Transactions of the ASME®

Technical Editor
ARTHUR J. WENNERSTROM
Senior Associate Editor
G. K. SEROVY
Associate Editors
Advanced Energy Systems
S. I. FREEDMAN
Environmental Control
H. E. HESKETH
Fuels and Combustion Technologies
R. E. BARRETT
Gas Turbine
S. KUO
Internal Combustion Engine
K. J. SPRINGER
Nuclear Engineering
S. M. CHO
Power
R. W. PORTER

BOARD ON COMMUNICATIONS
Chairman and Vice-President
K. N. REID, JR.

Members-at-Large
J. T. COKONIS
M. FRANKE
M. KUTZ
F. LANDIS
J. R. LLOYD
T. C. MIN
R. E. NICKELL
R. E. REDER
R. ROCKE
F. W. SCHMIDT
W. O. WINER

President, **R. ROSENBERG**
Executive Director,
D. L. BELDEN
Treasurer, **ROBERT A. BENNETT**

PUBLISHING STAFF
Mng. Dir., Publ., **J. J. FREY**
Dep. Mng. Dir., Pub.,
JOS. SANSONE
Managing Editor,
CORNELIA MONAHAN
Sr. Production Editor,
VALERIE WINTERS
Editorial Prod. Asst.,
MARISOL ANDINO

Transactions of the ASME, Journal of Turbomachinery (ISSN 0889-504X) is published quarterly (Jan., Apr., July, Oct.) for $95 per year by The American Society of Mechanical Engineers, 345 East 47th Street, New York, NY 10017. Second-class postage paid at New York, NY and additional mailing offices. POSTMASTER: Send address change to The Journal of Turbomachinery, c/o The AMERICAN SOCIETY OF MECHANICAL ENGINEERS, 22 Law Drive, Box 2300, Fairfield, NJ *07007-2300.*"

CHANGES OF ADDRESS must be received at Society headquarters seven weeks before they are to be effective. Please send old label and new address.

PRICES: To members, $27.00, annually; to nonmembers, $95.00.

Add $12.00 for postage to countries outside the United States and Canada.

STATEMENT from By-Laws. The Society shall not be responsible for statements or opinions advanced in papers or ... printed in its publications (B 7.1, para. 3).

COPYRIGHT © **1987** by the American Society of Mechanical Engineers. Reprints from this publication may be made on condition that full credit be given the *TRANSACTIONS OF THE ASME—JOURNAL OF* TURBOMACHINERY, and the author, and date of publication be stated.

INDEXED by Engineering Information

Journal of Turbomachinery

Published Quarterly by The American Society of Mechanical Engineers

VOLUME 109 • NUMBER 4 • OCTOBER 1987

TECHNICAL PAPERS

ANNOUNCEMENTS

Downloaded 01 Jun 2010 to 171.66.16.52. Redistribution subject to ASME license or copyright; see http://www.asme.org/terms/Terms_Use.cfm

D. C. Wisler
Manager, Turbomachinery Research,
Aircraft Engine Business Group,
General Electric Company,
Cincinnati, OH 45215
Mem. ASME

R. C. Bauer
Research Engineer,
General Electric Company,
Mem. ASME

T. H. Okiishi
Professor,
Department of Mechanical Engineering,
Iowa State University,
Ames, IA 50011
Mem. ASME

Secondary Flow, Turbulent Diffusion, and Mixing in Axial-Flow Compressors

The relative importance of convection by secondary flows and diffusion by turbulence as mechanisms responsible for mixing in multistage, axial-flow compressors has been investigated by using the ethylene tracer-gas technique and hot-wire anemometry. The tests were conducted at two loading levels in a large, low-speed, four-stage compressor. The experimental results show that considerable cross-passage and spanwise fluid motion can occur and that both secondary flow and turbulent diffusion can play important roles in the mixing process, depending upon location in the compressor and loading level. In the so-called freestream region, turbulent diffusion appeared to be the dominant mixing mechanism. However, near the endwalls and along airfoil surfaces at both loading levels, the convective effects from secondary flow were of the same order of magnitude as, and in some cases greater than, the diffusive effects from turbulence. Calculations of the secondary flowfield and mixing coefficients support the experimental findings.

1.0 Introduction

The importance of incorporating the effects of mixing into flowfield calculations for multistage, axial-flow compressors has become increasingly apparent, particularly in light of the trend toward higher stage loadings and lower aspect ratios. Such compressors tend to have more of their endwall flows affecting a larger fraction of the total flow, with the consequence that secondary flow, turbulence, and mixing require more careful evaluation. Much important work has been done in this area over the years [1-13]. Recently however, two differing analytical procedures for modeling the mixing in compressors have received a great deal of attention, and a short discussion of their main features is relevant to this paper.

Adkins and Smith [1] have put forward the concept that secondary flows are primarily responsible for both the spanwise mixing of flow properties and the deviation of blade row turnings from two-dimensional cascade theory. Their analysis is based upon inviscid, small-perturbation, secondary flow theory. They model spanwise mixing as a diffusion process, determining local values of the mixing coefficient from calculated secondary radial velocities. They also calculate secondary cross-passage velocities to use in estimating induced blade row under/overturning. Their model includes the effects of mainstream nonfree vortex flow, endwall boundary layers, blade end clearances, blade end shrouding, and blade boundary layer and wake centrifugation. It does not incorporate any effects of turbulent diffusion. The results of the application of their mixing theory in through-flow calculations were impressive.

Gallimore and Cumpsty [2], on the other hand, conclude that a random, turbulent type of diffusion process is the dominant mechanism of spanwise mixing and that the physical model of spanwise mixing based on deterministic, radial secondary flows is "inaccurate" [2] and "invalid" [3]. They conclude this from the results of their own experiments using two different, multistage, axial-flow compressors in which they found comparatively insignificant convection by secondary flows. They developed a simple, approximate method for estimating the value of the spanwise mixing coefficient in terms of stage geometry, loss and flow coefficient. They used this method, which does not include any effects of secondary flow, to incorporate spanwise mixing into through-flow calculations. Their results of modeling the flow for two other research compressors [3] were likewise impressive.

Our paper documents experimental work and analysis which show that facets of both mixing models are important and should be incorporated into through-flow calculations for multistage, axial-flow compressors.

2.0 Objectives

There were two primary objectives of this work. The first was to determine experimentally the relative importance of convection by secondary flows and diffusion by turbulence as mechanisms for mixing in multistage, axial-flow compressors. The second was to evaluate analytical models describing the flowfield, make comparisons with the experimental results, and recommend the most appropriate mixing model.

The following definitions will be helpful. Primary flow is defined as the two-dimensional cascade flow that would be predicted by a potential flow, blade-to-blade analysis. Secondary flow is defined as any flow that departs from the

---

Contributed by the Gas Turbine Division of The American Society of Mechanical Engineers and presented at the 32nd International Gas Turbine Conference and Exhibit, Anaheim, California, May 31-June 4, 1987. Manuscript received at ASME Headquarters February 3, 1987. Paper No. 87-GT-16.

Copyright © 1987 by ASME

Downloaded 01 Jun 2010 to 171.66.16.57. Redistribution subject to ASME license or copyright; see http://www.asme.org/terms/Terms_Use.cfm

primary flow. This, by definition, includes boundary layer skew.

3.0 Technical Approach

The overall technical approach used to achieve the objectives described earlier is presented.

3.1 Experimental Program. A test program was set up in the General Electric Low-Speed Research Compressor (LSRC) to measure secondary flowfields and diffusion rates in an imbedded stage of a multistage compressor. It was of prime importance to conduct the tests not only with good-quality blading, representative of current compressor design practice, but also in a facility large enough to make detailed measurements.

The ethylene tracer-gas technique and three-dimensional, slanted-hot-wire anemometry were used to measure secondary flows, fluid migration, diffusion rates, velocities and turbulence intensities for two loading levels. From these measurements the relative importance of secondary flows and turbulent diffusion in the mixing process could be determined.

3.2 Analytical Program. A thorough data-match analysis was conducted for the test compressor. The secondary flowfield was computed from the Adkins-Smith model and compared to the measurements. Mixing coefficients, based on both the Adkins-Smith model and the Gallimore-Cumpsty model, were also computed and compared with measurements. Recommendations for improvements to both models are made.

4.0 Test Vehicle and Apparatus

4.1 Low-Speed Research Compressor (LSRC). The LSRC is an experimental facility that duplicates the essential features of a small, high-speed-compressor flowfield in a large, low-speed machine where very detailed investigations of the flow can be made. The facility, which has a constant casing diameter of 1.524 m (60.0 in.), is described in [14]. The compressor was set up with four identical stages in order to simulate the repeating stage environment. The third stage was the test stage.

Table 1 Pitchline blading parameters

	Rotor		Stator	
Solidity	1.11		1.32	
Aspect Ratio	1.25		1.45	
Chord, cm (in)	9.12	(3.59)	7.90	(3.11)
Stagger, Deg.	49.05		20.27	
Camber, Deg.	32.32		53.39	
No. of Airfoils	54		74	
Axial Spacing, cm (in.)	2.79	(1.10)		

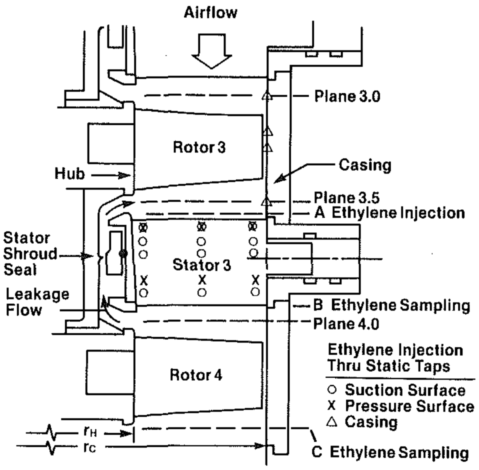

Fig. 1 Cross section of compressor test stage

Blading. Typical of modern designs, the compressor had high-hub/tip-ratio, low-aspect-ratio, high-solidity blading with shrouded stators and inlet guide vanes. The blading was a low-speed, aerodynamic model of stages 4–9 of a highly loaded, high-reaction, nine-stage HP compressor. A cross section showing the geometry of the test stage is given in Fig. 1 and blading details are given in Table 1.

Nomenclature

a = passage width at blade exit
C = percent circumferential stator pitch
c = chord
F = fraction of peak ethylene concentration
G = concentration of spreading ethylene gas
h = annulus height
I = percent radial immersion
IP = radial immersion for ethylene injection
L = normalizing length
L_s = axial stage length
l = stator shroud-seal-tooth clearance
m = mean flow direction in ethylene diffusion equation or mass flow
n = distance normal to axisymmetric stream surface of the main flowfield
P = pressure
$\bar{P}$ = fluid property subject to mixing

PS = pressure surface
q = dynamic head
SS = suction surface
R = $\sqrt{r^2+m^2}$
r = radial distance or spread of ethylene in plane perpendicular to mean flow direction
S = volume flow rate
TE = trailing edge
TI = turbulence intensity
T = measured torque minus tare torque
t = maximum airfoil thickness or phase lock increment
U = wheel speed
V = velocity
v' = random unsteadiness velocity
x = distance normal to primary flow streamline and normal to n direction
Z = axial coordinate
ϵ = mixing coefficient
η = efficiency = ψ'/ψ
ρ = density

ϕ = flow coefficient = $\dot{m}/\rho A U_t$
ψ' = pressure coefficient = $[\Delta P/1/2\rho U_T^2] \times$

$$\left[1-\frac{1}{2\gamma}\left(\frac{\Delta P}{P_1}\right) + \left(\frac{\gamma+1}{6\gamma^2}\right)\left(\frac{\Delta P}{P_1}\right)^2 + \ldots\right]$$

ψ = work coefficient = $T/(1/2\rho U_T^2\phi)$
ω = loss coefficient

Subscripts

C = casing
H = hub
i = instantaneous value
m = mean direction
r = radial
ref = reference
S = static conditions
t = tip
T = total conditions
z = axial
θ = circumferential

Downloaded 01 Jun 2010 to 171.66.16.57. Redistribution subject to ASME license or copyright; see http://www.asme.org/terms/Terms_Use.cfm

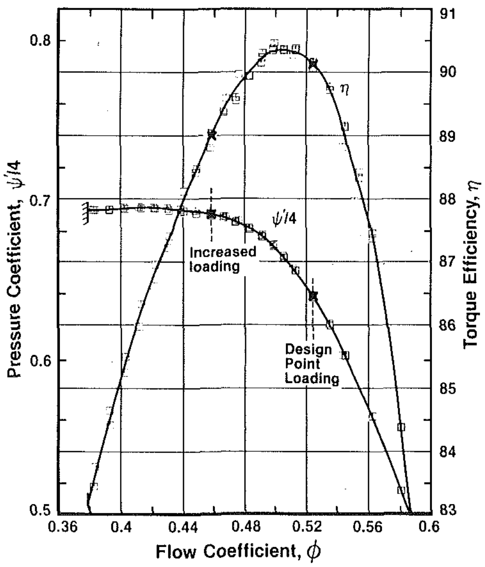

Fig. 2 Overall performance of test compressor

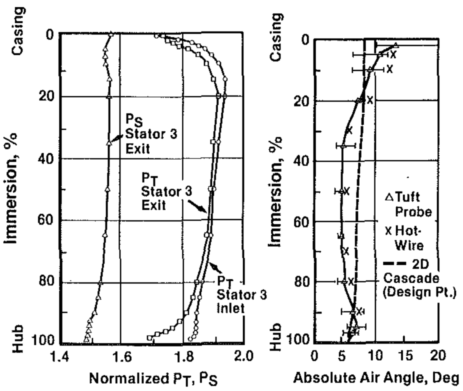

a) Design Point

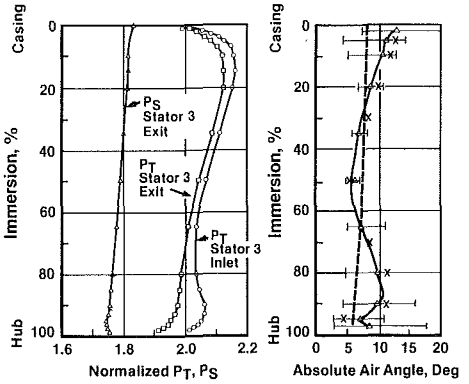

b) Increased Loading

Fig. 3 Radial variation of total pressure, static pressure, and stator exit air angle at (a) design point loading and (b) increased loading, pressure normalized by ½ ρU_T^2

Performance. Overall performance, shown as a four-stage average in Fig. 2, is based on measured airflow, measured work input (torque and speed), and measured pressure rise. Flow coefficient and pressure coefficient are accurate to within ±0.15 percent and efficiency is accurate to within ±0.15 point. Tests were conducted at the two loading levels shown in the figure. For the design-point loading, the flow coefficient was 0.525, the pressure coefficient was 0.639, and the efficiency was 90.2 percent. At increased loading these values were 0.458, 0.690, and 89.0 percent, respectively. Peformance data were obtained at 850 rpm. The ethylene and hot-wire studies were conducted at a reduced value of 600 rpm so that noise levels would be more tolerable for the researcher who spent over 250 hr making measurements very near the compressor casing. Tests showed that the difference in Reynolds numbers did not affect vector diagram quantities and consequently should not affect the conclusions of the work. Data were normalized by blade tip speed for comparisons.

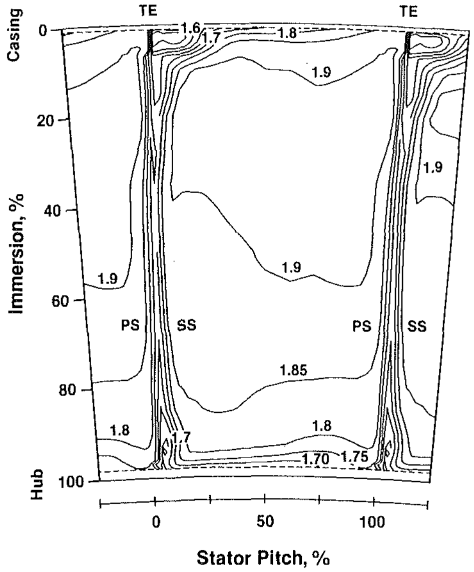

a) Design Point

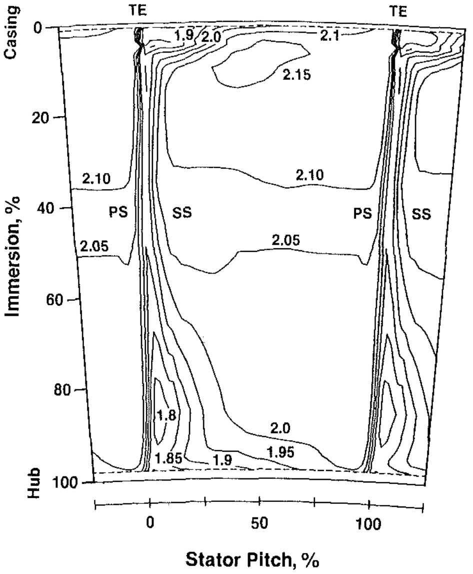

b) Increased Loading

Fig. 4 Contours of constant normalized total pressure at the Stator 3 exit (plane 4.0), $(P_T - P_{ref})/\frac{1}{2}\rho_{ref}U_T^2$

Detailed performance for Stator 3 is shown in Figs. 3 and 4. The measurements were made using single-element, traversing, total and static pressure probes, boundary layer probes, and flow angle probes. The results were circumferentially averaged. At the design point (Fig. 3*a*) the midpassage losses are typically lower, with increasing loss near the endwalls. The flow is generally well-behaved and the wakes, inferred from Fig. 4(*a*), are relatively thin across the span with no regions of large blockage. At increased loading (Fig. 3*b*) loss has increased and a more tip-strong radial distribution of total pressure has developed. A substantial thickening of the vane wakes from 60–100 percent immersion, with associated increased blockage, is evident in Fig. 4(*b*).

Downloaded 01 Jun 2010 to 171.66.16.57. Redistribution subject to ASME license or copyright; see http://www.asme.org/terms/Terms_Use.cfm

4.2 Ethylene Tracer-Gas Technique. The tracer-gas technique is well established, having been used successfully by others [2, 12, 13]. It involves introducing trace amounts of a nonreacting gas at some point in the flow and then sensing spatially varying concentrations of the entrained contaminant in a downstream sample plane. For these studies, ethylene was used as the tracer because it has nearly the same molecular weight as air and is therefore neutrally buoyant. Ethylene was injected into the flow using a crooked **L**-shaped injection probe similar to that used by Gallimore [2], whose tests showed minimum probe effects. Ethylene was also injected through casing and vane-surface static pressure taps. Injection rates were held constant at 80 cc/min through the probe and 60 cc/min through static taps. Increased rates of 120 cc/min and decreased rates of 30 cc/min showed no change in measured contour shape. Injection and sampling planes are shown in Fig. 1. Details of the system are given in [15].

Downstream sampling was done with a small, single-element total pressure probe. Ethylene concentration was determined by passing the sample through a flame ionization detector capable of sensing concentrations as low as 3–5 ppm.

4.3 Hot-Wire Anemometry System. Measurements of flow velocity (V_z, V_θ, V_r) and turbulence intensity were made at the inlet and exit of the third stator using a 45 deg, slanted-hot-wire anemometer system. The output of the anemometer was fed into a Kinetic Systems analog-to-digital converter running at a digitizing rate of 50 kHz. The data were taken using the phase-lock-average technique [16] which provided both the periodic and random unsteadiness. One-per-blade triggering was supplied by a pulse generator responding to a one-per-rev pulse from the compressor. Data were taken for the same two consecutive rotor blade passages, with each passage divided into 100 phase-lock increments. The hot wire was accurately calibrated in a nozzle flow.

The three-dimensional flow velocities were obtained at each measurement position as follows. Three angular orientations of the hot wire were selected to resolve the velocity vector. For each orientation, 300 revolutions of voltage data were taken and averaged. The velocity was obtained from these three average values by solving the appropriate hybrid, nonlinear equations given by Powell [17]. This was done for each of the 100 phase-lock increments.

Turbulence intensities were obtained as follows: For each of the 100 phase-lock rotor positions, instead of computing the average for the 300 sets of data, each of the individual sets was reduced to obtain instantaneous velocities V_i. Random unsteadiness velocities and turbulence intensities were then computed from equations (1)–(4). This method provides a very repeatable, time-averaged measure of relative turbulence level, even though velocity components were not measured simultaneously. The tight axial gaps did not allow fully three-dimensional probes to be used. Although data were also taken using the 12-orientation method of [11], they are not being reported until sign uncertainties in Reynolds stress terms are resolved.

$$\bar{V}(t) = \frac{\sum_{i=1}^{300} V_i(t)}{300} \qquad t = 1{,}100 \tag{1}$$

$$v'_{i_a}(t) = \bar{V}_a(t) - V_{i_a}(t) \qquad a = r, \theta, z \tag{2}$$

$$\bar{v}'(t) = \left[\frac{1}{3} \, \frac{\sum_{i=1}^{300} \left[v'^2_{i_r}(t) + v'^2_{i_\theta}(t) + v'^2_{i_z}(t) \right]}{300} \right]^{1/2} \tag{3}$$

$$TI = \frac{\bar{v}'(t)}{\bar{V}(t)} \times 100 \tag{4}$$

5.0 Ethylene Tracer-Gas Measurements

5.1 Technique for Interpreting Ethylene Contours. The ethylene tracer-gas results are presented as lines of constant ethylene concentration. To aid in understanding these results, the techniques for relating ethylene motion and contour shape to fluid motion are briefly discussed. The word "core" will refer to the region of peak ethylene concentration and the word "contour" will refer to all of the isoconcentration lines surrounding the core.

Core Migration. The movement of the core relative to its injection location results from a response to pressure gradients as the ethylene becomes entrained in the flow. Thus the core will move under the combined effects of primary and secondary flows.

Symmetric Contours. An ethylene contour that displays nearly circular or symmetric spreading with respect to the core axis results primarily from diffusion driven by nearly isotropic turbulence [18, 19]. In this case, the tracer-gas contours represent the time-averaged effects of the turbulence.

Distorted Contours. A distorted or skewed ethylene contour that exhibits marked elongation in one or more directions can result from secondary flows, gradients in either velocity and/or turbulence intensity in the flow, or all three. In turbine component flow Denton and Usui [12] and Moore and Smith [13] have observed stretched contours that were a result of secondary flows. Skewed contours have also been found in experiments carried out by Skramstad [20] in a turbulent boundary layer and by Hinze and Van der Hegge Zijnen [21] in the turbulent mixing zone of a planar free jet. In both cases, a thin, heated wire produced the contaminant. Their results showed skewness in the direction of greater mean velocity. Townsend [22] states that skewed distributions are typical in flows having strong gradients of turbulence intensity. Corrsin and Uberoi [23] postulated that the slightly skewed distributions they found in a turbulent round jet were due to a lateral turbulence gradient. Consequently, care must be exercised in deciding which of these causes produces contour distortion in the compressor. Transit times associated with mean fluid motion and turbulence levels are considered in making this evaluation.

5.2 Injection Upstream of Stator. Ethylene was injected upstream of the stator at Plane A shown in Fig. 1. Sampling was done in the downstream Plane B and the results are presented in Figs. 5 and 6. In these figures, the upstream injection positions are marked in the downstream plane with an X and the core positions of the contours found by sampling are marked with an O. Each injection-sampling pair is numbered. For example in Fig. 5(*b*), Core 9 was injected at 50 percent radial immersion and 53 percent stator pitch at Plane A. Its core was found at 50 percent immersion and 43 percent pitch in the sampling Plane B. Selected isoconcentration contours are shown for only some of the cores.

The core positions found in the downstream plane are connected with a line. Since the upstream injection was along a radial line at specific immersions, any distortion of this line in the downstream plane reveals important cross passage and radial features of the flow. This is the principal message in Fig. 5. The shapes and spacings of the contours reveal the magnitudes of secondary flows and turbulent diffusion in the stator passage. This is the main message in Fig. 6.

Evidence of Secondary Flow in Core Migration. The evidence for the existence of substantial secondary flow is found in core migration at both loading levels.

Core migration at the design point loading can be seen in Fig. 5(*a*), especially for the 53 percent pitch injection line. Near the casing from 0–20 percent immersion (Cores 1–7),

Downloaded 01 Jun 2010 to 171.66.16.57. Redistribution subject to ASME license or copyright; see http://www.asme.org/terms/Terms_Use.cfm

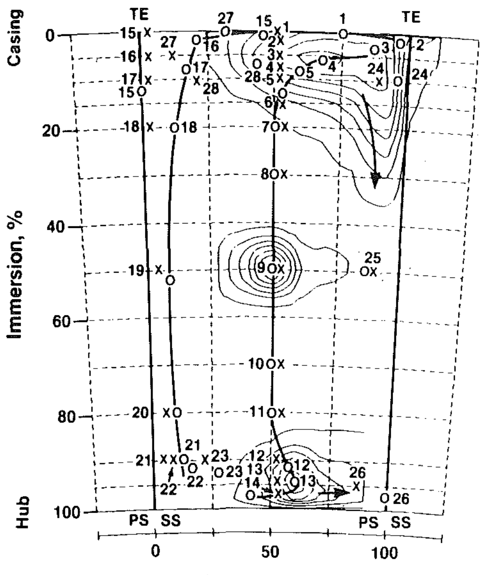

a) Design Point

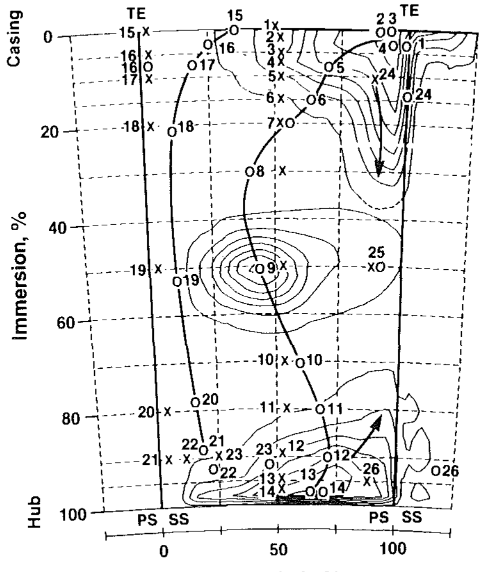

b) Increased Loading

Fig. 5 Ethylene core migration for two loading levels: (*a*) design point and (*b*) increased loading; injection upstream of Stator 3 at position X, sampling downstream of Stator 3 with core location at O; selected contours of min = 5 percent, max = 95 percent, delta = 15 percent

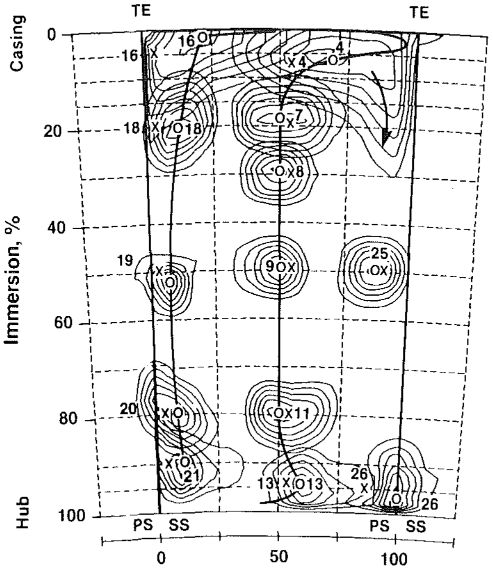

a) Design Point

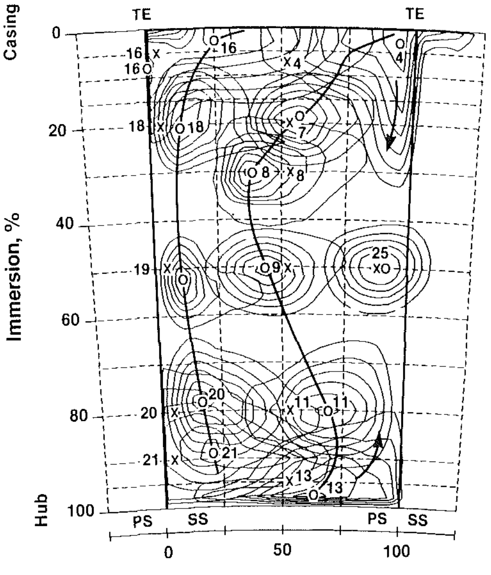

b) Increased Loading

Fig. 6 Ethylene contour spreading for two loading levels: (*a*) design point and (*b*) increased loading; injection upstream of Stator 3 at position X, sampling downstream of Stator 3 with core location at O, contours of min = 20 percent, max = 95 percent, delta = 15 percent

there is significant underturning as the cores are swept toward the pressure surface, revealing substantial cross-passage flow. There is also some radially outward flow toward the casing. For example, Core 3, which started at 53 percent pitch, has ended up at 80 percent pitch and closer to the casing. In the midpassage region from 20-80 percent immersion (Cores 7-11), there is a small amount of overturning as the core locations, which remain along a radial line, move slightly toward the suction surface. However, there is no radial motion in this region. Near the hub from 80-100 percent immersion (Cores 11-14), underturning first occurs as the cores move toward the pressure surface, although the effects are not so dramatic as those near the casing. Very near the hub at 97 percent immersion, Core 14 shows a marked overturning, probably resulting from the secondary flow effects of stator shroud leakage.

For the other design-point injection line at 3 percent pitch (Cores 15-21), suction surface boundary layer growth displaces the cores toward the pressure surface of the adjacent vane. Cores 15-17 and additional injection Cores 27 and 28 also show evidence of substantial underturning. The motion of Core 15 is particularly significant as the core splits into two regions of equal peak concentration. One peak moves circumferentially about 47 percent stator pitch and the other peak moves radially inward along the airfoil surface from 0 to 12 percent immersion. Cores 16, 27, and 28 show significant radially outward flow.

Core migration at increased loading is more dramatic, as seen in Fig. 5(*b*). Substantial underturning in the endwalls and overturning in the midstream was observed, with similar descriptive features, albeit enhanced, as discussed for design point operation. Near the casing, for example, Core 3 has moved from 53 to 93 percent pitch and from 5 to 0 percent immersion, showing a significant amount of cross-passage and radially outward spanwise flow. The motion of Core 24 is noteworthy. The core originates at 10 percent immersion, 87 percent pitch and moves to 14 percent immersion, 100 percent

Downloaded 01 Jun 2010 to 171.66.16.57. Redistribution subject to ASME license or copyright; see http://www.asme.org/terms/Terms_Use.cfm

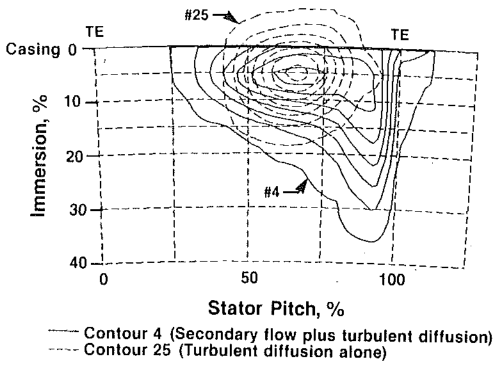

Fig. 7 Comparison of ethylene Contour 4 of Fig. 6(*a*) with Contour 25 of Fig. 6(*b*): Both contours have same turbulence intensity

pitch, giving evidence of secondary flow movement toward the pressure surface and radially inward along the stator vane.

Measurements of stator surface static pressure and wake thickness for increased loading, inferred from Fig. 4(*b*), show a thickened wake and increased blockage from 60–100 percent immersion, being most pronounced at 85 percent immersion. The ethylene contours respond to this increased blockage and the inlet skew as Cores 10–13 in Fig. 5(*b*) underturn and move toward the pressure surface. Flow adjustment in the midstream has occurred as the location of peak axial velocity shifts from 40–60 percent immersion at the design point to 15–30 percent immersion at increased loading. The motion implied by the other cores is evident in the figure.

Importantly, cross-passage motion occurs at both loading levels *all along the span, but spanwise motion occurs only near* the endwalls and vane edges. There is almost no radial movement of the cores from 20–80 percent immersion.

Evidence of Turbulent Diffusion. Substantial evidence for the existence of turbulent diffusion occurs at both loading levels.

At the design point in Fig. 6(*a*), the spread of ethylene in a nearly circular manner from 20–80 percent immersion is strong evidence of only turbulent diffusion in this region. However, near the endwalls, although increased turbulent diffusion is present, another mechanism is apparently acting to distort the contour shapes. This will be discussed in the next section.

At increased loading in Fig. 6(*b*), a marked increase in the level of turbulent diffusion occurs from 20–100 percent immersion. An increase of the distortion of the contours in the endwalls, particularly in the hub region, also occurs, again indicating the presence of an additional mechanism.

The data of Fig. 6 suggest a spanwise gradient of turbulent mixing at design point operation and a more uniform distribution at increased loading.

Evidence of Secondary Flow in Distorted Contours. There is significant distortion of the ethylene contours in the endwall regions at both loading levels in Figs. 5 and 6. The following evidence suggests that these distorted contours result from gradients in velocity due to secondary flow rather than from gradients in turbulence intensity. First, as suggested by data in Fig. 6(*b*) and confirmed by hot-wire data to be shown later, turbulence intensities at increased loading are nearly uniform from 0 to 80 percent immersion, indicating small gradients; yet, large distortions in the ethylene contours are apparent near the casing. Secondly, the motion of Cores 3, 13, and 24 in Fig. 5(*b*) indicates strong secondary flow. Thirdly, using measured average unsteadiness velocities to be shown later, one can infer that the fluid-particle transit times for flow across the stator are not nearly long enough to account for fluid motion from the core to the outermost portion of the distorted contour, if that motion resulted only from random unsteadiness.

Contour 4, at both loading levels near the casing in Figs. 5 and 6, shows significant cross-passage and radial motion as all segments of the contour stretch along the casing and bend and stretch along the pressure surface of the stator vane, indicating radially inward flow in the direction of the arrow. An estimate of the relative magnitudes of secondary flow and turbulent diffusion can be obtained by comparing Contour 25 at increased loading in Fig. 6(*b*) with Contour 4 at design point loading in Fig. 6(*a*). This comparison is made in Fig. 7. Both of these contours will be shown later to be influenced by nearly the same level of turbulence intensity. However, Contour 25 of Fig. 6(*b*) spreads by turbulent diffusion only and Contour 4 of Fig. 6(*a*) spreads by the combined effects of secondary flow and turbulent diffusion. It can be seen that turbulent diffusion accounts for only about 35–40 percent of the total spreading of the contour, the rest being attributed to secondary flow effects.

Contour 16, at both loading levels, confirms the strong crossflow toward the pressure surface near the casing. It also suggests radially inward flow along the suction surface of the vane.

Although near the casing only complete Contours 4 and 16 are presented in Fig. 6, all of the complete isoconcentration contours from 0–20 percent immersion (Contours 1–6, 15–17, 24, and 28) show this same secondary flow pattern, with the effect being quite intense from 0–10 percent immersion and diminishing by 20 percent immersion. Additional complete contours are presented in the appendix.

Near the hub, Contours 13 and 26 in Fig. 6(*a, b*) show cross-passage secondary flow toward the pressure surface and radially outward flow toward midstream, as indicated by the arrow. Very near the hub (96–100 percent immersion), Contour 13 in Fig. 6(*b*) shows cross-passage flow toward the suction surface with the Core showing radially inward flow. In the midstream, small pitchwise distortions of the contour shapes correlate with the previously described small tendency toward overturning.

Negative Loss Near Casing. The calculation of negative stator loss coefficients from measured data would, at first glance, imply a violation of the second law of thermodynamics, since the downstream total pressure would have to be higher than the upstream value in a vane row in which no work was input. However, negative loss coefficients for this stator are found near the casing as seen in the levels of total pressure from 0–4 percent immersion in Fig. 3(*a, b*). Similar findings are reported in [24]. One explanation is that secondary flows near the casing transport higher levels of total pressure radially outward as the flow proceeds through the vane row, thus raising the level of downstream total pressure very near the casing to a value higher than it would have otherwise been. This is exemplified by the radial motion of Core 3 from 5 to 0 percent immersion in Fig. 5(*b*).

5.3 Injection Through Static Pressure Taps on Stator Surfaces. Ethylene was injected into the boundary layer of the stator through static pressure taps at the positions shown in Fig. 1. Some of the concentration data acquired in the stator exit plane are displayed in Fig. 8 for nominal stator shroud-seal clearance and in Fig. 9 for increased clearance. All of the contours show the influence of turbulent diffusion, although the extent of the boundary layer tends to limit the size of the mixing zones. The contours near the endwalls also show the influence of secondary flow.

Nominal Leakage. Isoconcentration contours for 2.5 percent chord injection, nominal seal leakage, and design point operation are shown in Fig. 8(*a*). At 10 percent immersion, ethylene Core 29 is pressed tightly against the pressure surface

Downloaded 01 Jun 2010 to 171.66.16.57. Redistribution subject to ASME license or copyright; see http://www.asme.org/terms/Terms_Use.cfm

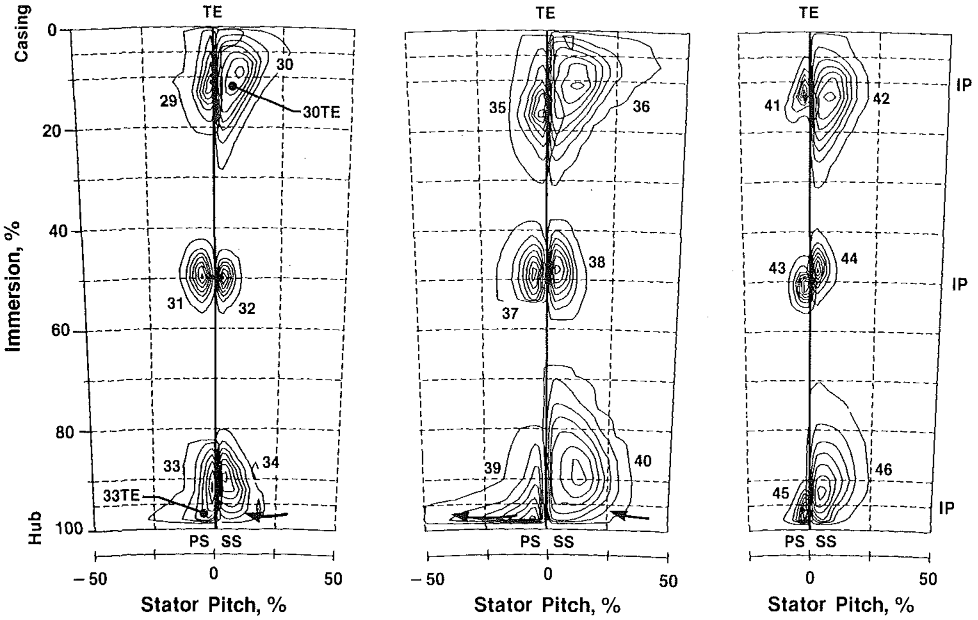

a) Design Point
2.5% chord injection

b) Increased loading
2.5% chord injection

c) Increased loading
70% c PS injection
80% c SS injection

Fig. 8 Ethylene contours for vane surface injection at 10, 50, and 95 percent radial immersion, sampling at vane trailing edge; *l/h* = 0.78 percent, contours of min = 5 percent, max = 95 percent, delta = 15 percent

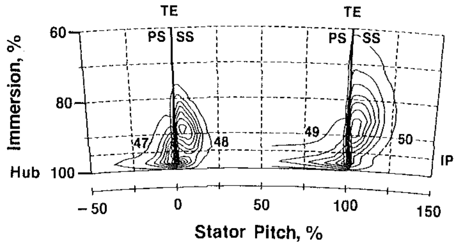

a) Design Point

b) Increased Loading

Fig. 9 Ethylene contours for vane surface injection at 95 percent immersion, increased stator shroud leakage, *l/h* = 1.56 percent; injection at 2.5 percent chord, sampling at vane trailing edge, contours of min = 5 percent, max = 95 percent, delta = 15 percent

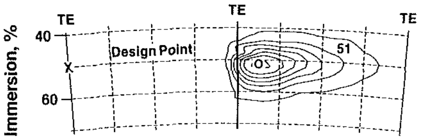

a) Spreading across Rotor 4, X = Stator 3 suction surface at 80% chord, O = downstream of Rotor 4 at Plane C

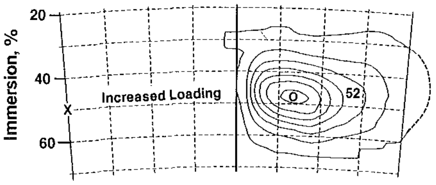

b) Spreading across Rotor 4, X = Stator 3 suction surface at 80% chord, O = downstream of Rotor 4 at Plane C

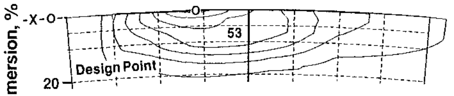

c) Spreading across Rotor 3, X = casing at 25% Rotor 3 chord, O = downstream of Rotor 3 at Plane 3.5

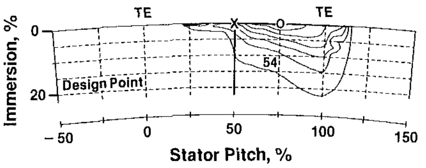

d) Spreading across Stator 3, X = casing upstream of Stator 3 at Plane 3.5, O = downstream of Stator 3 at Plane B

Fig. 10 Ethylene contour spreading showing enhancement of circumferential spreading and mixing by action of the rotor, X = injection location, O = sampling plane (ref. Fig. 1)

in response to the cross-passage flow seen in Fig. 5(*a*), while Core 30 shifts away from the suction surface probably in response to a thickened boundary layer and underturning. Furthermore, the stretching of Contours 29 and 30 along the vane surface suggests radially inward secondary flow, while the stretching of Contour 30 near the casing wall reflects cross-passage motion and underturning. At midspan, the nearly symmetric spreading of Contours 31 and 32 and the absence of core shifts suggest turbulent diffusion and no secondary flow. Near the hub, Cores 33 and 34 shift radially outward as they travel along both sides of the vane, probably in response to a thickening of the hub wall boundary layer and, for Core 34, the effects of overturning very near the hub. This overturning is seen in the stretching of Contour 33 toward the suction surface very near the hub. All of these trends are consistent with those discussed previously for Figs. 5(*a*) and 6(*a*). For near trailing edge injection, both Cores 30TE and 33TE in Fig. 8(*a*) show radially inward flow.

At increased loading, several effects are amplified as secondary flows increase. For 2.5 percent chord injection near the casing (Fig. 8*b*), the dramatic, radially inward shift of Core 35 from 10 to 17 percent immersion and the radially inward stretching of Contour 36 near the vane suction surface suggest strong inward secondary flows. Near the wall, cross-passage stretching of Contour 36 also suggests underturning. The midspan Core 38 moves radially out, probably in response to the thickened vane boundary layer from 60–100 percent immersion seen in Fig. 4(*b*). Near the hub, Core 39 shifts radially inward in response to stronger secondary flows along the vane

Downloaded 01 Jun 2010 to 171.66.16.57. Redistribution subject to ASME license or copyright; see http://www.asme.org/terms/Terms_Use.cfm

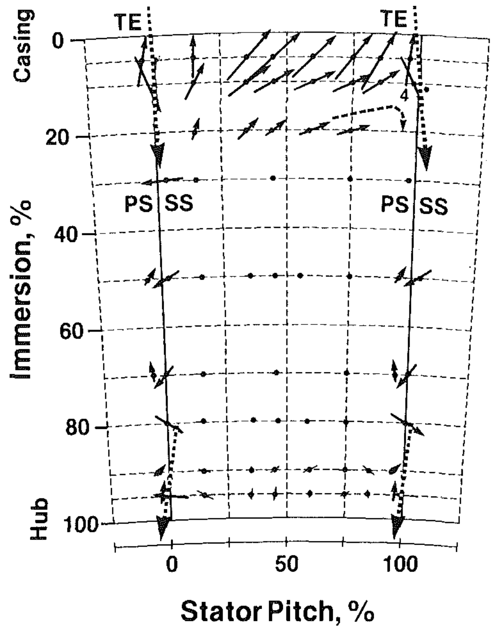

a) Design Point

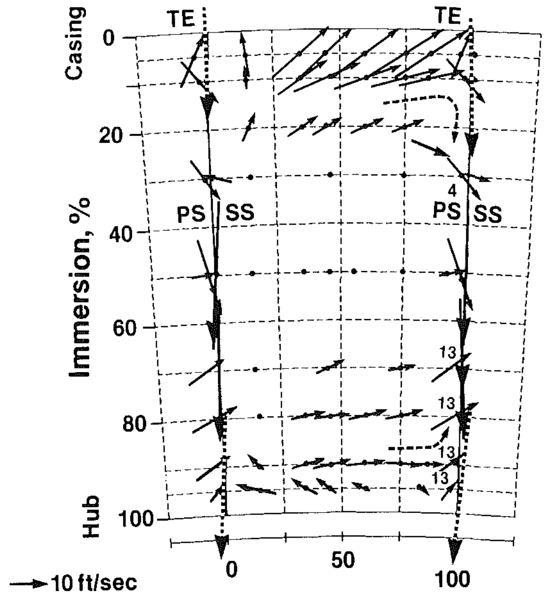

b) Increased Loading

Fig. 11 Secondary flow velocity vectors from hot-wire measurements at Stator 3 exit (plane 4.0)

edges. The core and contours are also pushed toward the pressure surface as a result of the blockage and increased cross-passage flow seen in Fig. 5(*b*). Very near the hub, pressure surface Contour 39 shows strong overturning in the direction of the arrow. On the suction surface, Core 40 moves significantly further from the vane surface than Core 34 did, in response to the much thicker boundary layer and wake. It also moves radially out, probably because of the effects of overturning very near the hub.

For near-trailing-edge injection at increased loading, Fig. 8(*c*), radially inward flow is seen for all pressure surface Cores 41, 43, and 45 and suction surface Core 42. Cores 44 and 46 move radially out for the reasons described above.

Increased Leakage. Isoconcentration contours for increased stator-shroud-seal leakage are shown in Figs. 9(*a*, *b*) for the two loading levels. Comparing design-point Contour 47 on the pressure surface in Fig. 9(*a*) with contour 33 in Fig. 8(*a*) shows enhanced overturning very near the hub wall at increased leakage. A similar comparison of Contours 49 and 39 for increased loading also shows stronger overturning very near the hub. Note that Core 50 remains very close to the suction surface compared to Core 40 in Fig. 8(*b*), indicating that increased leakage relieves the thickened vane boundary layers found at nominal leakage.

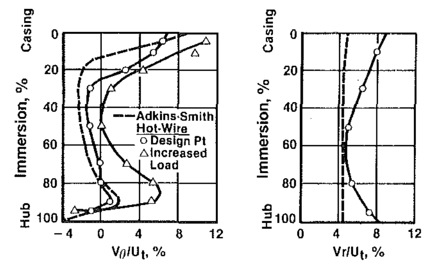

a) Average Circumferential Velocity at Stator 3 Exit

b) Maximum Radial Velocity in Rotor 3 Suction Surface Wake

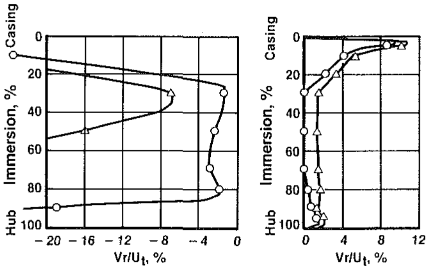

c) Peak Radial Velocity in Stator 3 Wake

d) Average Radial Velocity Outside Wake at Stator 3 Exit

Fig. 12 Secondary flow velocities shown as a percent of rotor tip speed, V_θ positive in direction of rotation, V_r positive radially outward toward casing

5.4 Injection Across the Rotor Passage. The action of the rotor in the mixing of the stator wake fluid was investigated by injecting ethylene through the suction surface static pressure tap of Stator 3 at 50 percent immersion and 80 percent chord and sampling downstream of rotor 4. The results are shown in Fig. 10(*a*, *b*) for the two loading levels. Note that Contour 52 in Fig. 10(*b*) results from the action of the rotor on Contour 44 in Fig. 8(*c*). Cores 51 and 52 and their contours remain distinguishable at the rotor exit, but the wake fluid is stretched and spread circumferentially across one stator passage with almost no radial shift of the core. Although the spanwise spreading appears to be greater for Contours 51 and 52 than it does for Contour 9 in Figs. 5(*a*, *b*), respectively, the diffusion rate is about the same. The difference appears because the axial distance from the injection point to the sampling plane is longer across the rotor, allowing more time for diffusion.

Apparently the low-momentum stator wake fluid and the endwall fluid, which were convected radially by secondary flow, are spread circumferentially across the passage by the action of the rotor. The spanwise mixing process is then completed by the action of turbulent diffusion. This whole process can take place without any radial shift of fluid cores in the midpassage region. Of course it is recognized that wakes can persist for many blade rows and it is not suggested that complete mixing occurs across one blade row.

Ethylene was also injected through casing static pressure taps upstream of the rotor and at 25 and 50 percent chord locations in the rotor passage, as seen in Fig. 1. A typical result for 25 percent chord injection, with sampling downstream of the stator, is shown in Fig. 10(*d*). The significantly increased circumferential sweeping caused by the rotor action compared to that of the stator is very apparent in

Downloaded 01 Jun 2010 to 171.66.16.57. Redistribution subject to ASME license or copyright; see http://www.asme.org/terms/Terms_Use.cfm

the figure. The radial spreading of the contours in Fig. 10(*c*) is also enhanced by the action of the tip clearance vortex.

5.5 Summary of Tracer Gas Results. The experimental results from the ethylene tracer gas studies show that considerable cross-passage and spanwise fluid motion can occur in a core compressor and that both secondary flow and turbulent diffusion can play important roles in the mixing process. In the midpassage region, turbulent diffusion appeared to be the dominant mixing mechanism. However, near the endwalls and along airfoil surfaces, the convective effects from secondary flow were of the same order of magnitude as, and in some cases greater than, the diffusive effects from turbulence. The evidence suggests that, in addition to being mixed by turbulent diffusion, the low-momentum fluid in the endwall is transported radially along the stator vane edges by secondary flow. The passing rotor then chops, turns, and transports this low-momentum fluid, spreading it circumferentially across the stator passage. The spanwise mixing process is then completed by turbulent diffusion.

The question arises, however, as to why some of these results differ from those of Gallimore and Cumpsty in which, having found comparatively insignificant spanwise convection by secondary flow in both of their Compressors A and B [2, 26], they conclude that the model of spanwise mixing by secondary flows is "inaccurate" [2] and"invalid" [3]. Several answers are possible. One is that, because the magnitude of secondary flow is configuration dependent, there was simply very little secondary flow in either Compressor A or B. However, further thought suggests additional possible answers. Compressor B, described in [26], had a very low peak efficiency of 76 percent, high endwall loadings, and untwisted blades. These features of this compressor would imply thick wakes and boundary layers which would generate high turbulent mixing that could dominate the flowfield. This is not typical of well-designed compressors operating at the design point. It should also be noted that the secondary flow model of Adkins and Smith was developed for design-point operation. Compressor A, described in [3, 26], is a different story. Although its efficiency of 86 percent is still somewhat low, its ethylene contours are different from those of Compressor B. In fact the contours from Compressor A show striking similarities to those of the present study, suggesting the presence of both secondary flow and turbulent diffusion in Compressor A. This can be seen by comparing the contours from the work of Gallimore and Cumpsty (Fig. 8 of [2]) with contours at similar locations from the present study (Contours 16, 9, 25, and 26 in Fig. 6*a* and Contour 54 in Fig. 10*d*). However additional data for Compressor A would be needed to give a definitive answer to the question asked above and determine whether contours showing strong secondary flow, like Contour 4 in Fig. 5(*a*) of the present study, are also present in Compressor A.

6.0 Hot-Wire Measurements

The three-dimensional measurements of the velocities upstream and downstream of the third stator were made using the hot-wire system described previously. Flow angles, shown in Fig. 3(*a, b*), and velocities compare favorably with values obtained from tuft probe and pressure measurements.

6.1 Secondary Flowfield. The secondary flowfield downstream of the stator was obtained from the three-dimensional hot-wire measurements by rotating these measurements onto a Trefftz-type plane, where the angle of rotation at each immersion was the two-dimensional cascade air angle obtained from a potential flow analysis. The results are shown in Figs. 11 and 12 for the two loading levels. The primary cascade flow at each measuring location appears as a dot in Fig. 11, indicating through-flow velocity coming out of the page toward the reader. The secondary flow appears as an arrow. The radially outward flow angles near the casing appear large in Fig. 11 because only secondary velocities are shown. Average radial flow angles, computed from the complete three-dimensional vectors are 8.4, 5.0, and 2.9 deg at 5, 10, and 20 percent immersion at the design point and 12.1, 6.0, and 3.9 deg at increased loading.

Design Point. At the design point in Figs. 11(*a*) and 12, cross-passage velocities toward the pressure surface and radial velocities toward the casing were found from 0–20 percent immersion. This is consistent with the core migration and underturning observed with the tracer gas near the casing in Fig. 5(*a*). At 10 percent immersion and 95 percent stator pitch, the arrow labeled "4" in Fig. 11(*a*) indicates radially inward flow consistent with the distorted Contour 4 in Fig. 5(*a*). In the vane wake, large, radially inward velocities were measured. However, because hot-wire orientation and calibration limits of the system were exceeded in this region, there are significant reservations about the magnitude of these wake velocities. Therefore they are "dotted" vectors in Fig. 11. The direction of the wake flow is correct and consistent with a mass flow balance in the casing region.

Elsewhere, a very small amount of overturning was seen at midspan and some underturning was seen at 90 percent immersion, but in general, these were small compared to those observed near the casing. No significant radial flow was found from 30–80 percent immersion, which is consistent with the results shown in Fig. 5(*a*).

Since phase-lock averaging was used, the velocities within the rotor suction-side wake could be determined. The radial components of these velocities, presented in Fig. 12(*b*), show radially outward flow of the order of 5–8 percent of the rotor tip speed at all spanwise locations, indicating rotor wake centrifugation.

Increased Loading. At increased loading in Figs. 11(*b*) and 12, the secondary-flow velocities increase, with higher cross-passage and radially outward velocities near the casing and large radially inward velocities in the vane wake. At 80 and 90 percent immersion, increased underturning is seen, but at 95 percent immersion overturning is present. Radial velocities in the midspan region were minimal except in the wake. This is consistent with the core motions shown in Fig. 5(*b*). Vectors labeled 4 and 13 in Fig. 11(*b*) are consistent with the distortion toward midspan of Contours 4 and 13 in Fig. 6(*b*).

6.2 Turbulence Intensity. Measurements of turbulence intensity in the endwall and midstream regions were made ahead of and behind Stator 3. The results for two adjacent rotor passages are presented in Fig. 13. Being phase-lock averaged, these measurements also show the variation in level of random unsteadiness as the rotor wakes pass fixed locations relative to the stator. For reference, the turbulence intensity of the flow entering the compressor ahead of the IGV's was 2.6 percent. Two different types of flowfields were observed depending on loading levels. The details are presented in the following.

Design Point. At the design-point loading in Fig. 13(*a, b*), a midstream region of lower turbulence intensity can be clearly distinguished from the endwall regions of higher intensities. Upstream at 50 percent immersion in Fig. 13(*a*), turbulence intensity levels of 5–6 percent over 90 percent of the blade passing time were measured, with levels increasing as the rotor wake passed. Downstream in Fig. 13(*b*), turbulence levels outside the wake at 50 percent immersion increased slightly, partly as a result of decreased mean velocity levels.

The turbulence levels described above for the midstream are easily distinguished from the levels in the endwalls, particularly in the downstream plane, Fig. 13(*b*). In the endwalls, turbulence levels increased to 18–22 percent over the blade pass-

Downloaded 01 Jun 2010 to 171.66.16.57. Redistribution subject to ASME license or copyright; see http://www.asme.org/terms/Terms_Use.cfm

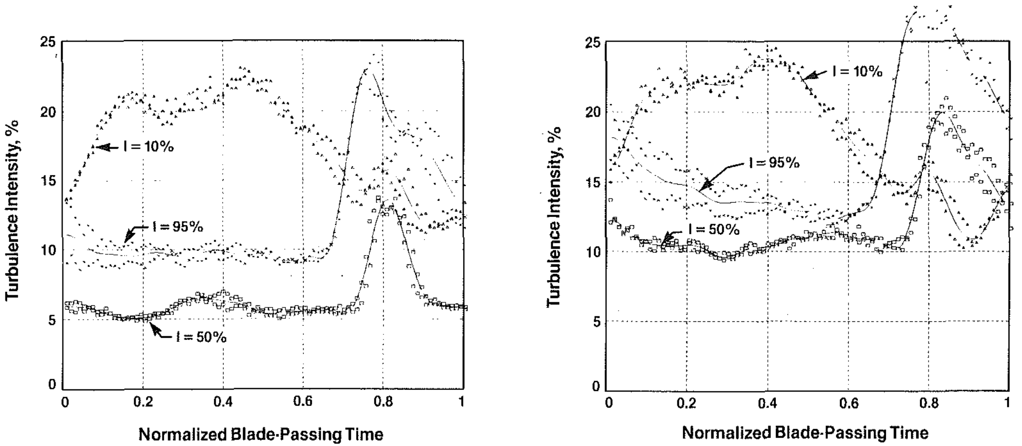

a) Design Point, Upstream of Stator 3, C = 50%

c) Increased Loading, Upstream of Stator 3, C = 50%

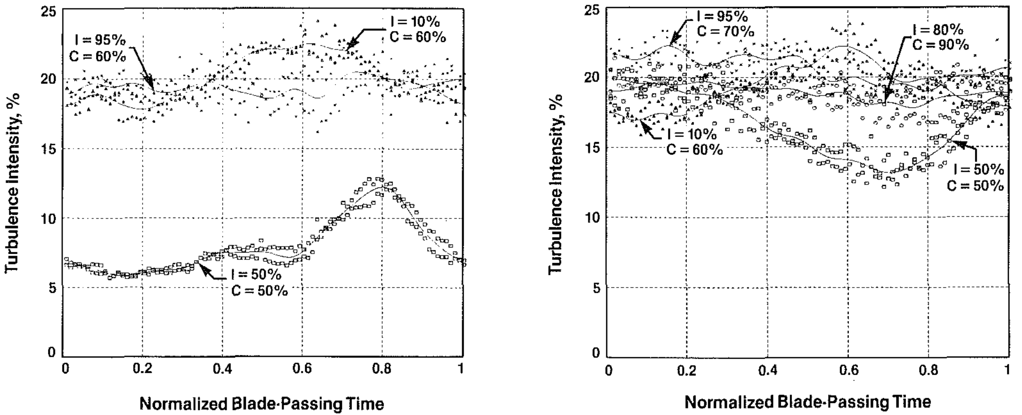

b) Design Point, Downstream of Stator 3

d) Increased Loading, Downstream of Stator 3

Fig. 13 Phase-lock averaged, turbulence intensity measurements for Stator 3, *I* is percent immersion, *C* is percent stator pitch

Table 2 Average random unsteadiness velocities at the Stator 3 exit plane shown as percent of rotor tip speed

A. Design Point

Imm	C	v'_z	v'_θ	v'_r
5	60	10.9	11.9	10.9
10	90	9.7	9.7	9.5
20	90	8.2	7.8	9.4
50	50	3.9	3.9	4.4
90	90	6.0	5.8	6.4
95	60	8.7	7.9	9.7

B. Increased Loading

Imm	C	v'_z	v'_θ	v'_r
10	60	8.2	8.2	7.8
10	90	9.4	8.8	9.4
25	90	7.8	7.5	8.9
50	50	6.9	7.1	7.6
80	80	6.0	8.1	8.5
95	70	8.4	7.6	10.4

Table 3 Ratio of turbulence levels for design-point Contour 4 to those for increased-loading Contour 25 (ref. Fig. 7)

%Immersion	5	7	10	10	16	20	25	Avg
% Circum	50	87	50	90	80	90	87	Value
Ratio	1.22	0.98	1.19	1.15	0.94	1.02	0.70	1.03

ing time. Near the casing, these higher levels are associated with tip clearance effects, endwall boundary layers, etc. Near the hub, there were no tip clearance effects since the stators were shrouded, but there were shroud leakage, rotor wake diffusion, endwall boundary layers and flow separation off of the shroud trailing edge (see Fig. 1). The intense rotor hub wake is clear in Fig. 13(*a*).

The average unsteadiness velocities (v'_z, v'_θ, and v'_r) are shown in Table 2(*A*). Interestingly, at each immersion and circumferential position, the average unsteadiness velocities are nearly equal, $v'_z \approx v'_\theta \approx v'_r$. This is indicative of nearly isotropic turbulence and explains why many of the contours in Figs. 5 and 6 are nearly circular. This also supports the conclusion that secondary flow, not turbulent diffusion, is primarily responsible for the contour distortions near the endwalls in Figs. 5 and 6. In the 2.7 ms it takes the fluid to travel across the stator, the fluid in the endwall region could diffuse radially and circumferentially about 1.25 cm (0.5 in.), based on the velocities in Table 2(*A*). This would account for only 35–40 percent of the spreading of Contour 4 in Fig. 5.

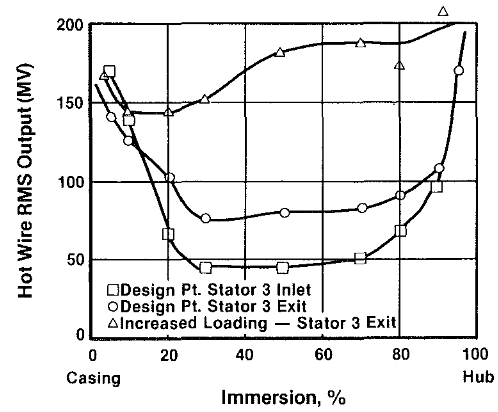

Fig. 14 Radial variation of total unsteadiness at Stator 3 exit

The spanwise and circumferential differences in levels of

Downloaded 01 Jun 2010 to 171.66.16.57. Redistribution subject to ASME license or copyright; see http://www.asme.org/terms/Terms_Use.cfm

Table 4 Spanwise secondary velocities from Adkins-Smith model. Velocities on pressure side of stator outside the wake shown as percent of rotor tip speed, Stator 3 exit, V_r positive radially out toward casing.

Imm	0	5	10	20	30	50	70	80	90	100
V_r	0	−4.3	−9.1	−10.3	−6.2	−1.3	2.5	4.1	3.3	0

random unsteadiness were also estimated qualitatively by using a single-element, straight hot-wire probe. This probe was rotated until maximum output was achieved. Figure 14 presents rms voltages, indicative of average unsteadiness velocities including rotor wakes. Clearly the region from 30–70 percent immersion is easily distinguished from the endwall region, thus giving merit, for engineering purposes, to the concept of a so-called circumferential average, free-stream region bounded by endwall boundary layers. These lower levels were observed at all circumferential locations except near the vane edges where the levels increased. This is in contrast to the results presented by Gallimore and Cumpsty in [2] but is consistent with the spanwide differences in the spread of ethylene contours in Fig. 6(*a*).

Increased Loading. At increased loading downstream of the stator in Fig. 13 (*d*), a more uniformly high level of turbulence intensity was observed across the whole span, as described in [2], with little distinction between the midstream and endwall regions. The uniformly high level of unsteadiness velocities all across the span is also shown qualitatively in Fig. 14. These findings are consistent with the contour spreads in Fig. 6(*b*) and indicate behavior similar to what was described by Gallimore and Cumpsty [2] as being typical of multistage, axial-flow compressors.

It will be recalled that the comparison in Fig. 7 provides an estimate of the relative contribution of secondary flow and turbulent diffusion in causing distortions in ethylene contours. This comparison relied on the fact that design-point Contour 4 of Fig. 6(*a*) was influenced by nearly the same average level of turbulence intensity as increased-loading Contour 25 in Fig. 6(*b*). Data to support this are shown in Table 3. In this table, turbulence levels covering the major expanse of Contour 4 are shown normalized by the levels at the location of Contour 25. The average ratio of 1.03 indicates the nearly equal levels of turbulence intensities for these two regions.

The same conclusion regarding the isotropic nature of the unsteadiness velocities ($v_z' \approx v_\theta' \approx v_r'$) can be drawn from Table 2(*B*) at increased loading as was drawn at the design point. In particular the unsteadiness velocities in the first three rows of Table 2(*B*) were taken at the radial and circumferential locations covering the major expanse of Contour 4 in Fig. 5(*b*). Their nearly equal levels support the conclusion that secondary flow, not turbulent diffusion, is primarily responsible for contour distortion.

6.3 Summary of Hot-Wire Results. The experimental results from the hot-wire measurements are consistent with the results of the tracer gas studies and show that a secondary flowfield with considerable cross-passage and spanwise fluid motion can occur in an HP compressor. Radially inward velocities were found along the vane edges which would transport the low-momentum fluid near the casing toward midspan. Radially outward velocities were found in the rotor wakes, indicating wake centrifugation. Also the spanwise distribution of the level of turbulence intensity depended upon loading. At the design point, the midstream unsteadiness level was distinctly lower than that near the endwalls. At increased loading, the unsteadiness level was uniformly high across the span, with the midstream level nearly indistinguishable from the endwall level.

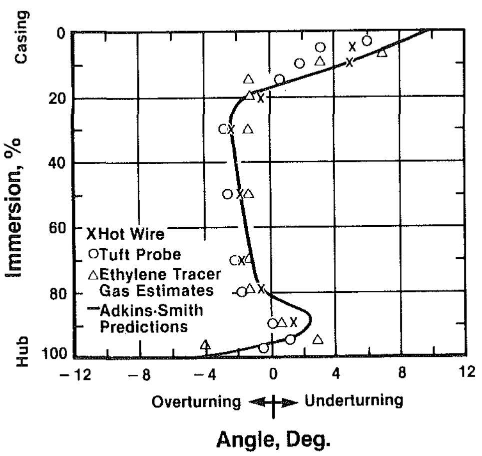

Fig. 15 Radial variation of under/overturning at Stator 3 exit

7.0 Secondary Flow and Mixing Analysis

An axisymmetric analysis was conducted to obtain a complete description of the flowfield in the test compressor. It included calculations of the secondary flow and mixing coefficients.

7.1 Analysis Procedure. The analysis method of Adkins and Smith [25, 1] was applied to the test compressor operating at the design point. In the five years since [1] was published, application of the method to additional data sets has led to the refinement of some of the empirical constants in the model, and these have been incorporated in the present analysis.

The exit air angles of the primary flow used in the analysis differed from those calculated with a potential flow, cascade analysis by an amount that ranged over the span from 2.2 to 0.3 deg for the rotors and from 2.2 to 1 deg for the stators. These departures from potential flow, along with a blockage coefficient of 0.945, were necessary to match measured overall pressure rise and airflow at the test speed. The departure angles were reduced smoothly from tip to hub in a manner which led to excellent agreement between calculated and measured radial distributions of circumferential-average total pressure, static pressure, flow angle and loss coefficient, with agreement comparable to that shown in [1].

7.2 Cross-Passage and Radial Velocities. The circumferential-average, cross-passage secondary velocities V_θ, computed from the model in [1], are shown in Fig. 12(*a*) to be in reasonable agreement with the values measured by the hot wire at the design point.

The spanwise secondary velocities on the pressure side of the stator outside the wake were computed from the model in [1]. These velocities, shown in Table 4, indicate radially inward flow along the pressure surface in the outer portion of the annulus and radially outward flow in the inner portion. These directions are consistent with the results in Figs. 6, 8, and 11.

The maximum values of radial velocities in the rotor wake as computed from the wake centrifugation model in [1] are compared in Fig. 12(*b*) to those measured by phase-lock averaging with the hot wire. In the midspan region, the overall agreement is good. In the endwalls, the model underpredicts the velocities.

7.3 Under/Overturning. For the compressor designer, one of the most important aspects of the secondary flow analysis is the calculation of blade-row under/underturning. This critical item, which has been largely overlooked in some discussions of the correct mixing model, is important because it guides the designer in setting the blading. The radial variation in

Downloaded 01 Jun 2010 to 171.66.16.57. Redistribution subject to ASME license or copyright; see http://www.asme.org/terms/Terms_Use.cfm

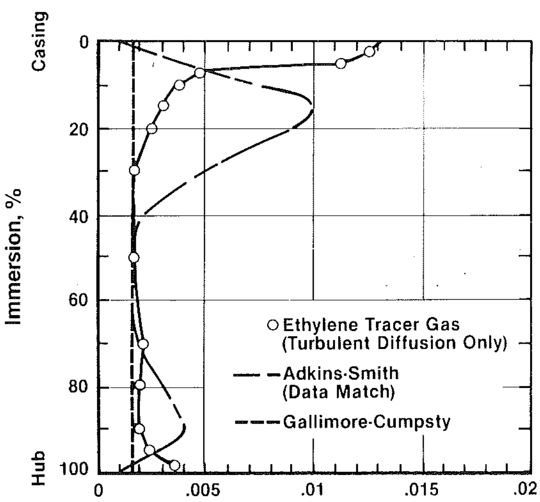

Fig. 16 Radial variation of mixing coefficient at Stator 3 exit

under/overturning, predicted by the model in [1], is in quite good agreement with those values inferred from the ethylene tracer-gas studies and from the tuft probe measurements (two-dimensional cascade angle minus measured angle), as seen in Fig. 15. The method for estimating under/overturning from the tracer-gas studies is given in [15].

In general, the Adkins-Smith model predicted the secondary flowfield reasonably well.

7.4 Mixing Coefficients. The spanwise mixing in [1] is modeled as a diffusion process, where the mixing coefficient ϵ is related to the calculated spanwise secondary velocities. The mixing equation is of the form

$$\frac{\partial \bar{P}}{\partial Z} = \epsilon \frac{\partial^2 \bar{P}}{\partial n^2} \tag{5}$$

where

$$\epsilon = \frac{Z}{a} \int_0^a \frac{V_n^2}{V_z^2}\, dx$$

The radial distribution of this suitably normalized mixing coefficient computed from the model in [1] is shown in Fig. 16. The value of the normalized mixing coefficient is high near the casing and lower near the midspan, with an overall average value for the entire compressor 2.57×10^{-3}. Comparisons with other mixing coefficients will be made later.

8.0 Turbulent Diffusion and Mixing Coefficients

As discussed earlier, the presence of turbulent diffusion is seen everywhere in the compressor flowfield. This was established by both ethylene spreads and hot-wire measurements. In this section, methods are presented for estimating the mixing coefficients resulting from turbulent diffusion as seen in the ethylene spreads and from measured loss coefficients using the method described in [2].

8.1 Hinze Model for Mixing. Estimates of mixing coefficients ϵ that would produce the observed ethylene spreads can be obtained by assuming that the tracer gas diffuses from a point source in a uniform flow, with the diffusion velocity being normal to the mean flow direction. Hinze [18] gives the equation for the concentration G of the spreading gas as

$$G = \frac{S}{4\pi\epsilon R} \exp\left[-V_m (R-m)/2\epsilon\right] \tag{6}$$

where the peak concentration occurs along the meanflow axis. It is shown in [2] that the amount of the spread of ethylene r can be estimated from equation (6) as

$$\frac{r}{L} = -\left[4 \frac{\epsilon}{V_m L} \frac{m}{L} \ln F\right]^{1/2} \tag{7}$$

Equation (7) was used to estimate the radial variation of mixing coefficients from the observed ethylene spreads for Contours 1 through 14 in Fig. 5(*a*). The value of r for the ethylene contours was taken as the distance from the core to the 20 percent contour. For nearly circular contours, r was taken along the radial direction to get spanwise mixing effects. For distorted contours, the minimum distance from the core to the 20 percent contour was taken, since it is thought that this distance is most representative of the contribution of turbulent diffusion to mixing. This conclusion is based on the findings described in Fig. 7. The mixing coefficients are presented in Fig. 16 and will be discussed later.

8.2 Gallimore Cumpsty Model. An approximate method for calculating the mixing coefficient for a multistage compressor was developed in [2] and is expressed as

$$\frac{\epsilon}{V_z L_s} = \frac{At}{L_s}\left[\frac{2\omega(t/L_s)}{3\phi^2}\right]^{1/3} \tag{8}$$

where

$$A = \left[\frac{\overline{u'v'}}{q^2}\right]^{1/2}$$

Equation (8), which gives an overall stage-average value of the mixing coefficient, was used with the airfoil thickness t, measured loss coefficient ω, flow coefficient ϕ, and values of A from [2, 26], to compute the mixing coefficient for the test compressor. A value of 1.75×10^{-3} was computed for design point operation. Since mixing was found to be uniform across the span in [2, 26], this value of 1.75×10^{-3} is assumed constant radially [27]. The result is presented in Fig. 16.

9.0 Mixing Discussion

As stated in the introduction, this paper documents experimental work and analysis which show that mixing from both secondary flow and turbulent diffusion is important and should be included in through-flow calculations for the mixing coefficients shown in Fig. 16.

Since the Adkins-Smith model [1] was used in a data-match mode and certain constants were adjusted to give agreement with measured data, the model is assumed to give an estimate of the levels and radial distribution of overall mixing coefficient required for a good date match. However, Adkins and Smith attribute all of this mixing to secondary flow and it is clear from Fig. 16 that not all of it should be. There is an underlying level of mixing by turbulent diffusion seen across the whole span. The amount of mixing which should be attributed to secondary flow can be obtained by subtracting the ethylene tracer-gas (turbulent diffusion) mixing coefficients from the Adkins-Smith values, both of which are shown in the figure. This subtraction shows that, near the casing from 0-30 percent immersion, secondary flow should contribute more than turbulent diffusion as supported by discussions associated with Figs. 5-7. In the midstream from 30-70 percent immersion, secondary flow should contribute very little to the spanwise mixing as supported by the shape of Contour 9 in Fig. 6(*a*) and by the lack of any measured radial velocity from the hot-wire studies. Near the hub, some mixing by secondary flow is again needed.

On the other hand, the level of mixing predicted by the Gallimore-Cumpsty model [2] and shown in Fig. 16 gives a good estimate of the mixing by turbulent diffusion in the midspan region as seen by comparing it with the levels obtained by the tracer-gas studies. However, in the endwalls especially near the casing, the model underpredicts both the measured mixing by turbulent diffusion and that attributed to secondary flow.

It is apparent from both [1] and [2] that incorporating any reasonable level of mixing into a through-flow calculation im-

Downloaded 01 Jun 2010 to 171.66.16.57. Redistribution subject to ASME license or copyright; see http://www.asme.org/terms/Terms_Use.cfm

proves things. However, our data show that to model the flow more realistically, the Adkins-Smith mixing coefficient in equation (5) needs to be modified by adding the contribution of turbulent diffusion and re-evaluating the empirical constants in the model to reduce the effects of secondary flow to again achieve good data matches. On the other hand, Gallimore and Cumpsty need to add a secondary flow contribution to their mixing coefficient shown in equation (8).

10.0 Conclusions

The following conclusions are drawn from the results of the ethylene tracer-gas studies, hot-wire measurements and data-match/mixing analyses for this multistage compressor study.

- Both secondary flow and turbulent diffusion were found to play important roles in the mixing process. This is in contrast to the conclusions of [2] in which the dominant mechanism causing spanwise mixing in multistage compressors was found to be a random, turbulent-type diffusion.
- Considerable cross-passage and spanwise fluid motion can occur in a compressor. Near the endwall and along airfoil surfaces, the convective mixing effects of secondary flow were of the same order of magnitude as, and in some cases greater than, the diffusive effects from turbulence.
- Outside the vane wake, spanwise motion transported fluid from the endwalls toward midspan along vane surfaces.
- Inside the vane wake, flow moved radially inward.
- Flow was centrifuged radially outward in the rotor suction-side wake.
- Turbulent diffusion effects were found everywhere. In the so-called freestream region, turbulent diffusion appeared to be the dominant mixing mechanism.
- Secondary flow and turbulent diffusion increase with compressor loading. The relative importance of the two should be configuration dependent.
- The appropriateness and accuracy of modeling the flow in multistage compressors as a so-called circumferential-average free-stream region bounded by two endwall boundary layers apparently depends upon loading level and design parameters. At the design-point loading, the midstream turbulence level was distinctly lower than levels near the endwalls, giving merit to the model. Levels of mixing varied radially. This is in exception to the conclusions of Gallimore and Cumpsty [2]. At increased loading, the midstream region was indistinguishable from the endwall regions, indicating the inappropriateness of the model. This is in agreement with the conclusions in [2].
- For more realistic models of the mixing process, the Adkins-Smith secondary flow mixing model [1] should be modified to incorporate the effects of turbulent diffusion and the Gallimore-Cumpsty diffusion mixing model [2] should be modified to incorporate the effects of secondary flow.
- The evidence suggests the following mixing process. In addition to being mixed by turbulent diffusion, the low-momentum fluid in the endwalls is convected radially by secondary flow. The passing rotor then chops, turns, and transports both this convected fluid and the wake fluid, spreading them circumferentially. The mixing process is then completed by turbulent diffusion. Similarly low-momentum fluid is convected radially outward in the rotor suction-side wake and is chopped by the next stator. This whole process can take place without any radial shift of fluid cores in the midpassage region and helps explain the existence of the repeating stage condition.

Acknowledgments

The authors are indebted to Dr. Hyoun-Woo Shin for his assistance in carrying out the hot-wire measurements and to Mr. Donald Menner for his tireless efforts in operating the LSRC during the test program. The authors also wish to thank the Aircraft Engine Business Group of the General Electric Company for permission to publish this paper.

References

1 Adkins, G. G., Jr., and Smith, L. H., Jr., "Spanwise Mixing in Axial-Flow Turbomachines," ASME Journal of Engineering for Power, Vol. 104, 1982, pp 97-110.

2 Gallimore, S. J., and Cumpsty, N. A., "Spanwise Mixing in Multistage Axial Flow Conpressors: Part 1—Experimental Investigation," ASME Journal of Turbomachinery, Vol. 108, 1986, pp. 2-9.

3 Gallimore, S. J., "Spanwise Mixing in Multistage Axial Flow Compressors: Part 2—Throughflow Calculations Including Mixing," ASME Journal of Turbomachinery, Vol. 108, 1986, pp. 10-16.

4 Smith, L. H., Jr., "Secondary Flow in Axial-Flow Turbomachinery," *Trans. of the ASME*, Vol. 77, No. 7, Oct. 1955, pp. 1065-1076.

5 Hawthorne, W. R., "The Growth of Secondary Circulation in Frictionless Flow," *Proc. Camb. Phil. Soc.*, Vol. 51, No. 4, 1955, p. 737.

6 Hearsey, R. M., "A Revised Computer Program for Axial Compressor Design, Vol. 1," ARL TR 75-001, Vol. 1, Aerospace Research Laboratories, Wright Patterson Air Force Base, Jan. 1975.

7 Lakshminarayana, B., and Horlock, J. H., "Leakage and Secondary Flows in Compressor Cascades," ARC, R&M No. 3483, Mar. 1965.

8 Herzig, H. Z., and Hansen, A. G., "Three-Dimensional Compressor Flow Theory and Real Flow Effects, Aerodynamic Design of Axial-Flow Compressors," NASA SP-36, I. A. Johnson and R. O. Bullock, eds., National Aeronautics and Space Administration, Washington, DC, 1965, Chap. XIV.

9 Hansen, A. G., and Herzig, H. Z., "Secondary Flows and Three-Dimensional Boundary Layer Effects, Aerodynamic Design of Axial-Flow Compressors," NASA SP-36, ibid.

10 Horlock, J. H., and Lakshminarayana, B., "Secondary Flows: Theory, Experiment and Application in Turbomachinery Aerodynamcis," *Annual Review of Fluid Mechanics*, Vol. 5, 1973, p. 247.

11 Kuroumaru, M., Inoue, M., Higaki, T., Abd-Elkhalek, F., and Ikui, T., "Measurement of Three Dimensional Flow Field Behind an Impeller by Means of Periodic Multi-sampling With a Slanted Hot Wire," *JSME*, Vol. 25, No. 209, 1982, pp. 1674-1681.

12 Denton, J. D., and Usui, S., "Use of a Tracer Gas Technique to Study Mixing in a Low Speed Turbine," Paper No. 81-GT-86, 1981.

13 Moore, J., and Smith, B. L., "Flow in a Turbine Cascade – Part 2: Measurement of Flow Trajectories by Ethylene Defection," ASME Journal of Engineering for Gas Turbines and Power, Vol. 106, 1984, pp. 409-413.

14 Wisler, D. C., "Loss Reduction in Axial-Flow Compressors Through Low-Speed Model Testing," ASME Journal of Engineering for Gas Turbines and Power, Vol. 107, 1985, pp. 354-363.

15 Bauer, R. C., "Fluid Migration and Mixing in a Multistage, Axial-Flow Compressor," M.S. Thesis, Iowa State University, 1987.

16 Gostelow, J. P., "A New Approach to the Experimental Study of Turbomachinery Flow Phenomena," ASME Journal of Engineering for Gas Turbines and Power, Vol. 99, 1977, pp. 97-105.

17 Powell, M. J. D., "A Hybrid Method for Nonlinear Equations," Mathematics Branch, Theoretical Physics Division, Atomic Energy Research Establishment, Harwell, Berkshire, England, Computer Journal, 1970, pp. 87-161.

18 Hinze, J. O., *Turbulence, An Introduction to Its Mechanism and Theory*, McGraw-Hill, New York, 1959, Chap. 5.

19 Bradshaw, P., *An Introduction to Turbulence and Its Measurements*, Pergamon Press, Ltd., Oxford, England, 1971.

20 Skramstad, cited in: J. O. Hinze, *Turbulence, An Introduction to Its Mechanism and Theory*, McGraw-Hill, New York, 1959, p. 342.

21 Hinze, J. O., and Van der Hegge Zijnen, B. G., "Local Transfer of Heat in Anisotropic Turbulence," *Proceedings of the General Discussion on Heat Transfer*, ASME/Institution of Mechanical Engineers, London, 1951, pp. 188-191.

22 Townsend, A. A., *The Structure of Turbulent Shear Flow*, Cambridge University Press, Cambridge, England, 2nd ed., 1976.

23 Corrsin, S., and Uberoi, M. S., "Spectra and Diffusion in a Round Turbulent Jet," NACA Report No. 1040, 1951.

24 Dring, R. P., and Joslyn, H. D., "Axial Compressor Stator Aerodynamics," ASME Journal of Engineering for Gas Turbines and Power, Vol. 107, 1985, pp. 485-493.

25 Smith, L. H., Jr., "The Radial-Equilibrium Equation of Turbomachinery," ASME Journal of Engineering for Power, Vol. 88, 1966, pp. 1-12.

26 Gallimore, S. J., "Spanwise Mixing in Multi-stage Axial Compressors," Ph.D. Dissertation, Dept. of Engineering, Cambridge University, Sept. 1985.

27 Gallimore, S. J., Private Communication.

APPENDIX

Some additional ethylene contours are presented in Figs. 17 and 18 to provide a more complete picture of the secondary flow and turbulent diffusion occurring near the casing endwall.

Downloaded 01 Jun 2010 to 171.66.16.57. Redistribution subject to ASME license or copyright; see http://www.asme.org/terms/Terms_Use.cfm

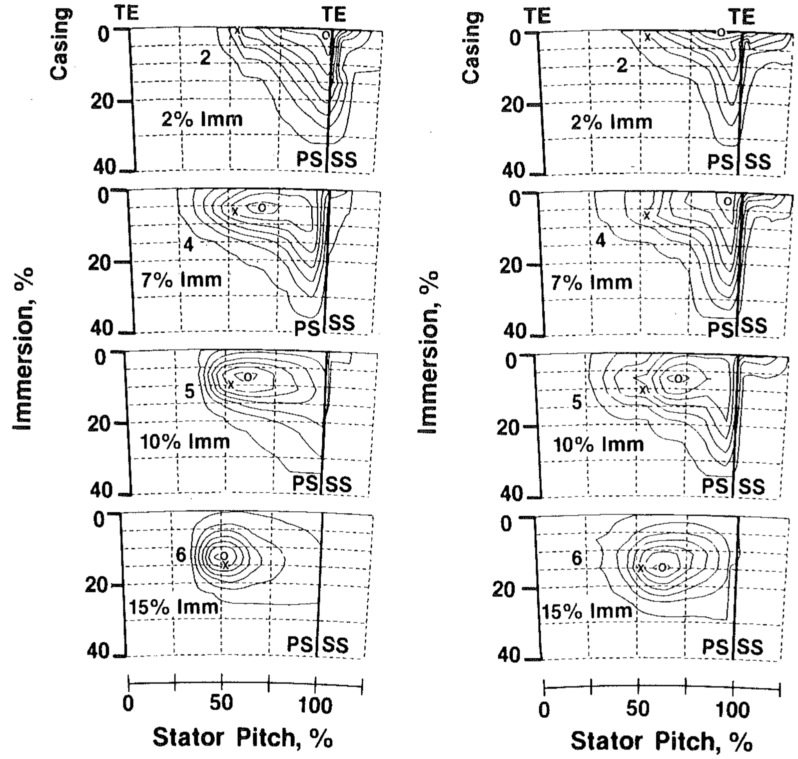

a) Design Point

b) Increased Loading

Fig. 17 Ethylene contours at various immersions for two loading levels: (*a*) design point and (*b*) increased loading; injection upstream of Stator 3 near midpitch at position "X", sampling downstream of Stator 3 with core location at "O"; contours of min = 5 percent, max = 95 percent, delta = 15 percent

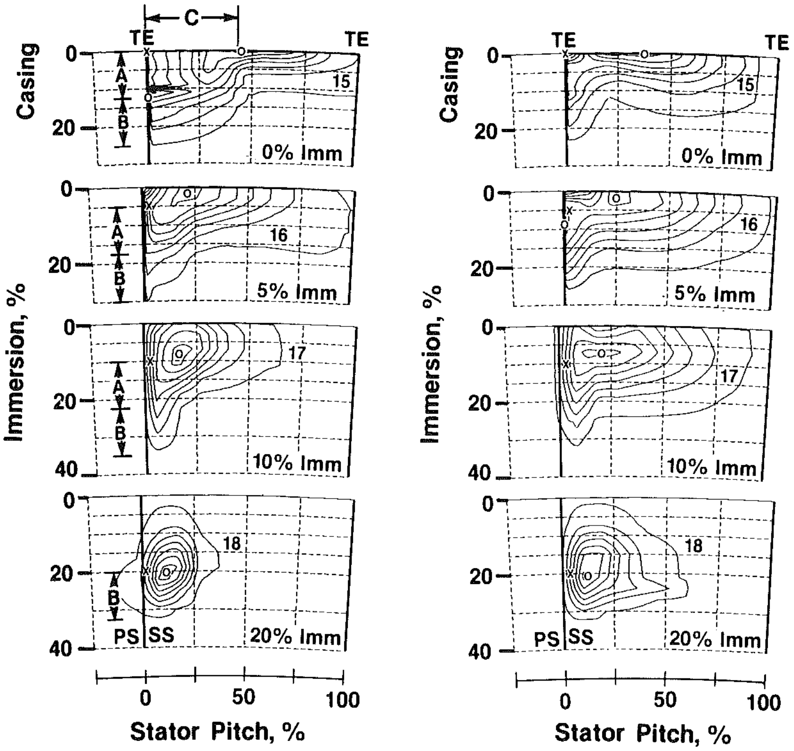

a) Design Point

b) Increased Loading

A = Radial Convection by Secondary Flow
B = Turbulent Diffusion
C = Circumferential Convection by Secondary Flow

Fig. 18 Ethylene contours at various immersions for two loading levels: (*a*) design point and (*b*) increased loading; injection upstream of Stator 3 near the leading edge at position "X", sampling downstream of Stator 3 with core location at "O"; contours of min = 5 percent, max = 95 percent, delta = 15 percent

Downloaded 01 Jun 2010 to 171.66.16.57. Redistribution subject to ASME license or copyright; see http://www.asme.org/terms/Terms_Use.cfm

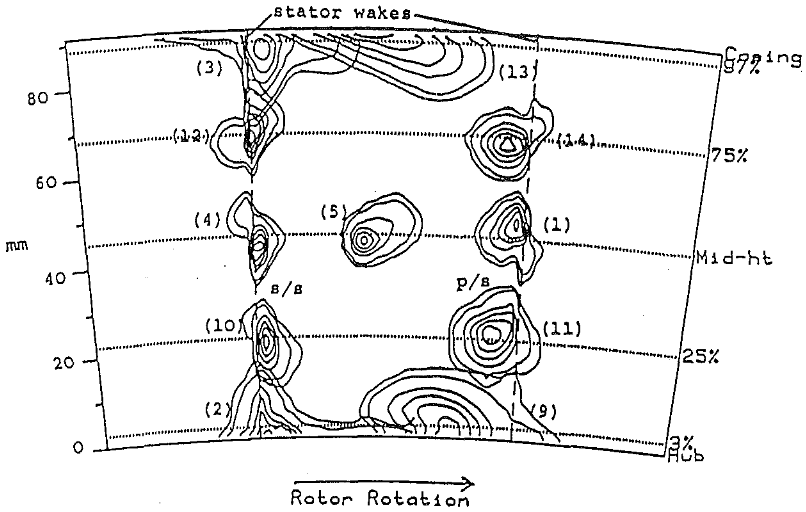

Fig. A1 Cranfield four-stage compressor: injection upstream of Stator 3; sampling downstream of Stator 3; 90, 70, 50, 30, 10, and 5 percent contours

Downloaded 01 Jun 2010 to 171.66.16.57. Redistribution subject to ASME license or copyright; see http://www.asme.org/terms/Terms_Use.cfm

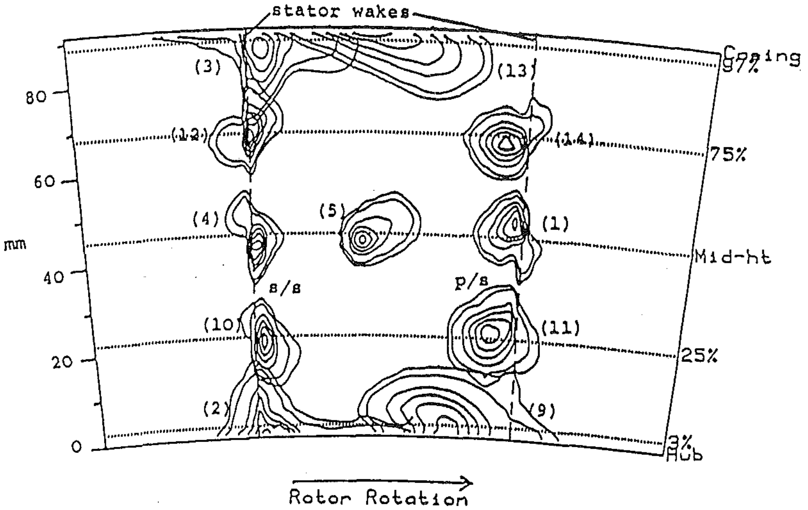

Fig. A1 Cranfield four-stage compressor: injection upstream of Stator 3; sampling downstream of Stator 3; 90, 70, 50, 30, 10, and 5 percent contours

DISCUSSION

S. J. Gallimore[1] and N. A. Cumpsty[2]

Note. The following discussion was written on the paper circulated prior to the oral presentation at the 32nd International Gas Turbine Conference and Exhibit in Anaheim, June 1987. The discussion was made available to the authors in time for them to respond to the comments made. The paper as presented was modified to take account of some of the suggestions made and this is true of the paper to appear in the journal as well. To some extent, therefore, our discussion has been superseded by the paper which now appears. For completeness it seems more appropriate to submit the original discussion, modified only where we wish to change the emphasis, and allow the evidence of the paper to show where the alterations have taken place.

The authors are to be congratulated on a fine piece of work and an excellent paper. Their research represents a very thorough investigation into mixing and secondary flow in multistage axial flow compressors and provides us with many valuable data. We do, however, have some reservations about the interpretation of the data and these are set out below.

In reference [2] of the present paper we presented evidence of the mixing of ethylene in two compressors. Contours for the better compressor, Compressor A, were presented but for convenience they are reproduced again here as Fig. A1. The similarity between this and Fig. 6 of the paper is very striking. As noted by Wisler et al. the efficiency of Compressor A was not very high at the time when the ethylene tests were carried out, about 86 percent. It should also be noted that the design point results of Wisler et al. were taken at higher flow than for peak efficiency and that at their increased loading condition the conclusions at which they arrive regarding turbulence level across the span are similar to those we came to using Compressor A.

The authors have used the measurement of ethylene concentration contours to infer the relative importance of secondary flow and turbulent mixing. In discussing their ideas we will concentrate on the results obtained near the pressure surface and the outer casing, since this is where the effects were largest. The problem arises from the differences in interpretation based on looking at the core of the ethylene contours and at the shape of the contours. The contours for test 4 shown in Figs. 5(*a*) and 5(*b*) and also Figs. 6(*a*) and 6(*b*) show considerable distortion of the contour with a distortion radially inward near the pressure surface for the low concentration contour. The arrows drawn in the figures and the discussion emphasize the authors' conclusion that this distortion is predominantly the result of secondary flow. What is very noticeable, however, is that the core of contour 4 has moved very little in the radial direction; what radial motion there has been is in the radially outward direction, the opposite sense to the arrows drawn on the figure. For test 24 with injection near the pressure surface-casing corner there is no radial movement of the core at design point and a small movement from 10 to 14 percent immersion at the operating point with increased loading. Because the injection for test 24 was close to the pressure surface this is a key observation.

One would certainly expect to see the secondary flow reflected in the movement of the core, since the secondary flow will bring about a convection of the entire concentration field, and one does see this in the circumferential movement for many of the tests, but in every case with no more than a small radial movement. We also showed [2] that there was significant circumferential transport by secondary flow but very little in the radial direction. The large arrows in Figs. 5 and 6 are, we believe, very misleading indeed, for the radial component of the secondary flow is small. It follows that its contribution to the radial mixing by the mechanism proposed by Adkins and Smith must likewise be small.

If the secondary flow is not producing the radial distortion of the ethylene contours for tests such as number 4 shown in Figs. 5 and 6 some other explanation must be offered. We believe that the authors have provided just such evidence in their test number 29, shown in Fig. 8(*a*), in which ethylene was injected from a tapping on the stator pressure surface at 2.5 percent chord. The core of the contours measured downstream has hardly moved radially from the 10 percent immersion point at which it was injected. The radial spread of the contours very close to the surface is very pronounced, being much greater than that in the circumferential direction, and the radial spreading is similar in both the radially inward and outward directions. The absence of a radial shift and of any very pronounced asymmetry of the contours indicates that some mechanism other than convection by radial secondary flow is responsible for the pattern. For injection at the same position but at the increased loading, test 35 shown in Fig. 8(*b*), the entire pattern is shifted radially inward by about 3 percent of span, and this movement can be realistically attributed to radial secondary flow. The extensive radial spread

---

[1] Rolls-Royce Limited, Derby, United Kingdom.

[2] Whittle Laboratory, University of Cambridge, Cambridge, United Kingdom.

Copyright © 1987 by ASME

Downloaded 01 Jun 2010 to 171.66.16.57. Redistribution subject to ASME license or copyright; see http://www.asme.org/terms/Terms_Use.cfm

of the contours in tests 29 and 35 must be attributed to locally anisotropic turbulence with larger components in the radial direction than the circumferential. The comparison shown in Fig. 7 is probably very misleading because it compares cases with different, but unknown, levels of turbulence anisotropy.

The anisotropy suggested by the ethylene test 29 is not reflected in the unsteady velocities measured with a hot wire and presented in Table 2(A) which, as the authors rightly point out, indicate very nearly isotropic turbulence. The anisotropy is probably occurring very near to the blade surface so that it could not be measured by the hot wire. The spread of ethylene seen for test 4 in Fig 6(*a*) is explainable as a circumferential spreading near the casing (partly turbulent but with a significant secondary flow contribution) followed by increased radial spreading by turbulence close to the blade surface. The ethylene spreads shown by the contours are the integrated effect through the whole blade passage and cannot be inferred only from the velocity or turbulence quantities measured downstream of the trailing edge.

Contours for test 4 show that very near to the casing there is a marked circumferential spreading in the direction away from the pressure surface whereas the core has moved toward the pressure surface. The measured velocities in Fig. 11 show that the secondary flow near the casing is toward the pressure surface. We believe that this is further evidence of local anisotropy, this time in the immediate vicinity of the casing wall with the larger component of turbulence being in the circumferential direction. The effect again probably occurred too close to the wall to be measured with the hot wire.

Figure 11 shows the secondary velocities measured downstream of the stator deduced from hot-wire measurements. This shows very high radial velocities in the wake region; at only 5 percent in from the casing wall the radial velocity is about 50 percent of the free-stream velocity. This seems somewhat improbable. We would be interested to know what checks were made in order to verify that the slant hot wire is valid in the very steep velocity gradients which would be found in the wake region. If the measurement of mean velocity is inaccurate does it mean that the turbulence measurements are also suspect in this region?

The radially inward velocities measured at 10 percent immersion near the pressure surface appear very similar to the design and increased loading conditions, Figs. 11(*a*) and 11(*b*). This would seem to be inconsistent with the lack of movement of the core at the design flow (test 24 in Fig. 5(*a*) and test 29 in Fig. 8(*a*)) and the radially inward movement at the increased loading (test 24 in Fig. 5(*b*) and test 35 in Fig. 8(b)). Would the authors care to comment on this?

The authors used the method of Adkins and Smith in a data-match mode to analyze their experimental results. Figure 15 shows excellent agreement between predicted and measured flow exit angles from stator 3. This combined with the reported good agreement with total and static measurements implies that the secondary flow effect on the under/overturning has been predicted well. There are, however, some points that it would be useful to have clarified. The Adkins and Smith model of mixing relies on calculation of radial secondary velocities, some deduced from consideration of radial flow in the blade boundary layer and some derived from the calculated cross passage (i.e., circumferential) flows. Figure 15 shows that the cross passage flows have been well predicted but it does not follow the radial velocities deduced from them are also correct. Considering results of prediction of radial secondary velocities for Compressor B of [2], kindly provided for us by Dr. L. H. Smith, we concluded that the radial components were overestimated, even though the match with measurement of other variables in the flow was good. It would therefore shed some light and perhaps clarify the importance of the secondary flow to radial mixing if the authors would provide a picture of the predicted secondary flow field for comparison with the measurements given in Fig. 11 of their paper. (This also assumes that some confirmation can be given or obtained that the radial velocities measured and shown in Fig. 11, in particular in the wake close to the casing, are correct.)

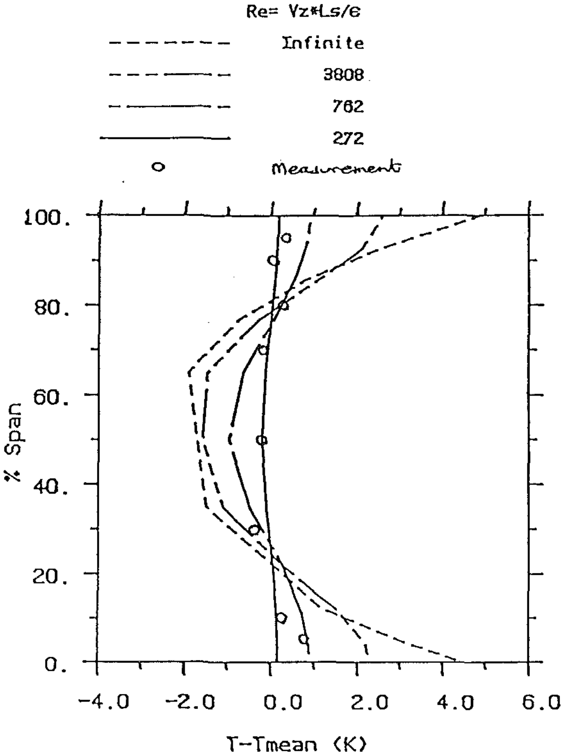

Fig. A2 **Effect of mixing level on calculated exit total temperature profiles for lower aspect ratio compressor 3S1**

The calculation of exit total pressure profiles in a throughflow method is affected by several inputs. In particular the input loss distribution and spanwise mixing interact to provide the apparent outlet loss profile across a blade row. This is even true if the loss is derived from measurements upstream and downstream of a blade row; there is no unique combination of loss and mixing. This is illustrated by the fact that for some cases the measured outlet pressure profiles can be predicted satisfactorily by throughflow methods with and without mixing included, but with different input loss distributions. It is therefore necessary to consider the mixing level and the spanwise loss distribution together. Would the authors indicate how they tackled this problem in using the Adkins and Smith method for Figs. 14, 15, and 16?

In [3] one of us (SJG) showed that the results predicted by a throughflow method were not very sensitive to the level of mixing used; it was very important to include some mixing but altering the level produced surprisingly little alteration. The relevant figure from [3] is reproduced here as Fig. A2 and from this it can be seen that with only 36 percent of the level of mixing assumed to be correct the predicted temperature profile is sufficiently close to the measured value to be considered satisfactory. (This is one reason that we chose to take the level of mixing as constant across the span since it simplifies the prediction of mixing level and its inclusion in a progam without any obvious loss in accuracy.) The corollary to this insensitivity to the level of mixing is that using the data-match method to infer the level of mixing from measured profiles of stagnation pressure and temperature is unlikely to be accurate. In light of this we would suggest that mixing levels shown in Fig. 16 derived from the Adkins and Smith method in data-match mode may not represent either the true level of mixing or the true spanwise mixing profile. We would expect there to

Downloaded 01 Jun 2010 to 171.66.16.57. Redistribution subject to ASME license or copyright; see http://www.asme.org/terms/Terms_Use.cfm

be increased mixing near the hub and casing just as the measurements of the present authors show.

Conclusions

1 The authors are to be congratulated on an excellent piece of research.

2 The evidence they show for the shifts in the positions of the *core* of the ethylene contours indicates that radial secondary flows are small. On their evidence the radial secondary flow cannot be contributing significantly to the radial mixing.

3 Close to the blades the mixing seems to be anisotropic with larger radial components than circumferential. (Very close to the casing the mixing is also anisotropic but with the circumferential component dominant.) The hot-wire measurements would not have been close enough to the surfaces to be able to detect this.

4 The contours for test 4 shown in Fig. 6(*a*) are explainable in terms of the nearly isotropic mixing a small distance out from the solid surfaces and anisotropic mixing very close to the surfaces. The authors attribute this feature to deterministic secondary flow near the pressure surface of the blade although there is little evidence of such motion from the ethylene tests with injection on the blade, Fig. 8, or from the measurements of secondary velocities where the radial component seems to be most pronounced on the suction surface.

5 The radial velocities measured in the wake near the outer casing seem to be rather high and we suspect that the hot-wire measurements could be in error because of the high shear in that region. We would like to hear the authors' comments on this.

6 The use of the Adkins and Smith method to infer the mixing level is unsatisfactory because of the demonstrated insensitivity of the calculated pressure profiles, etc., to the mixing level and also because other influential inputs such as blade loss are required in the implementation of the method. We would like to have the authors' comments on this and some clarification on how they input the loss distributions to the program.

Addendum to Discussion

We would like to supplement the original discussion with the following comments:

The revised paper includes a comment dealing with conclusion number 5 about large radial velocities in the wake region.

The appendix shows contour 15 splitting to give one core moving radially and another circumferentially, which clarifies the author's arguments in favor of substantial contributions to mixing by radial secondary flow. We do not dispute the existence of radial components of secondary flow and we welcome any clarification that the authors can provide. What we believe is that the radial secondary flows are generally small and are restricted to localized regions near the blade-surface endwall corners. This is reflected by the fact that only contour 15 shows significant radial motion of the core at the design point while contours 16, 17, 18, and 30 show no substantial movement of the core, although they are very close to where it was seen for contour 15.

We also believe that the prediction method used overestimates the magnitude of the radial components of secondary flow (as was confirmed orally by Dr. L. H. Smith at the meeting) and that the overwhelming contribution to the radial mixing is from a random process, which for brevity we called turbulent diffusion. In this connection we hope that the authors will address our conclusion number 6.

We suggested that anisotropy of turbulence is relevant and hard to measure in a compressor with a hot wire. The anisotropy of turbulence close to the surface is well documented in the literature of boundary layers; it is usual for the turbulent velocities to be substantially larger in directions parallel to the surface than normal to it. As remarked in our discussion, we believe that this can provide an important contribution to the distortion of the measured contours, such as those in Fig. 8 as well as contour 4, and we hope that the authors will address this point. We also hope that they will explain the absence of any substantial radial movement of the cores of contours 29 and 30 when, by the arguments advanced on the basis of contour 15, one would expect such movement.

L. H. Smith, Jr.[3]

I would like to thank my colleagues at General Electric and Professor Okiishi for the depth of the research presented in this paper.

When Adkins and I chose to represent the three-dimensional motions in an embedded blade row with linearized inviscid secondary flow models [1], we knew that these could not possibly account for all the important features of the real flow. We were pleasantly surprised when our method was found to match quite nicely the overturning, underturning characteristics of the circumferential-average flow as shown in our paper and again in the present paper, and use of our analysis is now commonplace in the design and development of compressors at GE.

Until recently there have been few data available on spanwise fluid motions with which to judge the accuracy of our approximations in that regard. The ethylene tracer-gas core location measurements given in the present paper indicate that the symmetric cellular flow pattern of our linearized inviscid secondary flow model is very much distorted and the spanwise velocities are generally lower than calculated, at least in a multistage compressor stator row. The measurements also show that turbulent diffusion plays a major role in mixing, which should surprise no one. But the origin and magnitude of the turbulence then come into question. It is suggested by this discusser that the secondary flows calculated by Adkins and Smith, while not always correct in detail, do spring from phenomena that are bound to agitate the flow and cause turbulent mixing, and that these agitations should be more or less proportional to the strengths of the secondary flows calculated. With this view it doesn't really matter much how the mixing is divided between secondary flow convection and turbulent diffusion; the end result is the same, and that end result has been found to be a satisfactory representation of the circumferential-average properties of the flow.

C. Weber[4]

The authors have shown, beyond any reasonable doubt, that aerodynamic mixing in a blade row of an axial compressor is due to the combined effects of secondary flow (i.e., deviations from the flow field as would be given by a two-dimensional blade-to-blade potential flow analysis) and of turbulent diffusion. For this I believe they deserve our hearty congratulations. Their paper makes it very clear that the experimental activities required to show this constitute a task of very major proportions. I do have one question concerning the analytical method described in the paper and an alternative to it. A little background information leading up to my question follows.

The analytical method the authors used to model the mixing

---

[3] Aircraft Engine Business Group, General Electric Company, Cincinnati, OH 45215.

[4] The Elliott Company, Compressor Development Engineering, 62-3, Jeannette, PA 15644.

Downloaded 01 Jun 2010 to 171.66.16.57. Redistribution subject to ASME license or copyright; see http://www.asme.org/terms/Terms_Use.cfm

was based largely on that given by Adkins and Smith [1]. Of course, they recommend, ". . .the Adkins-Smith mixing coefficient be modified by adding the contribution of turbulent diffusion and re-evaluate the empirical constants in the model to reduce the effects of secondary flow to again achieve good data matches." There is an alternative method for calculating more directly the combined effects of secondary flow and turbulent diffusion; two examples of papers that illustrate the method are the reference by Hah [W1] and the reference by Rhie [W2]. Both of these papers contain a figure that is identical in spirit to the authors' Fig. 11 (but for a stationary turbine cascade rather than for an axial compressor blade row). The Adkins-Smith approach is, most certainly, based on a great deal of empiricism. In contrast, the approach via computational fluid dynamics (CFD) exemplified by [W1, W2] is much more direct with far less empiricism (it still has some empiricism in it, though; for example, in the turbulence model). On the other hand, the CFD approach requires far more computation time; thus each method has its advantages and its disadvantages.

My question is this: Based on their experience with the Adkins-Smith type of model for mixing, can the authors comment on the relative merits of continuing work on the development of models like that of Adkins-Smith versus the three-dimensional CFD type of model? Should work continue on Adkins-Smith type models, or should we devote all resources to CFD type models, or should we continue to develop both?

References

W1 Hah, C., "A Navier-Stokes Analysis of Three-Dimensional Turbulent Flows in Turbine Blade Rows at Design and Off-Design Conditions," ASME *Journal of Engineering for Gas Turbines and Power*, Vol. 106, 1984, pp. 421-429.

W2 Rhie, C. M., "A Pressure Based Navier-Stokes Solver Using Multigrid Method," AIAA 24th Aerospace Sciences Meeting, Reno, NV, Jan. 1986, Paper No. AIAA-86-0207.

B. R. Vittal[5] and A. K. Sehra[6]

The authors of this paper are to be congratulated for a very good piece of work concerning the mixing process in multistage axial compressors. Experimental results presented in this paper are not only useful for better understanding of the secondary flow, turbulence, and mixing phenomena but also provide benchmark data for developing and validating the mixing models. This work is of vital importance to compressor designers.

The basic question addressed in this paper is whether it is secondary flow or turbulent diffusion that is the key element in the spanwise mixing process. Adkins and Smith [1] initially postulated the mixing process as an inviscid phenomena resulting from the convection of fluid properties by secondary velocity field. Gallimore and Cumpsty [2], based on their experimental investigation, concluded that this is not valid and that the mixing is due to diffusion resulting from random, high-intensity turbulence. The authors of this paper, using an experimental procedure similar to that of [2], have now come to the conclusion that both secondary flow and turbulent diffusion play important roles in the mixing process.

Before presenting our observations/comments on the work presented in this paper, we would like to mention, in addition to the above question, several other questions that need to be addressed for modeling the mixing phenomenon in multistage axial compressors. These include: (1) How accurately can we predict the secondary flows in a multistage compressor; (2) what phenomena are responsible for generating the high level of turbulence (or superturbulence) observed in multistage compressors; and (3) is it necessary to accurately model secondary flows and turbulent diffusion for predicting the mixing effect on the spanwise redistribution of temperature and pressure?

Our experience with endwall boundary layer/secondary flow calculations indicates that the predicted boundary layer thickness and associated deviation angles, downstream of the front stage, are considerably different from the experimental measurements. This discrepancy becomes more pronounced in the case of highly loaded, nonrepeating stages. In our view, the current endwall boundary layer and secondary flow models are not able to predict the secondary flow field in a multistage compressor accurately. Furthermore, computing secondary flows due to various phenomena, patching them, and then tracing the fluid properties is a rather cumbersome task. This is not ideally suited for the typically large number of iterations required for establishing stagewise and spanwise work distributions.

As far as the generation of the superturbulence is concerned, we feel that the chopping of the wakes (generated by the upstream blade row) is one of the phenomena responsible for it. Secondary flows, due to tip clearance and endwall boundary layers, are the other candidate phenomena that can play an important role in generating the high level of turbulent intensity observed in multistage axial compressors. This also implies that the superturbulence, generated by any or all of the above phenomena, is perhaps the final process that causes spanwise mixing. Having said this, we would like to present the following observations in support of this hypothesis:

- Through the stator passage, Figs. 5 and 6 do show substantial core migration in the endwall regions of the flow; but these core migrations are primarily restricted to the crossflow direction. In fact, these figures seem to suggest that the fluid particle is not really able to move from the endwall region to the midspan, or vice versa. A possible explanation is that the onset of the crossflow causes a substantial increase in the turbulent diffusion leading to the spanwise mixing. The mixing model presented in [1] is based on the assumption of physical motion of the fluid particle in the spanwise direction and is, therefore, not consistent with the experimental observations presented in this paper.

- In the rotor passage, as shown in Fig. 10, the secondary flows do not seem to be playing a dominant role in spanwise mixing because the rotor chops the incoming wakes and distributes them circumferentially. The spanwise mixing process is then completed by turbulent diffusion. Again this suggests (although the onset of the mixing process is initiated by wake chopping) the final process responsible for spanwise mixing is the turbulent diffusion.

- The authors have inferred from the turbulent intensity levels shown in Fig. 13 that the secondary flows are making a substantial contribution to the spanwise mixing. This is not as clear to us. The turbulent intensity levels are different at hub, midspan, and tip regions at stator 3 inlet for both the design point condition as well as for increased loading. Even at the stator 3 exit, in the case of a design point run, there exists a spanwise gradient of turbulent intensity. Only for the increased loading case, at the exit of the stator, is there no appreciable gradient. This suggests that the skewed contours at the endwalls may very well be due to nonuniform gradients in turbulent intensity.

- The authors have tried to show that there is a fair amount of difference between the mixing coefficients calculated based on turbulent diffusion and secondary flows, with the model of [1] showing better agreement with test values than that of [2].

---

[5] Development Engineer, Advanced Compressors, Allison Gas Turbine Division.

[6] Supervisor, Advanced Compressors, Allison Gas Turbine Division.

Downloaded 01 Jun 2010 to 171.66.16.57. Redistribution subject to ASME license or copyright; see http://www.asme.org/terms/Terms_Use.cfm

We are not able to comment on this figure since the exact details of the input used for computing mixing coefficient with the model of [1] are not very clear from this paper. A better comparison on the validity of these models could have been made if the authors had presented the spanwise distribution of temperature instead of mixing coefficient. Gallimore and Cumpsty have shown that the absolute level of mixing coefficient used in the throughflow calculation is not critical. It would have been interesting if the authors had presented additional results comparing the two models on different multistage compressors.

Based on the above observations we feel that although secondary flows play an important role in initiating the spanwise mixing process, the turbulent diffusion is the dominant process that causes the transport of energy and momentum in the spanwise direction. We also feel that Gallimore's procedure [3] for modeling the spanwise mixing is more suitable for integration with throughflow analysis.

We would again like to congratulate the authors for this valuable contribution for improving the understanding of the mixing phenomenon in multistage axial flow compressors.

G. J. Walker[7]

1 Introduction

The authors have reported a careful and comprehensive study which convincingly demonstrates that both secondary flow and turbulent diffusion may contribute significantly to mixing in multistage axial-flow compressors. This work puts in perspective the relative importance of these two mixing mechanisms and points the way to further refinements in the modeling of flow in axial turbomachinery.

The principal aim of this contribution is to discuss in more detail the circumferential transport of fluid particles arising from wake dispersion and the relative motion within individual wakes.

2 Wake Dispersion

An idealized model for the dispersion of inlet guide vane (IGV) wakes by an axial compressor rotor, as proposed by Smith [D1], is shown in Fig. D1. Downstream of the rotor, the IGV wake fluid is spread over an avenue of discontinuous segments terminated by the wakes of the rotor blades which have produced their dispersion. Each segment is oriented at an angle to the local mean flow direction due to the longer residence time in the rotor of fluid particles passing over the rotor blade pressure surface. Fluid particles emanating from any fixed source upstream of the rotor would produce a similar streakline pattern (sometimes referred to by British workers as "the old school tie effect").

The difference in time required for initially adjacent particles to pass over the upper and lower surfaces of an aerofoil in cascade is given approximately [D2, D3] by

$$\Delta t = \Gamma / W_\infty^2 \tag{1}$$

where Γ is the circulation per blade and W_∞ is the vector mean relative velocity. The circumferential extent of the wake dispersion (indicated by length AC in Fig. D1) is then

$$\Delta y = \Gamma U / W_\infty^2 \tag{2}$$

where U is the rotor speed. Finally substituting

$$\Gamma = s_{\text{rotor}} W_z (\tan \alpha_1 - \tan \alpha_2) \tag{3}$$

where s is the circumferential blade spacing, W_z is the axial velocity, and α_1, α_2 are the relative flow angles to axial upstream and downstream of the rotor, gives

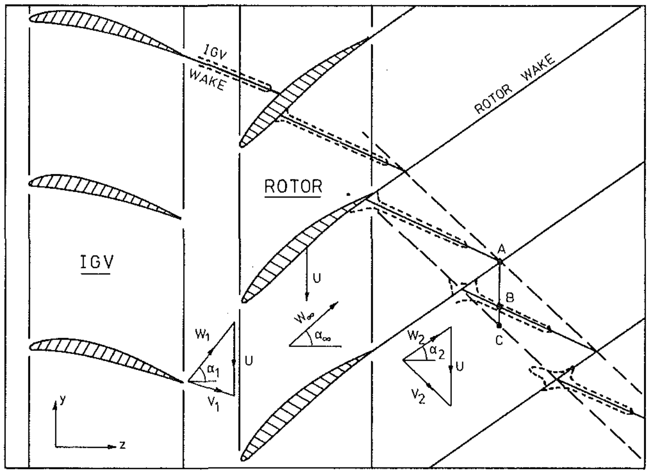

Fig. D1 Idealized model of IGV wake dispersion by a rotor (after Smith [D1])

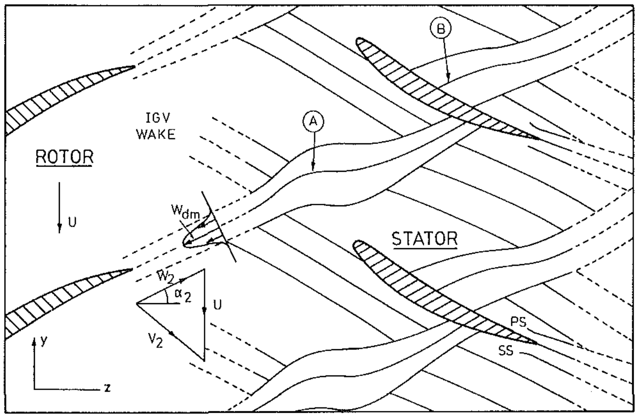

Fig. D2 Instantaneous flow pattern through stator row of a single-stage compressor with IGV showing location of blade wakes (from Lockhart and Walker [D4])

$$\Delta y / s_{\text{rotor}} = (1/\phi) \cos^2 \alpha_\infty (\tan \alpha_1 - \tan \alpha_2) \tag{4}$$

where $\phi = W_z/U$ is the local flow coefficient and $\cos \alpha_\infty = W_z/W_\infty$.

Equation (4) may be recast in terms of lift coefficient C_L by writing

$$C_L \sigma \simeq 2 \cos \alpha_\infty (\tan \alpha_1 - \tan \alpha_2)$$

where σ is the solidity, which yields

$$\Delta y / s_{\text{rotor}} = (C_L \sigma)_{\text{rotor}} \cos \alpha_\infty / 2\phi \tag{5}$$

Thus the relative circumferential extent of the dispersion of fluid elements by a rotor is seen to depend on the blade configuration, blade loading, and flow coefficient. For a fixed configuration, C_L, α_∞, and ϕ will vary in a related manner along the machine characteristic and it is valid to say that the dispersion is dependent on blade loading. At the initial design stage, however, there is some latitude for independent variation of the parameters on the right-hand side of equation (5).

Some experimental observations of IGV wake dispersion in a single-stage compressor by Lockhart and Walker [D4] are shown in Fig. D2. Using the observed values of flow angles for this test, equation (4) predicts a circumferential dispersion of 0.39 s_{rotor}. The circumferential spacing of the parallel IGV wake segments (distance AB in Fig. D1) is computed to be 0.28 s_{rotor}; this agrees well with the observed spacing of IGV wake segments in Fig. D2. Smith [D1] reached similar conclusions about the accuracy of this simple model from his observations of flow in a first stage of the General Electric Low-Speed Research Compressor.

---

[7] Senior Lecturer in Mechanical Engineering, University of Tasmania, Hobart, Tasmania, Australia; Mem. ASME.

Downloaded 01 Jun 2010 to 171.66.16.57. Redistribution subject to ASME license or copyright; see http://www.asme.org/terms/Terms_Use.cfm

The performance of this model in the multistage environment is examined by comparing with the observations of the present study at midpassage. At the design flow (where ϕ is based on average axial velocity and $U_t = 0.52$) the local pitchline value of ϕ is 0.62; the corresponding rotor relative flow angles at inlet and outlet are 57 and 41 deg, respectively [D6]. (Note from [14] that the rotor blades typically operate at large negative incidence to simulate high-speed flow conditions.) The circumferential dispersion is then computed to be 0.6 s_{stator}, and this may be compared with the spreading of Core 51 across Rotor 4 shown in Fig. 10(*a*). Assuming the core spreading to be caused by a combination of isotropic turbulent diffusion and circumferential dispersion by the rotor, the contribution from dispersion is given by the difference in circumferential and spanwise extent of the concentration contours. For the lowest concentration contour in Fig. 10(*a*) this gives 0.5 s_{stator}, which is of the correct order but lower than the calculated value. Non-isotropic diffusion in the stator blade boundary layer would have contributed to a lower experimental dispersion value. Agreement would be less good for the higher concentration contours, which are more symmetric.

3 Relative Flow Within Rotor Wakes

Downstream of a rotor there will be a circumferential transport of fluid particles in the absolute frame associated with the relative motion within the rotor blade wakes (directed toward the rotor trailing edge as shown in Fig. D2). This flow is assumed to dominate over those associated with the more highly decayed wakes of blade rows further upstream. Assuming the maximum defect in relative velocity within the rotor wake (W_{dm}) is small, and neglecting any interference from upstream blade wakes and downstream stator vanes, the maximum circumferential dispersion which can occur as the flow convects an axial distance Δz is approximated by

$$\Delta y/\Delta z = (W_{dm}/W_2)\tan\alpha_2 \tag{6}$$

There will be an associated mean flow displacement, but this will be smaller in magnitude by a factor principally dependent on the ratio of rotor wake displacement thickness to rotor blade spacing (typically only a few percent).

There are two significant mechanisms which may modify the relative flow within the rotor wakes and reduce the circumferential transport below that given by equation (6). First, the mixing due to chopped upstream stator wake segments impinging on the rotor wakes acts to restrict the relative flow within the rotor wakes; the avenues of chopped stator wake segments effectively form barriers against which low-energy rotor wake fluid accumulates. This phenomenon, which was examined by Lockhart and Walker [D4] in a single-stage compressor, can be seen occurring at location A in Fig. D2. The relative flows will also be restricted by interposition of a downstream stator causing accumulation of rotor wake fluid on the stator vane pressure surfaces (as at location B in Fig. D2). The latter phenomenon was investigated by Kerrebrock and Mikolajczak [D5] in a single-stage rotor–stator unit. These two mechanisms, although similar in effect, are distinctly different physical processes. They may interfere to some extent and their relative importance will depend on the circumferential location of the upstream stator wake avenues relative to the downstream stator vanes.

Finally, the above model of secondary flow within the rotor wakes is compared with the observations of ethylene core migration through Stator 3 presented in Fig. 5 of the paper. In this case the axial distance between injection and sampling planes is about 1.3 s_{stator} and the effective mean value of α_2, allowing for rotation of rotor wake segments through the stator passage, is about 60 deg. The relative rotor wake defect W_{dm}/W_2 is likely to be in the range 0.1 to 0.2 and should increase with loading as the rotor wakes thicken and take longer to decay. On these assumptions, the maximum circumferential dispersion predicted by equation (6) varies from 0.22 to 0.45 s_{stator}. As in Section 2 above, the calculated circumferential dispersion is compared with the excess in circumferential spreading over spanwise spreading for the lowest concentration contours of core 9. This gives about 0.2 s_{stator} for the design loading case in Fig. 5(*a*) and 0.4 s_{stator} for the increased loading case in Fig. 5(*b*). These figures are comparable in magnitude to the calculated values, and the contour skewing indicates a secondary flow in the expected direction toward the stator pressure surface. The agreement is less favorable for the higher concentration contours, but this is to be expected due to the variation in velocity defect across the wake.

The associated mean core movement would be of order 0.01 s_{stator} and quite negligible. The mean core movements at the middle of the stator passage in Fig. 5(*a*) are generally in the direction of the suction surface, indicating the dominant effect of other opposing secondary motions in the bulk flow. The latter effects are even more marked for the increased loading case in Fig. 5(*b*).

4 Concluding Remarks

The foregoing discussion of the particular secondary flows associated with wake dispersion and relative motion within wakes supports the authors' hypothesis regarding the relative importance of secondary flows and turbulent diffusion as mechanisms for mixing in axial turbomachines. The simple models presented here are in fair agreement with experiment and indicate that the wake dispersion is the more significant of the two circumferential transport mechanisms. The analysis further emphasizes the dependence of secondary flows on configuration and blade loading that was noted in the paper.

References

D1 Smith, L. H., Jr., "Wake Dispersion in Turbomachines," ASME *Journal of Basic Engineering*, Vol. 88, 1966, pp. 688–690.

D2 Smith, L. H., Jr., "Secondary Flow in Axial-Flow Turbomachinery," *Trans. ASME*, Vol. 77, 1955, pp. 1065–1076.

D3 Preston, J. H., "A Simple Approach to the Theory of Secondary Flows," *The Aero. Quarterly*, Vol. V, 1954, pp. 218–234.

D4 Lockhart, R. C., and Walker, G. J., "The Influence of Viscous Interactions on the Flow Downstream of an Axial Compressor Stage," *Proc. 2nd Int. Symposium on Air-Breathing Engines*, Sheffield, United Kingdom, Mar. 1974.

D5 Kerrebrock, J. L., and Mikolajczak, A. A., "Intra-stator Transport of Rotor Wakes and Its Effect on Compressor Performance," ASME *Journal of Engineering for Power*, Vol. 92, 1970, pp. 359–368.

D6 Wisler, D. C., private communication, June 1987.

K. D. Papailiou[8]

The authors must be congratulated for an excellent work, which, I am sure, will be very useful for future development in wall shear layer research.

Their work concerns, as well, previous work cited in references [1–3] of the subject paper. Consequently, my remarks will necessarily concern these works as well.

Generally speaking, the mechanisms from the literature that result in spanwise mixing are also recognized by the authors and put into evidence by their experimental results. In this respect, I would like to mention that blade-to-blade cross flow and dihedral effects contribute indirectly to intensifying the spanwise mixing mentioned by the authors.

Personally, I would like to make the following remarks concerning the experiments and the experimental setup:

1 The experimental compressor has a high hub/tip ratio, so that the dihedral effects on secondary flows are reduced and, in any case, not really mentioned by the authors.

---

[8] Professor, National Technical University of Athens, Athens, Greece.

Downloaded 01 Jun 2010 to 171.66.16.57. Redistribution subject to ASME license or copyright; see http://www.asme.org/terms/Terms_Use.cfm

2 The transport of low-energy material along the blade surfaces or inside the blade wakes (blade boundary layers, wakes, and part of secondary flows) is caused by spanwise static pressure gradients. The corresponding radial movements were recognized very early and experimental evidence of their existence and magnitude can be found as early as 1954 ([P1], Figs. 284–287). It is interesting to note that there have been proposed secondary flow optimization procedures [P2, P3] based on preventing this mechanism to function and that the authors' measurements show that, for increased loading, where the spanwise static pressure gradient is stronger, this transport is also stronger.

3 The contribution of the secondary vorticity to secondary flow and the radial and blade-to-blade movements associated with it must be, in my opinion, considered separately from the contribution mentioned in (2) above. For the compressor case, inlet skew (inlet secondary vorticity) is an important parameter, independent of spanwise static pressure gradients.

Concerning the authors' measurements, my opinion is that, if the experiments were conducted for nominal speed, the secondary flow effects would be more pronounced, because the contribution of the rotating speed to the upstream row secondary vorticity would have been different.

In addition, it must be pointed out that for other cases (higher camber compressor rows or turbines) the secondary vorticity and the resulting spanwise mixing may be stronger.

4 With respect to spanwise mixing due to turbulence, in addition to any attempt to model it, I would like to point out that it doesn't depend only upon the magnitude of the existing time-wise fluctuations, be they random or not, but also upon their frequency. Bradshaw [P4] pointed out this effect when he evaluated the dramatic difference between the influence of external flow unsteadiness and external flow turbulence on shear layer behavior. Consequently, it could be important to state, along with the time varying quantities, the rms of the part that corresponds to frequencies above, say, 8000–10,000 Hz. Additionally, it would be helpful to possess some knowledge about the effect of frequency upon the spreading rate of ethylene.

5 I do not have at my disposal a complete set of the experimental results, but I would suspect from the general experimental layout that the inlet casing boundary layer is very thick and that it occupies a good part of the blade height. Additionally, in the case of the test stage, I suspect that the hub and tip shear layers are merged, especially for the increased loading case for which they seem to interact strongly. Consequently, free-stream turbulence is a term that cannot be applied here as there is no free stream. In addition the high turbulence levels measured for increased loading seem to be present as a consequence of the strong interaction of the hub and tip shear layers.

With respect to the interpretation of the measurements and the corresponding modeling of the flow, I would like to observe the following:

6 It is important to bear in mind that our model is a circumferentially averaged one (meridional plane model) and that it must, necessarily, contain all contributions to the spanwise mixing. In addition, a turbulent mixing process depends not only upon the value of the diffusion coefficient, but also upon the existing local gradients of the flow quantities that are transported. Consequently, a calibration of the mixing process model is necessary, as, during the circumferential averaging, information is lost and certain terms are neglected. Even when the basic equations are used, as in the case of the calculation method presented in [P5], semi-empirical information is necessary in order to replace this information loss.

I am mentioning this reference for three reasons: (*a*) The coefficients controlling the diffusion processes are also those controlling the dissipation of kinetic energy, as the theory suggests; (*b*) the equations of motion are formally solved, including the effects of the secondary vorticity and velocity field; (*c*) the agreement between theory and experiment for multistage compressors is good, in spite of the fact that external turbulence level effects have not been taken into account.

Concerning the first reason given above, I would like to point out that in the case of the methods of Adkins and Smith [1] and Gallimore and Cumpsty [2], the mechanism for dissipation of kinetic energy is represented by loss correlations, so that this mechanism has been rendered independent from that of the diffusion process. In addition, neither the position where the losses have been generated nor their magnitude seems to be the same. Consequently, one cannot be sure whether part of the diffusion process has been taken into account when locating the losses. Furthermore all the other mechanisms enhancing spanwise mixing directly or indirectly and not being accounted for individually must be included somehow in the calculation procedure.

Concerning the second reason given above, I would like to point out that in the case of the other two methods, some empirical input, or so I understood reading the papers, was taken from the experimental results so that the injected information had already taken into account the spanwise mixing process. In addition, from Gallimore's calculations ([3], Fig. 9), I concluded that the value of the mixing coefficient could vary considerably, still giving acceptable results.

Concerning the third reason given above, I would like to point out that there seems to exist one more method giving satisfactory predictions for multistage compressor wall shear layer behavior, which is different from the ones described in [1–3].

Such a state of affairs, as it was described above, would render the comparison of the methods very difficult, even if all the details of each calculation were known, which they aren't. In fact, I would refrain totally from concluding that any of the above methods is "inaccurate" or "invalid." I would rather conclude that engineering methods of calculation, relying heavily on measurements, intuition, and creativity, have been developed in many cases of extreme complexity and lack of complete physical understanding such as the one I have been discussing. These methods have been very helpful for the engineer and very good machines have been designed with them.

References

P1 Johnsen, I. A., and Bullock, R. O., eds., "Aerodynamic Design of Axial-Flow Compressors," NASA SP 36, Washington, DC, 1965.

P2 Prumper, H., "Application of Boundary Layer Fences in Turbomachinery," in: *Boundary Layer Effects in Turbomachines*, J. Surugue, ed., AGARD AG-164, 1972.

P3 Gallus, H. E., and Kümmel, W., "Secondary Flows and Annulus Wall Boundary Layers in Axial Flow Compressor and Turbine Stages," in: *Secondary Flows in Turbomachines*, AGARD CP-214, 1977.

P4 Bradshaw, P., "Prediction of Turbulent Shear Layers in Turbomachines," presented at Symposium on Fluid Mechanics, Acoustics and Design of Turbomachinery, Pennsylvania State, 1974, NASA SP-304.

P5 Brochet, J., and Falketti, F., "Secondary Flow Calculation in Multistage Axial Flow Compressors," VIII ISABE, Cincinnati, OH, 1987.

B. Lakshminarayana[9]

The present authors as well as the authors of the earlier papers on this topic (Adkins and Smith, 1982; Gallimore and Cumpsty, 1986; Gallimore, 1986) should be commended for doing a very thorough investigation of the mixing effects in axial flow compressors. I feel that the data and the interpreta-

---

[9] Evan Pugh Professor of Aerospace Engineering, The Pennsylvania State University, University Park, PA 16802.

Downloaded 01 Jun 2010 to 171.66.16.57. Redistribution subject to ASME license or copyright; see http://www.asme.org/terms/Terms_Use.cfm

tion presented by Wisler et al. are consistent with observations by the Penn State group (e.g., B. Lakshminarayana et al., 1982; Ravindranath and Lakshminarayana, 1980, 1981; Reynolds and Lakshminarayana, 1979).

Mixing is a complex phenomenon caused by the mean flow, as well as the periodic and random unsteadiness in the flow. Momentum transport depends upon the local acceleration, convective acceleration, pressure gradient, and viscous and turbulent diffusion. If the flow is uniform (one dimensional) and steady, the mixing is mainly caused by the turbulent motion or molecular motion. Most compressors operate with large velocity gradients in blade boundary layers, wakes, and end-wall regions. In a multistage environment, the cross and radial flow component exit. The mean velocity can be decomposed into a time-averaged value, periodic components (depending upon the history of the flow, this may include components such as V_{1p} and V_{2p} due to first and second stages, respectively) and a random component V' as shown below by the transverse momentum equation (say blade to blade)

$$\frac{\partial V}{\partial t}+U\frac{\partial V}{\partial x}+V\frac{\partial V}{\partial y}+W\frac{\partial V}{\partial z}$$

$$=-\frac{1}{\rho}\frac{\partial p}{\partial y}+\mu_t\left(\frac{\partial^2 V}{\partial x^2}+\frac{\partial^2 V}{\partial y^2}+\frac{\partial V}{\partial z^2}\right)$$

where $V=\bar{V}+V_{1p}+V_{2p}+V'$; μ_t = turbulent eddy viscosity; $\bar{V}$ is the time-averaged velocity. It is evident from this equation that mixing is caused by convection by time-averaged velocity, the periodic unsteady component, and turbulent diffusion. V' is the turbulence component. Neither Gallimore and Cumpsty (1986) nor Wisler et al. (1987) decompose the turbulence component in this manner. Hence, the terminology used in these papers would include not only the random component but also the periodic component. The periodic component is a mean velocity and cannot be considered as turbulence. Hence, there is confusion with regard to the usage of the terminology "turbulent diffusion." Turbulent diffusion should be used only to identify the diffusion caused by the random fluctuation and not by the periodic fluctuation due to the upstream wakes.

Vast amounts of data available for turbulent shear flows (e.g., jets and wakes) indicate that both the convection by the mean velocity and the diffusion by turbulence dominate the transport. For example, the turbulent energy budget for a jet shown in Fig. 4.8 of Tennekes and Lumley (1972) indicates that this is indeed true.

The mixing process is caused by both the mean velocity field and the turbulent field. Consider for example the wake mixing, leakage flow, and vortex formation and mixing downstream of a rotor. The wake thickening near the tip of a rotor blade and the wake thinning at the root of a blade, as well as transport of secondary vorticity toward the suction side of the blade, are all caused mainly by the mean motion and to some extent by turbulence. The data presented recently by Lakshminarayana et al. (1987) indicate that the leakage flow and vortex are transported both by mean flow and turbulent fluctuations. Both these phenomena are equally important. The absence of a well-defined leakage vortex downstream demonstrates the effect of turbulent diffusion, distortion, and mixing by radial flows present in the wake. Within the passage, the vortex is transported inward by the radial mean flow. It is well known that a vortex decays and diffuses in both laminar and turbulent flows even though the diffusion is different for the turbulent case. Hence, it is misleading to think that the diffusion is caused purely by the mean velocity field or purely by the turbulent flow field. It is caused by both effects. One effect will dominate over the other depending upon the mean velocity gradient and turbulent intensities.

Wisler et al. and Gallimore and Cumpsty [2] have measured the flow downstream of the stator. In such a case, the turbulent diffusion may dominate over the mean velocity near the midspan, since the spanwise velocities are small in the case of stators. But Adkins and Smith (1982) have included mixing downstream of a rotor, where the mean velocities in the spanwise direction are likely to be substantial. The mixing downstream of a rotor will be dominated by the mean velocity field as well as the turbulent field, depending on the magnitude of the radial velocity or the spanwise velocity. We have taken extensive measurements downstream of a rotor and found considerable radial velocities near the trailing edge (Ravindranath and Lakshminarayana, 1980, 1981; Reynolds and Lakshminarayana, 1979). Hence, both radial velocity and turbulence would be major contributors to the mixing near the trailing edge of the blade. Far downstream, the turbulent fluctuations would tend to dominate the wake mixing as well as the spanwise mixing.

If the mixing is due to turbulence alone, the mixing and distortion of ethylene contours will be random and distorted, unless the turbulence is isotropic. Our measurements in the wake and in the end-wall region suggest turbulence is not isotropic. For example diffusion inside the wake of a stator (Fig. 8) is caused by both turbulence and normal velocity in the wake, as evidenced by equation (1). Even though turbulent diffusion may dominate, the contribution by mean velocity cannot be ignored. For a rotor wake, both these effects are equally important.

What precautions did the authors take to make sure that the ethylene injection technique provided quantitative information? Ethylene injection itself creates turbulence in the field. For example, injection on the blade surface would result in mixing of the mainstream flow with the crossflow jet, resulting in turbulence production and quick spreading of the ethylene gas. How much of this spreading/mixing is caused by this phenomenon and how much of it from the mean velocity and turbulence in the undisturbed stream must be investigated. We have used ammonia for flow visualization on a blade and noticed it is very sensitive to slot shape and injection velocity. If the injection velocity is high, the ammonia jet diffuses very rapidly, providing a thick trace on ozalid paper. The sharp holes likewise accelerated the diffusion processes. It will be useful to evaluate the extent of diffusion close to the injection point as well as several diameters downstream and see what happens before it reaches the blade.

It is interesting to note that prediction of the radial temperature profiles shown in Fig. 7 of Adkins and Smith [1] and Fig. 8 of Gallimore [3] shows remarkable resemblance, yet each author attributes this to entirely different phenomena. This dilemma can be attributed to empirical constants used by these authors. Gallimore utilizes a mixing coefficient one order of magnitude higher than that for a flat plate boundary layer. Such high values are unacceptable from physical considerations. Adkins and Smith likewise use many empirical coefficients. Such empiricism masks the underlying phenomena of mixing and may lead to misleading conclusions.

What is needed at this time is some detailed measurement of the flow field including the turbulence quantities, and evaluation of the transport by mean velocity, periodic unsteady components, and turbulence intensities through the use of the equations of motion and the data. This can be done if the measurements are taken at very close intervals to include such quantities as the turbulence intensity and correlation. This is the only way to resolve the controversy generated by Gallimore and Cumpsty, and Adkins and Smith.

It would be useful to access the vast amount of data available from Penn State, Cambridge University, UTRC, and GE low-speed compressors and evaluate the mixing phenomena through use of equations governing the mixing.

Downloaded 01 Jun 2010 to 171.66.16.57. Redistribution subject to ASME license or copyright; see http://www.asme.org/terms/Terms_Use.cfm

I am firmly convinced, based on the data of Wisler et al. as well as on Penn State data, that mixing downstream of a compressor is caused by both mean velocity components and turbulent diffusion.

References

Lakshminarayana, B., Pouagare, M., and Davino, R., 1982, "Three Dimensional Flow Field in the Tip Region of a Compressor Rotor Passage – Part 1: Mean Velocity Profiles and Annulus Wall Boundary Layer; Part 2: Turbulence Properties," ASME *Journal of Engineering for Power*, Vol. 104, pp. 760–781.

Lakshminarayana, B., Zhang, J., and Murthy, K. N. S., 1987, "An Experimental Study on the Effects of Tip Clearance on Flow Field and Losses in an Axial Flow Compressor Rotor," presented at the 8th International Air Breathing Engines Conference, Cincinnati, OH, June 16–19, 1987.

Ravindranath, A., and Lakshminarayana, B., 1980, "Mean Velocity and Decay Characteristics of the Near- and Far-Wake of a Moderately Loaded Compressor," ASME *Journal of Engineering for Power*, Vol. 102, pp. 535–548.

Ravindranath, A., and Lakshminarayana, B., 1981, "Structure and Decay Characteristics of Turbulence in Near- and Far-Wake of a Moderately Loaded Compressor Rotor Blade," ASME *Journal of Engineering for Power*, Vol. 103, pp. 131–140.

Reynolds, B., and Lakshminarayana, B., 1979, "Characteristics of Lightly Loaded Fan Rotor Blade Wakes," NASA CR-3188.

Tennekes, H., and Lumley, J. L., 1972, *A First Course in Turbulence*, MIT Press, Cambridge, MA.

W. B. Roberts[10]

Questions

1 Section 4.1 indicates that the overall performance data were obtained at 850 rpm and the ethylene and hot-wire studies were done at a speed of 600 rpm. Furthermore, the paper states that, "tests showed that the difference in Reynolds numbers did not affect the vector diagram quantities and consequently should not affect the conclusions of the work." Could the authors be more specific, i.e., what was the difference in blade chord Reynolds number between the two speeds; was at least one performance data point taken at the lower speed to compare with the higher speed data of Fig. 2; and what other hard data lead to the conclusions stated above?

2 Explain the term "unsteadiness velocities" as used in Section 6.2 and Fig. 14. Is this an approximate indicator of turbulence intensity? If so, is there an approximate relation between the two?

Comments

1 The ethylene trace and hot-wire measurements as seen in Figs. 5, 6, 8, 11, 13, and 14 show that near the design point there is a relatively large "core flow" region with secondary flow confined to the endwalls. This indicates that simple "design point" secondary flow loss and deviation models that use the concept of a core flow combined with a secondary endwall flow are valid for multistage compressors.

2 The turbulence intensity data shown in Fig. 14 are a significant contribution to the body of knowledge concerning the flow in multistage axial compressors. Were any measurements made of the scale of the turbulence?

3 Section 9.0 states that, "the Adkins–Smith model was used in a data-match mode and certain constants were adjusted to give agreement with measured data. . . . " This and other observations lead me to the conclusion that there is no current model or code that is completely independent of its database.

4 Considering the high quality and quantity of data presented in this paper, it would be greatly beneficial to turbomachinery designers, analysts, and code developers if the blading geometry used in this testing was published or otherwise made available.

Authors' Closure

We greatly appreciate the considerable time, effort, and thought expended by those who provided excellent discussions of our paper. These individuals are authorities in the field and we respect their opinions. We also appreciate having had some of these discussions in time to supply additional supporting data and clarification at the formal presentation of the paper at the 32nd International Gas Turbine Conference in Anaheim. The enthusiastic, thoughtful, and lengthy discussion following this presentation was very useful and gratifying. We are indebted to the session organizer, Dr. Herbert Law, who encouraged and facilitated this discussion. Finally, we continue to enjoy the many hours of in-depth and friendly discussions we've had with Dr. Simon Gallimore and Dr. Nick Cumpsty on this subject.

Having studied the large number of discussions thoroughly and having noted the commonality of certain questions and comments, we have organized our closure by addressing this commonality rather than addressing each discussion separately. This appeared to us to be the more logical approach. Most of the additional supporting figures presented in our closure and in the appendix of the paper were also presented at Anaheim. We believe we have successfully addressed all of the issues raised by the discussers; consequently, all of our conclusions remain unchanged.

The following eight issues were raised by the discussers: (1) data interpretation questions associated with small radial core movement but large radial contour distortions, (2) an alternative explanation for contour distortion by local anisotropic turbulence instead of secondary flow, (3) the effect of the rotor on the mixing process including circumferential transport, (4) random and periodic components and frequency of the turbulence, (5) the effects of Reynolds number on the results, (6) precautions taken to obtain quantitative ethylene measurements, (7) velocity levels in the vane wake, and (8) the Adkins–Smith data match procedure and the mixing models. Each of these issues is addressed below.

1 Data Interpretation Questions Associated With Small Radial Core Motion but Large Radial Contour Distortions. A major question is raised by Dr. Gallimore and Dr. Cumpsty (their paragraphs 4–6 and Conclusion 2) and by Dr. Vittal and Dr. Sehra (their bullet 1) about our conclusion that secondary flow causes the large radial contour distortions. Specifically, Gallimore and Cumpsty correctly point out that Contours 4 in Figs. 5(*a*, *b*) show considerable radially inward distortion along the pressure surface while Cores 4 move only a small amount in the radially outward (opposite) direction. However, they then reason that since the secondary flow should be reflected in the movement of the core and the radial core motion is small, it follows that radial secondary flows are also small and therefore cannot cause the large radial contour distortions seen in the data. Thus the secondary flow contribution to the radial mixing mechanism proposed by Adkins and Smith must likewise be small.

While we recognize the logic of the above reasoning and considered it ourselves when originally trying to understand the flow, we think our conclusion that secondary flow causes this distortion near the vane surface is supported by the data . However, this issue cannot be resolved by examining Contour 4 alone. Further insight is needed and this is found in the additional data supplied in Figs. 17 and 18 of the appendix. These data show a transition in the core motion and contour shape from large distortions to nearly circular contours as one proceeds through the endwall region from the casing to 15 percent immersion. Both pressure side and suction side contours are shown. To understand Contour 4, the contour in question, one first needs to examine design-point Contours 17 and 15.

The mirror-image similarity between the pressure-side Con-

---

[10] Flow Application Research, Fremont, CA 94539.

Downloaded 01 Jun 2010 to 171.66.16.57. Redistribution subject to ASME license or copyright; see http://www.asme.org/terms/Terms_Use.cfm

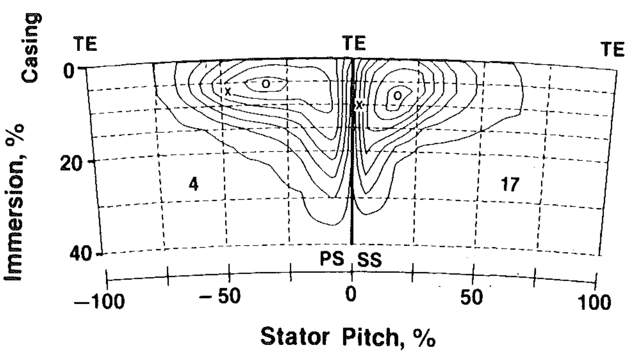

Fig. 19 Comparison of ethylene Contour 4 in Fig. 17(*a*) with Contour 17 in Fig. 18(*a*); design point loading

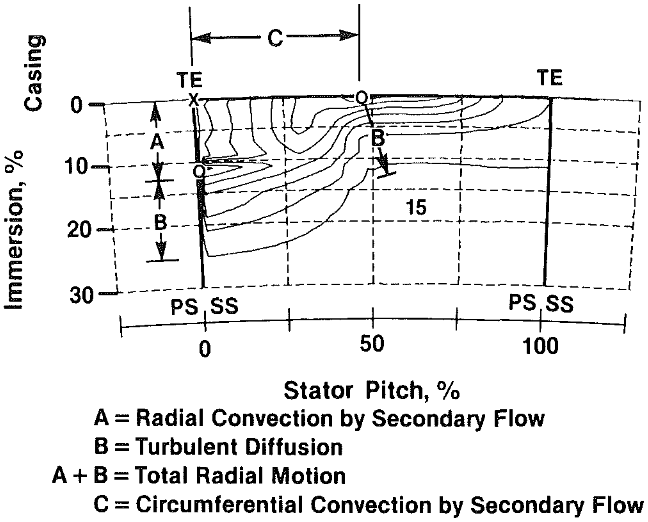

Fig. 20 Ethylene Contour 15 showing split core with both radial and circumferential convection by secondary flow and with turbulent diffusion; design point loading

tour 4 at 7 percent immersion in Fig. 17(*a*) and the suction-side Contour 17 in Fig. 18(*a*) is clearly seen in Fig. 19. Both show large, radially inward contour distortion or stretching along the airfoil surface, substantial circumferential core motion and a small amount of radially outward core motion. The cause of the stretching of Contour 17 will become clear when Contour 15 at 0 percent immersion, shown in Figs. 18(*a*) and 20, is examined.

Injection Point 15 was located at the vane leading edge at the casing. This important data point in Fig. 20 shows a split core motion. In the radial direction Core 15 moves from 0 to 12 percent radial immersion, nearly all the way through the endwall region. This distance is marked "A" in the figure. The radial velocity computed from this core motion is about 10 percent of rotor tip speed. The total radial excursion of ethylene from the injection point is "A + B," where "B" is attributed to turbulent diffusion. Clearly the radial convection by secondary flow, "A," and the diffusion by turbulence, "B," are the same order of magnitude. The significance of the circumferential motion, "C," was never questioned.

The reason for the spanwise stretching of Contour 17 along the vane surface now becomes clear when the radial lengths "A" and "B" from Fig. 20 are placed on Contour 17 in Fig. 21, beginning at the injection point. "A + B" accounts for the total inward radial spread of ethylene. Even though Core 17 is swept circumferentially by the cross-passage flow and a small amount radially outward, a significant fraction of the ethylene becomes entrained in the radially inward secondary flowfield near the vane surface producing the observed contour distortion. Turbulent diffusion is responsible for the additional spreading.

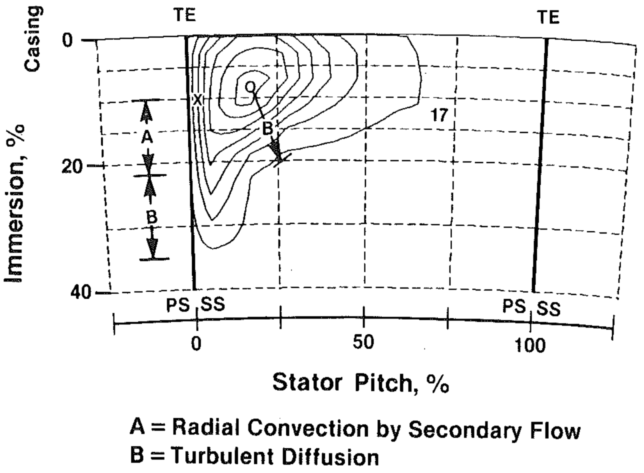

Fig. 21 Analysis of ethylene Contour 17 showing contributions of secondary flow and turbulent diffusion to total radial spreading; design point loading

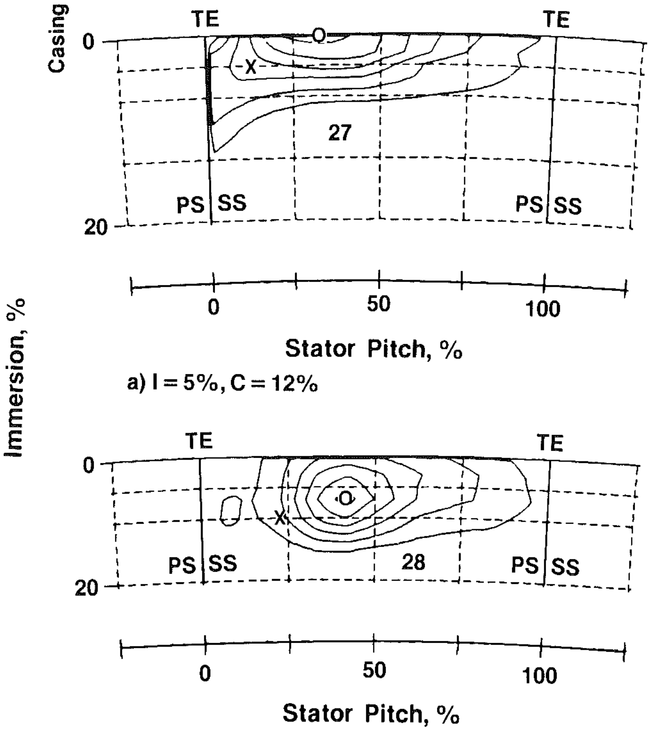

a) I = 5%, C = 12%

b) I = 10%, C = 21%

Fig. 22 Ethylene Contours 27 and 28 (see Fig. 5); design point loading

In fact, the distance "A + B" is shown in Fig. 18(*a*) to account for all of the radial motion shown inside the endwall region, while the distance "B" is shown to account for all the motion outside this region at 20 percent immersion.

The comparison in Fig. 19 suggests that the Contour 4 pattern is exhibiting similar features. Additional evidence will be presented to substantiate this under Issue 2.

Furthermore, the distance "B" in Figs. 20 and 21 is the same as the minimum distance from the core to the outermost contour. We think that this distance best represents the contribution of turbulent diffusion to mixing in any direction as described in Fig. 7 and Section 8.1.

Gallimore and Cumpsty state in the fifth paragraph of their discussion that they measured very little radial transport by secondary flow, as evidenced by their Fig. A1. In examining this figure, it seems to us that there are very few data from which to draw this conclusion in the critical region from the

Downloaded 01 Jun 2010 to 171.66.16.57. Redistribution subject to ASME license or copyright; see http://www.asme.org/terms/Terms_Use.cfm

casing to their 75 percent height position (see our Section 5.5). Moreover we suggest that their Contour 3 in their Figure A1 moves radially inward along the suction surface for the same reasons that our Contours 15, 16, and 17 do in Fig. 18(*a*).

Some more of our additional data in Fig. 22 show the full Contours 27 and 28 at the design point (see Fig. 5*a*). Most of the secondary flow is, as expected, circumferential. However even here, the radial diffusive motion by no means overwhelms the radial convective motion. In fact on average for Contour 27 in Fig. 22(*a*), the fluid is diffused from 5 to 11 percent immersion and is convected from 5 to 0 percent immersion.

The core motion, we think, shows only the localized aspects of the secondary flow motion. If the core doesn't become entrained in the secondary flow, it doesn't show the motion. Core 15 in Fig. 18(*a*) was injected at a point where it showed both radial and circumferential motion. Cores 16 and 17 were injected slightly farther from the vane suction surface, were immediately affected by the strong crossflow, and didn't show the radial feature. Cores 1-6 in Fig. 5 were injected at 53 percent stator pitch and were not convected into the regions of secondary flow that distorts the contours.

The contours, on the other hand, show a more global picture. As regions of the contour become entrained in the secondary flow field, they respond, as evidenced by Contours 2, 4, 5, 15, 16, and 17 in Figs. 17 and 18.

We have shown in this section that: (1) Secondary flow effects and turbulent diffusion effects are of the same order of magnitude in the endwall region and (2) there can be significant radial stretching of the contours near the vane surface due to secondary flow with little corresponding radial core motion.

2 *An Alternative Explanation for Contour Distortion by Local Anisotropic Turbulence Instead of Secondary Flow.* Gallimore and Cumpsty (Paragraphs 6-8 and Conclusions 3 and 4) suggest that the distortion of Contour 4 along the pressure surface is caused by local anisotropic turbulence while Vittal and Sehra (bullet 3) advocate that all of the contour skewing is caused by turbulence gradients. We will conclude from the data presented in Figs. 23 and 24 that the skewing caused by these effects accounts for only about ½ of the total contour skewing in the spanwise direction. The rest must be attributed to secondary flow.

The extent of mixing by turbulence was approximated in several ways as shown in Fig. 23. First, average random unsteadiness velocities were measured at the locations indicated by the solid dots in the figure (see Section 6.2). The radial components of unsteadiness velocity v_r', measured at the stator inlet and exit, were nearly identical. Values of v_r' for the stator exit were previously presented in Table 2. The product of v_r' and the fluid transit time across the stator represents the average distance for diffusion by turbulence at 90 percent stator pitch near the pressure surface. This diffusive distance is plotted in Fig. 23. Note that the measurements were made at the region in question for Contour 4.

Secondly, ethylene was also injected very near the pressure surface at the locations shown for design-point Contours 24 and 29 in Fig. 24(*a*). These are the contours that Gallimore and Cumpsty refer to as key observation points. We agree that they are key, but for reasons that are different from those of Gallimore and Cumpsty. We think they are key because they are a direct measure of the maximum amount of spreading that could be caused by turbulent diffusion very near the pressure surface, regardless of whether or not anisotropic turbulence is present. This diffusion distance for Contour 24 is also plotted on Fig. 23.

Finally the measured spreading of Contour 25 at increased loading, shown previously in Fig. 7, is plotted in Fig. 23.

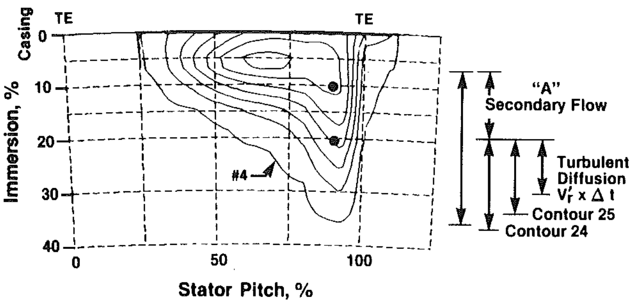

—— Contour 4 (Secondary flow plus turbulent diffusion)

Fig. 23 Evaluation of the relative contributions of secondary flow and turbulent diffusion to the radial distortion of Contour 4

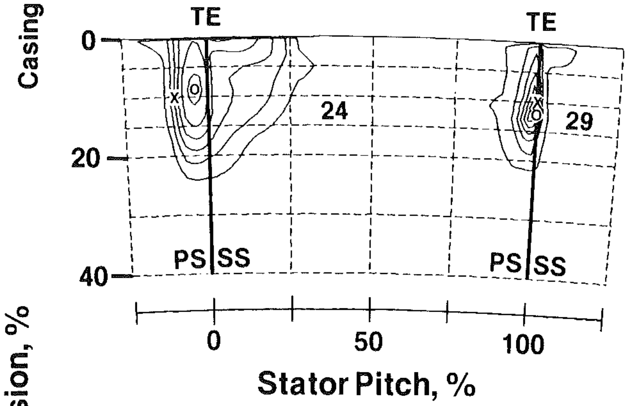

a) Design Point

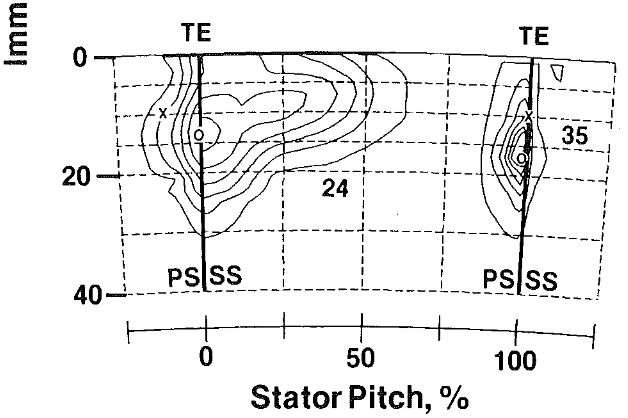

b) Increased Loading

Fig. 24 Ethylene contours for injection near pressure surface and through static tap on pressure surface (see Figs. 5 and 8)

It is clear that turbulent diffusion lengths in Fig. 23 can account for only about ½ of the radial inward spreading observed for Contour 4. An additional length, very similar to radial distance "A" described earlier in Fig. 20, is needed to explain the total radial motion of ethylene. We attribute this additional length, which produces the contour distortion, to the secondary flow motion created as the cross-passage flow impinges on the pressure surface. Consequently the arrows in Figs. 5 and 6 are not misleading.

We also think that the oblong contour patterns exhibited by Contours 24, 29, and 35 in Figs. 8 and 24 result from the strong cross-passage motion pushing toward the vane pressure surface as indicated by the hot-wire measurements in Fig. 11. In fact the cross-passage flow is strong enough that ethylene is swept past the leading edge at both loading levels for Contours 24 in Fig. 24 and is convected circumferentially on the suction side. The reason that design-point Cores 24 and 29 show little

Downloaded 01 Jun 2010 to 171.66.16.57. Redistribution subject to ASME license or copyright; see http://www.asme.org/terms/Terms_Use.cfm

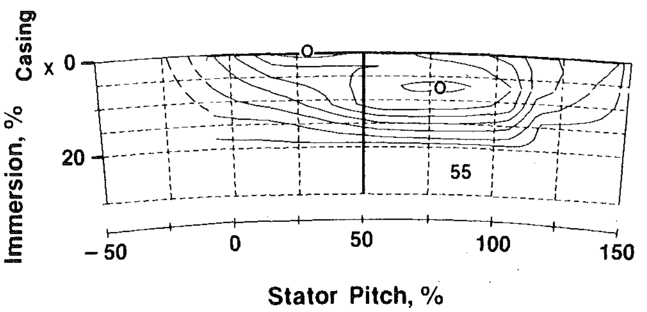

Fig. 25 Ethylene contours and split cores showing mixing action of the rotor, X = casing injection at 25 percent Rotor 3 chord, O = downstream of Rotor 3 at Plane 3.5

radial motion in Figs. 5(*a*) and 24(*a*) is easily explained. Very near the pressure surface, the cross-passage flow creates a type of stagnation point at 10 percent immersion. The radial secondary flow, shown by the arrow in Fig. 6(*a*), is farther from the pressure surface for Contour 24. As secondary flows increase for the increased loading point, there is stronger cross-passage flow and more flow being pushed into the corner as seen in Fig. 5(*b*). Secondary flows increase and now, in response, Cores 24 and 35 show radial motion with Core 35 moving from 10 to 17 percent immersion in Fig. 24(*b*). Also the radial secondary flow, shown for contour 4 in Fig. 5(*b*), is now closer to the pressure surface, as one would expect from the above analysis. Compare Fig. 17(*a*) with Fig. 17(*b*).

In summary for Issues 1 and 2, we have shown that:

(*a*) There can be significant radial distortion of the contours near the vane surface due to secondary flow with little corresponding radial core motion.

(*b*) Secondary flow effects were shown to be of the same order of magnitude as turbulent diffusion effects in the endwall region.

(*c*) With both secondary flow and turbulent diffusion shown to be important in the mixing process, the original conclusions in Section 10 of the paper remain valid.

We believe that these findings should be configuration dependent.

3 *Effect of the Rotor on the Mixing Process Including Circumferential Transport.* Vittal and Sehra (bullet 2) have concluded from the data in Fig. 10 that secondary flows in the rotor passage do not seem to be playing a dominant role in the spanwise mixing process. We understand how this conclusion would be reached from the data presented. However, the additional data in Fig. 25 show that in the endwall region the rotor influence on spanwise mixing can be significant. The split-core data show that a large concentration of ethylene has been convected from the casing to nearly 8 percent immersion, a radial distance halfway through the endwall boundary layer. The radial velocity computed from this core motion is about 8 percent of rotor tip speed. This implies a strong secondary flow in the endwall region of the rotor.

On another point, one of the important aspects of the secondary flow that has been neglected by some is its influence on circumferential mixing and under/overturning. We have tried to emphasize this in the paper in Section 7.3 and in the last conclusion in Section 10. To this end we have entitled our paper "mixing" not "spanwise mixing." It is satisfying to see that the results of Dr. Walker's careful analysis of the circumferential transport of fluid particles arising from wake dispersion and the relative motion within wakes are consistent with our measurements.

4 *Random and Periodic Components and Frequency of the Turbulence.* Prof. Papailiou, Prof. Lakshminarayana, and Dr. Roberts all addressed some aspects of the turbulence structure.

We agree with those discussers who propose that details of the unsteady (periodic and aperiodic) flow field as well as the time-averaged flow are fundamentally important because of their influence on mixing in the compressor. We have addressed some aspects of each of these flow components in our paper as clarified below.

Time-averaged flow information helped clarify the influence of secondary flow on mixing. The ethylene tracer gas results we provided are obviously a time-averaged record of flow mixing that occurred between injection and sampling planes. The hot-wire data displayed in Fig. 11 and Figs. 12(*b*, *c*) were also time-averaged. Further, some of these time-averaged hot-wire data were circumferentially averaged as well and are shown in Figs. 12(*a*, *d*).

Phase-lock averaged hot-wire information helped address the influence of the random and periodic nature of the flow on mixing. Phase-lock data appear in Fig. 13. All flow unsteadiness that was not periodic with respect to the rotor blade passing frequency was considered to be a measure of "turbulence intensity." Turbulence intensity values (equations (1)–(4)) are indicative of the combined extent of fluctuation or unsteadiness velocities, v_z', v_θ', and v_r' on either side of the phase-lock averaged flow and do not include any unsteadiness due to periodic occurrences such as rotor blade wakes. Some third-stage rotor blade wakes are discernible as regions of higher turbulence intensity in Fig. 13. Rotor wakes from blade rows further upstream could not be detected as easily and were assumed to be mixed out. Also, third-stage rotor wakes were much less noticeable near the casing at the stator row entrance, near both endwalls at the stator exit, and at all spanwise locations at the stator exit for increased loading flow. Average values of phase-lock averaged, unsteadiness velocity components that were not periodic with respect to rotor blade passing frequency were summarized in Table 2 for fixed locations in the stator 3 exit plane.

The flow unsteadiness data shown in Fig. 14 represent approximate values of "total unsteadiness" at different spanwise locations in the stator row. Since an rms average of the continuous analog signal from the hot-wire anemometer was involved, periodic (including rotor wakes) and aperiodic (including turbulence) unsteadiness were included. The result is an indication of the level of fluctuation of flow, at a point in space, about the time-averaged flow there. The trends in ethylene diffusion we observed were greatly clarified by the unsteady flow data.

We did not attempt to assess the scale of turbulence in the LSRC. Space limitations within the compressor prevented us from using an appropriate probe for this kind of measurement.

From our time-averaged and unsteady flow data we concluded that secondary flows and turbulence were both very important facets of flow mixing. We also concluded that wake chopping, a periodic flow effect, was another important aspect of mixing.

5 *Effects of Reynolds Number on the Results.* Dr. Roberts asked for clarification of the effects of the differences in Reynolds number on the results discussed in Section 4.1. Testing was conducted at two blade chord Reynolds numbers of 3.6 and 2.5 × 10^5, the latter being used for the ethylene and hot-wire tests. A complete set of overall performance data was taken at each Reynolds number. Except for the expected small reduction in pressure rise capability at the reduced Reynolds number, the features of the two pressure-flow characteristics were identical.

6 *Precautions Taken to Obtain Quantitative Ethylene Measurements.* In response to Prof. Lakshminarayana's question, the following precautions were taken for the ethylene measurements.

Downloaded 01 Jun 2010 to 171.66.16.57. Redistribution subject to ASME license or copyright; see http://www.asme.org/terms/Terms_Use.cfm

An injection probe was designed following the careful work of Dr. Gallimore [2, 26, 27].

The flame ionization detector (FID) was carefully calibrated and maintained. First the FID was calibrated and tested extensively to verify signal linearity and absence of zero drift. Secondly, FID calibrations were performed often during actual testing. Thirdly, leak checks were performed each day. Lastly, voltage signals were also monitored to watch for signal abnormalities.

To determine the effects of injection rates through the probe and through the surface static pressure taps, we conducted tests in which the injection rates were varied. For example, vane surface injection rates were halved and doubled relative to the test injection flow rate. This resulted in no change in core location and ethylene spreading, both radially and circumferentially. Sampling rates were also halved resulting in no change in core location and, importantly, no change in the extent of ethylene spread.

Periodic FID calibration, careful design and placement of injection and sampling probes, along with proper injection and sampling flow rates yielded the accurate, quantitative ethylene data shown in the paper.

7 Velocity Levels in the Vane Wake. Gallimore and Cumpsty (Paragraph 9 and Conclusion 5) point out that the magnitudes of the radial velocities measured in the stator wake in Fig. 11 seem to be rather high, perhaps improbably high. We agree. In fact, we realized that the original statement in Section 6.1 about the hot-wire calibration limits being exceeded in the stator wake (only) was not strong enough. We added an additional clarifying sentence in this section. However, the direction of this velocity vector in the stator wake and all other velocities are correct.

8 The Adkins-Smith Data Match Procedure and the Mixing Models. Most of the discussers have commented on various aspects of the Adkins-Smith data match procedure, the resulting mixing coefficients, and/or the mixing models. Their comments generally fall into the following categories: (*a*) procedural, (*b*) empiricism, (*c*) insensitivity or inaccuracy with respect to level of mixing and flow details, and (*d*) ease of application.

8(a) Procedural matters. Some concern was raised by Gallimore and Cumpsty in their Paragraph 12 and Conclusion 6 about how loss was input during the data match procedure because of its potential influence on the results.

In applying the Adkins-Smith analysis method to any design, it is only necessary to specify base (profile) losses representative of the cascade airfoil sections involved and a number indicating the proximity to stall. In the present case, spanwise uniform values of base loss coefficient of 0.025 for rotors and 0.020 for stators were employed, and the design point loading was taken to be 85 percent of the stall loading. The endwall loss model described in the appendix of [1] was invoked automatically by the computer program and this loss was added to the base loss to obtain the total loss before mixing. No "special handling" of losses was involved in the analysis. Comments on the other influential inputs were given in Section 7.1.

The suggestion was made by Vittal and Sehra (bullet 4) that a comparison of the radial distribution of temperature rather than mixing coefficients would have been a better measure of the relative validity of the models. Although we would have liked to do this, it was not practical for at least two reasons. First, detailed temperature distributions are not normally measured in the LSRC because the temperature rise across each rotor row in this low-speed device is not large. Instead, work input to the fluid is determined from overall measured torque. Secondly, we did not have access to the Gallimore code to predict a temperature distribution for our test condition. Some discussers have suggested that data bases in the major research organizations be accessed for mixing calculations or that additional comparisons of the two mixing models be made on different multistage compressors. In principle we agree. In practice, the task of getting data released is Herculean.

8(b) Empiricism. It was observed by Dr. Roberts (Comment 3) that there is no current model or code that is completely independent of its data base. This is our understanding also. On the one hand prudent designers must rely on models and codes that are well grounded physically. Although recognizing the importance of distinguishing the details of the flow physics for research purposes, the designer's primary interest centers on obtaining a satisfactory representation of the circumferential-average properties of the flow. Thus for them, as Dr. Smith stated, it doesn't really matter how the mixing is divided between convection and diffusion and whether the model is always correct in every detail. This, we believe, is the case for both the Adkins-Smith model and the Gallimore-Cumpsty model. Designers become calibrated with respect to such models. On the other hand, CFD code developers and other researchers need to understand the flow physics in detail. For these individuals detailed flow information, including level and radial variation of mixing, is very useful.

In response to Dr. Weber's question, we think that for some time to come there will be a need for both empirical methods and CFD approaches; thus development of both should continue.

8(c) Insensitivity/inaccuracy with respect to level of mixing and flow details. The difficult issue of insensitivity to mixing level and inaccuracy, raised by Gallimore and Cumpsty in Paragraph 13 and Conclusion 6 and by Vittal and Sehra in Bullet 4, needs careful evaluation. The sensitivity issue addresses how much the predicted flowfield solution changes when mixing level is changed. The accuracy issue addresses how closely the predicted mixing levels agree with the actual mixing levels.

What we did in our research was to measure the mixing, sort out as intelligently as we could the relative contributions of secondary flow and turbulent diffusion to this mixing, observe how well the models predict the experimental results, and recommend improvements. The models were exercised with no "special handling" and the reader is referred to Section 9.0 for details.

With respect to the issue of insensitivity to mixing level, Dr. Gallimore [3] concluded that the results predicted by his throughflow method were not very sensitive to the level of mixing used. Because of this, Gallimore and Cumpsty then conclude that levels of mixing inferred from measured profiles of total pressure and temperature by the Adkins-Smith method are unlikely to be accurate.

If only total pressure and temperature were being considered, then to a certain extent we would agree. However, there was more to our analysis than this. These other implications must be considered before conclusions are drawn about insensitivity and inaccuracy.

Several questions need to be answered. How sensitive is the Adkins-Smith method to the level of mixing used? How accurate are the computed mixing coefficients? To what accuracy do users want their answers? How do these findings impact the designer?

With the above in mind, we exercised the Adkins-Smith model by allowing the secondary flows to be computed but by inputting our own levels of mixing. We used radially constant mixing coefficients at each calculation station, with the level set to be a fraction of the mass-averaged value calculated by Adkins-Smith.

Downloaded 01 Jun 2010 to 171.66.16.57. Redistribution subject to ASME license or copyright; see http://www.asme.org/terms/Terms_Use.cfm

Table 5 Air angles at Stator 3 inlet predicted by the Adkins-Smith model for various levels of mixing; angles in deg

Mixing level	20 percent immersion	Casing—0 percent immersion	Difference
1.0 × Adkins-Smith	40.8	52.0	11.2
0.36 × Adkins-Smith	38.3	57.0	18.7
			Difference = 7.5

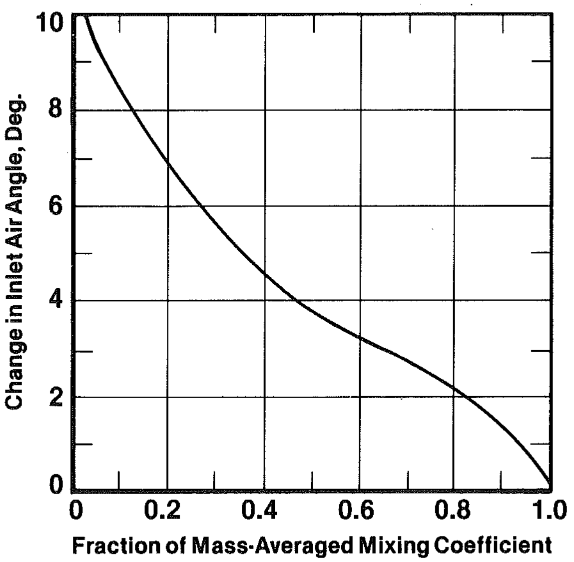

Fig. 26 Sensitivity of stator inlet air angles at the casing to variations in mass-averaged levels of mixing coefficient

One result in Fig. 26 shows the change in the air angle at the stator inlet as a function of the level of mixing. It is seen that with a mass-averaged level of mixing equal to 0.36 times the level assumed to be correct (the same fraction used by Gallimore in [3]), the air angles near the casing were 5 deg different. Another result presented in Table 5 shows that the difference in air angles from 20 percent immersion to the casing for the 36 percent mixing level case was 7.5 deg larger than the difference in air angles for the 100 percent mixing case, although the total pressure profiles were reasonably the same. These are significant differences relative to determining incidence and stagger angle for blade settings. In order to get air angles to agree to within less than 2 deg near the casing, the mass-averaged mixing level shown in Fig. 26 had to be at least 0.80 times the value assumed to be correct. In our paper, data matches of air angles were within 2 deg. In the pitchline region, little difference in the solution was seen for any reasonable level of mixing used.

Consequently, we concluded that when the secondary crossflows are incorporated and air angles are well matched, particularly in the endwalls, the Adkins-Smith solution is more sensitive to the average level of mixing coefficient than one would infer from the conclusions of Dr. Gallimore. The level of the mixing coefficient is important. This is because computed secondary flows change vector diagrams and mixing coefficients in an iterative manner.

Accuracy is another question. Although the mixing levels can be predicted from measured data to within 0.80 times "an assumed-to-be-correct value," it does not necessarily follow that these predicted coefficients are actually the correct values. This is because the mixing calculation in the Adkins-Smith model was calibrated from a limited data base.

A measure of the accuracy of the computed mixing coefficients can be assessed from the data in Fig. 16. It has already been shown that secondary flow and turbulent diffusion are the same order of magnitude near the casing. Therefore one could obtain a good estimate of the total mixing coefficient by doubling the experimental values shown in Fig. 16 near the endwalls and leaving the remaining experimental values unchanged. After doing this, we conclude that the Adkins-Smith model is a reasonably good predictor of the experimentally determined mixing coefficient, both in mass-averaged level and in radial distribution. However the predicted values are still high near 20 percent immersion.

Does the Adkins-Smith model overpredict radial velocities? Based on core movements shown in Figs. 5, 20, and 25 and on hot-wire measurements outside of the stator wakes, we compute maximum radial velocities in the endwall region to be about 9-10 percent of the rotor tip speed. This is about the level predicted by the Adkins-Smith model and shown in Table 4 at 10 percent immersion. The predicted radial velocities are too high between 20 and 50 percent immersion. Circumferential velocities are well predicted. The Adkins-Smith model does not predict the details of the secondary flowfield very well as measured in Figs. 5, 6, and 11, and in this sense it is inaccurate.

Thus these issues return to the criteria used to judge when the solution is "good enough." This is generally determined by the designer. If the design system being used does not do well in the endwall region and designers are forced to second guess the flowfield there anyway, then we would agree that the level of mixing doesn't much matter.

However this conclusion should not be made universal. The Adkins-Smith throughflow model has been constructed to give better predictions in the endwall region. Design experience assimilated to date using this model is producing confidence that the calculated air angles in this region can be used in setting blade angles. One of the authors (DCW), who is responsible for the design of research blading, thinks that the 7.5 deg variance in incidence angle or blade setting angle described earlier in Table 5 is too large and would have a serious impact upon the design approach.

Mixing levels computed in the design process must be tied to the physics of the flow and must respond to those changes in the design parameters that change mixing levels. If this doesn't happen, the designer is faced with problems as illustrated below. A parametric study was conducted in which vector diagrams having various levels of mixing were evaluated. For the case where spanwise gradients of circulation were significantly increased relative to a base level, the Adkins-Smith model predicted a significant increase in mixing. However the Gallimore-Cumpsty model, because of the axial velocities and stage lengths involved, predicted a decrease in mixing. The dilemma faced by a designer, who may want a design that increases mixing for example, is obvious.

8(d) Ease of application. For ease of applicability, we fully agree that the Gallimore-Cumpsty mixing model is much easier to integrate into a throughflow calculation.

General Comments

In summary, we have shown that both secondary flow and turbulent diffusion can play important roles in the mixing process in axial flow compressors. While recognizing the very valuable work of Adkins and Smith in secondary flow and Gallimore and Cumpsty in turbulent diffusion, we think that a more complete picture of mixing emerges when there is a synthesis of these two mechanisms as explained in our paper.

We are indebted to the American Society of Mechanical Engineers for providing the international forum in which the paper, the discussions, and our closure can be presented. We hope that this will provide the technical community with a better understanding of this complex mixing phenomenon.

Downloaded 01 Jun 2010 to 171.66.16.57. Redistribution subject to ASME license or copyright; see http://www.asme.org/terms/Terms_Use.cfm

Throughflow Analysis of a Multistage Compressor Operating at Near-Stall Conditions

R. P. Dring

H. D. Joslyn

United Technologies Research Center,
East Hartford, CT 06108

Because of their speed and efficiency, two-dimensional steady flow calculations will continue to play a significant role in the compressor aerodynamic design process. For this reason, an assessment of throughflow theory was undertaken based on detailed measurements obtained in a large-scale rotating compressor rig. This assessment is focused specifically on the compressor aerodynamics at near-stall conditions, since the three dimensionality of the flow is at its worst under these circumstances and the assumptions of axisymmetry in the theory will be tested far more severely than at design conditions. This assessment demonstrates that a reasonably accurate prediction can be achieved but that major discrepancies can occur near the endwalls where blockage is high. It has also been demonstrated that large errors can be incurred when the spanwise description of blockage is inaccurate in its detailed distribution or in its level.

Introduction

Throughflow modeling of turbomachinery provides the spanwise description of the velocity triangles and the thermodynamic properties of the flow at the various streamwise locations within and between the airfoil rows. This analytical procedure is at the heart of the design system in that it provides the inlet and exit velocity triangles that the airfoils are designed to produce. However, since the flow in turbomachinery is usually highly three dimensional and unsteady, throughflow theory can only be expected to provide an approximate description of the flow since it is fundamentally a steady, axisymmetric theory. Specifically, the nonaxisymmetry in the flow and the unsteadiness that it produces can presently only be included in the theory in an approximate manner. Thus, the theory can be expected to provide an accurate description of the flow in regions where the nonaxisymmetry is minimal. As the nonaxisymmetry in the flow becomes more severe the accuracy of the prediction will be degraded.

An assessment of this aspect of throughflow theory is presented in [1, 2] where a modern finite element throughflow procedure was provided with detailed aerodynamic input from a benchmark experiment carried out in a large-scale two-stage compressor operating at nominal design point conditions. Data were also available from the experiment to carry out detailed comparisons with the computed results. This assessment showed that while indeed an extremely accurate prediction could be achieved in the core flow region given adequate input there was, however, a loss in accuracy near the endwalls where the nonaxisymmetry in the flow was most severe. Similar conclusions were reached in a somewhat more detailed assessment of throughflow theory that was carried out using a benchmark data set acquired on a large-scale single-stage compressor rotor also operating at nominal design point conditions [3].

In an effort to understand better the impact of nonaxisymmetry in the flow on the accuracy of throughflow theory, the present assessment has been carried out. This assessment is based on benchmark data acquired on the same two-stage compressor as in [1, 2], but with the compressor operating at near-stall conditions. The nominal design point flow coefficient (C_x/U_m) for the compressor is 0.51 and the near-stall value is 0.45. The compressor goes into rotating stall at about 0.44. The effect flow coefficient has on the aerodynamics of the second stage stator is presented in [4]. In going from the design value to the near-stall value the nonaxisymmetry of the flow aft of the stator had increased dramatically in terms of wake width, depth, and spanwise penetration of the high-loss region near the hub. The nature of the flow downstream of the second-stage rotor and stator of the two-stage compressor operating at near-stall conditions can be seen in Fig. 1. The rotor exit flow has been plotted as contours of rotary total pressure and the stator exit flow has been plotted as contours of absolute total pressure. The dominant contributions to the nonaxisymmetry of the flow are the hub corner stall regions on both the rotor and the stator and the tip leakage flow on the rotor. The stator hub corner stall has grown to the point that near the hub it fills the channel between the airfoils. Additional information about the rotor and stator aerodynamics, and in particular surface flow visualization showing the corner stall regions, can be found in [4, 5]. Suffice it to say here that these flows will provide a good test of the ability of throughflow theory as it is presently formulated to account for the effects of severe nonaxisymmetry in the flow.

Contributed by the Gas Turbine Division of The American Society of Mechanical Engineers and presented at the 32nd International Gas Turbine Conference and Exhibit, Anaheim, California, May 31-June 4, 1987. Manuscript received at ASME Headquarters February 4, 1987. Paper No. 87-GT-51.

Copyright © 1987 by ASME

Downloaded 01 Jun 2010 to 171.66.16.57. Redistribution subject to ASME license or copyright; see http://www.asme.org/terms/Terms_Use.cfm

(a) ROTOR EXIT (ROTARY TOTAL PRESSURE)

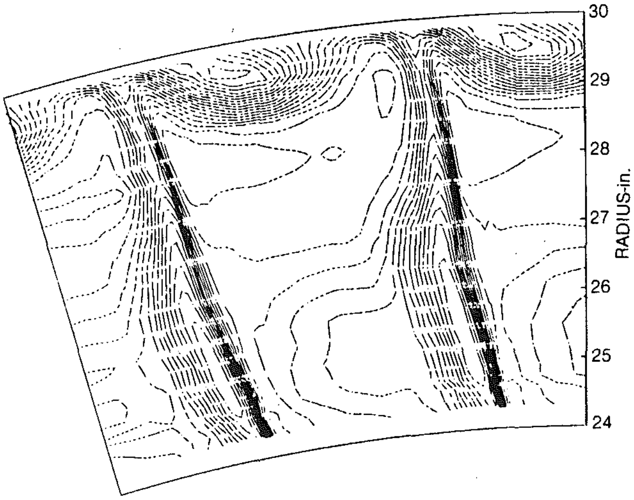

(b) STATOR EXIT (TOTAL PRESSURE)

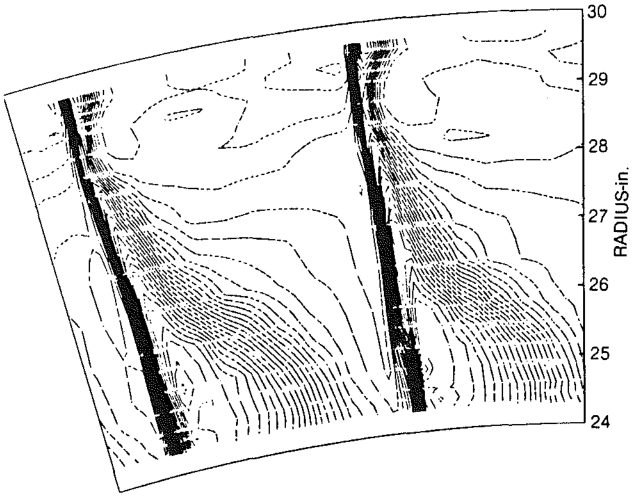

Fig. 1 **Second-stage rotor and stator exit total pressure contours, ΔC_{PT} = 0.025, (cl/B) = 0.041, ϕ = 0.45**

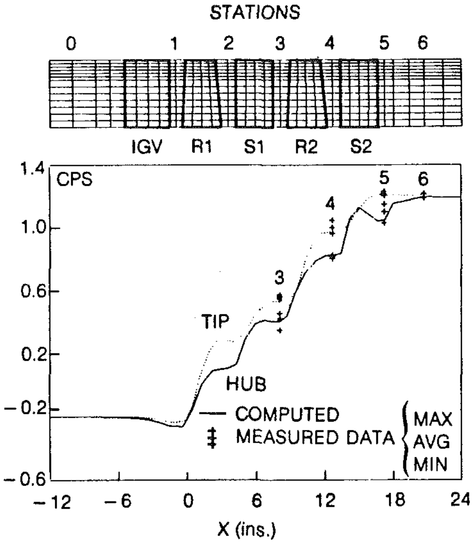

Fig. 2 **Two-stage compressor throughflow analysis, hub and tip static pressures, (cl/B) = 0.041, ϕ = 0.45**

Background

The throughflow analysis of Habashi and Youngson [6, 7] will be used in the assessment. This is a very practical and efficient finite element procedure with great geometric flexibility. It has been demonstrated to be in excellent agreement with the more historical approach using streamline curvature methods. The calculation requires as input geometric information describing the flowpath hub and tip contours as well as the airfoil tangential thickness distributions (mechanical blockage). The calculation also requires sufficient aerodynamic input to define the flow fully. There are a number of options here but for the present assessment the aerodynamic input will be in terms of row-by-row spanwise distributions of airfoil total pressure loss, flow deviation angle, and blockage. This is the same type of input that was used in the design point assessments of [1-3]. These references also contain rather detailed descriptions of (1) throughflow theory and the significance of aerodynamic blockage, (2) the benchmark data sets, (3) the way in which the aerodynamic inputs – loss, deviation, and blockage – were calculated from the benchmark data sets, (4) some additional aerodynamic input considerations related to the aerodynamic blockage within the airfoil rows and its decay due to mixing between airfoil rows, and (5) the analytical simulation procedure by which in both the experiment and the analysis the first stage was used to provide the inlet conditions for the highly instrumented second stage. These descriptions can be found in [1] and for the sake of brevity they will not be repeated here. Finally, because of the importance of blockage to the modeling of nonaxisymmetric effects in throughflow analysis it is pointed out here that the model of

Nomenclature

B = airfoil chord
C = absolute flow speed
C_p = pressure coefficient $= (P-P_{T0A})/Q_{Um}$
C_x = axial component of velocity
cl = rotor tip clearance
$\bar{K}$ = blockage factor
P = pressure
Q_{Um} = dynamic pressure based on midspan wheel speed = $\frac{1}{2} \rho U_m^2$
r = radial distance
U_m = wheel speed at midspan
W = relative flow speed
x = axial distance
α = absolute yaw angle (from axial)
β = relative yaw angle (from axial)
ρ = fluid density
ϕ = flow pitch angle (from axial)
Φ = flow coefficient = C_x/U_m

Subscripts

A = absolute frame of reference
m = midspan
r = radial
R = rotating frame of reference
S = static
T = total
x = axial
θ = tangential
0 = compressor inlet station
1, . . . , 5 = compressor axial stations

Superscripts

$-a,(A)$ = pitchwise area average
$-m,(M)$ = pitchwise mass average

Downloaded 01 Jun 2010 to 171.66.16.57. Redistribution subject to ASME license or copyright; see http://www.asme.org/terms/Terms_Use.cfm

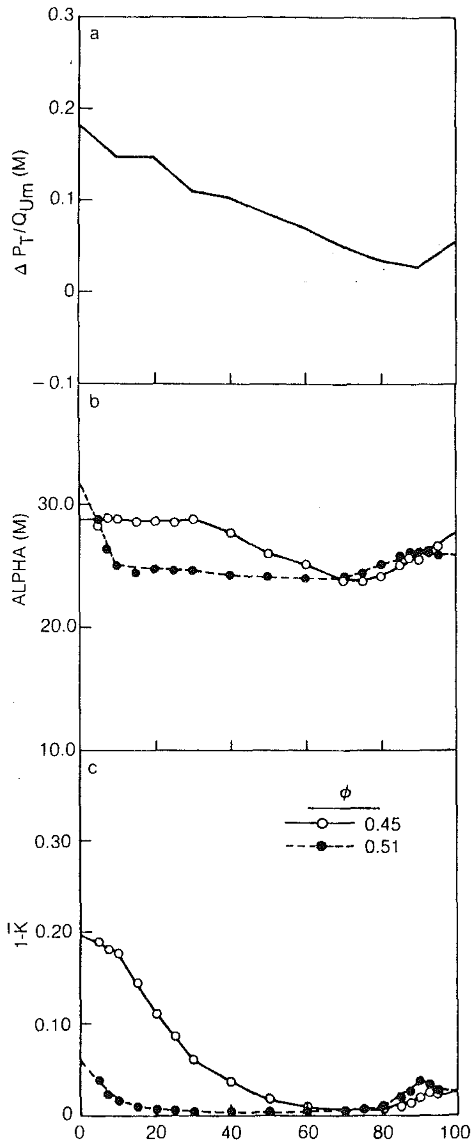

Fig. 3 Two-stage compressor throughflow analysis, input first stator exit, Station 3, $(cl/B) = 0.041$, $\phi = 0.45$ and 0.51

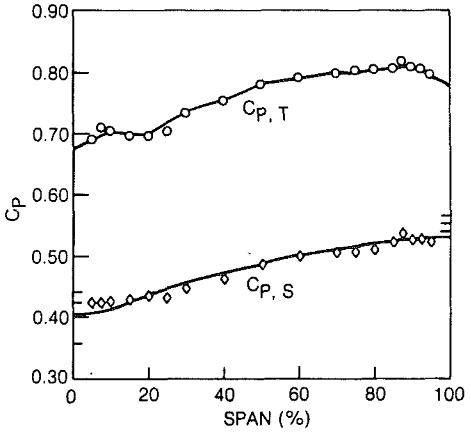

Fig. 4 Two-stage compressor first-stage stator exit, Station 3, $(cl/B) = 0.041$, $\phi = 0.45$

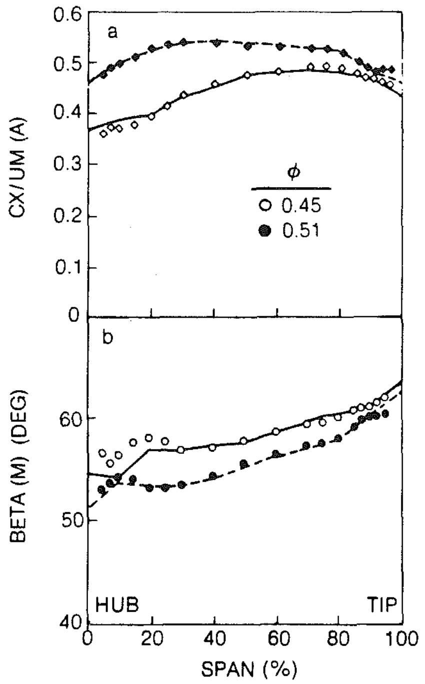

Fig. 5 Two-stage compressor first-stage stator exit, Station 3, $(cl/B) = 0.041$, $\phi = 0.45$ and 0.51

aerodynamic blockage employed in the present work is discussed in detail in [1, 8].

The following discussion will be focused on the input data and on the comparison between the measured and the computed results for the compressor operating at near-stall conditions with two levels of second-stage rotor tip clearance, $(cl/B) = 0.041$ and 0.007. This will be followed by a discussion of the sensitivity of the computed results to the nature of the aerodynamic blockage distributions.

Two-Stage Compressor (Large Rotor Tip Clearance, $cl/B = 0.041$)

A summary of the comparisons between the measured data and the computed results for the two-stage compressor is presented in Figs. 2-10. This comparison is made at the near-stall flow coefficient ($\phi = 0.45$) and at the larger of the two second-stage rotor tip clearances tested ($cl/B = 0.041$).

The computational grid of the finite element solution for this case is shown at the top of Fig. 2. There are four elements (stations) in each airfoil row and two between adjacent rows. The stations between adjacent rows correspond to the traverse planes (1-5). The grid has radial divisions of 10 percent span out to 70 percent span and 5 percent divisions from there to the tip. The refined grid near the tip was required in order to describe accurately the strong gradients that occur due to rotor tip leakage. Figure 2 also shows the computed variation of the static pressure along the annulus hub and tip (plotted in line with the grid above). The measured data are also indicated by the symbols (+). Groups of three symbols are shown for most cases ($\mp$). These correspond to the maximum, pitchwise average, and minimum static pressures measured on blade-to-blade arrays of static pressure taps on the annulus at Stations 3-6. In general the agreement between the computed and measured results is excellent. In most cases the computed value is within the measured maximum/minimum range and close to the average. The only exception is at the second rotor exit (Station 4) at the tip where the measured average is greater than the computed value by 0.03 (i.e., 3 percent of $\frac{1}{2}\,\rho U_m^2$). The relatively large difference between the maximum and

Downloaded 01 Jun 2010 to 171.66.16.57. Redistribution subject to ASME license or copyright; see http://www.asme.org/terms/Terms_Use.cfm

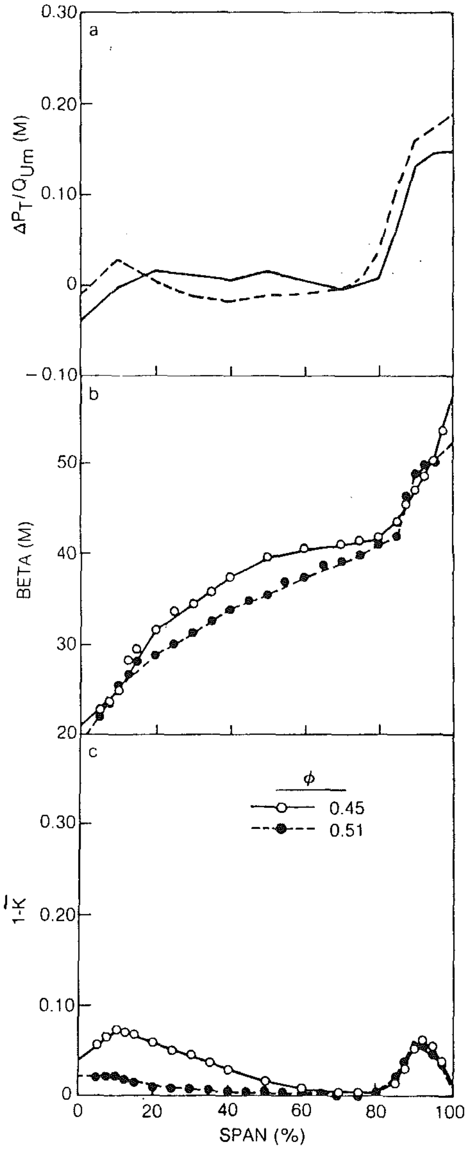

Fig. 6 Two-stage compressor throughflow analysis, input second rotor exit, Station 4, (*cl/B*) = 0.041, ϕ = 0.45 and 0.51

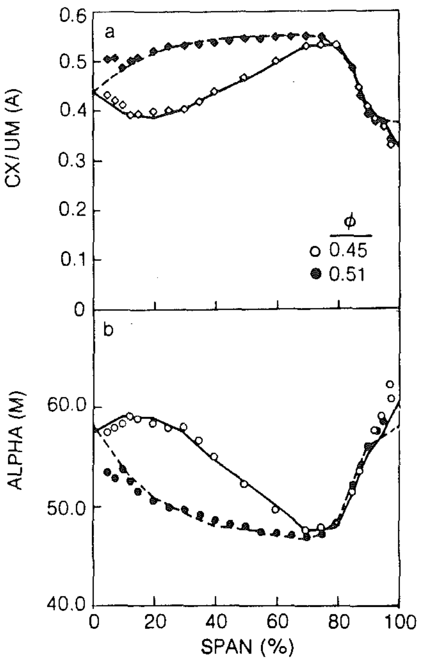

Fig. 7 Two-stage compressor second-stage rotor exit, Station 4, (*cl/B*) = 0.041, ϕ = 0.45 and 0.51

minimum static pressures at most locations is a good indication of the importance of determining a good pitchwise average value from measured data.

The input to the throughflow analysis at the first stator exit is shown in Fig. 3. Spanwise distributions of deviation and blockage are shown for both the design condition (ϕ = 0.51) and for the near-stall condition (ϕ = 0.45). This figure clearly shows the increases in deviation and blockage that occur near the first stator hub as the compressor was throttled down. The loss is from the first stator leading edge to the trailing edge but the flow angle and blockage plotted are for the downstream traverse plane at Station 3. The blockage profiles at the trailing edge and at Station 3 were made identical and the angle distributions at the two locations differ only slightly. The measured data (symbols) as well as the actual distributions used in the calculation (curve) are both shown. The first stator loss profile was adjusted to provide agreement between the measured and computed distributions of absolute total pressure at Station 3. This agreement is shown in Fig. 4 along with the measured and computed static pressure distributions which are also in good agreement. The average and the minimum and maximum static pressures measured on the hub and tip at this station are plotted at 0 and 100 percent span.

The area-averaged axial velocity ($C_x \cdot \bar{K}$) and relative yaw angle profiles at the first stator exit (Station 3) are shown in Fig. 5. The profiles are shown for both the design and near-stall conditions. The measured and computed axial velocity at ϕ = 0.45 are in excellent agreement except near the hub. The agreement here is not as precise as what was achieved at the design condition due to the much higher blockage at the hub for the near-stall case (Fig. 3*c*). The relative yaw angle also shows a deterioration in the agreement between the measured and computed results at the lower flow coefficient, the difference being typically 2 deg out to 20 percent span.

The input to the throughflow analysis at the second rotor exit (Station 4) is shown in Fig. 6. Here again the spanwise distributions of the measured data as well as the actual profiles used in the calculation are shown for loss, deviation, and blockage. The profiles for both the design condition (ϕ = 0.51) and the near-stall condition (ϕ = 0.45) are included in the figure. The main difference between the two flow conditions is that at the near-stall condition the loss and deviation in the midspan region are considerably higher and the blockage near the hub is increased substantially. The large rotor tip clearance (*cl/B* = 0.041) has caused a region of locally high loss, deviation, and blockage. It is these distributions which necessitated the refined radial grid from 70 to 100 percent span (Fig. 2). Figure 7 shows the measured and computed axial velocity and absolute yaw angle at the second rotor exit. The axial velocity for both the design and near-stall cases is well predicted except very close to the hub and tip.

The input to the throughflow analysis at the second stator exit is shown in Fig. 8 for both the design and near-stall flow conditions. There has been a significant increase in the loss due to the dramatic growth in hub corner stall. The stall has also caused an increase in deviation in the midspan region but a dramatic reduction in deviation (a considerable increase in turning) near the hub. The corner stall has caused a major increase in blockage from 75 percent span to the hub and a small reduction in blockage near the tip. The axial flow speed and the relative yaw angle at the second stator exit are shown in Fig. 9. The axial velocity and the relative flow angle are shown for both flow coefficients. The axial velocity is well predicted except close to the hub and tip. The relative yaw is also

Downloaded 01 Jun 2010 to 171.66.16.57. Redistribution subject to ASME license or copyright; see http://www.asme.org/terms/Terms_Use.cfm

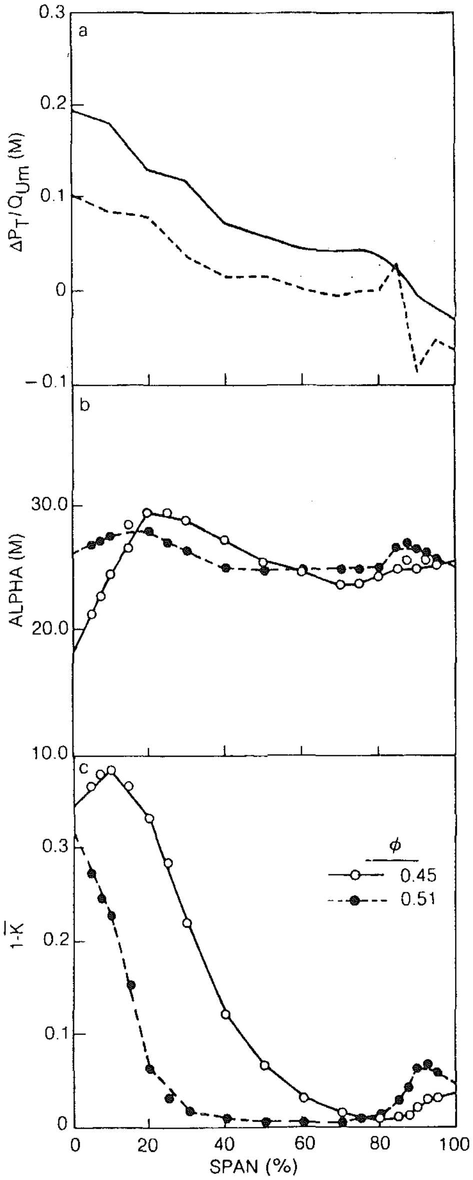

Fig. 8 Two-stage compressor throughflow analysis input, second-stage stator exit, Station 5, $(c/B) = 0.041$, $\phi = 0.45$ and 0.51

well predicted except in the hub region where large differences exist between the measured and computed results (~6 deg). In general, excellent agreement has been obtained at this stator exit station except near the hub where the blockage for this near-stall case is exceptionally high over a large fraction of the span (Fig. 8*c*).

The second-stage rotor inlet and exit (Stations 3 and 4) relative total and static pressures are shown in the top half of Fig. 10. Similar absolute frame quantities for the second stator (Stations 4 and 5) are shown in the bottom half of Fig. 10. Because the rotor and stator loss are input the differences between the inlet and exit total pressures in Fig. 10 are identical with the measured values. The assessment of the prediction, then, is based on how well the inlet total pressure profiles are predicted. The agreement between the measured and computed results is in general excellent. The static pressure profiles are in general well predicted as to level and trend. This suggests that whereas the definition of blockage used in this assessment [8] cannot be defended on a formal basis, all the same it does appear to account for the major impact of blockage on the velocity and static pressure fields.

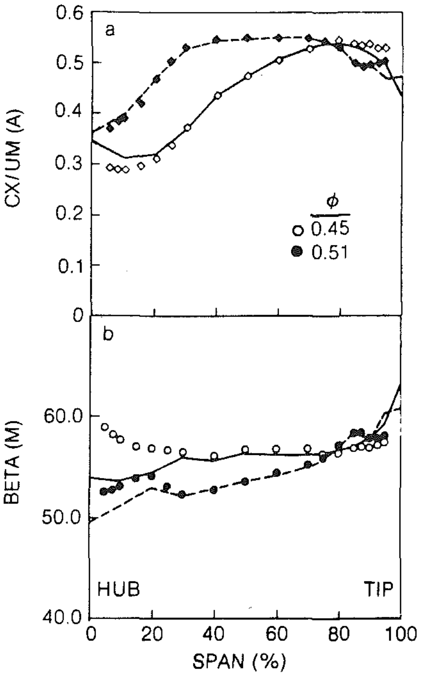

Fig. 9 Two-stage compressor second-stage stator exit, Station 5, $(c/B) = 0.041$, $\phi = 0.45$ and 0.51

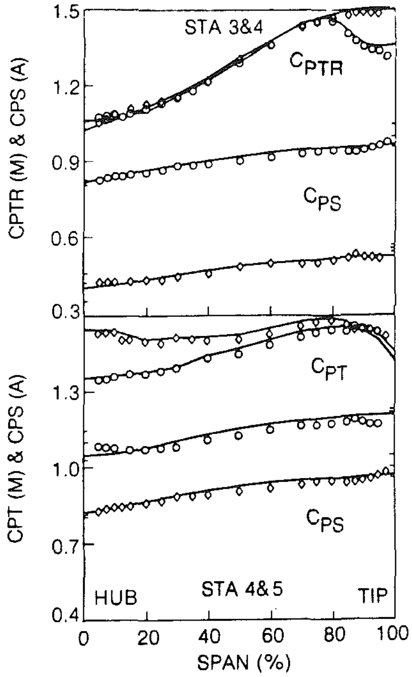

Fig. 10 Two-stage compressor throughflow analysis, second rotor and stator inlet and exit conditions, $(c/B) = 0.041$, $\phi = 0.45$

Looking back over this assessment of throughflow theory (Figs. 2–10) one is led to the conclusion that, given the adequate input, there is every expectation that a reasonably accurate prediction will result and that the major inaccuracies will be in the endwall regions where blockage is high. This assessment represents a particularly challenging demonstration of the robust nature of throughflow theory because of the strongly three-dimensional flow mechanisms that were present in the data base due to the large rotor tip clearance [5] and due to the large region of hub corner stall, especially on the second stator [4].

Downloaded 01 Jun 2010 to 171.66.16.57. Redistribution subject to ASME license or copyright; see http://www.asme.org/terms/Terms_Use.cfm

Two-Stage Compressor (Small Rotor Tip Clearance, $cl/B = 0.007$)

A second set of data had been acquired on the two-stage compressor with the second-stage rotor running at a tip clearance which was much smaller than that which existed in the previous comparisons ($cl/B = 0.007$ versus 0.041). The relevance to the present assessment is that this reduced tip clearance produced a rotor exit flow field in which the three-dimensional effects and the general distortion of the flow field were greatly reduced relative to the large clearance case. For this reason it is to be expected that the throughflow calculation will predict the measured flows more accurately than for the large clearance case.

The computational grid and the computed flow path hub and tip static pressures for the small tip clearance case are shown in Fig. 11 along with the measured static pressures at Stations 3-6. The major difference between these results and those for the large clearance case (Fig. 2) occurs between the second-stage rotor and stator (Station 4). The measured data are changed only slightly relative to the large clearance case. The major difference is that the predicted static pressure at the tip is now in excellent agreement with the average measured static pressure. This improved agreement between the measured and computed rotor exit tip static pressure at the present near-stall condition is very similar to the results for the design point case [1, 2]. Unlike the design point case, however, the present near-stall case also showed a variation in the rotor inlet hub and tip static pressures as the tip clearance was reduced. This can be seen by comparing Figs. 2 and 11 at Station 3. At both the hub and the tip the measured static pressures are slightly lower (by typically $\Delta C_p = 0.01$). The computed value at the tip hasn't changed but at the hub the computed value has dropped significantly ($\Delta C_p = 0.07$). This lower hub static pressure is due to the higher hub blockage for the small clearance case. The hub blockage $(1 - \bar{K})$ at Station 3 increased from 0.20 (Fig. 3*c*) to 0.32 with the reduction in rotor tip clearance.

In general, the comparisons between the measured and computed results for the large and small second-stage rotor tip clearance cases demonstrated that increasing rotor tip clearance can complicate the flow by introducing strong three-dimensional effects. Not surprisingly the throughflow analysis gave a more accurate prediction of the less complicated flows at the smaller tip clearance.

Sensitivity Analysis

A number of calculations have been carried out in order to determine the sensitivity of the computed results to specific details of the input data. A similar sensitivity analysis had been carried out at the design flow coefficient, $\phi = 0.51$ [1, 2]. That analysis indicated several things which are summarized here: (1) The axial turning distribution within the airfoil rows had only a very weak impact outside of the airfoil rows; (2) since blockages were only measured at locations somewhat downstream of the airfoil trailing edges, i.e., at Stations 3, 4 and 5, these measured profiles were used at the trailing edge plane. The sensitivity analysis showed this to be a useful and accurate assumption since a large increase (1.5×) in trailing edge blockage only had a significant impact at the trailing edge plane and practically no impact on the next downstream plane; (3) it was shown that replacing the measured spanwise distributions of blockage with a constant value (equal to the average at each plane) had a significant impact on the spanwise distributions of static pressure and incidence; (4) airfoil mechanical blockage had little impact on the computed results outside of the airfoil rows; (5) the removal of all aerodynamic blockage caused a large change in the levels and spanwise distributions of incidence and blockage. The distribution changes were very similar to those produced by simply using a spanwise constant blockage; (6) finally, it was also shown that for these low-speed cases a coarse grid (leading and trailing edge stations only) gave a surprisingly accurate result.

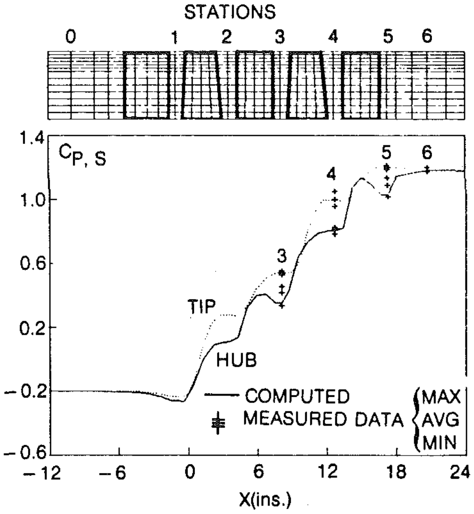

Fig. 11 Two-stage compressor throughflow analysis, $(cl/B) = 0.007$, $\phi = 0.45$

The sensitivity analysis for the present near-stall case ($\phi = 0.45$) was carried out for the small rotor tip clearance ($cl/B = 0.007$). In addition, it was focused purely on the effect of aerodynamic blockage. First, the impact of removing the aerodynamic blockage within the airfoil rows will be demonstrated. Second, the added effect of using a spanwise uniform aerodynamic blockage will be shown. Finally, a case will be run with no aerodynamic blockage, either within or between airfoil rows. In all cases the mechanical blockage due to airfoil thickness will be retained.

Case A: No Aerodynamic Blockage Within Airfoil Rows. As discussed in [1, 2] some aerodynamic blockage had been added within the airfoil rows to produce a smooth transition from the high mechanical blockage at the 25 percent chord locations (9 to 13 percent) to the high aerodynamic blockage at the trailing edge planes (locally as high as 40 percent, Fig. 8). Aerodynamic blockage was added between these two locations due to the relatively low mechanical blockage there (typically 2 to 7 percent). The aerodynamic blockage within the blade rows could be justified as simulating the blockage due to the hub corner stall and the rotor tip leakage (Fig. 1). The effect of removing this blockage was most significant within the blade rows. Eliminating the blockage caused a pressure maximum on the hub within the first stator and also a slightly stronger local hub maximum within the second stator. The incidence change was extremely small over most of the span and the maximum change was less than one degree at the hub. The changes in static pressure were also small, reaching a maximum at the hub of typically $\Delta C_p \approx 0.01$. This is about 2 percent of the stage static pressure rise. Thus, although the inclusion of aerodynamic blockage within the airfoil rows produces a smoother static pressure rise, it has only a relatively weak impact in the gaps between airfoil rows.

Case B: No Aerodynamic Blockage Within Airfoil Rows and Spanwise Constant Aerodynamic Blockage Between Airfoil Rows. The spanwise distributions of aerodynamic blockage input at the traverse planes (and at the trailing edge planes) vary strongly with span (Figs. 3*c*, 6*c*, and 8*c*). Since historically, spanwise distributions of blockage have not been available to the analyst it would be of value to know the

Downloaded 01 Jun 2010 to 171.66.16.57. Redistribution subject to ASME license or copyright; see http://www.asme.org/terms/Terms_Use.cfm

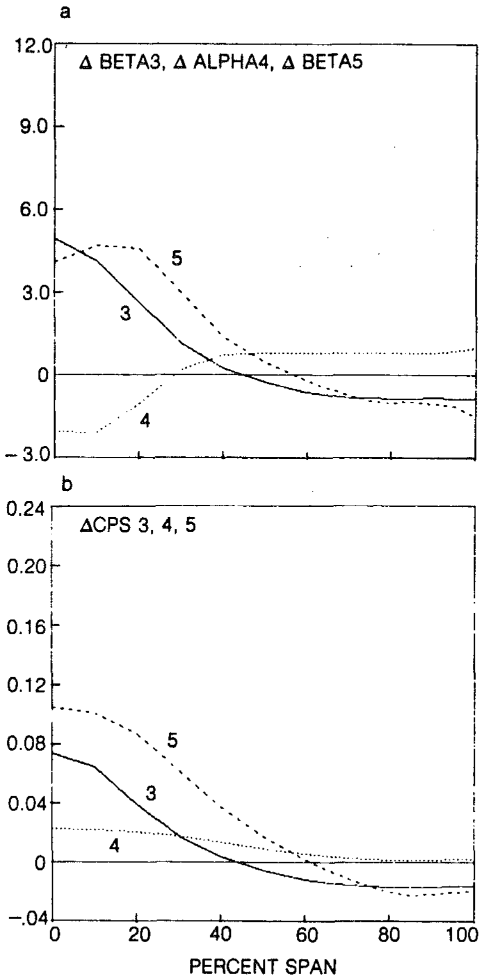

Fig. 12 Two-stage compressor throughflow analysis, $(c l/B) = 0.007$, $\phi = 0.45$; Case B: no aerodynamic blockage within airfoil rows and aero blockage $\neq f(\text{span})$

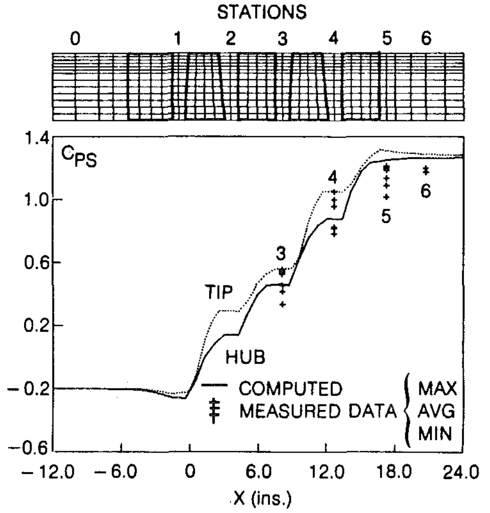

Fig. 13 Two-stage compressor throughflow analysis, $(c l/B) = 0.007$, $\phi = 0.45$; Case C: no aerodynamic blockage

magnitude of the errors incurred by simply using a constant value of blockage across the span. This was investigated by taking the spanwise mass-averaged aerodynamic blockage at the trailing edge, traverse, and leading edge planes from the base case ($\phi = 0.45$, $c l/B = 0.007$) and substituting these constant values from hub to tip at each axial station. At the first stator trailing edge and at Station 3 a constant blockage of 6.8 percent ($\bar{K} = 0.932$) was used instead of the measured distribution (Fig. 3*c*). At the second rotor exit and at Station 4 a constant value of 3.1 percent was used in place of the measured profile (Fig. 6*c*). At the second stator exit and at Station 5 a constant value of 11.3 percent was used in place of the measured profile which reached a maximum value of 39 percent at the hub (Fig. 8*c*). As in Case A above, the aerodynamic blockage within the airfoil rows had also been eliminated. Figure 12 shows how this case differs from the base case in terms of the spanwise distributions of static pressure and incidence at the three traverse planes. The changes plotted represent Case B values minus the base case values. At the first and second stator exits (Stations 3 and 5) the changes are large in comparison to the changes at the second rotor exit (Station 4). This is due to the relatively low level of blockage at the rotor exit compared to the stator exits, 3.1 percent versus 6.8 and 11.3 percent. The evidence for this

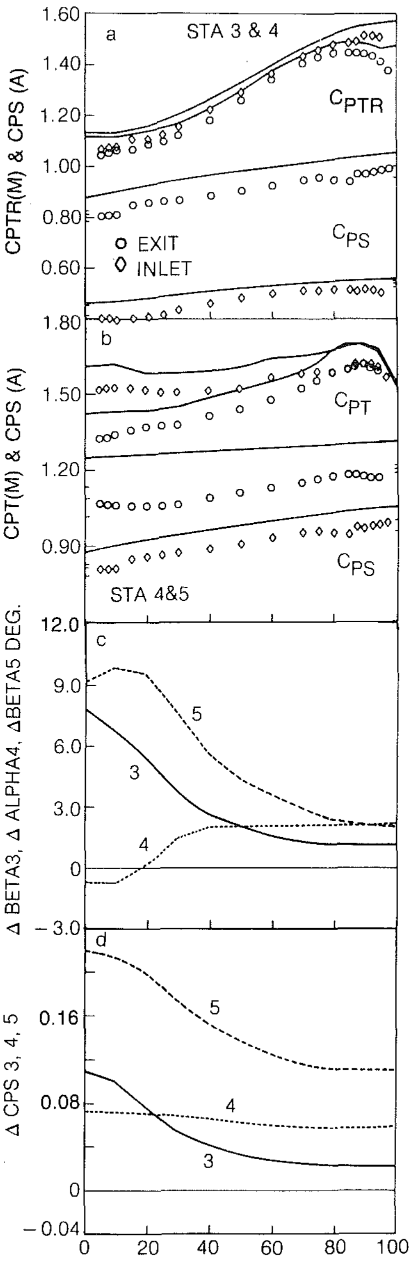

Fig. 14 Two-stage compressor throughflow analysis $(c l/B) = 0.007$, $\phi = 0.45$; Case C: no aerodynamic blockage

Downloaded 01 Jun 2010 to 171.66.16.57. Redistribution subject to ASME license or copyright; see http://www.asme.org/terms/Terms_Use.cfm

can also be seen in the blockage profiles for the large clearance case (Figs. 3*c*, 6*c*, and 8*c*). The high levels of blockage near the hub at the stator exit cause a major change to occur at the hub (Fig. 12) when they are replaced with a much lower constant value. For example, at the hub at the second stator exit the spanwise constant blockage has caused an increase in the hub static pressure (ΔC_{PS}) of 0.10, or 29 percent of the stator exit dynamic pressure. It has also increased the relative flow angle (incidence on the downstream row) by about 4 deg. The conclusion here is that using the correct spanwise distribution of blockage is important in correctly predicting the flow. For this case there is a local 1 deg error in incidence for every 7 percent error in local blockage. From this comparison it is clear that the computed flows are sensitive to the spanwise distribution of aerodynamic blockage. The sensitivity to the level of blockage will be considered below in Case C.

Case C: No Aerodynamic Blockage. As an assessment of a worst case condition in terms of blockage a calculation was carried out without any aerodynamic blockage ($\bar{K} = 1$) either within or between airfoil rows. Since the impact of eliminating aerodyamic blockage within the airfoil rows was negligible, as demonstrated in Case A, the major impact of the present case will be in eliminating aerodynamic blockage between the airfoil rows (at the trailing edge, traverse, and leading edge planes). The computed flowpath static pressure distribution is shown in Fig. 13. Comparison of these results with the base case (Fig. 11) shows that the elimination of blockage has had a major impact throughout the compressor and especially at the second stator trailing edge where the measured aerodynamic blockage had been large (39 percent near the hub). The computed spanwise distributions of the second rotor and stator, inlet and exit, total and static pressures are compared with the measured distributions in Figs. 14(*a*) and 14(*b*). In addition, the differences between this prediction and the base case prediction of the spanwise distributions of the incidence on downstream airfoils and static pressure are shown in Fig. 14(*c*) and 14(*d*). The absence of blockage has caused significant errors in the total and static pressures. At the first stator exit traverse plane (Station 3) Fig. 14(*d*) shows that the static pressure error (ΔC_{PS}) reaches a maximum of about 0.10 and that at the second rotor exit traverse plane (Station 4) it is typically 0.08. At the second stator exit traverse plane (Station 5) the static pressure error is typically 0.14 and it rises to 0.22 at the hub. These errors correspond to 53 and 83 percent, respectively, of the second stator exit dynamic pressure. At this plane the computed incidence for a downstream rotor (Fig. 14*c*) would be in error by typically 5 deg and by 10 deg near the hub. The positive incidence error indicates a rotor relative inlet angle which is 10 deg too high.

By comparing Case C (with no blockage) to Case B (with constant aerodynamic blockage between the airfoil rows) it is possible to isolate the effect of the level of aerodynamic blockage from the effect of the spanwise distribution of aerodynamic blockage. Comparing Figs. 12(*a*) and 12(*b*) (Case B) with Figs. 14(*c*) and 14(*d*) (Case C) indicates that the spanwise distribution of aerodynamic blockage has a significant impact on the spanwise distributions of static pressure and incidence and that the level of aerodynamic blockage has a significant impact on the levels of static pressure and incidence. The differences between Cases B and C from the base case are very similar in spanwise variation but they are significantly different in level. In this qualitiative sense these results are identical to what was observed in the sensitivity analysis of the design point case [1, 2].

Conclusions

An assessment of throughflow theory has been carried out by comparing the prediction of a modern finite element throughflow analysis with a benchmark data base acquired on a two-stage compressor operating at near-stall conditions. The benchmark data base was used to supply the aerodynamic input required by the analysis including loss, deviation, and blockage. The following conclusions were drawn:

1 It is essential to obtain an accurate pitchwise average of the hub and tip static pressures for comparison with a throughflow analysis. The circumferential variation can be a large fraction of the hub-to-tip difference (Figs. 2 and 11).

2 Given adequate input, there is every expectation that a reasonably accurate prediction will result (Figs. 2–10). The major discrepancies occur near the endwalls where blockage is high.

3 The description of aerodynamic blockage [8] used in this and the previous assessments [1–3] has produced an accurate prediction of most aspects of the flow field.

4 The levels of blockage in the two-stage compressor increased dramatically as the flow coefficient was reduced from the design value to the near-stall value. On the second stator the local hub blockage reached a maximum of 39 percent and extended out to 70 percent span (Fig. 8*c*).

5 There has been a general deterioration in agreement between the measured and computed results in going from the design to the near-stall condition. This disagreement is most severe in regions of high blockage (e.g., Fig. 9).

6 The measured and computed results were in closer agreement for the case with the small rotor tip clearance than for the large clearance (Figs. 2 and 11). This is to be expected due to the more strongly three-dimensional nature of the flow with the large rotor tip clearance.

7 For this low-speed flow case computed results at locations between adjacent airfoil rows were mainly dependent on the blockage profile at that location and only weakly dependent on the blockage within the airfoil rows.

8 The computed results are strongly dependent on the spanwise distribution of aerodynamic blockage. It was demonstrated that using the correct level of blockage but the wrong distribution (i.e., a constant) produced significant errors in both static pressure and incidence (Fig. 12). At the second stator exit the local static pressure error was 30 percent of Q and the local incidence error was 4 deg.

9 The spanwise distribution of aerodynamic blockage has a significant impact on the spanwise distributions of static pressure and incidence and the level of aerodynamic blockage has a significant impact on their levels (Figs. 12–14). At the second stator exit with all blockage removed the local static pressure error was 83 percent of Q and the local incidence error was as high as 10 deg.

10 All of the various shortcomings of throughflow theory brought to light in this assessment are closely related to regions of high blockage. It appears that a more precise formulation of throughflow theory will be required to resolve these difficulties. Such a formulation must include a formal treatment of the various averaging processes that are used to deal with the nonaxisymmetries that exist in the flow, i.e., the area-averaged continuity equation, the area-average radial momentum equation, and the mass flux weighted average conservation quantities (see for example [9]).

Acknowledgments

The two-stage compressor data were acquired under funding from the Pratt and Whitney Engineering Division of UTC and from the United Technologies Research Center. This assessment of throughflow theory was carried out under Navy funding under the direction of Dr. Raymond Shreeve, Contract No. N00014-85-C-0657.

Downloaded 01 Jun 2010 to 171.66.16.57. Redistribution subject to ASME license or copyright; see http://www.asme.org/terms/Terms_Use.cfm

References

1 Dring, R. P., and Joslyn, H. D., "Through-Flow Modeling of a Multi-Stage Compressor: Part I – Aerodynamic Input," ASME Journal of Turbomachinery, Vol. 108, No. 1, 1986, pp. 17–22.

2 Dring, R. P., and Joslyn, H. D., "Through-Flow Modeling of a Multi-Stage Compressor: Part II – Analytical-Experimental Comparisons," ASME Journal of Turbomachinery, Vol. 108, No. 1, 1986, pp. 23–31.

3 Dring, R. P., and Joslyn, H. D., "Through-Flow Modeling of Axial Turbomachinery," ASME *Journal of Engineering for Gas Turbines and Power*, Vol. 108, No. 2, 1986, pp. 246–253.

4 Joslyn, H. D., and Dring, R. P., "Axial Compressor Stator Aerodynamics," ASME *Journal of Engineering for Gas Turbines and Power*, Vol. 107, 1985, pp. 485–493.

5 Dring, R. P., Joslyn, H. D., and Wagner, J. H., "Compressor Rotor Aerodynamics," *Viscous Effects in Turbomachines*, AGARD-CP-351, Copenhagen, Denmark, June 1–3, 1983, Paper No. 24.

6 Habashi, W. G., and Youngson, G. C., "A Transonic Quasi 3-D Analysis for Gas Turbine Engines Including Split-Flow Capability for Turbofans," *International Journal for Numerical Methods in Fluids*, Vol. 3, 1983, pp. 1–21.

7 Habashi, W. G., "Numerical Methods for Turbomachinery," in: *Recent Advances in Numerical Methods in Fluids*, C. Taylor and K. Morgan, eds., Pineridge Press, United Kingdom, 1980, Chap. 8.

8 Dring, R. P., "Blockage in Axial Compressors," ASME *Journal of Engineering for Gas Turbines and Power*, Vol. 106, 1984, pp. 712–714.

9 Hirsch, Ch., and Dring, R. P., "Through-Flow Models for Mass and Momentum-Averaged Variables," ASME Journal of Turbomachinery, Vol. 109, 1987, pp. 362–370.

Downloaded 01 Jun 2010 to 171.66.16.57. Redistribution subject to ASME license or copyright; see http://www.asme.org/terms/Terms_Use.cfm

Stall Cell Development in an Axial Compressor

A. D. Jackson
Turbine Design Engineer,
Peter Brotherhood Ltd.,
Peterborough PE4 6AB, United Kingdom

An experimental investigation of stall inception and stall cell development in a single-stage axial compressor is described. The stall inception was found to be naturally nonrandom: By artificially perturbing the flow the inception could be accurately fixed at a known location in the compressor. The stall cell was first detected behind the rotor at a small distance from the tip. The stall cell grew very rapidly in circumferential extent, but slowly in radial extent. After reaching the hub the cell decreased in size before reaching full development as a single full span rotating stall cell. Relationships between various parameters of the stall cell growth are presented. The growth is explained in terms of the cell blockage, and the mechanism for multiple stall inception is discussed.

Introduction

Rotating stall remains a major problem in the design and operation of axial compressors. It restricts the operating range, indirectly reduces the efficiency (because of the need to provide a stall margin between the running line and the surge line), and may threaten the physical integrity of the compressor. There has recently been a resurgence of interest in rotating stall, the work of Day et al. [1, 2] inspiring a number of studies of the stall cell structure [3-5]. After the work of Greitzer [6, 7], and encouraged by the problem of "stagnation stall" in some recent aircraft gas turbines, many theoretical studies of the compressor system have also been reported.

However, although stall inception has received considerable theoretical treatment, the basic mechanism for inception has still to be elucidated. A description of stall inception is required to provide a model for numerical methods, and to enable more accurate correlations for the stall point. While the prediction of the stalling flow rate and pressure rise of a compressor system and the details of the fully developed stall cell have been the subject of many studies, very little experimental work has been reported on the inception and development of the stall cell.

The steps in the stall initiation sequence can be classified in the following way: As the throttle is closed on an axial compressor, the flow rate will decrease and the pressure rise increase until the compressor is on the point of stall. A further reduction in flow rate will cause stall inception: here "stall inception" is used to describe only the process which starts the sequence of events leading to rotating stall. The stall inception is followed by the "stall cell development," a period of typically ten rotor revolutions during which the stall cell grows from a very small cell to "fully developed rotating stall."

The literature on stall inception and stall cell development is minimal. Lakwani and Marsh [8, 9] give the time for stall cell growth as seven to ten revolutions on an isolated rotor, but make no measurements during the stall cell development. Greitzer [6] shows the change in stall cell angular extent with time after inception to give the timescale for the stall transient in a discussion of the compressor system instability. The work that has been found most relevant to stall cell development is that of Emmons et al. [10], which gave the classic explanation for stall propagation. Although the basic concept forms only one paragraph of their paper, the ideas will be shown to explain most of the observed features of the stall cell growth.

The nature of stall inception has also been treated in papers on the effect of casing treatment and tip clearance on compressor performance. A number of mechanisms for stall inception have been proposed: Blade stall (limiting incidence on a bladerow) was first proposed by Emmons et al. [10] as the basic mechanism for propagating stall. Wall stall, the separation of the annulus boundary layer, has been discussed by Greitzer et al. [11]. The relationship between blade stall and wall stall has also been described in terms of blockage behind the rotor tip by Smith and Cumpsty [12]. Freeman [13] has taken the results of Smith and Cumpsty and related them to some early measurements from the current program [14], and suggested that stall inception may be due to collapse of the tip clearance vortex.

The primary goal of the research work described here was to elucidate the detailed fluid mechanics of the stall inception. This has proved difficult due to the problems associated with locating and identifying the stall cell at, or shortly after, inception. In the course of the investigations a number of techniques for examining stall inception were developed. The basic approach was to develop a method for capturing the developing stall cell, and examine a large number of stall inception events. The results of this work showed that many features of the stall inception were naturally nonrandom due to small discrepancies in the blading. By making adjustments to the blading and blockage in the rig it was found possible to fix the inception to a known rotor blade and annulus position, thus opening the way to future detailed measurements of stall inception itself.

The second objective of the research was to provide a basic

Contributed by the Gas Turbine Division of The American Society of Mechanical Engineers and presented at the 31st International Gas Turbine Conference and Exhibit, Düsseldorf, Federal Republic of Germany, June 8-12, 1986. Manuscript received at ASME Headquarters February 21, 1986. Paper No. 86-GT-249.

Copyright © 1987 by ASME

Downloaded 01 Jun 2010 to 171.66.16.57. Redistribution subject to ASME license or copyright; see http://www.asme.org/terms/Terms_Use.cfm

description of the stall cell development. Precise relationships for the important parameters of the stall cell development were not sought, and the experimental procedure was intended to give an overview of the features rather than detailed measurements of the flow structure. For this reason the experimental approach was relatively simple, relying on the analysis of a large amount of basic data. The results give some graphic impressions of the stall cell development and some qualitative relationships between the main parameters.

A basic description of the stall cell development is proposed to explain the experimental observations, which include the delay between inception and the initial stall cell deceleration, the rapid circumferential growth compared to the radial growth, and the stability of the part-span stall cell during the middle stages of the development. The blockage model of Emmons et al. [10] can be used to explain many of the features of the cell. An interesting application of, and supporting evidence for, the blockage model is given in an analysis of secondary stall inception.

Experiment

In this section the rig and instrumentation are described, followed by a brief discussion of the steady-state performance which has relevance to the stall inception. The problems of investigating stall inception are then discussed in more detail and related to a description of the experimental techniques and interpretation of the results.

A large single-stage compressor of 0.7 hub-tip ratio was used for the project. The stage was intended to model the behavior of a modern aircraft high-pressure compressor stage at low speed. There were 51 blades on the rotor and 36 on the stator, giving midspan solidities of 1.43 and 1.01, respectively. The outer diameter of the rig is 1.524 m and the blades were 228.6 mm long. The rotor and stator were of C4 section on a circular arc camber line, with chords of 110 mm and 114.6 mm, respectively. The design was free vortex at a flow coefficient of 0.6; the rotor speed was 500 rpm. The air is drawn in through a bellmouth with a 6.6:1 contraction ratio into a parallel annulus. The hub bullet is supported by fifteen 6 mm struts upstream of the rotor and 50 mm struts downstream of the stator. An annular diffuser precedes the throttle, which is formed of 12 flat vanes.

The rig and steady-state performance have been described in more detail by Dong et al. [16] and Jackson [14]. The most important features with respect to the stall inception are the loading levels along the blade span. The diffusion factor decreases from hub to tip on both rotor (0.63 to 0.5) and stator (0.65 to 0.58) at the stall point; the stator is more highly loaded than the rotor. This would suggest a likelihood of separation and thus the probability that the stall would initiate at the stator hub. The region of separation that was found even at the peak efficiency flow coefficient of 0.55 is reported and discussed by Dong et al. [16]. However, it will be shown, from direct measurement of the stall inception, that the stall was first detected near the rotor tip, notwithstanding the greater diffusion factors elsewhere.

The instrumentation comprised a number of standard constant temperature hot-wire anemometers. These were positioned with one wire upstream of the rotor and up to six arrayed radially behind the rotor, and sometimes one wire downstream of the stator. For a standard hot-wire probe the variation in apparent velocity with yaw angle relative to the true velocity is within 10 percent of the cosine of the yaw angle for angles of less than 60 deg. By mounting the wires perpendicular to the axial and radial directions, the magnitude of the axial velocity could be measured with acceptable accuracy provided the radial velocity could be assumed small. However, reverse flow could not be differentiated by this method, but had to be inferred in stall cells where the velocity passed through zero. Reverse flow regions were found in fully developed stall cells and also within the stall cell during stall cell development.

At the outset the experimental method adopted was based on the assumption that the location of the stall inception was likely to be random within a particular blade row, occurring at an unknown time. Conventional ensemble averaging techniques cannot be used during the stall inception and stall cell development because the cell is not periodic in size or speed. Because of the likely randomness in position it was also not possible to ensemble across stall events. Thus the data had to be examined in a relatively unprocessed and thus unfamiliar form, with the turbulence and random unsteadiness masking the stall inception. The flow is generally nonsteady and the first clear evidence of stall occurs long after its inception when the cell is quite large; the inception event is not distinguishable, without guidance, from the background unsteadiness.

The results were acquired by a computer via an analog-to-digital converter, using a continuous recording routine to remove the uncertainty in the time of the inception. The compressor would be run in its unstalled condition with the data logging program operating. The throttle would then be closed very slowly so that the compressor operating point was essentially steady and throttle changes of the period of data collection could be ignored. The leading edge of the first stall cell of appreciable size was detected using a hot wire upsteam of the rotor. The data were then stored with a predetermined amount of data recorded on either side of the trigger. In this way attention could be focused on the inception, using a high logging frequency and short time after the trigger; or on the stall cell development, using a low logging frequency and recording most of the results after the first detected cell. The data were filtered at half the logging frequency to avoid aliasing, according to the Nyquist criterion; to produce low frequency results the data were also digitally filtered during processing.

A number of stall events were recorded in each experimental series, so that the repeatability of the stall inception could be analyzed. A small magnet was buried in the tip of one rotor blade to provide a once-per-rev pulse, which enabled the rotor position to be related to the instrumentation and the developing stall cell. Results from downstream of the rotor were unsteady, and the edges of the stall cell could not be distinguished clearly. For this reason, a single hot wire upstream of the rotor was used to provide quantitative measurements of the position of the stall cell relative to the rotor trigger pulse, the period of revolution of the stall cell and the circumferential extent of the stall cell. A second upstream wire at a different circumferential location was used to estimate the speed of the stall cell. The radial array of wires downstream of the rotor was used to determine the radial extent of the cell, and to investigate the nature of the inception.

Stall Inception

A typical set of results is presented in Fig. 1. The approximate axial velocities from six hot wires positioned (reading from the top): behind the stator, 0.131 span from the hub; behind the rotor at 0.488, 0.751, 0.882, and 0.969 span from the hub; and upstream of the rotor 0.869 span from the hub. The stall cell is first detected at time 1, extending over 14 percent of the circumference – about seven rotor blade pitches. The stall cell is most clearly visible downstream of the rotor at 0.882 and 0.751 span. At 0.969 and 0.488 span there are local increases in flow rate, which may be due to the blockage of the developing stall cell. There is no indication of stall behind the stator hub.

A second appearance of the stall cell at time 2 shows that the cell has developed much further. A local increase in the

Downloaded 01 Jun 2010 to 171.66.16.57. Redistribution subject to ASME license or copyright; see http://www.asme.org/terms/Terms_Use.cfm

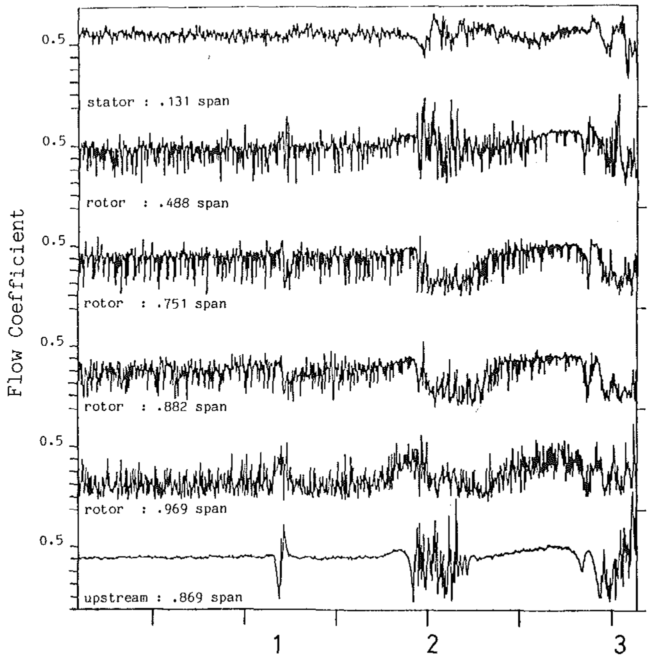

Time - Record Léngth 0.667 seconds

Rotor trigger positions are shown on the time axis

Fig. 1 Stall inception showing three appearances of the stall cell and a small secondary cell

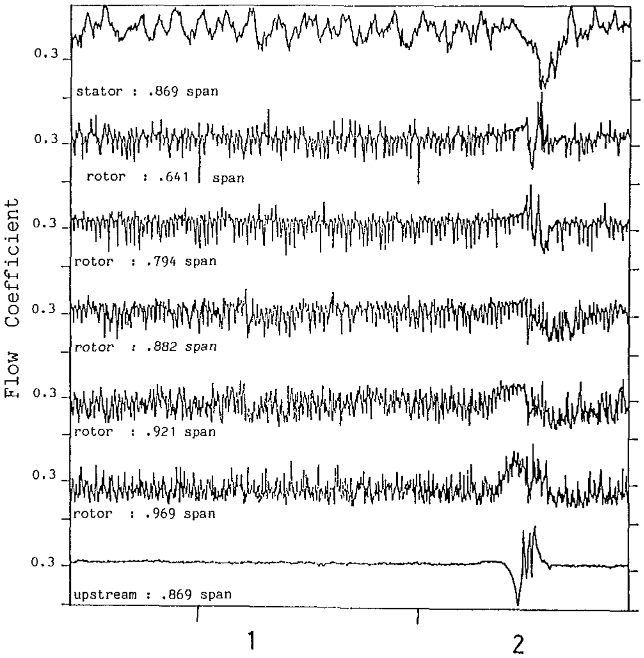

Time - Record Length 0.3 seconds

Fig. 2 Stall inception observed at high frequency, showing the stall cell shortly after inception

flow rate as the cell approaches is most apparent 0.969 span downstream of the rotor. This is due to the upstream flow being turned by the blockage of the stall cell, as described by Emmons et al. [10]: A slight decrease in the flow rate at the trailing edge of the cell (where the rotor is stalling) can be observed downstream of the rotor. At time 2 the cell has extended beyond midspan and has been detected downstream of the stator near the hub.

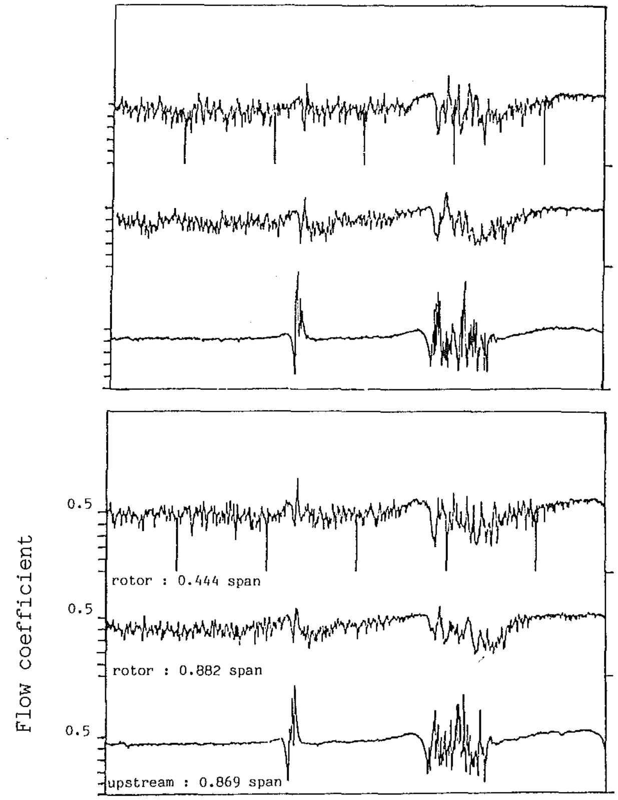

Time - Record Length 0.667 seconds

Fig. 3 Two stall events recorded from the same series, showing repeatable features

A third appearance of the cell at time 3 is preceded by a small secondary stall cell which has little circumferential extent but reaches over more than half the span in radial extent. (This phenomenon is not due to reversed flow, but rather to the formation of a second stall cell, and is discussed in detail later.) The flow rate outside the stall cell has increased: This can be seen upstream of the rotor as an increase in axial velocity, and downstream of the rotor as a decrease in the depth of the blade wakes. At 0.969 span downstream of the rotor there is a dramatic increase in the mean axial velocity as the annulus boundary layer becomes thinner due to the increased unstalled flow rate.

The data shown in Fig. 1 are typical of several hundred stall events that have been studied on the compressor. In most cases the stall cell started near the tip, and a single full-span rotating stall always resulted. (There was evidence for stall at the stator hub in only two cases. The evidence for stall inception on the rotor near the tip was overwhelming.) Figure 2 shows high-frequency measurements of a stall cell shortly after stall inception. The stall cell is clearly visible at time 2, extending through the annulus boundary layer and affecting the flow behind the stator. The stall cell is detected earlier at time 1, but only on wires located downstream of the rotor at 0.926 and 0.882 span. The circumferential influence of the cell appears to be two to three blade pitches, but the radial development is very limited. There is no evidence of the cell at 0.969 span, which suggests that the inception mechanism is not related to annulus boundary layer separation.

The standard experimental sequence for investigating stall inception was to take ten sets of results for given probe positions and logging frequency, in order to observe any repeatable features of the stall cells among the background unsteadiness. During the course of such investigations it was noted that results from different stall events were sometimes

Downloaded 01 Jun 2010 to 171.66.16.57. Redistribution subject to ASME license or copyright; see http://www.asme.org/terms/Terms_Use.cfm

much alike. Figure 3 shows limited results from two stall events from the same series. The most significant features are the similar size of the stall cell at first detection and the position of the rotor trigger relative to the stall cell. These features suggest the same rotor blade and circumferential position for the inception. In addition, the rotational speed to the second appearance is the same, and even the larger features of the unsteadiness within the stall cell are the same. The effect of overlaying the full results is uncanny, suggesting a highly repeatable process with a small amount of unsteadiness rather than a random process.

Nine of the ten results in this series showed the stall cell at the same position relative to the rotor, with some variation in the stall cell size. This suggested that there was a tendency within the compressor for stall to initiate on one rotor blade at a small number of circumferential positions. The level of distortion required to fix the position of the stall inception uniquely was then investigated.

In order to fix the inception in the stationary frame of reference, a wire mesh (of solidity 0.392) was used to reduce the flow through a single stator passage, thus causing a distortion to the flow and forcing the rotor to work at a lower local flow coefficient. The stagger of a single rotor blade was reduced in order to increase the flow incidence onto the blade and hence the likelihood of fixing the inception at that (known) blade. A systematic series of tests directed to reducing the distortion required to fix the inception is described in detail in [14]. If the blade stagger was reduced too much then multiple stalling resulted, but if the change in stagger was insufficient, then the inception occurred on more than one blade, showing a preference due to small differences in the blading. In the best results all ten stall events had the same measured lag with a small scatter. With such a high degree of repeatability, ensemble averaging across the stall events might be possible with sufficient computing power.

Although the stall inception was fixed in the stationary frame of reference, it has not proved possible to move the inception around the circumference. A series of experiments to validate the effect of moving the stator mesh around the circumference gave inconclusive results: In all the experiments the position of the stall cell relative to the rotor and size of the cell at first appearance remained constant. This was perhaps caused by a distortion within the compressor greater than that produced by the mesh. Such a distortion might be caused by dirt in the intake screens, inlet distortion (perhaps a ground vortex), the hub support struts, or variable tip clearance on the stator blades at the hub [16].

Given sufficient distortion of the flow and restaggering a single blade, the stall inception could be fixed in both rotor and stator frames of reference. The stall inception could be moved from one blade to another by changing the individual blade staggers: The decrease in stagger required varied from blade to blade as stall occurred preferentially on some parts of the rotor. The overall impression of the investigation was that the stall inception was not random, but was strongly influenced by small discrepancies in the blading.

Stall Cell Development

Figure 4 shows velocity traces from seven hot wires during the stall transient; the positions of the hot wires from the hub are shown on the figure. The lowest record is the axial velocity from a single hot wire located one axial chord upstream of the rotor, 0.869 span from the hub, just outside the annulus boundary layer. A rake of hot wires was mounted 1.7 axial chords downstream of the rotor. The record length is 2 s, and the data have been digitally filtered at 50 Hz to remove the unsteadiness due to the blade passing frequency. The positions of the rotor trigger and appearances of the stall cell are noted on the horizontal axis.

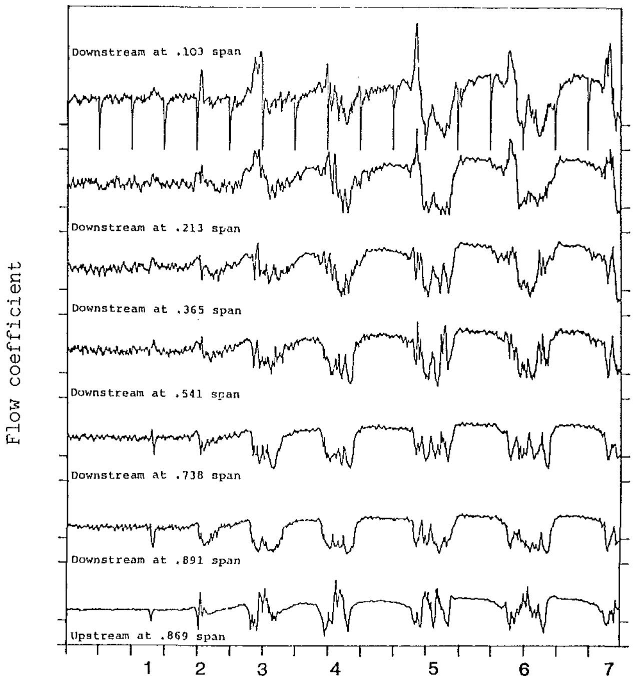

Time Axis - Record length 2 seconds
(Rotor trigger positions indicated)

Fig. 4 Stall inception and stall cell development, filtered to remove blade passing frequency

At time 1 the cell is recorded upstream of the rotor and at 0.891 and 0.738 span downstream of the rotor. There is also a small increase in the flow at 0.541 span, caused by the blockage of the small stage cell. At time 2 the stall cell has increased in size and developed radially to 0.365 span, with the blockage causing an increase in flow at the hub. At time 3 the stall cell is fairly well developed at the tip and has extended to about 0.213 span. There is a dramatic increase in the local flow rate near the hub, but the flow pattern suggests that the stall cell has not yet extended to the hub, but rather that the blockage caused by the part-span stall cell has caused an increase in the flow rate near the hub.

At time 4 the stall cell has reached the hub, after about six rotor revolutions from inception. There is a considerable decrease in the stall cell speed observed by a stationary observer because the larger stall cell rotates faster relative to the rotor, suggesting that the mechanism for propagation has been strengthened as the fully developed stall cell becomes established. At time 5 the shape of the stall cell indicates that the stall cell has reached full development. The overall sequence (which has been observed in many stall events) is: (*a*) inception at a small distance from the rotor tip; (*b*) growth of a part-span stall cell with the stall cell increasing in circumferential, radial and axial extent while decelerating from near rotor speed at inception down to about 34 percent of the rotor speed, until it forms (*c*) a single fully developed full-span rotating stall cell.

Figure 5 gives an alternative presentation of the same results: The edges of the cell have been estimated to be where the local velocity is more than 2 m/s above or below the axial velocity of the flow outside the stall cell. The stall cell circumferential extent has been estimated as a fraction of the stall cell period of rotation from Fig. 4. This is an approximation because the stall cell decelerates during its development and the probes are located at only a single circumferential position. However the extremely rapid circumferential development compared to radial development and the transi-

Downloaded 01 Jun 2010 to 171.66.16.57. Redistribution subject to ASME license or copyright; see http://www.asme.org/terms/Terms_Use.cfm

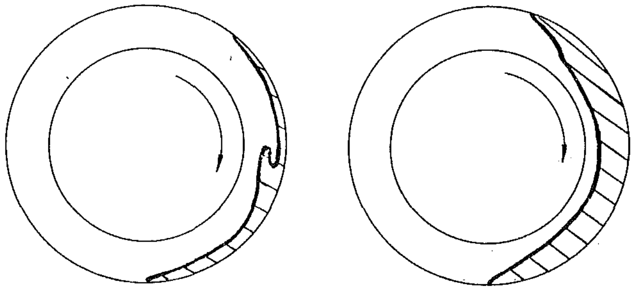

Second Appearance. Third Appearance.

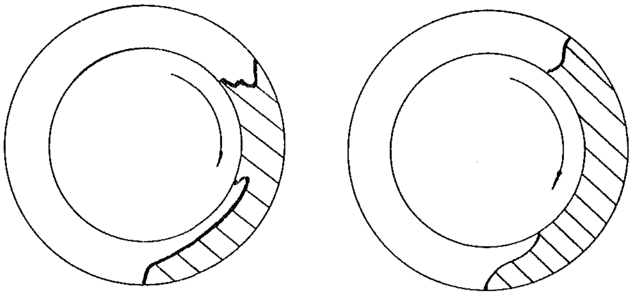

Fourth Appearance. Fifth Appearance.

Fig. 5 The compressor annulus showing the stall cell from Fig. 4 at its second to fifth appearances

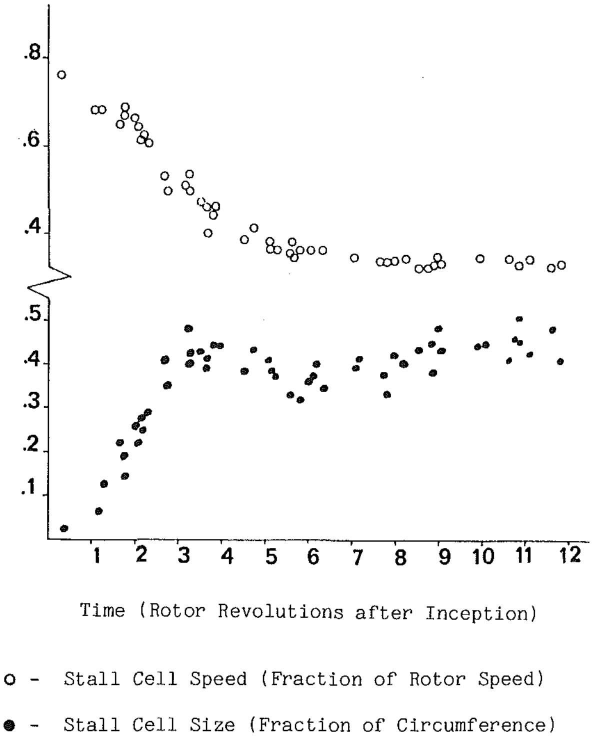

Fig. 6 Variation of the stall cell speed and size with time after inception

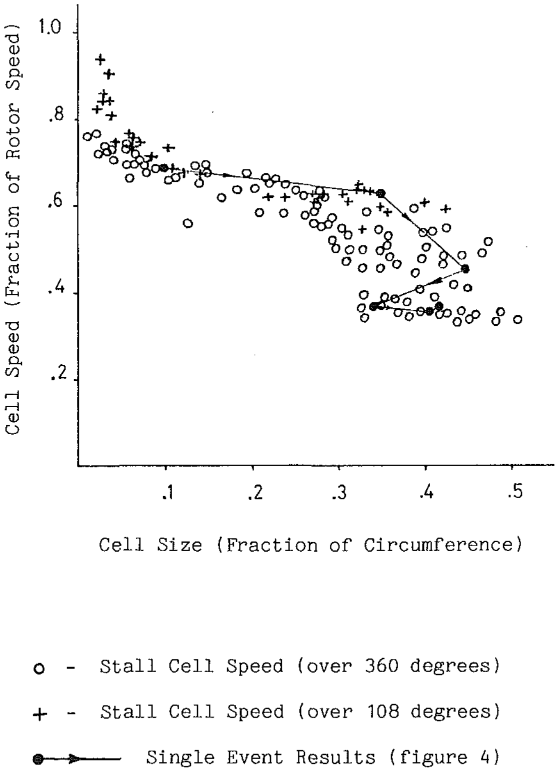

Fig. 7 Variation of the stall cell speed with stall cell size

tion from part-span to full-span stall are clear in this view. When the stall cell reaches the hub and forms a full-span cell the circumferential extent decreases.

Figure 6 shows the variation of the stall cell mean speed and size with time. The time at inception has been estimated for ten stall events of which Fig. 4 shows one, and the figure is intended to show the trend rather than detailed results. The stall cell speed is the reciprocal of the period of rotation, and is thus the average speed over one revolution. The speed drops steadily from around 76 percent of the rotor speed over its first revolution to 34 percent of the rotor speed at full development after about eight rotor revolutions after inception.

The stall cell size increases rapidly to about 40 percent of the circumference (defined as rotor period divided by the stall cell period). The stall cell size (measured by a single wire upstream of the rotor) drops slightly before rising to about 44 percent of the circumference at the stall throttle setting.

Figure 7 shows the stall cell speed plotted against the stall cell size. Here it is clear that the stall cell speed is not a function of the cell size when the cell extends over more than 25 percent of the annulus. The results from a single stall event (Fig. 4) are highlighted (solid circles) in order to show the variation through the stall cell development. By reference to Fig. 4, it can be seen that the stall cell size and speed fall when the stall cell reaches the hub. A reduction in speed in the stationary frame of reference is equivalent to an increase in speed relative to the rotor. The driving mechanism for the propagation of the stall cell has been strengthened. This is possibly due to the "active" cell becoming established across the span.

With a second hot wire upstream of the rotor circumferentially displayed from the first, the stall cell speed can be measured more accurately. The crosses on Fig. 7 show the speed measured with two upstream sensors at 108 deg separation, for the earliest part of the development. The inception time could not be determined with sufficient accuracy to plot these results against time, so the stall cell size is used as the abscissa. When first detected the stall cell speed is 95 percent of the rotor speed. After inception, the stall cell begins to extend by stalling at its trailing edge, but at the leading edge unstalling will not begin until there is sufficient blockage to turn the flow upstream of the rotor. Thus the leading edge of the stall cell will rotate at the rotor speed for a time, which is estimated to be about 0.5 rotor revolutions. Once the leading edge on the rotor has begun to unstall there is a rapid deceleration to around 61 percent of the rotor speed, after which the speed is constant until the stall cell reaches the hub. (No data

Downloaded 01 Jun 2010 to 171.66.16.57. Redistribution subject to ASME license or copyright; see http://www.asme.org/terms/Terms_Use.cfm

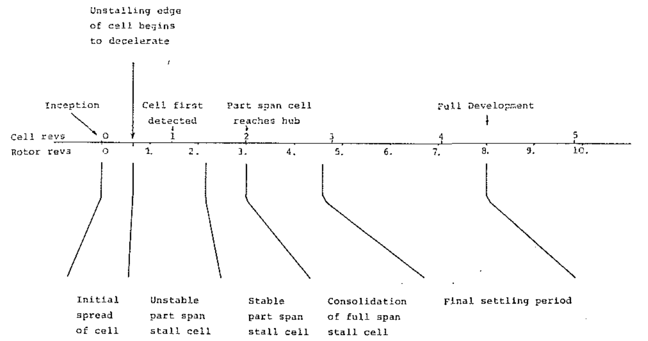

Fig. 8 A typical sequence of events leading from unstalled flow through stall inception and stall cell development to fully developed rotating stall

are available for the later stages of development.) In the later stages of the part-span stall cell development the deceleration is very slow, and the speed measured over one revolution is similar to that measured over 108 deg. Thus the approximation involved in plotting Figs. 5 and 6 is valid for much of the stall cell development.

Discussion

The basic features of the stall cell development can be explained in the following way:

After the stall inception a small stall cell will be formed at about 90 percent span which might have a radial extent of 10 percent of the span and a circumferential extent of one blade pitch. The embryo cell is rotating at the rotor speed (Fig. 7). The flow is diverted around the small cell, causing an increase in the local flow rate above and below the cell, and also turning the flow at the leading and trailing edges of the cell.

As explained by Emmons et al. [10], rotor blades will show a reduced tendency to stall at the leading edge of the cell, and an increased tendency to stall at the trailing edge. The blockage provides a driving mechanism in the circumferential direction without a similar effect in the radial direction, so that the stall cell grows much more rapidly in the circumferential direction than in the radial direction (Fig. 5). Because of the hysteresis between stalling and unstalling for an individual blade, there will be a delay between the inception and the cell beginning to rotate relative to the rotor: Unstalling will not begin until the flow upstream of the rotor has been turned sufficiently by the cell blockage. Thus the stall cell speed (measured at the leading edge) will be the same as the rotor speed for a period which has been estimated to be as much as 0.5 rotor revolution after inception.

Figure 8 outlines the sequence of events, with a typical timescale also indicated. Once the stall cell has begun to decelerate and has extended to the tip, the development proceeds steadily toward the hub. During the early stages of the development growth is rapid, and the cell decelerates rapidly after separating from the inception blade: The stall cell might be described as an "unstable" part-span stall cell during this period (0.5 to 2.5 rotor revolutions after inception). As the cell approaches the hub, the flow between the cell and the hub may tend to inhibit the development of the cell, which thus forms a "stable" part-span cell, where the cell speed varies only slowly (Fig. 7). After about four rotor revolutions after inception the stall cell reaches the hub, and accelerates relative to the rotor. The cell size decreases slightly before approaching the final size which is determined by the throttle setting. A fully developed full-span rotating stall cell is formed after about five cell revolutions from inception, eight to ten rotor revolutions.

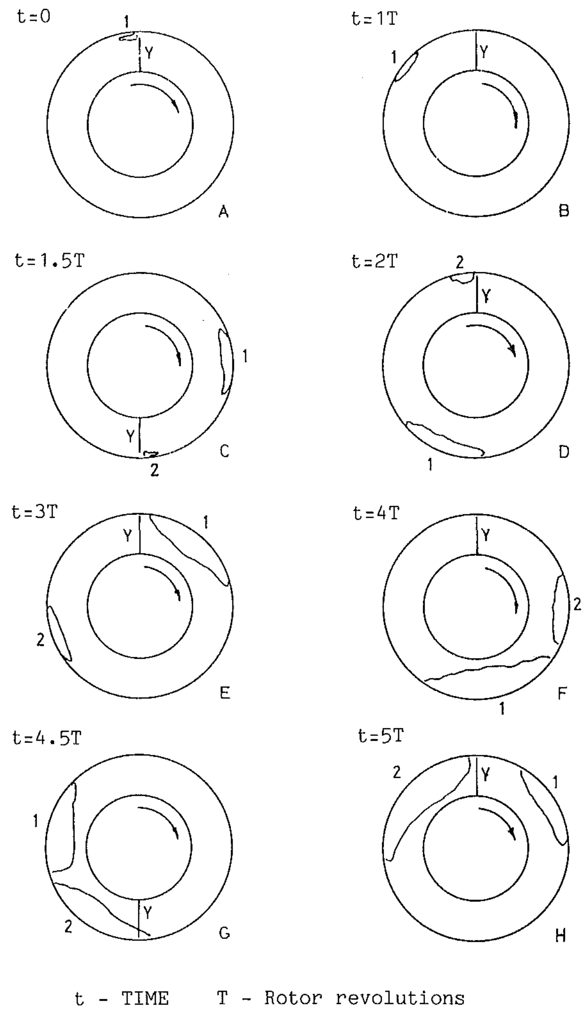

Fig. 9 Graphic description of multiple stall inception and the resulting interaction of the stall cells

Day and Cumpsty [9] have shown that the blockage model does not apply to the fully developed stall cell; thus during the stall cell development the cell changes from a "passive" cell, where the presence of the cell within the compressor is primarily to block the flow, to an "active" cell, where the flow within the stall cell dominates the compressor performance. The appearance of the flow within the developing stall cell (Fig. 4) suggests that this does not reach completion before the cell covers the whole span. The flow within the stall cell must drive the radial growth of the cell, because the effect of the cell blockage is to raise the velocity near the hub and to inhibit the radial growth. However, although the flow is clearly very complex, it is suggested that the development of the stall cell can be largely explained by using the concept of cell blockage first described by Emmons et al. [10].

Supporting Evidence – Multiple Stall Inception

Further evidence for the effects of the stall cell blockage can be gained from a study of multiple stall inception. In many stall events more than one stall cell was formed at some stage in the development, although only one cell resulted at full development. The type of multiple stall most often seen was due to repeat stalling on the inception blade. This was particularly apparent when a blade was restaggered to induce stall inception if the amount of restagger was larger than needed to fix the stall [14]. The sequence of events is illustrated in Fig. 9.

Inception occurs on a rotor blade Y, Fig. 9(*a*). As the cell develops it lags behind Y as the cell speed falls below the rotor speed, Fig. 9(*b*). Due to the blockage caused by the cell, blade Y will be able to operate unstalled as it moves out of the cell.

Downloaded 01 Jun 2010 to 171.66.16.57. Redistribution subject to ASME license or copyright; see http://www.asme.org/terms/Terms_Use.cfm

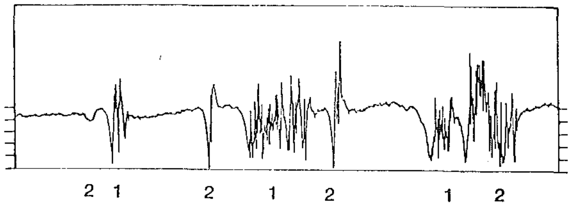

Record length 0.667 seconds

Hotwire at 0.969 span

Fig. 10 Inception and interaction of two stall cells, observed from upstream of the rotor

However, once the stall cell has moved far enough away from blade Y, the local flow rate will no longer be raised by the cell blockage and blade Y may stall again, Fig. 9(*c*). The first cell (1) is rotating at about 70 percent of the rotor speed and the new cell (2) is initially rotating at the rotor speed. Thus cell 2 will begin to catch up with cell 1, Figs. 9(*c-f*). Both the stalling and unstalling at the stall cell boundaries are driven by the blockage of the stall cells, and when cell 2 catches up with cell 1, the combined blockage will tend to increase the local flow rate between the two cells. The unstalling mechanism at the leading edge of cell 2 will be strengthened, but otherwise the cell will be unaffected. However, stalling will be inhibited at the trailing edge of cell 1, and cell 1 will decrease in size (Fig. 9*f*, *g*). As cell 1 becomes smaller it may coalesce with cell 2, or it may move away from cell 2 as its speed increases, Fig. 9(*h*). The sequence could then be repeated, but usually the unstalled flow rate has increased sufficiently to inhibit the development of small cells. Thus the cell that was initially formed (cell 1) will decay as cell 2 approaches full development (Fig. 9*g*).

Figure 10 gives experimental evidence of the sequence of events described above, with the two cells merging as cell 1 decays. Other examples of secondary inception are described in [14]. The most common example is when a second or third cell is formed at a late stage of the development (Fig. 1). Secondary cells often develop more rapidly in the radial direction as their circumferential growth is inhibited by the increasing unstalled flow rate and the presence of the primary cells, which rapidly eliminates the small cells.

The main reason for presenting and discussing Figs. 9 and 10 is to show how the cell blockage, in conjunction with experimental observations of the stall cell speed, can be used to explain the events following multiple stall inception within the single-stage compressor. This in turn strengthens the case for viewing the blockage of the small stall cell as the driving mechanism for the circumferential growth during the early stages of stall cell development.

Concluding Remarks

Observations of a large number of stall events have revealed that the stall was not stochastic. A study of stall inception has revealed that the stall is naturally located on a few rotor blades and annulus positions. With small perturbations to the compressor blading, it was found possible to fix stall inception to a known blade and annulus position, thus opening a new technique for the investigation of stall inception. Stall inception was initially observed to grow from near the tip, but detailed measurements have shown that the largest disturbance was at about 10 percent span from the tip. The early growth of the stall cell also showed signs of being highly repeatable and it was this which made it possible to detect the stall point and to study the fixing of the stall inception.

After the inception, the stall cell circumferential growth is driven by the blockage effect first described by Emmons et al. [10]. The leading edge of the cell rotates with the stalling blade for a short time before the blockage upstream is sufficient to reduce the incidence onto the stalling blade sufficiently to initiate unstalling. The stall cell then rotates as a part-span stall cell, growing more rapidly in circumferential than radial extent. The cell speed decreases as the cell grows in size. The stall cell is fairly stable as it approaches full-span development. Once the stall cell reaches the hub it decreases slightly in size; as this occurs there is a rapid deceleration. After about five stall cell revolutions a fully developed full-span rotating stall cell was formed.

The blockage effect can be used to explain many of the features of the stall cell development, for example the delay before the stalling blade first unstalls, and the rapid circumferential growth compared to the slower radial growth. A further application is to the multiple stall mechanism, where the second cell to initiate may reach full development at the expense of the first.

Further work on the stall inception is now in progress at the Whittle Laboratory. It is hoped that these results will stimulate research work on an interesting and relatively unexplored aspect of rotating stall.

Acknowledgments

This work was initiated by Dr. N. A. Cumpsty; to him go my thanks for his supervision and criticism. Mr. C. Freeman, Dr. T. P. Hynes, and Professor E. M. Greitzer all made valuable contributions during the project. The work was supported by Rolls-Royce Ltd.

References

1 Day, I. J., Greitzer, E. M., and Cumpsty, N. A., "Prediction of Compressor Performance in Rotating Stall," ASME Journal of Engineering for Power, Vol. 100, 1978, pp. 1–14.

2 Day, I. J., and Cumpsty, N. A., "The Measurement and Interpretation of Flow Within Rotating Stall Cells in Axial Compressors," *Journal of Mechanical Engineering Sciences*, Vol. 20, 1978, pp. 101–114.

3 Breugelmans, F. A. E., Mathioudakis, K., and Lambropoulos, L., "Measurement of the Radial Flow Along a Low Speed Compressor Blading During Unstalled and Stalled Operation," ASME Paper No. 83-TOKYO-IGTC-79.

4 Das, D. K., and Jiang, H. K., "An Experimental Study of Rotating Stall in a Multistage Axial-Flow Compressor," ASME Paper No. 83-TOKYO-IGTC-80.

5 Soundranayagam, S., and Balakrishnan, K., "A Model of Axial Impeller Stall," AIAA Paper No. 83-7077.

6 Greitzer, E. M., "Surge and Rotating Stall in Axial Flow Compressors. Part 1: Theoretical Compression System Model," ASME Journal of Engineering for Power, Vol. 98, 1976, pp. 190–198.

7 Greitzer, E. M., "Surge and Rotating Stall in Axial Flow Compressors. Part 2: Experimental Results and Comparisons With Theory," ASME Journal of Engineering for Power, Vol. 98, 1976, pp. 199–217.

8 Lakhwani, C. K., "The Onset of Rotating Stall in Axial Flow Compressors," Ph.D. Thesis, Cambridge University, 1973.

9 Lakhwani, C. K., and Marsh, H., "Some Observations of Stall Inception in an Axial Compressor Stage," *I. Mech. E. Conference Publication No. 3*, 1974.

10 Emmons, H. W., Pearson, C. E., and Grant, H. P., "Compressor Surge and Stall Propagation," *Trans. ASME*, Vol. 27, 1955, pp. 455–469.

11 Greitzer, E. M., Nikkanen, J. P., Haddad, D. E., Mazzawy, R. S., and Joslyn, H. D., "A Fundamental Criterion for the Application of Rotor Casing Treatment," ASME *Journal of Fluids Engineering*, Vol. 101, 1979, pp. 237–244.

12 Smith, G. D. J., and Cumpsty, N. A., "Flow Phenomena in Compressor Casing Treatment," ASME Journal of Engineering for Gas Turbines and Power, Vol. 106, 1984, pp. 532–541.

13 Freeman, C., "Effect of Tip Clearance on Compressor Stability and Engine Performance," in: V.K.I. Lecture Series *Tip Clearance Effects in Axial Turbomachines*, Apr. 1985.

14 Jackson, A. D., "Stall Inception in Axial Compressors," M.Sc. Thesis, Cambridge University, 1985.

15 Dong, Y., Gallimore, S. J., and Hodson, H. P., "Three-Dimensional Flows and Loss Reduction in Axial Compressors," ASME Journal of Turbomachinery, Vol. 109, 1987, pp. 354–362.

Downloaded 01 Jun 2010 to 171.66.16.57. Redistribution subject to ASME license or copyright; see http://www.asme.org/terms/Terms_Use.cfm

Unsteady Aerodynamic Measurements on a Rotating Compressor Blade Row at Low Mach Number[1]

L. W. Hardin
Research Engineer.
Mem. ASME

F. O. Carta
Supervisor, Aerodynamics.
Fellow ASME

J. M. Verdon
Principal Scientist.
Mem. ASME

United Technologies Research Center,
East Hartford, CT 06108

An experiment was conducted on a heavily instrumented isolated model compressor rotor to study the unsteady aerodynamic response of the blade row to a controlled pitching oscillation of all blades in an undistorted flow, and to a circumferential inlet flow distortion with nonoscillating blades. To accomplish this, miniature pressure transducers were embedded in the blades and the unsteady pressure time histories were recorded. Both phases of the experiment were performed over a wide range of flow coefficient, from $C_x/U_m = 0.6$ *to 0.95 in 0.05 steps, and data were taken at each condition for sinusoidal disturbances characterized by one, two, and four per revolution waves. Steady-state data were acquired for flow coefficients from 0.55 to 0.99 in 0.05 steps. In this paper the steady and unsteady results of the portion of this experiment dealing with oscillating blades are compared with analytical predictions, and the steady results are compared with experimental data from previous work. Although the model blades were instrumented at five spanwise stations, only the midspan measurements will be presented herein. The measured pressures for nonoscillating blades were in good agreement with the steady potential flow predictions (and with previous steady experimental data) when the measured exit angle was imposed as the downstream boundary condition for the analysis. It was found that a quasi-steady approach yielded marginally acceptable agreement with the experimental results for the lowest frequency tested. For the higher reduced frequencies, the experimental data could not be modeled in this manner. In contrast, a comparison of the measurements with the Verdon-Caspar unsteady potential flow theory produced generally good agreement except near the leading edge at high mean incidence (i.e., at low flow coefficient). At high incidence the blades in this experiment had very high steady pressure gradients near the leading edge and it is suspected that this may be responsible for the lack of agreement. The agreement was somewhat better at the higher frequencies.*

Introduction

The aim of all compressor rotor design systems is to provide a rational set of rules and criteria to maximize rotor performance within a safe operating regime. A necessary constituent of performance and safety is the predictability of unsteady aerodynamic blade response, both to outside stimuli and to self-excitation. Theoretical treatments of this type of problem require that certain assumptions be made to simplify the mathematical model (e.g., the assumption of two-dimensional potential flow is common). Similarly, experimental investigations often require that the experiment be run at lower speeds or in a larger scale to provide the necessary instrumentation capability. Full-scale tests typically permit only sparse instrumentation without alteration of the normal flow patterns. Thus, when the theory, model experiment, and full-scale measurements do not agree, it is not clear where the inaccuracy lies.

Several programs have been undertaken to address this problem. Theoretical studies have ranged from a linear blade row analysis in distorted flow (Adamczyk and Carta, 1973) to several nonlinear-based analyses of oscillating thick blades with camber (cf. Verdon et al., 1975; Verdon and Caspar, 1980; Verdon and Usab, 1986; Atassi and Akai, 1980). Linear cascade tests have been performed for several years to measure the unsteady response of oscillating two-dimensional blades (Carta and St. Hilaire, 1978, 1980; Fleeter et al., 1977; Boldman and Buggele, 1978) and to verify such experiments

---

[1] The United States Government is authorized to reproduce and distribute reprints of this paper for governmental purposes notwithstanding any copyright notation hereon.

Contributed by the Gas Turbine Division of The American Society of Mechanical Engineers and presented at the 32nd International Gas Turbine Conference and Exhibit, Anaheim, California, May 31-June 4, 1987. Manuscript received at ASME Headquarters February 19, 1987. Paper No. 87-GT-221.

Copyright © 1987 by ASME

Downloaded 01 Jun 2010 to 171.66.16.57. Redistribution subject to ASME license or copyright; see http://www.asme.org/terms/Terms_Use.cfm

by measuring the periodicity along the cascade leading edge (Carta, 1982, 1983). The last study was significant because it also provided a mutual validation of the Verdon and Caspar (1980) theory and the cascade experiment. Several unsteady rotor experiments have been performed at the United Technologies Research Center (UTRC). An initial program was run by Hardin (1978) under AFOSR sponsorship to generate a sinusoidal distortion pattern and to make limited measurements of the unsteady blade response using miniature pressure transducers. (This was a precursor to the experiment reported on herein.) In addition, a number of steady-state rotor experiments have been run by Dring et al. (1979, 1982) on the same model rotor and these provide a large well-documented body of steady baseline data for the current experiment.

Most of the work cited above was necessarily limited in scope, and in only a few instances was it possible to provide validation data. The original objective of this work was to address this need by providing unsteady rotating frame data from an extensive spanwise and chordwise array of pressure transducers, and to generate these data by two related stimuli: all blades oscillating in pitch in a uniform stream, and sinusoidal distortion of the flow approaching a nonoscillating blade row. This paper is based in part on a three-volume report to AFOSR (Hardin and Carta, 1985, 1986a, 1986b) documenting this effort. This experiment is believed to represent the first comprehensive study of the unsteady aerodynamics of a rotating multiblade system in which on-rotor measurements were made of the surface pressure and skin friction responses to the two cited disturbances, and in which comparisons were made with an appropriate aerodynamic theory. The current paper will deal only with the pressure measurements from the midspan measuring station for the pitching oscillations and their comparison with unsteady theory.

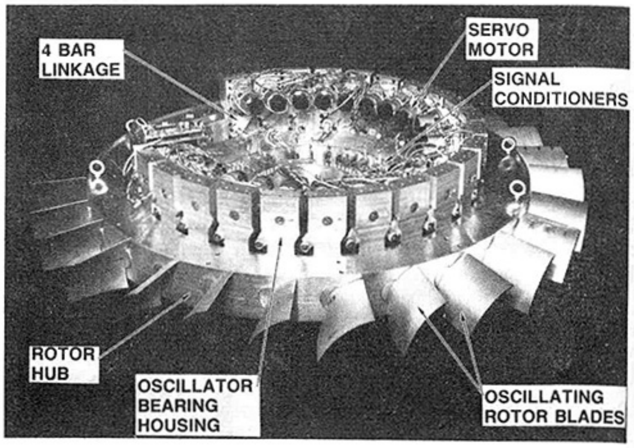

Fig. 1 Model rotor, partially disassembled

Experimental Equipment and Procedures

A series of unsteady aerodynamic experiments were carried out on an isolated rotor blade row model at UTRC in a Large-Scale Rotating Rig designated LSRR2. This is the second of two such rigs, identical in many respects to LSRR1, which was the vehicle for the steady-state experiments carried out on the same model geometry by Dring et al. (1982). In brief, air enters LSRR2 through a 12-ft-dia bellmouth fitted with 6-in. aluminum honeycomb at the inlet face to remove crossflow effects. The inlet contracts smoothly to the constant 5-ft outside diameter of the test section and the air passes through a series of fine mesh screens prior to entering the model blade row. The model section exhausts into a dump diffuser which houses the rotor drive motor (a variable speed d-c electric motor, rated at 200 hp (149 kW) and capable of speed regulation within ±0.1 rpm). The flow exhausts to the atmosphere through a centrifugal fan mounted downstream of the dump diffuser and equipped with a vortex valve for flow control. This is needed to offset any pressure drops through the system.

The isolated compressor model rotor is shown, partially disassembled, in Fig. 1. The model is 5 ft (1.52 m) in diameter, has a hub-to-tip ratio of 0.8, and consists of a single row of 28 blades. At the nominal operating condition of 510 rpm the Reynolds number, based on a 6-in. (15.2-cm) blade chord, is 5×10^5. Each blade is individually shaft-mounted in a bearing support and connected to a servomotor through a four-bar linkage [similar to that used by Carta (1983) in previous cascade experiments] to convert rotory motion of each motor to a sinusoidal pitching motion of each blade. Elastic blade deformations caused by aerodynamic loading were negligible. A rotating-frame servo electronics package (not shown) sets a constant frequency for all blades and an independent interblade phase angle for each blade, under command from a stationary frame computer. For steady-state (or nonoscillatory) operation the system is powered down and the blade oscillators are locked at their mean positions. On-board blade pressure transducers with on-rotor signal conditioning

Nomenclature

C_p = pressure coefficient
C_x = axial velocity, ft/sec (m/s), Fig. 2
C_x/U_m = flow coefficient at blade midspan
c = blade chord, ft (m), Fig. 2
f = frequency, Hz
N = number of disturbance cycles/rev (oscillation or distortion)
n = number of blades
P = pressure, psf (Pa)
P_{s1} = inlet static pressure, psf (Pa)
ΔP = pressure rise or difference, psf (Pa)
Q_{um} = dynamic pressure based on wheel speed at blade midspan, psf (Pa), Fig. 4
Q_{W1} = dynamic pressure based on relative inlet velocity, psf (Pa)
RPM = rotor speed, rpm
r = radius, ft (m)
r_m = mean radius, ft (m)
t = time, sec (s)
U = wheel speed, ft/sec (m/s), Fig. 2
W_1 = relative velocity in cascade reference frame, ft/sec (m/s), Fig. 2
x = blade chordwise coordinate, ft (m)
α = angle of attack ($=\beta_1^* - \beta_1$), Fig. 2
α_1 = first harmonic amplitude of α
β_1 = flow inlet angle, deg, Fig. 2
β_1^* = angle of tangent to mean camber line, deg, Fig. 2
ρ = fluid density, lb sec^2/ft^4 (kg/m^3)
σ = interblade phase angle, deg
τ = blade gap, ft (m), Fig. 2, or disturbance period, sec (s)
ω = reduced frequency based on full chord

Downloaded 01 Jun 2010 to 171.66.16.57. Redistribution subject to ASME license or copyright; see http://www.asme.org/terms/Terms_Use.cfm

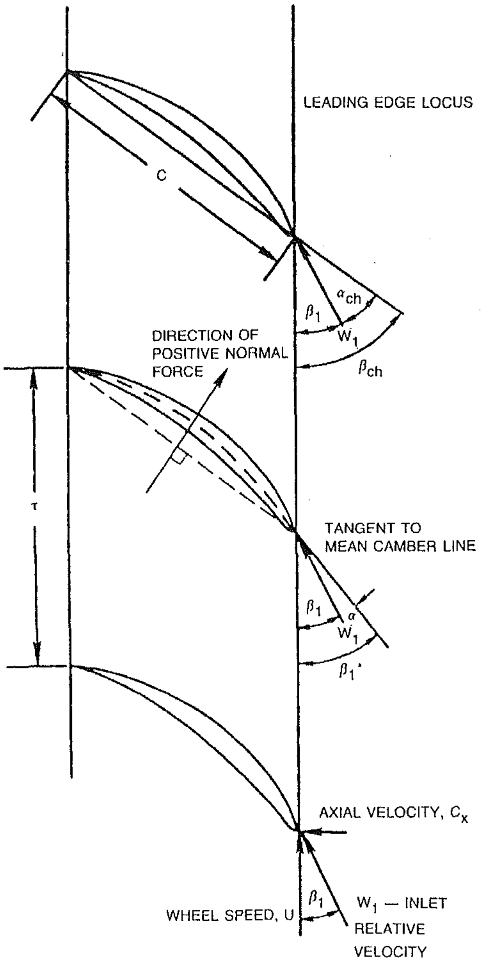

Fig. 2

interface to the same computer through the rig slip rings. The on-rotor signal conditioning renders any slip ring noise to be negligible. The unsteady data are synchronized to rotor revolution by means of a rig drive shaft encoder generating exactly 1024 pulses per revolution. These pulses control the sampling rate of the transient data system such that the 1024 samples stored in memory for each channel represent precisely one revolution of the rig. This permits the use of an efficient fast Fourier transform algorithm in reducing the data to Fourier coefficient form (where appropriate). The drive mechanisms and the data system are described in detail by Hardin and Carta, 1985.

The physical frequency of oscillation may be converted to a nondimensional reduced frequency, which is well established in the literature (e.g., Carta, 1982). The reduced frequency used in this experiment was based on the full blade chord and is defined as

$$\omega = 2\pi fc/W_1 \tag{1}$$

The interblade phase angle is a measure of the phase lag or lead of adjacent blades. Assuming that the n blades of a rotor are oscillating in a standing wave pattern (in the fixed frame), if N is the number of oscillations or distortion waves per revolution, then the magnitude of the interblade phase angle in radians is the circumferential arc divided by the number of blades per wave, or

$$|\sigma| = 2\pi/(n/N) = 2\pi N/n \tag{2}$$

The interblade phase angle is defined to be negative for a backward traveling wave in the rotating frame.

The original intent was to oscillate the blades at frequencies and interblade phase angles that would produce standing waves in the fixed frame of reference. This was true for the 1/rev disturbances. Unfortunately, an error was made in programming the microprocessor in the blade oscillator drive system, and for the 2 and 4 cycle/rev disturbances, the interblade phase angles for the oscillatory motion were 2 and 4 times those required for standing waves. Therefore neither of the higher order oscillatory waves was stationary in space. The relationship of the reduced frequency to the rig parameters, and a tabulation of both ω and σ for all run conditions, are found in the Appendix.

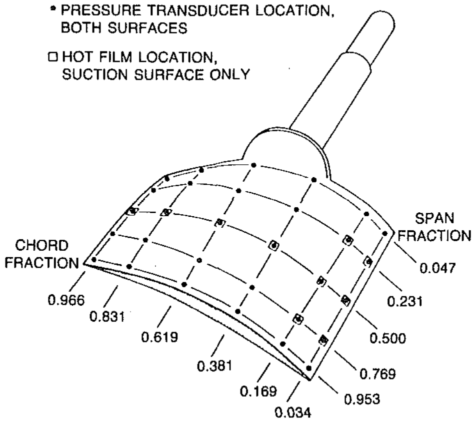

Fig. 3 Blade measuring stations

The nominal span and chord of each blade is 0.5 ft (15.2 cm) and the basic airfoil is a NACA 65-series thickness distribution superimposed on a nominal circular arc mean camber line, as tabulated by Dring et al. (1982). The blade geometry in the cascade reference frame at midspan (Fig. 2) shows the vector relationships of the flow entering the blade row. The important quantities for use in this paper are inlet angle β_1, indicating the direction of the inlet relative velocity, W_1, which in turn is the vector sum of the inlet axial velocity, C_x, and the wheel speed, U. These last two quantities, taken at blade midspan, define the flow coefficient, C_x/U_m, which is the fundamental reference parameter for the steady-state operation of the rig.

The original blades in Dring's experiment (1982) were machined from solid aluminum and would have had too much inertia to be successfully oscillated in pitch by the mechanism used in this experiment. Instead, a two-piece mold, cast from one of the original blades, was used to construct a set of stiff lightweight model blades, which consisted of a fiberglass-epoxy skin with a foamed epoxy core. Each blade was cast onto a hollow circular aluminum shaft with an internal support structure (cf. Hardin and Carta, 1985).

The primary blade instrumentation consisted of 60 miniature differential pressure transducers arranged in a double Gaussian array of six chordwise and five spanwise locations on both suction and pressure surfaces. This arrangement is shown in Fig. 3. The transducers, which were cylindrical Kulite XCQ-093 series, 0.093 in. (2.36 mm) diameter and 0.375 in. (9.53 mm) long, were molded into the blades during the construction process. Because of space and weight limitations the transducers were distributed over 12 blades. In the present application the data have been mathematically corrected to represent the response of a single blade at its mean angle of attack with angle increasing at the beginning of the unsteady time histories.

The differential transducers had a full-scale range of 2 psi (13.8 kPa) and were all referenced to inlet total pressure in the absolute reference frame as obtained from a Kiel probe upstream of the test section. This measured differential pressure was normalized on line by the dynamic pressure based on midspan wheel speed. Offline processing converted

Downloaded 01 Jun 2010 to 171.66.16.57. Redistribution subject to ASME license or copyright; see http://www.asme.org/terms/Terms_Use.cfm

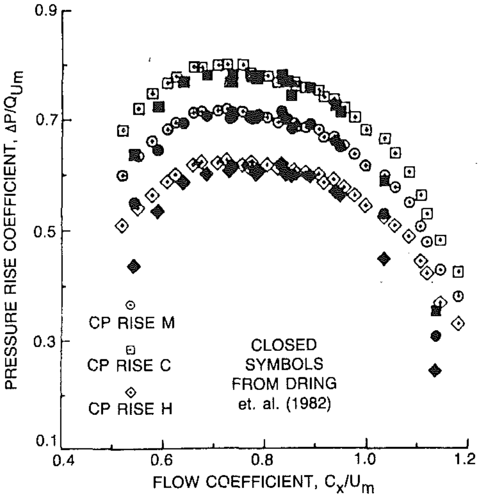

Fig. 4 Performance map

the data to a coefficient form more appropriate to the analysis of blade (or airfoil) aerodynamics, namely,

$$C_P = (P - P_{S1})/Q_{W1} \tag{3}$$

$$Q_{W1} = 0.5\rho W_1^2 \tag{4}$$

where Q_{W1} is the inlet relative dynamic pressure based on the inlet relative velocity W_1 (Fig. 2). The combination of inherent transducer stability and an accurate calibration over both pressure and temperature made it possible to use these transducers for both steady (or time-mean) and unsteady measurements.

Physics of the Experiment

Often, analytic treatments of the aerodynamic response of a blade row to gusts or oscillations assume that either the inlet static pressure or the inlet total pressure (or both) are uniform. However, instead of uniform inlet conditions it was found that circumferential variations existed in the inlet pressures for the oscillatory cases. This was not expected, but inspection of the data revealed its source. Atmospheric air was drawn into the rig through an inlet bellmouth and was passed through a series of fine screens to produce a total pressure drop in order to reduce turbulence. The model exhausted into a dump diffuser such that the exit pressure was also nominally uniform. However, when the blades of the model were oscillating sinusoidally, the variation in incidence angle produced a corresponding variation in the local static pressure rise generated by the rotor. This variation in static pressure rise in turn caused circumferential variations in the axial velocity, resulting in variations in the total pressure loss in the flow straightening screens upstream of the rotor. It thus became essential that comparison of theory and experiment account for these inlet pressure or velocity variations in some way.

This was accomplished in two steps. First, the effects of the circumferentially varying static pressure were nullified by using the instantaneous velocity and pressure upstream of the blade row in computing the pressure coefficient of equation (3). Second, the aerodynamic incidence angle rather than the geometric incidence was used in analyzing the data. The mechanical elements in the four bar linkages produced a geometric amplitude of ±2 deg for all oscillations. For the standing wave pattern of the $N=1$ disturbance it was possible to measure the total and static pressure variations circumferentially around the casing, compute the velocity perturbation, and convert this into an angular correction to the geometrically imposed oscillation. (It was found that for $N=1$ the 2 deg amplitude was reduced to 1.58 deg for a flow coefficient of $C_x/U_m = 0.8$, for example.) Thus treated, the experimental data may be safely compared to a theory which assumes uniform inlet conditions. It was not possible to make exact corrections for $N=2$ and 4 because these were not standing waves, and it was necessary to assume that the same results applied as those measured for $N=1$.

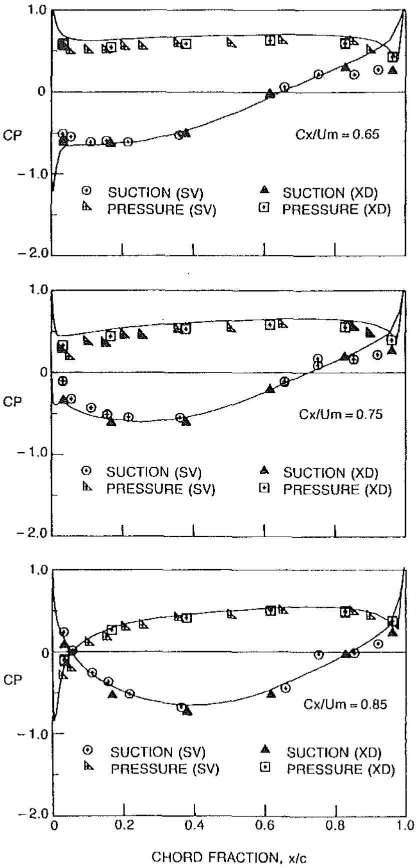

Fig. 5 Comparison of measured data to steady potential flow calculation at midspan

Steady-State Results

The first tests run in this experiment were undistorted, nonoscillating performance matching measurements to compare current rig pressure rise characteristics with those of Dring et al. (1982). These were run over a wide range of flow coefficients and the performance map of pressure rise coefficient, $\Delta P/Q_{Um}$, versus flow coefficient, C_x/U_m, is presented in Fig. 4 for the current experiment (open symbols) which agree very well with the Dring (1982) experiment (closed symbols) at the hub (*H*), midspan (*M*), and case (*C*). The only significant disagreement in results lies below $C_x/U_m = 0.6$ and above 0.95, which were the limits of operation for this experiment.

In addition to overall performance comparisons with previous data (obtained from case and hub static pressure measurements), steady blade surface pressure measurements comparable to those of Dring (1982) were also made. The measured pressures were compared to the predictions of a steady two-dimensional potential flow calculation (Caspar et al., 1980). This particular calculation allows one to select from a variety of downstream boundary conditions. Applying a simple Kutta condition yielded an exit flow angle which did not agree with the measured value (typically causing a 3 to 4 deg error) and predicted an erroneous pressure distribution on the aft portion of the blade. The behavior of the measured

Downloaded 01 Jun 2010 to 171.66.16.57. Redistribution subject to ASME license or copyright; see http://www.asme.org/terms/Terms_Use.cfm

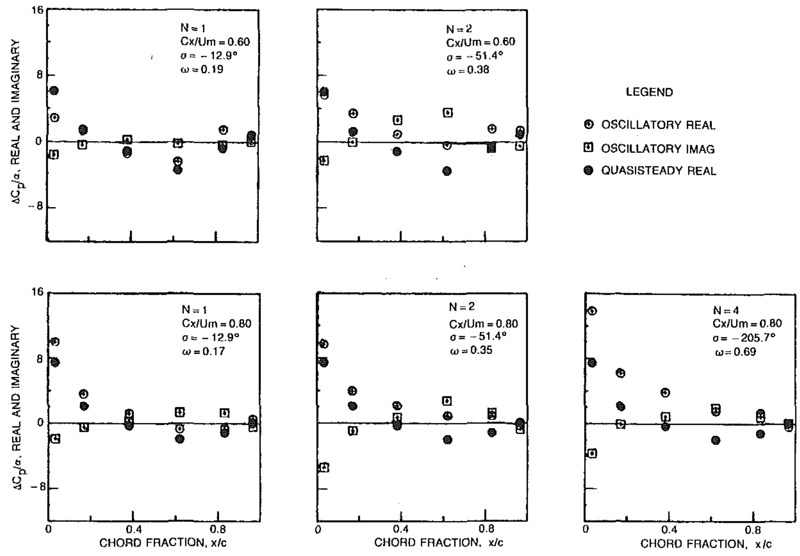

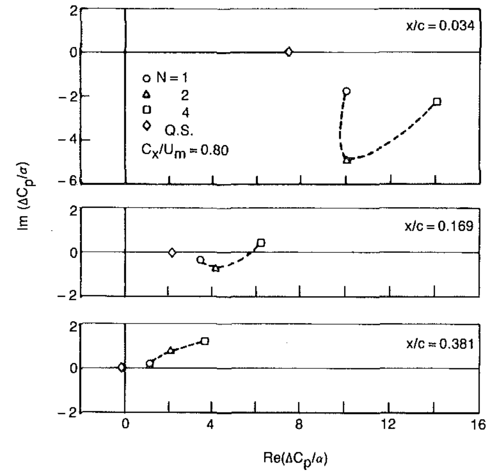

Fig. 6 Comparison of quasi-steady and unsteady chordwise pressures at midspan

Fig. 7 Phase plane comparison of quasi-steady and unsteady midspan pressures near the leading edge

pressures from both the current experiment and that of Dring, as well as the flow visualizations of Dring, indicate some trailing edge separation over virtually the entire range of flow conditions. The imposition of the measured exit flow angle as the downstream boundary condition brings the computed pressure distribution into close agreement with the experimental data. A direct consequence of this technique, however, is the appearance of a stagnation point at the trailing edge which is physically unrealistic. The results presented by Dring et al. (1982) empirically removed this stagnation point behavior, but no attempt has been made to do so for the present comparison.

A sample of the comparisons made as part of this study is shown in Fig. 5 for three values of C_x/U_m (0.65, 0.75, 0.85) in which the chordwise pressure distributions for both blade surfaces at midspan are shown for the Caspar (1980) theory (solid lines), the Dring (1982) scanivalve measurements (labeled SV), and the current measurements made with miniature pressure transducers (labeled XD). (These flow coefficients were chosen to match Dring's data and are not those for which unsteady data will be presented.) For both surfaces the measured data are in excellent agreement with each other, and in very good agreement with the theory except in the vicinity of the trailing edge suction surface where the measured pressure becomes flat, suggesting separation. Note that separation in a cascaded blade row is significantly different from isolated airfoil separation in that the trailing edge flow over the suction surface is restrained by the neighboring blade pressure surface. The net result is a thin separation layer which reduces the area through which the air outside the separation region must pass. Continuity requires that the fluid velocity be greater than without the separation, resulting in slightly lower pressures on both suction and pressure surfaces. This is clearly shown in Fig. 7(*a*) of the report by Hardin and Carta (1986a) in the comparison of the measured pressures and those predicted using the Kutta condition. (Further details and additional data samples are also found in this reference volume.)

Quasi-Steady Results

One of the simplest means of accounting for unsteadiness is the use of a quasi-steady approximation to determine the time-varying response of a blade to an unsteady stimulus. This method postulates that the unsteady behavior at sufficiently low reduced frequency may be modeled directly by the steady behavior, which is assumed to vary with time through the flow coefficient with no phase shift. The method would appear to have the advantage of including viscous effects to the extent that they are present in the steady data. In an analysis performed for this study, the quasi-steady response was constructed for each measurement station from the steady data taken over the range of flow coefficient values from 0.55 to 0.99. The data were curve fitted as a function of C_x/U_m and at each spanwise station the relationships

$$\beta_1 = \tan^{-1}(C_x/U_m) \tag{5}$$

$$\alpha = \beta_1^* - \beta_1 \tag{6}$$

(cf. Fig. 2) were used to relate the measured pressures to local incidence angle. For any combination of β_1 and β_1^* the instantaneous incidence angle, α, could be calculated (because β_1^* varies during oscillation), and from the variation in C_x/U_m around the circumference the pressure variation could be determined from the curve fit.

Because, by definition, the quasi-steady response is independent of time, there can be no lag between the motion and the response, whereas the actual unsteady data exhibit such a lag (or lead). It is customary to examine these responses in terms of their in- and out-of-phase first harmonic components, generally referred to as the real and imaginary components, respectively (cf. Carta, 1982). By this definition, there is no imaginary part to the quasi-steady response. Furthermore, because the quasi-steady response is constructed from the steady data taken from a nonoscillating blade row, the interblade phase angle of the data must necessarily be identically equal to zero.

Figure 6 displays the real and imaginary parts of the chordwise pressure difference coefficient, defined by the equation

$$\Delta C_p = C_{p(\text{pres})} - C_{p(\text{suct})} \tag{7}$$

for both the quasi-steady and the unsteady measured data, normalized with respect to the amplitude of the angle of attack variation. This normalization procedure expresses the oscillatory results in a convenient per-unit amplitude form. Positive pressure difference is defined as that which would produce a positive contribution to normal force (cf. Fig. 2). In Fig. 6, data taken at the midspan station are shown for flow

Downloaded 01 Jun 2010 to 171.66.16.57. Redistribution subject to ASME license or copyright; see http://www.asme.org/terms/Terms_Use.cfm

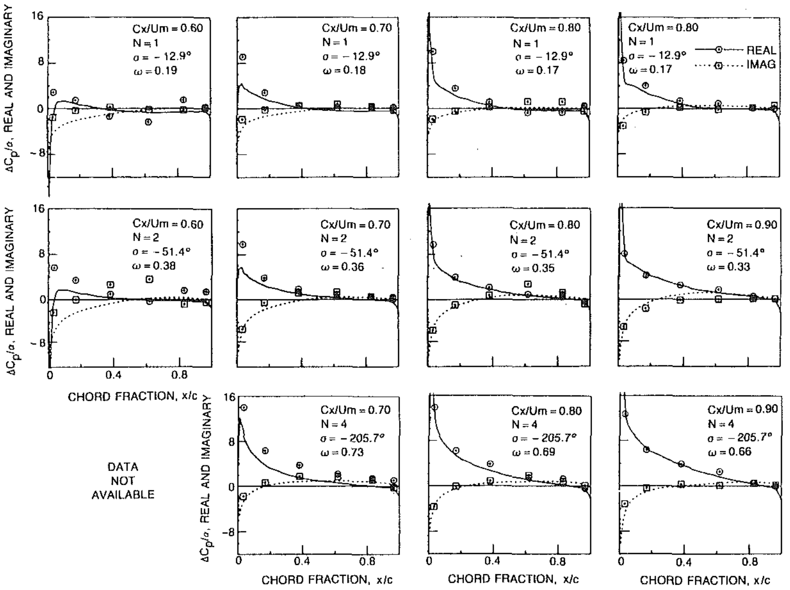

Fig. 8 Comparison of measured pressure distribution at midspan to potential flow calculation for three oscillatory frequencies

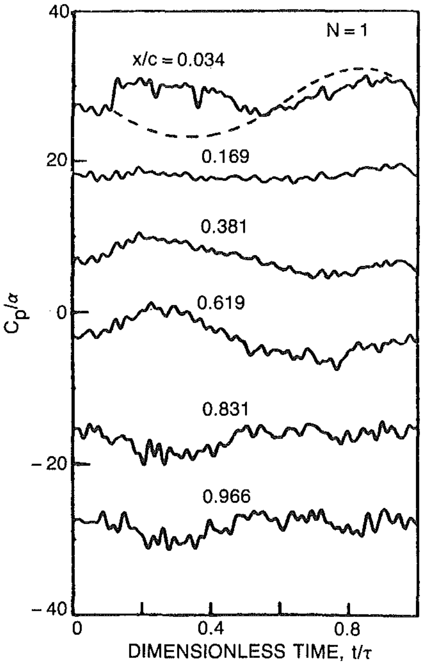

Fig. 9 Midspan suction surface time history at $C_x/U_m = 0.6$

coefficients of $C_x/U_m = 0.60$ and 0.80 (top and bottom rows) at the three frequencies, $N = 1$, 2, and 4 (left to right). (No data were taken for $C_x/U_m = 0.60$ and $N = 4$.) The open symbols are the unsteady data and the solid symbols are the quasi-steady data (real part only). A superficial examination of the left column for $N = 1$ indicates a reasonable match between the real part of the unsteady data and the quasi-steady results. With the exception of a large discrepancy at the leading edge (of as much as 30 percent) there is acceptable agreement between real parts over the rest of the chord, but with no imaginary part there can be no phase agreement. The situation is radically altered at $N = 2$ and 4 (second and third columns) where strong disagreement between the unsteady and quasi-steady response is found. The quasi-steady results in these two columns are identical to those in the first column because they are, by definition, invariant with frequency. In contrast, the real parts of the unsteady data for $N = 2$ and 4 change significantly from the $N = 1$ case (and from one another) to the extent that at $N = 4$, at all span stations, the error incurred in using quasi-steady results in place of unsteady data is enormous over the entire chord.

One possible way to model the unsteady response is to apply a first-order phase lag to the quasi-steady behavior. Consider the phase plane plots of Fig. 7 for the first three chordwise stations. In each panel the circle, triangle, and square symbols denote the measured complex values for $N = 1$, 2, and 4, respectively, while the diamond shows the quasi-steady value. (The dashed line merely connects the experimental points and does not necessarily represent an experimental variation.) Even if a simple phase shift were introduced into a modified quasi-steady formulation of the response it is obvious that this procedure could not possibly account for the observed amplification with reduced frequency. Furthermore, the measured phase angle does not exhibit a linear relationship with frequency. Thus, the use of quasi-steady results leads to large errors in all but the lowest frequencies, and the errors appear to grow with increasing frequency. Similar results will be obtained at other values of flow coefficient.

Comparison of Unsteady Oscillatory Data With Theory

As previously mentioned, unsteady data were recorded at flow coefficients ranging from 0.60 to 0.95 in 0.05 steps. The four flow coefficients, 0.60, 0.70, 0.80, and 0.90, were selected from these as being representative of the entire set. The linearized unsteady potential flow analysis of Verdon and Caspar (1980, 1984) for a cascade of blades having nonzero thickness and camber, operating in a subsonic, compressible flow was exercised at each of these flow coefficients at the three reduced frequencies. The basis of this theory is a linearized unsteady perturbation of a nonlinear steady potential flow (cf. Verdon, 1985). Hence, an essential first step in this analysis is to match the steady theory to the measured steady-state pressures (see above). It was shown earlier that the imposition of the measured exit flow angle at the downstream boundary of the solution domain results in large mean pressure gradients at the blade trailing edges. Consequently, a Kutta condition was used for the steady analysis in lieu of a prescribed exit flow angle to obtain the potential function describing smooth flow off the trailing edge. It must be noted that this is a compromise because the exit angle and steady surface pressures near the trailing edge thus obtained did not match the measured values.

The unsteady analysis was then used to compute the real and imaginary first harmonic components of the blade pressures at the blade midspan station, which were expressed in pressure difference coefficient form, as defined in equation (7). The comparisons of the potential flow calculations and the experimental data for the midspan measuring station are shown in Fig. 8 for three frequencies ($N = 1$, 2, 4 from top to bottom) and for four flow coefficients ($C_x/U_m = 0.6$, 0.7, 0.8, 0.9 from left to right). The real and imaginary parts of the data are denoted by the circles and squares, and of the theory by the solid and dashed lines, respectively. Overall, the agreement is very good. The experimental data and the theory show essentially the same behavior for flow coefficients from 0.70 to 0.90, with the data having slightly higher amplitude at the high reduced frequency. The decrease in amplitude of the data in going from $C_x/U_m = 0.70$ to 0.60 (Fig. 8) is caused by the formation of a separation bubble on the suction surface of the leading edge as evidenced by the abrupt rise in the leading edge pressure time history of Fig. 9. (This figure will be discussed presently, but in brief, the dashed line indicates the expected pressure variation for no separation. The pressure rise between $t/\tau = 0.1$ and 0.5 is therefore interpreted as a loss in leading edge suction caused by a local separation bubble.)

Downloaded 01 Jun 2010 to 171.66.16.57. Redistribution subject to ASME license or copyright; see http://www.asme.org/terms/Terms_Use.cfm

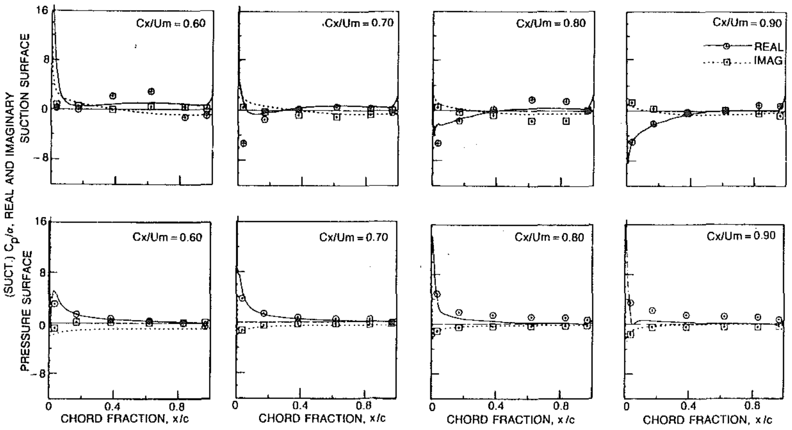

Fig. 10 Comparison of measured single surface pressure distribution to potential flow calculations for $N = 1$ ($\sigma = -12.9$ deg)

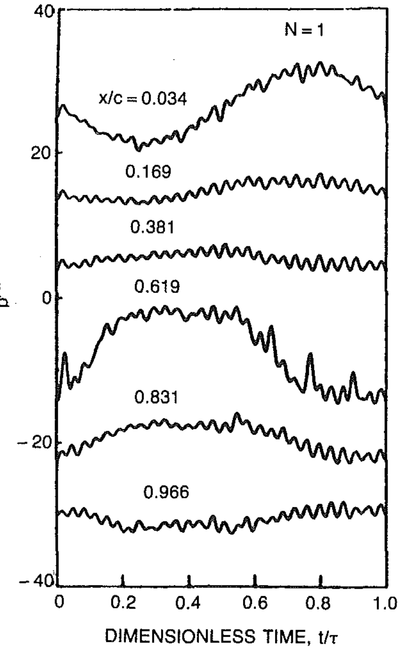

Fig. 11 Midspan suction surface time history at $C_x/U_m = 0.75$

The reduction in theoretical pressure difference at the leading edge for the 0.60 flow coefficient (and to a lesser extent for $C_x/U_m = 0.70$) is not presently understood. Based on the consistency of the experimental data up to the flow coefficient at which the separation bubble formed, one would expect that the inviscid theory would predict a continuation of this trend. Several possible reasons for this apparent deficiency have been considered and most have been discarded. For example, careful investigation has ruled out the possibility that this is a manifestation of the acoustical resonance phenomenon (cf. Appendix B in Carta, 1983).

The reader should note that the results of this linearized unsteady flow theory were previously compared to experimental data from a nonrotating oscillating cascade (Carta, 1982, 1983). In that work, good agreement was obtained for a blade row at or near design point and for a test matrix encompassing all combinations of eight interblade phase angles and three reduced frequencies. Furthermore, in the present study, a comparison of the predicted and measured pressures (real and imaginary parts) on the individual suction and pressure surfaces also shows good agreement between theory and experiment (cf. Fig. 10) except for the suction surface leading edge region at high mean incidence. These factors argue strongly that there are no inherent deficiencies in either the theoretical analysis or in the measurements.

Finally, it can be seen that the measured steady data do not show the sharp leading edge pressure gradient predicted by the steady theory (Fig. 5) at the high incidence conditions. Thus it is reasonable to expect that local viscous effects cause the differences between the experimental data and the theoretical prediction. If this is the case, it becomes necessary to understand the mechanisms by which these differences occur and ultimately to include local visous effects in theoretical unsteady aerodynamic models.

In summary, the theoretical formulation of Verdon and Caspar (1980, 1984) accurately predicted the surface pressure distributions on the oscillating blades over the entire chord for the lower mean incidence angles. At high incidence, the theory and experiment did not match at the leading edge. It is not clear whether or not this deviation is due to viscous phenomena present in the experimental data but neglected by the potential theory. Clearly, a more thorough investigation of steady and unsteady pressure behavior in the vicinity of a blade leading edge is needed.

Midspan Pressure Time Histories

To shed additional light on the behavior of the first harmonic chordwise plots of the previous section, a few selected time histories of the blade pressures at midspan will now be examined. The two figures discussed here represent a small fraction of the complete documentation in the AFOSR reports by Hardin and Carta (1986a, 1986b). Let us first consider Fig. 9, which contains the normalized suction surface pressure coefficient time plots for the six chordwise measuring stations, at a flow coefficient of 0.60. The mean pressure has been removed and the traces have been evenly spaced for clarity; therefore, the left-hand scale is only a measure of the amplitude of the unsteady part of the pressure. No motion plot is included here, but with a pitching motion of $\alpha = \alpha_1 \sin 2\pi ft$, zero displacement occurs at $t/\tau = 0.0$ and 0.5, with maximum and minimum displacement at 0.25 and 0.75, respectively. In this figure the leading edge station shows evidence of a leading edge separation bubble which initiates during the positive pitching motion at $t/\tau = 0.1$ as an abrupt increase in positive pressure (decrease in leading edge suction). This is also observed in the downstream stations, but with diminished amplitude. This is a straightforward occurrence of stall, with no ambiguities in the interpretation of the evidence. Not shown here is the pressure surface response which shows no evidence of separation.

When the data of Fig. 8 were first examined it was seen that there was an apparent anomaly in the real and imaginary values at $x/c = 0.619$ for the 0.70 and 0.80 flow coefficients, but the overall discrepancy was small enough to be considered within the data scatter band. Upon examining the data for the 0.75 flow condition, a dramatic variation in the suction surface pressure at $x/c = 0.619$ was discovered. The pressure coefficient time history for this location presented in Fig. 11 has the superficial appearance of an isolated separation, similar to the separation bubble near the leading edge that is depicted in Fig. 9. Investigation of data from adjacent spanwise stations for this range of flow coefficients and the flow visualization photographs obtained by Dring et al. (1982) ruled out the initial supposition that this behavior was due to spanwise flow. Plotting the data from the steady tests as a function of flow

Downloaded 01 Jun 2010 to 171.66.16.57. Redistribution subject to ASME license or copyright; see http://www.asme.org/terms/Terms_Use.cfm

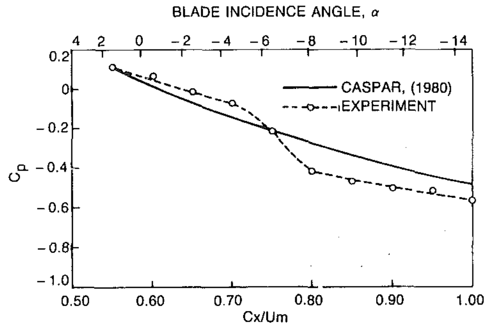

Fig. 12 Steady-state suction surface pressure at $x/c = 0.619$

coefficient (lower scale in Fig. 12) revealed an abrupt change in the suction surface pressure at $x/c = 0.619$ between flow coefficients of 0.70 and 0.80, and centered about a value of approximately 0.75. This behavior is not shown in the results from Caspar's 1980 steady potential flow theory (solid line) nor was it apparent in the comparison of the steady theory with the steady data in Fig. 5 (or in the earlier Dring (1982) experiment). Equations (5) and (6) provide a relationship between flow coefficient and α which was evaluated here for $\beta_1^* = 30.55$ at midspan, and is shown in the upper scale of Fig. 12. During the oscillation at a mean flow coefficient of 0.75, the mean incidence angle was −6.32 deg at $t/\tau = 0.0$, 0.5, and 1.0, and varied from −4.74 deg at $t/\tau = 0.25$ to −7.9 deg at $t/\tau = 0.75$. This range in α about the point $C_x/U_m = 0.75$ produces the apparent pressure rise (and consequent loss in lift) during the upstroke seen in Fig. 11. (It should be noted that the actual time history is phase shifted relative to the quasi-steady estimate.) Although it is not reasonable to suppose that the trailing edge separation region could extend this far forward (based on the flow visualization), it certainly appears that the separation does affect the pressures far upstream of the actual separation region.

These data and the accompanying discussion are presented to make several points. First, nonpotential flow behavior which might seem insignificant in comparing steady experimental data to a steady theory can produce extraordinary and unexpected unsteady behavior. Second, data for twice the number of flow conditions actually presented herein and for several spanwise stations were necessary to interpret the results properly. An evaluation with fewer data points might have resulted in erroneous conclusions regarding the agreement between the theory and the experiment and the physics of the flow field. Third, the applicability of the inviscid theory is questionable only for flow conditions which are equivalent to the incidence angle at which this abrupt change occurs and only over a region of small chordwise extent. Thus the potential theory yields good unsteady flow predictions even in the aft region of the blade where viscous effects seem to play a large role (by producing a confined region of local separation).

Conclusions and Observations

This is the first known investigation to bring together three experimental elements that have been studied separately in previous work: a heavily instrumented blade row, rotating in a realistic compressor model, with all blades oscillating in a prescribed motion under external command. The existence of this data set affords the researcher with a unique opportunity to examine, in detail, the unsteady response of a blade row to a prescribed oscillation and compare the results with theory.

Specifically, this program has demonstrated that:

- The experiment clearly confirmed the ability to measure precisely both the steady and unsteady components of the blade pressures with a single set of miniature, high-response pressure transducers.
- Data acquired for steady-state conditions matched previously acquired pneumatic data at all flow conditions, and agreed well with a steady potential flow solution.
- The quasi-steady response was in fair agreement with the in-phase part of the measured unsteady response for the lowest oscillation frequency. (The lack of an out-of-phase component to the quasi-steady response precluded any phase agreement with the unsteady data at all frequencies.) For the higher frequencies, the agreement of the in-phase part became progressively worse.
- The data acquired for the oscillatory conditions agreed with linearized unsteady potential flow predictions over virtually the entire chord for low to moderate incidence. At high mean incidence, there were discrepancies on the suction surface near the leading edge which appear to have been caused by local viscous effects. The agreement between theory and experiment was better for the higher frequencies.

Acknowledgments

This work was sponsored by the Air Force Office of Scientific Research, Bolling AFB, DC 20332, under Contract F49620-81-C-0088. It was performed under the technical direction of Dr. Anthony K. Amos at AFOSR.

In a program such as this one, involving the coordination of many complicated systems and disciplines, the authors were fortunate to have the personnel and equipment resources of UTRC to draw upon. They are indebted to many people for their help, and in particular to Messrs. Alfred F. Covino and John L. Kostic for building models and acquiring data, to Mr. Robert K. Thornton for his design of the closed loop blade oscillator circuit, and to Ms. Ruth Ann Rudewicz for her skill and patience in executing Verdon's analytical codes.

References

Adamczyk, J. J., and Carta, F. O., 1973, "Unsteady Fluid Dynamic Response of an Axial-Flow Compressor Stage With Distorted Inflow," Project SQUID Technical Report UARL-2-PU.

Atassi, H., and Akai, T. J., 1980, "Aerodynamics and Aeroelastic Characteristics of Oscillating Loaded Cascades at Low Mach Number. Part I: Pressure Distribution, Forces and Moments. Part II: Stability and Flutter Boundaries," ASME *Journal of Engineering for Power*, Vol. 102, No. 2, pp. 344–356.

Boldman, D. R., and Buggele, A. E., 1978, "Wind Tunnel Tests of a Blade Subjected to Midchord Torsional Oscillation at High Subsonic Stall Flutter Conditions," NASA TM 78998.

Carta, F. O., and St. Hilaire, A. O., 1978, "Experimentally Determined Stability Parameters of a Subsonic Cascade Oscillating Near Stall," ASME *Journal of Engineering for Power*, Vol. 100, No. 1, pp. 111–120.

Carta, F. O., and St. Hilaire, A. O., 1980, "Effect of Interblade Phase Angle and Incidence Angle on Cascade Pitching Stability," ASME *Journal of Engineering for Power*, Vol. 102, No. 2, pp. 391–396.

Carta, F. O., 1982, "An Experimental Investigation of Gapwise Periodicity and Unsteady Aerodynamic Response in an Oscillating Cascade: I, Experimental and Theoretical Results," NASA CR 3513.

Carta, F. O., 1983, "Unsteady Aerodynamics and Gapwise Periodicity of Oscillating Cascaded Airfoils," ASME *Journal of Engineering for Power*, Vol. 105, pp. 565–574.

Caspar, J. R., Hobbs, D. E., and Davis, R. L., 1980, "Calculation of Two-Dimensional Potential Cascade Flow Using Finite Area Methods," *AIAA Journal*, Vol. 18, No. 1, pp. 103–109.

Dring, R. P., Joslyn, H. D., and Hardin, L. W., 1979, "Experimental Investigation of Compressor Rotor Wakes," United Technologies Research Center Report R79-914183-15 (performed under AFAPL Contract No. F33615-77-C-2883).

Dring, R. P., Joslyn, H. D., and Hardin, L. W., 1982, "An Investigation of Axial Compressor Rotor Aerodynamics," ASME *Journal of Engineering for Power*, Vol. 104, pp. 84–96.

Fleeter, S., Novick, A. S., Riffel, R. E., and Caruthers, J. E., 1977, "An Experimental Determination of the Unsteady Aerodynamics in a Controlled Oscillating Cascade," ASME *Journal of Engineering for Power*, Vol. 99, No. 1, pp. 88–96.

Hardin, L. W., 1978, "An Experimental Study of the Response of a Turbomachine Rotor to a Low Frequency Inlet Distortion," Ph.D. Thesis submit-

Downloaded 01 Jun 2010 to 171.66.16.57. Redistribution subject to ASME license or copyright; see http://www.asme.org/terms/Terms_Use.cfm

ted to North Carolina State University, Raleigh, NC (also published as Air Force Report AFOSR-TR-79-0073, Dec. 1978, ADAO 64776).

Hardin, L. W., and Carta, F. O., 1985, "Unsteady Aerodynamics of a Rotating Compressor Blade Row at Low Mach Number. Vol. I – Experimental Facilities, Procedures, and Sample Data," UTRC Report No. R85-915767-3, prepared under USAFOSR Contract No. F49620-81-C-0088 (to be published as an AFOSR Technical Report).

Hardin, L. W., and Carta, F. O., 1986a, "Unsteady Aerodynamics of a Rotating Compressor Blade Row at Low Mach Number. Vol. II – Analysis of Experimental Results and Comparison With Theory," UTRC Report No. R86-915767-4, prepared under USAFOSR Contract No. F49620-81-C-0088 (to be published as an AFOSR Technical Report).

Hardin, L. W., and Carta, F. O., 1986b, "Unsteady Aerodynamics of a Rotating Compressor Blade Row at Low Mach Number. Vol. III – Experimental Data Base and Users Manual," UTRC Report No. R86-915767-5, prepared under USAFOSR Contract No. F49620-81-C-0088 (to be published as an AFOSR Technical Report).

Verdon, J. M., Adamczyk, J. J., and Caspar, J. R., 1975, "Subsonic Flow Past an Oscillating Cascade With Steady Blade Loading – Basic Formulation," in: *Unsteady Aerodynamics*, R. B. Kinney, ed., Vol. II of proceedings of a symposium held at the University of Arizona, Tucson, Mar. 18–20, 1975.

Verdon, J. M., and Caspar, J. R., 1980, "Subsonic Flow Past an Oscillating Cascade With Finite Mean Flow Deflection," *AIAA Journal*, Vol. 18, No. 5, pp. 540–548.

Verdon, J. M., and Caspar, J. R., 1984, "A Linearized Unsteady Aerodynamic Analysis for Transonic Cascades," *Journal of Fluid Mechanics*, Vol. 149, pp. 403–429.

Verdon, J. M., 1985, "Linearized Unsteady Aerodynamic Theory," Chap. 2 in *AGARD Manual on Aeroelasticity in Axial Turbomachines*, Vol. 1, *Unsteady Turbomachinery Aerodynamics*, M. F. Platzer and F. O. Carta, eds., AGARDograph No. 298, Mar. 1987.

Verdon, J. M., and Usab, W. J., Jr., 1986, "Application of a Linearized Unsteady Aerodynamic Analysis to Standard Cascade Configurations," NASA CR 3940.

APPENDIX

Reduced Frequency and Interblade Phase Angle

The reduced frequency is based on full blade chord and is defined as

$$\omega = 2\pi f c / W_1 \tag{8}$$

where the frequency f is given by $f = N$ [RPM]/60, and where N is the disturbance frequency in cycles/rev and RPM is the rotor speed. Thus,

$$\omega = 2\pi c N[\text{RPM}]/60_1 W_1 \tag{9}$$

From the geometry of Fig. 2, W_1 is related to the wheel speed, U, and the axial velocity, C_x,

$$W_1 = (U^2 + C_x^2)^{1/2} \tag{10}$$

and U is computed from the radial position and rotor rpm, $U = 2\pi r$[RPM]/60. When all of these equations are combined and written for mean passage height, r_m, the equation for reduced frequency is

$$\omega = \frac{cN}{r_m(1 + (C_x/U_m)^2)^{1/2}} \tag{11}$$

where $r_m = 2.25$ ft (0.686 m). It is seen that the reduced frequency will be a variable function of flow coefficient, which is tabulated at the end of this appendix.

The interblade phase angle was defined in the text as

$$|\sigma| = 2\pi N/n \tag{12}$$

and is negative for a backward-traveling wave relative to the rotor. This is the correct formulation for the standing wave, and is tabulated below in the first two columns for σ. It was noted that the function was programmed incorrectly for the oscillatory portion of the experiment such that the N in equation (12) was replaced by N^2. This is also tabulated below in the second two columns.

The following were the parameter values used in the experiment:

$n = 28$ blades

$N = 1, 2, 4$ cycles/rev

$c = 0.5$ ft (15.2 cm) chord

$r_m = 2.25$ ft (0.69 m) (midspan location)

RPM = 510 rpm

$C_x/U_m = 0.6, 0.65, 0.7, 0.75, 0.8, 0.85, 0.9, 0.95$

	σ for standing wave		σ for actual oscillation	
N	(rad)	(deg)	(rad)	(deg)
1	−0.2244	−12.86	−0.2244	−12.86
2	−0.4488	−25.72	−0.8976	−51.43
4	−0.8976	−51.43	−3.5904	−205.71

The reduced frequency values at midspan are:

C_x/U_m	ω ($N = 1$) ($f = 8.5$ Hz)	ω ($N = 2$) ($f = 17$ Hz)	ω ($N = 4$) ($f = 34$ Hz)
0.60	0.1906	0.3811	0.7622
0.65	0.1863	0.3726	0.7453
0.70	0.1821	0.3641	0.7282
0.75	0.1778	0.3556	0.7111
0.80	0.1735	0.3471	0.6941
0.85	0.1693	0.3386	0.6773
0.90	0.1651	0.3304	0.6607
0.95	0.1611	0.3222	0.6444

Downloaded 01 Jun 2010 to 171.66.16.57. Redistribution subject to ASME license or copyright; see http://www.asme.org/terms/Terms_Use.cfm

J. Z. Xu
Research Professor.

W. Y. Ni
Research Assistant.

J. Y. Du
Research Assistant.

Institute of Engineering Thermophysics,
Chinese Academy of Sciences,
Beijing, China

Numerical Solution of Stream Function Equations in Transonic Flows

In order to develop the transonic stream function approach, in this paper one of the momentum equations is employed to form the principal equation of the stream function which does not contain vorticity and entropy terms, and the other one is used to calculate the density directly. Since the density is uniquely determined, the problem that the density is a double-valued function of mass flux in the stream function formulation disappears and the entropy increase across the shock is naturally included. The numerical results for the transonic cascade flow show that the shock obtained from the present method is slightly weaker and is placed farther downstream compared to the irrotational stream function calculation, and is closer to the experimental data. From a standpoint of computation the iterative procedure of this formulation is simple and the alternating use of two momentum equations makes the calculation more effective.

Introduction

Numerical calculation of transonic flow field is now one of the most active areas of research in computational fluid dynamics. Among a wide variety of solutions the most common mathematical models are the Euler equations, the full potential equation, and the stream function equation.

The Euler equations are an exact inviscid model which can account for the vorticity and the nonisentropic effect and can capture shock waves correctly. Since the current approaches to solving these equations are the time-dependent methods, which are more complicated, reaching steady state requires a large number of iterations and a long computational time. In addition, since the state of the art of the computational algorithms is not so perfect, the existing Euler solutions have not attained the accuracy that the mathematical theory predicts.

The potential formulation is one of the classic methods to solve a subsonic flow field in fluid dynamics. The introduction of artifical compressibility (Hafez et al., 1978) and the recent developments in computational algorithms of second-order partial differential equations (e.g., Ballhaus et al., 1978; Holst, 1978) contribute a great deal to the method, and it has been proven to be a useful tool for the design and analysis of transonic flows. The appearance and development of the nonisentropic potential formulation (Klopfor and Nixon, 1983; Hafez et al., 1984; Osher et al., 1985; Xu et al., 1985; Xu et al., 1986a: Xu et al., 1986b) extend the range of its validity. The limitation of this model is the assumption of irrotationality of the flow.

The stream function formulation is an equivalent mathematical model to the Euler equations theoretically and in the two-dimensional case it has the same speed of computation as the potential formulation. However, the development and application of this formulation are severely limited due to the difficulty which comes from the fact that the density in the transonic regime is a double-valued function of the unknown stream function. Recently, several methods (Hafez and Lovell, 1983; Zhao, 1984; Ge, 1985; Wang, 1985; Wei, 1985) have been suggested to circumvent this difficulty and have made much progress. Moreover, there is another important problem to be solved, which is associated with the direct capture of the entropy variation or its influence on the gas parameters in a simple and reliable way.

In order to develop the transonic stream function calculations, in this paper one of the momentum equations is combined with the energy equation and utilized to form the principal equation of the stream function in which the terms concerning the vorticity and the entropy do not appear. Another momentum equation is used to calculate the density which contains the effect of the entropy directly. In this way the problem that the density is not a unique function of the mass flux disappears and the effect of the entropy increase across the shock is also taken into account naturally. Moreover, the present formulation is accurate and effective in computation due to the coordinated use of two momentum equations and the simple iteration procedure. So the main problems which limited the development and the application of the stream function calculations are readily solved.

Basic Idea

When a two-dimensional, adiabatic steady flow of a nonviscous gas is considered, the stream function may be introduced from the continuity equation. Substitution of it and the energy equation into one of the momentum equations

---

Contributed by the Gas Turbine Division of THE AMERICAN SOCIETY OF MECHANICAL ENGINEERS and presented at the 32nd International Gas Turbine Conference and Exhibit, Anaheim, California, May 31-June 4, 1987. Manuscript received at ASME Headquarters February 3, 1987. Paper No. 87-GT-18.

Copyright © 1987 by ASME

Downloaded 01 Jun 2010 to 171.66.16.57. Redistribution subject to ASME license or copyright; see http://www.asme.org/terms/Terms_Use.cfm

yields the principal equation of the stream function, which is a second-order partial differential equation. To simplify the computation, instead of vorticity and entropy, only two thermodynamic parameters, the density and the temperature, are included in this equation with the stagnation rothalpy, which is an invariant in a steady, adiabatic flow of an inviscid gas even across shock. By means of the artificial density and a proper difference scheme, this equation with certain boundary conditions may be solved numerically in the transonic region.

As the mass flux is calculated from the stream function equation, how to compute the density or the velocity components is the key problem of this approach. In the most current stream function methods, the density–mass flux relation is derived from the state equation, the energy equation, and the second law of thermodynamics or the isentropic relation, which is a two-valued equation.

To solve this problem correctly, it should be started from its origin. It is obvious that the crux of the problem is the density–mass flux relation from the energy equation and the second law of thermodynamics. Moreover, although the second law of thermodynamics offers an equation, a new thermodynamic quantity s is also introduced. It has no benefit in the shock-capturing calculations except that the entropy increase is obtained from the shock relations. On the other hand, it is noted that the entropy variation may be calculated from the momentum equations and the density containing the effect of the entropy may also be directly calculated from the momentum equations, and it is possible to compute the density from the momentum equation, which has not been taken as the principal equation of the stream function. In fact

$$\nabla p = R\nabla(\rho T) = R(\rho\nabla T + T\nabla\rho) \tag{1}$$

Then the density affected by the entropy may be evaluated from the momentum equations. Here, the density is determined uniquely through a first-order partial differential equation and its boundary conditions and there is no problem about two values, and the entropy increase across the shocks is involved naturally.

Since two momentum equations are used, the computed shock satisfies the Rankine–Hugoniot condition and the present model can really be applied to the nonisentropic and rotational flow, and is a precise and strict theoretical model equivalent to the Euler equations. From a computational standpoint it simplifies the iteration procedure and makes the computation well balanced and matching. In fact, in this formulation the whole calculation consists of the iterations between the stream function, the temperature, and the density, and the computations of stream function and density are carried out alternately. So it is simple and accurate. It is expected that this model will give impetus to the development of the transonic stream function computation.

Taking the cascade transonic flow on the surface of revolution as an example, the application of the present stream function model will be discussed. It is pointed out that this approach is also applicable to external flows and other internal flows.

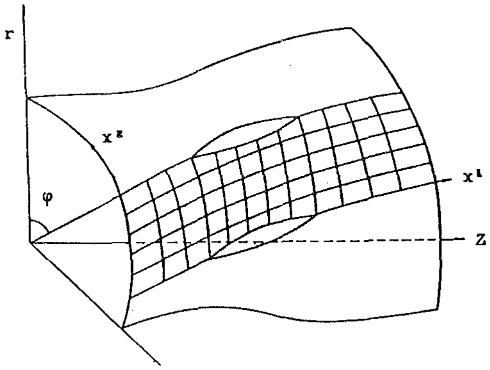

Fig. 1 Nonorthogonal coordinates on surface of revolution

Stream Function Equation on a Surface of Revolution and Its Numerical Solution

Consider a relatively steady and adiabatic flow of a nonviscous gas in a rotating blade. The basic equations are

$$\nabla\cdot(\rho\mathbf{W}) = 0 \tag{2}$$

$$\frac{DW}{dt} - |\omega|^2\mathbf{r} + 2\omega\times\mathbf{W} = -\frac{1}{\rho}\nabla p \tag{3}$$

$$\frac{dI}{dt} = 0 \tag{4}$$

$$p = \rho RT \tag{5}$$

$$I = h + \frac{(W)^2}{2} - \frac{(\omega r)^2}{2} \tag{6}$$

It is noted from equation (4) and the shock relations (Xu, 1980; Xu et al., 1982) that I is always a constant along a streamline. So it is convenient to rewrite equation (3) as

$$\mathbf{W}\times(\nabla\times\mathbf{V}) = \nabla I - \frac{R}{k-1}\nabla T + RT\nabla(\ln\rho) \tag{7}$$

When the partial derivatives along a stream surface are used, in the nonorthogonal curvilinear coordinates (Fig. 1) equations (2) and (7) become

$$(\tau\rho\sqrt{g}w^1)_{x^1} + (\tau\rho\sqrt{g}w^2)_{x^2} = 0 \tag{2a}$$

$$w^2[(w_2)_{x^1} - (w_1)_{x^2}] + 2\sqrt{g}w^2\omega^3 = I_{x^1} - \frac{R}{k-1}T_{x^1} + RT(\ln\rho)_{x^1} \tag{7a}$$

$$w^1[(w_1)_{x^2} - (w_2)_{x^1}] - 2\sqrt{g}w^1\omega^3 = I_{x^2} - \frac{R}{k-1}T_{x^2} + RT(\ln\rho)_{x^2} \tag{7b}$$

Nomenclature

a_{ij} = metric tensor elements of two-dimensional x^i coordinate system
h = enthalpy of gas per unit mass
I = relative stagnation rothalpy of gas per unit mass
k = ratio of specific heats of gas
l = generator of stream surface of revolution
L = blade chord in axial direction
M = relative Mach number
p = pressure of gas
R = gas constant
r = radius
T = absolute temperature of gas
$\mathbf{V}$ = absolute velocity of gas
$\mathbf{W}$ = relative velocity of gas
x^i = nonorthogonal curvilinear coordinates
β = relative flow angle
θ_{12} = angle between x^1 and x^2 lines
μ = artificial viscosity coefficient
ρ = density of gas
$\tilde{\rho}$ = artificial density
σ = relaxation factor
τ = normal thickness of S_1 stream filament
ψ = stream function
ω = angular velocity of rotor

Subscripts

0 = stagnation state
i = covariant component of vector

Downloaded 01 Jun 2010 to 171.66.16.57. Redistribution subject to ASME license or copyright; see http://www.asme.org/terms/Terms_Use.cfm

where τ is the thickness of the stream filament and the derivatives in these equations are all the derivatives along the stream surface.

From equation (2*a*) a stream function ψ may be defined

$$w^1 = \frac{1}{\sqrt{g}\tau\rho}\,\psi_{x^2}$$

$$w^2 = -\frac{1}{\sqrt{g}\tau\rho}\,\psi_{x^1}$$

Substituting these expressions into equation (7*b*) gives an equation in a weak divergence form

$$\left[\frac{1}{\rho}\,(A\psi_{x^2} - B\psi_{x^1})\right]_{x^2} - \left[\frac{1}{\rho}\,(B\psi_{x^2} - C\psi_{x^1})\right]_{x^1} = D \quad (8)$$

where

$$A = \sqrt{a_{11}}/(\tau\sqrt{a_{22}}\sin\theta_{12}), \qquad B = \cos\theta_{12}/(\tau\sin\theta_{12}),$$

$$C = \sqrt{a_{22}}/(\tau\sqrt{a_{11}}\sin\theta_{12}),$$

$$D = \frac{1}{w^1}\left[I_{x^2} - \frac{R}{k-1}\,T_{x^2} + RT(\ln\rho)_{x^2}\right] + E,$$

$$E = 2\omega\sin\sigma\sqrt{a_{11}a_{22}}\sin\theta_{12}$$

Equation (8) is the principal equation of the stream function. It is seen that besides the geometric quantities, only two basic thermodynamic parameters ρ and T appear in this equation. The boundary conditions are related to the flow condition. For the transonic flow in a cascade where the flow is subsonic at the inlet and outlet boundaries and it is supersonic in some region within the cascade, the boundary conditions are as follows:

(*i*) At the inlet boundary, the relative stagnation temperature and pressure and the mass flow are specified and ψ_{x^1} is assumed to be zero.

(*ii*) In the periodicity boundaries, $\psi_N - \psi_0 = G$.

(*iii*) Along the cascade surface, ψ = const.

(*iv*) At the outlet boundary, the relative flow angle is given and it is assumed that $\psi_{x^1} = 0$.

Because equation (8) is of mixed type in the transonic regime, the artificial density is introduced to ensure the stability of the computation in the supersonic grids

$$\tilde{\rho} = \rho - \mu\rho_s\Delta s \approx \rho - \mu_{i,j}\left(\frac{W^1}{W}\,\rho_{x^1}\Delta x^1 + \frac{W^2}{W}\,\rho_{x^2}\Delta x^2\right)$$

$$\mu_{i,j} = \mathrm{Max}\left[0,\ \bar{C}\left(1 - \frac{1}{\mathrm{M}^2_{i,j}}\right)\right]$$

where $\bar{C}$ ranges from 1 to 2.

To solve the discrete algebraic equations (8), the line relaxation procedure and the direct matrix solution procedure are used.

Density Equation and Its Numerical Solution

It has been pointed out that in order to overcome the nonuniqueness difficulty of density and to capture the entropy increase across the shock, the density should be computed from the momentum equation, which has not been employed as the principal equation of the stream function. For this reason the momentum equation along x^1 direction in the divergence form is utilized

$$\frac{1}{\sqrt{a_{11}}}\,[(\tau\rho W^1 W^1)_{x^1} + (\tau\rho W^1 W^2)_{x^1}\cos\theta_{12}]$$

$$+\frac{1}{\sqrt{a_{22}}}\,[(\tau\rho W^1 W^2)_{x^2} + (\tau\rho W^2 W^2)_{x^2}\cos\theta_{12}] + \frac{\tau}{\sqrt{a_{11}}}\,p_{x^1}$$

$$= \tau\rho\left\{\frac{(W^2)^2 - (W^1)^2}{\sqrt{a_{11}}}\,(\ln\sqrt{a_{22}})_{x^1}\right.$$

$$-\frac{2W^2(W^1 + W^2\cos\theta_{12})}{\sqrt{a_{22}}}\,(\ln\sqrt{a_{11}})_{x^2} - \frac{(W^2)^2}{\sqrt{a_{22}}}\,(\cos\theta_{12})_{x^2}$$

$$-(W^1 + W^2\cos\theta_{12})\left[\frac{W^1}{\sqrt{a_{11}}}\,(\ln\sin\theta_{12})_{x^1}\right.$$

$$\left.\left.+\frac{W^2}{\sqrt{a_{22}}}\,(\ln\sin\theta_{12})_{x^2}\right] + 2\omega W^2\sin\theta_{12} + |\omega|^2\,\frac{r_2}{\sqrt{a_{22}}}\right\}$$

Substitution of equation (1) into this equation yields

$$(\rho T)_{x^1} = -\frac{1}{\tau R}\left\{\left(\tau\frac{m^2}{\rho}\right)_{x^1} + \cos\theta_{12}\left(\tau\frac{mn}{\rho}\right)_{x^1}\right.$$

$$\left.-\sqrt{\frac{a_{11}}{a_{22}}}\left[\left(\tau\frac{mn}{\rho}\right)_{x^2} + \cos\theta_{12}\left(\tau\frac{n^2}{\rho}\right)_{x^2}\right]\right\}$$

$$+\frac{1}{\rho R}\left\{(n^2 - m^2)(\ln\sqrt{a_{22}})_{x^1} - 2n(m + n\cos\theta_{12})\sqrt{\frac{a_{11}}{a_{22}}}\,(\ln\sqrt{a_{11}})_{x^2}\right.$$

$$-\sqrt{\frac{a_{11}}{a_{22}}}\,n^2(\cos\theta_{12})_{x^2}$$

$$-(m + n\cos\theta_{12})\sqrt{a_{11}}\left[\frac{m}{\sqrt{a_{11}}}\,(\ln\sin\theta_{12})_{x^1}\right.$$

$$\left.\left.+\frac{n}{\sqrt{a_{22}}}\,(\ln\sin\theta_{12})_{x^2}\right] + 2\rho n\omega\sqrt{a_{11}}\sin\theta_{12} + \rho^2|\omega|^2 r_1\right\} \quad (9)$$

where $m = \rho W^1$, $n = \rho W^2$, and T is calculated from equation (4).

As opposed to the nonisentropic potential in which the density is computed according to the Poisson equation, a second-order partial differential equation derived from the momentum equations, a first-order equation for the density is obtained from only one of the momentum equations, and it is easily solved numerically. Since another momentum equation has been used as the stream function equation, the Rankine-Hugoniot relation is surely satisfied. On the contrary, any momentum equation is not concerned to the potential approach, so the use of the Poisson equation to calculate density is favorable to the accuracy of the computational results.

To solve equation (9) centered differences and the line relaxation procedure are used.

Finally, a brief comment on the extension of the present formulation to the three-dimensional flow is needed. In this case there exist two stream functions ψ^1 and ψ^2 (Giese, 1951)

$$\rho\mathbf{W} = \nabla\psi^1 \times \nabla\psi^2$$

In terms of ψ^1 and ψ^2 two of the momentum equations (7) yield two principal equations and the other one is used to calculate the density. So the three-dimensional problem may be solved numerically in a manner similar to the two-dimensional case.

Solution Procedure and Computational Results

The overall calculation procedure may be merged into the iteration between the calculations of equations (8), (4), and (9). At the beginning of calculation, an initial distribution of ψ may be calculated from equation (8) based on an estimated distribution of the gas quantities. Density ρ then may be computed by use of equations (4) and (9), and new variations of velocity and other variables are obtained. After these distributions are found, the next iteration begins and this procedure will continue until convergence is reached. Convergence is checked when the maximum relative change of the stream

Downloaded 01 Jun 2010 to 171.66.16.57. Redistribution subject to ASME license or copyright; see http://www.asme.org/terms/Terms_Use.cfm

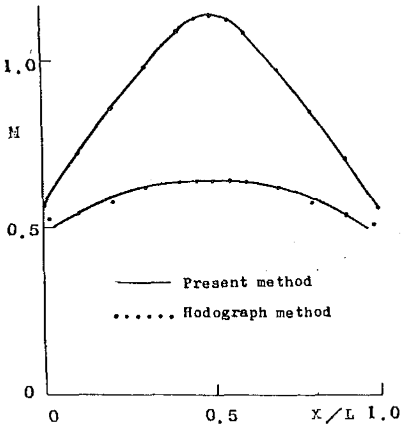

Fig. 2 Computational results for Hobson cascade

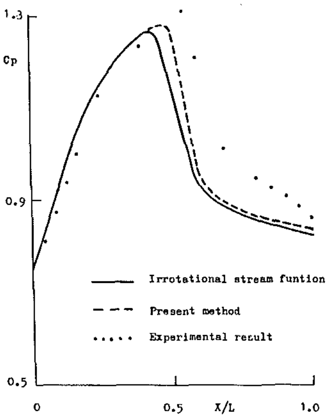

Fig. 3(*a*) Distribution of pressure coefficient

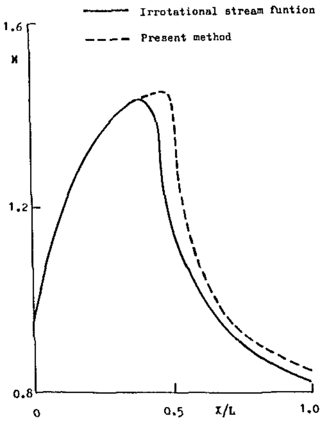

Fig. 3(*b*) Mach number contour

Fig. 3 Comparison of computational and experimental result for DCA 2-8-10 ($M_1 = 1.03$)

function is less than a prescribed precision, say, 1×10^{-4}. It is expected that compared with the irrotational stream function calculation, the convergence of the present model is a little bit better owing to the introduction of the entropy, and the total computing time is also a little bit less owing to the omission of the calculation about the two-valued problem of density. The calculation practice confirms these judgments.

A number of transonic cascade flows have been computed to evaluate the effectiveness of the present method. Some numerical results will be given below.

1 Hobson Cascade. The inlet conditions in the calculation are: $P^0 = 10{,}332$ kg/m^2, $T^0 = 288$ K, $\lambda_1 = 0.61$, $\beta_1 = 0.805$ arc; the outlet conditions are: $\beta_2 = -0.805$ arc, $P_2 = 8257.64$ kg/m^2. The computed distributions of Mach number (Fig. 2) show that the result of this method is in agreement with the original hodograph solution (Hobson, 1972), and is identical with the irrotational stream function calculation carried out by Wei (1985). The iteration numbers and the time of computation to achieve the same convergence precision for both stream function calculations are equivalent.

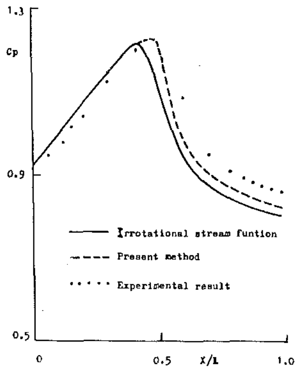

Fig. 4(*a*) Distribution of pressure coefficient

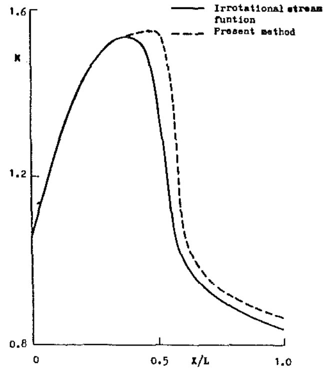

Fig. 4(*b*) Mach number contour

Fig. 4 Comparison of computational and experimental result for DCA 2-8-10 ($M_1 = 1.11$)

2 DCA 2-8-10 Cascade. The cascade geometries are given by Starken (1971). Two flow conditions are calculated:

(*i*) $M_1 = 1.03$, $\beta_1 = 61.8$ deg, $P_2/P_1 = 1.29$
(*ii*) $M_1 = 1.11$, $\beta_1 = 62.5$ deg, $P_2/P_1 = 1.35$

It is seen from the distributions of the pressure coefficients in Figs. 3(*a*) and 4(*a*) that the shocks computed by the present method are located one or two meshes downstream of those in the irrotational method, and are closer to the experimental data, while upstream of the shocks the results of both calculations are identical. In the calculations a 50×13 grid is used and the shocks are smeared in three-four meshes; correspondingly, in the Mach number contours (Figs. 3*b* and 4*b*) the positions of the maximum Mach number move downstream and their values are almost the same or increase slightly. On the other hand, the Mach number after the shocks increases. So the shocks are slightly weaker compared with the irrotational calculations, which is also in agreement with the test results.

3 $T_1-(18A_6I_{4b})08$ Cascade. The cascade shape is described by Savage et al. (1955). The inlet flow conditions: $M_1 = 0.832$ and $\beta_1 = 30$ deg, and the outlet condition $\beta_2 = 11.6$ deg, are given. The distribution of calculated Mach number is shown in Fig. 5 and compared with the time-dependent solution (Lu and Chen, 1984), the irrotational stream function calculation (Wei, 1985), and experimental data. In this case two shocks appear. Even so the present formulation gives a

Downloaded 01 Jun 2010 to 171.66.16.57. Redistribution subject to ASME license or copyright; see http://www.asme.org/terms/Terms_Use.cfm

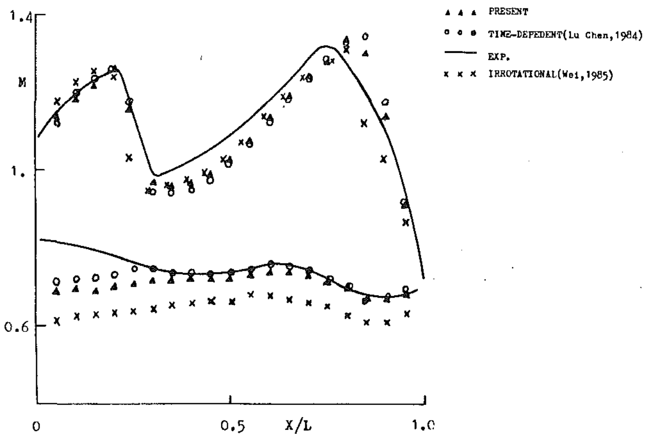

Fig. 5 Comparison of Mach number contours for T_1(18A6I4b)08 cascade

result very close to the Euler solution, as the theoretical analysis predicts. Both solutions are quite different from the irrotational calculation although the agreement between them and the experimental value is quite good. It proves that this model is exact in calculating transonic flow with shocks.

In these examples it is found that the iteration number of this method to achieve a prescribed precision is a little bit less, the computer code is simpler, and the computing time is shorter compared to the irrotational one.

Concluding Remarks

The stream function approach may be applied to solve rotational and nonisentropic flows, and its computation is very simple. To circumvent the difficulty in computing density from the mass flux in the transonic region and to capture the effect of entropy across the shock, it is proposed in this paper to solve the stream function from one of the momentum equations combined with the energy equation and to compute the density from another momentum equation.

The numerical results of the transonic cascade flows on the surface of revolution show that the shocks from the present model are slightly weaker and are placed one or two meshes farther downstream compared to the irrotational stream function calculations, and the agreement with the experimental data is also improved. It is also seen that the results of this formulation are very close to Euler solutions.

From a standpoint of computation the convergence of this method is a little bit better than the irrotational one due to the effect of entropy. Moreover, the alternate use of two momentum equations not only extends the range of calculation and improves the accuracy of the computation, but also simplifies the iteration procedure and saves computing time. All these will make the wide application of the stream function formulation to the transonic flow calculations possible, as in the subsonic case.

References

Ballhaus, W. F., Jameson, A., and Albert, J., 1978, "Implicit Approximate Factorization Schemes for the Efficient Solution of Steady Transonic Flow Problems," *AIAA J.*, Vol. 16, No. 6.

Ge, M. C., 1985, "A Stream Function Relaxation Method for Solving Transonic S_1 Stream Surface With Pre-determination of the Density," ASME Paper No. 85-GT-164.

Giese, J. H., 1951, "Stream Functions for Three-Dimensional Flows," *J. of Math. and Phys.*, Vol. 30, No. 1.

Hafez, M. M., Murman, E. M., and South, J. C., 1978, "Artificial Compressibility Methods for Numerical Solution of Transonic Full Potential Equation," AIAA Paper No. 78-1148.

Hafez, M., and Lovell, D., 1981, "Numerical Solution of Transonic Stream Function Equation," AIAA Paper No. 81-1017.

Hafez, M., Habashi, W., and Kotiuga, P., 1984, "Conservative Calculations of Non-isentropic Transonic Flows," AIAA Paper No. 84-1182.

Hobson, D., 1972, "The Hodograph Method for Design of Transonic Turbine Blades," CUED/A, Turbo-TR, 40.

Holst, T. L., 1978, "An Implicit Algorithm for the Conservative Transonic Full Potential Equation Using an Arbitrary Mesh," AIAA Paper No. 78-1113.

Klopfer, G. H., and Nixon, D., 1983, "Non-isentropic Potential Formulation for Transonic Flows," AIAA Paper No. 83-0375.

Lu, W. Q., and Chen, X. M., 1984, "An Improved Time-Dependent Method for Transonic Fow Calculation on S_1 Surface of Revolution," in: *Computational Methods in Turbomachinery*, IMechE.

Osher, S., Hafez, M., and Whitlow, W., Jr., 1985, "Entropy Condition Satisfying Approximations for Full Potential Equation of Transonic Flow," *Mathematics of Computation*, Vol. 44, No. 169.

Savage, M., Felix, R., and Emery, J., 1955, "High Speed Cascade Tests of a Blade Section Designed for Typical Hub Conditions of High-Flow Transonic Rotors," NACA RM L55 F07.

Starken, H., 1971, "Untersuchung der Strömung in Ebenen Überschall-Verzogerung Gitten," DLR FB 71-99, DFVLR, Institut für Luftstrahlantriebe.

Wang, Z. M., 1985, "Solution of Transonic S_1 Surface Flow by Successfully Reversing the Direction of Integration of the Stream Function Equation," ASME JOURNAL OF ENGINEERING FOR GAS TURBINES AND POWER, Vol. 107, No. 2, pp. 317-322.

Wei, X. M., 1985, "Relaxation Solution of Transonic Stream Function Equation on S_1 Stream Surface in a Turbomachine," MSc Thesis, Institute of Engineering Thermophysics, Chinese Academy of Sciences.

Xu, J. Z., 1980, "Shock Relations in Turbomachines," *Chinese J. of Mechanical Engineering*, Vol. 16, No. 3.

Xu, J. Z., et al., 1982, "An Aerothermodynamic Analysis of Transonic Compressor Rotors Containing Three-Dimensional Shocks," ASME JOURNAL OF ENGINEERING FOR POWER, Vol. 104, No. 2.

Xu, J. Z., Ni, W. Y., and Du, J. Y., 1985, "Non-isentropic Potential Equations and Their Application to Transonic Computation," presented at the 5th Conference of Chinese Society of Engineering Thermophysics.

Xu, J. Z., Du, J. Y., and Ni, W. Y., 1986a, "Numerical Computation of Non-isentropic Potential Equations for Transonic Cascade Flows," to be published in *Acta Aerodynamica Sinica* (in Chinese).

Xu, J. Y., Du, J. Y., and Ni, W. Y., 1986b, "Transonic Potential Formulation and Its Numerical Solution," presented at the Aerothermodynamics Conference of Heat Engines, Chinese Society of Engineering Thermophysics.

Zhao, X., 1984, "Solution of Transonic Flow Along S_1 Stream Surface Employing Non-orthogonal Curvilinear Coordinates and Corresponding Non-orthogonal Velocity Components," *Computational Methods in Turbomachinery*, IMechE.

Downloaded 01 Jun 2010 to 171.66.16.57. Redistribution subject to ASME license or copyright; see http://www.asme.org/terms/Terms_Use.cfm

D. S. Musgrave
Engineering Specialist.

N. J. Plehn
Engineer.

Williams International
Walled Lake, MI 48088

Mixed-Flow Compressor Stage Design and Test Results With a Pressure Ratio of 3:1

This paper presents a brief history of mixed-flow compressors, possible applications, and the design and measured performance of a recently tested 3:1 pressure-ratio stage. The stage is intended to run behind a multistage axial compressor; it has an envelope radius only 9.4 percent greater than the rotor tip radius. A tandem cascade diffusing system is used to promote flow range and thus aid matching to the axial stages. Compressor maps from the rig test are presented along with additional data (from static taps and exit rakes) that characterize the behavior of various elements of the stage.

Introduction

Axial compressor design technology has a well-documented history, with many cascade tests and data sets supporting an established technology base. Centrifugal compressor design has a more informal background and the initial progress was not as rapid, but the current design methodology is quite sophisticated. On the other hand, the mixed-flow compressor has a very modest history and it has rarely seen production.

A literature search revealed that most of the work on mixed-flow stages in the 1950s and 1960s was hampered by many of the same problems that confronted centrifugal designs of that era: radial element blades due to structural limitations, no experimental data base, limited computational ability, and serious problems with diffuser design.

Surprisingly, pump designers (working solely with incompressible fluids) have been quite successful at designing mixed-flow pumps and turbines for many years. Indeed, early mixed-flow designs for air could have been more successful if the existing pump designs were scaled and then corrected for compressibility.

Eventually, turbomachinery compressor designers developed powerful computational design tools for arbitrary geometry airfoils, brought centrifugal compressors to the point that they became competitive in some jet engines, and developed an understanding of fundamental compressible fluid mechanics for turbomachinery that permitted successful mixed-flow designs [1]. Published data on mixed-flow stages that were developed over the last ten years are still small, however. It is expected that the ultimate efficiency potential of the mixed-flow stage is quite high and that more widespread use will develop. This paper reports on one modern stage at 3.02:1 pressure ratio designed to exhibit wide range for matching to a series of axial stages. It is hoped that the results of this study will stimulate further investigation.

Applications

The mixed-flow stage is expected to be advantageous in situations in which the overall stage diameter is of critical importance or in designs in which several axial stages can be replaced by a single mixed-flow stage as a cost reduction.

Turbochargers of low to moderate pressure ratio are an obvious possibility, since an increase in the overall stage length could be less critical than the benefits of a reduction in the maximum stage diameter. Care would be needed to ensure that the pedestal support for the rotor minimizes the polar moment of inertia.

Conventional short-range missiles with turbojet or turbofan engines are similar in their requirements, since the maximum stage diameter is often established by a centrifugal compressor stage.

An example of substitution for axial stages would be that of high-pressure-ratio turbofan engines, which often use six to ten axial stages. The last axial stages are quite small and their entrance conditions and matching requirements limit their pressure ratio. For instance, the 3.02:1 pressure ratio stage presented in this paper could substitute for three axial stages with pressure ratios of 1.5, 1.44, and 1.4. If these small axials averaged only 86 percent efficiency each, then a mixed-flow stage with 85 percent efficiency overall would provide better performance and only three blade rows would be needed instead of six. The overall length is similar.

Program Goals and Preliminary Design

The mixed-flow stage was designed in tandem with a multistage axial compressor running on the same shaft. The major reason for using a mixed-flow stage was to eliminate three small axial stages. The corrected mass flow was selected to be in the 3 kg/s (6.6 lb/sec) size class. An efficiency goal of

---

Contributed by the Gas Turbine Division of THE AMERICAN SOCIETY OF MECHANICAL ENGINEERS and presented at the 32nd International Gas Turbine Conference and Exhibit, Anaheim, California, May 31-June 4, 1987. Manuscript received at ASME Headquarters February 3, 1987. Paper No. 87-GT-20.

Copyright © 1987 by ASME

Downloaded 01 Jun 2010 to 171.66.16.57. Redistribution subject to ASME license or copyright; see http://www.asme.org/terms/Terms_Use.cfm

Table 1 Rotor geometric and aerodynamic characteristics

GEOMETRY (HOT)			
NUMBER FULL BLADE		12	
NUMBER SPLITTER BLADES		12	
INDUCER HUB RADIUS	mm (inches)	68.6	(2.7000)
INDUCER TIP RADIUS	mm (inches)	99.95	(3.9350)
INDUCER TIP CLEARANCE	mm (inches)	0.25	(0.010)
INDUCER BLADE ANGLE (REF AXIAL) AT HUB	(degrees)	48.32	
INDUCER BLADE ANGLE (REF AXIAL) AT MEAN	(degrees)	54.65	
INDUCER BLADE ANGLE (REF AXIAL) AT TIP	(degrees)	58.55	
INDUCER L.E.R. AT HUB	mm (inches)	0.83	(0.0325)
INDUCER L.E.R. AT TIP	mm (inches)	0.25	(0.010)
INDUCER THROAT AREA	mm^2 (inches^2)*	8,574	(13.29)
IMPELLER EXIT RADIUS	mm (inches)**	122.7, 128.5, 134.6	(4.83, 5.06, 5.30)
IMPELLER EXIT BLADE ANGLE (REF RAD)	(degrees)**	19.9, 31.9, 48.96	
IMPELLER EXIT BLADE HEIGHT	mm (inches)	13.5	(0.5313)
IMPELLER EXIT BLADE CLEARANCE	mm (inches)	0.25	(0.010)
AERODYNAMICS			
STAGE DESIGN POINT CORRECTED FLOW RATE	kg/sec (lbm/sec)	2.89	(6.35)
STAGE DESIGN POINT CORRECTED SPEED	(rpm)	31,974	
STAGE DESIGN POINT PRESSURE RATIO (T-T)		3.02:1	
STAGE DESIGN POINT EFFICIENCY (T-T)		0.837	
INDUCER RELATIVE MACH NUMBER AT HUB		0.786	
INDUCER RELATIVE MACH NUMBER AT TIP		1.139	
INDUCER BLOCKAGE		0.020	
INDUCER INCIDENCE AT HUB	(degrees)	11.7	
INDUCER INCIDENCE AT MEAN	(degrees)	5.4	
INDUCER INCIDENCE AT TIP	(degrees)	1.5	
IMPELLER CORRECTED EXIT SPEED	m/sec (ft/sec)**	411, 430, 450	(1,347, 1,412, 1,479)
IMPELLER DEVIATION ANGLE	(degrees)**	9.2, 6.0, 4.3	
IMPELLER WORK FACTOR (Z)**		0.81, 0.68, 0.63	
IMPELLER EXIT RELATIVE AIR ANGLE (REF MER)	(degrees)**	30.5, 36.8, 54.1	
IMPELLER EXIT ABSOLUTE AIR ANGLE (REF MER)	(degrees)**	68.5, 58.2, 67.0	
IMPELLER EXIT RELATIVE MACH NUMBER**		0.40, 0.61, 0.53	
IMPELLER EXIT BLOCKAGE (AERO)**		0.13, 0.07, 0.18	
IMPELLER CORRECTED EXIT STATIC PRESSURE	(psia)**	26.5, 28.0, 29.1	
IMPELLER CORRECTED TEMPERATURE RISE	(°R)	229.3	
IMPELLER RELATIVE VELOCITY RATIO**		0.58, 0.68, 0.54	

*BASED ON PITCHES DETERMINED AT PLANE SECTION CUT RADII
**HUB, RMS, TIP

M-12321
12-1-86

Table 2 Diffusing system geometric and aerodynamic characteristics

GEOMETRY (HOT)			
VANELESS RAD RATIO, MEAN (MERIDIONAL/R)		1.14	
VANELESS INLET RADIUS, MEAN	mm (inches)	128.52	(5.060)
VANELESS PASSAGE HEIGHT – INLET	mm (inches)	13.48	(0.531)
VANELESS PASSAGE HEIGHT – EXIT	mm (inches)	13.33	(0.525)
STATOR ONE INLET MEAN RADIUS	mm (inches)	135.87	(5.349)
STATOR ONE INLET PASSAGE HEIGHT	mm (inches)	13.33	(0.525)
STATOR ONE INLET METAL ANGLE (REF MER)	(degrees)*	64.5, 59.0, 61.9	
STATOR ONE VANE NUMBER		27	
STATOR ONE VANE TYPE		DCA	
STATOR ONE SOLIDITY*		1.41, 1.17, 1.30	
STATOR ONE CAMBER	(degrees)*	16.6, 18.3, 11.2	
STATOR ONE CHORD	mm (inches)*	43.69, 37.85, 43.94	(1.72, 1.49, 1.73)
STATOR ONE T/C		0.040	
STATOR ONE LER	mm (inches)	0.25	(0.010)
STATOR ONE TER	mm (inches)	0.18	(0.007)
STATOR ONE EXIT MEAN RADIUS	mm (inches)	142.25	(5.600)
STATOR ONE EXIT PASSAGE HEIGHT	mm (inches)	10.09	(0.397)
STATOR ONE METAL ANGLE (REF MER)	(degrees)*	47.9, 40.7, 50.7	
STATOR TWO INLET MEAN RADIUS	mm (inches)	142.43	(5.607)
STATOR TWO INLET PASSAGE HEIGHT	mm (inches)	9.80	(0.386)
STATOR TWO INLET METAL ANGLE (REF MER)	(degrees)*	48.5, 48.6, 54.0	
STATOR TWO VANE NUMBER		54	
STATOR TWO VANE TYPE		DCA	
STATOR TWO SOLIDITY*		2.04, 1.96, 1.97	
STATOR TWO CAMBER	(degrees)*	47.5, 49.6, 52.0	
STATOR TWO CHORD	mm (inches)*	32.77, 32.51, 33.78	(1.29, 1.28, 1.33)
STATOR TWO T/C		0.045	
STATOR TWO LER	mm (inches)	0.23	(0.009)
STATOR TWO TER	mm (inches)	0.18	(0.007)
STATOR TWO EXIT MEAN RADIUS	mm (inches)	142.88	(5.625)
STATOR TWO EXIT PASSAGE HEIGHT	mm (inches)	8.91	(0.351)
STATOR TWO EXIT METAL ANGLE (REF MER)	(degrees)*	1.0, -1.0, 2.0	
ANNULAR DIFFUSER AREA RATIO		2.6:1	
ANNULAR DIFFUSER L/W		12.5	
AERODYNAMICS			
VANELESS DIFFUSER INLET MACH NUMBER*		0.94, 0.93, 0.80	
VANELESS DIFFUSER INLET AIR ANGLE (REF MER)	(degrees)*	68.5, 58.2, 67.0	
VANELESS DIFFUSER INLET BLOCKAGE		0.11	
VANELESS DIFFUSER CORRECTED INLET STATIC PRESSURE	(psia)*	26.5, 28.0, 29.1	
VANELESS PRESSURE RECOVERY (Cp)*		0.11, 0.10, 0.09	
STATOR ONE INLET MACH NUMBER*		0.87, 0.86, 0.76	
STATOR ONE INLET BLOCKAGE		0.11	
STATOR ONE INLET CORRECTED STATIC PRESSURE	(psia)*	28.7, 30.0, 30.4	
STATOR ONE INCIDENCE ANGLE	(degrees)*	6.2, -0.3, 4.5	
STATOR ONE DEVIATION	(degrees)*	8.0, 7.0, 8.0	
STATOR ONE LOSS COEFFICIENT (ω)*		0.057, 0.05, 0.05	
STATOR ONE DIFFUSION FACTOR D_f*		0.33, 0.25, 0.30	
STATOR TWO INLET MACH NO.*		0.68, 0.72, 0.59	
STATOR TWO INLET BLOCKAGE		0.11	
STATOR TWO INLET CORRECTGED STATIC PRESSURE	(psia)*	33.5, 33.8, 34.4	
STATOR TWO INCIDENCE ANGLE	(degrees)*	5.5, -2.1, 4.0	
STATOR TWO DEVIATION	(degrees)*	6.5, 7.0, 7.5	
STATOR TWO LOSS COEFFICIENT (ω)*		0.065, 0.05, 0.075	
STATOR TWO DIFFUSION FACTOR D_f*		0.62, 0.50, 0.70	
ANNULAR DIFFUSER EXIT MACH NUMBER		0.30	
ANNULAR DIFFUSER EXIT AIR ANGLE (REF AXIAL)	(degrees)	$\approx$15	

*HUB, RMS, TIP

M-12334
12-1-86

at least 0.837 (total-to-total) was specified as the minimum for the mixed-flow stage with a higher value desired.

Comparison with three axial stages indicated that the mixed-flow stage would be comparable in overall length and efficiency. The reduction in blade rows from three rotors and three stators to one rotor and two stators showed a significant cost advantage.

The weight and polar inertia of the mixed-flow stage would probably be higher than those of the three-stage axial compressor, with the exact differences dependent upon the design of the pedestal support for the rotor.

A flowpath outer diameter limit of 305 mm (12 in.) was established as a packaging constraint for the mixed-flow stage.

Additional goals arose from the aerodynamic requirement to match the mixed-flow stage to the axial ones without interstage bleed except, possibly, at startup. Thus, wide range was needed along with tolerance to a skewed entry profile. Finally, it was desired to use a cylindrical flowpath for connecting the axial stages to the mixed-flow stage in order to minimize axial length and ducting losses.

A computer code for matching axial stages to a centrifugal stage on the same shaft was modified and used extensively to study the various possibilities. "Meanline" or preliminary programs were also used to characterize the behavior of the axial stages or the mixed-flow one. This work was carried out in considerable depth since experience has shown that errors in diffusion levels, blade loading, and flow angles during the initial definition of a stage flowpath cannot be rectified during the detailed blading design regardless of the degree of sophistication of the final aerodynamic design programs.

Major matching parameters were speed and work-split (i.e., pressure ratio). Other significant items included axial stage exit radii (which determine both entrance axial Mach number and "inducer" relative Mach numbers), mixed-flow exit blade angles, and diffusion and relative turning projected for rotor and diffusing system. Key output variables were the tip relative Mach number of the first axial stage and its specific flow and the exit Mach numbers and angles from the mixed-flow rotor. Projected maps were generated for acceptable designs and then run through a map-merging program to obtain an overall map.

Specific speed of the mixed-flow stage was limited to 0.92 (nondimensional value) in order to avoid excessive shock losses on the first axial stage. An application that needed only the mixed-flow stage would run 30 to 40 percent faster with a much lower leading edge hub/tip ratio.

The final mixed-flow stage has a pressure ratio of 3.02:1, with corrected mass flow and speed of 2.89 kg/s (6.35 lb/sec) and 31,971 rpm, respectively. Its inducer hub radius of 68.6 mm (2.700 in.) and tip radius of 99.95 mm (3.935 in.) result in a high hub/tip ratio (0.686). Lower values, although desirable, were detrimental to the axial stages' surge margin and efficiency.

Meanline geometric and aerodynamic characteristics for the mixed-flow rotor and diffusing system are presented in Tables 1 and 2, respectively. It should be noted that the stage diameter of 294.6 mm (11.60 in.) is well under the 305-mm (12-in.) goal.

A splitter-bladed rotor (12-12 blades) was selected to gain choke margin, reduce incidence sensitivity, assist fabrication, and lower entrance losses.

The diffusing system employs a tandem stator arrangement with 27 vanes in the first row and 54 vanes in the second row. This design philosophy draws on previous experience with wide range diffusers for centrifugal stages. Briefly, the first row is lightly loaded and its low solidity allows acceptance of significant incidence variations resulting from changes in mass flow or entry profile. The second row is confronted with nearly constant incidence over various operating conditions, and hence its loading can be quite high. A meridional contraction is used on both rows to obtain the desired diffusion factors.

An annular diffuser completes the stage. It lowers the exit Mach number to a level consistent with the bounding collection plenum.

Axial length of the stage would be lowered for a production application by overlapping the stators and possibly reducing the rotor axial length. This stage, however, was designed to investigate the basic concept and allow individual stator fabrication (and substitution if necessary). A meridional view of the stage is presented in Fig. 1.

Detailed Design

Estimated total pressure and total temperature profiles from the last axial stage were available to assist in the detailed

Downloaded 01 Jun 2010 to 171.66.16.57. Redistribution subject to ASME license or copyright; see http://www.asme.org/terms/Terms_Use.cfm

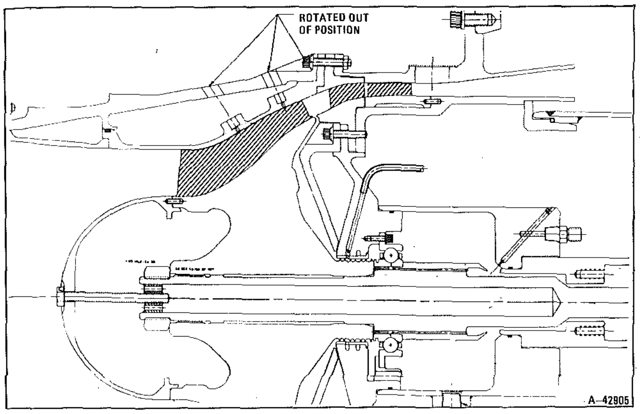

Fig. 1 Meridional view of the mixed-flow stage

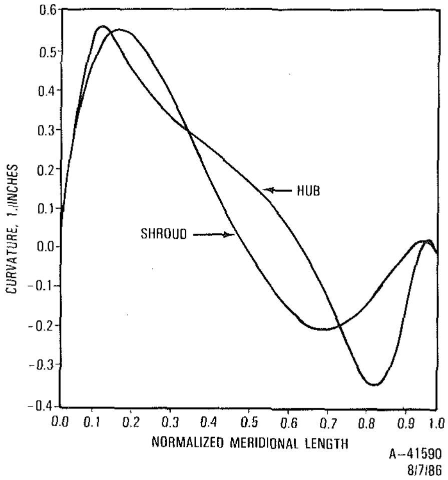

Fig. 2 Rotor meridional curvature levels

design of the blading. A spanwise variation of about 4 percent in total temperature was predicted along with a hub total pressure approximately 4.5 percent below the average value. Both incidence angles and blade loading distribution are dependent upon the predicted axial stage exit characteristics, but there was no guarantee of the accuracy of these estimates. Thus, the reduced entrance sensitivity of a splitter-bladed rotor with conservative loading was indicated.

Rotor flowpath was established in tandem with the blade loading calculations to control relative velocities and the distribution of the energy addition. A Bernstein-Bezier polynomial program determined the shape of the hub and shroud contours. In brief, this technique allows local control of an analytic curve through the use of "puppet points" that adjust the curve in the proximate region. Precise control of slopes and curvatures is possible throughout the flowpath.

Curvatures of 0.0 were obtained at the leading edge and trailing edge of both contours. Curvature increased in the "inducer" region to maximums of about 0.55, which then decreased to 0.0, obtained −0.2 to −0.3 after the inflection point, and then finally reached 0.0 at the rotor exit. This approach follows the philosophy of turning moderately in the initial region of the flowpath where the boundary layers are healthier. Curvature values throughout the rotor flowpath are shown in Fig. 2.

Maximum slopes of 33 deg and 45 deg were reached on the shroud and hub, respectively. These values are substantially below the 90 deg typical of centrifugal compressors and they result in substantially reduced secondary flows. An analogy with flow in curved pipes is quite appropriate.

Loading throughout the flowpath was also controlled using the Bezier-Bernstein technique. In this case, the vorticity derivative with respect to meridional distance was used as the adjustable curve.

The rms streamline loading is fairly conventional with moderate trailing region suction surface diffusion (Fig. 3).

Relative velocity ratios (neglecting loading) on the hub, rms, and tip streamlines are 0.58, 0.68, and 0.54, respectively.

Boundary layer calculations were made for the above three streamlines on both the pressure and suction surfaces for both the full blades and the splitters. These computations adjust the boundary layer behavior for the effects of blade loading, i.e., Richardson number. Although it is recognized that the calculations can only be approximate due to the very complex flow situation in mixed or centrifugal turbomachinery, they do serve as a semiquantitative guide to the highly nonlinear behavior that is typical of boundary layers, and thus they are of value in selecting surface velocities and loading distributions.

Separation was predicted for only three streamline surfaces. The full blade hub pressure surface showed a separation about 2/3 of the way through the flowpath. The hub loading reveals that this boundary layer almost makes it through the point of minimum velocity and it could well be successful given the stable character of hub pressure surface flows. A somewhat similar situation also exists on the full blade shroudline pressure surface.

Finally, a shroudline suction surface separation was predicted at about 90 percent of the way through the flowpath. No separations were predicted anywhere else. The splitter blade pressure and suction surface velocities were particularly stable, with shape factors on the order of 1.4 to 1.8. It was decided to accept the above situation since a reduction in blade loading or diffusion would create other potential efficiency costs in the remainder of the stage.

A careful integration of the inducer choke flow (using the estimated axial stage exit conditions) resulted in a choke margin of 3.8 percent. Although quite low, it was accepted since additional choke margin would require increased incidence levels and the current hub value of around 10.9 deg is considered fairly high.

Deviation angles were selected based upon centrifugal compressor practice; they were a function of the exit blade angle and they were distributed along the approach to the trailing edge.

Aerodynamic blockages within the rotor were based upon smoothed and interpolated displacement thicknesses from the output of the Richardson number-corrected boundary layer calculations. The rotor's aerodynamic loss distribution drew upon correlations for similar boundary layer characteristics in centrifugal stages. The losses projected at the trailing edge are nonlinear with minimum loss on the rms streamline and higher losses on both the hub and tip streamlines. Boundary layer calculations indicated that a fillet radius of 3.18 mm (0.125 in.) would be appropriate, and this value was used for both blade types. Detailed information regarding the rotor design is available from Table 1.

A "vaneless space" was used to reduce the dynamic interaction between the rotor and the cascade stator system. The 19 mm (0.748 in.) meridional spacing also results in a reduction of about 0.06 in Mach number at the stator leading edge. This is of significant benefit to the stage range. The Bezier-Berstein polynomial approach was used to contour the vaneless space in order to avoid any acceleration of flow due to curvature effects.

The cascade stator system was designed with particular attention to the strong three dimensionality of the flow exiting from the mixed-flow rotor. Double circular arc airfoils were used with variations in stagger and camber from hub to shroud [2, 3]. The first stator looked much like a pipe diffuser

Downloaded 01 Jun 2010 to 171.66.16.57. Redistribution subject to ASME license or copyright; see http://www.asme.org/terms/Terms_Use.cfm

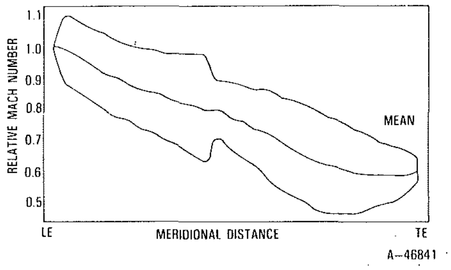

Fig. 3 Rotor blade loading, rms streamline

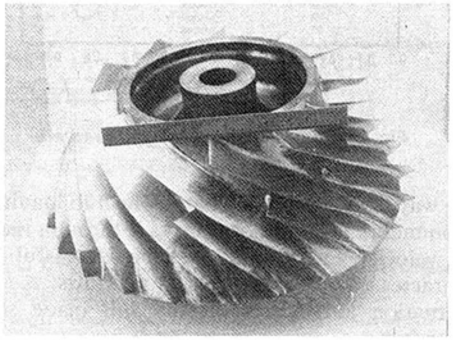

Fig. 4 Rotor after machining

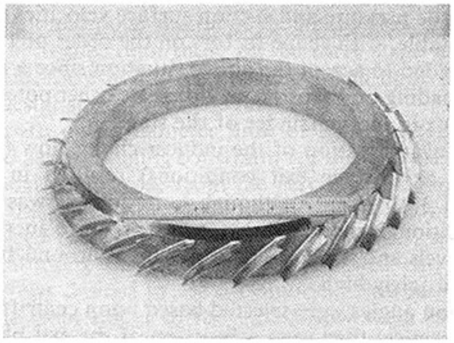

Fig. 5 First stator ring

at its entrance due to the difference in stagger between the mean section and the two wall sections.

The first stator had an rms streamline diffusion factor of 0.255 and an incidence close to 0 deg. Endwall incidences and diffusion factors were slightly higher. An overall choke margin of 7.8 percent was obtained. The second stator had similar incidences, but the rms diffusion factor was 0.5.

Lean angles along the first stator trailing edge of the cascade diffuser design were adjusted to align with the second stator leading edge lean distribution so that the stators could be offset in a realistic manner. A guide was used to determine the tangential and axial offsets along with experience on similar cascade arrangements [4]. A fillet radius of 1.14 mm (0.045 in.) was used on both vanes as a result of boundary layer calculations.

Stator design was the most difficult aspect of the project, since it combines a substantial diffusion (Mach 0.76 through 0.87 down to Mach 0.42) with a large amount of turning (an inlet air angle approximately 70 deg is reduced to approximately 7 deg).

An annular flare diffuser completes the stage. It lowers the exit Mach number to 0.30, and it reduces the chaotic flow that would result from dumping the flow at the second stator exit where measurements are made.

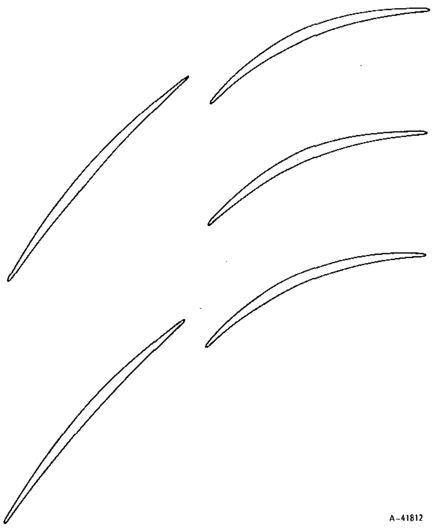

Fig. 6 Relative location of the two stators

Table 2 also presents detailed geometric and aerodynamic information for the diffusing system.

Stage Mechanical Design and Fabrication

The stage is a research project only, and hence, the arrangement of hardware and test rig was oriented toward obtaining instrumentation access, reasonable cost, and high reliability with little effort devoted to high-volume production or weight reduction.

The test rig could be easily modified to allow operation with the axial stages upstream. Rotor backface bleed level is metered, and shaft dynamics and other mechanical concerns are addressed.

The rotor was designed to handle stresses and temperatures of operation with axial stages upstream. A dynamics analysis indicated that all blade modes below the ninth would lie outside of the operating range.

Inspection slices were taken of the rotor blades (both types) and then compared to CAD/CAM sections of the aerodynamic definition. Very good agreement was obtained except that the blades were slightly thin in part of the trailing edge region. Figure 4 shows the rotor. Note the high blade wrap (large change in polar angle), the splitter arrangement, and the high inducer hub/tip ratio.

Average rotor surface finish was approximately 60 μin. rms. A slightly better value (about 32 μin. rms) would be desirable for production items.

A cover with an abradable shroud (aluminum polyamide) was used to permit running with the design clearance of 0.25 mm (0.010 in.) or less.

Both stators were also produced by Williams International using the pantograph technique. The first stator is highly three dimensional, as can be seen in Fig. 5. Stator one was brazed to its outer contour, while stator two has a constant outer radius which was designed to press fit into its casing. Relative stator location is revealed in the mean section sketches of Fig. 6.

Stator inspection revealed very good fidelity to the design contours although the fillet radius on the first stator was 2.29 mm (0.090 in.) instead of the print value of 1.14 mm (0.045 in.). No significant impact on the performance was anticipated.

As shown in the meridional view (Fig. 1), the annular flare exits outward. This was done solely to mate with an existing plenum; in an actual application it would diverge downward to maintain the envelope.

Downloaded 01 Jun 2010 to 171.66.16.57. Redistribution subject to ASME license or copyright; see http://www.asme.org/terms/Terms_Use.cfm

Table 3 Instrumentation description

LOCATION	TYPE	QUANTITY/NOTES
BELLMOUTH	P_S	2
	P_T(BAROMETER)	1
	T_T(AMBIENT)	2
STAGE ENTRANCE	P_S	3
	P_T	8 KIEL
	T_T	2 FIVE-ELEMENT RAKES
ROTOR	P_S	6 NEAR THROAT
	P_S	6 AT SHROUD EXIT
	P_S	3 AT HUB EXIT
	P_S	5 IN BACKFACE CAVITY
	T_S	4 IN BACKFACE CAVITY
	CLEARANCE	1 ROTADATA AT "KNEE" 1 ROTADATA AT TIP
STATOR ONE	P_S	3 AT LE HUB
	P_S	3 AT LE SHROUD
	P_S	3 AT SHROUD THROAT
	P_S	6 AT TE
STATOR TWO	P_S	4 AT TE SHROUD
	P_S	4 AT TE HUB
	P_S, DYNAMIC	2 ENTRANS AT TE
	P_T	13 ELEMENT RAKE AT HUB, 2 PITCHES
	P_T	2 KIELS NEAR TIP AND RMS
ANNULAR FLARE EXIT	P_T	3 FIVE-ELEMENT RAKES (WITH AXIALS UPSTREAM)
	T_T	3 FIVE-ELEMENT RAKES
PLENUM	P_S	3

M–12422
12/3/86

Rig Instrumentation

Instrumentation was installed to achieve twin goals of overall stage performance measurement and detailed intrastage element characterization.

The work input into the stage was measured using calibrated thermocouples at the stage entrance and exit. Two five-element inlet rakes were used along with three five-element rakes at the annular flare exit. Although not as accurate as a calibrated torquemeter, the temperature-based work input approach was estimated to read within 1 percent of the true mechanical work. The inlet thermocouples were located 0.28 m (11 in.) ahead of the rotor leading edge to avoid heat transfer and backflow effects.

Inlet total pressure was obtained from eight probes located at various radii near the stage entrance. Stage exit flow was expected to be skewed in both the radial and circumferential directions at the second stator exit. Hence, rakes were used at three different radii. One rake had 13 elements which spanned two full vane pitch. It was supplemented by Kiel probes and later by three five-element rakes at the flare exit for the combined test with the axial stages upstream.

Static taps with 0.51 mm (0.020 in.) holes were liberally sprinkled throughout the stage to provide information about the various stage elements. Two sets of three holes each were located near the rotor throat to assist in determining rotor choke. Rotor efficiency was computed using static pressures from six shroud taps and three hub taps at the rotor tip plus the measured work input of the stage. The taps were equally spaced circumferentially.

The first stator had six taps at its leading edge, three at its throat (shroud side only since it becomes sonic last), and six taps at the trailing edge. The second stator had eight trailing edge taps (four of each of the shroud and hub) to assist in the analysis of the exit flow field. Total pressure rakes were also located in this plane. Additional static taps were located in the rotor backface cavity to help model secondary flows and support the backface bleed settings. Finally, three static taps were located in the collection plenum to permit rating the stage on a total-to-static basis.

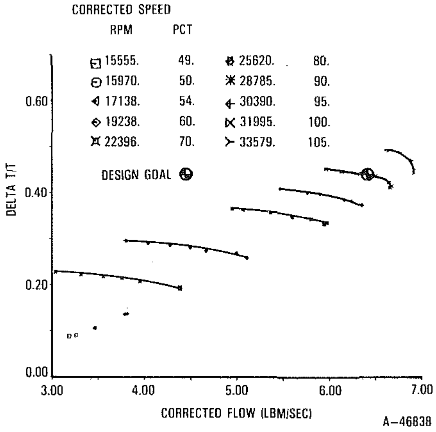

Fig. 7 Stage temperature rise data

Static temperature thermocouples were installed in the rotor backface region to monitor operating temperatures. They were especially useful during operation with the axial stages upstream since temperature levels were much hotter.

An accurate measurement of the rotor running clearance is essential in order to assess the efficiency potential of the stage and to provide feedback to the mechanical design group, Rotadata Ltd. Clearance probes were used at the rotor tip and "knee" during the test (Fig. 1). Also, nine rub tabs were installed (three at the leading edge, three at the "knee," and three at the tip) to provide a check of the Rotadata measurements after rig dissasembly.

An online data system provided an instantaneous CRT display of overall pressure ratio and efficiency, $\Delta T/T$, percent operating speed, corrected mass flow, backface bleed level, running clearance, and options for display of all other information. All the raw data were stored on disk for entry into a master data reduction program.

Two Entran high-response static pressure transducers were installed 120 deg apart at the stage exit. They were used to record the static pressure signal as the stage approached and entered surge. This information was taken to assist the study of stage matching with the axial stages upstream.

Additional instrumentation (vibration levels, bearing temperatures) was installed to monitor the mechanical health of the rig. Table 3 summarizes the type, location, and quantity of the instrumentation.

Analysis of the Test Rig Data

The compressor was assembled to achieve a design point running clearance of 0.25 mm (0.010 in.), and values of 0.18 to 0.36 mm (0.007 to 0.014 in.) were measured over most of the data recording using the Rotadata probes, with the tighter clearances achieved at the "knee" of the rotor. Running clearance could be varied somewhat during the test by adjustment of the air pressure to a thrust piston. Minimum measured running clearances, 0.33 mm (0.013 in.) at the tip and 0.05 mm (0.002 in.) at the "knee," were confirmed upon disassembly by the rub tabs.

Although the stage was designed for use with the estimated axial stages' exit conditions, the mixed-flow rig test was run with a clean inlet (ambient total pressure and temperature conditions), since its performance with the axial stages upstream would be measured later. The clean entry conditions result in inducer relative Mach numbers of 0.834 at the hub and 1.144 at the tip compared to design values of 0.786 and 1.139 as given in Table 1.

The test was run using corrected operating speeds of 70 through 105 percent with six or seven different mass flows at each speed. Mass flow was lowered from wide open throttle

Downloaded 01 Jun 2010 to 171.66.16.57. Redistribution subject to ASME license or copyright; see http://www.asme.org/terms/Terms_Use.cfm

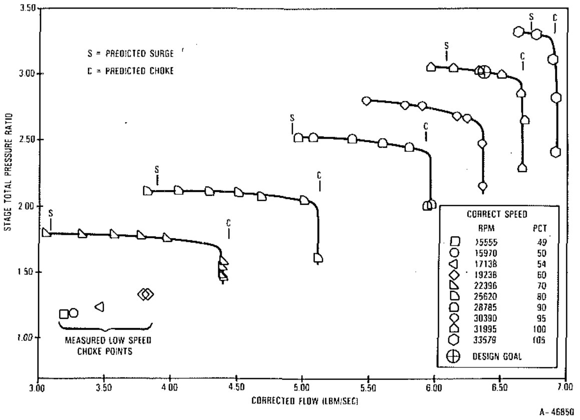

Fig. 8 Compressor map from rig data

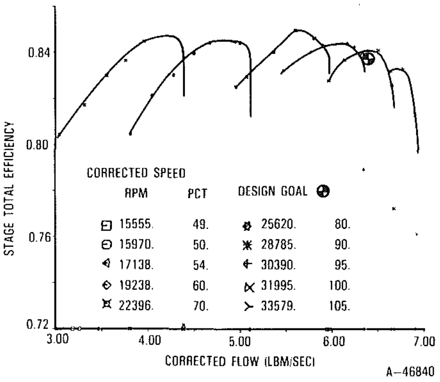

Fig. 9 Measured stage efficiencies

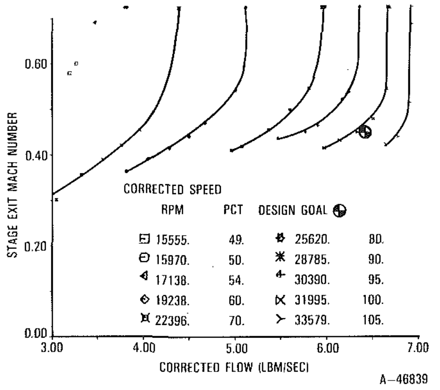

Fig. 10 Measured stage exit Mach number

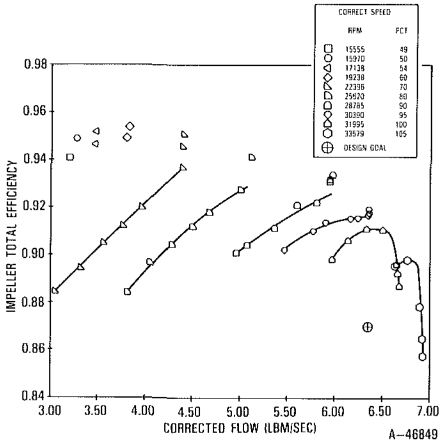

Fig. 11 Rotor efficiency calculated from rig data

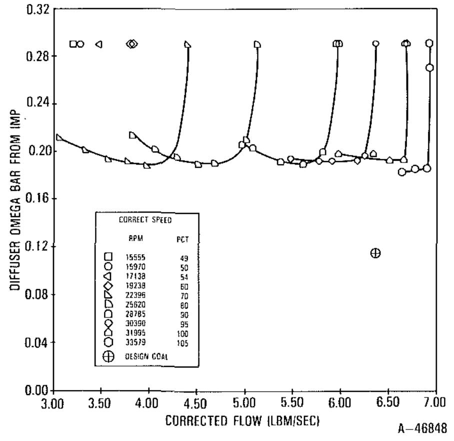

Fig. 12 Measured diffusing system $\bar{\omega}$

down to audible surge with the lowest mass flow point taken just slightly above surge. Several minutes elapsed between each data point recording to allow the rig to reach thermal equilibrium. In addition to the full-speed line data, several wide open throttle points were taken at 50, 54, and 60 percent speeds.

The measured $\Delta T/T$ for the test is shown in Fig. 7. The data quality is quite good, and $\Delta T/T$ at the 100 percent speed design massflow point is easily within 1 percent of the projected value. Rotor choke at 100 and 105 percent speeds is also apparent. Figure 8 plots the overall total pressure ratio (at the second stator exit) versus corrected mass flow. Also shown are the projected surge (S) and choke (C) flows for the various speeds.

The design pressure ratio was met and the flow range is good. Also shown on the plot are the chokeflows for 50, 54, and 60 percent speeds. This information was of value in studying the startup match to the axial stages.

Predicted surge mass flows were made solely on the basis of the diffusion factor on the first stator. A mean diffusion factor of 0.55 was used as the limiting value for this stator, and the accuracy of this simple technique appears good. Rotor shroudline relative velocity ratio was monitored during the effort, and rotor stall would precede stator stall at low pressure ratios such as 50 to 60 percent speed operation.

Predicted choke flows are also quite good. They are based upon the throat conditions in the first stator for all speeds except 100 and 105 percent, where rotor inducer choke became a limiting factor.

Thus, straightforward monitoring of fluid mechanics did a good job of flagging the first stator as the controlling element for most of the speedlines. Clearly, a better first stator could be expected to extend the flow range, which is already good. This could be accomplished by using a boundary layer driven airfoil design instead of the circular arc currently used and also by measuring the flowfield at the stator leading edge before designing this element.

Operation above 105 percent speed was not attempted since the flow range was being limited by rotor inducer choke. It should be noted that a mixed-flow stage designed with a lower hub/tip ratio for operation without upstream stages could accomplish a substantially higher pressure ratio. Pressure ratios of around 5:1 are indicated as not unreasonable by the design programs.

Total-to-total efficiencies at the second stator exit are shown in Fig. 9. These efficiencies are at or above the projected levels, with 84 percent reached at the design point and

Downloaded 01 Jun 2010 to 171.66.16.57. Redistribution subject to ASME license or copyright; see http://www.asme.org/terms/Terms_Use.cfm

peak efficiencies of around 84.5 percent at the lower speeds. As might be expected, the peak efficiencies are near the center of the flow range and, hence, they are usable.

These efficiences were achieved at ambient inlet conditions with a rotor having a surface finish of about 60 rpms. They are quite respectable for a machine in the 3 kg/s (6.6 lb/sec) flow size. Higher efficiencies were obtained in the combined tests with the axial stages upstream due to Reynolds number effects.

The second stator exit Mach number is shown in Fig. 10. It is at the projected 0.45 value at the design point, with other values depending strongly upon the operating condition.

Static taps allowed detailed tracing of the performance of the various stage elements. Figure 11 shows the rotor total efficiency calculated when the measured $\Delta T/T$ is used along with the nine static pressure taps at the rotor tip.

Loss coefficient for the diffusing system (vaneless gap and both stators) is shown in Fig. 12. Note the rather broad loss buckets when the flow is outside of choke. This is typical of low solidity cascades with a moderate entrance Mach number.

Accurate static pressure values are difficult to obtain across the skewed rotor exit flowfield. The level of static pressure measured will influence the division of the stage performance into rotor efficiency and diffusing system losses. Nevertheless, it seems likely that the rotor efficiency was significantly higher than the conservative design goal of 87 percent.

The test data of Fig. 11 were reduced using the design estimate of 7 percent rotor exit aerodynamic blockage. A rotor efficiency of 91 percent is shown at the design conditions. If the aerodynamic blockage was reduced to the unrealistic value of zero percent, the measured rotor efficiency would decrease only to 90 percent. Thus, losses in the vaneless region and the very low aspect ratio stators were probably higher than their design goal.

Static taps also allowed other information to be deduced, including the loss split between stators and when rotor or stators were in choked conditions. Static taps at the annular flare exit allowed calculation of the Mach number at this location. It is Mach 0.30 at the design point using the measured 1 percent loss in total pressure in the flare.

Summary and Conclusions

Specific speed of this mixed-flow compressor is fairly low due to the upstream axial stages, and thus much technology was drawn from centrifugal compressor capabilities, with only modest assistance from axial compressor methodology. It is encouraging that these design procedures could be used with very good predictive capability. Probably the biggest surprise from this effort was that there were no surprises!

During the several years following design completion, rig testing, and publication of this paper, several advancements have been made in design capabilities which should promote improved performance. For example, both stators would now be designed using arbitrary thickness and camberline distributions. The loading analysis is obtained from an inviscid Euler code coupled with a boundary layer postprocessor.

Matching the stage to a downstream burner could probably be done most compactly using a hybrid diffuser (a passive boundary layer control configuration) [5].

Rig testing of this stage with upstream axial stages has been accomplished with good results. The work was done under a classified contract which presents detailed information concerning the design and performance of the axial stages [6].

Acknowledgments

Sincere appreciation is given to Williams International for permission to publish this paper, and to compression systems leader Ed Worth and test engineers Dennis Roemer and Sharon Wilson for their valuable assistance.

References

1 Dodge, J. L., et al., "Mixed-Flow Compressor Program," Parts I, II, and III, AFWAL-TR-80-2047, May 1982.

2 Pampreen, R. C., "The Use of Cascade Technology in Centrifugal Compressor Vaned Diffuser Design," ASME Paper No. 72-GT-39, 1972.

3 Senoo, Y., Hayami, H., and Ueki, H., "Low-Solidity Tandem-Cascade Diffusers for Wide-Flow-Range Centifugal Blowers," ASME Paper No. 83-GT-3, 1983.

4 Bammert, K., and Staude, R., "Optimization for Rotor Blades of Tandem Design for Axial Flow Compressors," ASME Paper No. 79-GT-125, 1979.

5 Adkins, R. C., Matharu, D. S., and Yost, J. O., "The Hybrid Diffuser," ASME *Journal of Engineering for Power*, Vol. 103, 1981, pp. 229–236.

6 Worth, E. M., et al., "Low-Cost, High-Performance Two-Stage Axial Compressor," AFWAL-TR-86-C2384 (Confidential), Dec. 1986 (to be published).

Downloaded 01 Jun 2010 to 171.66.16.57. Redistribution subject to ASME license or copyright; see http://www.asme.org/terms/Terms_Use.cfm

The Measurement of Boundary Layers on a Compressor Blade in Cascade: Part 1—A Unique Experimental Facility

S. Deutsch

W. C. Zierke

The Applied Research Laboratory,
The Pennsylvania State University,
State College, PA 16804

A unique cascade facility is described which permits the use of laser-Doppler velocimetry (LDV) to measure blade boundary layer profiles. Because of the need for a laser access window, the facility cannot reply on continuous blade pack suction to achieve two-dimensional, periodic flow. Instead, a strong suction upstream of the blade pack is used in combination with tailboards to control the flow field. The distribution of the upstream suction is controlled through a complex baffling system. A periodic, two-dimensional flow field is achieved at a chord Reynolds number of 500,000 and an incidence angle of 5 deg on a highly loaded, double circular arc, compressor blade. Inlet and outlet flow profiles, taken using five-hole probes, and the blade static-pressure distribution are used to document the flow field for use with the LDV measurements (see Parts 2 and 3). Inlet turbulence intensity is measured, using a hot wire, to be 0.18 percent. The static-pressure distribution suggests both separated flow near the trailing edge of the suction surface and an initially laminar boundary layer profile near the leading edge of the pressure surface. Probe measurements are supplemented by sublimation surface visualization studies. The sublimation studies place boundary layer transition at 64.2 ± 3.9 percent chord on the pressure surface, and indicate separation on the suction surface at 65.6 percent ± 3.5 percent chord.

I. Introduction

Over the past two decades, techniques for computing complex flows have become increasingly more sophisticated. Steger [1], Thompson [2], Rubin and Khosla [3, 4], Beam and Warming [5], and Briley and McDonald [6] have computed viscous flows at reasonable Reynolds numbers; Davis and Werle [7] and Johnston and Sockol [8] have studied viscous-inviscid interaction; and Edwards and Carter [9] and Melnik and Brook [10] have computed through separated regions. Further, all computations may now involve complex turbulence models, such as the models by Bradshaw et al. [11] and Launder et al. [12]. It is desirable that these techniques find their way into the turbomachinery design process. These numerical techniques are capable of very detailed predictions, but to be used with confidence, they should be tested against very detailed experimental data under typical flow conditions. As turbomachinery testing has generally been concerned with overall turbomachinery performance rather than with the details of the flow field, such data are lacking.

In order to provide some of the needed data, we used a one-component laser-Doppler velocimeter (LDV) to measure the two-dimensional periodic flow field about a double circular arc, compressor blade in cascade. Eleven boundary layer profiles were taken on both the pressure and suction surfaces of the blade; two profiles were taken in the near wake. All measurements were made at a chord Reynolds number (Re_c) of 500,000 (±1 percent) and an incidence angle of 5 deg (that is, the stagnation point is on the pressure surface). The turbulence intensity in the incident flow was 0.18 percent. With an incidence angle of 5 deg, the pressure surface exhibits a large region of laminar flow (up to roughly 60 percent chord); transition on the pressure surface appears to be incomplete. The suction surface profiles appear to separate both at the leading edge and again somewhat beyond midchord; the leading edge separation apparently reattaches by 2.6 percent chord. Using the terminology of Simpson et al. [13], we found incipient detachment to occur at 60 percent chord on the suction surface and transitory detachment to occur at 83 percent chord. Inlet and outlet five-hole probe measurements and blade static-pressure measurements supplement the blade boundary layer profiles. Surface flow visualization, through sublimation, complements the transition and separation region data.

Because of the unique requirements on a cascade facility suitable for LDV studies and the need for a thorough documentation of the flow field, we use Part 1 of the study to describe the facility and to present cascade results. Part 2

Contributed by the Gas Turbine Division of The American Society of Mechanical Engineers and presented at the 32nd International Gas Turbine Conference and Exhibit, Anaheim, California, May 31-June 4, 1987. Manuscript received at ASME Headquarters February 24, 1987. Paper No. 87-GT-248.

Copyright © 1987 by ASME

Downloaded 01 Jun 2010 to 171.66.16.57. Redistribution subject to ASME license or copyright; see http://www.asme.org/terms/Terms_Use.cfm

presents and discusses the suction surface boundary layers, while Part 3 presents and discusses the pressure surface boundary layers and the near wake. Before describing the facility and the cascade results, we will attempt to put the current study in perspective by describing previous detailed measurements both in rotating systems and in cascades.

II Historical Background

Several researchers have attempted to measure boundary layers on turbomachine blades. Evans [14] measured boundary layers at four chord (c) locations at midspan on the suction surface of a stator blade (c = 305.0 mm and Re_c = 500,000). The hot-wire measurements were made in an axial-flow compressor at three time-mean incidence angles on a row of stationary blades preceded by a row of rotating blades. The stator blades cut the wakes to the rotor blades and the rotor wake segments are subsequently transported through the stator passages. Since the wake segments involve low-velocity fluid, the boundary layer is subject to a periodically varying freestream, and the blade is subject to a periodically varying incidence angle. Ensemble-averaged velocity profiles eliminate the random unsteadiness caused by turbulence. However, the periodic unsteadiness is preserved. The ensemble-averaged velocity profiles at 30 and 50 percent chord show that the boundary layers alternate between laminar and turbulent because of the unsteady flow. As a result, the time-mean velocity profiles exhibited a larger boundary layer growth than was expected.

Anand and Lakshminarayana [15] measured boundary layers on the rotor blades of a rocket pump inducer using a three-sensor hot-wire probe rotating with the blades. Because of imbalances in the radial pressure force and inertia forces in the blade boundary layer, outward radial velocities develop in a rotor blade boundary layer and inward radial velocities develop in a stator blade boundary layer. Anand and Lakshminarayana [15] measured a significant outward radial component in the boundary layer velocity and found that this radial migration strongly influenced the chordwise velocity profiles.

Other experimenters have measured the boundary layers on rotor blades of axial-flow fans. Toyokura et al. [16] used rotating three-hole cobra probes to measure the three-dimensional boundary layers at six radial sections (c = 80.0 mm to 199.5 mm and Re_c = 300,000 to 500,000). The outward radial flow seemed to retard the predicted regions of transition and separation. Lakshminarayuana et al. [17] used rotating miniature x-configuration hot-wire probes for boundary layer measurements at five radial locations (c = 152.4 mm and Re_c = 280,000 at midchord). Rotating miniature x-configuration hot-wire probes were also used by Pouagare et al. [18] for numerous boundary layer measurements (c = 123.9 mm to 154.1 mm). In no case could the velocity profiles to be very well resolved.

Walker [19] made measurements similar to those of Evans [14]. Walker used a hot wire in an axial-flow compressor to measure boundary layers on a stator (c = 76.0 mm and Re_c = 30,000 to 200,000) downstream of both a row of rotating blades and a row of inlet guide vanes. He tried to correct for wall proximity using a method outlined by Wills [20], but still had difficulties matching the law of the wall. Low Reynolds number, large adverse streamwise pressure gradients, and rapidly changing boundary conditions (due to the periodic unsteadiness) were given as reasons for the absence of a logarithmic region.

Hodson [21] made hot-wire measurements in an axial-flow turbine at midspan on a rotor blade (c = 114.5 mm and Re_c = 315,000) downstream of a stator row. Once again, the periodic unsteadiness seemed to cause the boundary layer characteristics to vary between laminar and turbulent at some chordwise locations. Profile losses were larger than expected and this too was attributed to the unsteady flow.

Boundary layer measurements on turbomachine blades have yet to produce velocity profiles with enough detail and precision to compare with viscous computational codes. Therefore, our understanding of the physical nature of these complex, unsteady, three-dimensional boundary layers is far from complete. These flows are characterized by high turbulence levels, as well as by periodic unsteadiness caused by the interaction between stationary and rotating blade rows. "Blockage" effects exist because of the development of the end-wall boundary layers and the consequent contraction of the

Nomenclature

AR = aspect ratio
c = blade chord length
C_p = static pressure coefficient = $(p-p_1)/(\rho\, V^2{}_1/2)$
D = diffusion factor
H_{12} = first shape factor = δ^*/θ
i = incidence angle = $\beta_1-\kappa_1$
LDV = laser-Doppler velocimeter
M = Mach number
p = static pressure
P_T = total or stagnation pressure
r = radius
Re_c = blade chord Reynolds number = cV_1/ν
s = blade spacing
u = streamwise velocity
U_e = velocity at the boundary layer or wake edge
V = velocity
x = streamwise coordinate; or blade coordinate (see Appendix)
y = coordinate normal to the blade surface or across the wake; or blade coordinate (see Appendix)
β = flow angle measured from the axial direction
γ = stagger angle
δ^* = displacement thickness = $\int_0^\infty (1-u/U_e)dy$
δ_D = deviation angle = $\beta_2-\kappa_2$
ϵ = fluid turning or deflection angle = $\beta_1-\beta_2$
θ = momentum thickness = $\int_0^\infty (u/U_e)(1-u/U_e)dy$
κ = blade metal angle
ν = kinematic viscosity (= 0.150 cm^2/s for air)
ρ = fluid density (= 1.205 kg/m^3 for air)
σ = blade solidity = c/s
ϕ = camber angle = $\kappa_1-\kappa_2$
ω = total pressure loss coefficient = $(P_{T_1}-P_{T_2})/(\rho V_1^2/2)$

Subscripts

c = camberline
LE = leading edge
m = mean flow
p = pressure surface
TE = trailing edge
s = suction surface
x = axial direction
θ = tangential direction
1 = inlet (upstream five-hole probe measurement station)
2 = outlet (downstream five-hole probe measurement station)

Superscript

$\overline{\quad}$ = average over the blade passage

Downloaded 01 Jun 2010 to 171.66.16.57. Redistribution subject to ASME license or copyright; see http://www.asme.org/terms/Terms_Use.cfm

mainstream flow. The blade boundary layers are also affected by centrifugal and Coriolis forces associated with both the swirl and the blade rotation. The complex blade geometries and the complex flow field, including secondary flows, tip leakage, and trailing vorticity, make the analysis or measurement of turbomachine blade boundary layers very difficult.

Because of these difficulties, many researchers have sought a simple geometry which retains some of the physics of the flow in which to make their boundary layer measurements. A model that has proven effective in other areas of turbomachinery is the periodic, two-dimensional row of airfoils, commonly referred to as a cascade. Properly realized, a cascade should eliminate all of the complexities of the turbomachine except blade curvature, secondary flow, and the effect of freestream turbulence.

The first attempt to measure boundary layers on cascade blades was made by Peterson [22]. He used a three-hole cobra probe to measure blade boundary layers in a compressor cascade ($c = 123.8$ mm and $\mathrm{Re}_c = 300{,}000$). Several boundary layers were measured on both the suction and pressure surfaces for three different incidence angles. In an attempt to better model an actual turbomachine, Peterson [22] simulated the added diffusion caused by the radial distribution of axial velocity and the consequent streamline deviation. This added diffusion was created in the cascade by placing a perforated metal screen downstream of the blades. The measurements were not taken in the freestream, and therefore, the normal pressure gradient remains unknown. This lack of information leads to a problem in computing the edge velocity (which was probably inferred from the blade static-pressure distribution). The data are quite scattered, especially in the regions near separation, where the cobra probe fails. Peterson [22] reported no significant differences between measurements with an without the added diffusion.

Pollard and Gostelow [23] measured boundary layers on compressor cascade blades ($c = 152.4$ mm and $\mathrm{Re}_c = 200{,}000$) with a Pitot tube to examine the effect of leading edge roughness. Three suction surface boundary layers and one pressure surface boundary layer were measured on both blades with a smooth leading edge and with a leading edge roughened with polythene spheres. With no roughness, laminar separation occurred before transition. It appears that separation of the turbulent boundary layers near the trailing edge would be more likely to occur when leading edge roughness is present. These results agree with the Preston tube skin-friction measurements of Pollard and Gostelow [23]. The detail and precision of the data are unknown since no actual data points are given.

Evans [24] used compressor cascade blades ($c = 304.8$ mm and $\mathrm{Re}_c = 500{,}000$) for boundary layer measurements taken with a hot-wire anemometer probe. A problem with these data is that the blade boundary layers were tripped with a wire at 10 percent chord. Evans [24] argued that a turbulent boundary layer over most of the blade would better represent the high turbulence and unsteadiness levels usually encountered in a turbomachine. Instead, the artificially induced boundary layer development is rather misleading.

Problems of contamination, corrosion, erosion, and deposition have led to two investigations that dealt with the effects of surface roughness on cascade blade boundary layers. Bammert and Milsch [25] measured blade boundary layers in a compressor cascade ($c = 180.0$ cm and $\mathrm{Re}_c = 430{,}000$) with four different blade profiles to change the pitch, camber, and thickness of the blades parametrically. They used emery powder to develop the five roughness grades to be tested. A turbine cascade ($c = 17.50$ cm and $\mathrm{Re}_c = 560{,}000$) was used for the blade boundary layer measurements of Bammert and Sandstede [26] where four roughness grades were tested. Both investigations used a flattened Pitot tube which allowed measurements to be taken very close to the blade surface. Bammert and Sandstede [26] used a hot-wire anemometer to confirm the measurements made with the flattened Pitot tube. The studies showed that increasing surface roughness led to increases in both momentum thickness and skin friction and a forward shift of the regions of transition and separation.

Meauze [27] used a transonic compressor cascade ($c = 94.9$ mm, $\mathrm{Re}_c = 1{,}660{,}000$ for $M_1 = 0.70$, and $\mathrm{Re}_c = 2{,}120{,}000$ for $M_1 = 0.85$) for blade boundary layer measurements. He used total pressure probes to measure suction surface boundary layers for two inlet Mach numbers and four incidence angles. The flow recompression on the highly cambered blades results in laminar flow separation and subsequent turbulent reattachment. The thin laminar boundary layers upstream of this separation "bubble" were difficult to measure, so that the total-pressure profiles were only measured for turbulent boundary layers.

The trailing edge boundary layers on both the suction and pressure surfaces of a compressor cascade blade ($c = 203.2$ mm and $\mathrm{Re}_c = 478{,}000$) were measured with a hot-film probe by Hobbs et al. [28]. The two profiles are very detailed and precise; they show a nearly separated profile on the suction surface, and also a pressure surface profile typical of favorable pressure gradients.

Recently, Hodson [21] has presented blade boundary layer data measured in a turbine cascade ($c = 114.5$ mm and $\mathrm{Re}_c = 315{,}000$) with a hot-wire probe. Although no data points are reported, the velocity profiles on the suction surface show laminar flow until 78 percent chord followed by laminar separation and no reattachment.

All prior investigations have used hot-wire or pressure probes to make boundary layer measurements. There are three potential problems: First, a periodic two-dimensional cascade flow is difficult to establish and the probe may distort it; second, some boundary layers are likely to be small compared to the probe dimensions; and third, separated regions, if present, cannot be conveniently studied. For these reasons, the current study used the LDV technique. The need for optical access to the blade row for the LDV technique places some unique restrictions on the types of flow controls that may be employed in the cascade. In particular, continuous blade pack suction to restrict the side wall boundary layer growth is no longer possible. A description of the cascade facility and a documentation of the resulting flow field form the body of this, Part 1, of the study.

III Cascade Tests

The cascade wind tunnel has a 0.37 m by 0.64 m test section with a maximum air speed of approximately 35 m/s. Tunnel turbulence control is through a honeycomb with a 3.18-mm cell size, several settling screens in the diffuser section, and a nine-to-one contraction. Over the speed range of 24-35 m/s, the tunnel operated with a freestream turbulence level of 0.18 ± 10 percent as measured by a hot-wire anemometer. Figure 1 shows a schematic of the open return facility.

The blade section used in the tests is a compressor blade designed at the NASA Lewis Research Center (see [29]). The blade section is a double circular arc blade with 65 deg of camber[1] and a 228.6 mm chord length. Both the leading and trailing edges were machined to a 9.14-μm radius. The blade aspect ratio is 1.61. The five cascade blades were made of aluminum and were anodized black to minimize laser reflections. Camber line and thickness relationships necessary to construct the blades (or for computation) are given in the Appendix. To insure proper alignment, the blades were carefully

---

[1] A design condition was that the blade show some trailing edge separation of the suction surface turbulent boundary layer at zero incidence angle. With the available cascade geometry, this leads to a large camber angle.

Downloaded 01 Jun 2010 to 171.66.16.57. Redistribution subject to ASME license or copyright; see http://www.asme.org/terms/Terms_Use.cfm

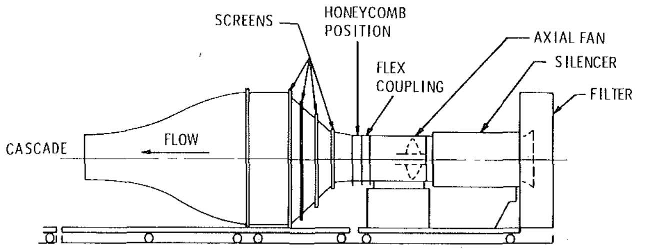

Fig. 1 Open return wind tunnel

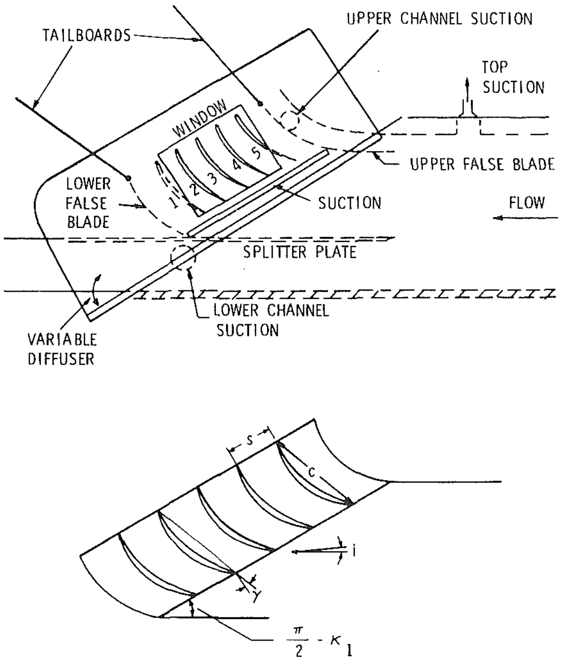

Fig. 2 Cascade test section with flow controls

positioned in two inserts [aluminum and Plexiglas[2] (on the optics side], which were in turn mounted to the plywood walls of the cascade test section. The test section is shown in Fig. 2. For the case to be reported, the cascade had a solidity of 2.14. The stagger angle was 20.5 deg. The important cascade and flow angles are defined in Fig. 2.

As current computer codes assume a two-dimensional, periodic cascade flow, one must take data in such a flow field for it to be of use. Two dimensionality, of course, implies that the velocities and angles of the flow are substantially the same in spanwise planes, while periodicity supposes that velocities and flow angles show only minimal variations from blade passage to blade passage, both upstream and downstream of the blade row. For the five-bladed cascade used here, periodicity was taken to mean periodicity over three blade passages centered at the minimum velocity point of the middle blade wake. In order to satisfy the condition of continuity for a two-dimensional, incompressible cascade flow, the axial velocity must be held constant throughout. From a practical standpoint then, flow periodicity and two-dimensionality could be determined, for a uniform inlet flow, by examining the axial-velocity ratio and flow angles determined at the exit plane. This was quite useful as these outlet measurements could be made simply and quickly, thus allowing us to check the cascade flow daily.

Two dimensionality and periodicity are normally controlled in cascades by using continuous suction over the entire blade pack.[3] Continuous suction was not possible in the current experiment because of the need for laser access. Alternate flow control was examined in some detail. Returning to Fig. 2, we note that there are many potentially useful flow controls. That is, it is possible in principle to control the flow by adjusting the position of the lower false blade, the upper false blade, the variable diffuser, and the tailboards (as well as the relative position of the tailboards), or by adjusting the magnitude (and distribution) of the top suction, side suction, and lower and upper channel suction. In practice, the lower and upper false blades were each set at nominally one blade spacing from blades 1 and 5, respectively. The diffuser was set to minimize the flow angle at the splitter plate. Lower channel suction was not required. Top and upper channel suction were provided through the same 5-hp blower, which was run at full power. A baffle system was used to adjust the relative amounts of suction provided at the top and upper channel, and the baffling along with slight adjustments to the upper false blade position were used to insure a horizontal flow at the upper false blade leading edge. The tailboards were most useful in controlling the relative exit angles of the flow; that is, they could be adjusted so that the exit angle across the cascade in a blade-to-blade direction was constant outside of the wake regions. The periodicity, however, was found to be most influenced by the amount and distribution of the sidewall suction. Side suction was provided by a 10-hp centrifugal blower operated at full power. Side suction distribution was controlled by a complex baffling system. Six suction ducts were located at a half-blade spacing on either side of each of the blades. Each of the individual ducts had a separate baffle control, and was adjusted by the simple but tedious procedure of changing a baffle position and then examining the resulting outlet flow. Presumably, the control of side suction distribution controlled the size of the sidewall boundary layer at its intersection with the blade pack leading edge line – in a sense controlling the virtual origin of the corner disturbances. Control of sidewall suction distribution then implied a control of the "blockages," caused by corner disturbance contamination, of each blade passage individually and hence control of the individual blade angles of attack. Once set, the stability of the periodicity obtained on a day-to-day basis was excellent.

The two dimensionality and periodicity of the cascade flow were determined by conducting measurements of the cascade inlet and outlet velocity profiles using five-hole probes. These probes are capable of resolving the three components of velocity as well as the relative yaw and pitch angles of the flow. Treaster and Yocum [30] give a complete description of the five-hole probes employed in the study. The probes were calibrated at a speed of 30.5 m/s in an open jet air facility over the range of pitch and yaw angles of +30 deg to −30 deg. Reynolds number effects on the probes have been shown to be small (see [30]).

All inlet and outlet five-hole probe surveys were referenced to a Pitot-static probe located 25.4 mm upstream of the blade pack leading edge line. The probe protruded approximately 150 mm into the flow – well outside of the sidewall boundary layer. The probe was located along a parallel to the leading edge line at a position between blades 3 and 4 at which the inlet velocity was roughly equal to the average of the measured inlet velocities.

Cascade inlet flow profiles were documented by five-hole probe measurements approximately 38 mm upstream of and parallel to the leading edge line. Outlet flow profiles were measured parallel to the trailing edge line and one-half chord downstream of this line. A nearly real-time data acquisition/reduction system was used for the velocity measurements. In each case the five-hole probe and Pitot-static probe

---

[2] A glass insert was later placed within the Plexiglas to improve the LDV signal.

[3] Note that the control here seems to be over the growth of channel corner disturbances. An attempt to use a slightly divergent wall, commonly used to compensate for boundary layer growth, failed.

Downloaded 01 Jun 2010 to 171.66.16.57. Redistribution subject to ASME license or copyright; see http://www.asme.org/terms/Terms_Use.cfm

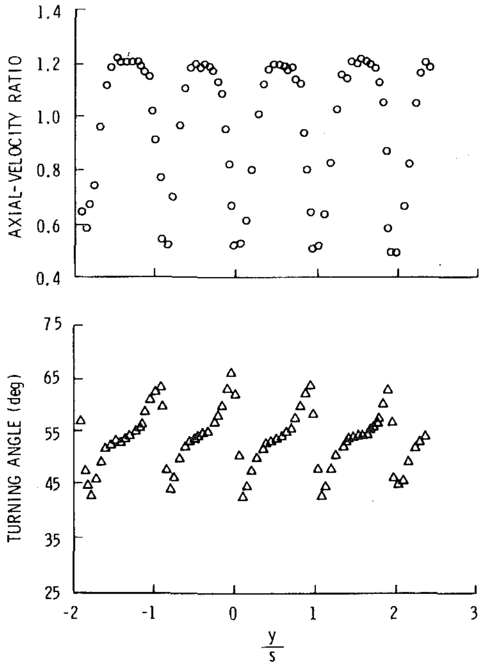

Fig. 3 Five-hole probe outlet survey

BLADE GEOMETRY

$C = 228.6$ mm $\sigma = 2.14$ $\kappa_1 = 53^\circ$

$S = 106.8$ mm $AR = 1.61$ $\kappa_2 = -12^\circ$

$r_{LE} = r_{TE} = 9.14\ \mu m$ $\gamma = 20.5^\circ$ $\phi = 65^\circ$

MEASURED FLOW CONDITIONS

$Re_c \approx 500{,}000$ $V_x = 17.55$ m/sec $\bar{\beta}_m = 39.9^\circ$

$i = -5^\circ$ $\bar{\beta}_2 = 4^\circ$ $\bar{\epsilon} = 54^\circ$

$\beta_1 = 58^\circ$ $\bar{V}_2 = 17.59$ m/sec $\bar{\delta}_D = 16^\circ$

$V_1 = 33.11$ m/sec $\bar{V}_m = 22.88$ m/sec $\bar{\omega} = 0.151$

$(\bar{C}_p)_2 = 0.463$

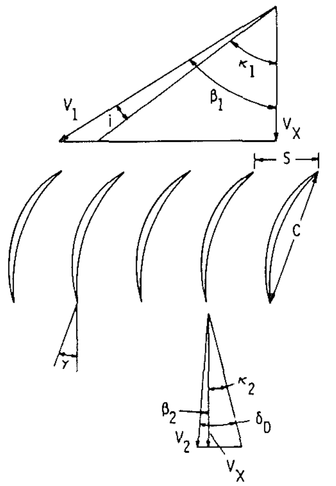

Fig. 4 Blade geometry and flow conditions

data were sent to seven separate pressure transducers. These seven pressure signals as well as a test section temperature signal were scanned by a multiplexer/scanner, smoothed on a multimeter through a 100 cycle (1 2/3 sec) integration, and sent for reduction to a VAX 11/782. Velocities, velocity ratios, and flow angles could be displayed on a video terminal, written on a line printer, or plotted on a flat-bed plotter.

Inlet velocity surveys were made after the outlet flow had been determined to be satisfactory. Good periodicity and spanwise consistency were apparent, as was some streamline bending induced by the presence of the blades. An average inlet velocity was found to be 33.11 m/s (from the average gage static and total pressures of $P_1 = -414.3$ Pa and $P_{T_1} = 246.1$ Pa), with an average incidence angle of 5 deg. Chord Reynolds number, based on the inlet velocity, was 500,000 with an observed ±1 percent variation on a day-to-day basis. Figure 3 shows a typical outlet flow profile and the equivalent turning angles. The periodicity of the flow is clearly excellent. The axial-velocity ratio is determined by averaging the local axial-velocity ratio over three blade passages, centered at the minimum velocity-ratio point of the center blade wake. In the calculation, the inlet flow is assumed to be spatially constant at its average value (the Pitot-static tube reading). The average axial-velocity ratio was found to be 1.0; on a day-to-day basis the variation was within ± 3 percent. The flow turning angle averaged across the three center blade passages was 54 deg. Figure 4 shows the blade geometry and the inlet and outlet flow measurements.

Measurements have been taken to help quantify the losses in total pressure across the cascade. Additional quantities can be computed to compare with design limits on diffusion rate and static-pressure rise within the cascade. The difference between the blade-passage-averaged flow angle in the outlet flow and the exit blade "metal" angle is the deviation angle. For the current study, the deviation angle was measured to be 16 deg, which is very large.[4] Nondimensionalizing by the inlet dynamic pressure, the blade-passage-averaged total pressure loss coefficient was 0.151 and the blade-passage-averaged static-pressure rise coefficient was 0.463. Note that the static-pressure rise coefficient was probably affected by the positioning of the tailboards. An equation for the total pressure loss coefficient was developed by Lieblein and Roudebush [31] where

$$\bar{\omega} = 2\left(\frac{\theta}{c}\right)\frac{\sigma}{\cos\beta_2}\left(\frac{\cos\beta_1}{\cos\beta_2}\right)^2$$

$$= 1-\left[\left(\frac{\theta}{c}\right)\frac{\sigma H_{12}}{\cos\beta_2}\right]^{-3}\left(\frac{2H_{12}}{3H_{12}-1}\right)$$

A value of 0.172 for ω can be calculated from this equation using five-hole probe measurements and LDV measurements of the trailing edge boundary layers. The loss in total pressure across the cascade is related to the amount the flow is diffused through the blade passage. Lieblein et al. [32] derived a diffusion factor where

$$D = 1-\frac{V_2}{V_1}+\frac{V_{\theta_1}-V_{\theta_2}}{2\sigma V_1}$$

$$= 1-\frac{\cos\beta_1}{\cos\beta_2}+\frac{\sin\beta_1-\cos\beta_1\tan\beta_2}{2\sigma}$$

Designers normally place a limit between 0.5 and 0.6 on D when designing a blade row (depending upon span location). This limit is based on a large number of cascade performance tests. Values of D greater than this limit result in large increases in total-pressure loss because the larger amount of diffusion causes the blade boundary layers to separate. Using a blade-passage-averaged value of the outlet flow angle allows a value of 0.658 for D to be computed for the current study. This value of D indicates a risk of separation.

---

[4] Although large, a 16-deg deviation angle is not unexpected, as the design condition called for a zero incidence angle. Experiments at lower incidence angles are planned.

Downloaded 01 Jun 2010 to 171.66.16.57. Redistribution subject to ASME license or copyright; see http://www.asme.org/terms/Terms_Use.cfm

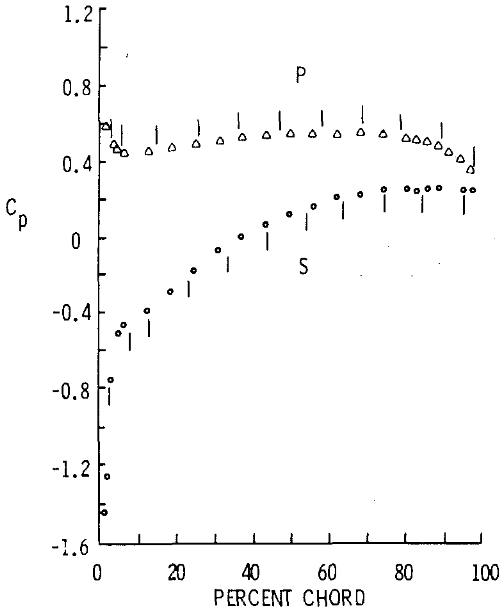

Fig. 5 Blade static-pressure distribution (the vertical line segments represent the locations of LDV measurements: *P* is the pressure surface; *S* is the suction surface)

Ideally, blade static pressure would be measured on the center blade of the cascade – the one intended for LDV measurements – but the two types of measurements had somewhat conflicting requirements. That is, an aerodynamically smooth (0.8 μm estimated surface roughness) surface was desired for the LDV surveys, while the conveying tubes required for the pressure measurements inevitably led to a somewhat roughened surface. To work around this problem, we instrumented the suction surface of the upper blade, 4 (see Fig. 2), and the pressure surface of the lower blade, 2, with 24 pressure taps; we instrumented the center blade, 3 pressure and suction surfaces with 6 and 7 taps, respectively. Since the flow was periodic, the pressure distribution could be obtained from blades 2 and 4 as well as from blade 3. After checking this by comparing the results of the pressure distributions from blades 2 and 4 against the data from blade 3 (the agreement was excellent), we interchanged blade 3 with the uninstrumented blade, 5, for the LDV surveys. Data acquisition and reduction, for the static-pressure distribution, were similar to that described for the five-hole probe data with the exception that a scanner valve was used to switch the pressure data, hole-by-hole, to a single transducer during data acquisition.

The blade static-pressure distribution appears in Fig. 5. The vertical lines in Fig. 5 indicate the locations at which LDV surveys were made. Integrating this distribution gives a lift coefficient of 0.952. The 5-deg incidence angle dramatically affects the pressure distribution. The large favorable gradient on the pressure surface suggests that the boundary layers near the leading edge will be laminar; transition should be looked for on the pressure surface. The unfavorable gradient at the leading edge of the suction surface implies a leading edge separation. The rather flat pressure profile near the trailing edge of the suction surface suggests that the flow may be separated there. The rapid and continuous changes of pressure on both the pressure and suction surfaces offer little hope of finding equilibrium boundary layers. In addition, the inviscid velocity field within the blade passage will be under the influence of a normal pressure gradient, and one cannot anticipate a constant freestream velocity region.

Following the sublimation method used by Holmes and Obara [33], we used surface flow visualization to help determine the location of the anticipated trailing edge separation on the suction surface, and the transition on the pressure surface. An air brush was used to coat the blade with a mixture of naphthalene and acetone in a 1:8 solid-to-solvent volume ratio. Preliminary tests determined that a run time of nine minutes was sufficient to set up the visualization pattern. For each run the center blade was removed, the naphthalene/acetone mixture was applied, and large particles were dusted off. The blade was then replaced in the cascade and removed after the 9-min run time, allowing the sublimation pattern to be photographed. A sufficient number of tests were taken so that a meaningful mean and Student's *t* test deviation could be obtained. Evidence of two-dimensionality was much more apparent in the suction surface separation pattern then in the pressure surface transition pattern. This is perhaps an indication of the importance of the local surface roughness in determining the transition point for the very thin boundary layers encountered. With 95 percent confidence, separation was found to occur at 65.5 percent chord on the suction surface with a deviation of ±3.5 percent chord. Transition was found on the pressure surface to be at 64.2 ± 3.9 percent chord to the same level of confidence.

IV Conclusions

There is a need for detailed and precise data, taken in geometries of interest to workers in turbomachinery, to support the growing potential of computational fluid dynamics to the design process. In the current three-part study, we attempt to provide some of these data by making detailed LDV measurements of the flow field about a double circular arc compressor blade in cascade.

The need for laser access to the blade pack makes the customary use of continuous blade pack suction to establish a two-dimensional, periodic flow field in the cascade impossible. Instead, a combination of strong suction just upstream of the blade pack and tailboards are used to create a two-dimensional, periodic flow field at a chord Reynolds number of 500,000. In creating this flow field, we found it particularly important to be able to control the strength of the upstream suction, discretely, in the blade-to-blade direction.

Details of the inlet and outlet flow are documented using five-hole pressure probes. These measurements are supplemented by both blade static-pressure measurements and sublimation flow visualization studies. At the measured incidence of 5 deg the pressure gradient data suggests the possibility of a very complicated flow field. In particular, the strong favorable gradient at the leading edge of the pressure surface indicates a probable laminar boundary layer near the leading edge with the probability of transition on that surface. The large adverse gradient at the leading edge of the suction surface indicates a leading edge separation (obvious at this incidence), while the region of constant pressure past 60 percent chord on the suction surface indicates separation there. Diffusion factors, calculated through the technique derived by Lieblein et al. [32] also indicate separation. Sublimination flow visualization studies show transition near 64 percent chord on the pressure surface and separation at 65 percent chord on the suction surface.

Part 2 of the current study documents the flow field on the suction surface of the blade. Particular attention is paid to the region of separation, which begins near 60 percent chord. Part 3 of the study documents both the pressure surface and near-wake flow fields. In general, these detailed measurements agree with the physical picture obtained from the pressure gradient measurements, incidence angle measurements, and flow visualization studies quite well.

Acknowledgments

We would like to extend our appreciation to NASA Lewis

Downloaded 01 Jun 2010 to 171.66.16.57. Redistribution subject to ASME license or copyright; see http://www.asme.org/terms/Terms_Use.cfm

for supporting this work (NASA Grant NSG-3264) and to the NASA Lewis personnel for their advice and patience. A special thanks goes to Mr. Nelson Sanger who acted as the grant manager. Professor Robert E. Henderson and Professor Blaine R. Parkin gave valuable support throughout the research project. Other engineering and technical personnel at the Garfield Thomas Water Tunnel were instrumental in the success of the project. Finally, we give a special thanks to the many students who assisted us with the data acquisition and analysis.

References

1 Steger, J. L., "Implicit Finite-Difference Simulation of Flow About Arbitrary Two Dimensional Geometries," *AIAA Journal*, Vol. 16, 1978, pp. 679-686.

2 Thompson, J., "Numerical Solution of Flow Problems Using Body-Fitted Coordinate Systems," in: *Computational Fluid Dynamics*, Lecture at von Karman Institute, W. Kollmann, ed., Hemisphere Publication, New York, 1980, p. 1.

3 Rubin, S. G., and Khosla, P. K., "Navier-Stokes Calculations With a Coupled Strongly Implicit Method. Part I – Finite Difference Solutions," *Computers and Fluids*, Vol. 9, No. 2, 1981, p. 163.

4 Rubin, S. G., and Khosla, P. K., "A Composite Velocity Procedure for the Incompressible Navier-Stokes Equations," *8th International Conference on Numerical Methods in Fluid Mechanics*, Springer-Verlag, 1982, pp. 448-454.

5 Beam, R. M., and Warming, R. F., "An Implicit Factored Scheme for the Compressible Navier-Stokes Equations," *AIAA Journal*, Vol. 16, No. 4, 1982, pp. 393-402.

6 Briley, W. R., and McDonald, H., "Three-Dimensional Viscous Flows With Large Secondary Velocity," *Journal of Fluid Mechanics*, Vol. 144, 1984, pp. 47-77.

7 Davis, R. T., and Werle, M. J., "Progress on Interacting Boundary-Layer Computations at High Reynolds Number," *Numerical and Physical Aspects of Aerodynamic Flows*, T. Cebeci, ed., Springer-Verlag, New York, 1981.

8 Johnston, W., and Sockol, P., "Viscous-Inviscid Interactive Procedure for Rotational Flow in Cascades of Airfoils," *AIAA Journal*, Vol. 22, No. 9, 1984, pp. 1281-1282.

9 Edwards, D. E., and Carter, J. E., "A Quasi-Simultaneous Finite Difference Approach for Strongly Interacting Flow," presented at the Third Symposium on Numerical and Physical Aspects of Aerodynamics Flow, Jan. 21-29, 1985.

10 Melnik, R. E., and Brook, J. W., "The Computation of Viscid/Inviscid Interaction on Airfoils With Separated Flow," Gruman Aerospace Corporation Report RE-697, Apr. 1985.

11 Bradshaw, P., Ferriss, D. H., and Atwell, W. P., "Calculation of Boundary Layer Development Using the Turbulent Energy Equation," *Journal of Fluid Mechanics*, Vol. 28, 1967, pp. 593-616.

12 Launder, B. E., Reece, G. J., and Rodi, W., "Progress in the Development of a Reynolds Stress Turbulence Closure," *Journal of Fluid Mechanics*, Vol. 68, 1975, pp. 537-566.

13 Simpson, R. L., Chew, Y.-T., and Shivaprasad, B. G., "The Structure of a Separating Turbulent Boundary Layer. Part 1. Mean Flow and Reynolds Stresses," *Journal of Fluid Mechanics*, Vol. 113, 1981, pp. 23-51.

14 Evans, R. L., "Boundary Layer Development on an Axial-Flow Compressor Stator Blade," ASME JOURNAL OF ENGINEERING FOR POWER, Vol. 100, 1978, pp. 287-293.

15 Anand, A. K., and Lakshminarayana, B., "An Experimental Study of Three-Dimensional Turbulent Boundary Layer and Turbulent Characteristics Inside a Turbomachinery Rotor Passage," ASME JOURNAL OF ENGINEERING FOR POWER, Vol. 100, 1978, pp. 676-690.

16 Toyokura, T., Kurokawa, J., and Kimoto, Y., "Three-Dimensional Boundary Layer Flow on Rotating Blades," *Transactions of the JSME*, Vol. 25, 1982.

17 Lakshminarayana, B., Govindan, T. R., and Hah, C., "Experimental Study of the Boundary Layer on a Turbomachine Rotor Blade," in: *Three-Dimensional Turbulent Boundary Layers*, IUTAM Symposium, Berlin, Mar. 29-Apr. 1, 1982.

18 Pouagare, M., Galmes, J. M., and Lakshminarayana, B., "An Experimental Study of the Compressor Rotor Blade Boundary Layer," ASME JOURNAL OF ENGINEERING FOR GAS TURBINES AND POWER, Vol. 107, 1985, pp. 364-373.

19 Walker, G. J., "The Turbulent Boundary Layer on an Axial Compressor Blade," ASME Paper No. 82-GT-52, 1982.

20 Wills, J. A. B., "Correction of Hot Wire Readings for Proximity to a Solid Boundary," *Journal of Fluid Mechanics*, Vol. 12, 1962, pp. 388-296.

21 Hodson, H. P., "The Development of Unsteady Boundary Layers on the Rotor on an Axial-Flow Turbine," AGARD-CP-351, June 1983.

22 Peterson, C. R., "Boundary Layer on an Airfoil in a Cascade," Gas Turbine Laboratory Report No. 49, Massachusetts Institute of Technology, Dec. 1958.

23 Pollard, D., and Gostelow, J. P., "Some Experiments at Low Speed on Compressor Cascades," ASME JOURNAL OF ENGINEERING FOR POWER, Vol. 89, 1967, pp. 427-436.

24 Evans, B. J., "Effects of Free-Stream Turbulence on Blade Performance in a Compressor Cascade," Ph.D. Dissertation, Cambridge University, Cambridge, UK, 1971.

25 Bammert, K., and Milsch, R., "Boundary Layers on Rough Compressor Blades," ASME Paper No. 72-GT-48, 1972.

26 Bammert, K., and Sandstede, H., "Measurements of the Boundary Layer Development Along a Turbine Blade with Rough Surfaces," ASME JOURNAL OF ENGINEERING FOR POWER, Vol. 102, 1980, pp. 978-983.

27 Meauze, G., "Transonic Boundary Layer on Compressor Stator Blades as Calculated and Measured in Wind Tunnel," Fourth International Symposium on Air Breathing Engines – ISABE, Apr. 1-6, 1979.

28 Hobbs, D. E., Wagner, J. H., Dannenhoffer, J. F., and Dring, R. P., "Experimental Investigation of Compressor Cascade Wakes," ASME Paper No. 82-GT-299, 1982.

29 Sanger, N., "Double Circular Arc Compressor Blades," NASA Lewis DCA4; "65 Degree Camber Centerline and Thickness Equations," Private Communication, Nov. 1980.

30 Treaster, A. L., and Yocum, A. M., "The Calibration and Application of Five-Hole Probes," *Transactions of the Instrument Society of America*, Vol. 18, No. 3, 1979, pp. 23-24.

31 Lieblein, S., and Roudebush, W. H., "Theoretical Loss Relations for Low-Speed Two-Dimensional-Cascade Flow," NACA TN 3662, 1956.

32 Lieblein, S., Schwenk, F. C., and Broderick, R. L., "Diffusion Factor for Estimating Losses and Limiting Blade Loadings in Axial-Flow-Compressor Blade Elements," NACA RM E53D01, June 8, 1953.

33 Holmes, B. J., and Obara, C. J., "Observations and Implications of Natural Laminar Flow on Practical Airplane Surfaces," Aircraft Systems and Technology Conference, Thirteenth Congress of ICAS and AIAA, Seattle, WA, Aug. 22-27, 1982, ICAS-82-5.1.1.

APPENDIX

Equations for the Double Circular Arc Blades

The equations for the pressure surface, suction surface, and camberline of the double circular arc blades used in the current study can be written as

$$x_p^2 + [y_p + 219.7]^2 = 246.8^2$$

$$x_s^2 + [y_s + 149.5]^2 = 189.1^2$$

and

$$x_c^2 + [y_c + 179.4]^2 = 212.8^2$$

All of the dimensions are in millimeters. The origin of the coordinate system used here is located on the chord line at midchord. The x coordinate is parallel to the chord, while the y coordinate is normal to the chord.

Downloaded 01 Jun 2010 to 171.66.16.57. Redistribution subject to ASME license or copyright; see http://www.asme.org/terms/Terms_Use.cfm

J. Padovan

F. K. Choy

Department of Mechanical Engineering,
The University of Akron,
Akron, OH 44325

Nonlinear Dynamics of Rotor/Blade/Casing Rub Interactions

This paper considers the transient analysis of rub problems in high-speed rotating equipment that involve interactions between the rotor, blades, and casing. Special emphasis is given to ascertaining the participation characteristics of turbine/impeller blades during the overall rub event. To generalize the scope of the work, single and multiple blade rub events are considered including the effect of such system parameters as imbalance magnitude, blade/rotor stiffness, system damping, and rub interface friction characteristics.

Introduction

Perhaps the single most catastrophic periods in the life of rotating equipment are the imbalance excitation/base motion induced rotor/blade/casing rub events. Rubbing between rotors and casing has been recognized as one of the major causes of machine failure. If not outright fatal, such behavior leads to worn seals and hence degraded performance. Without a general understanding of the dynamics of rotor/blade/casing rub interactions, it is difficult for designers of rotating equipment to plan/design rub site management features.

A large number of transient dynamics studies of rotor-bearing systems under the effects of imbalance excitations and base motion have been reported in the literature. Most of these are limited to the preliminary rub onset stage of behavior (Adams, 1980; Choy et al., 1978; Gunter, 1978; Kirk and Hibner, 1976) wherein the vibration amplitude just exceeds the enclosed clearances. In this context, there is little qualitative/quantitative work which attempts to simulate the complete global dynamics of the system during rub events. Some work has been performed on the correlation between analytical and experimental results during rub interaction (Bently, 1974; Black, 1968; Childs, 1979; Enrich, 1969). These are typically limited to steady-state operating conditions for simple rotors. Childs (1979) has reported a parametric study on the stability of rotor systems during steady state rub. Nelson and Kascak (1983) have performed a limited number of case studies on the rotor/casing rub interaction problem. The authors have undertaken a series of comprehensive studies to define the role of casing stiffness, frictional effects, and imbalance magnitudes during transient rub interactions (Choy and Padovan, 1985, 1986, 1987). To date the rubs have been modeled as interfacial problems involving concentric cylindrical surfaces. In this context, the effects of blade casing interactions have yet to be directly considered by the modeling process. This is an important shortcoming in view of the fact that the tight clearances in modern high-performance turbines/impellers tend to lead to blade rubs.

In view of the foregoing, the main objective of this paper is to develop a basic understanding of the highly nonlinear dynamics of rotor/blade/casing systems during transient rub interactions. The study will be divided into two major thrusts, namely: (*a*) the modeling of the dynamics of rotor systems under various effects including imbalance, friction, blade stiffness as well as the number of blades participating during the rub event, and (*b*) the investigation of blade displacements and stresses as they relate to buckling, and fatigue failure of impeller/turbine blades during rub interactions. A simplified nonlinear analytical model will be used to demonstrate this analysis. Generalized conclusions will be then drawn from the results of parametric studies performed using the model.

Development of Rub Model

In order to investigate the dynamics of rotor/blade/casing during rub interactions, a simplistic rotor/bearing system will be employed. The model possesses the following general characteristics:

(*i*) The rotor bearing assembly is assumed to be a Jeffcott rotor simulation (see Fig. 1).

(*ii*) Linearized effective damping and stiffness characteristics are assumed at the rotor geometric center.

(*iii*) The turbine/impeller blades are assumed to be fixed at the rotor mounting (cantilevered).

(*iv*) Compared to rotor blade flexibility, the casing is assumed to be rigid.

(*v*) Only light rub conditions are considered such that the tangential force generated from friction varies linearly with the radial force exerted by the rotor. In other words, a Coulomb type of frictional relationship is used. No material removal is considered at this stage.

(*vi*) The rotor is assumed to operate initially in a steady state condition with an inbalance eccentricity e_{uo}. It is then suddenly excited by an additional imbalance eccentricity e_{us} ($e_u = e_{uo} + e_{us}$).

Contributed by the Gas Turbine Division for publication in the JOURNAL OF TURBOMACHINERY. Manuscript received by the Gas Turbine Division February 26, 1986.

Copyright © 1987 by ASME

Downloaded 01 Jun 2010 to 171.66.16.57. Redistribution subject to ASME license or copyright; see http://www.asme.org/terms/Terms_Use.cfm

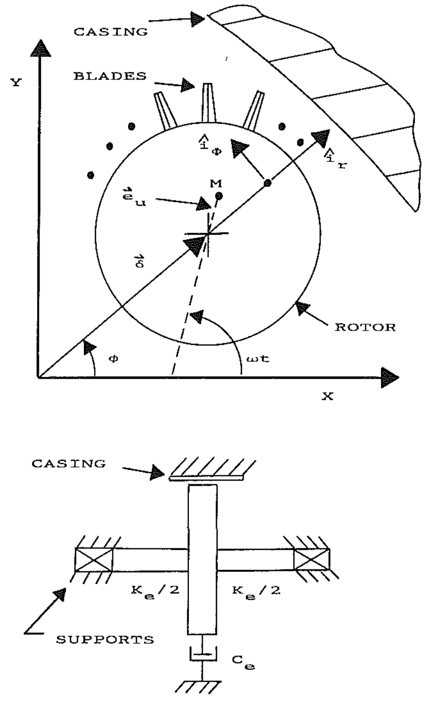

Fig. 1 Rotor-casing geometry

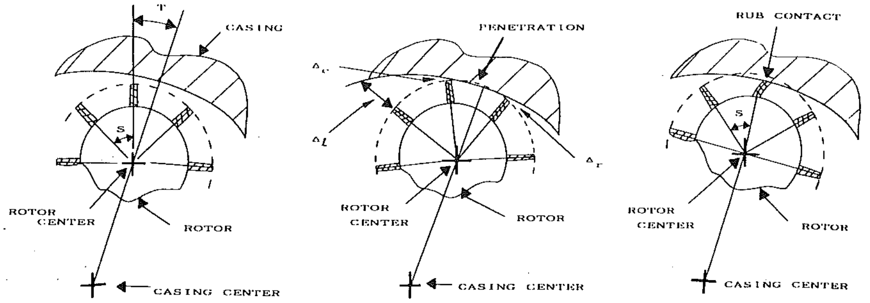

Fig. 2 Blade-casing contact geometry

With the above assumptions, the response of the rotor before, during, and after rub interaction can be separated into the following five regimes of operation, namely:

(*i*) No rotor/casing contact
(*ii*) Rub initiation with single blade contact
(*iii*) Rub interaction with multiple blade contact
(*iv*) Rub interaction separation with single blade contact
(*v*) Separation

Before rotor/blade/casing contact, the rotor motion vector δ is smaller than the radial clearance c. During this period, the rotor motion is dominated by the imbalance and the initial operating conditions. Noting the cylindrical coordinate geometry defined in Fig. 1, the equations of motion of the noncontacted rotor can be cast in the following component form:

i_r *direction*

$$m(\ddot{\delta}-\dot{\phi}^2\delta)+C_e\dot{\delta}+K_e\delta$$
$$=me_u\{\omega^2(\cos\theta\cos\phi+\sin\theta\sin\phi)-\alpha(\cos\theta\sin\phi-\sin\theta\cos\phi)\}+F_x\cos\phi+F_y\sin\phi \tag{1}$$

i_ϕ *direction*

$$m(\ddot{\phi}\delta+2\dot{\phi}\dot{\delta})+C_e\dot{\phi}\delta=me_u\{\omega^2(\sin\theta\cos\phi-\cos\theta\sin\phi)-\alpha(\sin\theta\sin\phi+\cos\theta\cos\phi)\}-F_x\sin\phi+F_y\cos\phi \tag{2}$$

During the initial and final phase of a rub interaction, typically only a single blade participates. In terms of the geometry defined in Fig. 2, a two-blade rub initiation process can occur if the minimum clearance is achieved when the rotor orientation is such that $T=S/2$. Overall, noting Appendix A, contact initiation and separation are signaled by the following clearance criteria:

$$\Delta_c<0 \tag{3}$$

$$\Delta_l,\ \Delta_r>0 \tag{4}$$

The equations of motion associated with the contacted condition are given by the expressions

i_r *direction*

$$m(\ddot{\delta}-\dot{\phi}^2\delta)+C_e\dot{\delta}+K_e\delta+F_N=m\,e_u\{\omega^2(\cos\theta\cos\phi+\sin\theta\sin\phi)-\alpha(\cos\theta\sin\phi-\sin\theta\cos\phi)\}+F_x\cos\phi+F_y\sin\phi \tag{5}$$

and

i_ϕ *direction*

$$m(\ddot{\phi}\delta+2\dot{\phi}\dot{\delta})+C_e\dot{\phi}\delta+\mu F_N=me_u\{\omega^2(\sin\theta\cos\phi-\cos\theta\sin\phi)-\alpha(\sin\theta\sin\phi+\cos\theta\cos\phi)\}-F_x\sin\phi+F_y\cos\phi \tag{6}$$

where F_N is the normal and μF_N the tangential friction force

Nomenclature

A = cross-sectional area
C = radial clearance
Ce = effective damping
C_e = imbalance eccentricity
C_{eo} = original imbalance eccentricity
C_{es} = suddenly increased eccentricity
E = Young's modulus
F_N = normal rub force
F_x, F_y = external load in x and y directions
I = area moment of inertia
K_e = effective stiffness
l_b = length of impeller blade
m = effective rotor mass
R_c = rotor bore radius
R_r = casing inside radius
S = blade spacing angle
T = angle between preceding blade and line of contact
$W(x)$ = blade bending deflection
α = rotor center angular precession acceleration
δ = normal rotor displacement
Δ_c, Δ_l, Δ_r = distance between blade tip and casing
θ = mass center phase angle
μ = coefficient of friction
ϕ = rotor center precession angle
$\dot{\phi}$ = rotor center angular precession

Downloaded 01 Jun 2010 to 171.66.16.57. Redistribution subject to ASME license or copyright; see http://www.asme.org/terms/Terms_Use.cfm

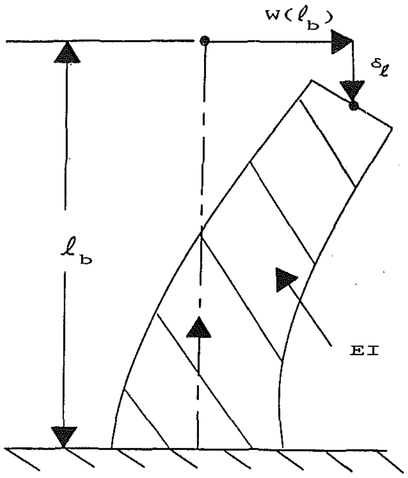

Fig. 3 Deflected blade geometry

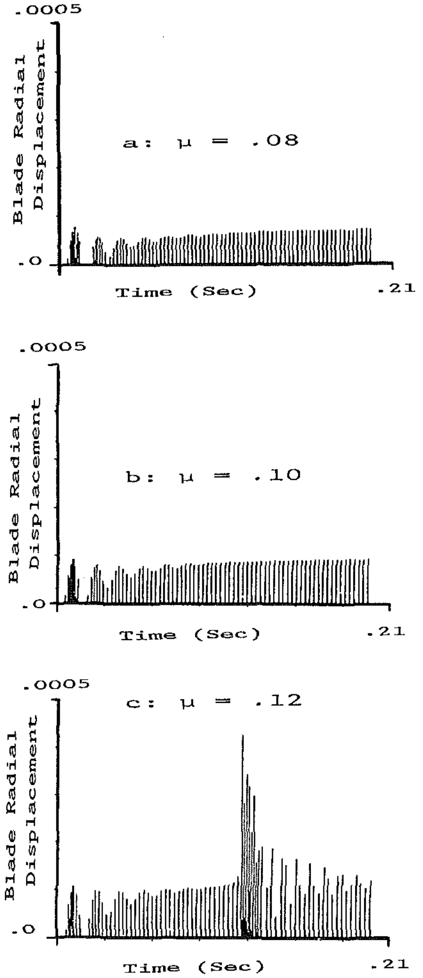

Fig. 4 Effects of friction on blade radial displacement

between the blade tip and the casing. Noting Appendix B, the normal force F_N varies nonlinearly with the deformation of the blade and can be expressed by the following nondimensional form:

$$F_N = \frac{\pi^2 EI}{4l^2_D}\bar{F}_N \tag{7}$$

such that

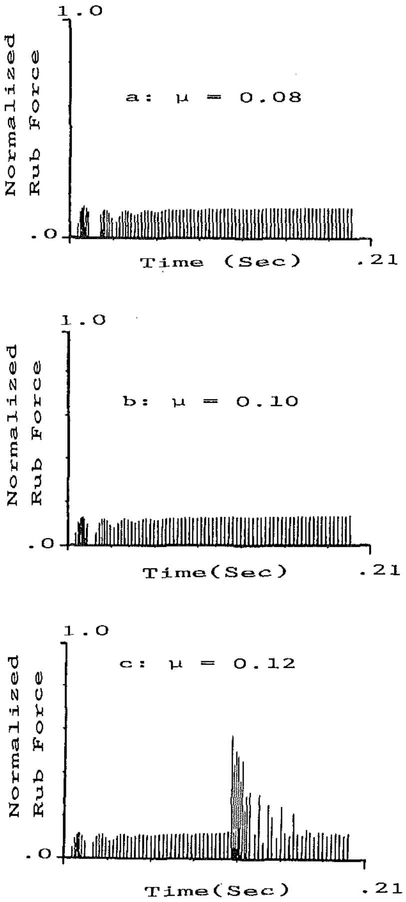

Fig. 5 Effects of friction on rub force

$$\bar{F}_N = \frac{\frac{\pi}{2}\sqrt{\frac{\delta_l}{l_b}}}{\mu + \frac{\pi}{2}\sqrt{\frac{\delta_l}{l_b}}} \tag{8}$$

where Δ_l is the radial displacement in the i_r direction of the blade, l_b the length of the blade, and $\bar{F}_N$ is a nondimensionalized parameter defined by the ratio of the radial force and the blade buckling load $(\pi^2 EI/4l_b^2)$.

For the case of multiple blade participation, the normal force exerted on the rotor will be represented by

$$F_N = \frac{\pi^2}{4}\sum_{i=1}^{n}\frac{E_i I_i}{l_{bi}^2}\bar{F}_{Ni} \tag{9}$$

such that

$$\bar{F}_{Ni} = \frac{(\pi/2)\sqrt{\frac{\delta_{li}}{l_{bi}}}}{\mu + \frac{\pi}{2}\sqrt{\frac{\delta_{li}}{l_{bi}}}} \tag{10}$$

where n is the number of blades participating in the rub interaction and F_{Ni}, E_i, and I_i are respectively the normal load, Young's modulus, and moment of inertia of the ith blade. Based on equation (9), the maximum blade stress can be expressed as a combination of the radial and tangential forces exerted on the blade tip. It is given by the relation

$$\sigma = F_N\left(\frac{\mu l_b C}{I} + \frac{1}{A}\right) \tag{11}$$

In order to simulate sudden blade loss conditions, the rotor

Downloaded 01 Jun 2010 to 171.66.16.57. Redistribution subject to ASME license or copyright; see http://www.asme.org/terms/Terms_Use.cfm

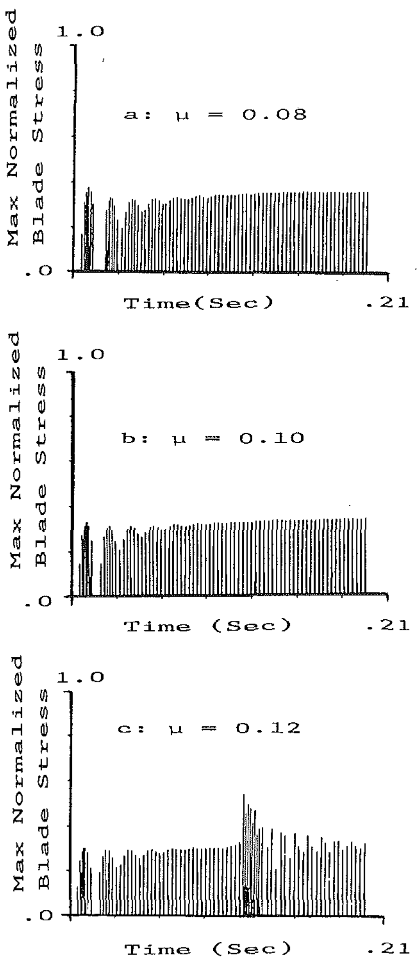

Fig. 6 Effects of friction on maximum blade stress

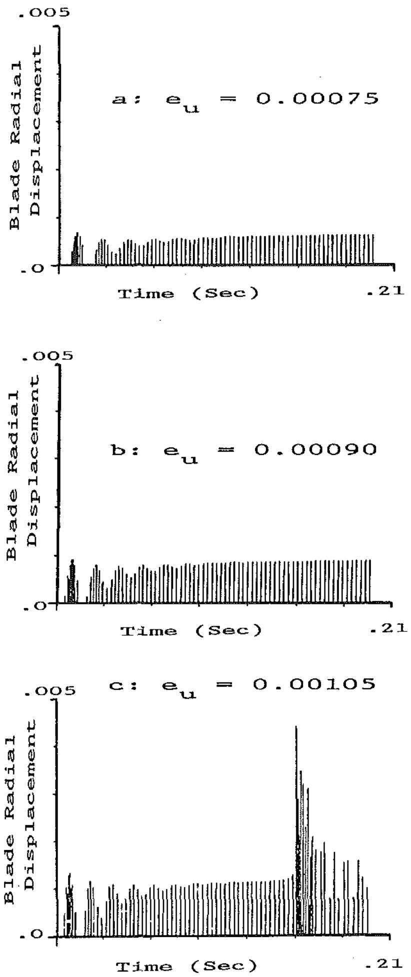

Fig. 7 Effects on unbalance eccentricity on blade radial displacement

Table 1 Rotor/blade/casing data for transient study

Rotor weight	4 lbs (17.792 nt.)
Equivalent stiffness	10,000 lb/in. (17511.8 nt/cm)
Equivalent damping	0.5 lb.-sec/in. (0.8756 nt-s/cm)
Rotor radius	1.5 in. (3.81 cm)
Casing radial clearance	0.003 (0.0762 mm)
Original imbalance eccentricity	0.001 in. (0.00254 mm)
External X-direction load	0.0 lb. (0.0 nt)
External Y-direction load	0.0 lb. (0.0 nt)
Blade radial length l_b	1.0 in. (2.54 cm)
Blade thickness h	0.0625 in. (0.15875 cm)
Blade width b	0.5 in. (1.27 cm)
Spacing between blades	20 deg (0.349 rads)
Fictional coefficient	0.1
Rotational speed of rotor	9072 rpm
Beta value for integration	0.25

system is assumed to possess an original imbalance e_{uo} and to be operating in an initially steady-state condition. An additional imbalance of e_{us} is then suddenly induced in the system. Using the steady-state behavior as an initial condition, a Newmark-Beta type of integration scheme is used to evaluate the velocity and displacement vectors at the next time step. Note, once contact between blade tips and the motor casing occurs, the forces exerted on the rotor are highly nonlinear. Thus a self-adaptive numerical scheme is introduced such that variable time step sizes are used to provide a better solution to the nonlinear transient motion. An in-depth discussion of the parametric studies in blade/casing rub interaction will be presented in the next section.

Discussion of Results

In the preceding section Jeffcott-type field equations were developed. These model rub interactions in rotating equipment involving the effects of blade stiffness, friction, rotor stiffness, and inertia as well as system damping. This includes handling such problems as load imbalance (eccentricity), seismic inputs, etc. Based on the model developed, this section will discuss the results of benchmark studies considering the effect of blade stiffness, friction, and load imbalance. Overall the numerical experimentation will include parametric studies involving such system response characteristics as

(*i*) Blade radial displacement
(*ii*) Normalized rub force
(*iii*) Maximum blade stresses
(*iv*) Incidence and separation angles
(*v*) Backward whirl and
(*vi*) Typical rotor orbits

As noted, due to the inherent nonlinearity of the governing field equations, numerical integration must be employed to yield the requisite solution. In particular, this involved the use of a Newmark-Beta type algorithm wherein time stepping was automatically updated. This enables the handling of the tight time stepping requirements generated during the contact/impact, separation, and rubbing processes. Because of the severity of the onset of backward whirl, this approach proved especially useful.

In the context of the foregoing, Figs. 4–14 illustrate various aspects of the overall response characteristics of the system

Downloaded 01 Jun 2010 to 171.66.16.57. Redistribution subject to ASME license or copyright; see http://www.asme.org/terms/Terms_Use.cfm

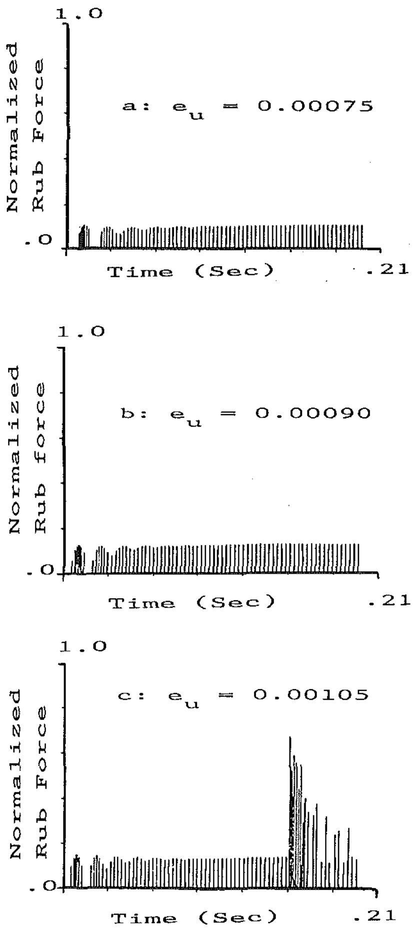

Fig. 8 Effects of unbalance eccentricity on rub force

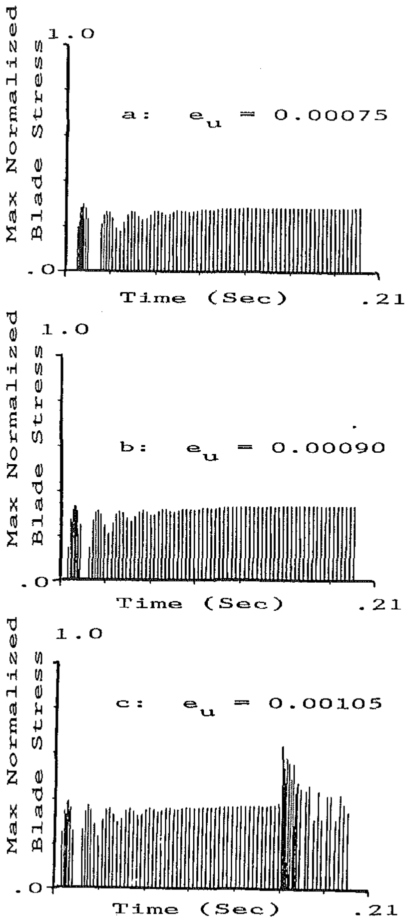

Fig. 9 Effects of unbalance eccentricity on maximum blade stress

defined by the model depicted in Table 1. For instance, considering the effect of changes in friction coefficient, Figs. 4–6 illustrate the resulting influence on the radial blade displacement, normalized net rub forces, and maximum blade stresses. As can be seen, increasingly higher displacement, load, and stress fields are induced as the friction coefficient is raised. Recalling the blade clearance expression developed earlier, the displacements noted in Fig. 4(*c*) exceed the multiple blade contact criteria. In this context the maximum stresses are blunted by multiple blade participation. This phenomenon is clearly seen by comparing Figs. 4(*c*) and 6(*c*). In particular while the radial displacement response shows very sharp peaky results, the maximum blade stresses are somewhat blunted in the same region of response time. This is a direct result of load sharing among several blades. Regardless, it follows that blades undergoing rubs can have severely reduced fatigue lives. In fact if pushed far enough, they can be forced into a low cycle fatigue threshold of behavior. In the context of Figs. 4(*a*–*c*), this is especially true as the rubbing surfaces friction characterisitc are increased during successive rub events. This follows from the increased wear of the surfaces involved.

Figures 7–9 illustrate the effects of increasing the load eccentricity. Similar to friction, raising the load imbalance causes significant increases in the maximum blade stress and hence the overall excursion in stress cycling. Noting Fig. 7(*a*), since the multiple blade clearance has again been exceeded, the growth in maximum stress is blunted due to load sharing. Such is not the case for the net rub force which shows operationally the same peakiness as the rotor displacement profile.

Continuing, Figs. 10–13 illustrate the effects of increases in bladestiffness. As would be expected, as the overall blade stiffness increases, the overall rotor displacement vector is reduced in amplitude. In contrast to this, the maximum blade stresses are increased with stiffness. This is clearly seen in Fig. 12. The effects of friction eccentricity and blade stiffness on the rub intiation and separation angles are depicted in Fig. 13. Noting Figs. 13(*a*, *b*) backward whirl is initiated when the angles of incidence and separation reach $\pi/2$ radians. At such points, the rub forces are maximized. This of course yields high blade stress. Such behavior is clearly seen in Figs. 6(*d*) and 9(c). As noted earlier, such stresses are blunted when multiple blade contacts are involved. Such behavior is also depicted by comparing the sharp contrasts between the rub forces and the resulting blade stresses. Lastly, Fig. 14 illustrates the rotor center trajectory for a given set of system parameters. Also depicted are the variations in whirl displacement and associated speed. As noted earlier, during the onset of backward whirl, angles of incidence and separation undergo transitions through $\pi/2$ radians. This is clearly depicted in the trajectory illustrated in Fig. 14(*b*).

Conclusions

In summary, the current work has developed modeling methodologies which enable the handling of rotor blade casing rub interactions. Based on the benchmark studies, the modeling has revealed the occurence of high-stress fluctuations and hence potential low/high cycle fatigue problems. In future studies, the modeling will be generalized by employing more comprehensive modal and FE solution methodologies. Such generalizations will enable more definitive component life predictions. Overall the current work has led to the following conclusions:

Downloaded 01 Jun 2010 to 171.66.16.57. Redistribution subject to ASME license or copyright; see http://www.asme.org/terms/Terms_Use.cfm

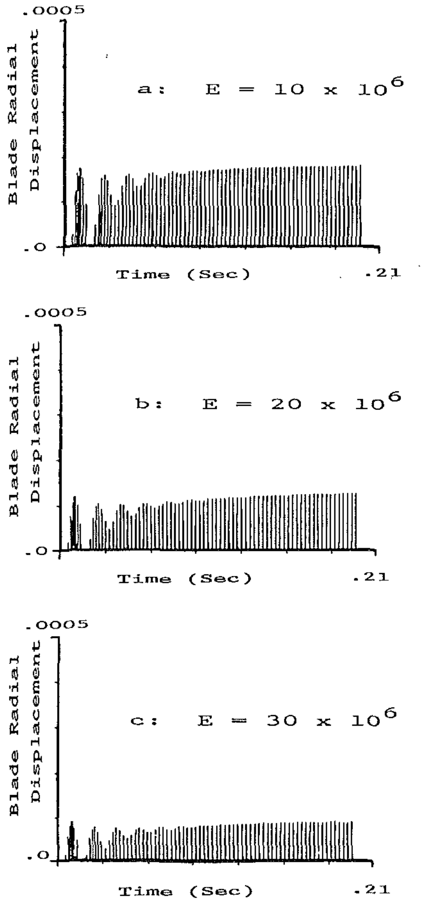

Fig. 10 Effects of blade stiffness on radial tip displacement

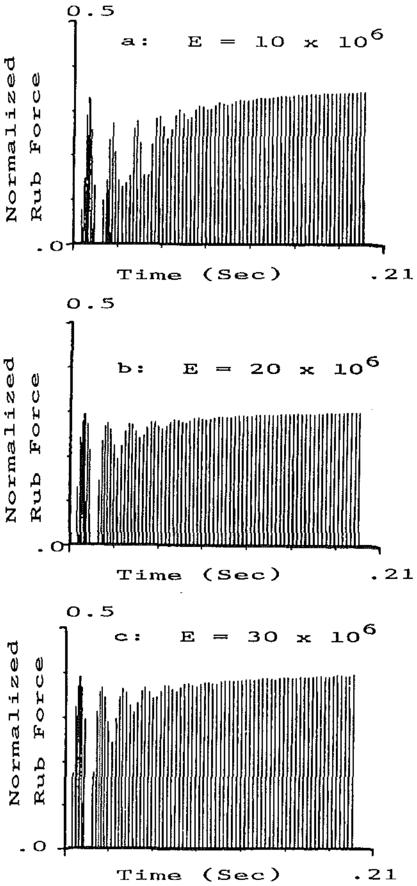

Fig. 11 Effects of blade stiffness on rub force

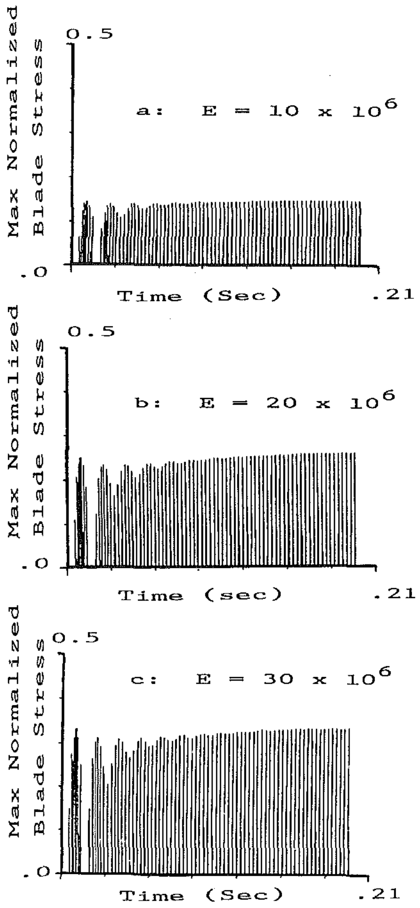

Fig. 12 Effects of blade stiffness on maximum stress

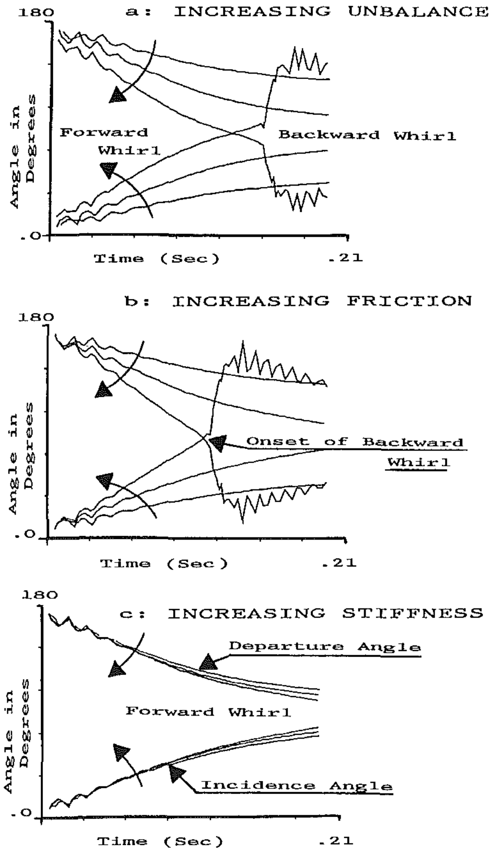

Fig. 13 Effects of friction, unbalance eccentricity, and blade stiffness on the angles of incidence and separation

Downloaded 01 Jun 2010 to 171.66.16.57. Redistribution subject to ASME license or copyright; see http://www.asme.org/terms/Terms_Use.cfm

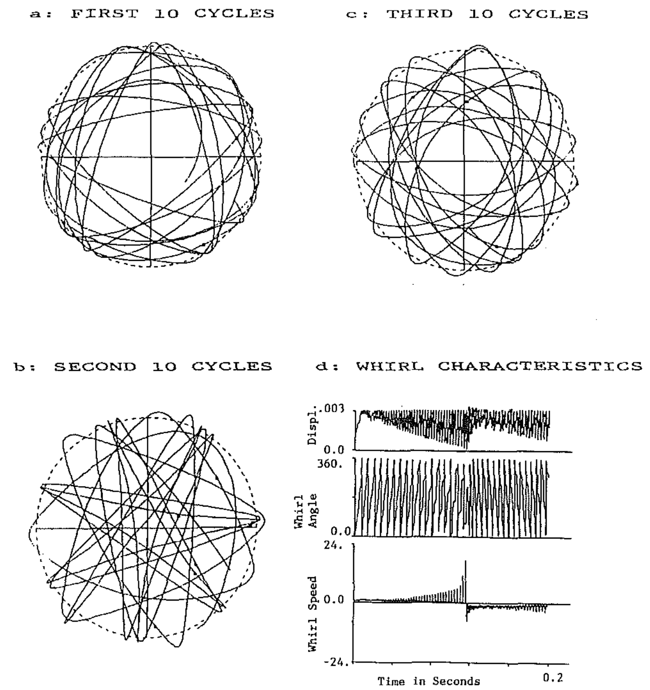

Fig. 14 Typical rotor orbits with rubs and backward whirl development: $\mu = 0.12$, $E = 30 \times 10^6$, $e_u = 0.0009$.

1 The increase in friction coefficient and imbalance of the system causes a dramatic steepening of the angles of incidence and separation of the rotor rub trajectory. This leads to an earlier onset of backward whirl. It is noted that increases in blades stiffness have a much smaller effect on the onset of backward whirl orbits.

2 Rub forces, blade displacement, and blade stresses are maximized during the onset of backward whirl orbits.

3 Rub forces and maximum blade stresses increase with increases in frictional coefficient, imbalance, and blade stiffness of the system. In contrast blade displacement decreases with the increase in blade stiffness.

4 The use of a self-adaptive time-stepping integration scheme is necessary to enable accurate simulation of the highly nonlinear rub interaction especially in the regimes where backward whirl motions are initiated.

5 Multiblade rub interactions tend to lead to a saturation (leveling off) of the growth of maximum stresses.

References

Adams, M. L., 1980, "Nonlinear Dynamics of Flexible Multibearing Rotors," *Journal of Sound and Vibration*, pp. 129-144.

Bently, D. E., 1974, "Forced Subrotative Speed Dynamic Action of Rotating Machiners," ASME Paper No. 74-DET-16.

Black, H. F., 1968, "Interaction of a Whirling Rotor With a Vibrating Stator Across a Clearance Annulus," *Journal of Mech. Eng. Science*, Vol. 10, No. 1, pp. 1-12.

Childs, D. W., 1979, "Rub Induced Parametric Excitation in Rotors," ASME *Journal of Mechanical Design*, Vol. 10, No. 4, pp. 640-644.

Choy, K. C., Gunter, E. J., and Allaire, P. E., 1978, "Fast Fourier Transform Analysis of Rotor-Bearing Systems," *Topics in Fluid Film Bearing and Rotor Bearing System Design and Optimization*, ASME, New York.

Choy, K. C, and Padovan, J., 1985, "Investigation of Rub Effects on Rotor-Bearing-Casing System Response," *Proceedings of the 40th Mechanical Failures Prevention Group Symposium*, Gaithersburg, MD.

Choy, F. K., Padovan, J., and Li, W., 1986, "Seismic Induced Nonlinear Rotor-Bearing-Casing Interaction of Rotating Nuclear Component," *Proceedings of ASME 1986 PVP Conference*, Chicago, IL.

Choy, F. K., and Padovan, J., 1985, "Nonlinear Transient Analysis of Rotor-Casing Rub Events," submitted to *Journal of Sound and Vibration.*

Enrich, G. E., 1969, "The Dynamic Stability of Rotor-Stator Radial Rubs in Rotaing Machinery," ASME *Journal of Engineering for Industry*, Vol. 91, pp. 1025-1028.

Gunter, E. J., Choy, K. C., and Allaire, P. E., 1978, "Modal Analysis of Turborotor Using Planar Modes Theory," *Journal of Franklin Institute*, Vol. 305, No. 4, pp. 221-243.

Kirk, R. G., and Hibner, D. H., 1976, "A Note on Blade Loss Dynamics of Rotor-Bearing Systems," ASME *Journal of Engineering for Industry*, Vol. 98, No. 2, pp. 437-504.

Nelson, H. D., Meacham, W. L., Fleming, D. P., and Kascak, A. F., 1983, "Nonlinear Analysis of Rotor-Bearing Systems Using Component Mode Synthesis," ASME *Journal of Engineering for Power*, Vol. 105, pp. 606-614.

APPENDIX A

Blade-Casing Proximity Check

In checking for blade-casing contact, several potential scenarios may occur, namely

(*i*) No contact
(*ii*) Single-blade contact
(*iii*) Multiblade incursions

Figure 2 illustrates the geometric characteristics associated with items (*i*)-(*iii*). Considering the geometry of the no-contact case, the clearance of the closest blade must be monitored. Noting Fig. 2, the noncontact phase itself consists of two stages namely the penetration or nonpenetration of the clearance circle of the blades with the casing. For the nonpenetrating case, the minimum clearance is defined by the expression

$$\Delta_{\min} = R_c - |\delta| - R_r - l_b > 0 \tag{A1.1}$$

such that $|\delta|$ denotes the magnitude of the rotor deflection $\boldsymbol{\delta}$. For the next phase of noncontact, $\Delta_{\min} < 0$. Noting Fig. 2 the deepest point of penetration of the blade clearance circle and the casing is colinear with the vector $\boldsymbol{\delta}$. By keeping an accurate account of shaft rotation, the relative orientation of the various blades to the point of deepest penetration can be ascertained. For a given blade-to-blade spacing angle S and orientation angle T, the various blade clearance illustrated in Fig. 2 take the form

$$\Delta_c = (R_r + l_b + c) - [(R_r + l_b)^2 + |\delta|^3 - 2(R_r + l_b)\,|\delta| \cos(\pi - T)]^{1/2} \tag{A1.2}$$

$$\Delta_l = (R_r + l_b + c) - [(R_r + l_b)^2 + |\delta|^2 - 2(R_r + l_b)\,|\delta| \cos(\pi - S - T)]^{1/2} \tag{A1.3}$$

and

$$\Delta_r = (R_r + l_b + c) - [(R_r = l_b)^2 + |\delta|^2 - 2(R_r + l_b)\,|\delta| \cos(\pi - T)]^{1/2} \tag{A1.4}$$

For no contact, it follows that $(\Delta_c, \Delta_l, \Delta_r) > 0$.

Once single-blade contacts is initiated, it follows that for $T \leq S/2$, $\Delta_l < 0$. For multiple-blade contacts, either or both Δ_l and Δ_r are > 0. If more than three blades are in contact, then relations similar to (A1.2-A1.4) can be established for each such blade. Overall the various contact criteria take the form:

(*i*) *No contact or penetration*

$$\Delta_{\min} > 0 \tag{A1.5}$$

(*ii*) *Penetration but no contact*

$$\Delta_{\min} < 0$$

$$T \leq \frac{S}{2} \tag{A1.6}$$

$$\Delta_c < 0$$

Downloaded 01 Jun 2010 to 171.66.16.57. Redistribution subject to ASME license or copyright; see http://www.asme.org/terms/Terms_Use.cfm

(*iii*) *Single-blade contact*

$$T \leq \frac{S}{2}$$

$$\Delta_c < 0$$

$$(\Delta_l, \Delta_r) > 0 \tag{A1.7}$$

(*iv*) *Multiblade contact*

$$T \leq \frac{S}{2}$$

$$(\Delta_c, \Delta_l, \Delta_r) < 0 \tag{A1.8}$$

APPENDIX B

Blade Stiffness and Stresses

For the current purposes, the blade behavior is assumed to be governed by largely linear kinematics. Since a full three-dimensional or even two-dimensional elasticity description is beyond current computational capabilities, we shall employ a beam type analogy. In this context, noting Fig. 3 the mechanical energy balance in a simple configuration blade takes the form

$$\frac{1}{2}\int_0^{l_b} EI\left(\frac{d^2W}{dX^2}\right)^2 ds = \frac{1}{2}F_N U + \frac{1}{2}\mu F_N W(l_b) \tag{A2.1}$$

where the radial deflection is given by the expression

$$U \approx \frac{1}{2}\int_0^{l_b} \frac{dW(X)}{dX} dX \tag{A2.2}$$

such that E, I, W, U, F_N and μ are, respectively, the Young's modulus, moment of inertia, circumferential deflection, radial deflection, normal blade tip force, and the friction coefficient associated with the blade end. Since the blade deformation can be approximated by

$$W(X) = W(l_b)\left(1 - \cos\left(\frac{\pi X}{2l_b}\right)\right) \tag{A2.3}$$

based on (A2.1) and (A2.2), the radial and circumferential tip deflections are given by the expressions

$$W(l_b) = \frac{\mu F_N}{\dfrac{EI\pi^2}{32l_b^3} - \dfrac{F_N\pi^2}{8l_b}} \tag{A2.4}$$

and

$$\delta_l = \frac{\pi^2}{16l_b}\left\{\frac{\mu F_N}{\dfrac{EI\pi^4}{32l_b^3} - F_N\dfrac{\pi^2}{8l_b}}\right\}^2 \tag{A2.5}$$

Noting classic bending theory, the critical stress associated with the deformation state is given by

$$\sigma = F_N\left(\mu\frac{l_bC}{I} + \frac{1}{A}\right) \tag{A2.6}$$

where C and A are, respectively, the cross-sectional thickness and area of the blade.

Based on (A2.5), the force-radial deflection behavior of the blade is defined by the expression

$$\bar{F}_N = \frac{\dfrac{\pi}{2}\sqrt{\dfrac{\delta_l}{l_b}}}{\mu + \dfrac{\pi}{2}\sqrt{\dfrac{\delta_l}{l_b}}} \tag{A2.7}$$

where $\bar{F}_N$ is the normalized force

$$\bar{F}_N = \frac{4l_b^2}{\pi^2 EI}F_N \tag{A2.8}$$

In similar context, the force-circumferential deflection relation takes the form

$$W(l_b) = \left(\frac{8l_b}{\pi^2}\right)\frac{\mu\bar{F}_N}{1 - \bar{F}_N} \tag{A2.9}$$

Downloaded 01 Jun 2010 to 171.66.16.57. Redistribution subject to ASME license or copyright; see http://www.asme.org/terms/Terms_Use.cfm

W. Tabakoff
Professor.
Fellow ASME

M. F. Malak
Graduate Research Assistant.
Student Mem. ASME

Department of Aerospace Engineering
and Engineering Mechanics,
University of Cincinnati,
Cincinnati, OH 45221

Laser Measurements of Fly Ash Rebound Parameters for Use in Trajectory Calculations

This paper describes an experimental method used to find particle restitution coefficients. The equations that govern the motion of solid particles suspended by a compressible gas flow through a turbomachine depend on the restitution coefficients. Analysis of the data obtained by a laser-Doppler velocimeter (LDV) system of the collision phenomenon gives the restitution ratios as a function of the incidence angle. From these ratios, the particle velocity components after collision are computed and used as the initial conditions to the solution of the governing equations of motion for particle trajectories. The erosion of metals impacted by small dust particles can be calculated by knowing the restitution coefficients. The alloy used in this investigation was 410 stainless steel.

Introduction

Gas turbines operating in areas where the atmosphere is polluted by small solid particles and industrial gas turbines burning coal as fuel are examples of machines operating under particulate two-phase flow conditions. The presence of solid particles in the working media leads to a performance deterioration of these engines both structurally and aerodynamically.

Under two-phase flow conditions, the gas and particles experience different degrees of turning as they flow through the blade channels. This is mainly due to the differences in their inertia. The major interacting force between the gas and particles is the viscous drag. The degree of turning and acceleration or deceleration achieved by the particles depends on the ratio of the viscous forces to the inertial forces experienced by the particles. This results in a concentration gradient across the blade channel and causes a change in the properties of gas and particles. The net result is a change in the blade surface pressure distribution, which alters the engine performance during the period of particle ingestion.

If the particles are of erosive nature, the problem becomes more complicated. The impact of particles on the blade surfaces can cause severe erosion damage, leading to structural failure of the blades. This damage is manifested by pitting and cutting of the blade leading and trailing edges, and a general increase in the blade surface roughness. The overall effect of the above phenomena, from the aerodynamic viewpoint, is an increase in total pressure loss across the blade row.

The use of pulverized coal as fuel in many power plants and industrial establishments is inevitable both in the present and in the future. The major problem confronting earlier developers of coal-burning turbines is the serious erosion of turbine blades and other metal parts by the suspension of fly ash in hot combustion gases. It is possible to remove approximately 85 percent by weight of the ash in these gases using cyclones. However small particles ranging in size between 1 and 15 μm still pass through the cyclones and enter the turbine. Typical ash concentrations for such a turbine are about 0.00027 mg/cm^3 (7.8 mgm/ft^3). The damage is caused principally by erosion of the leading and trailing edges of the stator and rotor blades. A thorough knowledge of the various parameters which influence the extent of erosion damage is required to improve the life and the aerodynamic performance of turbomachinery operating in an ambient of particulate flow. This paper presents an experimental method used to determine the particle restitution coefficients which are used for trajectory calculations in turbomachinery and in the new derived equations to calculate the material erosion.

Experimental Setup

The experimental setup is shown schematically in Figs. 1 and 2. It consists of an erosion wind tunnel, a laser-Doppler velocimeter (LDV) system, a data acquisition system, and a solid particle feeder.

Erosion Wind Tunnel. An existing erosion wind tunnel was used in this investigation [1]. The major advantage of this tunnel is that the primary variables of fluid velocity, particle velocity, particle flow rate, and particle sizes can be controlled in a representative aerodynamic environment. Provisions are made in the tester design to allow variation between the angle of attack of the abrasive particle and the surface of the test specimen.

Figure 1 is a schematic description of the apparatus to fulfill these objectives. The equipment functions as follows. A measured amount of dry fly ash is placed into the particle feeder A. The particles are fed into secondary air source and carried up to the particle injector C, where it mixes with the main air supply B. The particles are then accelerated by the

---

Contributed by the Gas Turbine Division of The American Society of Mechanical Engineers and presented at the 30th International Gas Turbine Conference and Exhibit, Houston, Texas, March 18–21, 1985. Manuscript received at ASME Headquarters January 7, 1985. Paper No. 85-GT-161.

Copyright © 1987 by ASME

Downloaded 01 Jun 2010 to 171.66.16.57. Redistribution subject to ASME license or copyright; see http://www.asme.org/terms/Terms_Use.cfm

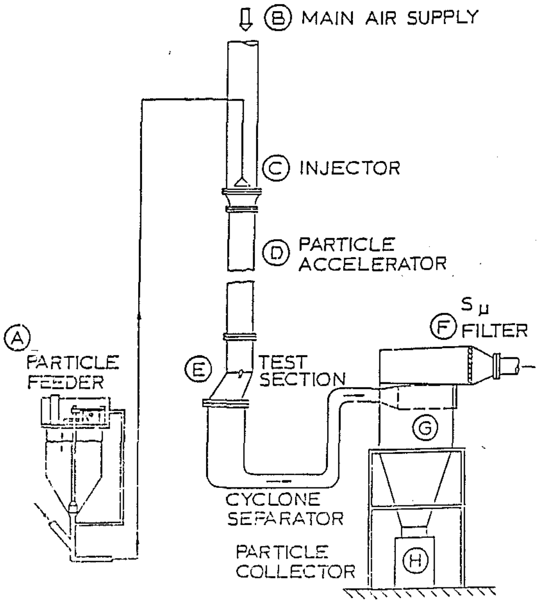

Fig. 1 Erosion research facility

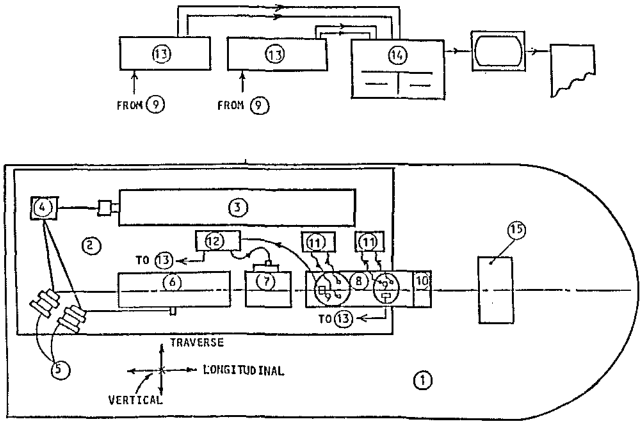

(1)	THE PLATFORM
(2)	THE OPTICAL SYSTEM TABLE
(3)	5 WATT ARGON LASER
(4)	DISPERSION PRISMS
(5)	2 ONE-INCH DIAMETER MIRRORS
(6)	BEAMSPLITTERS AND POLARIZATION ROTATORS
(7)	FREQUENCY SHIFTER
(8)	BACKSCATTER RECEIVING OPTICS WITH COLOR SEPARATORS
(9)	PHOTODETECTOR
(10)	250 MM COLLECTING LENS
(11)	PHOTOMULTIPLIER
(12)	FREQUENCY DOWNMIXER
(13)	DATA PROCESSOR
(14)	PDP 11/MINC 23 MINI-COMPUTER
(15)	THE TEST SECTION

Fig. 2 Schematic showing the experimental setup

high-velocity air in a constant-area duct D, and impact the specimen in the test section E. The test dust is then separated from the air by a cyclone separator G, and collected in the container H. The test air is further filtered through a commercial 5-μm filter F.

The test section is designed so that the particle-laden air is channeled over the specimen and the aerodynamics of the fluid surrounding the blade sample are preserved. This section contains several interchangeable inserts so that the flow properties can be determined using conventional instrumentation and the particle trajectories can be recorded using high-speed photographic or laser methods.

Laser and Optics (LDV System). The optical components of the laser-Doppler anemometer were arranged in the backward scatter mode (Fig. 2) to measure two simultaneous velocity components of a single particle. A two-color 5-W argon-ion Spectra physics, model 164-09 is used as laser source. The laser beams are brought into one common measuring volume using a transmitting lens of 250 mm focal length. The crossing angle for the incident 1.5-mm-dia beams is 11.05 deg. The LDV and the measuring volume characteristics are shown in Table 1.

Table 1 LDV characteristics

Color	blue	green
Wavelength, μm	0.488	0.5145
Firing spacing, μm	2.534	2.672
Diameter of measuring volume at the $1/e^{-2}$ intensity location, mm	0.1045	0.1097
Length of measuring volume at the $1/e^{-2}$ intensity location, mm	1.08	1.134
Number of stationary fringes	41	41

Table 2 Fly ash size distribution (percent)

Under 5 μm	62
5-10 μm	17
10-20 μm	20
Over 20 μm	1

Data Acquisition System. Two signal processors, TSI model 1990 and on-line Minc 11/23, are used to acquire synchronized data for the simultaneous measurement of two velocity components. The minimum time for a particle to cross the measuring volume was evaluated to be 1.4 μs. Accordingly the synchronization condition was set to 1 μs, which is the time out between the two data ready pulses received from both signal processors. A time out of 5 μs, after each valid synchronized data point is tagged in the computer, allows the particle to clear the measuring volume. The data acquisition program thus insures that sampling data are not obtained more than once from the same particle.

Particle Feeder. The particles from the feeder A (Fig. 1) are carried up to the particle injector. The feeder is designed as a vessel to operate at high air pressures. However, the pressure is equalized above and below the plunger by a bypass line. This allows the system to be calibrated under gravity feed conditions. Further, an electric eye records the plunger rpm in order to maintain operating conditions. The metering orifice is designed to be replaceable. In this manner, a larger (or smaller) orifice may be used, along with corresponding rod diameter, to allow versatility of the feeder. In this investigation the air flow was seeded with fly ash with size distribution as shown in Table 2.

Development of Particle Rebound Correlations

The erosion of metals impacted by small dust particles as well as the rebound dynamics of these particles can only be described in a statistical sense. This becomes obvious when one examines the number of geometric situations that might occur at impact. After a given incubation period, the target material will become pitted with craters and in fact after a slightly longer period, a regular ripple pattern may form on the eroded surface. Thus the local impact angle between the small particle and the eroded surface may deviate considerably from the geometric average. Further, the particles themselves are irregular crystalline in shape with several sharp corners. As a particle approaches the specimen the orientation of the particle is, for the most part, random. Thus, some particles will impact on a flat surface and do very little work on the target material. Others will impact with a corner oriented in a manner that removes material in a method similar to that of a cutting tool.

The restitution coefficient or restitution ratio is a measure of the kinetic energy exchange between two objects upon impact. Since erosion is a function of the energy exchange between the erodent particle and the material impacted, the restitution ratio will give a good indication of the behavior of

Downloaded 01 Jun 2010 to 171.66.16.57. Redistribution subject to ASME license or copyright; see http://www.asme.org/terms/Terms_Use.cfm

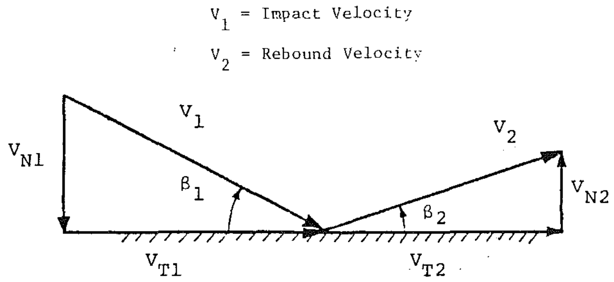

Fig. 3 Velocity and angle notations

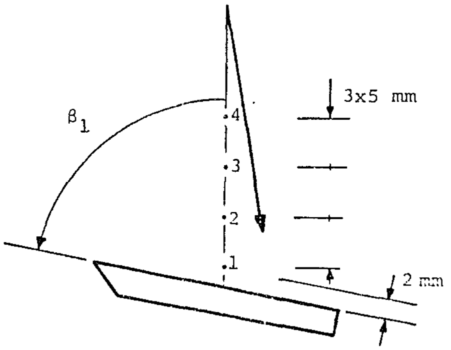

Fig 4 Impingement velocity measurement locations

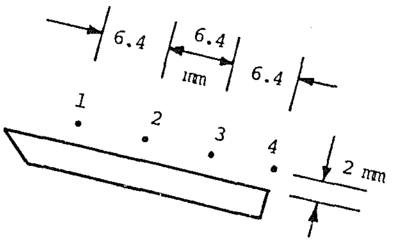

Fig. 5 Rebounding velocity measurement locations

the particle-material interaction. In this investigation an erosive impact occurs when the contaminant particle is much harder than the target material. This investigation was limited to ductile target materials, upon which the particle will create local stresses high enough to cause plastic flow in the target material.

Grant et al. [2] were the first to investigate thoroughly the rebound characteristics of high-speed eroding particles. The study was carried out on annealed 2024 aluminum alloy. The data were described using histograms to illustrate their statistical distribution. It was concluded that the restitution ratio V_2/V_1, which is directly related to the kinetic energy lost during impact, does not give sufficient information in regard to erosion. With this in mind, the restitution ratio was broken down into a normal velocity restitution ratio V_{N2}/V_{N1}, as shown in Fig. 3 (the normal component of the particle velocity after impact/the normal component of the particle velocity before impact), and a tangential velocity restitution ratio V_{T2}/V_{T1} (the tangential component of the particle velocity after impact/the tangential component of the particle velocity before impact). It was found that the normal velocity restitution ratio does not significantly contribute to ductile erosion. Most probably the kinetic energy is dissipated by plastic deformation of the target material without significant material removal.

Table 3 Summary of the impingement velocity at $\beta_1 = 60$ deg

Location above the sample	Normalized incidence velocity					
	Tangential		Normal		Total	
	SSM*	SD†	SSM	SD	SSM	SD
1	0.544	±0.11	0.897	±0.094	1.05	±0.144
2	0.463	±0.046	0.863	±0.09	0.98	±0.101
3	0.473	±0.058	0.867	±0.094	0.988	±0.11
4	0.465	±0.0725	0.865	±0.087	0.982	±0.11

---

*SSM = Sample Statistical Mean.
†SD = Standard Deviation.

Table 4 Normalized average impingement velocities at different impact angles

Incidence angle β_1	Normalized incidence velocity					
	Tangential		Normal		Total	
	SSM*	SD†	SSM	SD	SSM	SD
15	0.962	±0.083	0.253	±0.093	0.955	±0.0766
30	0.862	±0.046	0.503	±0.092	0.989	±0.06
45	0.672	±0.048	0.709	±0.087	0.977	±0.06
60	0.463	±0.046	0.863	±0.09	0.98	±0.059
75	0.234	±0.079	0.966	±0.088	0.994	±0.073

---

*SSM = Sample Statistical Mean.
†SD = Standard Deviation.

Measurement Technique

The LDV system was used to measure the impact and rebound velocities and angles on 410 stainless steel samples for different incidence angles. Wakeman and Tabakoff [3] show no significant tendency for the velocity or angle restitution ratios to vary with increasing target temperature. Therefore, this investigation was conducted at room temperature 21°C (70°F). Some of the results obtained for impact angle, $\beta_1 = 60$ deg, are listed in Table 3. The velocities are normalized with respect to the particle velocity at the center of the test section, which was 98 m/s (320 ft/sec). The impinging particle velocities were measured at four points above the stainless steel sample as shown in Fig. 4.

Inspection of the results in Table 3 shows that the impingement velocity has not changed too much from point 2 to point 4. At the point 1 location, the results obtained include the velocities of the smaller fly ash particles, less than 2 μm, which follow the air flow streamlines without hitting the specimen surface. Therefore the velocity at point 2 was selected to represent the impingement velocity for all impacting angles. Measurements for five incidence angles β_1 were performed and a summary of the normalized average and standard deviation of the impingement velocities is shown in Table 4. The standard deviation is large due to the irregularly shaped fly ash particles, and the size variation (standard deviation) causes the particles to deviate randomly from the air flow path.

The rebounding velocities were measured at four points located on a line 2. mm above and parallel to the specimen surface, as shown in Fig. 5, for all impacting angles. It was found that the variations of the rebounding velocities at these four points were within the standard deviation.

The average rebounding velocities were measured and normalized with respect to the corresponding impact velocities listed in Table 4, for the different impacting angles and the results are shown in Table 5.

Figures 6–9 illustrate typical histograms of the restitution ratios for the fly ash impacting at $\beta_1 = 60$ deg over a stainless steel sample target material. The vertical axis in these figures

Downloaded 01 Jun 2010 to 171.66.16.57. Redistribution subject to ASME license or copyright; see http://www.asme.org/terms/Terms_Use.cfm

Table 5 Mean restitution coefficients at different incidence angles

Incidence angle β_1	Directional coefficient $e_\beta = \beta_2/\beta_1$	Velocity restitution coefficients				
		Tangential $e_T = V_{T2}/V_{T1}$		Normal $e_N = V_{N2}/V_{N1}$		Total $e_V = V_2/V_1$
	SSM*	SSM	SD†	SSM	SD	SSM
15	0.933	0.867	±0.116	0.823	±0.38	0.865
30	0.74	0.698	±0.176	0.493	±0.225	0.652
45	0.578	0.7	±0.199	0.352	±0.283	0.528
60	0.64	0.76	±0.204	0.362	±0.146	0.51
75	0.6	1.6	±0.217	0.37	±0.157	0.49

*SSM = Sample Statistical Mean
†SD = Standard Deviation

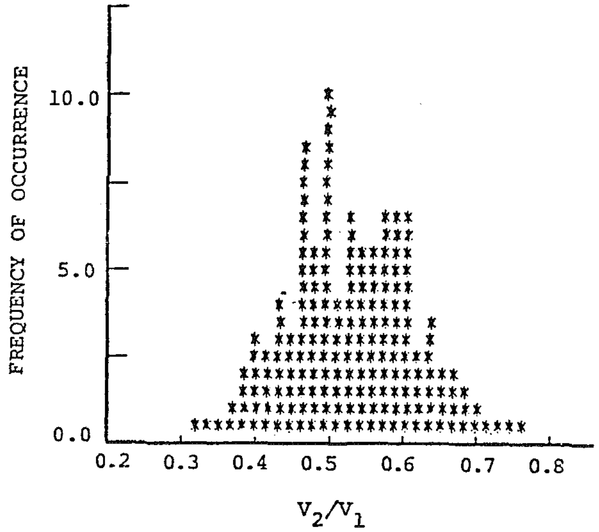

Fig. 6 Erosive particle velocity restitution ratio distribution

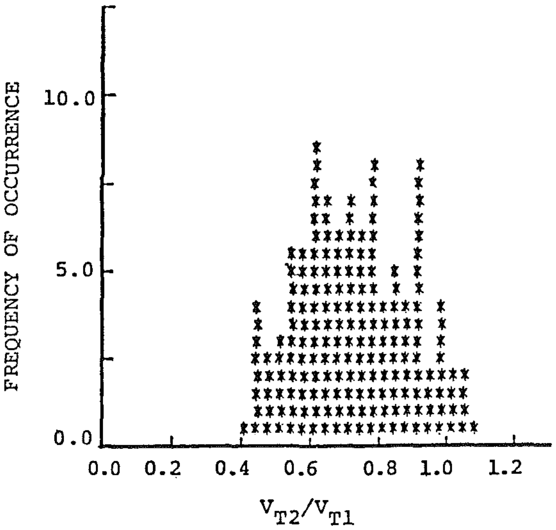

Fig. 8 Erosive particle tangential velocity restitution ratio distribution

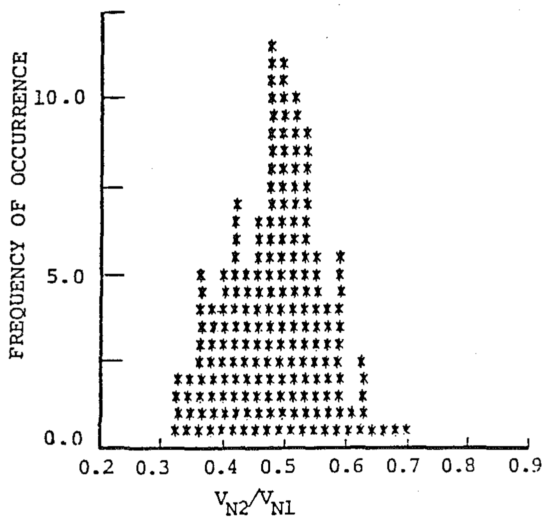

Fig. 7 Erosive particle normal velocity restitution ratio distribution

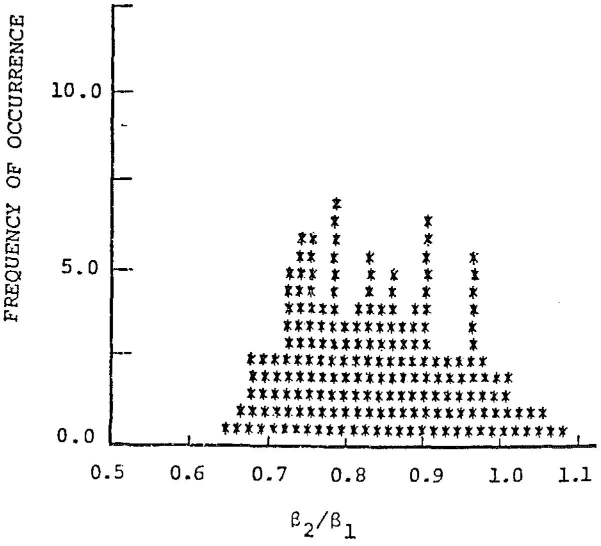

Fig. 9 Erosive particle directional coefficient distribution

represents the number of times that the restitution ratio was found to be between the limits designated by the scale at the horizontal axis. The wide distributions of the data are due to the variation of the particle sizes and shape irregularity. The ratio of the particle velocity after and before impact, V_2/V_1, is plotted against the angle of attack β_1 as shown in Fig. 10. Since the statistical distributions are of importance, the shapes of these distributions are cross plotted on the figure. The parameter V_2/V_1 is directly related to the kinetic energy lost during impact. The spread in these data indicates the variable condition of the surfaces and the orientation of the particle at impact. It is evident from this figure that V_2/V_1 decreases as the impact angle β_1 inreases from 0 to 75 deg.

The directional coefficient (β_2/β_1) is plotted in Fig. 11 versus the impact angle β_1. Again, these data are plotted with their statistical distributions. The minimum directional coefficients have been found at $\beta_1 = 45$ deg.

Figures 12 and 13 show the normal ($V_{N2}/V_{N1} = V_2$ sin

Downloaded 01 Jun 2010 to 171.66.16.57. Redistribution subject to ASME license or copyright; see http://www.asme.org/terms/Terms_Use.cfm

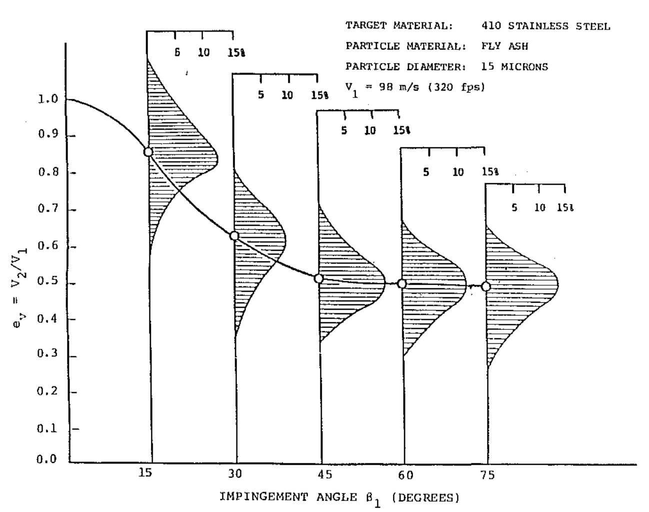

Fig. 10 Influence of impact angle on the erosive particle velocity restitution coefficient

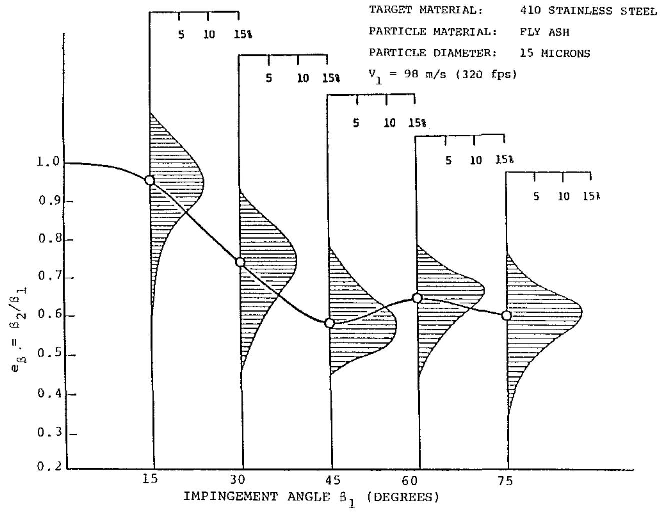

Fig. 11 Influence of impact angle on the erosive particle directional coefficient

$\beta_2/V_1 \sin\beta_1$) and tangential ($V_{T2}/V_{T1} = V_2\cos\beta_2/V_1\cos\beta_1$) restitution coefficients respectively plotted against the impact angle β_1. The trend of the data observed in Fig. 12 is very similar to that for the directional coefficient β_2/β_1 at small angle of impact. The statistical data distribution of Fig. 13 appears to be reasonably tight and well formed. The average value of V_{T2}/V_{T1} when analyzed supports the theory that erosion is proportional to a particle kinetic energy loss at impact. The maximum erosion of the material tested (410 stainless steel) occurs at $\beta_1 \simeq 30$ deg. This is also the point where V_{T2}/V_{T1} reaches a minimum. These results indicate that the normal component of velocity does not contribute significantly to ductile erosion. Most probably the kinetic energy is dissipated by plastic deformation of the target material without significant material removal.

The solid lines in Figs. 10–13 represents a least-squares polynomial curve fit of the mean value of the restitution parameters and may be expressed by the equations

$$e_V = V_2/V_1 = 1.04577 - 0.90847\,\beta_1 + 0.30702\,\beta_1^2 + 0.05695\,\beta_1^3$$

$$e_\beta = \beta_2/\beta_1 = 1.03642 - 0.38746\,\beta_1 - 0.51442\,\beta_1^2 + 0.45094\,\beta_1^3$$

$$e_N = V_{N2}/V_{N1} = 1.07474 - 1.19738\,\beta_1 + 0.16584\,\beta_1^2 + 0.27733\,\beta_1^3$$

$$e_T = V_{T2}/V_{T1} = 0.97903 + 0.15987\,\beta_1 - 2.14461\,\beta_1^2 + 1.74705\,\beta_1^3$$

where β_1 is measured in radians.

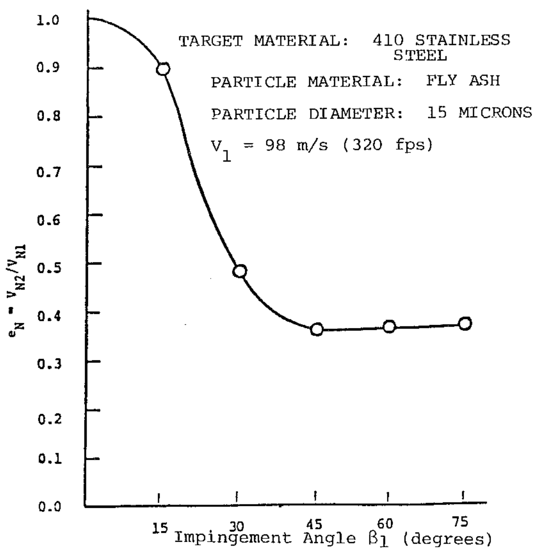

Fig. 12 Influence of impact angle on erosive particle normal velocity restitution ratio

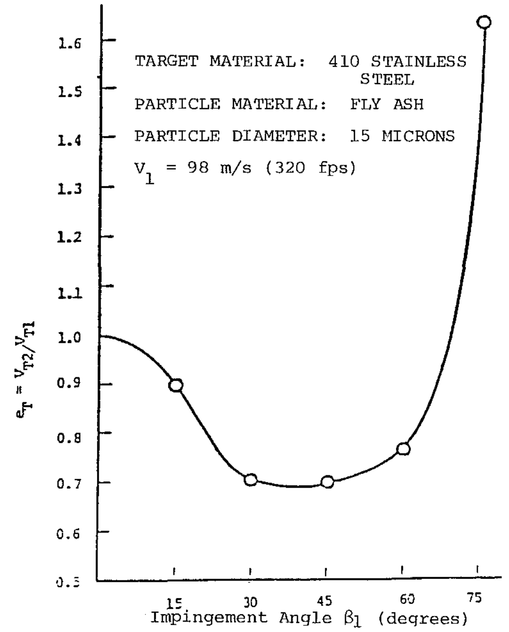

Fig. 13 Influence of impact angle on erosive particle tangential velocity restitution ratio

The above expressions may be used in the erosion equations developed by Grant and Tabakoff [2] to predict the erosion behavior of the materials. Furthermore, they are important data for the particle trajectories in turbomachinery utilizing coal.

In addition, Figs. 14 and 15 show the comparison of the normal and tangential restitution ratios for larger particles (quartz 200 μm) as reported by Tabakoff et al. [4] with the present data obtained for small particles (15 μm fly ash). To date most of the industries were using restitution parameters that we obtained earlier by high-speed photography techniques for large particles. Such parameters cannot give good results when applied to fly ash because of the difference in the particle size. Therefore presently we are continuing to study the restitution parameters for future turbine alloys that will be exposed to fly ash.

Downloaded 01 Jun 2010 to 171.66.16.57. Redistribution subject to ASME license or copyright; see http://www.asme.org/terms/Terms_Use.cfm

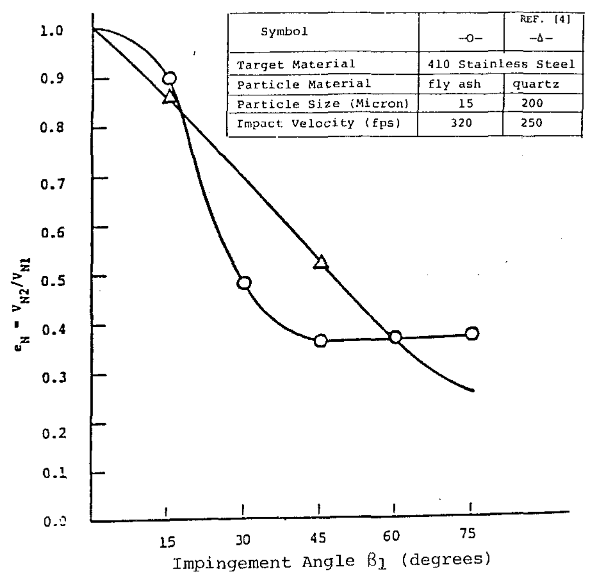

Fig. 14 Influence of impact angle on erosive particle normal velocity restitution ratio for two different particle sizes

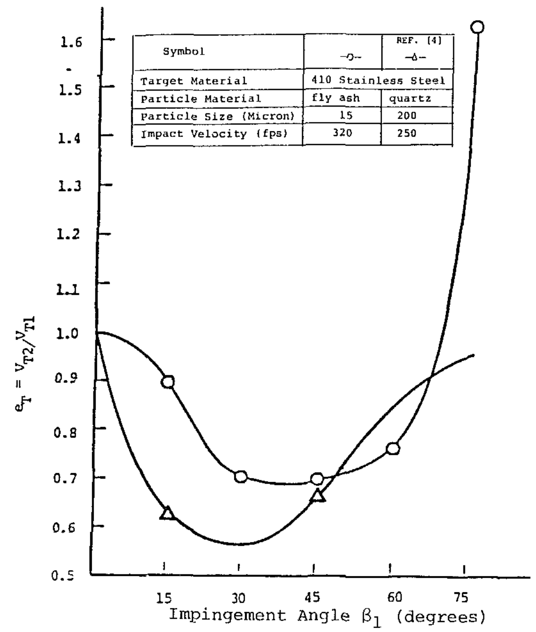

Fig. 15 Influence of impact angle on erosive particle tangential velocity restitution ratio for two different particle sizes

Conclusions

The dynamic impact characteristics of erosive fly ash particles impacting a 410 stainless steel material with resulting rebound have been investigated experimentally. The results of this investigation have led to the following conclusions:

1 The kinetic energy lost by the particle can be expressed in terms of restitution coefficients. In theory, this parameter should then be proportional to the resulting erosion.

2 The restitution ratio decreases as the particle impact angle increases.

3 Directional coefficients (β_2/β_1) and restitution ratios for different alloys are different.

4 Particle restitution coefficients for particle sizes below 40 μm can be measured only with an LDV system.

5 The restitution parameters for fly ash particles were measured for the first time, and the data obtained can be of great benefit for trajectory calculations in turbomachinery or other systems exposed to such particles.

Uncertainty Analysis

The limited sample uncertainty analysis of Kline and McClintock [5] was used. The final velocities were found to have an uncertainty of 3 percent.

Acknowledgments

This research work was sponsored by U.S. Department of Energy Advanced Research and Technology Development Fossil Energy Material Program.

References

1 Tabakoff, W., and Wakeman, T., "Test Facility for Material Erosion at High Temperature," ASTM Special Publication 664, 1979, pp. 123–135.

2 Grant, G., and Tabakoff, W., "Erosion Prediction in Turbomachinery Resulting From Environmental Solid Particles," *Journal of Aircraft*, Vol. 12, No. 5, 1975, pp. 471–478.

3 Wakeman, T., and Tabakoff, W., "Measured Particle Rebound Characteristics Useful for Erosion Prediction," ASME Paper No. 82-GT-170.

4 Tabakoff, T., Grant, G., and Ball, R., "An Experimental Investigation of Certain Aerodynamic Effects on Erosion," AIAA 8th Aerodynamic Testing Conference, Bethesda, MD, July 8–10, 1974, AIAA Paper No. 74-639.

5 Kline, S. J., and McClintock, F. A., "Describing Uncertainties in Single-Sample Experiments," *Mechanical Engineering*, Jan. 1953, p. 3.

Downloaded 01 Jun 2010 to 171.66.16.57. Redistribution subject to ASME license or copyright; see http://www.asme.org/terms/Terms_Use.cfm

R. A. Strub
Chairman of Working Group.

L. Bonciani
Nuovo Pignone.

C. J. Borer
Dresser Industries.

M. V. Casey
Sulzer Escher Wyss.

S. L. Cole
Ingersoll-Rand.

B. B. Cook
Transamerica Delaval.

J. Kotzur
MAN Gutehoffnungshuette GmbH.

H. Simon
Mannesmann Demag.

M. A. Strite
Elliott, United Technologies.

Process Compressor Subcommittee,
International Compressed Air and
Allied Machinery Committee (ICAAMC)

Influence of the Reynolds Number on the Performance of Centrifugal Compressors

This work is the result of an investigation based on numerous test data supplied by major compressor manufacturers in USA and in Europe. The main objective of the work is to propose improved formulae for the correction of the efficiency, the head, and the flow as influenced by the Reynolds number variation between workshop tests and specified conditions, carried out with the same machine. Tests on hand have shown that a sufficiently good correlation between measured and predicted values can be obtained with the proposed formulae. In addition a proposal is made for the allowable range, taking into account the inherent limitations for accurate testing at low Reynolds numbers. As a conclusion to this study it is recommended that the proposed formulae and allowable range be reviewed by the ASME, the ISO, or any other appropriate associations for adoption in revised test codes for centrifugal compressors.

Introduction

It is generally recognized that a variation of the Reynolds number between workshop tests and specified conditions influences the performance of turbomachines and more specifically of centrifugal compressors.

Most of the correction formulae proposed in the past are generally considered to be inadequate. Some of the formulae are too complicated to use, some others have no clear physical meaning, and some of the formulae can lead to excessively high correction of the efficiency. If the efficiency is modified by the Reynolds number, it follows that the head-flow characteristics of the compressor will also change. Many existing correction procedures do not include this.

The purpose of the present work is to propose simple, easy-to-use, and physically consistent formulae for efficiency, head, and flow corrections. In addition a recommendation for the allowable deviation between the test and the specified Reynolds number is proposed.

An exhaustive list of references concerning the above subject is given in the excellent work of Wiesner [1]. This work clearly shows that the correction formula for efficiency as given in the ASME PTC-10 Code leads to unacceptably high efficiency corrections. As a consequence a manufacturer carrying out workshop tests at a low Reynolds number will be favored over other suppliers conducting tests closer to specified conditions. This is clearly to the detriment of the customer and as a result no Reynolds correction is usually made.

The present paper provides an analysis of test data supplied by the major compressor manufacturers in the USA and in Europe. Some of the results of this work have been referred to in recent ASME publications by Simon and Bulskamper [7], Strub [8], and Casey [9].

Contributed by the Gas Turbine Division of The American Society of Mechanical Engineers and presented at the 32nd International Gas Turbine Conference and Exhibit, Anaheim, California, May 31-June 4, 1987. Manuscript received at ASME Headquarters January 30, 1987. Paper No. 87-GT-10.

Copyright © 1987 by ASME

Downloaded 01 Jun 2010 to 171.66.16.57. Redistribution subject to ASME license or copyright; see http://www.asme.org/terms/Terms_Use.cfm

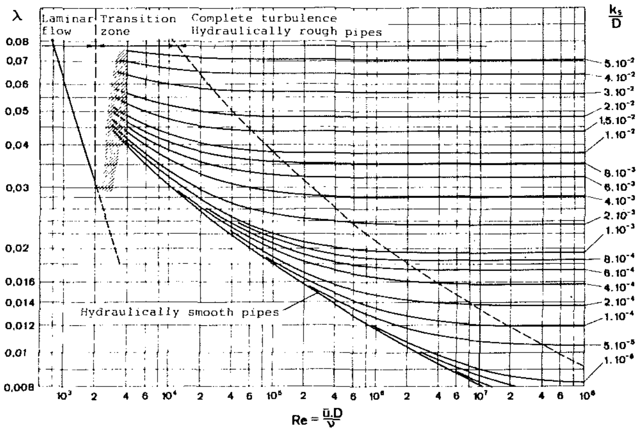

Fig. 1 Friction factor for turbulent flow in rough pipes

Basic Assumptions and Formulae

Assumptions. The prime interest of this study is to provide simple formulae for efficiency, head, and flow corrections as influenced by a change of the Reynolds number between workshop tests and specified conditions. As a consequence the centrifugal compressor is the same machine in both cases, which means that the geometry and the relative surface roughness are identical.

In order to take into account the fact that part of the losses are independent of the Reynolds number, the total losses are split up into two portions. Near the best efficiency point the portion of the Reynolds independent losses can be represented by a constant fraction of 0.3. This value varies according to various authors between 0 and 0.5 [1]. The losses due to friction are assumed to be dependent on a representative value of the friction coefficient λ according to the Moody diagram for pipe friction (Fig. 1). The representative value of λ is related to a reference Reynolds number and to a reference relative roughness of the compressor. Appropriate definitions for these reference values are given below.

The mean flow velocity in the flow channels of a compressor stage is approximately given by half its tip speed, $U_2/2$, and the mean hydraulic diameter D_h by twice the outlet tip width b_2. Thus a representative value of the Reynolds number for a stage is given by

$$\mathrm{Re} = \frac{U_2/2 \cdot 2b_2}{\nu} = \frac{U_2 \cdot b_2}{\nu} \tag{1}$$

in which ν is the kinematic viscosity at the inlet total condition. This definition is taken as the reference value.

The technical roughness R_a denotes the roughness average from the center line of the peaks and has been found to be the most suitable roughness value for the definition of machining work. Its definition [2] is

$$R_a = (1/l) \int_0^l |y| \cdot dx \tag{2}$$

which is equivalent to the values used in English language publications: CLA – center line average (UK); AA – arithmetic average (USA).

The reference roughness R_a is the average roughness for the impeller and its diffuser and can be either measured or taken from the manufacturer's drawing (agreement between manufacturer and customer). The roughness values are taken inside the impeller on one blade, on the disk, and on the shroud near to the outer diameter. The values for the diffuser are taken on the side walls and in the middle of one blade near the inlet diameter.

The effect of the roughness on turbulent pipe flow is characterized by the equivalent sand roughness k_s, as given in the Moody diagram. The equivalent sand roughness k_s of a machined surface with a technical roughness of R_a is defined as the diameter of the closely packed uniform sand grains that lead to the same friction losses. Various references [3-5] show that the ratio of k_s to R_a lies typically between 1.5 and 2.4 and in this study we have assumed that k_s is roughly twice R_a. The representative relative roughness of the stage is then given by

$$\frac{k_s}{D_h} = \frac{2R_a}{2b_2} = \frac{R_a}{b_2} \tag{3}$$

This definition of the relative roughness is used as a reference value.

In multistage compressors, for the sake of simplification, we take the reference values of Reynolds number and relative roughness of the first stage to represent each stage group.

The correction method applies only to the internal hydraulic losses and, therefore, the leakage losses across the balancing piston and the mechanical losses must be accounted for separately.

Formula for Efficiency Correction. The proposed formula for efficiency correction in the neighborhood of the best efficiency point is given by

$$\frac{1-\eta_{sp}}{1-\eta_t} = \frac{0.3 + 0.7\dfrac{\lambda_{sp}}{\lambda_{cr}}}{0.3 + 0.7\dfrac{\lambda_t}{\lambda_{cr}}} \tag{4}$$

Instead of taking friction factors directly from the Moody diagram the following generally accepted equations are used: von Karman equation for friction factor at critical Reynolds number

$$\frac{1}{\sqrt{\lambda_{cr}}} = 1.74 - 2\log_{10}\left\{2\frac{R_a}{b_2}\right\} \tag{5}$$

Colebrook equation for friction factor at specified operating conditions

$$\frac{1}{\sqrt{\lambda_{sp}}} = 1.74 - 2\log_{10}\left\{2\frac{R_a}{b_2} + \frac{18.7}{\mathrm{Re}_{sp} \cdot \sqrt{\lambda_{sp}}}\right\} \tag{6}$$

Colebrook equation for friction factor at test operating conditions

Nomenclature

b_2 = impeller outlet width
D_2 = impeller outlet diameter
D_h = hydraulic diameter
k_s = equivalent sand roughness
R_a = technical roughness
Re = Reynolds number
U_2 = impeller tip speed
η = polytropic efficiency

λ = friction coefficient
μ = polytropic head coefficient = $\Delta H_p/u_2^2$
μ_{in} = work coefficient = $\Delta H/u_2^2$
ν = kinematic viscosity
ρ = density
ϕ = flow coefficient = $\dot{V}/U_2D_2^2$

Subscripts

cr = refers to critical Reynolds number
ref = reference conditions
sp = specified operating condition
t = test operating condition

Downloaded 01 Jun 2010 to 171.66.16.57. Redistribution subject to ASME license or copyright; see http://www.asme.org/terms/Terms_Use.cfm

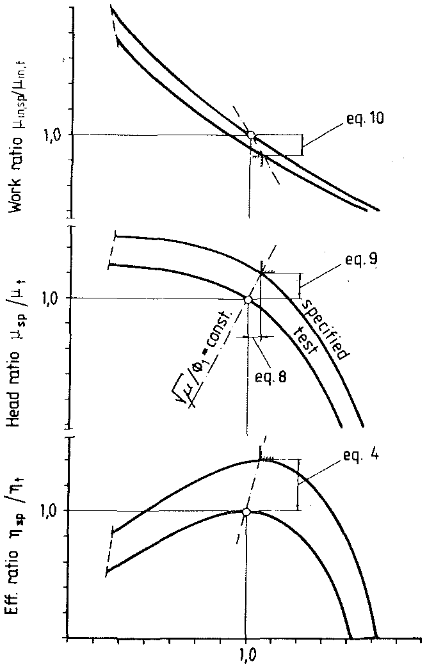

Fig. 2 Illustration of correction procedure

$$\frac{1}{\sqrt{\lambda_t}} = 1.74 - 2\log_{10}\left\{2\frac{R_a}{b_2} + \frac{18.7}{\mathrm{Re}_t \cdot \sqrt{\lambda_t}}\right. \tag{7}$$

In equation (5), λ_{cr} is the value of the pipe flow friction factor attained as the Reynolds number tends to infinity. This is not to be confused with the critical value at the transition from laminar to turbulent flow.

Formula for Head, Flow, and Work Input Correction. According to the consulted literature [1] and to the experience of the manufacturers contributing to this paper, there is a definite increase in both head coefficient and flow coefficient with an increase in Reynolds number. To a first approximation the head-flow characteristic changes in such a way that a typical reference point (e.g., the point of best efficiency) moves along a parabola. The change in head and flow with increasing Reynolds number resembles the change due to a small speed increase and can be approximated by

$$\frac{\phi_{sp}}{\phi_t} = \sqrt{\frac{\mu_{sp}}{\mu_t}} \tag{8}$$

In the neighborhood of the best efficiency point, roughly half of the increase in the efficiency appears as an increase in head, and this leads to the following formula:

$$\frac{\mu_{sp}}{\mu_t} = 0.5 + 0.5\left\{\frac{\eta_{sp}}{\eta_t}\right\} \tag{9}$$

With a knowledge of the efficiency and head coefficient corrections the correction for the work input can be calculated from the relationship $\mu_{in} = \mu/\eta$ and gives the following formula:

$$\frac{\mu_{in_{sp}}}{\mu_{in_t}} = 0.5 + 0.5\left\{\frac{\eta_t}{\eta_{sp}}\right\} \tag{10}$$

Application of Formulae to Test Data. These equations define the change in the best efficiency point on the performance characteristics. The shift in other points can then be calculated by noting that the shape of the characteristic remains essentially unchanged, and that other points can be transferred proportionally.

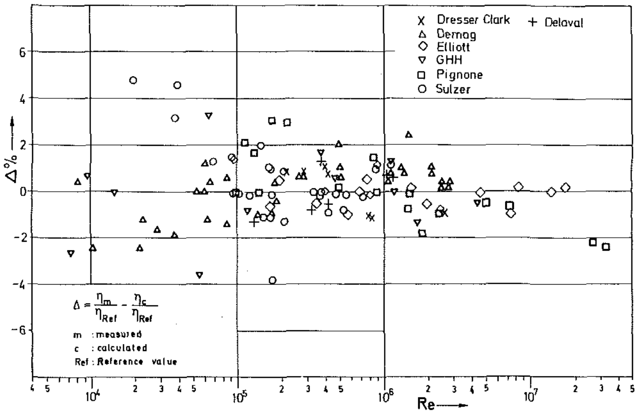

Fig. 3 Deviation between measurement and calculation

The full correction procedure is illustrated in Fig. 2 and is summarized below:

(*i*) At the best efficiency point on the test characteristic the ratio $(1-\eta_{sp})/(1-\eta_t)$ is calculated according to equation (4).

(*ii*) From this ratio η_{sp}/η_t is found.

(*iii*) Equation (9) is used to calculate the ratio μ_{sp}/μ_t, equation (8) to calculate the ratio ϕ_{sp}/ϕ_t, and equation (10) to calculate the ratio $\mu_{in_{sp}}/\mu_{in_t}$ at the best efficiency point.

(*iv*) The ratios η_{sp}/η_t, μ_{sp}/μ_t, ϕ_{sp}/ϕ_t, and $\mu_{in_{sp}}/\mu_{in_t}$ calculated at the best point are taken to be the same at all points of the measured test characteristic.

(*v*) The measured test points are now transferred to the new specified characteristic with these fixed ratios.

Checking of the Proposed Formulae With Test Data

Test data for 31 compressor groups (17 multistage and 14 single-stage compressors) leading to about 120 test points have been submitted by various manufacturers engaged in this study and compared to the prediction with the corresponding formula.

In order to avoid specifying the absolute values of the efficiency, which are confidential to the individual manufacturers, the efficiencies are presented as a ratio to a reference value. This reference value of efficiency has been chosen at a Reynolds number within the tested range in order to give the least scatter between the calculated curve according to the proposed formula and the available measurement points. This gives the same importance to all the measurement values and only by this means can the scatter be defined.

The deviation of the measured efficiency ratio from the calculated efficiency ratio given by the curve for all of the test results is plotted in Fig. 3. This figure demonstrates an almost equal distribution of the deviation (scatter) for all sets of data, thus showing that the proposed formula is acceptable for practical purposes. This figure also shows that the scatter for tests at low Reynolds numbers is greater than that at high Reynolds numbers. A large scatter can be expected when performing tests at low pressure or at low peripheral speed, which leads to low driving power.

It is worth remembering that owing to the complexity of the phenomena influencing the efficiency when a compressor is tested away from specified conditions, no correction formula, however sophisticated it may be, will be able to match all the practical testing conditions. This is the reason for proposing a formula which has at least the merit of being simple and which gives results which are certainly within the range of accuracy of the measurements.

Two manufacturers have presented data for the variation of head and flow coefficients with Reynolds number. These data

Downloaded 01 Jun 2010 to 171.66.16.57. Redistribution subject to ASME license or copyright; see http://www.asme.org/terms/Terms_Use.cfm

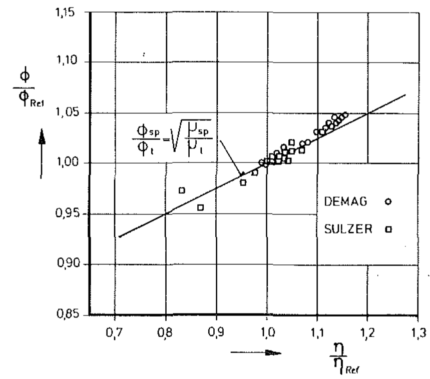

Fig. 4 Correlation between measured and calculated values for the flow coefficient ϕ

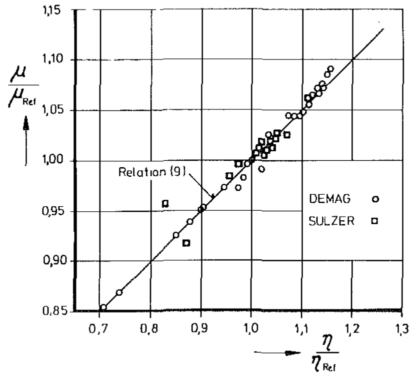

Fig. 5 Correlation between measured and calculated values for the head coefficient μ

are shown in Figs. 4 and 5 and demonstrate the good correlation with the proposed formulae (8) and (9).

Allowable Range

The range of application of the correction formula and the choice of a suitable test Reynolds number are influenced by two factors:

- the accuracy of the correction formula at different Reynolds numbers
- the reliability of tests carried out at reduced suction pressures or low driving power.

It is recommended that the limit of applicability be discussed between the customer and the manufacturer and agreed between them.

The limit of accuracy of the correction formula for efficiency has been established on the assumption that the correction formula is sufficiently accurate when used in a range where the hydraulic losses change by less than ±20 percent. These limits are shown in Fig. 6. The limits are very wide at high Reynolds number and become smaller as the Reynolds number is reduced.

The limits determined by the inaccuracy in the measurements are more difficult to establish. Tests carried out at reduced suction pressure require less power input and a smaller mass flow which lead to a reduced accuracy of the power measurement. In order to ensure that the limits of accurate measurements are not exceeded it is suggested that tests at reduced suction pressure only be carried out on the condition that the Reynolds number ratio of $\mathrm{Re}_t/\mathrm{Re}_{sp} > 0.1$ can be maintained.

The suggested limit of application of the ICAAMC formula is derived from the two limits discussed above and is shown in Fig. 6.

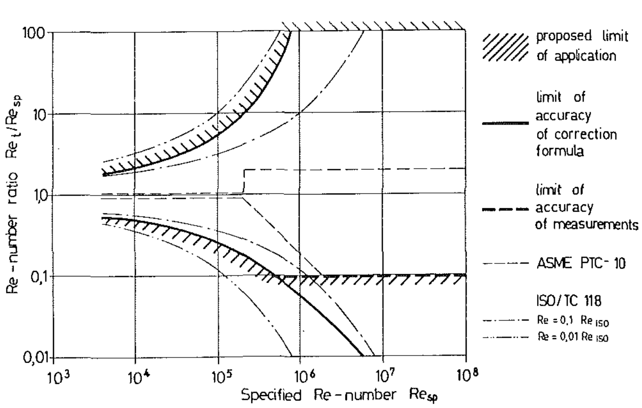

Fig. 6 Proposed allowable range of application

The upper limit of this range is, in practice, not very relevant as it would mean a very high test pressure that may be impossible because of the mechanical limitations at the casing. The narrow range of application at low Reynolds numbers corresponds well to the limited accuracy of test measurements in this region.

The previous limits defined by ASME PTC-10 Code were considered too narrow. In view of the better accuracy of the new correction formula these limits can now be enlarged. The previous limits defined by ISO Code TC-118, which are based on the work of Davis [6] and specify the range in which no correction need be applied, were considered inappropriate.

Conclusions and Recommendations

The present study leads to the following conclusions and recommendations for the workshop testing of centrifugal compressors:

1 The proposed formulae provide good agreement between test and specified conditions for efficiency, head, and flow corrections.

2 The allowable range should be limited, especially for low specified Reynolds numbers, and a suggestion is given on Fig. 6.

3 It is recommended that the proposed formulae and the proposed allowable range be reviewed by ASME, the ISO, or any other appropriate associations dealing with such problems for adoption in revised test codes for centrifugal compressors.

References

1 Wiesner, F. J., "A New Appraisal of Reynolds Number Effects on Centrifugal Compressor Performance," ASME *Journal of Engineering for Power*, Vol. 101, 1979, pp. 384-396.

2 DIN Standard 4762.

3 Grein, H., "Some Considerations on the Surface Roughness on Wetted Components of Hydraulic Machines," Escher Wyss News, No. 1, 1975.

4 Koch, C. C., and Smith, L. H., "Loss Sources and Magnitudes in Axial Flow Compressors," ASME *Journal of Engineering for Power*, Vol. 98, 1976, pp. 411-424.

5 Nixon, R. A., and Cairney, W. D., "Scale Effects in Centrifugal Cooling Water Pumps for Thermal Power Stations," NEL Report No. 505, National Engineering Laboratory, Glasgow, 1972.

6 Davis, H., "Equivalent Performance Parameters for Turboblowers and Compressors," *Trans. ASME*, Vol. 80, 1958.

7 Simon, H., and Bulskamper, A., "On the Evaluation of Reynolds Number and Relative Surface Roughness Effects on Centrifugal Compressor Performance," ASME *Journal of Engineering for Gas Turbines and Power*, Vol. 106, 1984, pp. 489-501.

8 Strub, R. A., Discussion contribution to [7] above.

9 Casey, M. V., "The Effects of Reynolds Number on the Efficiency of Centrifugal Compressor Stages," ASME *Journal of Engineering for Gas Turbines and Power*, Vol. 107, 1985, pp. 541-548.

Downloaded 01 Jun 2010 to 171.66.16.57. Redistribution subject to ASME license or copyright; see http://www.asme.org/terms/Terms_Use.cfm

A. Engeda
Research Assistant.

M. Rautenberg
Professor, Head.

Institute of Turbomachinery,
University of Hannover,
Hannover, Federal Republic of Germany

Comparisons of the Relative Effect of Tip Clearance on Centrifugal Impellers

Why do some centrifugal impellers exhibit high sensitivity to tip clearance losses while others don't? This may be understood by considering the geometric and fluid mechanics design parameters of the impellers. On the basis of experiments on five pumps of different specific speed, the relative effect on the stage performances of the pumps due to tip clearance is studied and earlier works in the field are discussed.

Introduction

Although tip clearance effects on turbomachinery performance have been studied for many years, and the necessity for reliable information is ever increasing, an exact method of calculation of these effects currently does not exist and test data must be relied upon to aid in the development of models to predict these effects.

Several models have been proposed for modeling tip flows, to predict tip losses. With the exception of tip-pressure measurements to measure unloading effects, no detailed confirmation of the methods was given. The most widely used model is that proposed by Rains [1] which suggests that the dominant tip flow mechanism is an inviscid imbalance. Lakshminarayana [2] proposed a theoretical model which predicted the aerodynamic efficiency loss due to tip clearance losses. Wood [3], using a series of experiments, reported extensive results to compare the hydraulic performance of the models, and he presented slip correlations for varying degrees of tip clearance which he compared with the slip prediction of Acosta [4]. Senoo et al. [5] presented a relationship between change of input power due to a change of tip clearance and the effective blockage at the impeller tip, on the basis of pressure distribution measurement along the shroud.

This present work was initiated due to the lack of reliable correlation of tip clearance losses of centrifugal impellers and lack of systematic identification of the tip clearance flow as related to the particular impeller.

On the basis of experimental investigations of five centrifugal pump impellers, of specific speed 0.33, 0.57, 0.83, 1.23, and 1.51, the present work studies the relative effect of tip clearance on the stage performance of centrifugal impellers.

Flow Through an Impeller and Its Effect on Tip Clearance Losses

It is well established now that in most cases the clearance flow consists essentially of a jet of fluid issuing as a vortex sheet on the low pressure surface of the blade. A survey of literature shows that three major effects are associated with tip clearance, as shown in Fig. 1: (1) secondary flow due to pressure gradients across the flow passage; (2) leakage of the flow past the tip clearance because of pressure differential across the blade tip; (3) the boundary layer "scraping" effect caused by the blades moving relative to the wall boundary layer and scraping fluid from it.

A fluid vortex is created by both the clearance flow and the boundary layer scraping, according to Hoshide et al. (6); these phenomena are additive. As shown in Fig. 1, the leakage flow

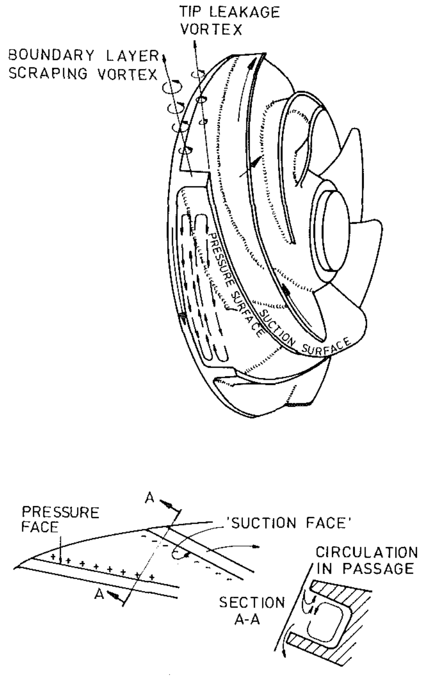

Fig. 1 Flow patterns of a semi-open impeller

Contributed by the Gas Turbine Division of The American Society of Mechanical Engineers and presented at the 32nd International Gas Turbine Conference and Exhibit, Anaheim, California, May 31–June 4, 1987. Manuscript received at ASME Headquarters January 30, 1987. Paper No. 87-GT-11.

Copyright © 1987 by ASME

Downloaded 01 Jun 2010 to 171.66.16.57. Redistribution subject to ASME license or copyright; see http://www.asme.org/terms/Terms_Use.cfm

through the tip clearance is intercepted by the secondary flow along the shroud which moves from the pressure side of the blade to the suction side of the adjacent blade, and the flow with low velocity near the shroud moves into the channel between blades. Even though tip clearance effects on centrifugal impellers have the above tendencies, the magnitude and severity of the effects is very much different for each impeller. An investigation of flow pattern by Senoo [7] showed a more complex pattern as affected by tip clearance flow than that of Howard et al. [8]. Senoo's impeller was of the mixed flow type while that of Howard et al. was a radial impeller.

Impeller internal flow solutions require an extensive geometric description of the blading, but often impeller design is made using a reduced number of variables, commonly: specific speed, suction specific speed, diffusion limitations, and exit flow angle. One of the important factors governing the impeller performance is the design of channel area changes along the flow path from inlet to outlet. Internal diffusion limitations for centrifugal impellers are widely discussed in the literature; Karassik et al. [9] gave 1.0–1.3 as the range for high hydraulic efficiency in pumps. In order to judge whether a particular blade shape is likely to lead to high impeller efficiency, it is essential to consider the distribution of the relative velocity along the flowpath. Laboratory tests have confirmed theoretical calculations which predict a significant velocity gradient depending upon the shape of the impeller and the position of the blade leading edge [10].

In an impeller passage the maximum velocity is not in the center of the passage, but nearer to the wall with greater convex curvature. But this is so only if flow separation does not occur; otherwise the velocity maximum can be nearer the other wall, which may have smaller convex or even a concave curvature. On the wall with flow separation, reverse flow may set in. This situation can prevail in some impellers, even at design point. When flow separation occurs, the Coriolis forces can set flows into motion which go crosswise to the main flow.

Mizuki et al. [11] reported, from investigation on three impellers, that in the impeller having the smallest radius of curvature at the shroud side separation was observed. They concluded that a large total pressure loss region appeared near the shroud and that the impeller efficiency decreased that much. They further reported that the separation produced a strong secondary flow component that flowed from the shroud toward the hub and that the secondary flow became stronger in the impeller having a lower aspect ratio. Senoo [12] is right in stating that tip clearance loss is influenced by the distribution of relative velocity in the impeller.

To estimate clearance effect, Pfleiderer [13] suggested an empirical formula, obtained experimentally, which can be represented as:

$$\begin{aligned} \phi_{opt}/\phi_0 &= 1-\alpha\lambda \\ \psi_{opt}/\psi_0 &= 1-\beta\lambda \\ \eta_{max}/\eta_{0-max} &= 1-\gamma\lambda \end{aligned} \tag{1}$$

where the numerical constants $2\,\alpha=\beta=\gamma=1.3\sim3$. This gives a simple linear effect of the clearance, which is shown in Figs. 5 and 6 not to be the case. However, within the range of small clearances the formulae give a good approximation.

Murakami et al. [14] suggested that

$$\begin{aligned} \psi_{opt}/\psi_0 &= (n/n_0)^2 \\ \phi_{opt}/\phi_0 &= (n/n_0) \end{aligned} \tag{2}$$

where n is a speed under zero clearance and n_0 is a speed at a particular clearance to give the same head and flow as zero clearance. This relationship implies that $\psi_{opt} \propto \phi^2_{opt}$; at present the amount of available evidence is too scarce to enable one to arrive at such final conclusions. In Fig. 6 this relationship is shown to be violated by pump Ns 0.57.

Hoshide et al. [6] gave an efficiency correlation with the head and power change due to tip clearance

$$\frac{\eta_{max}}{\eta_{0-max}} = \frac{\psi_{opt}}{\psi_0} \times \frac{\mu_0}{\mu_{opt}} \tag{3}$$

The discrepancy between the values calculated using equation (3) and the actual test results is too big to qualify the above relationship as reliable.

Hesselgreaves [15] published a modified form of the Rains [1] analysis. He presented a good correlation between tip clearance and efficiency. His results provide a rapid method of estimating efficiency losses due to tip clearance changes for mixed and axial flow machines.

The Investigated Impellers and Setup

The five investigated impellers are shown in Fig. 2. The meridional profiles of the five impellers are composed of circular arcs with inlet tangent angles of zero degree.

The five test pumps were typical commercial centrifugal pumps with end suction and volute construction. Initially the impellers were fully shrouded, then the front shroud was machined off to give a semi-open impeller with an identical shape to the shrouded one. The semi-open impeller was then fitted with a new front casing, shown in Fig. 2, having the same shroud contour.

The running clearance between the impeller vanes and the stationary casing was varied by a chain-gear drive, which changed the clearance without losing the symmetric position of the impeller outlet relative to the casing. The axial clearance variation was accurately read by a dial gauge. The impeller geometric data are given in Fig. 2.

The experimental setup consists of the investigated pump, booster pump, supply tank, and cooling system. The test loop has been specially designed for conducting performance and cavitation tests over the full range of pump operation. The physical outputs of the various parameters (pressure, flowrate, rotational speed, torque, and temperature) are measured and converted to electrical signals, and then are read by a data

Nomenclature

b = blade height
g = gravitational constant
H = pump total head
Ns = $\omega(Q)^{1/2}/(gH)^{3/4}$ = specific speed
P = power input to machine
Q = volume flow rate
r = impeller radius
U = peripheral velocity
V = absolute velocity
Vu_2/U_2 = $P/\rho Q\ U_2^2$ = an estimate
Z = number of blades
β = blade angle
δ = tip clearance
η = QgH/P = overall efficiency
λ = δ/b = tip clearance ratio
μ = $2P/2\pi b_2 r_2 U_2^3$ = power coefficient
ρ = density
ϕ = $Q/2\pi r_2 b_2 U_2$ = flow coefficient
ψ = $2gH/U_2^2$ = head coefficient
ω = angular speed

Subscripts

0 = at zero tip clearance
1 = at impeller inlet
2 = at impeller exit
m = meridional component
max = maximum
opt = optimal
u = tangential component

Downloaded 01 Jun 2010 to 171.66.16.57. Redistribution subject to ASME license or copyright; see http://www.asme.org/terms/Terms_Use.cfm

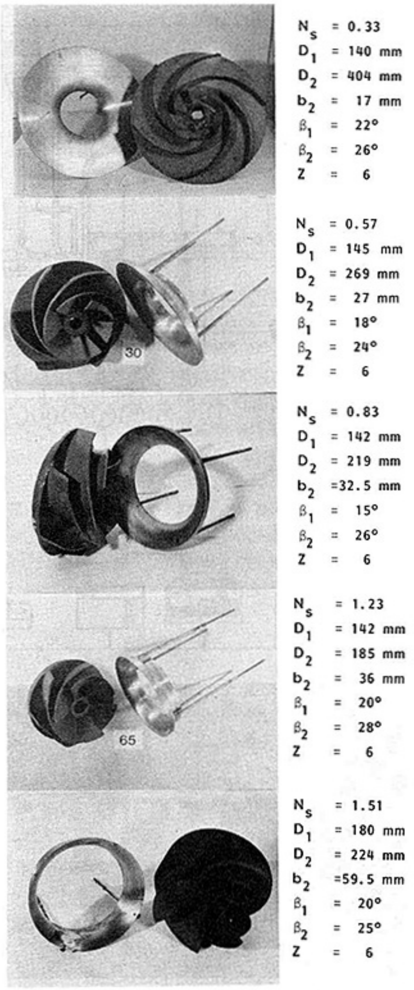

Fig. 2 The tested impellers

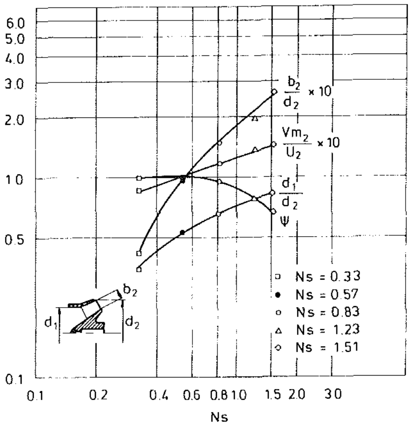

Fig. 3 Design characteristics of the five tested impellers: Ψ and Vm_2/U_2 extrapolated to zero tip clearance

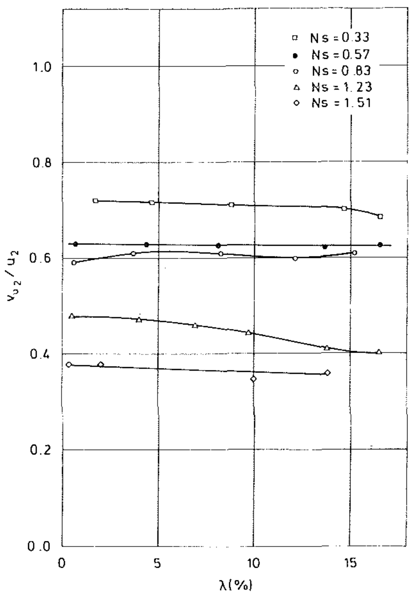

Fig. 4 Effect of tip clearance on the tangential component of the velocity

acquisition/control unit, which can scan up to 30 channels. The data acquisition/control unit is commanded by a desktop computer.

Pressure measurements are carried out using pressure transducers with a ±0.2 percent full-scale accuracy. The transducers are calibrated before testing, using a weight-type reference gauge. Flowrate is measured using a calibrated electromagnetic flowmeter, which was controlled by way of calibration against a calibration tank with precision 0.1 percent. Torque was measured using a calibrated torque meter, which has a full-scale accuracy ±1 percent. Angular speed was measured by an electronic counter; the pulses are proportional to the pump speed. All measurement devices were checked and controlled before and after each test. Although the uncertainties were within a fairly good tolerance, that the relative errors in impeller comparison measurement could be less is a further encouragement.

The experimental setup used for the investigation and the measurement technique involved are schematically shown in Fig. 7. Assuming independent parameter error generation, the uncertainties in measurements, nondimensionalized and normalized, are summarized as follows:

Nondimensionalizing error (percent)				
Quantity:	Ψ		ϕ	μ
Uncertainty:	±0.4		±0.2	±1.4
Normalizing error (percent)				
Quantity:	Ψ/Ψ_0	ϕ/ϕ_0	μ/μ_0	η/η_0
Uncertainty:	±0.8	±0.42	±2.7	±2.9

Discussion of Results

The essential geometric information for the tested impellers is summarized in Fig. 3, where the various geometric ratios are given as a function of the optimum specific speed *Ns* of each type. Low specific speed impellers are characterized by high head, requirement of ample usage of centrifugal effect, higher ratio of outer to inner impeller radius, and small flow passages that do not cause excessive flow velocities because the flowrate is small. As a result of this the loss of head in low specific speed impellers is more, leading to lower maximum efficiency. The maximum efficiency also tends to drop at higher specific speeds due to lack of proper guidance of the fluid by the impeller blades which in turn is due to shorter blade length and smaller blade lap.

All characteristic parameters have been nondimensionalized, and since the local pressure gradient is largest near the outlet tip of the impeller, the clearance ratio δ/b at outlet tip was taken as the representative value.

Effects of the tip clearance on the pump performance characteristics at each maximum efficiency point are shown in Fig. 5 for a constant speed and a changing clearance ratio. Each performance parameter is presented as a percentage ratio of its corresponding value at zero clearance, which was found by extrapolation from Fig. 6.

Downloaded 01 Jun 2010 to 171.66.16.57. Redistribution subject to ASME license or copyright; see http://www.asme.org/terms/Terms_Use.cfm

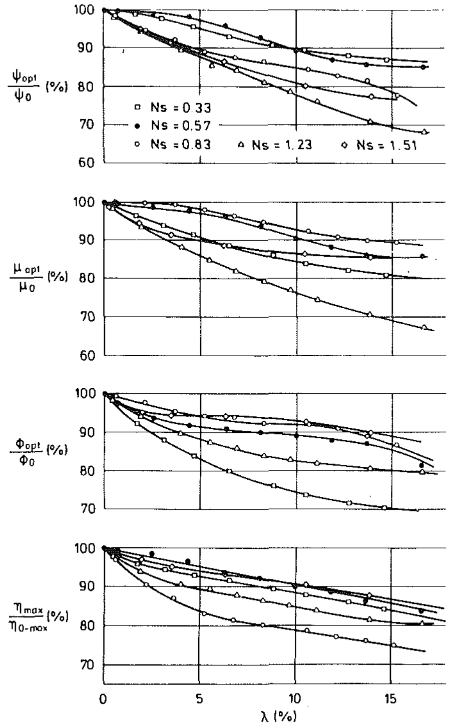

Fig. 5 Comparison of the effects of tip clearance on the performance of the five test pumps: *Ns* = 0.33, 0.57, 0.83, 12.3, and 1.51

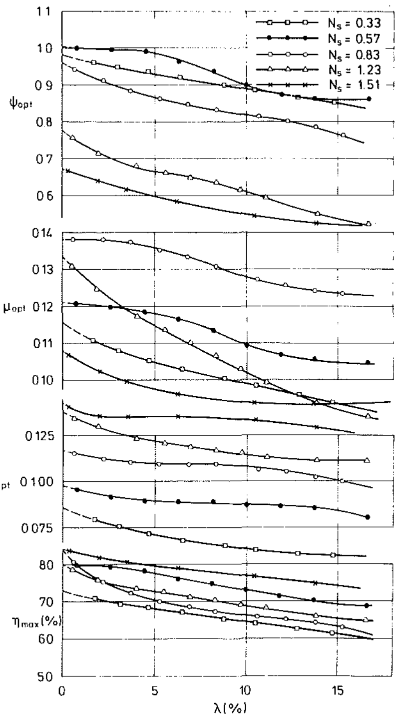

Fig. 6 The effects of running clearance on the optimal performance characteristics of the five test pumps

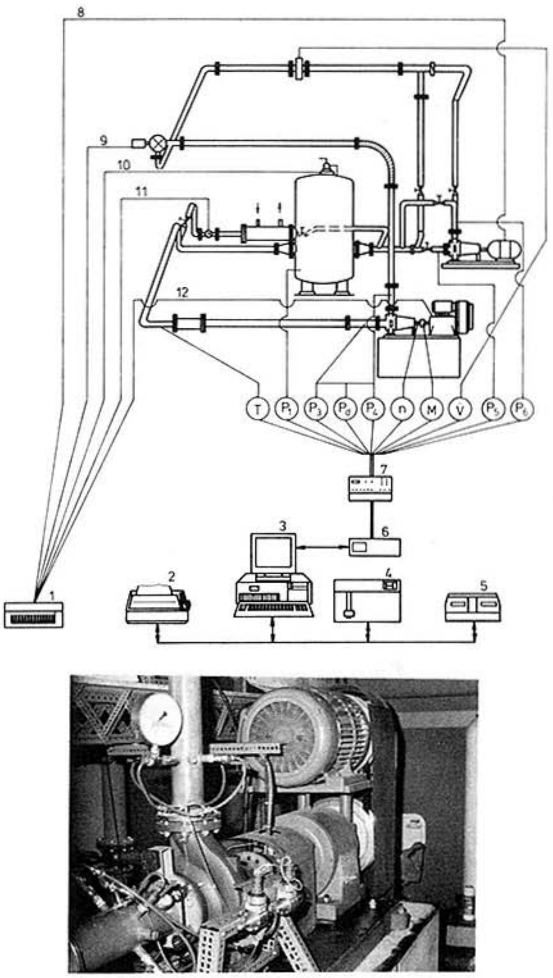

1. Control desk
2. Printer
3. Desk computer
4. Plotter
5. Floppy set
6. Data control/Acquisition unit
7. Power supply and amplifier
8. Booster pump control
9. Main throttle valve
10. NPSH control
11. Colling-system control
12. Speed control

T	Temperature
P_1	Tank pressure
P_3	Inlet pressure
P_d	Pressure difference
P_4	Outlet Pressure
n	Rotational speed
M	Torque
$\dot{V}$	Flowrate
P_5	Inlet pressure
P_6	Outlet pressure

Fig. 7 Experimental setup and measurement technique used

The tangential component of the absolute velocity at the impeller exit was estimated from the measured shaft torque and flowrate. The effect of tip clearance on the tangential component of the absolute velocity at impeller exit for optimal flowrate is shown in Fig. 4. With the exception of pump impeller of *Ns* = 1.23, the tangential component of the absolute velocity is seen to be hardly influenced by the tip clearance variation.

Figure 5 shows overall efficiency decrement as the tip clearance increases showing a tendency similar to those reported in other studies. Leakage loss increases with increase in tip clearance due to increase in flow passage. As a result of this the developed head falls for a constant flow due to: (1) increase in drag as a consequence of the clearance flow; (2) reduction in blade loading; (3) reduction of effective blade size. The decrease in the developed head is directly followed by the decrease in input power. But as seen in all cases in Fig. 5 the efficiency also decreases considerably with increase in tip

Downloaded 01 Jun 2010 to 171.66.16.57. Redistribution subject to ASME license or copyright; see http://www.asme.org/terms/Terms_Use.cfm

clearance. This means that the rate of decrease of developed head is much higher than that of input power. It is interesting to note that in the first 3.5 percent of clearance ratio each impeller had a different rate of change of efficiency with clearance ratio, but tends to be constant for all impellers at higher clearance ratios.

Conclusions

Although the efficiency variation with tip clearance ratio showed a patterned tendency, with the middle specific speed pump $Ns = 0.83$ being the most sensitive to clearance losses and the higher and lower specific speed pumps being less sensitive, the investigation shows that simple relationships between developed head variation with clearance ratio and input power variation with clearance ratio are difficult to imagine. A clearer dependency of clearance effects on specific speed, which might have been hoped, is not observed here.

The problem of tip losses could most likely be better understood from a detailed impeller geometry, impeller relative velocity distribution measurements, and secondary flow analysis.

Acknowledgments

The authors wish to thank KSB-Stiftung and Stiftung Volkswagenwerk for their encouragement and financial support. In addition thanks are due to Mr. J. Köster, who prepared the test setup.

References

1 Rains, D. A., *Tip Clearance Flows in Axial Compressors and Pumps*, California Institute of Technology, Hydrodynamic and Mechanical Engineering Laboratories, Pasadena, CA, 1954.

2 Lakshminarayana, B., "Methods of Predicting the Tip Clearance Effects in Axial Flow Machinery," ASME *Journal of Basic Engineering*, Vol. 92, 1970.

3 Wood, G. M., Welna, H., and Lamers, R. P., "Tip Clearance Effects in Centrifugal Pumps," *Trans. ASME*, Vol. 87, 1965.

4 Acosta, A. J., "Potential Flow Through Radial Flow Turbomachine Rotors," Hydraulic Laboratory, CIT Report E. 19.4.

5 Ishida, M., and Senoo, Y., "On the Pressure Loss Due to the Tip Clearance of Centrifugal Blowers," ASME *Journal of Engineering for Power*, Vol. 103, 1981.

6 Hoshide, R. K., and Nielson, C. B., "Study of Blade Clearance Effects on Centrifugal Pumps," NASA CR-120815, Nov. 1972.

7 Senoo, Y., Yamaguchi, M., and Nishi, M., "A Photographic Study of the Three-Dimensional Flow in a Radial Compressor," ASME *Journal of Engineering for Power*, Vol. 90, 1968.

8 Howard, J. H. G., and Kittmer, C. W., "Measured Passage Velocities in a Radial Impeller With Shrouded and Unshrouded Configuration," ASME *Journal of Engineering for Power*, Vol. 97, 1975.

9 Karassik, I. J., Krutzsch, W. C., Fraser, W. H., and Messina, J. P., *Pump Handbook*, 2nd ed., McGraw-Hill, New York.

10 Bunges, J. H., and Op De Woerd, J. G. H., "Centrifugal Pump Performance Prediction by Slip and Loss Analysis," *I. Mech. Engrs.*, C 178/82.

11 Mizuki, S., Ariga, I., and Watanabe, I., "Investigations Concerning the Blade Loading of Centrifugal Impellers," ASME Paper No. 74-GT-143, Dec. 1974.

12 Senoo, Y., and Ishida, M., "Pressure Loss Due to the Tip Clearance of Impeller Blades in Centrifugal and Axial Blowers," ASME *Journal of Engineering for Gas Turbines and Power*, Vol. 108, 1986.

13 Pfleiderer, C., *Die Kreiselpumpen, 5. Auflage*, Vol. 99, Springer-Verlag, Berlin, 1961.

14 Murakami, M., and Minemura, K., "Effects of Running Clearance of Semi-Open Impeller Pumps Under Air Admitting Conditions," *Bulletin of the JSME*, Vol. 19, No. 136, 1976.

15 Hesselgreaves, J. E., "A Correlation of Tip Clearance/Efficiency Measurements on Mixed-Flow and Axial-Flow Turbomachines," NEL Report No. 423, July 1969.

Downloaded 01 Jun 2010 to 171.66.16.57. Redistribution subject to ASME license or copyright; see http://www.asme.org/terms/Terms_Use.cfm

Effect of Geometry on the Performance of Radial Vaneless Diffusers

Zhu Yingkang[1]
Visiting Scholar.

S. A. Sjolander
Associate Professor
Assoc. Mem. ASME

Department of Mechanical
and Aeronautical Engineering,
Carleton University,
Ottawa, Canada K1S 5B6

The paper presents measurements of the steady aerodynamic characteristics of a series of five radial vaneless diffusers with walls varying from mildly divergent to strongly convergent. The static pressure recovery was determined and the flow was traversed at the inlet and the outlet of the diffuser for a broad range of flow rates in each case. It was found that wall convergence results in a negative (stabilizing) slope in the pressure rise curve for the diffuser. Furthermore, at high flow rates convergence was found to reduce the pressure recovery far less than one would expect and at intermediate flow rates convergence actually improved the pressure recovery. The better-than-expected performance is thought to be closely related to the observed improvement in the flow uniformity at the diffuser outlet when convergent walls are used.

Introduction

Vaneless radial diffusers continue to be used widely with industrial centrifugal compressors and many experimental and analytical studies have investigated their steady and unsteady aerodynamic behavior.

The main geometric parameters affecting the diffuser performance are: (*a*) the ratio of inlet height to radius, b_3/R_3, (*b*) the ratio of outlet radius to inlet radius, R_4/R_3, and (*c*) the diffuser wall taper angle. The first of these appears to have received the greatest attention. Simple one-dimensional, viscous calculations (e.g., Van den Braembussche, 1985) show that for a given radius ratio the losses are lower and the static pressure recovery is higher for larger values of b_3/R_3, because of the smaller wetted area relative to the flow area. However, for a given mass flow rate, larger values of b_3/R_3 also imply smaller values of flow angle α_3, which brings the diffuser closer to the critical angle for flow reversal and rotating stall (Jansen, 1964a). In fact, calculations by Senoo and Kinoshita (1977) have shown that the critical flow angle itself is lower for narrower diffusers and this seems to be confirmed by experiment (e.g., Van den Braembussche et al., 1980; Kinoshita and Senoo, 1985). The radius ratio has also received some attention. For $b_3/R_3=0.116$, Abdel-Hamid (1983) found that the critical flow angle increased with increasing radius ratio. On the other hand, Kinoshita and Senoo (1985) found that the critical angle was insensitive to the ratio for their very slender diffusers ($b_3/R_3=0.0257$ and 0.0153).

All of the studies mentioned considered only parallel-walled diffusers. The various studies of the aerodynamic factors in diffuser performance, such as circumferential flow nonuniformity (e.g, Johnson and Dean, 1966, and Senoo and Ishida, 1975) and axial flow nonuniformity (e.g., Jansen, 1964b and Senoo et al., 1977), likewise have concentrated on constant-height diffusers.

Recently, Ludtke (1983) reported the results of a series of tests for a centrifugal compressor stage using diffusers with four different wall shapes: parallel, parallel following a rapid contraction, constant area (mildly tapered), and strongly tapered. Significant improvements in the compressor surge margin were obtained with the tapered diffusers, although there was also some reduction in efficiency. On balance, the constant-area diffuser appeared best since it gave a substantial improvement in surge margin with minimum efficiency penalty. Unfortunately, Ludtke's measurements of only overall stage performance do not reveal how the convergent diffusers improved the surge margin nor what aerodynamic penalties, such as reduced static pressure recovery, were incurred by using taper. Eckardt (1975, 1976) also used a constant-area diffuser in his detailed study of the impeller flow field, but the flow behavior in the diffuser was not reported. Eckardt (1980) did present total pressure profiles measured at the inlet and outlet of the diffuser for three different flow rates; these profiles show a noticeable improvement in the total pressure uniformity between inlet and outlet. The only experimental study of which we are aware that focuses specifically on the flow in diffusers with contoured walls is the work of Sherstyuk and Sokolov (1966) and Sherstyuk and Kosmin (1969). The authors examined the effects of a rapid contraction at the diffuser inlet as well as convergent and divergent walls. The results are presented as curves of static pressure recovery effectiveness (defined as $\Delta P_{s_{\text{actual}}}/\Delta P_{s_{\text{ideal}}}$) and the highest effectiveness was reportedly obtained with 2 deg of convergence. Since only wall static pressure measurements were made it is

---

[1] Permanent address: Department of Power Machinery Engineering, Xi'an Jiaotong University, Xi'an, Shaanxi Province, The People's Republic of China.

Contributed by the Gas Turbine Division of The American Society of Mechanical Engineers and presented at the 32nd International Gas Turbine Conference and Exhibit, Anaheim, California, May 31–June 4, 1987. Manuscript received at ASME Headquarters February 17, 1987. Paper No. 87-GT-169.

Copyright © 1987 by ASME

Downloaded 01 Jun 2010 to 171.66.16.57. Redistribution subject to ASME license or copyright; see http://www.asme.org/terms/Terms_Use.cfm

Table 1 Geometry of rotors

Impeller	A	B	C	D	E
No. of Blades	24	12	12	12	12
β_1, deg	55	55	55	55	30
β_2, deg	30	30	60	90	60

$D_1 = 64$ mm $D_2 = 223$ mm
Blade thickness = 1.6 mm

again not clear precisely why the convergent diffuser performed better.

The present paper reports the results of a series of measurements made in five radial vaneless diffusers with constant inlet height and radius ratio but with varying degrees of wall taper from mildly divergent to strongly convergent. The objectives were fairly modest, namely to examine the effect of wall taper on the diffuser steady aerodynamic characteristics, in the hopes of understanding why the stable operating range of the machine is broadened by diffuser convergence and of determining any tradeoffs, such as reduced pressure recovery, which must be accepted. To this end only mean quantities were measured.

Experimental Facility and Procedure

Experimental Facility. The experimental facility used in the present investigation is shown schematically in Fig. 1. The same apparatus was used by Abdel-Hamid (1983, 1987) in his studies of vaneless diffuser instability. Five different rotors were used, to provide a variety of flow distributions at the inlet to the diffuser. All rotors were shrouded; other details of their geometries are summarized in Table 1. The tests were conducted at a constant rotor speed of 5000±50 rpm. With a rotor diameter of 223 mm the corresponding blade tip speed was 58.4 m/s so that all measurements were made at essentially incompressible conditions. Calculations show that the blade inlet angle for rotors A to D is well-matched to the flow incidence for 5000 rpm and the observed range of flow rates; rotor E therefore had very high positive incidence at all running conditions. The flow rate was varied with the throttle valve in the intake and by clamping screens of different porosities over the diffuser exhaust.

The geometries of the five diffusers tested are summarized in Fig. 2. Measurements were made at two stations located at $1.045R_2$ and $1.655R_2$ where R_2 is the rotor tip radius. The diffuser performance was therefore determined over a radius ratio R_4/R_3 of 1.584. The outlet measurement station is 10 mm upstream of the diffuser discharge. The passage height was varied with interchangeable hub walls having slopes from

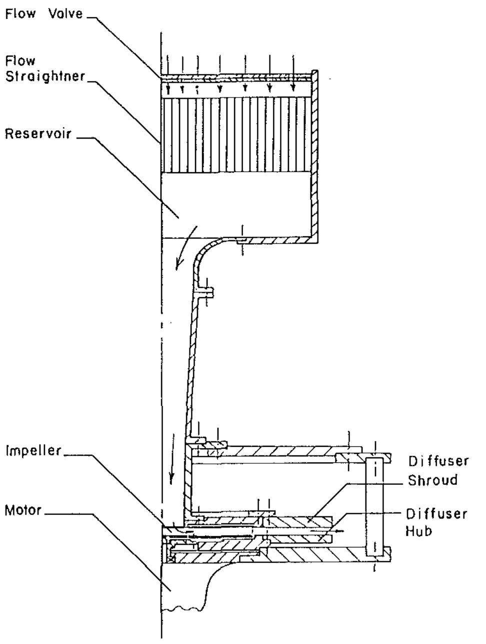

Fig. 1 Schematic drawing of experimental facility

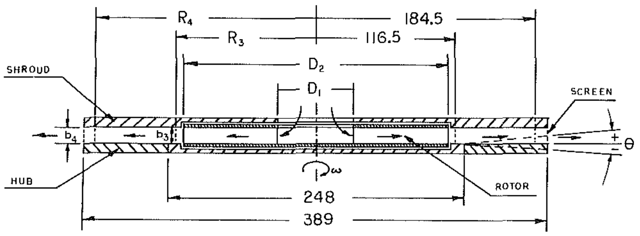

Fig. 2 Geometry of diffusers; all dimensions in mm

	Diffuser 1	2	3	4	5
θ, deg	−3	0	3	5.5	8.2
θ', deg	2.7	0	2.7	4.9	7.3
b_3, mm	12.9	12.9	12.9	12.9	12.9
b_4, mm	16.1	12.9	9.7	7.1	4.2
A_4/A_3	1.98	1.58	1.19	0.87	0.52

$R_4/R_3 = 1.58$ $b_3/R_3 = 0.111$

Nomenclature

A = radial area
b = diffuser height
B = b/R_3 = ratio of height to radius
B_f = radial velocity distortion parameter (equation (5))
C_p = static pressure recovery coefficient (equation (4))
$\dot{m}$ = mass flow rate
P_0 = total pressure
P_s = static pressure
r = radial coordinate
R = radius
R' = r/R_3 = radius ratio
v = resultant velocity
v_r = radial component of velocity
v_t = tangential component of velocity
z = axial coordinate
α = flow angle, measured from the tangential direction
β = rotor blade angle, measured from the tangential direction
θ = nominal wall convergence angle
θ' = effective wall convergence angle (for linear variation in height from R_3 to R_4)
ρ = density
Ω = $(P_{0_3} - P_{0_4})/\frac{1}{2}\rho v_3^2$ = total pressure loss coefficient

Subscripts

1, 2, 3, 4 = rotor inlet, rotor tip, diffuser inlet, diffuser outlet

Superscript

$\bar{\ }$ = mean value

Downloaded 01 Jun 2010 to 171.66.16.57. Redistribution subject to ASME license or copyright; see http://www.asme.org/terms/Terms_Use.cfm

−3 deg (divergent) to 8.2 deg (convergent). Because of the mechanical design of the original facility, the wall slope began 7.5 mm downstream of the inlet measurement station. As a result, the effective taper angles, corresponding to linear variations in height between R_3 and R_4, were −2.7 to 7.3 deg. The inlet height, b_3, was constant at $0.116R_2$ or $0.111R_3$. The ratio of the areas at the outlet and inlet measurement stations A_4/A_3 varied from 1.98 to 0.52.

Experimental Procedure. The diffuser flow was traversed at the two measurement stations using a standard United Sensor cobra probe. The probe was used in the nulling mode; that is, the probe was rotated until the side-hole pressures were equal and the center-hole pressure was taken as the total pressure. The inferred flow direction is estimated to be accurate to ±0.5 deg. Measurements were typically made at five locations across the axial height of the diffuser; the positioning accuracy is estimated at ±0.25 mm. The objective was to provide sufficient data to obtain reasonable mean values of flow quantities such as mass flow rate and total pressure. As shown in Figs. 7 to 9, the flow quantities varied fairly gradually in the bulk of the flow and the measurements were sufficient to characterize the overall profiles, although they of course do not give details about the boundary layers. For integration purposes, the two additional points at the walls provided by the no-slip condition were included. Based on the observed repeatability of the measurements, the values of total pressure are estimated to be accurate to better than ±5 percent of the mean dynamic pressure at the station in question. The wall static pressures were measured using 0.5-mm-dia taps located at the same radius as the mouth of the cobra probes but displaced 90 deg circumferentially. The static pressure measurements are estimated to be accurate to ±2 percent of the inlet dynamic pressure. All pressures were measured with manometers or pressure transducers using pneumatic circuits which damped out most of the pressure fluctuations because of their fairly long tubes and substantial volumes.

The resultant velocity distributions in the diffuser were calculated from the probe total pressures assuming that the static pressures measured on the shroud wall apply across the flow. Radial and tangential components were then calculated using the flow angles obtained from the probe. The velocity components were averaged separately. The rationale for this is that in simple design calculations the inlet conditions to the diffuser will be known in component form, the average radial component of velocity being obtained from the mass flow rate and the average tangential component being known from angular momentum considerations. Thus our average values were calculated as follows:

$$\bar{v}_r = \frac{\int_0^b \rho 2\pi r v_r dz}{\rho 2\pi r b} \tag{1}$$

$$\bar{v}_t = \frac{\int_0^b \rho 2\pi r^2 v_t v_r dz}{r\dot{m}} \tag{2}$$

The average flow angle at the diffuser inlet α_3 is then arctan $(\bar{v}_r/\bar{v}_t)$. The average total pressure was obtained by mass averaging in the usual way

$$\bar{P}_0 = \frac{\int_0^b P_0 \rho 2\pi r v_r dz}{\dot{m}} \tag{3}$$

and the average dynamic pressure was then calculated by subtracting the measured wall static pressure.

The radial components of velocity at the two diffuser stations were integrated to obtain the mass flows. These were compared with the mass flow calculated from two static pressures measured on the intake contraction. This latter mass flow should be very reliable. At higher flow rates, the three mass flows agreed very well, being typically within 5 percent of each other. However, at very low flow rates the mass flow inferred from the diffuser inlet measurements was consistently higher than the other two. This is probably mainly due to the circumferential flow nonuniformity, which will be more pronounced at low flow rates. As noted above, the inlet measurement station is at $1.045R_2$, at which point the mixing-out of the blade-to-blade flow nonuniformity will not yet be complete. Evidently, the mean total pressure which we obtain with our slow response instrumentation is higher than the actual mean value. An additional source of error is the uncertainty in the probe angles which, for small values of α_3, can lead to significant errors in the mass flow rates. We examined the effect of scaling the velocity distribution at the diffuser inlet to give the same mass flow rate as the intake. However, if we added the scaled dynamic pressure distribution to the measured wall static pressure, the new average value of the total pressure was in some cases less than that obtained at the diffuser outlet. This suggests that the nonuniform flow also affected the wall static pressure measurement, making the measured average lower than the actual mean value. Since we have no basis for applying corrections to both the probe total pressure and the wall static pressure measurements, we have chosen to present the data as measured. It is worth noting that in the pressure coefficient

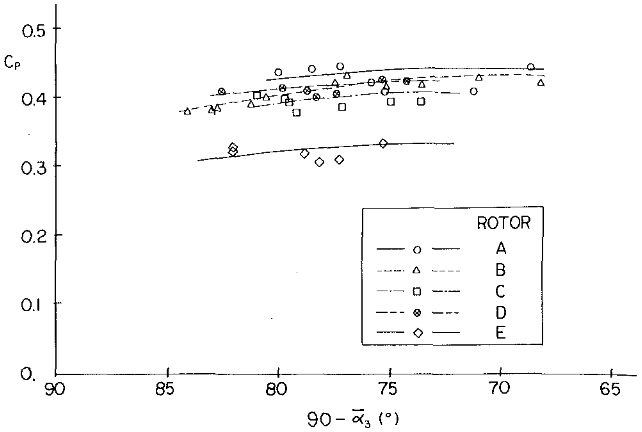

Fig. 3 Effect of rotor geometry on static pressure recovery (parallel-walled diffuser)

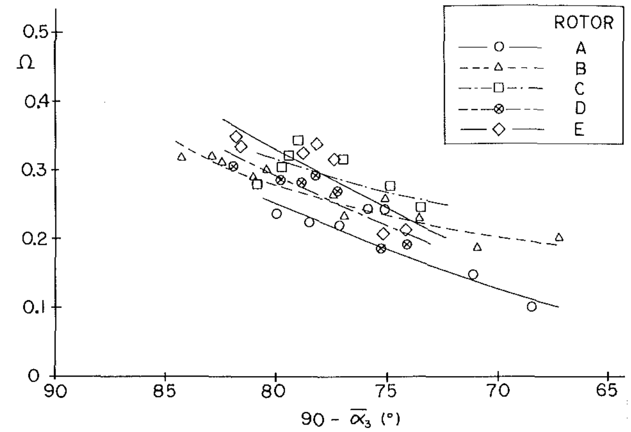

Fig. 4 Effect of rotor geometry on total pressure losses (parallel-walled diffuser)

Downloaded 01 Jun 2010 to 171.66.16.57. Redistribution subject to ASME license or copyright; see http://www.asme.org/terms/Terms_Use.cfm

$$C_p = \frac{P_{s4} - P_{s3}}{\frac{1}{2}\rho v_3^2} \tag{4}$$

the effects of the underestimated P_{s3} and overestimated $\frac{1}{2}\rho v_3^2$ are to some degree offsetting. Nevertheless, the values of C_p presented for low values of α_3 should be treated with some caution. The measured data are available (Zhu and Sjolander, 1986) to anyone wishing to analyze it in alternative ways.

From our measurements we have concluded that flow uniformity is an important factor in the performance of the tapered diffusers. Senoo (1984) (as discussed by Van den Braembussche, 1985) has investigated the effect of radial flow distortion in constant height diffusers and found that poor uniformity reduces the pressure recovery and increases the losses. The calculations of Senoo and Kinoshita (1977) likewise suggested that radial flow distortion had a significant influence on the critical angle for reverse flow. Senoo (1984) defined a radial velocity distortion parameter B_f, where

$$B_f = \frac{\int_0^b \rho v_r^2 dz \Big/ \int_0^b \rho v_r dz}{\int_0^b \rho v_r dz \Big/ \int_0^b \rho dz} \tag{5}$$

and we have adopted this as a measure of flow nonuniformity in our work.

Experimental Results

Effect of Rotor Geometry. Measurements were first made with the parallel-walled diffuser using the five available rotors. The objectives were, firstly, to establish the repeatability and scatter of the pressure coefficient data, and secondly, to determine the sensitivity of the diffuser performance to the details of the rotor design.

Figure 3 shows the static pressure recovery coefficients and Fig. 4 the total pressure loss coefficients plotted against the diffuser inlet flow angle, the usual parameter used to represent flow rate. We estimate our pressure coefficients to be accurate to ±0.015; this does not include the systematic errors introduced by circumferential flow nonuniformity, which we are unable to quantify. As expected, the pressure recovery deteriorates and the losses rise at low flow rates.

It is evident from Figs. 3 and 4 that the diffuser performance is quite similar for rotors A to D. For rotor E the static pressure recovery was noticeably lower and the losses were slightly higher. As noted earlier, rotor E has high positive incidence at all flow rates when run at 5000 rpm and should therefore produce a highly distorted flow. This was partly confirmed by the values of Senoo's distortion parameter B_f, which were higher for this rotor than for others. The observed hub-to-shroud distortion and the undoubted circumferential distortion probably account for the reduced static pressure recovery. However, from the results for rotors A to D we conclude that, provided the rotor is well-designed and well-matched, the diffuser performance is not very sensitive to such details of the rotor design as the number of blades or the outlet sweep angle. The performance of the tapered diffusers was therefore measured for one rotor only (rotor B for diffusers 1 to 4 and rotor A for diffuser 5), but we believe that the results have broad validity.

Effects of Diffuser Wall Taper. A simple analysis outlined in the Appendix shows that for a constant-height diffuser with no losses the pressure rise curve, C_p versus α_3, has zero slope. With a loss variation such as we observed for our range of α_3, the slope becomes everywhere positive. On the other hand, for convergent diffusers the pressure rise curve has a negative slope. A first-order criterion for stability of a compressor stage is that the overall pressure rise curve should have a negative slope (e.g., Greitzer, 1981). Since the overall curve is the resultant of the pressure rise curves for the rotor and the diffuser, the negatively sloped curve predicted for the convergent diffusers is clearly stabilizing to the machine as a whole. This would seem to be the simplest explanation for the improved surge margin observed by Ludtke (1983) when he used convergent diffusers. The simple analysis also indicates that convergence substantially reduces the pressure recovery at higher flow rates. The reason for this is clear: As α_3 increases, reduction in the radial component of velocity becomes increasingly important to the pressure recovery. Thus the reduced deceleration (or even acceleration, with sufficient convergence) shows up as a significant decrease in the pressure rise. A prime objective of the present study was to determine the pressure recovery penalty incurred in real diffusers by using wall convergence.

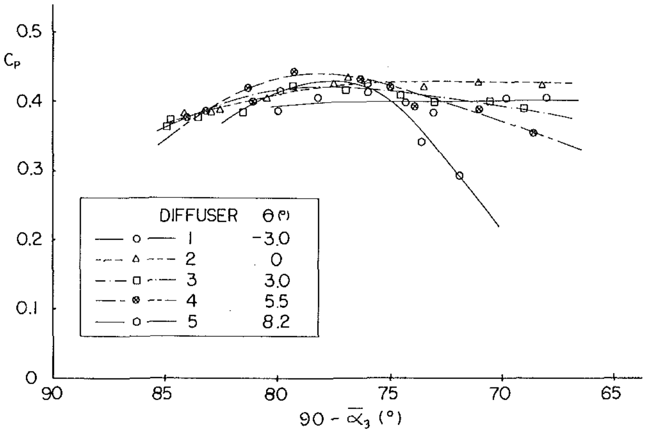

Fig. 5 Effect of diffuser geometry on static pressure recovery

Figure 5 shows the static pressure recovery curves obtained for the five diffusers. As noted earlier, measurement errors introduced by circumferential flow nonuniformity cast some doubt on the absolute values of C_p. However, the relative magnitudes should be correct since most of the measurements were made with a single rotor which, at a given flow rate, would give essentially identical inlet conditions to all the diffusers. The behavior of the curves is generally consistent with the simple analysis. For sufficient convergence (about 3 deg in our case) the effects of the taper more than offset the effects of the losses to produce a pressure rise curve with a stabilizing negative slope. Furthermore, an interesting and surprising result was the fact that the reduction in pressure recovery due to wall convergence was not nearly as large as the simple analysis would suggest. In fact, in the middle of the flow range, the highest pressure recovery was obtained with the 5.5 deg diffuser.

Part of the explanation for the unexpected behavior of the pressure recovery probably lies in the differing loss characteristics of the diffusers. Figure 6 shows the total pressure loss coefficients plotted against the inlet flow angle, as before. At higher flow rates, convergence appears to reduce the losses very substantially; for example, by a factor of about two as the taper increases from 0 to 5.5 deg. The reasons for this are not completely clear. It may be related to changes in the path length as the fluid particles pass through the diffuser. By increasing the radial component of velocity, convergence shortens the path length and therefore reduces the effective wetted area. One-dimensional calculations show that the changes in the average path length are not very large for our range of taper angles. However, the radial velocity distortion present in the real flows makes these calculations a little misleading. The path length for the fluid close to the walls,

Downloaded 01 Jun 2010 to 171.66.16.57. Redistribution subject to ASME license or copyright; see http://www.asme.org/terms/Terms_Use.cfm

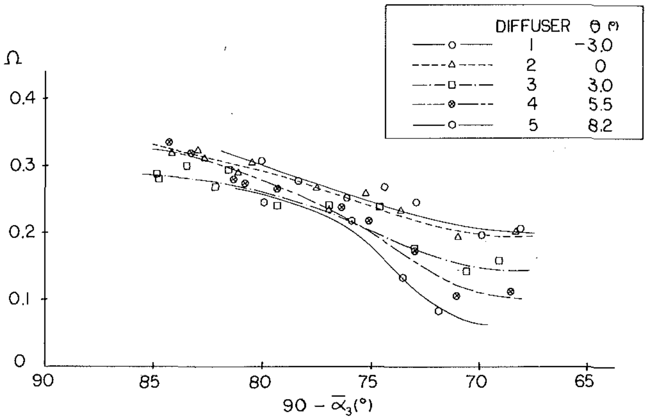

Fig. 6 Effect of diffuser geometry on total pressure losses

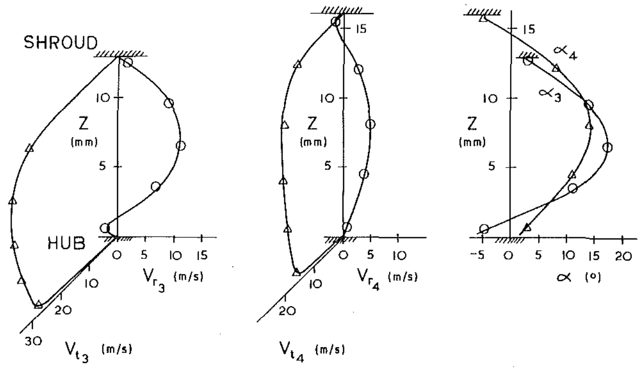

Fig. 7 Velocity and flow angle distributions ($\theta = -3$ deg, $\alpha_3 = 10$ deg)

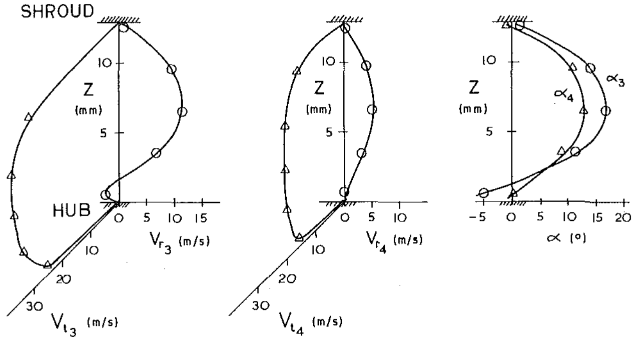

Fig. 8 Velocity and flow angle distributions ($\theta = 0$ deg, $\alpha_3 = 9.5$ deg)

which is the important length for skin friction losses, can be considerably larger than the mean path length. The significance of flow nonuniformities will be considered further, but in any event the observed reduction in losses must partly account for the retained pressure recovery in the convergent diffusers.

We believe that the relationship between wall taper and flow uniformity plays a part in the static pressure recovery behavior and probably also the loss behavior of the convergent diffusers. Figures 7 to 9 show the velocity and flow angle distributions at the inlet and outlet of three of the diffusers for a mean inlet flow angle of about 10 deg. Subjectively, there is an improvement in the uniformity of the radial velocity distribution as the diffuser becomes convergent. To quantify this effect, we calculated Senoo's radial velocity uniformity parameter B_f at inlet and outlet for all of our cases; these results are shown in Fig. 10. For the divergent, constant-height, and mildly convergent diffusers the nonuniformity is seen to increase between inlet and outlet. At higher flow rates,

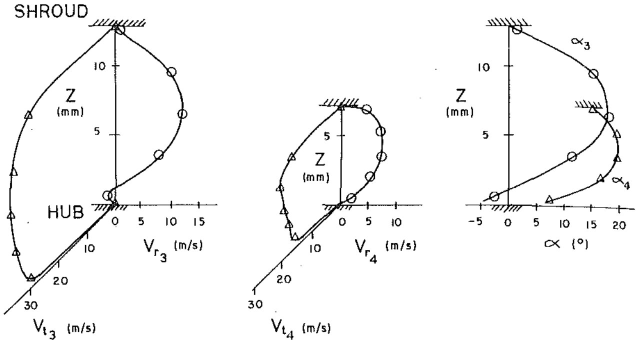

Fig. 9 Velocity and flow angle distributions ($\theta = 5.5$ deg, $\alpha_3 = 10.7$ deg)

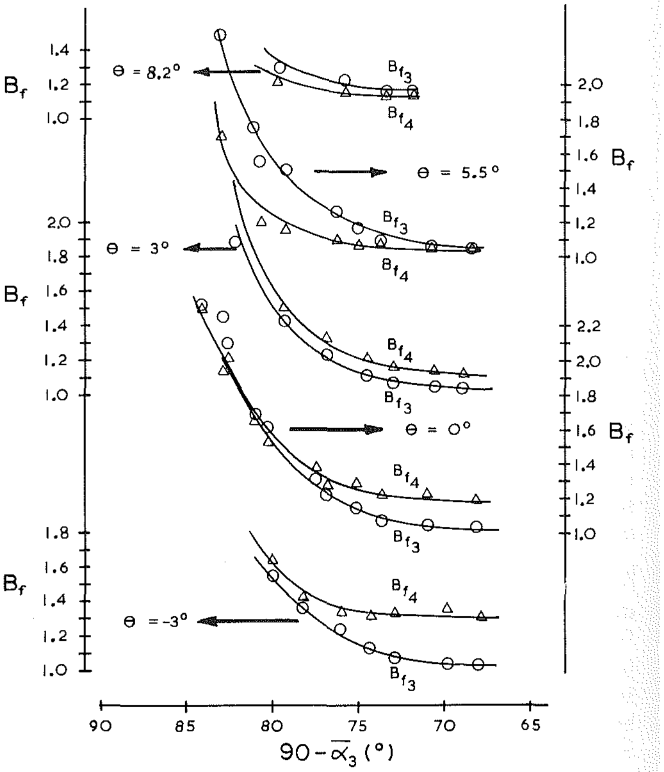

Fig. 10 Relationship between wall taper angle and radial velocity uniformity

this would be attributed to boundary layer growth on the walls of the diffuser; at lower flow rates the regions of flow reversal, seen in Figs. 7 and 8, also contribute to the nonuniformity. Both the boundary layer displacement effect and the flow reversal produce blockage which reduces the effective flow area, raises the outlet dynamic pressure, and therefore reduces the outlet static pressure. By contrast, for 5.5 and 8.2 deg of convergence Fig. 10 shows that the flow uniformity actually improves between inlet and outlet, as suggested by Fig. 9. As a result, the flow blockage decreases in the radial direction and this will to some degree offset the height reduction produced by the taper. This would appear to be an additional, and probably important, reason for the better-than-expected pressure recovery in the convergent diffusers.

The improvement in flow uniformity in the convergent diffusers may also account in part for their lower losses. As shown by Fig. 9, the improved uniformity increases the flow angle close to the walls and therefore shortens the path length of the fluid that is in immediate contact with the walls. This should to some extent reduce the skin friction losses. In addition, the better uniformity reduces the velocity gradients away

Downloaded 01 Jun 2010 to 171.66.16.57. Redistribution subject to ASME license or copyright; see http://www.asme.org/terms/Terms_Use.cfm

from the walls and will therefore reduce the viscous dissipation as well as the turbulence production in the interior of the flow.

Finally, wall convergence is seen to reduce or eliminate the flow reversal, which is associated with rotating stall, toward the outlet of the diffuser. For our ratio of inlet height to radius, this may be of limited benefit since the flow reversal appeared first at the inlet. However, there is some evidence (e.g., Senoo and Kinoshita, 1977) that for wider diffusers, flow reversal appears first toward the outlet. For such cases, a convergent diffuser could be doubly beneficial in terms of overall machine stability, through the negatively sloped pressure rise curve as well as by delaying the onset of flow reversal near the outlet.

Conclusions

Our measurements have shown that a small amount of wall convergence can have several beneficial effects on the steady aerodynamic performance of radial vaneless diffusers. In the first place, sufficient convergence results in a stabilizing negative slope to the pressure recovery curve; this helps to explain the improved surge margin observed by Ludtke (1983) for centrifugal compressor stages with convergent diffusers. An additional and surprising result was the fact that wall convergence resulted in far less reduction in static pressure recovery than one would expect. In fact, at intermediate flow rates the best pressure recovery was obtained with the 5.5 deg convergent diffuser. The convergent diffusers also had the useful characteristic of suppressing flow reversal toward the outlet of the diffuser. This could delay the appearance of rotating stall in wide diffusers where the stall appears to be triggered by the onset of flow reversal near the outlet.

There appear to be several interrelated reasons for the better-than-expected performance of the convergent diffusers. We believe that an important factor is the observed improvement in the uniformity of the radial velocity distribution. At the largest convergence angles, the outlet flow was actually more uniform than the inlet flow. The corresponding reduction in aerodynamic blockage to some extent offsets the reduction in physical area and helps to explain the retained pressure recovery. The better uniformity also had the beneficial effect of shortening the path length for the fluid in the streamtubes closest to the walls. This should reduce the skin friction losses and explains, at least in part, the substantially lower total pressure losses which we measured in the convergent diffusers at our higher flow rates.

Based on our results we would recommend that a small amount of wall convergence be used routinely when designing radial vaneless diffusers. However, our results are too limited to define an optimum amount of convergence. For our family of diffusers, a nominal convergence angle between 3 and 5.5 deg appears best, giving the highest pressure recovery in the middle flow rates, and a negative slope for the pressure rise curve. It is interesting to note that our "best" diffuser would have roughly constant flow area, as was also the case for Ludtke's best diffuser. This may be a useful rule of thumb for choosing the convergence angle for different values of inlet height to radius.

Acknowledgments

Financial support for this study provided by the Natural Sciences and Engineering Research Council of Canada under Grant No. A1671 is gratefully acknowledged.

References

Abdel-Hamid, A. N., 1983, "Effects of Vaneless Diffuser Geometry on Flow Instability in Centrifugal Compression Systems," *Canadian Aeronautics and Space Journal*, Vol. 29, No. 3, pp. 259-266.

Abdel-Hamid, A. N., 1987, "A New Technique for Stabilizing the Flow and Improving the Performance of Vaneless Radial Diffusers," ASME JOURNAL OF TURBOMACHINERY, Vol. 109, pp. 36-40.

Eckardt, D., 1975, "Instantaneous Measurements in the Jet-Wake Discharge Flow of a Centrifugal Compressor Impeller," ASME *Journal of Engineering for Power*, Vol. 97, pp. 337-345.

Eckardt, D., 1976, "Detailed Flow Investigation Within a High-Speed Centrifugal Compressor Impeller," ASME *Journal of Fluids Engineering*, Vol. 98, pp. 390-399.

Eckardt, D., 1980, "Flow Field Analysis of Radial and Backswept Centrifugal Compressor Impellers. Part I: Flow Measurements Using a Laser Velocimeter," in: *Performance Prediction of Centrifugal Pumps and Compressors*, S. Gopalakrishnan et al., ed., ASME, Mar., pp. 77-86.

Greitzer, E. M., 1981, "The Stability of Pumping Systems," ASME *Journal of Fluids Engineering*, Vol. 103, No. 2, pp. 193-242.

Jansen, W., 1964a, "Rotating Stall in Radial Vaneless Diffusers," ASME *Journal of Basic Engineering*, Vol. 86, pp. 750-758.

Jansen, W., 1964b, "Steady Fluid Flow in a Radial Vaneless Diffuser," ASME *Journal of Basic Engineering*, Vol. 86, pp. 607-619.

Johnston, J. P., and Dean, R. C., Jr., 1966, "Losses in Vaneless Diffusers of Centrifugal Compressors and Pumps: Analysis, Experiment, and Design," ASME *Journal of Engineering for Power*, Vol. 88, pp. 49-60.

Kinoshita, Y., and Senoo, Y., 1985, "Rotating Stall Induced in Vaneless Diffusers of Very Low Specific Speed Centrifugal Blowers," ASME *Journal of Engineering for Gas Turbines and Power*, Vol. 107, pp. 514-519.

Ludtke, K., 1983, "Aerodynamic Tests on Centrifugal Process Compressors – the Influence of the Vaneless Diffusor Shape," ASME *Journal of Engineering for Power*, Vol. 105, pp. 902-909.

Senoo, Y., 1984, "Vaneless Diffusers," in: *Flow in Centrifugal Compressors*, VKI LS 1984-07.

Senoo, Y., and Ishida, M., 1975, "Behavior of Severely Asymmetric Flow in a Vaneless Diffuser," ASME *Journal of Engineering for Power*, Vol. 97, pp. 375-387.

Senoo, Y., and Kinoshita, Y., 1977, "Influence of Inlet Flow Conditions and Geometries of Centrifugal Vaneless Diffusers on Critical Flow Angle for Reverse Flow," ASME *Journal of Fluids Engineering*, Vol. 99, pp. 98-102.

Senoo, Y., Kinoshita, Y., and Ishida, M., 1977, "Asymmetric Flow in Vaneless Diffusers of Centrifugal Blowers," ASME *Journal of Fluids Engineering*, Vol. 99, pp. 104-110.

Sherstyuk, A. N., and Kosmin, V. M., 1969, "The Effects of the Slope of Vaneless Diffuser Walls on the Characteristics of a Mixed-Flow Compressor," *Thermal Engineering*, Vol. 16, pp. 116-121.

Sherstyuk, A. N., and Sokolov, A. I., 1966, "Meridional Profiling of Vaneless Diffusers," *Thermal Engineering*, Vol. 13, pp. 64-69.

Van den Braembussche, R. A., 1985, "Design and Optimization of Centrifugal Compressors," in: *Thermodynamics and Fluid Mechanics of Turbomachinery*, A. S. Ucer et al., eds., Martinus Nijhoff Publishers, Dordrecht, Vol. II, pp. 829-885.

Van den Braembussche, R. A., Frigne, P., and Roustan, M., 1980, "Rotating Non-uniform Flow in Radial Compressors," AGARD CP-282, Paper 12.

Zhu, Yingkang, and Sjolander, S. A., 1986, "Effect of Wall Taper on the Steady Aerodynamic Performance of Radial Vaneless Diffusers: Experimental Data," Carleton University, Dept. of Mechanical and Aeronautical Engineering, Technical Report.

APPENDIX

A very approximate analysis is made to examine the effect of various parameters on the C_p versus α_3 relationship.

Assuming one-dimensional incompressible flow, from continuity

$$rbv_r = R_3 b_3 v_{r3}$$

and if the diffuser height varies linearly with a convergence angle θ then

$$v_r = \frac{v_{r3}}{R'\left(1 - \tan\theta \dfrac{(R'-1)}{B_3}\right)}$$

where $R' = r/R_3$ and $B_3 = b_3/R_3$. Neglecting the moment due to the skin friction, angular momentum is conserved, so that

$$rv_t = R_3 v_{t3}$$

Then since

$$P_s = P_0 - \tfrac{1}{2}\rho(v_r^2 + v_t^2)$$

the static pressure recovery coefficient is given by

Downloaded 01 Jun 2010 to 171.66.16.57. Redistribution subject to ASME license or copyright; see http://www.asme.org/terms/Terms_Use.cfm

$$C_p = \frac{P_s - P_{s3}}{\frac{1}{2}\rho v_3^2} = 1 - \frac{1}{R'^2}\left[\frac{\sin^2\alpha_3}{\left(1 - \frac{(R'-1)}{B_3}\tan\theta\right)^2} + 1 - \sin^2\alpha_3\right] - \Omega(\alpha_3)$$

where

$$\Omega = \frac{P_{0_3} - P_0}{\frac{1}{2}\rho v_3^2}$$

is the total pressure loss coefficient.

For a constant-height diffuser ($\theta = 0$)

$$C_p = 1 - \frac{1}{R'^2} - \Omega(\alpha_3)$$

and neglecting losses, the slope of the pressure recovery curve, $\partial C_p/\partial\alpha_3$, is zero. For our range of flow rates, Ω varies inversely with α_3. Thus $\partial\Omega/\partial\alpha_3$ is negative and the slope of the pressure rise curve will be positive. At higher values of α_3, Ω may rise again but the slope of the pressure rise curve is of greatest concern at low values of α_3.

For tapered diffusers without losses, it is easily shown that $\partial C_p/\partial\alpha_3 < 0$ if the diffuser is convergent ($\theta > 0$); Fig. A1 shows the predicted pressure recovery curves for the diffuser geometries used in our experiment. For an actual diffuser with losses, sufficient convergence will therefore offset the effects of the losses to produce a pressure recovery curve with a negative slope, as we observed in our experiment.

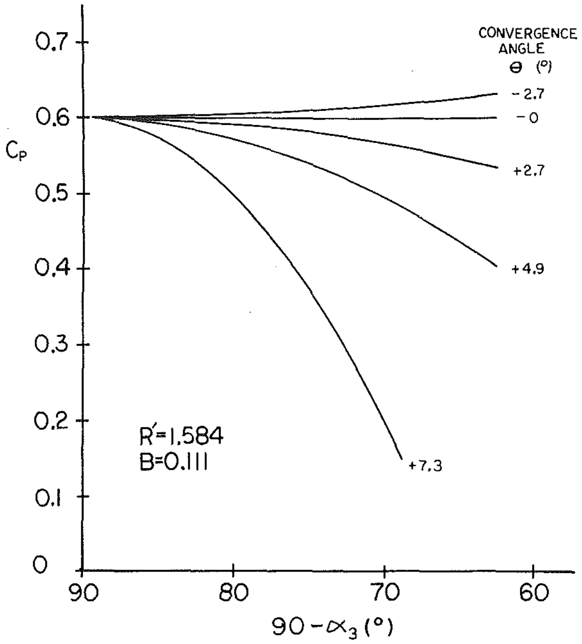

Fig. A1 Predicted static pressure recovery (no losses)

Downloaded 01 Jun 2010 to 171.66.16.57. Redistribution subject to ASME license or copyright; see http://www.asme.org/terms/Terms_Use.cfm

G. E. Andrews

J. Durance

C. I. Hussain

S. N. Ojobor

Department of Fuel and Energy,
University of Leeds,
Leeds, LS2.9JT, United Kingdom

Full Coverage Impingement Heat Transfer: Influence of the Number of Holes

The choice of hole diameter in impingement cooling requires the number of holes to be specified and design information is provided for this purpose. The correlations for impingement cooling usually take geometry effects into account by using the pitch-to-diameter ratio (X/D) *and this is independent of the number of holes and specified purely by the desired pressure loss at a given flow rate. Impingement heat transfer from a square array of holes was studied for a range of coolant flows* G *from 0.1 to 1.8 kg/sm^2 at a fixed* X/D *of approximately 10. The number of holes per unit surface area* N *was varied by a factor of 70 at a constant gap-to-hole diameter ratio* Z/D *of 4.5 and constant gaps of 3 mm and 10 mm. It was shown that there was a range of* N *over which there was only a small influence on heat transfer at constant* G. *However, heat transfer fell at large* N *due to crossflow effects and at low* N *due to inadequate surface coverage of the impingement flow.*

1 Introduction

Impinging air jets are extensively used for internally cooling turbine blades because of their high convective heat transfer coefficients [1–29]. Impingement cooling may also be used for cooling gas turbine combustor walls [1–6], and the technique offers the possibility of reducing present wall film cooling air flow requirements. For blade cooling, the air usually exits at the trailing edge of the blade, so that each successive row of holes experiences a crossflow of air from the upstream holes, which may influence the impingement heat transfer [6–8, 11–13, 19, 21]. For combustor wall cooling, configurations with and without crossflow are possible [3–6]. The authors [5, 30–33] have shown that full coverage discrete hole film cooling (effusion cooling) offers efficient film cooling at low coolant flow rates. It has design considerations similar to those of impingement cooling and is ideally suited to a combination with impingement cooling. This impingement/effusion design has the main coolant pressure loss at the impingement holes and a low pressure loss and hence film blowing rate at the effusion holes. This design has been shown to have a cooling performance close to the ideal transpiration cooling at low coolant flow rates [5, 33].

In the present work impingement configurations that are applicable to full coverage impingement/effusion cooling of combustor walls are studied. This involves a full flame tube design pressure loss of approximately 3 percent and minimum crossflow. Future work will investigate the influence of the addition of the effusion holes. The range of geometries investigated also covers those of interest in turbine blade cooling. Identification of the minimum number of holes that can be used in a full coverage application, without reducing the mean surface-averaged heat transfer, is important for the minimization of the manufacturing complexity and cost of the combustor design. Large numbers of holes involve small hole diameters, for the same design pressure loss and also small impingement gaps. Both these factors are generally to be avoided in combustor designs, although they may be feasible in turbine blades due to the smaller surface areas to be cooled.

The choice of hole diameter in an impingement cooling design, for a specified coolant mass flow, is a function of the design pressure loss and the number of holes per unit surface area N [1, 2, 4]. The pressure loss defines the pitch-to-diameter ratio X/D, and a wide range of these has been investigated by the authors for a fixed N of 4306 m^{-2} [2]. Other authors have also investigated the X/D parameter or the related hole area per unit surface area A [7, 10, 23, 28]. However, the number of holes per unit surface area N, which defines the pitch X, has received little study and the only previous work was that of Chance [7]. In the present work X/D has been held constant at approximately 10.5 and N varied by a factor of 70, giving a hole diameter variation by a factor of over 7. This is a much wider range of variables than in any previous investigation.

2 Impingement Array Designs

The factors influencing the design of impingement cooling systems are the mass flow per unit surface area G, the desired pressure loss $\Delta P/P$ percent, and the impingement geometry defined by the hole diameter D, the hole pitch X, and the impingement gap Z [1, 2, 4, 6]. A specified design G and $\Delta P/P$ percent defines the required open area per unit surface area A, as

$$A = G\,(Cd\,P)^{-1}(2/RT\,\Delta P/P)^{-0.5} = (GRT)\,(\mathrm{UP})^{-1} \qquad (1)$$

For this design value of A the hole diameter is specified in terms of A and N by

---

Contributed by the Gas Turbine Division of The American Society of Mechanical Engineers and presented at the 32nd International Gas Turbine Conference and Exhibit, Anaheim, California, May 31–June 4, 1987. Manuscript received at ASME Headquarters February 6, 1987. Paper No. 87-GT-93.

Copyright © 1987 by ASME

Downloaded 01 Jun 2010 to 171.66.16.57. Redistribution subject to ASME license or copyright; see http://www.asme.org/terms/Terms_Use.cfm

Table 1 Impingement plate configurations

N, m^{-2}	D, mm	X, mm	X/D	A, percent	t/D	Array
26,910	0.64	6.10	9.53	0.86	9.92	25×25
17,222	0.76	7.62	10.03	0.78	8.36	20×20
9688	0.94	10.16	10.81	0.67	6.76	15×15
4306	1.41	15.24	10.81	0.67	4.50	10×10
1076	2.84	30.48	10.73	0.68	2.24	5× 5
689	3.55	38.10	10.73	0.68	1.79	4× 4
388	4.70	50.80	10.81	0.67	1.35	3× 3

$$D=(4A/\pi N)^{0.5} \tag{2}$$

The number of holes per unit surface area N is specified by the hole pitch X as

$$N=X^{-2} \tag{3}$$

The hole pitch-to-diameter ratio X/D is given by the value of A, as

$$X/D=(\pi/4A)^{0.5} \tag{4}$$

The impingement hole Reynolds number Re is defined by G, A, and N as

$$\mathrm{Re}=(4/\pi AN)^{0.5}G/\mu \tag{5}$$

In the present work a design G of 0.5 kg/sm^2 at ambient T and P was used with a design $\Delta P/P$ of 3 percent. This was a low mass flow combustor wall cooling impingement geometry with an application to impingement/effusion cooling where the effusion design has a low pressure loss [5]. For this design condition, N has been varied over a wide range as detailed in Table 1. The impingement plate thickness t was 6.35 mm throughout. The variation in t/D was not a significant factor as all the values were greater than unity and hence the hole flow was reattached to the walls and there was no major change in the pressure loss characteristics [30].

3 Experimental Apparatus and Procedure

The experimental apparatus [1] consisted of a filtered and metered compressed air supply to an insulated 152-mm-square plenum chamber with two flow distribution grid plates. The 152-mm-square Nimonic 75 impingement test plate was bolted to the plenum chamber and then bolted at the four corners through 10-mm-dia. PTFE spacing rods of equal length, to the impingement target plate. The four corner spacer rods were interchangeable so that the impingement gap Z could be varied. This experimental configuration gave an air exit on all four sides of the impingement gap, thus minimizing the influence of crossflow in the impingement gap. The authors have previously shown that the present experimental configuration gives good agreement with a single sided impingement gap exit configuration provided that $Z/D > 2$ [6]. Crossflow effects only became significant for $Z/D < 2$ for the present X/D of 10.5 [6].

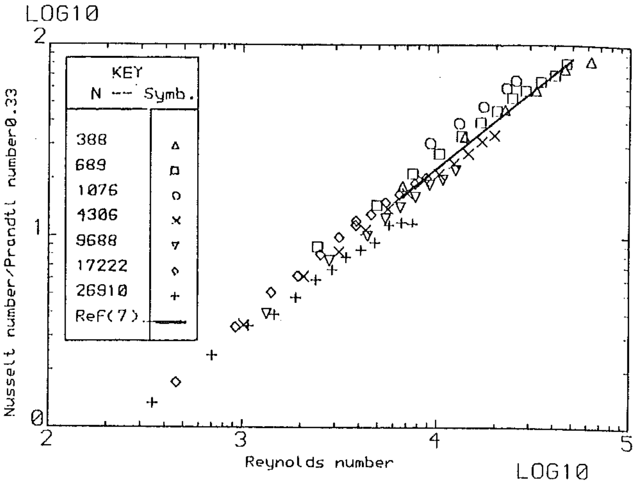

Fig. 1 Influence of Re on heat transfer, at $Z/D \sim 4.5$

The 152-mm-square impingement target plate was instrumented with 14 Type K grounded junction mineral insulated thermocouples, which were recorded with a temperature resolution of 0.1 K. This target plate was heated with a silicon rubber electrical mat heater, which was well insulated. The 152-mm-square mat heater gave a uniform electrical heat dissipation and the electrical energy was measured using a digital wattmeter. A temperature difference of approximately 30 K between the impingement air and the target plate was maintained by setting the electrical power for each flow rate. The impingement plates were also instrumented with at least five mineral insulated Type K grounded junction thermocouples and the mean temperature was used in the definition of the coolant supply temperature. The heating of the impingement plate was significant [4, 5], especially at low G, and this has not been realized by previous workers. It is caused by three-dimensional recirculation within the impingement gap and between the impingement jets and measurement of the mean convective heat transfer to the impingement plate is in progress by the authors.

The present method of using a solid metal heat transfer plate measures a surface-averaged heat transfer coefficient for

Nomenclature

A = hole area per unit surface area
As = heat transfer target plate area, m^2
Cd = hole discharge coefficient
D = hole diameter, m
G = coolant flow per m^2 surface area, kg/sm^2
h = heat transfer coefficient, equation (6)
Ic = crossflow parameter, equation (9)
k = thermal conductivity of the coolant, W/mK
L = distance from the start of the crossflow, m
n = number of upstream impingement holes
N = number of holes per unit surface area, m^{-2}
Nu = Nusselt number, equation (7)
Nu_0 = Nusselt number for zero crossflow
P = coolant supply static pressure, Pa
ΔP = pressure loss across the impingement plate, Pa
Pr = Prandtl number
Q = electrical heat supply, equation (6)
R = gas constant for air = 284 J/kgK
Re = Reynolds number, equation (5)
t = impingement plate thickness, m
T = mean target surface temperature, K
Tm = log mean temperature of the coolant and impingement plate temperatures, K
U = mean impingement jet velocity, m/s
Uj = local impingement jet velocity, m/s
Uc = crossflow mean velocity, m/s
X = hole pitch, m
Z = impingement gap, m
μ = coolant viscosity, Ns/m^2

Downloaded 01 Jun 2010 to 171.66.16.57. Redistribution subject to ASME license or copyright; see http://www.asme.org/terms/Terms_Use.cfm

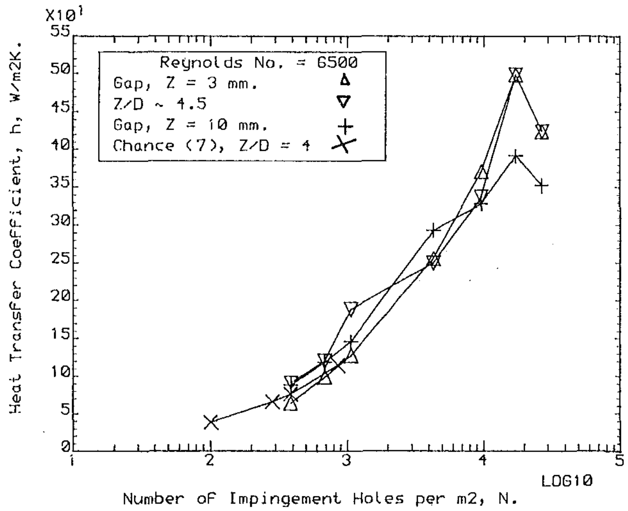

Fig. 2 Influence of hole density on heat transfer coefficients; Re = 6500

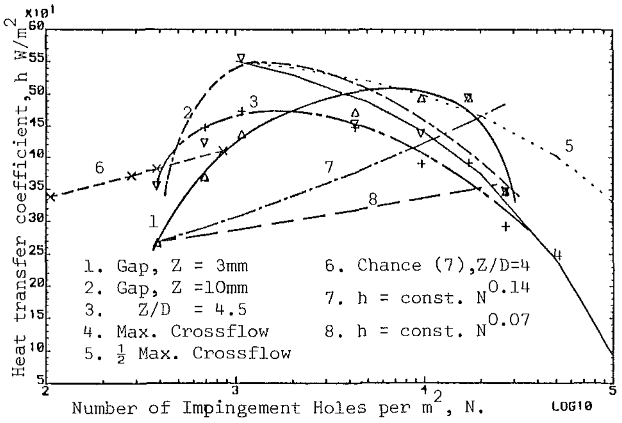

Fig. 3 Influence of hole density on h at G = 1.2 kg/sm^2

the impingement jet array. This technique has also been used by Friedman and Mueller [10] and Hollworth and Berry [17]. For each flow rate the system was allowed half an hour to come to thermal equilibrium before all the temperatures were recorded. The target plate was very close to a uniform temperature and hence the deviations from the mean heat transfer coefficient were small and generally less than 10 percent. The influence of N on the target plate temperature distribution was relatively small.

The average impingement convective heat transfer coefficient h was determined from

$$h = Q/As\ (T - Tm) \tag{6}$$

where Q is the electrical heat supply (watts) minus an allowance of 3 percent for heat losses [7, 17, 21]. The major errors in the present work were associated with equation (6), particularly the determination of the two temperatures. The temperatures were recorded with a 0.1°C resolution, but there were small temperature variations across the plates [3-5]. The temperature difference in equation (6) is between two average temperatures and with a temperature difference as low as 10-20°C at high flow rates, the error in this could be significant. The maximum error at high flow rates was a 1°C surface variation with a 10°C difference giving a 10 percent maximum error in h; generally the error was less than this. All other errors were below 1 percent except for the coolant mass flow, which was 5 percent using calibrated variable area flow meters.

Impingement heat transfer results are usually correlated by a dimensionless equation of the form of

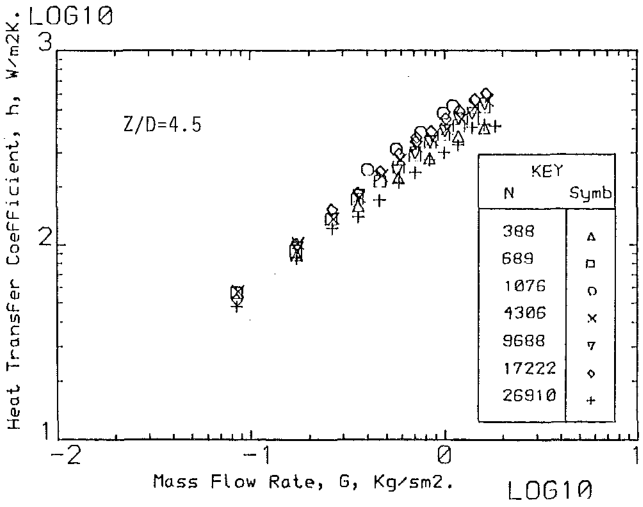

Fig. 4 Effect of coolant flow on h at Z/D = 4.5

$$\mathrm{Nu} = hD/k = C(X/D)^a\ (Z/D)^b\ \mathrm{Re}^y\ \mathrm{Pr}^{0.33} \tag{7}$$

In the present work X/D was constant and the influence of N on the constant C and the exponent y was investigated.

4 Influence of the Number of Holes per Unit Surface Area N

4.1 Constant Z/D = 4.5. The authors have previously investigated the influence of A or X/D at a constant Z/D of 4.5 [2]. This Z/D was shown [1] to be in the central region of the range of Z/D which gave little influence on the impingement heat transfer at the present X/D of 10.5. Thus a Z/D of 4.5 was a useful value to use for the present investigations. The results are shown in the form of equation (7) in Fig. 1 for a range of N from 388 to 26,910 m^{-2} and for a range of G from 0.1 to 1.8 kg/sm^2. Although the influence of N was small at a constant Re, there were significant differences. At an Re of 10,000 there was a factor of 2 between the lowest results for N = 26,910 m^{-2} and the highest for N = 1076. Figure 1 also shows that the present results are in very good agreement with those of Chance [7] for 96 < N < 856 at a Z/D of 4 and X/D of 11, which are the only previous results for the influence of N and are for geometries very close to the present work. Chance reported no difference in the results for the three values he investigated. The present wider range of N shows that this conclusion of Chance may not be generally valid and may only apply for a limited range of N.

The influence of N on the impingement convective heat transfer coefficient h is shown at a constant Re of 6500 in Fig. 2. There was a strong increase in h with N up to N = 17,222. Figure 2 also demonstrates good agreement with the results of Chance [7]. The increase in h was mainly controlled by the increase in coolant mass flow, G, with N that was necessary to maintain a constant Re, as shown by equation (5). For this reason it was considered preferable to investigate the influence of N at a constant coolant mass flow G, as shown in Fig. 3 for G = 1.2 kg/sm^2. This value of G gave the maximum influence of N, as shown in Fig. 4.

The variation of h with G for a range of N is shown in Fig. 4 for a constant Z/D of 4.5. For a fixed G the influence of N was slightly less than that at constant Re in Fig. 1. There was clearly a sharp fall in heat transfer for N below approximately 1000 m^{-2}; at an N of 300 it was only 64 percent of that at 1000. For higher N there was a reduction in h, especially at very high values of N. Within the range 1000 < N < 20,000 Fig. 3 shows that h varied only +/− 10 percent from the mean

Downloaded 01 Jun 2010 to 171.66.16.57. Redistribution subject to ASME license or copyright; see http://www.asme.org/terms/Terms_Use.cfm

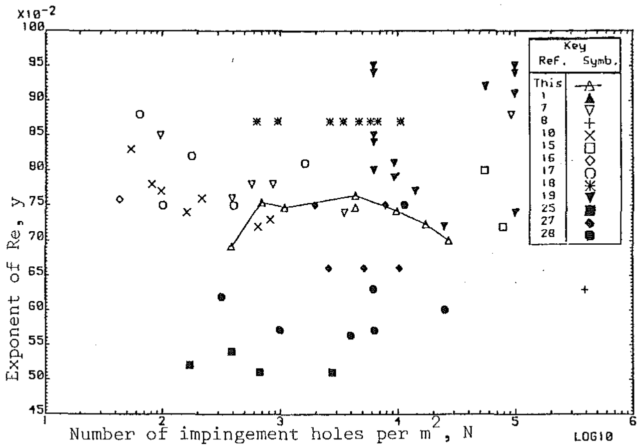

Fig. 5 Influence of hole density *N* on Re exponent *y*

value of 500 W/m^{2}K and this was not a significant variation. Hence, h may be concluded to be relatively insensitive to N within this range. The data of Chance [7] are also shown in Fig. 3 and cover the range of N where a sharp reduction in heat transfer was found in the present work. However, Chance found a smaller influence of N in this range, although there was a significant reduction.

The Reynolds number exponent y in equation (7) depends on N, as can be seen from the slightly different gradients in Fig. 1. The variation of y with N is shown in Fig. 5 to be small but significant and indicates that equation (7) with a fixed value of y may not be an adequate correlation of impingement heat transfer data. The authors have previously [1, 2] reviewed the data of other workers for the Re exponent y and this shows a large variation from 0.5 to 0.95. Figure 5 shows that the data for y of different investigators show a large scatter and no correlation with N. However, the data of the other workers in Fig. 5 refer to different X/D and Z/D at each value of N; only the present work and that of Chance have kept other variables constant as N was varied. Figure 5 does illustrate that many workers have used very low values of N in their investigations and the present work shows that the applicability of those data to the large N region may produce significant errors in the heat transfer predictions. This is the situation with some of the turbine blade impingement cooling investigations. The authors have also previously shown that y is a function of Z/D at constant X/D [1], a function of X/D at constant Z/D [2], and a function of X/D at constant Z [4]. However, in all these situations a good correlation ($+/-$ 10 percent) of the data could be obtained using equation (7) with a fixed mean value for y of 0.72 and Fig. 5 shows that this is a reasonable value for a wide range of N.

Equation (7) for the present constant X/D and A may be shown to predict that h depends on N to the power 0.14 for the 0.72 value of y and a constant G and Z/D. This predicts an increase in h by 81 percent from the lowest to the highest N of the present work. The gradient of this line is marked on Fig. 3 and shows a relatively poor agreement with the experimental results at constant Z/D. However, there is a better agreement with the results of Chance. The present results indicate that equation (7) does not take into account all the effects of N.

4.2 3-mm Impingement Gap *Z*. Previous work by the authors showed that the influence of Z/D was not large for the present X/D of 10.5 [1]. In the present work D increased as N decreased and hence for a constant Z/D there was a relatively large impingement gap at low N. In gas turbine applications there are practical limits on the maximum impingement gap and for turbine blades 3 mm is a typical value for Z. Thus, where the impingement hole diameter is an experimental variable, there are practical advantages in keeping Z constant. The authors have previously investigated for a constant Z the influence of impingement hole porosity, A, or X/D at constant N [4]. It was shown that for $2 < Z < 12$ mm there was little influence of Z on the impingement heat transfer and on the influence of A or X/D.

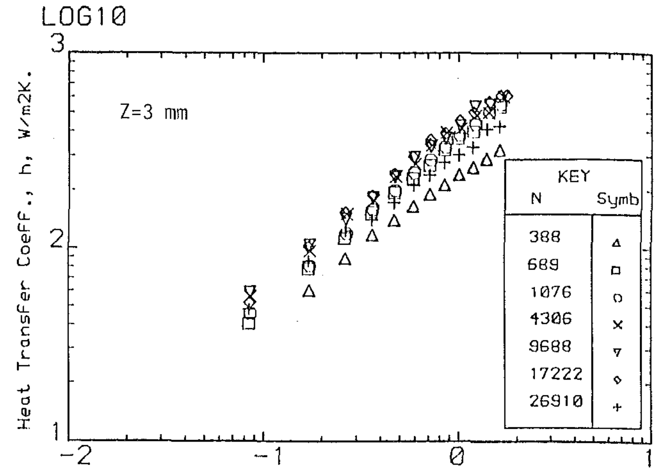

Fig. 6 Effect of coolant flow on *h* at $Z = 3$ mm

The variation of h with coolant mass flow G at a constant Z of 3 mm is shown in Fig. 6 for a range of N from 388 to 26,910 m^{-2}. Comparison of this with Fig. 4 for a constant Z/D shows a slightly greater influence of N. This is shown more clearly in Fig. 3 where, for a constant G, h increased with N up to a maximum at approximately N = 20,000 m^{-2}. This indicates that for a turbine blade cooling application a large value of N should be used. This is equivalent to the use of a small pitch and the above maximum value of N corresponds approximately to a 7-mm pitch, which is similar to many turbine blade cooling designs. However, the increase in h with N is greatest in the region of $N < 1000$, as was the case for the constant Z/D situation. The lower values of h at low N are likely to be due to the fall in h at low Z/D that has been observed by several workers [1]. At $Z = 3$ mm and an X/D of 10, Z/D is less than unity for $N < 1000$ and is only 3 for N = 10,000. Thus the trends of h with N at Z = 3 mm are likely to be due to Z/D effects. However, the sharp fall in h below N = 1000 is greater than Z/D effects would predict [1].

Equation (7) for a constant Z, X/D, and G may be shown, using a 0.14 value for the Z/D exponent b [1], to predict a 0.07 exponent for the dependence of h on N. Figure 3 shows that this is in poor agreement with the experimental results, which show a much stronger increase in h with N up to N = 10,000. However, equation (7) does predict a very small influence of N at constant Z, which is the situation found for $1000 < N < 10{,}000$ for Z = 3 mm. This suggests that equation (7) may be valid for a defined range of N, with other factors being of importance at low and high N.

The sharp fall in heat transfer at low N is considered to be due to a breakdown in the surface coverage of the impingement heat transfer. Impingement jets have an annular ring of high turbulence around the jet which promotes the high heat transfer. In impingement jet arrays these turbulence regions interact to give a good surface coverage. However, if the hole pitch is made sufficiently large, then at some stage this interaction will cease giving rise to lower convective heat transfer rates at the mid regions between the holes and hence a lowering of the mean surface averaged heat transfer. The present sharp deterioration in heat transfer at an N of approximately 1000 corresponds to a pitch of 30 mm. Clearly this is unlikely to occur in any turbine blade impingement jet array design, as

Downloaded 01 Jun 2010 to 171.66.16.57. Redistribution subject to ASME license or copyright; see http://www.asme.org/terms/Terms_Use.cfm

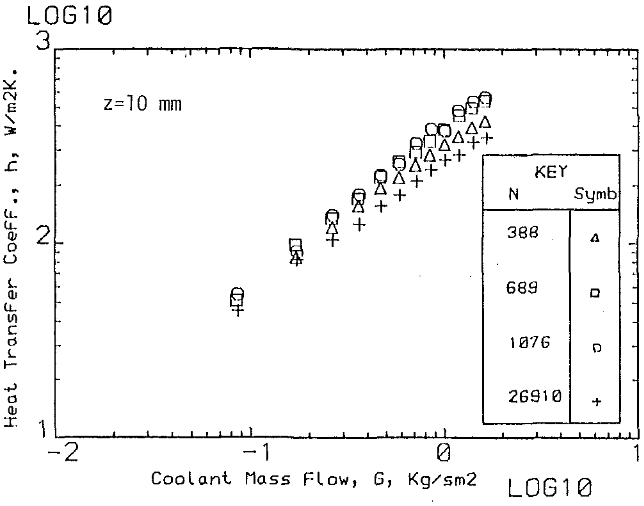

Fig. 7 Effect of coolant flow on *h* at *z* = 10 mm

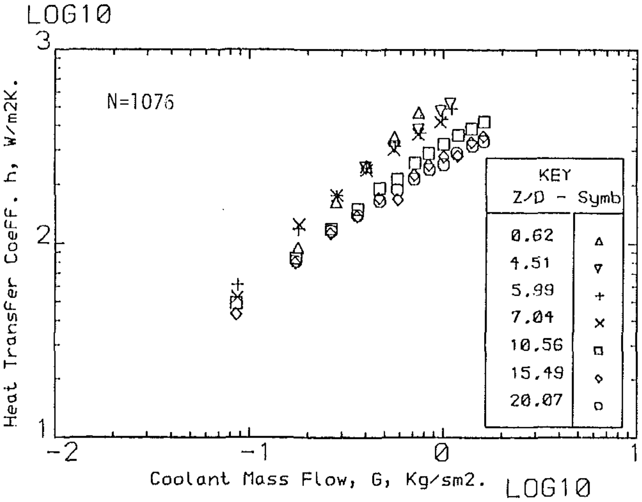

Fig. 8 Effect of *Z/D* of *h* for *N* = 1076

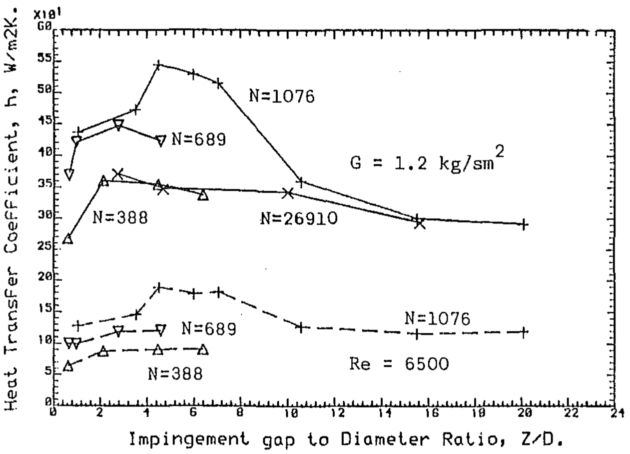

Fig. 9 Influence of *Z/D* on *h* at fixed *G* and Re

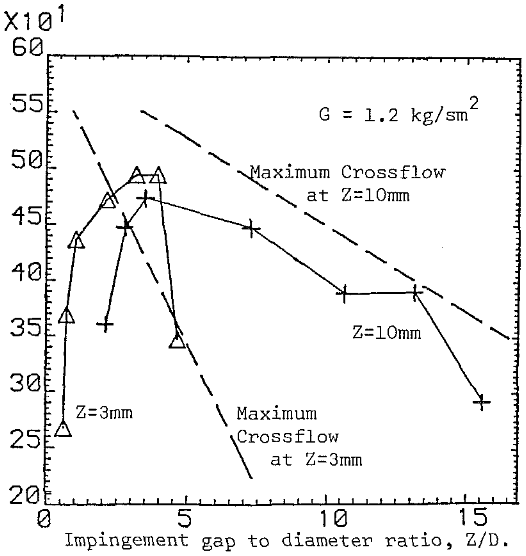

Fig. 10 Influence of *Z/D* on *h* at *G* = 1 kg/sm^2

it is too close to the blade dimensions. However, it is quite feasible for full coverage combustor wall cooling applications. Thus the fall in heat transfer at low *N* is only likely to be a problem in combustor applications. Conversely, the fall in heat transfer at very high values of *N*, shown in Fig. 3, is of importance mainly for turbine blade designs and the reasons for this will be discussed below in terms of the crossflow effects.

4.3 10-mm Impingement Gap *Z*. The variation of *h* with *G* for a range of *N* and a constant impingement gap of 10 mm is shown in Fig. 7. This shows a reduced influence of *N* compared with the situation with a 3-mm gap. The variation of *h* with *N* at constant *G* of 1.2 kg/sm^2 is shown in Fig. 3 and is significantly different than for the 3-mm gap, with a peak *h* at low *N*. The reason for this is again associated with the variation of *Z/D* with *N*. At an *N* of 1000, *Z/D* is over 3 and is 15 for the highest value of *N* tested. Previous work on the *Z/D* effect has shown that heat transfer falls significantly once *Z/D* is greater than approximately 5 [1].

4.4 Influence of *Z/D* at Constant *N*. The influence of *Z/D* has been studied previously by the authors [1] for the present *X/D* and an *N* of 4306 m^{-2}. Figure 8 shows the influence of *Z/D* for *N* = 1076 which demonstrates similar results to those found previously for *N* = 4306. The heat transfer was approximately constant for *Z/D* up to 7 and then fell significantly for higher *Z/D*. This reduction may be associated with the end of the impingement jet potential core, high heat transfer being associated with the maximum jet velocities of the potential core striking the target plate. The influence of *Z/D* on *h* for a constant *G* of 1.2 kg/sm^2 and constant Re of 6500 is shown in Fig. 9 for a wide range of *N*. For all except *N* = 1076, the influence of *Z/D* was relatively weak with a slow deterioration in heat transfer as *Z/D* was increased. However, for *N* = 1076 there was significantly higher heat transfer in the *Z/D* range 4–8, as also shown in Fig. 8. This was responsible for the peak in the heat transfer at this value of *N* and a *Z/D* of 4.5 in Fig. 3. The reason for this different behavior at this value of *N* is not known and is being investigated for other values of *N* in the 600–4000 range.

4.5 Influence of *Z/D* at Constant *Z*. The variation of *N* at constant *Z* causes a consequent variation in *Z/D*. Thus, the results in Fig. 3 may be presented as a function of *Z/D* as shown in Fig. 10. This shows that the maximum heat transfer occurs at a *Z/D* of approximately 4 for both values of *Z*. This gives the optimum number of holes as 17,222 for the 3-mm gap and 1076 for the 10-mm gap, as shown in Fig. 3. Thus the use of a *Z/D* of 4, as an optimum design parameter, gives a convenient method for choosing the optimum value of *N* once a convenient value for *Z* has been selected.

5 Effect of *N* on the Crossflow Influence

Impingement cooling involves the flow of impingement air

Downloaded 01 Jun 2010 to 171.66.16.57. Redistribution subject to ASME license or copyright; see http://www.asme.org/terms/Terms_Use.cfm

along the impingement gap to the downstream exit position. This is maximized in a situation with a single-sided exit as in a turbine blade, but is still significant in the present four-sided exit configuration. The influence of the crossflow on the impingement jet is strongly dependent on the impingement geometry. For a fixed length L of combustor wall or turbine blade surface the number of upstream impingement jets n increases with N. The influence of the crossflow is thus a function of N.

The authors [6] have previously investigated the design factors that influence the magnitude of the crossflow effect. They showed that crossflow had two separate influences: firstly, the influence of flow generated pressure gradients in the impingement gap that could lead to a flow maldistribution between the jets and secondly, an influence of crossflow on the impingement heat transfer. It was shown [6] that flow maldistribution would only be a problem if the ratio of the impingement jet to crossflow velocities Uj/Uc was less than two. The maximum value of this velocity ratio, in the plane of the last row of impingement jets, is defined by the impingement geometry as given by

$$Uj/Uc = Z/nAX = Z/LA \qquad (8)$$

where L is the length of wall to be cooled ($=nX$). For the present geometry and a single-sided exit this gives a value of Z below 2 mm before flow maldistribution would be a problem [6]. With a four-sided exit the value of Z is less than 1 mm. Thus, in the present work flow maldistribution did not occur.

Several workers have shown that crossflow may decrease the impingement heat transfer [7, 9, 11, 13, 15, 19–21, 24–29]. Chance [7] and Kercher and Tabakoff [19] have shown that the influence of crossflow may be correlated by the parameter Ic defined [6] by

$$Ic = \pi nD/4X = \pi LDN^{0.5}/4X = (\pi/4A)^{0.5} L\ N^{0.5} \qquad (9)$$

It should be noted that Ic does not depend on Z/D, but only on the impingement plate geometry. Chance showed a linear correlation between the decrease in heat transfer and Ic, given by

$$\mathrm{Nu}/\mathrm{Nu}_0 = 1 - 0.236\ Ic \qquad (10)$$

where Nu_0 is the heat transfer in the absence of any crossflow. For the present X/D of approximately 10.5 and maximum impingement gap length L of 152 mm it may be shown that the crossflow effect is a direct function of the square root of N, as

$$\mathrm{Nu}/\mathrm{Nu}_0 = 1 - 0.00269\ N^{0.5} \qquad (11)$$

Equation (11) gives the maximum possible influence of crossflow as a function of N. With the present four-sided exit to the impingement gap it is likely that a length of half the test plate would be more appropriate and the constant in equation (11) would be reduced to a half of the above value. Both the maximum and half maximum crossflow effect as a function of N are compared with the experimental results in Fig. 3. A value of Nu_0 has been chosen to make the predictions pass through the point $h=550$ at $N=1000$. The results show a fair agreement with the experimental data at constant Z/D, although the present high value of Nu at $N = 17{,}222$ is off the predicted trend, even at half the maximum crossflow effect. The present surface-averaged heat transfer measurements will underestimate the crossflow influence. However, it may be concluded that the main reason for the fall in heat transfer at high values of N is the influence of crossflow. Figure 10 shows the predicted maximum crossflow influence as a function of Z/D, at the two values of Z used, with the variation in Z/D caused by the variation in N. Again the predictions have a fair agreement with the experimental results. Future work will investigate the crossflow influence using a single-sided exit geometry and any change in the present optimum values of N will be determined.

6 Conclusions

The number of impingement holes N influences the surface average impingement heat transfer coefficient, but there is a range of N from 1000 to 20,000 where this influence is small.

At low values of N it is considered that the reduction in heat transfer is due to inadequate surface coverage of the high turbulence region around each impingement jet.

At high values of N the reduction in heat transfer has been shown to be caused by the influence of crossflow in the impingement gap.

For combustor wall cooling with a typical Z of 10 mm, it was shown that the optimum number of holes was approximately $N = 1000/\mathrm{m}^2$.

For turbine blade applications with a typical value of Z of 3 mm it was found that the optimum value of N was approximately $20{,}000/\mathrm{m}^2$.

The influence of Z/D on heat transfer was small but significant and of the same magnitude over a wide range of N.

Acknowledgments

We would like to thank the UK Science and Engineering Research Council for research grant GR/D/53029 in support of this work. Some of the test geometries were manufactured by Ruston-GEC Gas Turbines and we would like to thank M. F. Cannon for technical discussions.

References

1 Andrews, G. E., and Hussain, C. I., "Impingement Cooling of Gas Turbine Components," *High Temp. Tech.*, Vol. 2, 1984, pp. 99–106.

2 Andrews, G. E., and Hussain, C. I., "Full Coverage Impingement Heat Transfer: the Influence of Impingement Jet Size," *I. Chem. E. Symp. Series*, No. 86, 1984, pp. 1115–1124.

3 Andrews, G. E., and Hussain, C. I., "Impingement Cooling Using Large Arrays of Holes," *Proc. 11th Annual I. Chem E. Research Meeting*, 1984, pp. 86–91.

4 Andrews, G. E., Asere, A. A., Hussain, C. I., and Mkpadi, M. C., "Full Coverage Impingement Heat Transfer: the Variation in Pitch to Diameter Ratio at Constant Gap," *Heat Transfer and Cooling in Gas Turbines*, AGARD-CP-390, 1985, pp. 26.1–26.12.

5 Andrews, G. E., Asere, A. A., Hussain, C. I., and Mkpadi, M. C., "Transpiration and Impingement/Effusion Cooling of Gas Turbine Combustion Chambers," *7th International Symposium on Air Breathing Engines*, AIAA, Beijing, 1985, pp. 798–801.

6 Andrews, G. E., and Hussain, C. I., "Full Coverage Impingement Heat Transfer: the Influence of Channel Height," *8th International Heat Transfer Conference*, 1986, pp. 1205–1211.

7 Chance, J. L., "Experimental Investigations of Air Impingement Heat Transfer Under an Array of Round Jets," *Tappi*, Vol. 57, 1974, pp. 108–112.

8 Chupp, R. E., Helms, H. E., McFadden, P. W., and Brown, T. R., "Evaluation of Internal Heat Transfer Coefficients for Impingement Cooled Turbine Aerofoils," AIAA Paper No. 68-564, 1968.

9 Dyban, E. P., Mazur, A. I., and Golovanov, V. P., "Heat Transfer and Hydrodynamics of an Array of Round Impinging Jets With One-Sided Exhaust of Spent Air," *International Journal of Heat and Mass Transfer*, Vol. 23, 1980, pp. 667–676.

10 Friedman, S. J., and Mueller, A. C., "Heat Transfer to Flat Surfaces," *Proc. General Discussions on Heat Transfer*, I. Mech. E., London, 1951, pp. 138–142.

11 Florschuetz, L. W., Truman, C. R., and Metzger, D. E., "Streamwise Flow and Heat Transfer Distribution for Jet Array Impingement With Initial Crossflow," ASME *Journal of Heat Transfer*, Vol. 103, 1981, pp. 337–342.

12 Florschuetz, L. W., and Isoda, Y., "Flow Distribution and Discharge Coefficient Effects for Jet Array Impingement With Initial Crossflow," ASME *Journal of Engineering for Power*, Vol. 105, 1983, pp. 296–304.

13 Florschuetz, L. W., and Metzger, D. E., "Heat Transfer Characteristics for Jet Array Impingement With Initial Crossflow," ASME Paper No. 83-GT-28, 1983.

14 Gardon, R., and Akfirat, J. C., "Heat Transfer Characteristics of Impinging Two Dimensional Air Jets," ASME *Journal of Heat Transfer*, Vol. 88, 1966, pp. 101–108.

15 Gauntner, J. W., Gladden, H. J., Gauntner, D. J., and Yeh, F. C., "Crossflow Effects in Impingement Cooling of a Turbine Vane," NASA TM X-3029, 1974.

16 Hilgeroth, E., "Heat Transfer From a Jet Stream at Right Angles to the Exchange Surface," *Chemie.Ing.Techn.*, Vol. 37, 1965, pp. 1264–1272.

17 Hollworth, B. R., and Berry, R. D., "Heat Transfer From Arrays of

Downloaded 01 Jun 2010 to 171.66.16.57. Redistribution subject to ASME license or copyright; see http://www.asme.org/terms/Terms_Use.cfm

Impinging Jets With Large Jet-to-Jet Spacing," ASME *Journal of Heat Transfer*, Vol. 100, 1978, pp. 352-357.

18 Huang, G. C., "Investigations of Heat Transfer Coefficients for Air Flow Through Round Jets Impinging Normal to a Heat Transfer Surface," ASME *Journal of Heat Transfer*, Vol. 85, 1963, pp. 237-245.

19 Kercher, D. M., and Tabakoff, W., "Heat Transfer by a Square Array of Round Air Jets Impinging Perpendicular to a Flat Surface," ASME JOURNAL OF ENGINEERING FOR POWER, Vol. 92, 1970, pp. 73-82.

20 Metzger, D. E., and Korstad, R. J., "Effects of Crossflow on Impingement Heat Transfer," ASME *Journal of Engineering for Power*, Vol. 94, 1972, pp. 35-41.

21 Saad, N. R., Majumdar, A. S., Messeh, A. W., and Douglas, W. J. M., "Local Heat Transfer Characteristics for Staggered Arrays of Circular Impinging Jets With Crossflow," ASME Paper No. 80-HT-23, 1980.

22 Obot, N. T., Majumdar, A. S., and Douglas, W. J. M., "The Effect of Nozzle Geometry on Impingement Heat Transfer Under a Round Turbulent Jet," ASME Paper No. 79-WA/HT-53, 1979.

23 Daane, R. A., and Han, S. T., "An Analysis of Air Impingement Drying," *Tappi*, Vol. 44, 1961, pp. 73-80.

24 Stoy, R. C., and Ben-Haim, Y., "Turbulent Jets in a Confined Crossflow," ASME *Journal of Fluids Engineering*, Vol. 95, 1973, pp. 551-556.

25 Hrycak, P., "Heat Transfer From a Row of Impinging Jets to Concave Cylindrical Surfaces," *International Journal of Heat Mass Transfer*, Vol. 24, 1981, pp. 407-419.

26 Florschuetz, L. W., Metzger, D. E., and Truman, L. R., "Jet Array Impingement With Crossflow Correlation of Streamwise Resolved Flow and Heat Transfer Distribution," NASA-CR-3373, 1981.

27 Tabakoff, W., and Clevenger, W., "Gas Turbine Blade Heat Transfer Augmentation by Impingement of Air Jets Having Various Configurations," ASME *Journal of Engineering for Power*, Vol. 94, 1972, pp. 51-60.

28 Metzger, D. E., Florschuetz, L. W., Takeuchi, D. I., Behee, R. D., and Berry, R. A., "Heat Transfer Characteristics for Inline and Staggered Arrays of Circular Jets With Crossflow of Spent Air," ASME *Journal of Heat Transfer*, Vol. 101, 1979, pp. 526-531.

29 Florschuetz, L. W., Berry, R. A., and Metzger, D. E., "Periodic Streamwise Variations of Heat Transfer Coefficients for Inline and Staggered Arrays of Circular Jets With Crossflow of Spent Air," ASME *Journal of Heat Transfer*, Vol. 102, 1980, pp. 132-137.

30 Andrews, G. E., and Mkpadi, M. C., "Full Coverage Discrete Hole Wall Cooling: Discharge Coefficients," ASME *Journal of Engineering for Power*, Vol. 106, 1984, pp. 183-192.

31 Andrews, G. E., Gupta, M. L., and Mkpadi, M. C., "Full Coverage Discrete Hole Wall Cooling: Cooling Effectiveness," *International Journal of Turbo Jet Engines*, Vol. 2, 1985, pp. 213-225.

32 Andrews, G. E., Asere, A. A., Gupta, M. L., and Mkpadi, M. C., "Full Coverage Discrete Hole Film Cooling: the Influence of Hole Size," *International Journal of Turbo Jet Engines*, Vol. 2, 1985, pp. 213-225.

33 Andrews, G. E., Asere, A. A., Mkpadi, M. C., and Tirmahi, A., "Transpiration Cooling: Contribution of Film Cooling to the Overall Cooling Effectiveness," *International Journal of Turbo Jet Engines*, Vol. 3, 1986.

Downloaded 01 Jun 2010 to 171.66.16.57. Redistribution subject to ASME license or copyright; see http://www.asme.org/terms/Terms_Use.cfm

Heat Transfer to Arrays of Impinging Jets in a Crossflow

B. R. Hollworth
Associate Professor,
Mechanical Engineering Department,
Gonzaga University,
Spokane, WA 99258

G. H. Cole
Senior Program Specialist,
Idaho National Engineering Laboratories,
Idaho Falls, Idaho 83415

Convective heat transfer measurements are reported for staggered arrays of round turbulent air jets impinging upon a heated flat surface. Spent air was constrained by skirts to exit at one end of the test section, thus establishing a crossflow. Geometric variables included the jet hole diameter d, *the streamwise spacing* X *and spanwise spacing* Y between jet holes, and the standoff distance Z *between the orifice plate and the target plate. Three patterns of holes, all having* d = *3.5 mm, were tested. Their* (X,Y) *were* (4d, 4d), (4d, 8d), and (8d, 4d). *Values of the standoff were* Z = d, 2d, *and* 3d; *and tests were run for 4, 6, and 8 rows of holes. The airflow was varied to achieve a range of mean jet Reynolds number from 2500 to 25,000. Microfoil heat flux sensors were used to determine streamwise variations in (spanwise-averaged) heat transfer. Excellent resolution was obtained by employing a sensor whose streamwise dimension is considerably less than one hole diameter* d. *Heat transfer profiles were periodic, with a peak corresponding to each spanwise row of holes. Such peaks were displaced in the steamwise direction by the crossflow, and those nearest the exhaust end of the channel exhibited the largest deflections. Array-averaged heat transfer coefficients were obtained by numerically averaging the local measurements; values agree well with the results of other experiments on similar impingement-with-crossflow systems.*

Introduction

Impinging fluid jets have a number of applications in situations where very high rates of convective heat or mass transfer are required. Some of these include the tempering of glass, the heat treating of some metals, the spot-cooling of electronic components, and the drying of paper stock and photographic film.

Impinging jet systems have become an accepted technique for cooling components in the hot sections of gas turbine engines; in fact, the gas turbine industry has been responsible for a considerable portion of the experimentation needed to generate heat transfer data for such systems. An important application, within this context, is the cooling of gas turbine airfoils (blades and vanes) using relatively low-temperature compressor discharge air as the coolant. The airfoil is made hollow, and an internal manifold directs cooling air jets at the midchord portion of the blade skin to achieve the necessary reduction in skin temperature. Ordinarily, the spent coolant is removed through slots at the trailng edge of the airfoil, so that the flow field within the airfoil consists of a crossflow of spent air, flowing toward the trailing edge, superimposed upon and interacting with the various individual cooling jets.

It has long been recognized that the presence of this crossflow may have a considerable effect on the convective heat transfer characteristics of the impinging jets through its interference with them. As a result, a number of experimental studies have been conducted to measure convective heat transfer for such systems, with special attention paid to determining the effects of the crossflow. Bouchez and Goldstein (1975), Sparrow, et al. (1975), and Hollworth and Bowley (1975) measured convective heat transfer rates for a single impinging jet in a crossflow, while Metzger and Korstad (1971) made measurements for a single spanwise row of jets. Several investigators have measured heat transfer for arrays of jets (consisting of multiple spanwise rows) discharging into a rectangular passage, with spent air withdrawn at one end; these include Kercher and Tabakoff (1970), Chance (1974), Saad et al. (1980), Behbahani and Goldstein (1983), and Metzger et al. (1978, 1980, 1981, 1985). Finally Gauntner and co-workers (1973, 1974) measured convection rates in actual turbine airfoils cooled by arrays of jets.

For some engineering calculations, such as the determination of the total coolant flow for a given application, it is sufficient to know only the average heat transfer coefficient. The studies of arrays of jets with crossflow cited above all contain such information. However, the distribution of (spanwise-averaged) heat transfer for impinging jet systems tends to be highly nonuniform. The calorimeters used to measure "local" heat flux in these studies (with the exception of those used by Saad et al. (1980) and Florschuetz et al. (1980)) have tended to be fairly large, having a chordwise dimension generally on the order of chordwise spacing X between jets.

It is the purpose of the present paper to report detailed measurements of (spanwise-averaged) heat transfer for arrays of impinging jets. High resolution was obtained by using microfoil heat flux sensors whose chordwise length is approximately $0.3d$, where d is the jet hole diameter. Sensors were at-

---

Contributed by the Gas Turbine Division of THE AMERICAN SOCIETY OF MECHANICAL ENGINEERS and presented at the 32nd International Gas Turbine Conference and Exhibit, Anaheim, California, May 31–June 4, 1987. Paper No. 87-GT-198.

Copyright © 1987 by ASME

Downloaded 01 Jun 2010 to 171.66.16.57. Redistribution subject to ASME license or copyright; see http://www.asme.org/terms/Terms_Use.cfm

Table 1 Test program

Arrays tested	$(\bar{X}, \bar{Y})$	(4, 4), (4, 8), (8, 4)
Jet Reynolds number	Re	3000, 5000, 10,000, 25,000
Standoff between jet plate and target plate	$\bar{Z}$	1, 2, 3
Number of spanwise rows of jets	N	4, 6, 8

tached to a movable heated target plate which was traversed slowly past the arrays of jets to obtain continuous heat transfer profiles which clearly show the effect of spent air flow on local impingment heat transfer over the entire chordwise length of each jet array.

Heat transfer measurements were made for ranges of coolant flow and geometry which are fairly typical of gas turbine cooling applications. The nondimensional test parameters which were varied in this study include the jet Reynolds number Re, the chordwise spacing between jet holes $\bar{X} \equiv X/d$, the spanwise spacing between jet holes $\bar{Y} \equiv Y/d$ the standoff between the jet orifice plate and the target plate $\bar{Z} \equiv Z/d$, and the number of spanwise rows of jets N. Figure 1 shows the impingement configuration that was tested, and Table 1 summarizes the test parameters and their ranges of variation. All possible combinations listed in the table were run, so that the total program consisted of 108 tests. For all the arrays tested, the jets were formed by square-edged circular orifices (with $d = 3.5$ mm) drilled in a flat plate (thickness = 3.5 mm). They were flow-calibrated and found to have an average discharge coefficent of 0.79 over the range of Re used in the heat transfer tests. All three arrays of jets were staggered by displacing alternating spanwise rows by $X/2$ in the spanwise direction. It was felt that this arrangement would produce more uniform heat transfer than inline arrays, and would be less likely to allow formation of chordwise hot streaks on the surface being cooled. The test fluid was air near STP, which has a Prandtl number of 0.72.

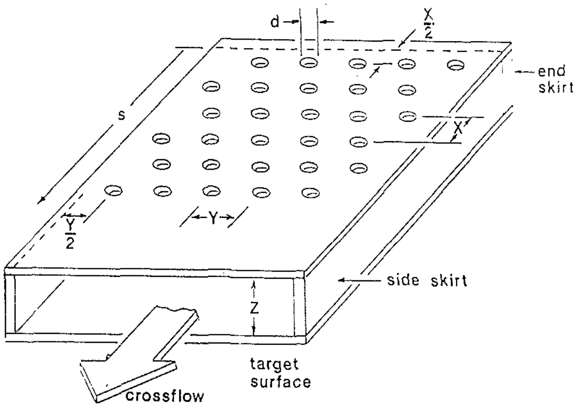

Fig. 1 Test geometry and nomenclature

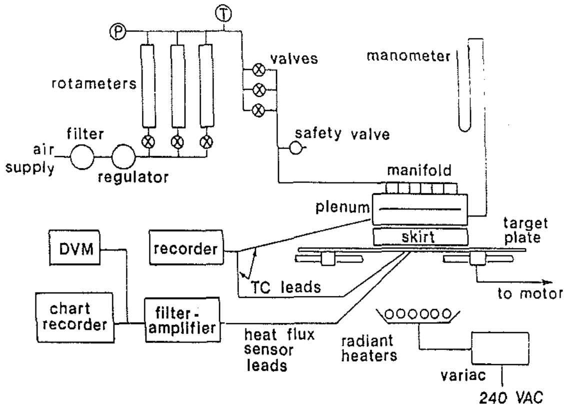

Fig. 2 Test apparatus

Experimental Apparatus and Procedures

The test apparatus is shown in Fig. 2. It consists of a jet plenum, a moving impingement plate, a stationary array of radiant heaters to heat the impingement plate, an air supply system, and instruments to measure and record the appropriate pressures, temperatures, airflow, and heat fluxes.

The air supply circuit consists of high-accuracy (±1 percent) rotameters to measure flow to the impingement rig, with hand-operated valves to set and control the flow rate. A pressure regulator and filter are installed upstream of the flow meters. Pressure and temperature are measured immediately downstream from the rotameters to correct indicated flow rates for off-calibration conditions. Laboratory quality air is supplied from a reciprocating compressor and arrives at the test rig at room temperature.

The air plenum is a solid block of aluminum, with outside dimensions 38 mm × 203 mm × 762 mm, hollowed out to inside dimensions of 152 mm × 559 mm. The "lid" of the plenum is an aluminum plate with a manifold to decelerate and evenly distribute the incoming air. A baffle is located immediately beneath the inlet ports to avoid a ram effect at the jet orifices. The bottom face of the plenum consists of (interchangeable) plates containing the arrays of jets to be tested; these plates are 3.5-mm-thick steel, bolted to the plenum using countersunk machine screws.

Nomenclature

d = jet orifice diameter, mm
G = coolant flow rate per unit area of target surface, kg/s-m^2
h = spanwise-averaged convective heat transfer coefficient, W/m^2-°C
H = dimensionless quantity defined by equation (6)
k = thermal conductivity of test fluid, W/m-°C
$\dot{m}$ = total coolant flow rate, kg/s
n = total number of jet orifices in array
N = number of spanwise rows of orifices
Nu = Nusselt number based on spanwise-averaged heat transfer coefficent = hd/k
$\overline{\text{Nu}}$ = area-averaged Nusselt number
Pr = Prandtl number
q = local spanwise-averaged heat flux, W/m^2
q_r = heat flux due to radiation, W/m^2
Re = average jet Reynolds number for array, equation (4)
s = distance measured in streamwise direction, mm
T_0 = jet plenum temperature, °C
T_p = copper target plate temperature, °C
T_s = target plate surface temperature, °C
X = streamwise spacing of orifices, mm
$\bar{X}$ = X/d
Y = spanwise spacing of orifices, mm
$\bar{Y}$ = Y/d
Z = normal distance between jet orifice plate and target plate, mm
$\bar{Z}$ = Z/d
μ = test fluid dynamic viscosity, Pa•s

Downloaded 01 Jun 2010 to 171.66.16.57. Redistribution subject to ASME license or copyright; see http://www.asme.org/terms/Terms_Use.cfm

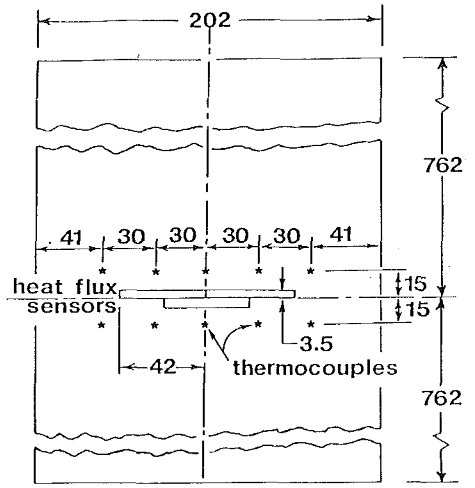

Fig. 3 Instrumented target plate (all dimensions in mm)

The array of jets impinges upon a movable target plate which is heated from beneath by a stationary array of six quartz lamps with a total power rating of approximately 3.6 kW. The plate surface facing the lamps is painted flat black so as to absorb most of the incident radiant heat. The target plate is 6.4-mm-thick copper, 202 mm (in the spanwise direction) × 1524 mm (in the chordwise direction). Spanwise-averaged heat transfer is measured using commercially available microfoil heat flux devices. Three of them are glued with epoxy to the target plate at the locations shown in Fig. 3. Each such device contains a linear array of 28 separate heat flux sensors (approximately 1 mm by 1 mm) spaced 1.5 mm apart. A typical sensor consists of two thermopiles deposited on opposite faces of a Kapton thermal barrier, with this assembly sandwiched between two more thin sheets of Kapton. Overall thickness is about 0.1 mm. The thermopiles within a given sensor are wired so that their emf's opposite each other, and the net output is a millivolt-level signal proportional to local heat flux. Finally, the 28 sensors are wired in series so that the signal (at the device level) is proportional to spanwise-averaged heat flux. The manufacturer furnishes a calibration (for each device, not for each sensor) accurate to ±5 percent. Hollworth and co-workers (1978, 1985) have previously used microfoil sensors (individually) to measure the highly nonuniform heat transfer due to a single isolated impinging jet. Our data showed good agreement with those obtained by other investigators using various other types of heat transfer gages. Two of the sensors, placed end to end and wired in series (so their output voltage signals add), are used when traversing the "wide" ($\bar{Y}=8$) jet arrays; the remaining sensor is used when traversing the two "narrower" ($\bar{Y}=4$) arrays. The rest of the impingement surface is masked with Kapton sheet having the same thickness (and thermal inpedance) as the sensors themselves; this assures a fairly isothermal surface during testing.

The target plate is mounted on four pillow blocks, and this assembly is moved at constant speed along rails past the jet array, in the direction of the crossflow. The heat flux sensors are connected to a strip-chart recorder, so that a continuous trace corresponding to spanwise-averaged heat flux is generated as the instrumented target plate is traversed past the array of cooling jets. The recorder was periodically checked against a precision digital voltmeter to assure accuracy of the traces. Tests were conducted to determine what effect the traverse speed would have on the heat transfer measurements. It was determined by Cole (1978) that it is permissible to traverse at a speed of approximately 0.70 mm/s without these measurements deviating significantly from those obtained from a steady-state test.

Ten Type J (iron-constantan) thermocouples were imbedded in the target plate near the heat flux sensors, as shown in Fig. 3. These were used to determine the temperature T_s of the convecting surface, with suitable correction (see Date Reduction section) for the temperature drop across the heat flux sensors. In addition, two thermocouples in the jet plenum were used to measure the total temperature T_0 of the coolant, and one attached to the orifice plate was used to correct the measured heat flux for radiation effects. During the tests, the output signals of the thermocouples were continuously monitored with a multichannel recorder.

In operation, the spent air is confined by three balsa wood skirts (see Fig. 1) to exit at the open end of the channel formed between the orifice plate and the target plate. These skirts serve also as spacers to set the standoff distance Z; a set of spacers was made for each value of Z for which heat transfer measurements were made. The skirt at the closed end of the channel was located a distance $X/2$ upstream from the first row of holes. The distance between the two side skirts was always set such that the flow field was the same as that which would occur if the array were infinite in the spanwise direction. The array of jets was positioned over the copper plate (see Fig. 3) in such a way that the heat flux sensor(s) measured a spanwise-averaged heat flux for three jets near the centerline of each array.

To set up a typical test run (i.e., a traverse), the jet array to be tested was bolted to the plenum and the assembly installed above the target plate with the centerline of the jet array directly above the centerline of the heat flux sensors on the target plate. Three skirts of the appropriate height Z were put in place between the orifice plate and the impingement plate. A pointer attached to the stationary plenum was set such that the traverse start point ($s=0$) aligned with zero on a scale (graduated in jet diameters) fastened on the target plate. The air flow rate was adjusted (using the manually operated valves shown in Fig. 2) to obtain the desired Re. The quartz heaters were turned on and the powerstat adjusted until the desired target plate temperature was obtained. Sufficient time was allowed to pass to permit the air flow and impingement plate temperatures to come to steady-state.

The target plate was then traversed manually beneath the jet array to make sure that the heat flux sensor output signals did not exceed the range set for the strip chart recorder, and to make sure that the remainder of the instrumentation was functioning satisfactorily. A zero pen position was established by shorting the two heat flux sensor leads, thereby simulating zero heat transfer. Finally, the target plate was backed up several jet diameters past $s=0$, and the plate connected to the drive motor, which was turned on to begin the actual heat transfer traverse. As the pointer approached $s=0$, the recorders were started and event marks were put on the heat flux and temperature traces simultaneously as the pointer passed through $s=0$. During the traverse, the following data were read and recorded:

- indicated air flow
- air temperature and pressure at rotameters
- plenum temperature and pressure
- orifice plate temperature
- chart speed and recorder sensitivity
- ambient pressure and temperature.

Also during the traverse, visual checks were performed periodically to make sure that neither the air flow or plate temperature T_p varied significantly. Several event marks were put on the charts at various s/d (read from the scale attached to the target plate) to insure that if either the traverse speed or chart speed changed during the traverse, it would be apparent upon later inspection of the traces.

When the pointer came to that value of s corresponding to

Downloaded 01 Jun 2010 to 171.66.16.57. Redistribution subject to ASME license or copyright; see http://www.asme.org/terms/Terms_Use.cfm

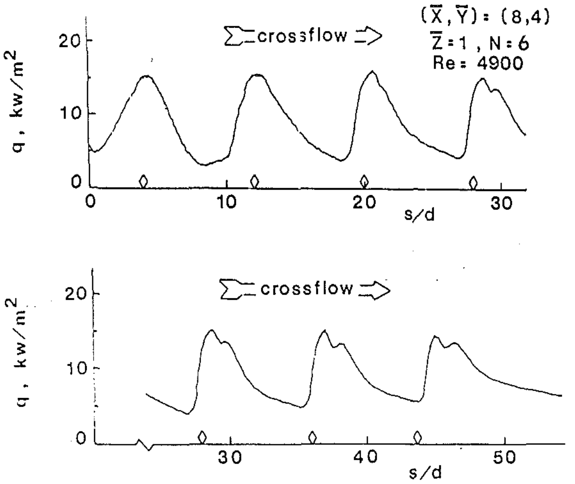

Fig. 4 Typical heat flux trace

the end of a traverse (a distance X downstream from the last spanwise row of holes), event marks were put on both traces, clearly indicating the termination point for the traverse. Since both traverse speed and chart speed were constant, it became a simple matter to relate horizontal distances on the traces to the corresponding positions of the heat flux sensors relative to the jet arrays during the traverse.

Data Reduction

Raw data from these tests were available as continuous plots of heat flux sensor output (in mV) and temperature. The traces generated by the heat flux sensor were converted to plots of local (spanwise-averaged) heat flux q using calibrations furnished by its manufacturer. Figure 4 shows a typical plot of q versus streamwise position produced in this fashion. The ◇ symbols on the horizontal axis indicate locations of spanwise rows of coolant holes.

To calculate local heat transfer coefficients, discrete values of heat flux sensor signal were read from the original millivolt versus position traces at intervals corresponding to one jet hole diameter. These values were subsequently read into our mainframe computer, which reduced the data and produced corresponding heat transfer profiles in terms of appropriate dimensionless variables. The local impingement surface temperature T_s was deduced from the measured plate temperature T_p, the heat flux, and the thickness and thermal conductivity of the sensor (both supplied by the manufacturer) assuming one-dimensional conduction through the sensor. Details are given by Cole (1978). The local spanwise-averaged film coefficient was then computed using

$$h = \frac{q - q_r}{T_s - T_0} \tag{1}$$

where q is a small correction for radiation and h is based here on the difference between the impingement surface temperature and the jet plenum (stagnation) temperature. The uncertainty in our reported measurements of heat transfer is determined by the errors inherent in the devices and methods used to obtain the heat fluxes and temperatures which appear in equation (1). Using the method suggested by Holman (1978), we estimated the uncertainty in our values of local h to be ±9 percent. Local heat transfer coefficients were incorporated into a local Nusselt number given by

$$\mathrm{Nu} = \frac{hd}{k} \tag{2}$$

and a space-averaged Nusselt number for each array was calculated from

$$\overline{\mathrm{Nu}} = \frac{1}{s_{\max}} \int_0^{s_{\max}} \mathrm{Nu}\, ds \tag{3}$$

The integral was computed numerically (using the trapezoidal rule) as part of the data reduction computer routine. The average was calculated from the upstream skirt ($s=0$) to a point X downstream from the last spanwise row of holes.

Strictly speaking, the local recovery temperature T_r should be used instead of T_0 in equation (1). Behbahani and Goldstein (1983) show distributions of T_r for a staggered array with $\bar{Z}=2$ and $\bar{Z}=4$ at $\mathrm{Re}=15{,}000$; T_r and T_0 differ by no more than 0.25°C. Owing to our higher maximum Re (25,000 as compared to their 15,000) and smaller d (3.5 mm as compared to their 5.0 mm) our highest jet velocities are about 2.4 times theirs. The difference between T_r and T_0 for our test conditions should, then, exceed the values which they indicate. In fact, based on some of our earlier work (Hollworth and Berry, 1978) for an array of jets in a modest crossflow, we estimate that local T_r may differ from T_0 by as much as 1.0°C for this experiment. This represents only about 2 percent of our nominal ΔT, so that the impact upon our reported heat transfer coefficients is minimal. On the other hand, the advantage associated wih basing h upon $(T_s - T_0)$ is apparent. The total temperature is easily measured in the jet plenum, and a single value applies for the entire array.

Finally, the total coolant flow $\dot{m}$ was used to define an average jet Reynolds nunber Re using

$$\mathrm{Re} = \frac{\dot{m}/n}{(\pi/4)d^2}\,\frac{d}{\mu} \tag{4}$$

where n is the total number of jet orifices in the array. All air properties (k, μ, Pr) are evaluated at a "film" temperature halfway between T_0 and T_s using properties tabulated by Kreith (1973).

Results

Traces of local heat flux were used to generate plots of local heat transfer coefficients using the formulae given in the Data Reduction section. Figures 5–7 show typical profiles, and profiles for the rest of the test cases are given by Cole (1978). The local heat transfer coefficient and the chordwise position are expressed in nondimensional form as $\mathrm{Nu}/\mathrm{Pr}^{1/3}$ and s/d, respectively. The symbols on the curves do not represent discrete data points, but rather indicate where the analog raw data were digitized for computer analysis. It should be noted, also, that the Prandtl number Pr was not varied in these tests; the conventional assumption $\mathrm{Nu} \sim \mathrm{Pr}^{1/3}$ was used. For all tests, the plenum temperature T_0 was nominally equal to room temperature. For the majority of tests, the plate temperature T_p was kept at about 95°C. A few tests were run, however, with $T_p = 60°\mathrm{C}$, and the resulting distributions of h were found to be identical (to within our estimated experimental uncertainty) to those obtained with $T_p = 95°\mathrm{C}$.

As will be discussed in some detail later, the shapes of the heat transfer profiles vary considerably with both geometry and cooling flow. However, there are general conclusions which apply to all of them. The first, and most obvious, is that the streamwise distribution of heat transfer is very nonuniform. The profiles consist of a series of heat transfer peaks and valleys, with one peak corresponding to each row of holes. For jet orifice rows near $s=0$ (i.e., the first few rows), the peaks are symmetric and occur at positions nearly opposite the corresponding row of jet orifices. However, peaks near the test section exhaust are skewed (nonsymmetric) and may be displaced several jet diameters downstream from the corresponding row of holes, due to the crossflow. Other investigators such as Behbahani and Goldstein (1983) and Florschuetz et al. (1980) have observed similar behavior. The crossflow is, of course, cumulative and increases monotonical-

Downloaded 01 Jun 2010 to 171.66.16.57. Redistribution subject to ASME license or copyright; see http://www.asme.org/terms/Terms_Use.cfm

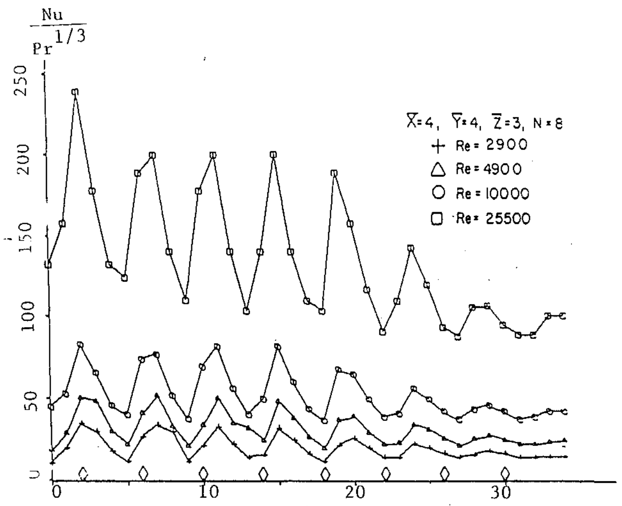

Fig. 5(*a*) $\bar{Z} = 3$, $N = 8$

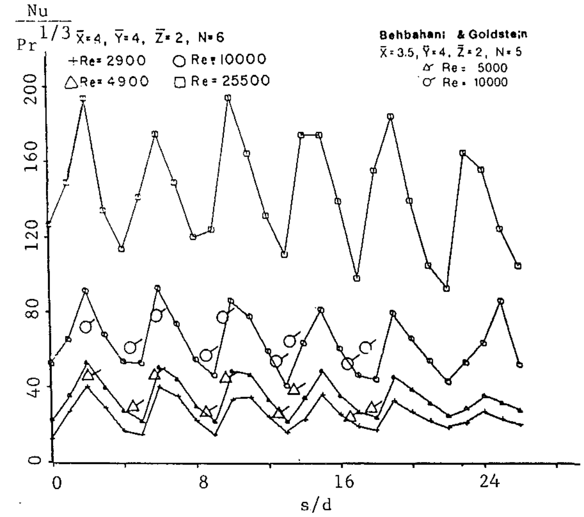

Fig. 5(*b*) $\bar{Z} = 2$, $N = 6$

Fig. 5 Heat transfer profiles for $(\bar{X}, \bar{Y}) = (4, 4)$

ly with s. Thus, the resultant distortion and displacement of heat transfer peaks likewise increase with s.

Figures 5(*a*) and 5(*b*) show heat transfer distributions for the array $\bar{X} = \bar{Y} = 4$. For fixed $\bar{Z}$ and N these profiles tended to have the same general shapes, with h values increasing, of course, with array Reynolds number. This held true for all $\bar{Z}$ and N for which data were taken. The magnitude of the heat transfer coefficient (peak or average) is nearly constant for the first four-five rows, and any significant "degradation" of heat transfer due to the crossflow (in cases where it does occur) appears farther downstream. Such a dropoff in heat transfer near the exhaust end of the enclosure was most pronounced at large Z; this effect is shown clearly by Fig. 5(*a*) for $\bar{Z} = 3$. Similar behavior has been noted by other investigators. For example, Florschuetz et al. (1980) show periodic variations in spanwise-averaged heat transfer for a staggered array with $\bar{X} = 5$, $\bar{Y} = 4$, $N = 10$ at $\mathrm{Re} = 15{,}000$. Such degradation in heat transfer is evident in their data (Fig. 3) for $\bar{Z} = 3$. For smaller plate-to-plate spacing this effect becomes less pronounced. For example, our data for $\bar{Z} = 2$ (Fig. 5(*b*)) show a decrease in (peak) heat transfer of only about 12 percent between the first and last rows of an array with $N = 6$.

It is difficult to find data generated by other investigators at

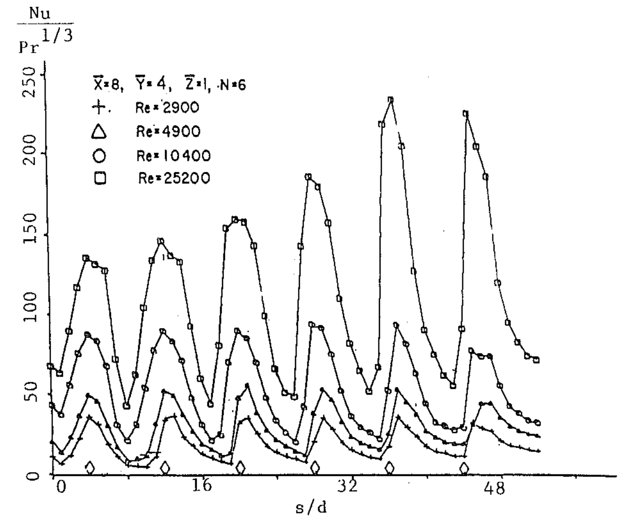

Fig. 6(*a*) $\bar{Z} = 1$, $N = 6$

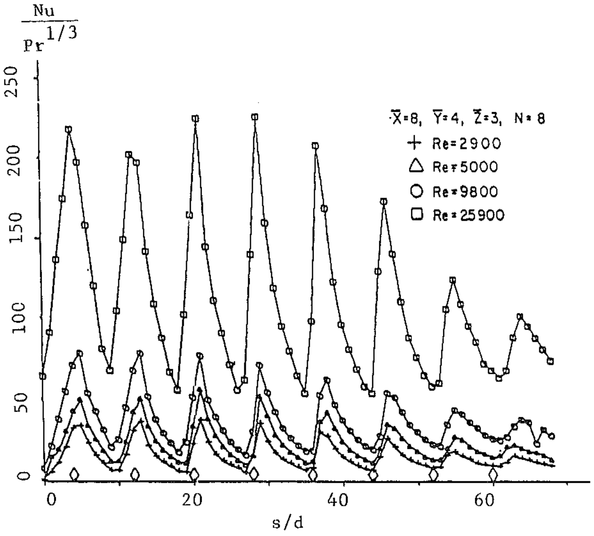

Fig. 6(*b*) $\bar{Z} = 3$, $N = 8$

Fig. 6 Heat transfer profiles for $(\bar{X}, \bar{Y}) = (8, 4)$

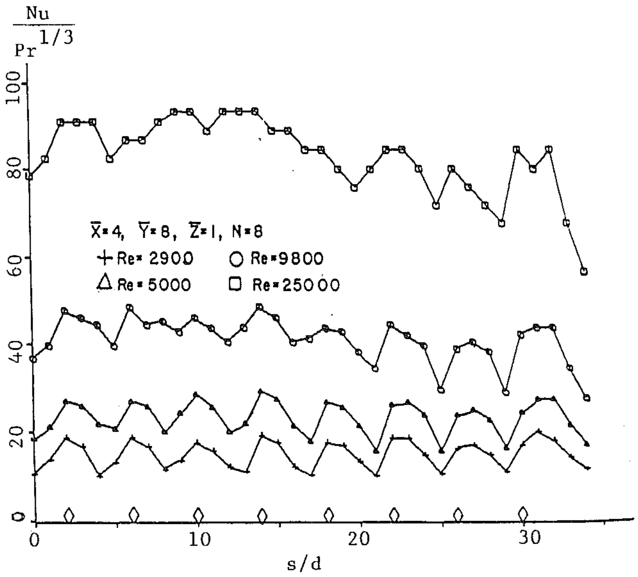

Fig. 7 Heat transfer profiles for $(\bar{X}, \bar{Y}) = (4, 8)$

Downloaded 01 Jun 2010 to 171.66.16.57. Redistribution subject to ASME license or copyright; see http://www.asme.org/terms/Terms_Use.cfm

test conditions which exactly match our own, so that a direct comparison of results can be made. Behbahani and Goldstein (1983) measured spanwise-averaged heat transfer for a staggered array nearly identical to our array of Fig. 5; theirs has $N=5$, $\bar{X}=3.5$, and $\bar{Y}=4$. Heat transfer maxima and minima were extracted from their profiles for Re = 5000 and 10,000 at $\bar{Z}=2$, and are shown on Fig. 5(*b*) along with our results. Peaks do not line up due, of course, to the difference in $\bar{X}$ between the two arrays. The agreement in the mean level of heat transfer is quite satisfactory, although their data show somewhat less dramatic peaks and valleys than do our own. The streamwise length of their heat transfer gage was $L=5d$ while ours had $L<d$. Thus, the "local" h values given in their paper undoubtedly reflect more truncation due to streamwise smearing than do those that we report.

Figures 6(*a*) and 6(*b*) show heat transfer profiles for the array $(\bar{X}, \bar{Y})=(8, 4)$. The relatively large streamwise spacing between holes is responsible for there being relatively little overlap of the impingement zones and relatively low heat transfer coefficients in those areas halfway between adjacent spanwise rows. Figure 6(*a*) was chosen for inclusion in this paper because it was one of several test cases where the induced crossflow does not produce relative degradation of heat transfer near the exit end of the channel, but, in fact, actually enhances heat transfer. This occurred for all tests of the (8, 4) array and (to a lesser degree) in tests of the (4, 4) array at $\bar{Z}=1$. The same tendency was observed by Saad et al. (1980) and Florschuetz et al. (1980) at small $\bar{Z}$. This particular geometry (small $\bar{Z}$ and small $\bar{Y}$) provides a relatively small cross-sectional area through which spent air may flow. As Kercher and Tabakoff (1970) showed, a fairly substantial static pressure gradient (dp/ds) may be built up in the channel under these conditions, with the lowest pressure occurring near the exit plane. If the jet plenum (i.e., stagnation) pressure is constant over the entire length of the array, then the pressure difference (and the flow rate per hole) is minimum at the closed end of the channel ($s=0$) and increases continuously with s. Thus, the increased heat transfer which is apparent at the discharge end occurs primarily because the local jet flow is highest. At larger standoff ($\bar{Z}=2$ and 3), heat transfer is fairly uniform for the first four–five rows and decreases quite considerably at the last few rows. This behavior is shown in Fig. 6(*b*).

Finally, Fig. 7 gives spanwise-averaged heat transfer for the array $(\bar{X}, \bar{Y})=(4, 8)$. These profiles show characteristics that are common to all of the test cases run for this array. First, the profiles were very "smooth" in that periodic streamwise fluctuations in h were small compared to its mean value. However, the sizes of the fluctuations remained nearly constant as the flow (i.e., Re) was varied. This is in contrast to the behavior exhibited by both of the arrays with $\bar{Y}=4$, for which an increase in Re causes both the mean and fluctuating components to become larger. In fact some of the runs made for the wide ($\bar{Y}=8$) array at our highest Re (25,000) show heat transfer profiles which are "washed out" to the extent that some of the peaks associated with spanwise rows of holes are indistinguishable. Further work to better understand the behavior exhibited by this particular array (especially at high Re) would be worthwhile. It should be noted, however, that because the fluctuating components are small for this array (seldom more than 10–20 percent of the mean component), the experimental uncertainty in our data (±9 percent of the sum of these components) is not inconsequential. This array had the largest $\bar{Y}$ of any tested so that it provided the largest flow area for the spent flow. Therefore, those effects associated with a strong crossflow (such as the heat transfer degradation or enhancement observed near the exhaust end of the target surface for the narrower $\bar{Y}=4$ arrays) were largely absent for $\bar{Y}=8$. For example, Fig. 7 shows virtually identical heat transfer "hills" opposite each spanwise row in the array; and the same held true for all other tests on this array.

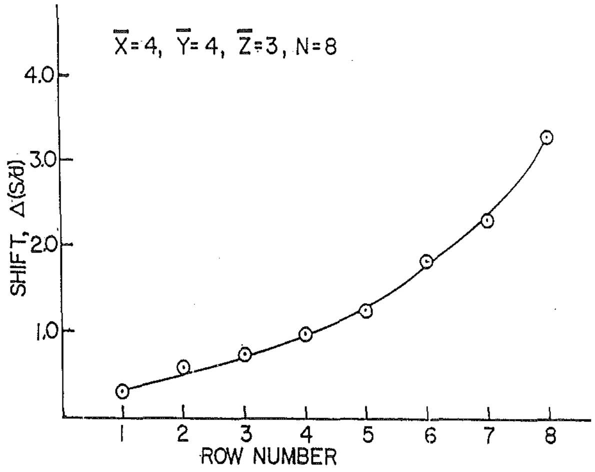

Fig. 8 Shift of heat transfer peaks

The crossflow deflects the cooling jets downstream and results in a corresponding shift of their impingement points. In general, jets are deflected most when the crossflow is strongest. Therefore, large deflections occur in arrays containing many spanwise rows, and rows near the exit plane are affected most profoundly. The mean crossflow mass flux is higher for the two narrow ($\bar{Y}=4$) arrays; and the downstream shift of a given row of jets is typically two–three times that of the same row in the $\bar{Y}=8$ array. The displacement of the impingement (i.e., maximum heat transfer) point(s) tends to be roughly proportional to $\bar{Z}$ for the narrow arrays and nearly independent of $\bar{Z}$ for the wide array. In all cases, the amount of shift is insensitive to Reynolds number. Figure 8 shows the downstream displacements ($\Delta S/d$) for each row of jets of the 8-row version of array (4, 4) at $\bar{Z}=3$. Based on the observations above, this geometry should (and does) yield especially large displacements. For example, the heat transfer peak for the last row of holes is shifted nearly 4 orifice diameters.

Although Figs. 5–7 offer excellent streamwise resolution, some detail has still been lost in the process of converting from the original continuous heat flux traces. Figure 4 is the trace from which the "Re = 4900" curve of Fig. 6(*a*) was constructed, and the loss of detail is readily seen by comparing the two. First, it is apparent that some heat transfer peaks and troughs have been truncated. This occurs because the original strip chart displays were digitized at points one jet diameter apart and Figs. 5–7 were computer-plotted by connecting successive points with straight line segments. Another detail that is lost are the small twin cusps (see Fig. 4) that appear near the jet rows' stagnation points. These occur quite regularly for the arrays (4, 4) and (8, 4) only at the smallest standoff, $\bar{Z}=1$. They resemble, somewhat, those observed by Gardon and coworkers (1962, 1965) for circular and slot jets at small standoff, except that they have been distorted somewhat by the skewing effect of the crossflow. Such cusps appear first on the heat transfer peaks near the exhaust end of the channel. As Re is increased, the cusps become more pronounced and spread to peaks farther upstream. Figure 4 clearly shows cusps on the three peaks near the exit, and one beginning to form on the fourth peak from the exit.

For each test case, space-averaged heat transfer coefficients were calculated using equation (3) and plotted against Reynolds number. Figure 9 shows a typical plot, for the array $(\bar{X}, \bar{Y})=(4, 4)$ at $\bar{Z}=3$; and similar plots for the remaining cases are given by Cole (1978). Kercher and Tabakoff (1970) and Chance (1974) tested square jet arrays and their correlations for $\bar{Z}=3$ and $N=6$ rows are shown, also, for com-

Downloaded 01 Jun 2010 to 171.66.16.57. Redistribution subject to ASME license or copyright; see http://www.asme.org/terms/Terms_Use.cfm

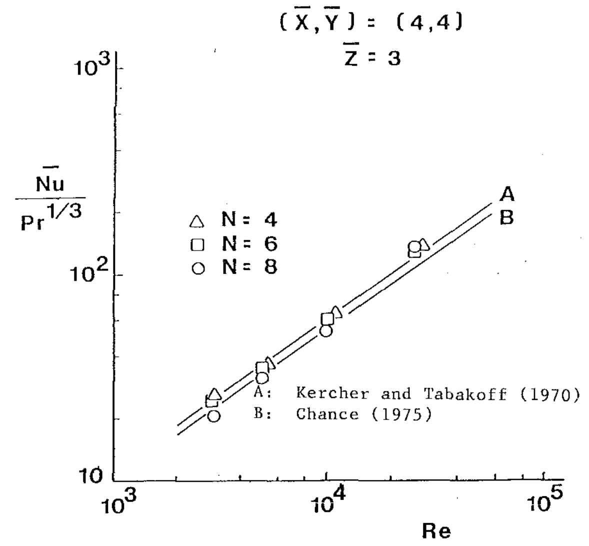

Fig. 9 Typical variation of average heat transfer with Reynolds number

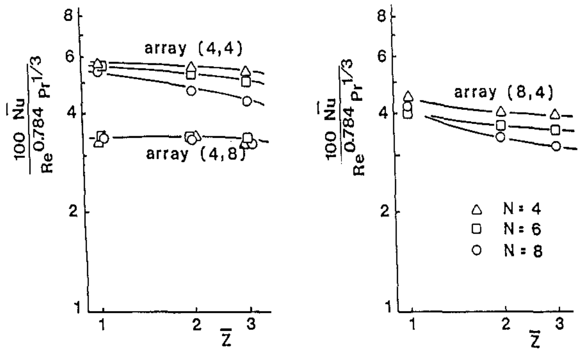

Fig. 10 Effects of geometry on average heat transfer

parison. Agreement is quite satisfactory. In fact, comparisons were made in a number of other cases where test conditions were similar, and good agreement was likewise obtained. The behavior of these data (see Fig. 9) suggests a relationship of the form

$$\mathrm{Nu}/\mathrm{Pr}^{1/3} \sim \mathrm{Re}^{m} \tag{5}$$

The least-squares method was used to determine the best value of the exponent m for each geometry tested. Values ranged between 0.71 and 0.86, with a mean value of 0.784. The only discernible trend was that m tended to decrease somewhat with $\bar{Z}$; this trend was observed also by Hollworth and Berry (1978) in an earlier study where square arrays of widely spaced ($\bar{X}>10$) jets impinged, and spent air was withdrawn along all four edges of the target surface.

Despite the variations of m discussed above, data correlated well using

$$H \equiv \frac{\overline{\mathrm{Nu}}}{\mathrm{Re}^{0.784}\,\mathrm{Pr}^{1/3}} = f(\text{array}, \bar{Z}, N) \tag{6}$$

and Fig. 10 shows average heat transfer coefficients for all geometries tested, displayed using this format. The vertical coordinate for each point on the graph is the average of the H values measured at the four values of Re (i.e., Re = 3000, 5000, 10,000, and 25,000). The deviation between this average value and values at the various Re (for a given geometry) were usually less than the experimental uncertainty (±9 percent) inherent in the measurements of h. The largest such deviation was 14 percent, and only 3 (of 27) were greater than 9 percent.

From inspection of Fig. 10, it is possible to pick out several effects of system geometry upon average heat transfer. For the $(\bar{X}, \bar{Y}) = (4, 8)$ array, the flow area for spent air is largest. Hence, the crossflow is relatively weak and its effect on Nu is minor. Thus, the heat transfer is virtually independent of the number of rows N. For this array, the effects of variations in standoff $\bar{Z}$ are negligible as well.

The two narrow arrays behave similarly, though array (4, 4) yields higher heat transfer than does array (8, 4). This occurs, of course, because the former has twice as many jets per unit heat transfer area and (at the same Re) twice the coolant flow. Because of the more powerful crossflow naturally associated with these arrays with $\bar{Y}=4$, the heat transfer performance is considerably more dependent upon the number of spanwise rows. In terms of average heat transfer, increasing N always degrades performance, and the effect becomes more pronounced at large $\bar{Z}$. At $\bar{Z}=3$, the average heat transfer is decreased by roughly 20 percent in increasing N from 4 to 8 for both arrays. It is worth noting, also, that the standoff $\bar{Z}$ has a fairly strong effect upon Nu, especially at large N. In both cases, $\bar{Z}=1$ appears to be optimum, and Nu is again reduced by roughly 20 percent in increasing $\bar{Z}$ from 1 to 3.

It is especially interesting to compare the performances of the arrays (4, 8) and (8, 4), as both have the same cooling hole density and, therefore, the same coolant flow at fixed Re. Although the relative strength of the crossflow is greater for the narrow array (8, 4), it nevertheless yields somewhat higher average heat transfer than does (4, 8). Hollworth and Bowley (1975) observed that a superimposed crossflow tends to elongate impinging jet footprints in the x direction while narrowing them in the y direction. Thus the formation of streamwise avenues of low heat transfer between coolant jets in an array with large $\bar{Y}$ would be more pronounced than the formation of spanwise bands of low heat transfer in an array with large $\bar{X}$. We suggest, then, that the better heat transfer offered by the narrow array (8, 4) is attributable to the better surface "coverage" which it provides.

In most applications, it is desirable to heat or cool a surface of fixed area with a minimal expenditure of fluid. Therefore, in order to rate the performamce of several jet arrays, one must compare this average convective heat transfer rates at *constant coolant flow per unit area of target surface.* To facilitate such a "fair" comparison of the three arrays tested, average heat transfer coefficients $\mathrm{Nu}/\mathrm{Pr}^{1/3}$ were replotted against a Reynolds number Re* based on the air flow G per unit area of cooled surface. This modified Reynolds number is defined as $\mathrm{Re}^* = Gd/\mu$, so that constant Re* corresponds to constant G. This graph is shown by Cole (1978) but is not included in this paper because of space limitations. On this basis, the two arrays with lowest hole density (i.e., (4, 8) and (8, 4)) were consistently better than array (4, 4). The average heat transfer rate for (8, 4) exceeded that of (4, 4) by anywhere from 20 to 50 percent (depending upon both N and $\bar{Z}$), while the difference for array (4, 8) relative to (4, 4) varied from roughly 0 to 30 percent. This tendency of patterns with fewer holes per unit area (and more flow per hole) to yield higher heat transfer was observed also by Hollworth and Berry (1978) in the earlier study discussed above.

Conclusions

Spanwise-averaged heat transfer coefficients were measured for three staggered arrays of impinging air jets. Spent air was constrained to exit at one end of the array, thus establishing a crossflow. Significant conclusions resulting from this study are the following:

1. The streamwise distribution of (spanwise-averaged) heat transfer is periodic, with one heat transfer peak per row of cooling jets. The nonuniformity of the heat transfer distribution is most pronounced at large $\bar{X}/\bar{Y}$.

Downloaded 01 Jun 2010 to 171.66.16.57. Redistribution subject to ASME license or copyright; see http://www.asme.org/terms/Terms_Use.cfm

2. Heat transfer peaks may be shifted considerable distances downstream by the induced crossflow; deflections of as much as four jet diameters were observed in these tests. It would therefore be good design practice to extend the cooled surface somewhat past the end of the array to take advantage of the "residual" cooling from the (deflected) last row of holes.

3. At constant coolant flow per unit heat transfer area, arrays with low hole density consistently yield higher average heat transfer than the array with more holes per unit area.

4. For the two arrays with equal hole density ((4, 8) and (8, 4)), the former consistently produces lower average heat transfer. The authors attribute this to streamwise bands of low heat transfer (which would correspond to hot streaks in a "real" cooling application), which occur when the spanwise hole spacing is large.

References

Behbahani, A. I., and Goldstein, R. J., 1983, "Local Heat Transfer to Staggered Arrays of Impinging Circular Air Jets," ASME *Journal of Engineering for Power*, Vol. 105, pp. 354-360.

Bouchez, J. P., and Goldstein, R. J., 1975, "Impingement Cooling From a Circular Jet in a Crossflow," *International Journal of Heat and Mass Transfer*, Vol. 18, pp. 719-730.

Chance, J. L., 1984, "Experimental Investigation of Air Impingement Heat Transfer Under an Array of Round Jets," *Tappi*, Vol. 57, No. 6, pp. 108-112.

Cole, G. H., 1978, "Heat Transfer to Arrays of Impinging Jets in a Crossflow," Mechanical and Industrial Engineering Department, Clarkson University, Potsdam, NY, Report No. MIE-038.

Florschuetz, L. W., Berry, R. A., and Metzger, D. E., 1980, "Periodic Streamwise Variations of Heat Transfer Coefficients for Inline and Staggered Arrays of Circular Jets With Crossflow of Spent Air," ASME *Journal of Heat Transfer*, Vol. 102, pp. 132-137.

Florschuetz, L. W., Truman, C. R., and Metzger, D. E., 1981, "Streamwise Flow and Heat Transfer Distributions for Jet Array Impingement With Crossflow," ASME *Journal of Heat Transfer*, Vol. 103, pp. 337-342.

Florschuetz, L. W., Metzger, D. E., and Su, C. C., 1984, "Heat Transfer Characteristics of Jet Array Impingement With Initial Crossflow," ASME *Journal of Heat Transfer*, Vol. 106, pp. 34-41.

Gardon, R., and Cobonpue, J., 1962, "Heat Transfer Between a Flat Plate and Jets of Air Impinging on It," in: *International Developments in Heat Transfer*, ASME, New York, pp. 454-460.

Gardon, R., and Akfirat, J., 1965, "Heat Transfer Characteristics of Impinging Two-Dimensional Air Jets," ASME Paper No. 65-HT-20.

Gaunter, J. W., and Livingood, J. N. B., 1973, "Engine Investigation of an Impingement-Cooled Turbine Rotor Blade," NASA TM X-2791.

Gaunter, J. W., Gladden, H. J., Gaunter, D. J., and Yeh, F. C., 1974, "Crossflow Effects of Impingement Cooling of a Turbine Blade," NASA TM X-3029.

Hollworth, B. R., and Bowley, W. W., 1975, "Heat Transfer Characteristics of an Impinging Jet in a Crossflow," ASME Paper No. 75-WA/HT-100.

Hollworth, B. R., and Berry, R. D., 1978, "Heat Transfer From Arrays of Impinging Jets With Large Jet-to-Jet Spacing," ASME *Journal of Heat Transfer*, Vol. 100, No. 2, pp. 352-357.

Hollworth, B. R., and Gero, L., 1985, "Entrainment Effects on Impingment Heat Transfer," ASME *Journal of Heat Transfer*, Vol. 107, pp. 910-915.

Holman, J. P., 1978, *Experimental Methods for Engineers*, 3rd ed., McGraw-Hill, New York, pp. 44-51.

Kercher, D. M., and Tabakoff, W., 1970, "Heat Transfer by a Square Array of Round Air Jets Impinging Perpendicular to a Flat Surface Including the Effect of Spent Air," ASME *Journal of Engineering for Power*, Vol. 92, No. 1, pp. 73-82.

Kreith, F., 1973, *Principles of Heat Transfer*, 3rd ed., Intext, New York-London, p. 636.

Metzger, D. E., and Korstad, R. J., 1971, "Effects of Crossflow on Impingement Heat Transfer," ASME Paper No. 71-GT-1.

Metzger, D. E., Florschuetz, L. W., Takeuchi, D. I., Behee, R. D., and Berry, R. A., 1978, "Heat Transfer Characteristics for Inline and Staggered Arrays of Circular Jets With Crossflow of Spent Air," *Proceedings of Gas Turbine Heat Transfer Conference*, ASME Winter Annual Meeting, San Francisco, Dec. 1978, pp. 9-19.

Saad, N. R., Mujumdar, A. S., Abdelmessah, W., and Douglas, W. J., 1980, "Local Heat Transfer Characteristics for Staggered Arrays of Circular Impinging Jets With Crossflow of Spent Air," ASME Paper No. 80-HT-23.

Sparrow, E. M., Goldstein, R. J., and Rouf, M. A., 1975, "Effects of Nozzle-Surface Separation Distance on Impingement Heat Transfer for a Jet in a Crossflow," ASME *Journal of Heat Transfer*, Vol. 97, pp. 528-533.

Downloaded 01 Jun 2010 to 171.66.16.57. Redistribution subject to ASME license or copyright; see http://www.asme.org/terms/Terms_Use.cfm

S. Wittig
Mem. ASME

V. Scherer

Lehrstuhl und Institut für Thermische
Strömungsmaschinen,
Universität Karlsruhe (TH),
Karlsruhe, Federal Republic of Germany

Heat Transfer Measurements Downstream of a Two-Dimensional Jet Entering a Crossflow

Nusselt and Stanton numbers have been evaluated in and behind the recirculating zone produced by a two-dimensional jet entering a crossflow. The momentum flux ratio of the jet to the main flow was varied from 1.44–8.4 and measurements of the static pressure distribution and of the flow field by a five-hole probe were performed. A relation between the location of the reattachment point of the flow and the maximum of heat transfer was observed. Comparisons with available data are made. The experiments are intended for the verification of calculational codes.

Introduction

The knowledge of the parameters influencing the heat transfer mechanism in separated flows is of dominant interest in various practical engineering applications. The utilization of numerical codes for the prediction of the heat transfer in separated flows is dependent on reliable experimental data with well-known boundary conditions. In the present study, the perpendicular injection of a two-dimensional jet into a crossflow has been examined. This configuration, for example, can be considered as a first approximation of the mixing region of a combustion chamber.

Velocity and temperature fields in similar experimental setups have been measured by our group and by various other authors [1, 2]. Also, the influence on film cooling effectiveness of a mixing jet entering a combustion chamber is well known [3, 4]. However, the heat transfer is more difficult to determine. In the present study the recirculating zone is induced by a jet entering the main flow. Experimental data concerning this problem are scarce. However, similar observations can be derived from impinging jets. Kumuda et al. [5], for example, examined heat transfer from a free jet to a flat plate. An inclination angle of 30–60 deg was realized in the study with crossflow not present. Oyakawa and Mabuchi [6] investigated heat transfer by a dual jet discharging into a rectangular duct. The flow separated and an augmentation of heat transfer was detected due to the reattachment effect of the jets. Several other recent studies were concerned with impinging jet experiments with and without crossflow [7, 8]. The heat transfer pattern—in contrast to the present study—was determined at the wall opposite the entering jet.

In spite of the differences in the experimental studies cited, the same general features for heat transfer in separated flows with reattachment can be detected: The heat transfer coefficients show a maximum close to the reattachment point of the flow, with peak values higher than those for turbulent boundary layers. This contradicts the Reynolds analogy for heat transfer.

Recent studies detected the point of maximum heat transfer well upstream of reattachment [9]. Suzuki et al. also showed that the maximum Nusselt number can be correlated with the turbulence intensity measured close to the wall ($y = 4$ mm). This leads to the conclusion that the structure of turbulence in the vicinity of the wall determines the heat transfer process. Inside the separation bubble itself, heat transfer rates are relatively low. Vogel and Eaton [10] compared the behavior of the boundary layer within the recirculating zone with the development of a laminar boundary layer. Downstream of reattachment a turbulent boundary layer reoccurs. Typical flat plate values were obtained at a certain distance downstream. Bradshaw and Wong [11] detected a disturbed boundary layer far downstream of reattachment. The wake component especially is affected by this disturbance.

The maximum Nusselt number can be correlated with the main flow or the jet Reynolds number. Experiments concerned with impinging jets on a flat plate without crossflow show a 0.58 exponential dependence on jet Reynolds number [5]. Additional influence parameters on the heat transfer mechanism such as the geometry and the turbulence level of the flow also play an important role.

In the present study, a similar behavior of heat transfer coefficients can be expected: a distinct peak value close to the reattachment of the flow, low values in the separation bubble itself, and a fast recovery to turbulent flat plate values downstream of reattachment. From the previous studies of our group [1, 12], it can be expected that as a second nondimensional scale factor besides the Reynolds number the momentum flux ratio has to be considered. This parameter determines the length of the separation bubble.

The goal of the present study, therefore, was to generate detailed flow and heat transfer measurements outside and within the separation bubble induced by a jet entering a

---

Contributed by the Gas Turbine Division of The American Society of Mechanical Engineers and presented at the 32nd International Gas Turbine Conference and Exhibit, Anaheim, California, May 31–June 4, 1987. Manuscript received at ASME Headquarters February 10, 1987. Paper No. 87-GT-119.

Copyright © 1987 by ASME

Downloaded 01 Jun 2010 to 171.66.16.57. Redistribution subject to ASME license or copyright; see http://www.asme.org/terms/Terms_Use.cfm

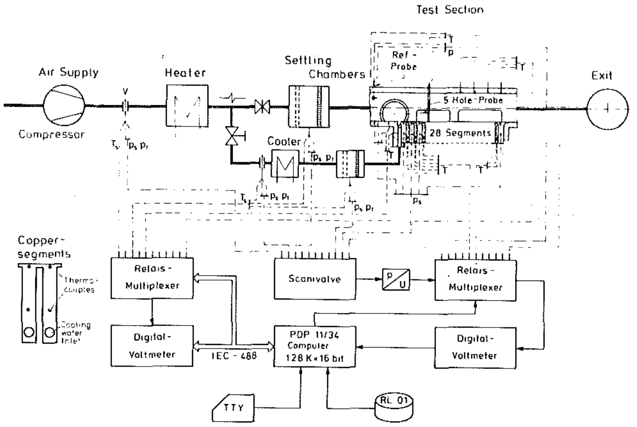

Fig. 1 Schematic layout of test rig

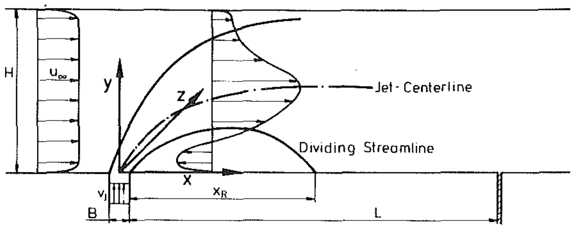

Fig. 2 Test section and notation

crossflow. The results were to be compared with extended codes derived from previous studies [1, 12, 16].

Experimental Apparatus

The major components of the experimental setup have been described previously by Rüd et al. [13, 14]. The setup consists of an electrical heater, the plenum chambers, and the test section itself (see Fig. 1). After heating, the air is divided into the main flow and the jet. Mass flow rates of both flows are measured by orifice meters and are individually controlled. Settling chambers are installed for each air stream and thus uniform flow distributions at the outlets of the connecting ducts to the test section are assured. The mixing jet, which can be cooled or heated, enters the test section through a slot of 125 × 6 mm. The slot spans the distance between the side walls of the rig. The channel height and length were fixed at 95 and 800 mm, respectively.

The test section is equipped with a 440 × 125 mm copper plate with an integral surface (see Fig. 1). It is divided into 28 insulated segments, each of which is cooled separately. Water is used as the cooling fluid, and is held at constant temperature with the aid of a thermostat. The mass flow rate in each segment can be controlled individually by valves. This cooling process ensures a constant flat plate temperature. On the other hand, the segmentation of the plate guarantees the local resolution of the heat transfer rates downstream of the injection slot. The heat flux within the cooled segments is derived from one-dimensional heat conduction analysis, i. e., from the temperature difference determined by thermocouple measurements in the segments. The Nusselt and Stanton numbers are obtained from the local heat flux. The assumption of one-dimensional heat conduction is supported by finite element heat conduction analysis. Measurements were performed of the static pressure distribution using static pressure taps drilled into the copper segments. Velocity and temperature profiles can be taken over the channel height at 10 different streamwise locations along the centerline of the channel. To check the two dimensionality of the flow, velocity profiles over the channel height and width were obtained.

The flow field was determined by a spherical five-hole probe with a sphere diameter of 2.9 mm and pressure tap diameters of 0.3 mm. A standardized calibration procedure [12] guarantees a fast conversion of the measured pressures into the three velocity components u, v, w. Data acquisition was accomplished with the aid of a "Scanivalve" and relay-multiplexer, both controlled by a minicomputer (PDP-11/34) as indicated in Fig. 1.

Experimental Conditions

In the present study, the momentum flux ratio J was varied from 1.44–8.4. The mean velocity determined with the orifice meters has been used. The typical characteristics of the flow are illustrated in Fig. 2. The main flow temperature was constant for each of the experimental runs, but varied between runs in the range from 104 to 185°C. The temperature of the mixing jet in this series of measurements was slightly below the main flow temperature due to heat losses. The wall temperature was kept nearly constant ($T_w = 30°\text{C}$). Therefore, wall-to-crossflow temperature ratios can be realized from 0.66 to 0.8. The Reynolds number of the crossflow was varied from 6×10^4 to 2×10^5, corresponding to main flow velocities from 17 to 53 m/s. The jet Reynolds numbers were held between 6×10^3 and 2.4×10^4, with resulting velocities of 28 to 107 m/s. The angle between the crossflow and jet axis was 90 deg for the experiments reported here. With previously described experimental conditions the reattachment length varied from 60 to 240 mm.

Nomenclature

B = slot width
cp = specific heat of air
c_p = pressure coefficient $= 2 \cdot (p_s - p_\infty)/(\rho_\infty u_\infty^2)$
H = channel height
J = momentum ratio $= \rho_j \bar{v}_j^2 / \rho_\infty \bar{u}^2$
L = copper plate length
Nu_H = Nusselt number $= \mathrm{St} \cdot \mathrm{Re}_H \mathrm{Pr}$
p = pressure
Pr = Prandtl number
$\dot{q}$ = heat flux
Re_j = jet Reynolds number $= \bar{v}_j \cdot B/\nu_j$
Re_H = Reynolds number based on channel height $= u_\infty H/\nu_\infty$
Re_{x_R} = Reynolds number based on distance from reattachment of the flow $= u_\infty (x - x_R)/\nu_\infty$
St = Stanton number $= \dot{q}_w/\rho_\infty u_\infty cp(T_{t,\infty} - T_w)$
T = temperature
$\bar{u}$, $\bar{v}_j$ = mean values of velocity determined by orifice meters
u, v, w = velocity in x, y, z direction
x = distance from center of slot
x_R = reattachment distance
x^* = distance where $x = 1/2 \cdot (c_{p,\max} - c_{p,\min})$
y = distance from the wall
z = direction at right angles to main flow direction
ξ = unheated starting length
ρ = density

Subscripts

∞ = freestream
j = jet
s = static
t = total
w = wall

Downloaded 01 Jun 2010 to 171.66.16.57. Redistribution subject to ASME license or copyright; see http://www.asme.org/terms/Terms_Use.cfm

Heat transfer coefficients are presented in terms of Stanton or Nusselt numbers with the inlet conditions used for reference (see Fig. 2).

$$\mathrm{St}=\frac{\dot{q}_w}{u_\infty \rho_\infty cp(T_{t,\infty}-T_w)} \tag{1}$$

For experiments with jet injection, the Nusselt number was used

$$\mathrm{Nu}_H=\mathrm{St}\ \mathrm{Re}_H\mathrm{Pr} \tag{2}$$

The channel height serves as a characteristic length scale, with the Prandtl number assumed to be 0.71.

Results and Discussion

Two Dimensionality of the Flow. In verifying the assumption of two-dimensional flow, detailed velocity and total pressure profile measurement were necessary. First, the main flow and the flow in the slot were examined separately. Main flow profiles in front of and behind the slot for the case of $J=0$ were measured with a pitot probe in x and y directions. For a traverse the measured profiles show deviations below 1 percent. A traverse across the jet length gives agreement within the range of ±1.2 percent. The existing boundary layers at the channel walls, of course, yield larger discrepancies in these regions. Velocity profiles along the centerline of the channel were determined at various distances upstream and downstream of the slot with the jet and crossflow present. The w components obtained are negligible. Typical values show data uncertainty of ± 0.5 m/s. This corresponds to flow angles of ± 0.5 deg. Additional velocity profiles were measured at off-centerline positions ($z/H=0$, ± 0.42) at $x/H=1.05$, 2.3. A satisfactory two dimensionality was found, except toward the end of the recirculating region.

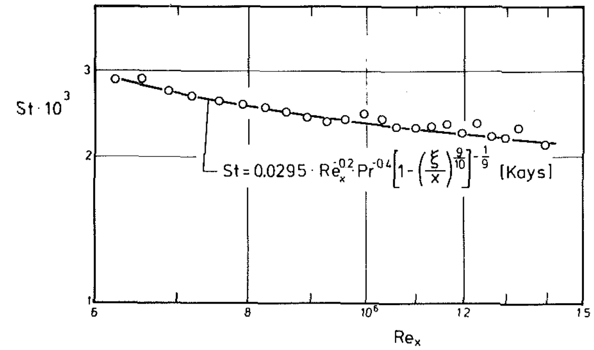

Fig. 3 Stanton number for flat plate experiments

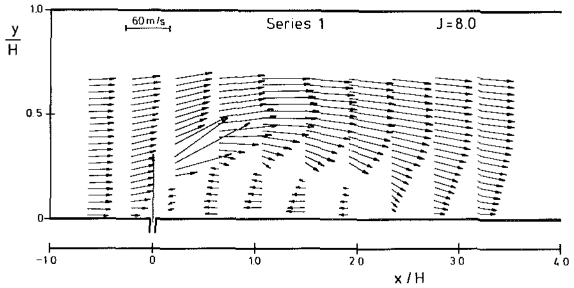

Fig. 4 Velocity vector diagram

To validate the heat transfer data, initial measurements were taken without the jet. The results obtained agree quite well with those recently reported by our group [13, 14] and Kays' theoretical correlation [15] (see Fig. 3). Boundary layer measurements at $x/H=0.21$ were used to calculate an effective boundary layer origin. In addition, the unheated starting length upstream of the copper plate has been taken into account. The results illustrate that, with the present experimental apparatus, reliable data for heat transfer coefficients were obtained.

Flow Field Distribution. Two different fluid temperature levels were chosen for the first experimental series ($T\simeq 105$°C, $T\simeq 175$°C). Of dominant interest was the influence of the momentum flux ratio on the developing flow field. The experimental conditions are summarized in Table 1. The velocity field was determined for each experimental run using the five-hole probe described earlier. A typical velocity vector distribution for $J=8.0$ is shown in Fig. 4. The shape of the recirculating zone is evident. The influence of the separation bubble on the velocity profiles upstream and downstream of the injection slot can be recognized quite well. Due to the displacement effect of the separation bubble, the velocity vectors are deflected in the first measurement plane at $x/H=-0.63$. The jet penetration into the flow leads to a velocity decay on the lower channel wall and to relatively high velocities in the center of the channel. Figures 5 and 6 illustrate the components of velocity vectors of Series 1 with their dependence on the momentum flux ratio. For high-momentum flux ratios the jet penetration height is strong (see $x/H=0.21$, 0.63) and

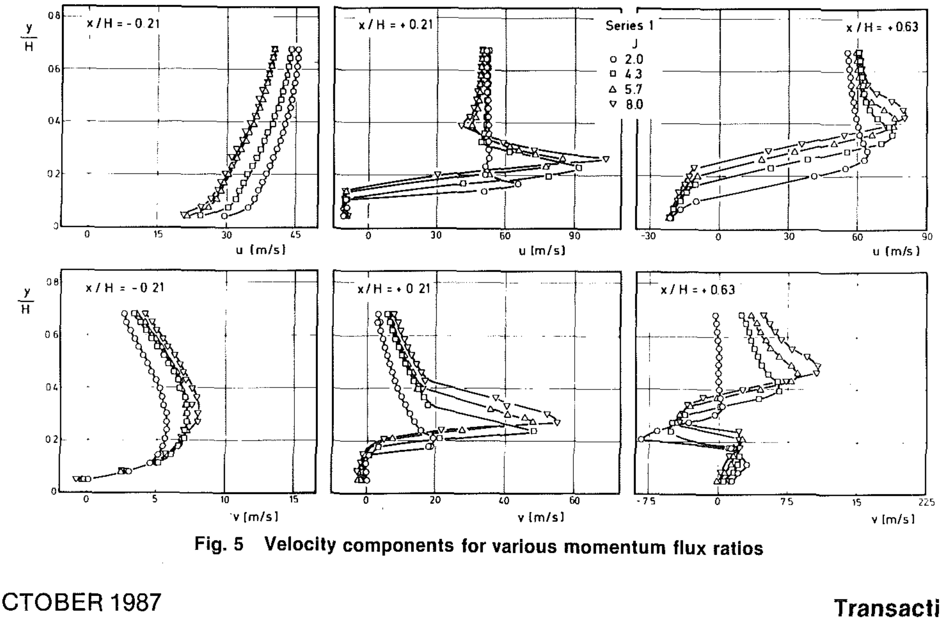

Fig. 5 Velocity components for various momentum flux ratios

Downloaded 01 Jun 2010 to 171.66.16.57. Redistribution subject to ASME license or copyright; see http://www.asme.org/terms/Terms_Use.cfm

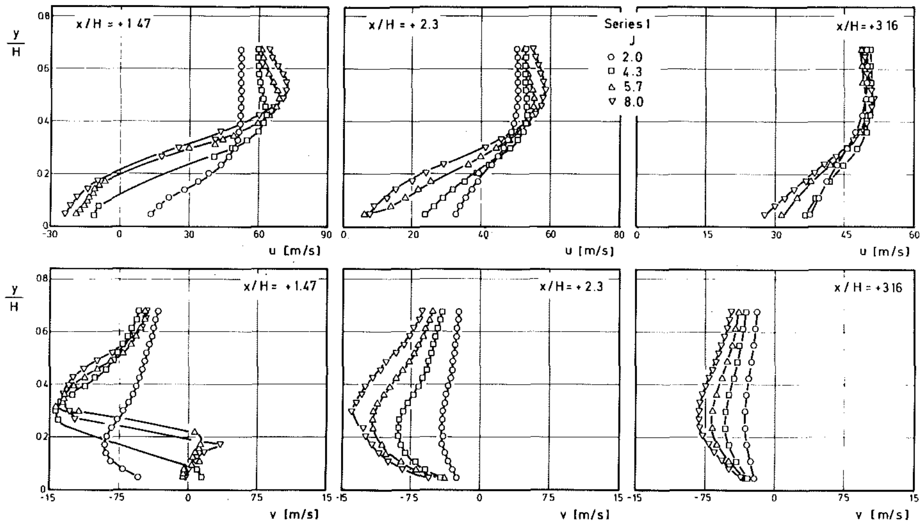

Fig. 6 Velocity components for various momentum flux ratios

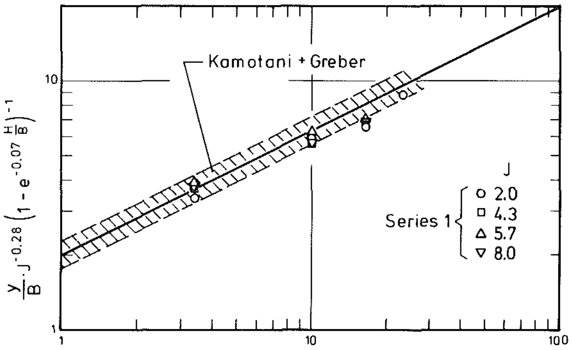

Fig. 7 Measured jet centerlines compared with the correlation of Kamotani and Greber

Table 1 Experimental conditions for experimental Series 1 and 2

	J	$Re_H \cdot 10^{-5}$	$Re_j \cdot 10^{-4}$	T_∞ [°C]	T_j [°C]	
○	2.0	1.71	1.44	104	97	SERIES 1
□	4.3	1.62	1.98	105	101	
△	5.7	1.37	1.97	112	107	
▽	8.0	1.33	2.24	116	111	
●	2.0	1.46	1.25	162	148	SERIES 2
■	3.5	1.25	1.44	169	156	
▲	5.4	1.05	1.51	167	155	
▼	7.3	0.88	1.47	184	171	

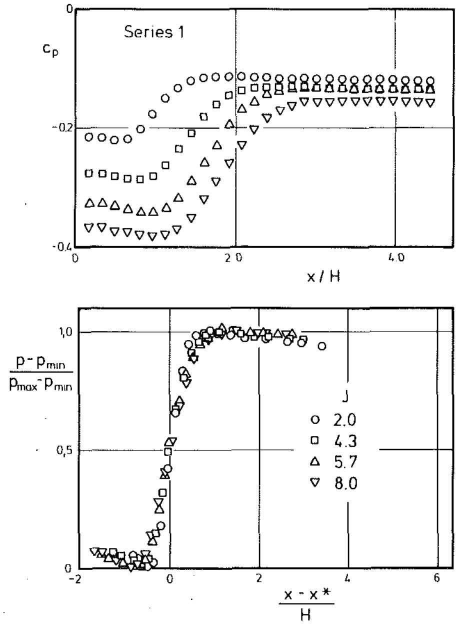

Fig. 8 (a) Influence of momentum flux ratio on static pressure distribution; (b) similarities in pressure distribution (Series 1)

the reattachment length increases ($x/H = 1.47$). The strong upstream influence of the separation bubble can be detected considering the v component at $x/H = -0.21$. With increasing momentum flux ratio, the v component increases strongly in the region of $0.1 < y/H < 0.5$. The low v velocities ($v < 3$ m/s) at the plane $x/H = 3.16$ indicate a nearly parallel flow for the case of $J = 2.0$, whereas for $J = 8.0$ the flow is still strongly disturbed. For comparison of the present results with values found in the literature [16], the location of the jet's velocity maximum, the jet centerline, was determined. Kamotani and Greber [2] have correlated the jet centerline as dependent on channel height-to-slot width ratio H/B and momentum flux ratio J. The lowest momentum flux ratio measured by Kamotani and Greber was 8. Most of the experimental data in the present study were below this value. Within this restriction, relatively good agreement is observed as shown in Fig. 7. These results are in agreement with another internal study conducted in the context of the work published earlier [16].

In trying to determine the flow characterisitcs, the static pressure distribution downstream of the injection slot is of interest. The pressure distribution in terms of pressure coefficients is plotted versus nondimensional x coordinate for Series 1 and 2 in Figs. 8(*a*) and 9(*a*). Similar results have been detected in backward-facing step experiments [17]. The high injection velocities induce negative pressure coefficients. In the recirculating zone, c_p reaches a minimum before rising to maximum values beyond the point of reattachment [18]. The figures illustrate the downstream shift of the minimum pressure value and the pressure rise with increasing momentum flux ratio. Therefore, the pressure distribution can be taken as reference for the reattachment length x_R. Figures 8(*b*) and 9(*b*) compare modified pressure coefficients, developed by Narayanan et al. [19] for backward-facing step experiments. The coordinate x^* is defined as the distance be-

Downloaded 01 Jun 2010 to 171.66.16.57. Redistribution subject to ASME license or copyright; see http://www.asme.org/terms/Terms_Use.cfm

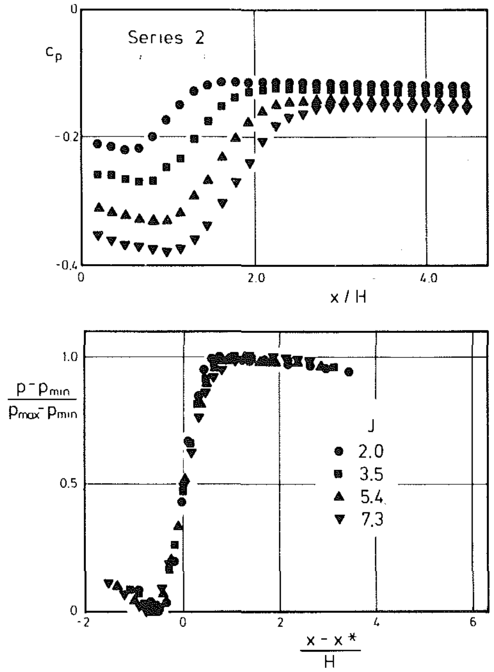

Fig. 9 (*a*) Influence of momentum ratio on static pressure distribution (Series 2); (*b*) similarities in pressure distribution (Series 2)

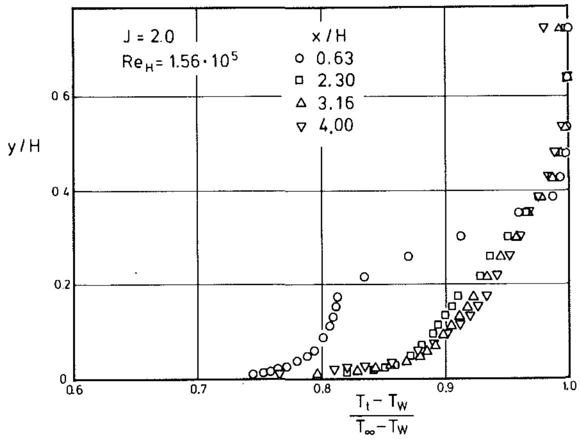

Fig. 10 Influence of momentum flux ratio on temperature distribution

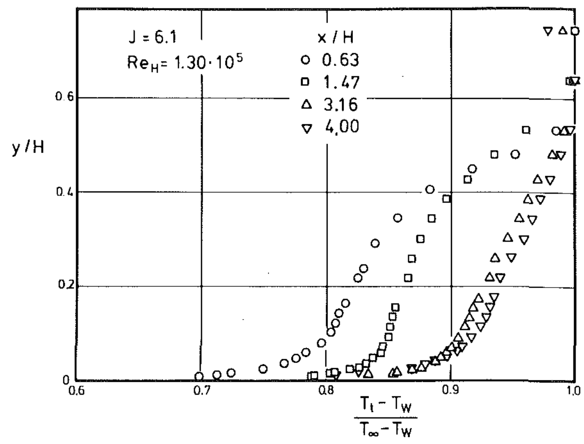

Fig. 11 Influence of momentum flux ratio on temperature distribution

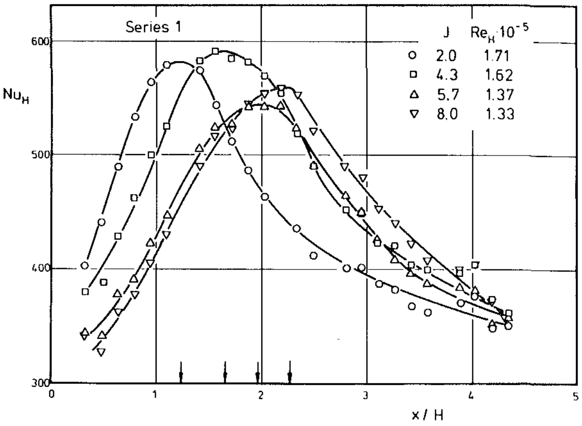

Fig. 12 Nusselt number versus streamwise coordinate (Series 1)

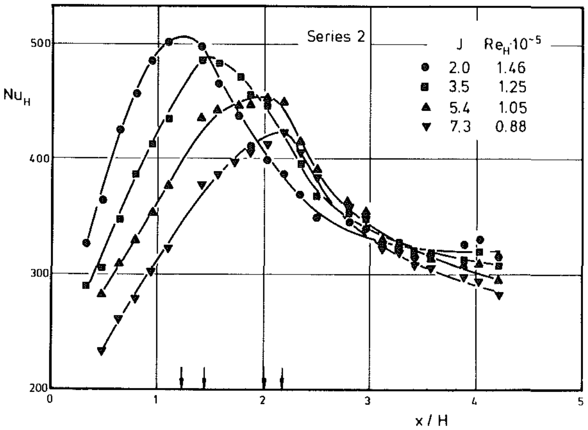

Fig. 13 Nusselt number versus streamwise coordinate (Series 2)

tween the center of the injection slot and the point on the x axis where the pressure rise is equal to $1/2\ (c_{p,\ \max} - c_{p,\ \min})$. This similarity pattern shows close agreement with the present experimental data.

Heat Transfer Measurements. It should be noted that the main emphasis of the present study was directed toward the heat transfer phenomena at the wall. The main flow as well as the mixing jet temperatures were, therefore, kept at similar levels. The momentum flux ratios were adjusted to cover those experienced in practical applications.

In analyzing the temperature field, eight temperature profiles (Figs. 10 and 11) were taken at various distances downstream of the slot, with the momentum flux ratio again as the dominant parameter. In Fig. 10 only the first plane ($x/H = 0.63$) is found within the recirculating zone for a relatively low momentum flux ratio. In contrast, the results plotted in Fig. 11 ($J = 6.1$) show two planes ($x/H = 0.63$, 1.47) which are within the region of separated flow. As can be seen from the profiles, principally two regions with strong temperature gradients exist inside the separation bubble. The first is located close to the wall and the second occurs in the shear layer at the edge of the recirculating zone. The outer region is due to the slightly lower temperature of the jet compared with the crossflow. Downstream of the flow reattachment, strong convective mixing effects are sufficiently high to reduce the outer temperature gradient.

Local Nusselt number profiles are plotted for Series 1 and 2 in Figs. 12 and 13. A distinct maximum of the Nusselt number is observed (indicated by arrows in Figs. 12 and 13), and is displaced downstream with increasing momentum flux ratio. A comparison of the streamwise location of peak Nusselt number with flow field characteristics leads to the conclusion that the location of maximum heat transfer rate occurs close to the point of reattachment of the flow. Therefore, in cor-

Downloaded 01 Jun 2010 to 171.66.16.57. Redistribution subject to ASME license or copyright; see http://www.asme.org/terms/Terms_Use.cfm

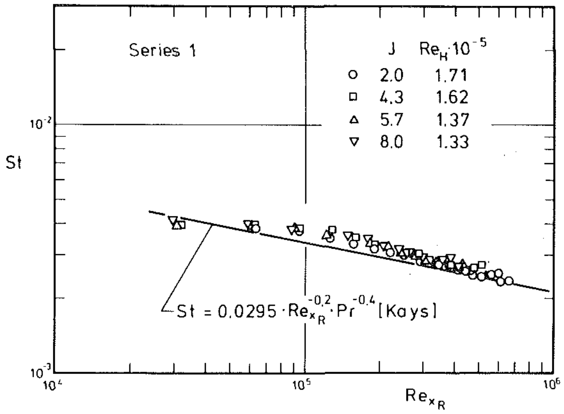

Fig. 14 Stanton number downstream of reattachment (Series 1)

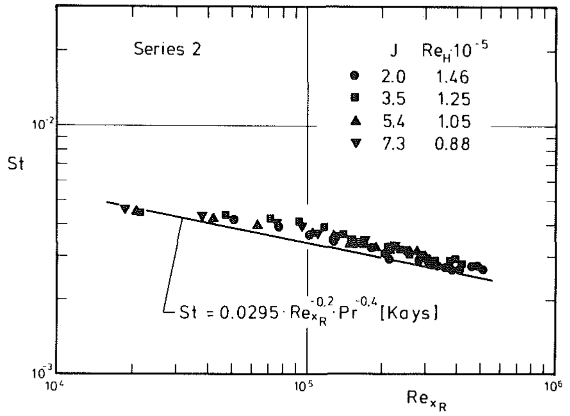

Fig. 15 Stanton number downstream of reattachment (Series 2)

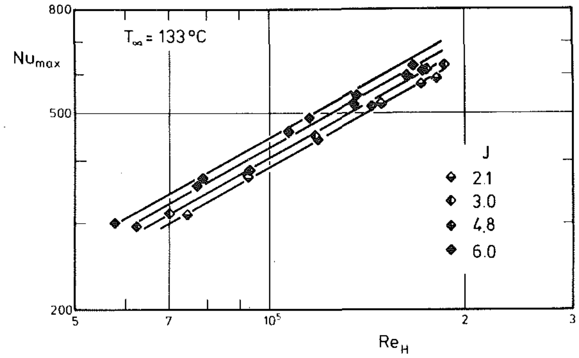

Fig. 16 Influence of momentum flux ratio on maximum Nusselt number

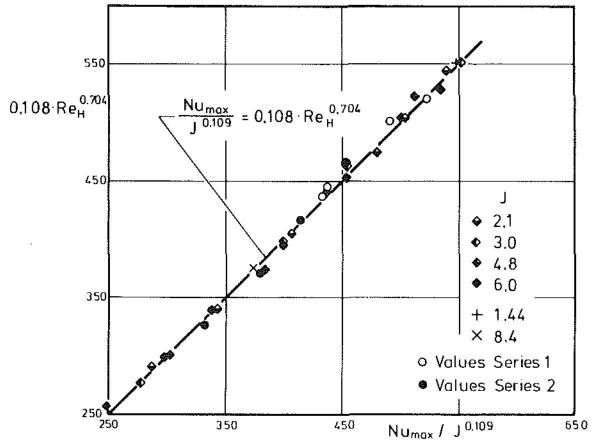

Fig. 17 Comparison of present correlation and measurements

relating the data it seemed to be justified to define the location of maximum heat transfer as the origin of a new turbulent boundary layer and to evaluate the local Stanton number as a function of Re_{x_R} as shown in Figs. 14 and 15. It is interesting to note that this correlation matches the functional dependence suggested by Kays [15] for turbulent boundary layer with constant surface temperature. An even better agreement between experimental results and the theoretical curve may be obtained taking into account Vogel and Eaton's [10] suggestion, that "the recovering boundary layer behaves much like a boundary layer with an unheated starting length upstream of the heated (cooled) section. The effective origin of the redeveloping thermal boundary layer lies downstream of reattachment." This modified approach was not taken here, due to the uncertainty in detecting the reattachment length and in fixing the effective origin of the recovering boundary layer.

In Figs. 12 and 13 no distinct dependence of Nu_{max} on crossflow Reynolds number or momentum flux ratio is obvious. Therefore, additional systematic experiments were performed, with a fixed momentum ratio and with varying crossflow Reynolds numbers. The results are shown in Fig. 16 using a logarithmic scale. They illustrate the increase of the maximum Nusselt number with increasing Reynolds number. With the aid of a least-square-fit analysis a mean exponential factor of 0.704 was obtained. The empirical correlation shows close agreement with the measured data.

$$Nu_{max} = 0.108\, Re_H^{0.704} \cdot J^{\,0.109} \qquad (3)$$

This equation represents all measurements, and also the results of Series 1 and 2, within an accuracy of 3 percent. This is shown in Fig. 17. These results lead to the conclusion, that for relatively small momentum flux ratios—in contrast to impinging jet experiments with crossflow [8]—the behavior of heat transfer coefficients is dominated by the main flow. The maximum Nusselt number depends much more heavily on the crossflow Reynolds number than on the momentum flux ratio and, therefore, on the jet Reynolds number.

Summary

In an attempt to provide a sufficient data base for the numerical analysis of practical applications especially in combustor design, detailed flow and heat transfer measurements downstream of a two-dimensional jet entering a crossflow have been presented. The heat transfer data show the typical characteristics of turbulent flows with separation and reattachment. A local augmentation of heat transfer caused by the reattachment of the jet and a rapid recovery to flat plate values downstream of reattachment were found. The peak Nusselt number has been correlated with the aid of an empirical formula as a function of the main flow Reynolds number and the momentum flux ratio. For low momentum flux ratios the heat transfer mechanism is obviously dominated by the characteristics of the crossflow. The dependence of Nusselt number on momentum flux ratio is much weaker than the dependence on the Reynolds number of the main flow. The reported results can be used for the validation of numerical calculational procedures concerning the heat transfer in separated flows.

Acknowledgments

The authors are indebted to the Deutsche Forschungsgemeinschaft (German Science Foundation) which supports the

Downloaded 01 Jun 2010 to 171.66.16.57. Redistribution subject to ASME license or copyright; see http://www.asme.org/terms/Terms_Use.cfm

work through the "Sonderforschungsbereich 167, High Intensity Combustors." Thanks are due to Dr. K. Rüd, Dr. B. Noll, and Prof. R. E. Mayle for their help and discussion throughout the work.

References

1 Wittig, S., Noll, B., Elbahar, O., and Willibald, U., "Einfluss von Mischluftstrahlen auf die Geschwindigkeits- und Temperaturverteilung in einer Querströmung," *VDI-Bericht*, No. 487, 1983.

2 Kamotani, Y., and Greber, I., "Experiments on Confined Turbulent Jets in Cross Flow," NASA CR-2392, 1974.

3 Köhler, J., and Beer, H., "Effectiveness Measurements for a Cooling Film Disrupted by a Row of Jets," *Int. Comm. Heat Mass Transfer*, Vol. 11, 1984, pp. 505-516.

4 Kadotani, K., and Goldstein, R. J., "On the Nature of Jets Entering a Turbulent Flow, Part B—Film Cooling Performance," ASME *Journal of Engineering for Power*, Vol. 101, 1979, pp. 466-470.

5 Kumuda, M., Mabuchi, I., and Oyakawa, K., "Generalized Correlation of Mass Transfer by Reattached Jet at Stagnation Point on a Plate," *Heat Transfer, Jap. Res.*, Vol. 3, 1974, pp. 93-104.

6 Oyakawa, K., and Mabuchi, I., "Heat Transfer by Dual Jet Discharged Into a Rectangular Duct," *B. JSME*, Vol. 22, 1979, pp. 1416-1423.

7 Goldstein, R. J., and Behbahani, A. I., "Impingement of a Circular Jet With and Without Cross Flow," *Int. J. Heat Mass Transfer*, Vol. 25, 1982, pp. 1377-1382.

8 Chong, Y. K., Hammond, G. P., Macaskill, C., and Ward, J., "An Experimental Study of Two-Dimensional Jet-Impingement Heat/Mass Transfer in a Confined Cross-Flow," *Proceedings of 8th International Heat Transfer Conference*, Vol. 3, San Francisco, CA, 1986, pp. 1225-1230.

9 Suzuki, K., Ida, S., and Sato, T., "Turbulence Measurements Related to Heat Transfer in an Axisymmetric Confined Jet With Laser-Doppler Anemometer," *Proceedings of 4th Symposium on Turbulent Shear Flow*, Karlsruhe, Germany, Sept. 1983, pp. 18.1-18.6.

10 Vogel, J. C., and Eaton, J. K., "Combined Heat Transfer and Fluid Dynamic Measurements Downstream of a Backward-Facing Step," ASME *Journal of Heat Transfer*, Vol. 107, 1985, pp. 923-929.

11 Bradshaw, P., and Wong, F. Y. F., "The Reattachment and Relaxation of a Turbulent Shear Layer," *J. Fluid Mech.*, Vol. 52, 1972, pp. 113-135.

12 Elbahar, O., "Zum Einfluss von Kühlluftstrahlen und Mischzonengeometrie auf die Temperaturprofilentwicklung in Gasturbinen Brennkammern," Diss., Inst. f. Therm. Strömungsmaschinen, Universität Karlsruhe, 1982.

13 Rüd, K., "Transitionale Grenzschichten unter dem Einfluss hoher Freistromturbulenz, intensiver Wandkühlung und starken Druckgradienten in Heissgasströmungen," Diss., Inst. f. Therm. Strömungsmaschinen, Universität Karlsruhe, 1985.

14 Rüd, K., and Wittig, S., "Laminar and Transitional Boundary Layer Structures in Accelerating Flow With Heat Transfer," ASME JOURNAL OF TURBOMACHINERY, Vol. 108, 1986, pp. 116-123.

15 Kays, W. M., *Convective Heat and Mass Transfer*, McGraw-Hill, New York, 1966.

16 Wittig, S. L. K., Elbahar, O. M. F., and Noll, B. E., "Temperature Profile Development in Turbulent Mixing of Coolant Jets With a Confined Hot Crossflow," ASME *Journal of Engineering for Gas Turbines and Power*, Vol. 106, 1984, pp. 193-197.

17 Moss, W. D., and Baker, S., "Re-circulating Flows Associated With Two-Dimensional Steps," *Aeronautical Quarterly*, Vol. 3, 1980, pp. 151-172.

18 Kottke, V., "Strömung, Stoff-, Wärme-und Impulsübertragung in lokalen Ablösegebieten," *Fortschr.-Ber. VDI-Z.*, Reihe 7, No. 77, 1983.

19 Narayanan, M. A. B., Khadgi, Y. N., and Viswanath, P. R., "Similarities in Pressure Distributions in Separated Flows Behind Backward-Facing Steps," *Aeronautical Quarterly*, Vol. 25, 1974, pp. 305-312.

Downloaded 01 Jun 2010 to 171.66.16.57. Redistribution subject to ASME license or copyright; see http://www.asme.org/terms/Terms_Use.cfm

Prediction of Film Cooling by a Row of Holes With a Two-Dimensional Boundary-Layer Procedure

B. Schönung

W. Rodi

Institute of Hydromechanics,
University of Karlsruhe,
Karlsruhe, Federal Republic of Germany

The present paper describes predictions of film cooling by a row of holes. The calculations have been performed by a two-dimensional boundary-layer code with special modifications that account for the basically three-dimensional, elliptic nature of the flow after injection. The elliptic reverse-flow region near the injection is leapt over and new boundary-layer profiles are set up after the blowing region. They take into account the oncoming boundary layer as well as the characteristics of the injected jets. The three dimensionality of the flow, which is very strong near the injection and decreases further downstream, is modeled by so-called dispersion terms, which are added to the two-dimensional boundary-layer equations. These terms describe additional mixing by the laterally nonuniform flow. Information on the modeling of the profiles after injection and of the dispersion terms has been extracted from three-dimensional fully elliptic calculations for specific flow configurations. The modified two-dimensional boundary-layer equations are solved by a forward-marching finite-volume method. A coordinate system is used that stretches with the growth of the boundary layer. The turbulent stresses and heat fluxes are obtained from the k–ϵ *turbulence model. Results are given for flows over flat plates as well as for flows over gas turbine blades for different injection angles, relative spacings, blowing rates, and injection temperatures. The predicted cooling effectiveness and heat transfer coefficients are compared with experimental data and show generally fairly good agreement.*

Introduction

The thermal efficiency of gas turbines can be improved by increasing the temperature at the inlet to the turbine section. With higher and higher inlet temperatures a reasonable lifetime of turbine blades can be ensured only by protecting them from the hot gas stream. For this, basically two different cooling methods are available. One method is internal convection cooling, which is often insufficient because of the relatively poor heat transfer characteristics of air. For especially exposed blades some means must therefore be taken to reduce the heat transfer from the hot gas to the outside surface of the blade. This can be achieved by film cooling, a method in which cooling air is injected into the mainstream in order to establish a protecting film on the blade surface. Because of design considerations, injection through slots is usually not possible and the cooling air must be introduced through discrete holes. A typical flow configuration for film cooling by a row of holes is shown in Fig 1. The injected jets generate a complex three-dimensional flow, in which flow reversal can occur near injection. Apart from the characteristics of the oncoming two-dimensional boundary layer, the flow resulting from the injection depends mainly on the injection angle α, the relative hole spacing s/D, the blowing rate $M = \rho_2 U_2 / \rho_e U_e$, and the diameter of the injection holes. It is primarily these parameters that have to be optimized in the design of a film cooling configuration. The influence of most of them has been studied separately, mainly for injection into boundary layers on flat plates. Under realistic conditions, however, systematic experimental

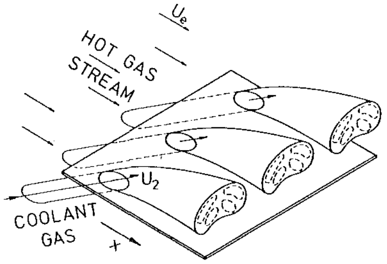

Fig. 1 **Flow configuration after injection by a row of holes**

Contributed by the Gas Turbine Division of The American Society of Mechanical Engineers and presented at the 32nd International Gas Turbine Conference and Exhibit, Anaheim, California, May 31–June 4, 1987. Manuscript received at ASME Headquarters February 10, 1987. Paper No. 87-GT-122.

Copyright © 1987 by ASME

Downloaded 01 Jun 2010 to 171.66.16.57. Redistribution subject to ASME license or copyright; see http://www.asme.org/terms/Terms_Use.cfm

parameter studies are very expensive, so that design engineers have a great need for prediction procedures.

As the flow field is strongly three dimensional in the vicinity of the injection holes, basically a three-dimensional calculation procedure is necessary. For injection through discrete tangential slots, Patankar et al. [1] presented such a procedure. Patankar et al. [2] analyzed the injection at high blowing rates from a single hole and Khan et al. [3] predicted the injection through a row of holes. In a series of publications, Bergeles et al. [4-6] analyzed the three-dimensional discrete-hole cooling process. As their method is based on a partially parabolic calculation procedure, it cannot handle regions with reverse flow. They calculated laminar as well as turbulent flows for single-row and multirow cooling configurations. Detailed computational studies of film cooling by a row of holes have been presented by Demuren [7], Demuren and Rodi [8], and Demuren et al. [9]. These authors used a locally elliptic calculation procedure, which can be applied also at higher blowing rates where regions with flow reversal occur. In their systematic study the last authors [9] analyzed the influence of the injection angle, the relative spacing, and the blowing rate on the cooling effectiveness with their three-dimensional calculation method.

For the three-dimensional calculation of film-cooling processes, numerical grids with 20,000 to 40,000 grid nodes have been used. With these, converged solutions required between 30 and 90 min of computing time (e.g., on a CDC 6600, IBM 360/195 or Siemens 7881). This time is far too long for carrying out parameter studies for the optimization of film cooling configurations. For such parameter studies, faster prediction methods are required, such as suitably extended two-dimensional boundary-layer procedures. Up to now only a few attempts have been made to extend boundary-layer codes for the prediction of film cooling processes. Herring [10] treated the boundary layer as a laterally averaged flow and introduced the effects of lateral nonuniformity through additional momentum and energy source terms. He obtained the nonuniformity interaction terms by an integral method, for which he assumed locally uniform flow, axisymmetry of the jets, and negligible interaction between the jets and the wall. The comparison with his own experimental results showed reasonable agreement, but only for blowing rates M smaller than 1. Crawford et al. [11] extended their boundary-layer program STAN5 by an injection model, which they derived with the aid of a one-dimensional momentum and energy balance. This model cannot account for the fact that because of the blockage effect of the injected jet the fluid velocity above the injected cooling jet can be higher than in the free stream. This overshoot cannot be neglected for higher blowing angles. Crawford et al. [11] modeled the additional lateral mixing by augmentation of the mixing length in their turbulence model. They compared their results with measurements for full-coverage film cooling at a blowing angle of $\alpha = 30$ deg and for two different relative spacings $s/D = 5$ and $s/D = 10$. The blowing rates were always below 0.8; the predicted Stanton numbers compared well with experimental data. Miller and Crawford [12] extended this work by applying basically the same film cooling model to injection from a row of holes, calculating also the film cooling effectiveness. For each cooling configuration, they had to adjust the two constants in their film cooling model. They compared their results for blowing rates smaller than 1, relative spacings larger than 2 and injection angles smaller than 45 deg; for these configurations they obtained good agreement with experimental data.

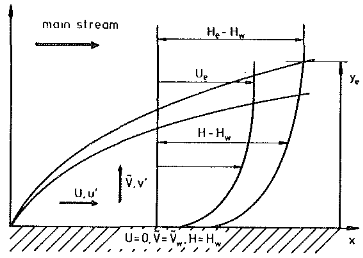

Fig. 2 (*x*, *y*) coordinate system

The present paper describes a new film cooling model for cooling by a row of holes which was incorporated into a two-dimensional boundary-layer procedure. First the governing mean-flow equations and the turbulence model are given. Then the special modifications are described, which account for the elliptic nature of the flow after the injection (injection model) and for the three dimensionality of the flow (dispersion model). The numerical solution procedure is given and results are presented for flows over flat plates as well as for flows over model gas turbine blades.

Boundary-Layer Equations

Mean-Flow Equations. The time-averaged boundary-layer equations in a plane, Cartesian coordinate system (see Fig. 2) may be written for two-dimensional flows as:

Nomenclature

$c_\mu, c_{\epsilon 1}, c_{\epsilon 2}, \sigma_k, \sigma_\epsilon$ = constants of the turbulence model
D = hole diameter
D_ϕ = dispersion term
f_μ, f_1, f_2 = damping functions of the turbulence model
H = total enthalpy
h = static enthalpy
I = momentum
k = turbulent kinetic energy
M = blowing rate
P = pressure
Pr, Pr_t = laminar/turbulent Prandtl number
q_w = wall heat flux
R = gas constant
Re_y, Re_T = turbulent Reynolds numbers
s = spacing
T = temperature
Tu = degree of turbulence, percent
U, V, W = velocity components
$\tilde{V}$ = mass("Favre")-averaged V velocity
x, y, z = Cartesian coordinates
α = injection angle
$\bar{\alpha}$ = laterally averaged heat transfer coefficient
Γ = diffusivity
δ = boundary-layer thickness
ϵ = dissipation rate
$\bar{\eta}$ = laterally averaged cooling effectiveness
θ = dimensionless temperature, tracer
μ = dynamic viscosity
μ_t = eddy viscosity
ξ, η = coordinates
ρ = density

Subscripts

e = free-stream value
prof = value after injection region
w = value on the wall
2 = injection value

Downloaded 01 Jun 2010 to 171.66.16.57. Redistribution subject to ASME license or copyright; see http://www.asme.org/terms/Terms_Use.cfm

Continuity equation

$$\frac{\partial}{\partial x}(\rho U)+\frac{\partial}{\partial y}(\rho\tilde{V})=0 \tag{1}$$

Momentum equation

$$\frac{\partial}{\partial x}(\rho UU)+\frac{\partial}{\partial y}(\rho\tilde{V}U)=-\frac{dP}{dx}+\frac{\partial}{\partial y}\left(\mu\frac{\partial U}{\partial y}-\rho\overline{u'v'}\right) \tag{2}$$

Transport equation for total enthalpy

$$\frac{\partial}{\partial x}(\rho UH)+\frac{\partial}{\partial y}(\rho\tilde{V}H)=\frac{\partial}{\partial y}\left\{\frac{\mu}{\mathrm{Pr}}\frac{\partial H}{\partial y}-\rho\overline{h'v'}\right. \tag{3}$$

$$\left.+U\left[\left(1-\frac{1}{\mathrm{Pr}}\right)\mu\frac{\partial U}{\partial y}-\rho\overline{u'v'}\right]\right\}$$

The total enthalpy is defined as the sum of the static enthalpy, the kinetic energy of the mean flow, and the turbulent kinetic energy. The density is calculated from the ideal-gas law

$$\rho=\frac{P}{RT} \tag{4}$$

which connects the pressure, temperature, and density.

For the solution of the parabolic differential equations (1)-(3), inlet conditions as well as boundary conditions are necessary. The inlet conditions must be known from measurements or from analytical models. Boundary conditions have to be prescribed along the wall and in the free stream.

At the wall ($y = 0$), the conditions are as follows:

$$U=0 \tag{5a}$$

$$\tilde{V}=\tilde{V}_w(x) \tag{5b}$$

$$H=H_w(x) \tag{5c}$$

$$\frac{\partial H}{\partial y}=-q_w(x)\frac{\mathrm{Pr}}{\mu_w} \tag{5d}$$

For the total enthalpy H, either the wall temperature (equation (5*c*)) or the wall heat flux (equation (5*d*)) can be specified. In the free stream ($y = y_e$) the distributions of the velocity and the total enthalpy are given:

$$U=U_e(x) \tag{6a}$$

$$H=H_e=\mathrm{const} \tag{6b}$$

Turbulence Model. The turbulent shear stress $-\rho\overline{u'v'}$ and the heat flux $-\rho\overline{h'v'}$ appearing in the transport equations (2) and (3) are calculated with a low-Reynolds-number version of the k-ϵ turbulence model. This version has been developed by Lam and Bremhorst [13] and is applicable to regions where the molecular viscosity is important. Like the standard k-ϵ model (see [14]), it used the eddy viscosity principle

$$-\rho\overline{u'v'}=\mu_t\frac{\partial U}{\partial y} \tag{7}$$

The eddy viscosity μ_t is related to the turbulent kinetic energy k and to its rate of dissipation ϵ by

$$\mu_t=f_\mu c_\mu \rho\frac{k^2}{\epsilon} \tag{8}$$

where f_μ is a damping function, which simulates the influence of the molecular viscosity. The distribution of k and ϵ over the flow field is determined from the following semi-empirical transport equations:

$$\frac{\partial}{\partial x}(\rho Uk)+\frac{\partial}{\partial y}(\rho\tilde{V}k)=\frac{\partial}{\partial y}\left[\left(\mu+\frac{\mu_t}{\sigma_k}\right)\frac{\partial k}{\partial y}\right]$$

$$+\underbrace{\mu_t\left(\frac{\partial U}{\partial y}\right)^2}_{P_k}-\rho\epsilon \tag{9}$$

$$\frac{\partial}{\partial x}(\rho U\epsilon)+\frac{\partial}{\partial y}(\rho\tilde{V}\epsilon)=\frac{\partial}{\partial y}\left(\mu+\frac{\mu_t}{\sigma_\epsilon}\right)\frac{\partial\epsilon}{\partial y}$$

$$+c_{\epsilon1}f_1\frac{\epsilon}{k}P_k-\rho c_{\epsilon2}f_2\frac{\epsilon^2}{k} \tag{10}$$

$$P_\epsilon$$

The constants used in the k-ϵ model are as follows: $c_\mu = 0.09$, $c_{\epsilon1} = 1.44$, $c_{\epsilon2} = 1.92$, $\sigma_k = 1.0$, $\sigma_\epsilon = 1.3$. As f_μ and the functions f_1 and f_2 simulate the influence of the molecular viscosity, they approach unity in a fully turbulent region. They are defined as follows [13]:

$$f_\mu=(1-\exp(-0.016\,\mathrm{Re}_y))^2\left(1+\frac{19.5}{\mathrm{Re}_T}\right) \tag{11a}$$

$$f_1=1+(0.06/f_\mu)^3 \tag{11b}$$

$$f_2=1-\exp(-\mathrm{Re}_T^2) \tag{11c}$$

where

$$\mathrm{Re}_T=\frac{\rho k^2}{\mu\epsilon}\sim\frac{\mu_t}{\mu} \tag{12a}$$

$$\mathrm{Re}_y=\frac{\rho\sqrt{k}y}{\mu} \tag{12b}$$

In this low-Reynolds-number version of the k-ϵ turbulence model, no wall functions for bridging the viscous sublayer are used as the differential equations are solved up to the wall. The boundary conditions for the turbulent kinetic energy k and its dissipation rate ϵ are:

wall ($y = 0$)

$$k=\frac{\partial\epsilon}{\partial y}=0 \tag{13}$$

free-stream ($y = y_e$)

$$U_e\frac{\partial k_e}{\partial x}=-\epsilon_e \tag{14a}$$

$$U_e\frac{\partial\epsilon_e}{\partial x}=-c_{\epsilon2}\frac{\epsilon_e^2}{k_e} \tag{14b}$$

For the calculation of the turbulent heat flux $-\rho\overline{h'v'}$ the eddy diffusivity concept is used and the eddy diffusivity is related to the eddy viscosity, leading to

$$-\rho\overline{h'v'}=\frac{\mu_t}{\mathrm{Pr}_t}\frac{\partial h}{\partial y} \tag{15}$$

where Pr_t is the turbulent Prandtl number.

Film Cooling Model

Three-Dimensional Elliptic Calculations. The flow generated by the injection of cooling air and sketched in Fig. 1 is normally elliptic and three dimensional. The calculation of this kind of flow with a two-dimensional boundary layer procedure is possible only when the elliptic region can be excluded and the three dimensionality of the flow is accounted for by additional terms. For this reason, two separate extensions of the two-dimensional boundary layer method are introduced in the present film cooling model:

1 Injection Model. The region near the injection is leapt over and new profiles are prescribed at a certain distance behind the blowing region. They take into account the characteristics of the oncoming boundary layer as well as the characteristics of the injected jets.

Downloaded 01 Jun 2010 to 171.66.16.57. Redistribution subject to ASME license or copyright; see http://www.asme.org/terms/Terms_Use.cfm

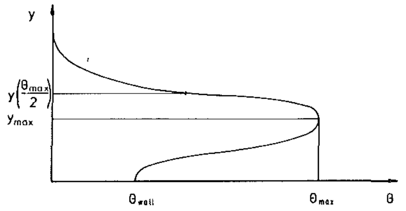

Fig. 3 Tracer profile after the injection

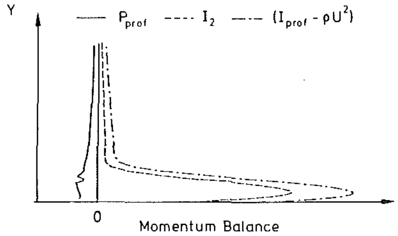

Fig. 4(*a*) Momentum distribution after injection (α = 10 deg, M = 2)

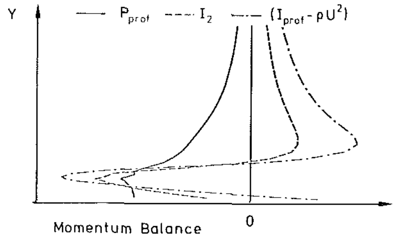

Fig. 4(*b*) Momentum distribution after injection (α = 90 deg, M = 1)

2 Dispersion Model. The three dimensionality of the flow is accounted for by so-called dispersion terms, which simulate the additional lateral mixing.

In order to obtain the information necessary for the development of the two abovementioned models, the three-dimensional calculations of Demuren et al. [9] have been analyzed in detail. In their systematic study, these authors covered the whole parameter range of practical interest for the injection angle (10 deg $\leq \alpha \leq$ 90 deg), the relative spacing ($1.5 \leq s/D \leq 5$), and the blowing rate ($0.5 \leq M \leq 2$). Apart from the continuity and momentum equations, they also solved a transport equation for the dimensionless temperature

$$\theta = \frac{T_{ad} - T_e}{T_2 - T_e} \tag{16}$$

using adiabatic wall boundary conditions. This dimensionless temperature θ can be regarded as a tracer for the trajectory and the spreading of the injected coolant air, and its value on the wall is equal to the adiabatic film cooling effectiveness. Analysis of the three-dimensional calculations has shown that the local distribution of θ can be used to correlate the injection profiles (injection model) and the dispersion terms (dispersion model). For this reason the following transport equation for θ has been introduced into the two-dimensional boundary-layer procedure:

$$\frac{\partial}{\partial x}(\rho U\theta) + \frac{\partial}{\partial y}(\rho \tilde{V}\theta) = \frac{\partial}{\partial y}\left(\frac{\mu_{eff}}{\mathrm{Pr}_{eff}}\frac{\partial \theta}{\partial y}\right) \tag{17}$$

with the boundary conditions

wall (y = 0)*:*

$$\frac{\partial \theta}{\partial y} = 0 \tag{18}$$

free-stream ($y = y_e$)*:*

$$\theta = 0 \tag{19}$$

The predicted θ distribution (always obtained with adiabatic boundary conditions) is for a tracer and is used only for correlating the injection profiles and the dispersion terms. The temperature distribution is calculated with the aid of the total enthalpy and not necessarily with adiabatic boundary conditions.

Injection Model. The x position for prescribing the boundary layer profiles after the injection region has been correlated with the aid of the three-dimensional results and depends on the diameter of the injection tube and its angle with the blade surface. The profiles are prescribed always at the first position, after which the dispersion terms showed similarity behavior. For each three-dimensional test case, the profiles of the velocity component in the mainstream direction and of the tracer were laterally averaged at this position and approximated by analytical functions. A typical profile for the distribution of the tracer θ is shown in Fig. 3. It is approximated by sine and exponential functions, and for its interpolation four constants are necessary for each test case. The prescription of the U velocity was derived wth the aid of the one-dimensional momentum balance

$$I_{\mathrm{prof}}(y) = \rho U^2(y) + I_2(y) - P_{\mathrm{prof}}(y) \tag{20}$$

In this equation the first term on the right-hand side characterizes the momentum distribution of the oncoming boundary layer. The distribution of the injected momentum is described by I_2, while P_{prof} characterizes the pressure distribution, which is not uniform after the injection. Two typical profiles for the injected momentum (I_2), the pressure (P_{prof}), and the difference in momentum with and without blowing ($I_{\mathrm{prof}} - \rho U^2$) are shown in Fig. 4. The profiles in Fig. 4(*a*) characterize the momentum distribution for a film cooling configuration with low injection angle (α = 10 deg) and high blowing rate (M = 2). In Fig. 4(*b*), the corresponding profiles for high injection angle (α = 90 deg) and medium blowing rate (M = 1) are given. Clearly a fundamentally different development of the injected jet can be seen, which behaves in Fig. 4(*a*) like a wall jet while in Fig. 4(*b*) it acts like an obstacle behind which a wake is formed. As with the tracer θ, the distributions of the injected momentum (I_2) and of the pressure (P_{prof}) are approximated by analytical functions. For this, six additional constants are necessary for each test case. The velocity distribution after the injection can then easily be calculated with the aid of equation (20). For the temperature distribution the following relationship is used:

$$T_{\mathrm{prof}}(y) = \theta(y)T_2 + (1 - \theta(y))T(y) \tag{21}$$

from which also the profile for the total enthalpy is calculated. The turbulent kinetic energy k of the injected jet is approximated by a parabolic distribution and superposed to the k profile of the oncoming boundary layer. Using this k distribution and assuming a mixing length distribution (ramp function) in the secondary layer, the profile for the dissipation rate ϵ is finally determined.

The ten constants necessary for generating the momentum and θ distributions are stored in the prediction code for 120 test cases; they are dependent on the injection angle α, the relative spacing s/D, and the blowing rate M. With this set of constants, film cooling configurations with the following parameters can be calculated:

$$\begin{aligned} 0 \text{ deg} < {} & \alpha \leq 90 \text{ deg} \\ 1.2 \leq {} & s/D \leq 10.0 \\ 0.0 \leq {} & M \leq 4.0 \end{aligned}$$

Downloaded 01 Jun 2010 to 171.66.16.57. Redistribution subject to ASME license or copyright; see http://www.asme.org/terms/Terms_Use.cfm

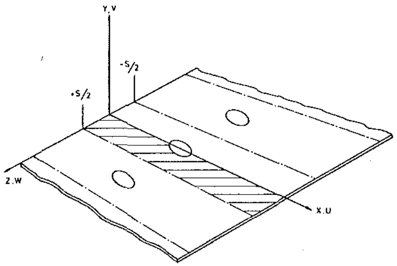

Fig. 5 Geometry for lateral averaging

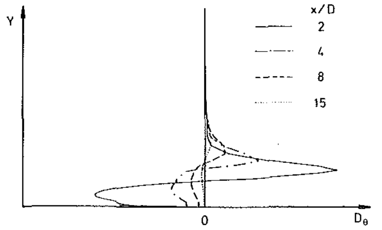

Fig. 6 Distribution of the θ dispersion at different streamwise locations

For a given film cooling configuration, three-dimensional interpolations are performed within the set of stored constants to get the specific values for the generation of the profiles after the blowing region. The generation of the profiles is such that the momentum of the prescribed boundary-layer profiles is always the sum of the momentum of the oncoming boundary layer and of the injected coolant fluid, i.e., momentum is conserved.

Dispersion Model. The dispersion terms describe the three dimensionality of the flow and can be derived formally by averaging laterally the three-dimensional transport equation, which can be written in a general form as follows:

$$\frac{\partial}{\partial x}(\rho U\phi)+\frac{\partial}{\partial y}(\rho V\phi)+\frac{\partial}{\partial z}(\rho W\phi)$$

$$=\frac{\partial}{\partial x}\left(\Gamma\frac{\partial\phi}{\partial x}\right)+\frac{\partial}{\partial y}\left(\Gamma\frac{\partial\phi}{\partial y}\right)+\frac{\partial}{\partial z}\left(\Gamma\frac{\partial\phi}{\partial z}\right)+S_\phi \quad (22)$$

with $\phi = (U, H, k, \epsilon, \theta)$. The dependent variables are separated as follows into a laterally averaged value $(\hat{\phi})$ and a laterally varying component (ϕ_z)

$$\phi=\hat{\phi}+\phi_z \quad (23)$$

The laterally averaged value is defined as

$$\hat{\phi}(x, y)=\frac{2}{s}\int_0^{s/2}\phi(x, y, z)dz \quad (24)$$

The separation according to (23) is introduced into the three-dimensional transport equations, which are then averaged over the shaded region shown in Fig. 5. The integration only needs to be performed over this region because of the periodicity of the geometry ($z = 0$ and $z = s/2$ are symmetry lines). This process results in the averaged transport equations, e.g., the ϕ equation

$$\frac{\partial}{\partial x}(\hat{\rho}\hat{U}\hat{\phi})+\frac{\partial}{\partial y}(\hat{\rho}\hat{V}\hat{\phi})=\frac{\partial}{\partial x}\left(\hat{\Gamma}\frac{\partial\hat{\phi}}{\partial x}\right)$$

$$+\frac{\partial}{\partial y}\left(\hat{\Gamma}\frac{\partial\hat{\phi}}{\partial y}\right)+\hat{S}_\phi$$

$$\underbrace{-\frac{2}{s}\int_0^{s/2}\frac{\partial}{\partial x}(\hat{\rho}U_z\phi_z)dz}_{D_{U\phi}}\underbrace{-\frac{2}{s}\int_0^{s/2}\frac{\partial}{\partial y}(\hat{\rho}V_z\phi_z)dz}_{D_{V\varphi}} \quad (25)$$

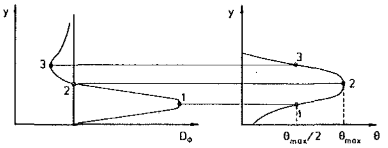

Fig. 7 Typical distribution of the dispersion term D_ϕ and the tracer θ

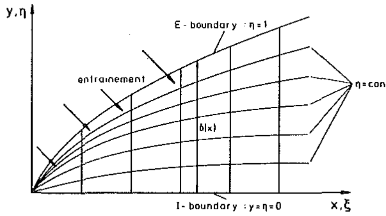

Fig. 8 (ξ, η) coordinate system

which includes in addition to the convection, diffusion, and source terms two dispersion terms $D_{U\phi}$ and $D_{V\phi}$. These have been calculated from the results of the three-dimensional calculations and were found to show similar behavior. For this reason the sum of $D_{U\phi}$ and $D_{V\phi}$ is modeled, and typical distributions for the θ-dispersion term $D_\theta = D_{U\theta} + D_{V\theta}$ are given in Fig. 6 at different streamwise locations. They show that D_θ is a sink in the near-wall region and a source further away from the wall which describes the lifting of the jet trajectory. This lifting is due to the lateral entrainment of the main gas stream below the injected jet. Further, it can be seen in Fig. 6 that the magnitude of the dispersion term decreases rapidly with increasing streamwise distance. Similar profiles to those sketched in Fig. 6 are obtained for the U-dispersion terms.

The dispersion terms for the U velocity and for the tracer θ are approximated with the aid of a dispersion model, which consists of three parts:

1 For the interpolation of the dispersion distributions parabolic functions are used.

2 The maxima and minima of the dispersion distributions are correlated by exponential functions. For this, five constants derived from the three-dimensional calculations are necessary for each test case.

3 The y positions of the maxima and minima are calculated from the θ distribution. This is illustrated in Fig. 7, where on the left-hand side a typical dispersion distribution and on the right-hand side a typical tracer profile is given; in addition, the corresponding y positions are marked.

The dispersion term for the total enthalpy is calculated from the θ dispersion as follows:

$$D_H=D_\theta c_p(T_2-T_e) \quad (26)$$

The dispersion terms D_U, D_H, and D_θ are added to equations (2), (3), and (17) as additional source terms in order to simulate the three dimensionality of the flow. The five constants for correlating the dispersion terms are stored for each test case. For a given film cooling configuration three-dimensional interpolations are then performed, as for the injection model.

Solution Procedure and Boundary Conditions

Finite Volume Method. The two-dimensional differential equations for the conservation/transport of mass (1), momentum (2), total enthalpy (3), turbulent kinetic energy (9), dissipation (10), and tracer θ (17) are solved with a parabolic forward-marching method. This employs a coordinate system (see Fig. 8), which adapts automatically to the growth of the boundary layer. With the aid of the equations

Downloaded 01 Jun 2010 to 171.66.16.57. Redistribution subject to ASME license or copyright; see http://www.asme.org/terms/Terms_Use.cfm

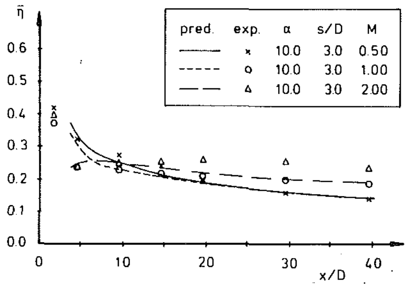

Fig. 9 Cooling effectiveness at different blowing rates; measurements of Kruse and Metzinger [15]

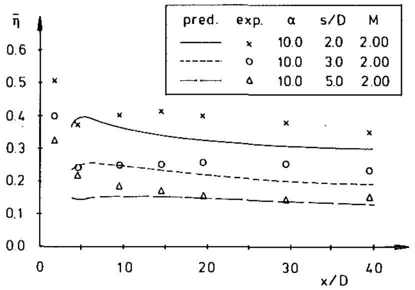

Fig. 10 Cooling effectiveness at different relative spacings; measurements of Kruse and Metzinger [15]

$$\xi = x \qquad \eta = \frac{y}{\delta(x)} \tag{27}$$

the transport equations have been transformed into the new coordinate system and integrated over finite control volumes. For the discretization in the normal direction hybrid differences are used, which are a combination of first-order upwind differences and second-order central differences, depending on the local Peclet number; in the main-flow direction an implicit discretization is applied. The resulting tridiagonal matrix is solved with a Thomas algorithm, which is a simplified version of a Gauss-elimination algorithm. The V-velocity component is obtained by integrating the continuity equation.

Boundary Conditions. Boundary conditions must be prescribed at the in-flow cross section, along the wall, and in the free stream. For the inlet profiles the momentum thickness Reynolds number, the form parameter $H_{12} = \delta_1/\delta_2$, and the intensity as well as a typical length scale of the free-stream turbulence have to be specified.

As boundary conditions along the wall and in the free stream, the above given formulae (5), (6), (13), (14), (18), and (19) are used. Laminar Couette flow is assumed in the near-wall control volume and formulae were derived which connect the value at the wall nearest grid point to the corresponding wall-flux (for instance wall shear stress or wall heat flux). Finally, the parameters for the film cooling configuration have to be specified: the injection angle α, the relative spacing s/D, the blowing rate M, the temperature of the injected fluid T_2, and the streamwise location of the blowing hole x_{bh}.

A typical calculation with 100 grid points in the normal direction took about 1 min CPU time on a Siemens 7881 computer.

Results

Flat-Plate Boundary Layers. The calculation method was applied first to various flat-plate situations studied experimentally by Kruse and Metzinger [15]. In these experiments the free-steam velocity was 65 m/s, the free stream turbulence level about 3 percent, and the oncoming boundary layer was fully turbulent. The main gas stream was heated to an excess temperature of 77°C and the cooling effectiveness was determined by extrapolating measured temperature profiles to the wall. For the first applications of the new model reported here, the density difference between main and coolant gas was neglected. Figure 9 compares predicted and measured laterally averaged cooling effectiveness $\bar{\eta}$ for different blowing rates M at an injection angle of 10 deg and a relative spacing of 3.0. It can be seen that the film cooling effectiveness increases slightly with increasing blowing rate. The cooling effectiveness for different relative spacings at the same injection angle and for $M = 2$ is given in Fig. 10. The $\bar{\eta}$ distributions are similar for all the spacings, but with increasing spacing the level of $\bar{\eta}$ decreases. This behavior indicates that the characteristics of the injected jets are similar for all the spacings. Finally, the influence of the injection angle on the cooling effectiveness is illustrated in Fig. 11. The different streamwise decay of the cooling effectiveness is due to the different jet characteristics at $\alpha = 10$ deg, and $\alpha = 45$ deg. At an injection angle of $\alpha = 10$ deg, the cooling jets are bent over immediately after injection and attach to the wall. At an angle of 45 deg, however, the jets penetrate into the main stream which results in smaller values of $\bar{\eta}$. The influence of these differences in the complex three-dimensional flow behavior on the cooling effectiveness is predicted quite well by the present two-dimensional film-cooling model.

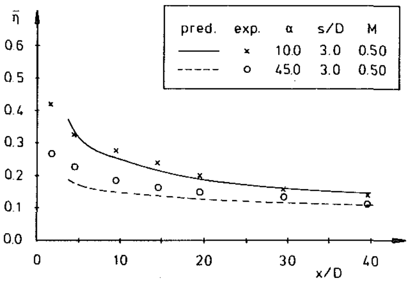

Fig. 11 Cooling effectiveness at different injection angles; measurements of Kruse and Metzinger [15]

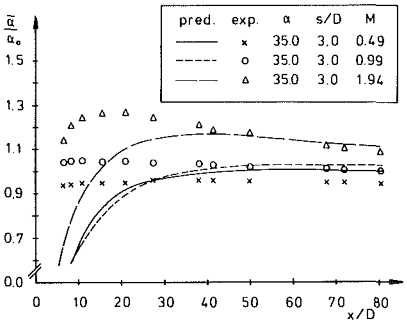

Fig. 12 Ratio of the heat transfer coefficient with and without film cooling; measurements of Eriksen et al. [16]

Eriksen et al. [16] measured the heat transfer coefficient for boundary layers on flat plates with and without film cooling. The injection angle was $\alpha = 35$ deg, the relative spacing $s/D = 3$, and the hole diameter $D = 11.8$ mm. The free stream had a velocity of $U_e = 30.5$ m/s and a turbulence level of $Tu = 0.5$ percent. Eriksen et al. [16] determined the heat transfer coefficient by imposing a constant wall heat flux q_w and measuring the wall temperature T_w. For $T_2 = T_e$, they defined the heat transfer coefficient as

$$\alpha = \frac{q_w}{T_e - T_w}$$

Figure 12 shows the predicted and measured ratio of the heat transfer coefficients with and without blowing. It can be seen

Downloaded 01 Jun 2010 to 171.66.16.57. Redistribution subject to ASME license or copyright; see http://www.asme.org/terms/Terms_Use.cfm

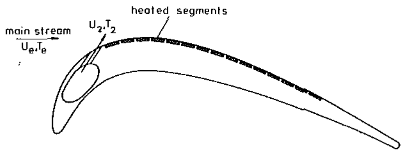

Fig. 13 Model turbine blade

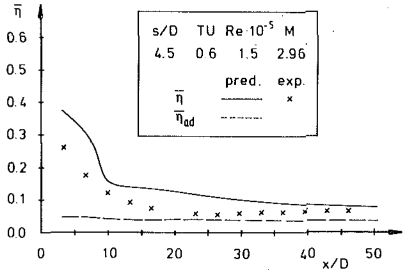

Fig. 14 Influence of the heated front part; $\bar{\eta} \hat{=}$ heated, $\bar{\eta}_{ad} \hat{=}$ adiabatic front part

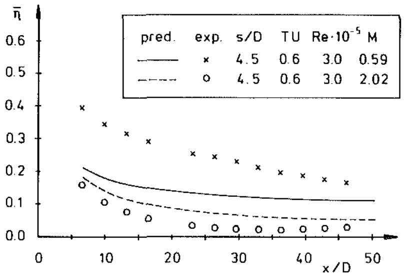

Fig. 15 Influence of the blowing rate on the cooling effectiveness; measurements of Rodi et al. [17]

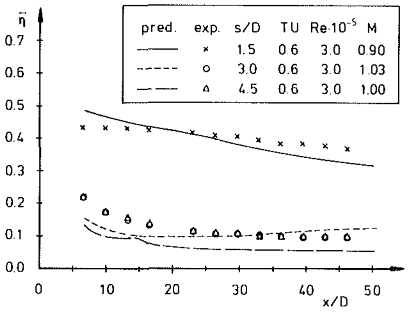

Fig. 16 Cooling effectiveness at different spacings; measurements of Rodi et al. [17]

that film cooling has a noticeable influence on the heat transfer coefficient only at higher blowing rates and results in higher heat transfer. At a blowing rate of $M = 0.99$, the values of the heat transfer coefficient are even somewhat below those without blowing. This effect is qualitatively well predicted, but quantitative agreement could be obtained only at larger distances ($x/D > 20$). The low predictions near the injection ($x/D < 20$) are probably due to an underestimation of the lateral mixing in the model.

Flow Over Model Turbine Blade. In the following, predictions are compared with results of our own measurements (see Rodi et al. [17]) in which film cooling effectiveness and heat transfer coefficients have been measured on an enlarged model of a relatively thin, highly curved turbine blade (see Fig. 13). The "cooling" gas was injected on the suction side through a row of holes at a relative surface distance of 25 percent and at an injection angle of $\alpha = 32$ deg. In the measurements of film cooling effectiveness, the secondary gas was actually heated (excess temperature up to 45°C), and this case was simulated in the calculations. The measurements have been performed for different blowing rates, relative spacings, free-stream Reynolds numbers, and turbulence levels, and the oncoming boundary layer has been laminar.

Cooling Effectiveness. Because of the relatively thin model turbine blade used in the experiments, it was not possible to achieve adiabatic wall conditions in the front part of the blade. Due to the discharge of heated gas in the cooling-effectiveness measurements, the wall temperature increased in front of the injection position. This effect was simulated in the calculations by prescribing the wall heat flux distribution in front of the injection and using adiabatic wall conditions after the injection, in close correspondence with the experimental situation. The wall heat flux distribution was obtained with the aid of a boundary-layer calculation for which the measured wall temperature distribution in front of the injection was prescribed as the wall boundary condition. The influence of the heated front part is more important for larger spacing because the oncoming temperature boundary layer is less disturbed between the injection holes and is therefore more dominant. The influence of the heated front part can be seen in Fig. 14, in which the cooling effectiveness predicted with and without heated front part, $\bar{\eta}$ and $\bar{\eta}_{ad}$ respectively, is given. In addition, measured $\bar{\eta}$ values are shown. In Fig. 15, the influence of the blowing rate M on $\bar{\eta}$ is displayed. With increasing M, both measurements and predictions show a decrease of cooling effectiveness. However, at the lower blowing rate, $\bar{\eta}$ is underpredicted considerably, especially near the injection. This is probably due to curvature effects, which induce the injected jet to attach more quickly to the wall and hence cause higher cooling effectiveness for $M < 1$. Experimental studies of curvature effects performed by Ito and Goldstein [18] have indicated this kind of influence, but so far too little is known about curvature effects so that they are not accounted for in the present prediction code. The influence of the spacing on the cooling effectiveness is given in Fig. 16, where the predictions show fairly good agreement with the measurements. Both yield a drastic decrease in cooling effectiveness when the relative spacing is increased from $s/D = 1.5$ to $s/D = 3.0$ and about the same values for the two higher spacings ($s/D = 3.0$ and $s/D = 4.5$). The predicted cooling effectiveness was compared with the measured one also for different Reynolds numbers and different free-stream turbulence levels [17]. Both parameters were found to have only a small influence: Increasing the Reynolds number results in slightly smaller cooling effectiveness and the opposite trend was observed for the free-stream turbulence. Both effects are well predicted with the present film cooling model.

Heat Transfer Coefficient. In a separate series of experiments, Rodi et al. [17] measured the wall heat flux for different blowing rates, spacings, Reynolds numbers, and free-stream turbulence levels. They determined the heat transfer coefficient by measuring the electric current required to maintain heated segments of the model surface at an isothermal level in excess of the mainstream temperature. In these experiments, secondary and primary air had the same temperature. The measurements revealed that the heat transfer coefficient in the far region ($x/D > 20$) depends considerably on the Reynolds number and blowing rate. On the other hand, variation of the relative spacing or the free-stream turbulence level resulted only in slight changes of the heat transfer coefficient. These effects are simulated well by the predictions. In Figs. 17–19, the measured and calculated heat transfer coefficients are compared for different spacings (Fig. 17), different Reynolds numbers (Fig. 18), and different blowing rates (Fig. 19). It should be mentioned that the marked in-

Downloaded 01 Jun 2010 to 171.66.16.57. Redistribution subject to ASME license or copyright; see http://www.asme.org/terms/Terms_Use.cfm

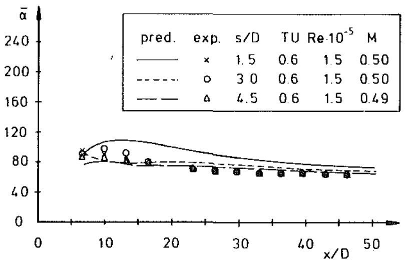

Fig. 17 Heat transfer coefficient at different relative spacings; measurements of Rodi at al. [17]

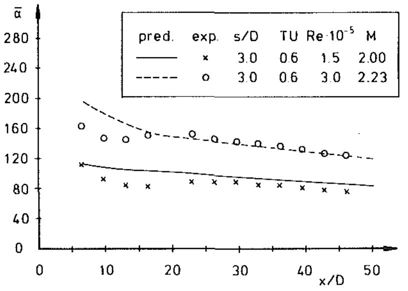

Fig. 18 Influence of the Reynolds number on the heat transfer coefficient; measurements of Rodi et al. [17]

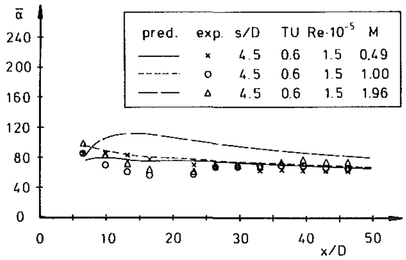

Fig. 19 Influence of the blowing rate on the heat transfer coefficient; measurements of Rodi et al. [17]

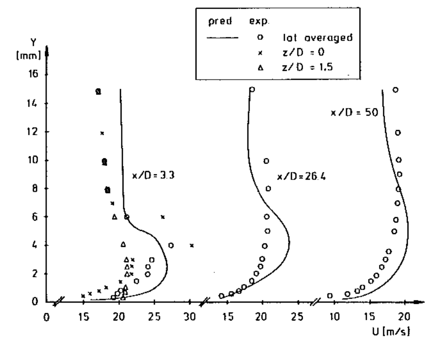

Fig. 20 Calculated and measured velocity distributions at different streamwise positions; measurements of Rodi et al. [17]

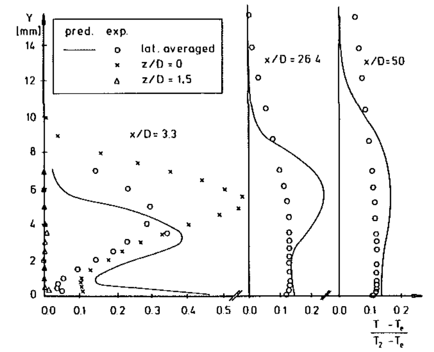

Fig. 21 Calculated and measured temperature distributions at different streamwise positions; measurements of Rodi et al. [17]

fluence of the Reynolds number on the heat transfer coefficient in Fig. 18 is not caused by film cooling effects but by differences in the characteristics of the oncoming boundary layer. The difference in Fig. 19 between the measured and predicted film cooling effectiveness for the blowing rate $M =$ 1.96 is due to the fact that, in the present film cooling model, the laminar-turbulent transition is simulated immediately after the injection. The measurements showed, however, that for this blowing rate the jet penetrates into the boundary layer and transition occurs farther downstream.

Laterally Averaged Profiles. Rodi et al. [17] also reported measurements of velocity and temperature boundary-layer profiles at different lateral and streamwise positions. The measurements were performed with hot wires and thermocouples. The profiles were laterally averaged to allow a comparison with the predictions, and sample results are shown in Figs. 20 and 21 for the case

$$M = 2, s/D = 3, Tu = 6 \text{ percent}, \mathrm{Re} = 1.5 \times 10^5$$

In order to demonstrate the three dimensionality of the flow, measured velocity profiles at the extreme lateral positions ($z/D = 0$ and $z/D = 1.5$) are included in Fig. 20 at a streamwise position of $x/D = 3.3$. The wall-jet nature of the boundary-layer profile can be seen clearly for $z = 0$ while the velocity profile at the symmetry plane between the holes shows only slight deviations from the usual boundary-layer profile. The velocity maximum for $z/D = 1.5$ is at a distance from the wall, which is smaller than the wall distance of the velocity maximum at the position $z/D = 0$. This is due to the kidney shape of the jet cross section sketched in Fig. 1. Comparisons between the measured, laterally averaged, and predicted velocity profiles at different streamwise positions are also given in Fig. 20. The differences in the free-stream velocity may be due to the difficulty of measuring absolute values with a hot-wire anemometer. At $x/D = 3.3$, the position as well as the value of the maximum velocity are calculated satisfactorily. However, the predicted redevelopment to an undisturbed boundary-layer profile is somewhat too slow.

The corresponding profiles for the temperature are given in Fig. 21. Even clearer than in the case of the velocity profiles, the wall jet behavior and an almost unchanged temperature profile in the plane between the holes can be seen. Compared with the measurements, the predictions show a smaller temperature-boundary-layer thickness and a slower redevelopment to a uniform temperature profile. The agreement between predictions and measurements is however good in the near-wall region.

Conclusions

A model was presented for simulating the effects of film cooling by a row of holes in a two-dimensional boundary-layer procedure. The model consists of two parts: an injection model, which generates boundary-layer profiles after the injection region, and a dispersion model, which simulates the three-dimensional effects. The model was devised to cover the whole range of practical interest of the parameters injection angle, relative spacing, and blowing rate. Results were presented for flows over flat plates as well as for flows over model gas turbine blades. In general, the predicted results agree satisfactorily with the measurements. To appreciate this, one should keep in mind the distinctly different kinds of three-dimensional flow patterns that can occur for different cooling

Downloaded 01 Jun 2010 to 171.66.16.57. Redistribution subject to ASME license or copyright; see http://www.asme.org/terms/Terms_Use.cfm

configurations. For low injection angles and high blowing rates, for example, the flow resulting from the injection behaves like a wall jet, whereas for higher injection angles a flow with wake character develops. Concerning the film-cooling effectiveness, the influence of the different parameters is predicted correctly and the quantitative agreement is satisfactory apart from configurations with low blowing rate. For these cases, curvature effects appear to be important, which are not accounted for in the present model. The predicted heat transfer coefficients are also in satisfactory agreement with the measurements, but for specific configurations (large relative spacings and high blowing rates), where the laminar-turbulent transition does not occur immediately after the injection, too-high heat transfer coefficients are predicted near the injection.

Future work should concentrate on the inclusion of curvature effects and the refinement of the transition model after the injection. Further, the present model should be extended to other film cooling configurations of practical interest such as film cooling with high density ratios or film cooling by more than one row of holes.

Acknowledgments

The research reported here was sponsored by the Forschungsvereinigung Verbrennungskraftmaschinen e.V. The calculations were carried out on the Siemens 7881 computer of the University of Karlsruhe. The authors should like to thank Mrs. R. Zschernitz for preparing the typescript.

References

1 Patankar, S. V., Rastogi, A. K., and Whitelaw, J. H., "The Effectiveness of Three-Dimensional Film-Cooling Slots—II Predictions," *Int. J. Heat and Mass Transfer*, Vol. 16, 1973, pp. 1665–1681.

2 Patankar, S. V., Basu, D. K., and Alpay, S. A., "Prediction of Three-Dimensional Velocity Field of a Deflected Turbulent Jet," ASME *J. Fluids Eng.*, Vol. 99, 1977, pp. 758–762.

3 Khan, Z. A., McGuirk, J. J., and Whitelaw, J. H., "A Row of Jets in Cross Flow," AGARD CP 308, 1982.

4 Bergeles, G., Gosman, A. D., and Launder, B. E., "The Prediction of Three-Dimensional Discrete Hole Cooling Processes: Part 1: Laminar Flow," ASME *Journal of Heat Transfer*, Vol. 98, No. 3, 1976, p. 379.

5 Bergeles, G., Gosman, A. D., and Launder, B. E., "The Prediction of Three-Dimensional Discrete-Hole Cooling Processes—Part 2: Turbulent Flow," ASME *Journal of Heat Transfer*, Vol. 103, 1981, p. 141.

6 Bergeles, G., Gosman, A. D., and Launder, B. E., "Double-Row Discrete Hole Cooling: An Experimental and Numerical Study," ASME JOURNAL OF ENGINEERING FOR POWER, Vol. 102, 1980, p. 498.

7 Demuren, A. O., "Numerical Calculations of Steady Three-Dimensional Turbulent Jets in Cross Flow," *Comp. Meth. Appl. Mech. Engg.*, Vol. 37, 1983, pp. 309–328.

8 Demuren, A. O., and Rodi, W., "Three-Dimensional Calculation of Film Cooling by a Row of Jets," *Proceedings of the Fifth GAMM Conference on Numerical Methods in Fluid Mechanics*, Rome, Italy, Oct. 5–7, 1983, pp. 49–56.

9 Demuren, A. O., Rodi, W., and Schönung, B., "Systematic Study of Film Cooling With a Three-Dimensional Calculation Procedure," ASME JOURNAL OF TURBOMACHINERY, Vol. 108, 1986, pp. 121–130.

10 Herring, H. J., "A Method of Predicting the Behavior of a Turbulent Boundary Layer With Discrete Transpiration Jets," ASME JOURNAL OF ENGINEERING FOR POWER, Vol. 97, 1975, p. 214.

11 Crawford, M. E., Kays, W. M., and Moffat, R. J., "Heat Transfer to a Full Coverge Film-Cooled Surface With 30° Slant-Hole Injection," NASA Contractor Report NASA CR-2786, 1976.

12 Miller, K. L., and Crawford, M. E., "Numerical Simulation of Single, Double and Multiple Row Film Cooling Effectiveness and Heat Transfer," ASME Paper No. 84-GT-112, 1984.

13 Lam, C. K. G., and Bremhorst, K. A., "Modified Form of the k-ϵ Model for Predicting Wall Turbulence," ASME *J. Fluids Eng.*, Vol. 103, 1981, pp. 456–460.

14 Launder, B. E., and Spalding, D. B., *Lectures in Mathematical Models of Turbulence*, Academic Press, London, 1972.

15 Kruse, H., and Metzinger, H., "Der Einfluss der Belochungsgeometrie auf die Filmkühlwirkung einer Lochreihe," *Deutsche Forschungs- und Versuchsanstalt für Luft- und Raumfahrt*, Interner Bericht IB 325-9-84, Köln, 1984.

16 Eriksen, V. S., and Goldstein, R. J., "Heat Transfer and Film Cooling Following Injection Through Inclined Circular Tubes," ASME *Journal of Heat Transfer*, Vol. 96, 1974, pp. 239–245.

17 Rodi, W., Haas, W. T., and Schönung, B., "Untersuchung des Grenzschichtverhaltens an Turbinenschaufeln unter Berücksichtigung von Filmkühlung und von lokalen Ablöseblasen," FVV-Forschungsberichte Heft 383-1, 1986.

18 Ito, S., Goldstein, R. J., and Eckert, E. R. G., "Film Cooling of a Gas Turbine Blade," ASME JOURNAL OF ENGINEERING FOR POWER, Vol. 100, 1978, p. 476.

Downloaded 01 Jun 2010 to 171.66.16.57. Redistribution subject to ASME license or copyright; see http://www.asme.org/terms/Terms_Use.cfm

R. J. Goldstein

P. H. Chen

Mechanical Engineering Department,
University of Minnesota,
Minneapolis, MN 55455

Film Cooling of a Turbine Blade With Injection Through Two Rows of Holes in the Near-Endwall Region

Measurements of film cooling on a simulated turbine blade are conducted using a mass transfer technique. Under the influence of the endwall, dramatic changes of film cooling performance occur on the convex surface of the blade as compared to the region where the flow is two dimensional. The result is a triangular region, where coolant is swept away from the surface by the three-dimensional vortex-driven flow present between adjacent blades. In order to predict the area of this unprotected region, the influences of several parameters including density ratio, blowing rate, and number of rows of injection holes are studied. The presence of the endwall affects the film cooling performance on the concave surface only slightly.

Introduction

To improve the performance of a gas turbine engine, the temperature of combustion gas entering the first-stage turbine has increased to as high as 1750 K, which is above the allowable limit for alloys presently used as turbine materials. An effective cooling system is required to protect the gas turbine blade from high-temperature failure. Surface film cooling combined with internal convection cooling and impingement cooling is widely used in the aircraft industry. A better understanding of this cooling system can improve the design of gas turbine engines. The present work focuses on film cooling using a plane simulated turbine blade cascade. Particular attention is directed to the influence of the endwall on the adiabatic wall effectiveness.

Adiabatic wall effectiveness is defined by

$$\eta_{aw} = \frac{T_{aw} - T_r}{T_2 - T_r} \tag{1}$$

Based on the definition of the adiabatic wall temperature, the heat transfer is defined by

$$q_w = h(T_w - T_{aw}) \tag{2}$$

Values of the heat transfer coefficient are generally close to those without coolant injection if the region near the injection holes is excluded. Close to the injection holes equations (1) and (2) are still valid; there, however, h must be determined, usually, in a separate experiment.

In the present study a heat/mass transfer analogy is used to investigate the film cooling effectiveness. A detailed discussion on the analogy is available in [1]. A gas mixture containing a tracer is injected into the mainstream. The concentration of the tracer is measured in samples drawn through taps, which are located on the surface of a simulated blade. The local impermeable wall effectiveness, analogous to the adiabatic wall effectiveness, is defined by

$$\eta_{iw} = \frac{C_{iw} - C_\infty}{C_2 - D_\infty} \tag{3}$$

As the concentration of the tracer in the mainstream is zero, the impermeable wall effectiveness can be calculated from

$$\eta_{iw} = \frac{C_{iw}}{C_2} \tag{4}$$

Prior studies [2, 3] of film cooling on a turbine blade were conducted in the central space of the blade to minimize the influence of the endwall. In these, the effect of blade-wall curvature on the performance of the film cooling was reported. However, the spans of most turbine blades are not long compared to their chord length. A recent work [4] found a close relation between the flow field in the endwall region and the film cooling. Measurements of the film cooling in a plane cascade showed that a passage vortex traveling from the adjacent blade apparently sweeps the coolant from the convex surface and produces a triangular region without film cooling protection.

An understanding of the flow field in the near endwall region is essential when conducting a study of film cooling on a turbine blade. Studies of the three-dimensional flow field within a turbine cascade passage have been described by others [5-8]. A review of recent investigations, including a summary of the currently accepted view of the flow field, is reported in [9].

Contributed by the Gas Turbine Division of THE AMERICAN SOCIETY OF MECHANICAL ENGINEERS and presented at the 32nd International Gas Turbine Conference and Exhibit, Anaheim, California, May 31-June 4, 1987. Manuscript received at ASME Headquarters February 19, 1987. Paper No. 87-GT-196.

Copyright © 1987 by ASME

Downloaded 01 Jun 2010 to 171.66.16.57. Redistribution subject to ASME license or copyright; see http://www.asme.org/terms/Terms_Use.cfm

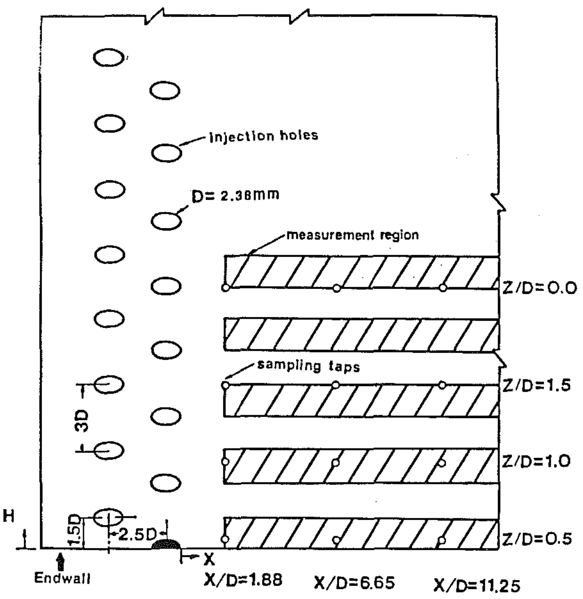

Fig. 1(a) Detail of test blade

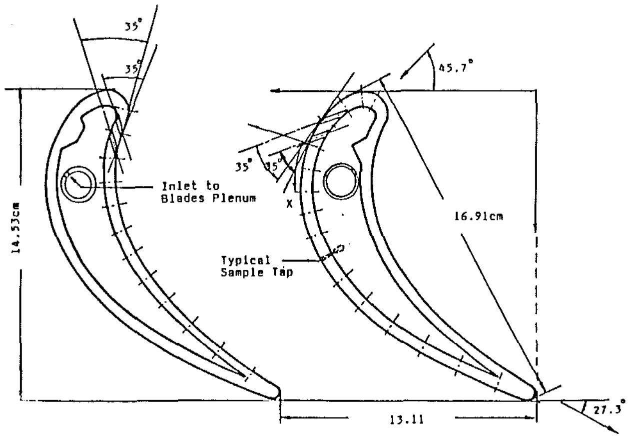

Fig. 1(b) Test blades

The present work is an extension of an earlier study done with a single row of holes, a single blowing rate, and a single density ratio. Herein the effects of density ratio, two rows of injection holes, and blowing rate on film cooling near an endwall are considered.

Experimental System and Test Conditions

Measurements are conducted in an open-cycle, low-speed wind tunnel using a plane cascade of six turbine blades [2]. Two central blades with injection holes face each other; four others are solid. Figure 1(*a*) shows the location of the injection holes and sampling taps. Two staggered rows of injection holes inclined at an angle of 35 deg are used. The angles of flow inlet and outlet with respect to the blades are shown in Fig. 1(*b*). The lateral positions of each of the four rows of sampling taps are Z/D = 0.0, 0.5, 1.0, and 1.5, respectively. Each row has seven sampling taps (only three are shown on Fig. 1*a*) located at different downstream positions. The central two blades can be moved in or out of the endwall using a positioning mechanism underneath the blades. For any single run, a blade is positioned at a fixed distance from the endwall with the lowest hole of the second row centered on the endwall. To assure uniform flow through each hole, the injection hole half embedded in the endwall is plugged. For each run, samples are drawn from all four rows of sampling taps. These represent the regions between different paired holes; that is, only one row of sampling taps lies inside the shaded area where the measurement region is. To get data for results between a given pair of holes (at fixed H/D), four different positionings of a blade are required. For a given blowing rate and density ratio, the blades are positioned in a dozen different locations to conduct a series of measurements before the two-dimensional flow region is reached. Note that the shaded area only covers half the space between a given pair of holes, as the sampling taps were designed for a study in the central span of the blades where the flow is symmetric around the injection hole.

The injected flow is produced by mixing refrigerant-12 or helium with air. Two density ratios, R = 2.0 and 0.96, are used. For the measurements on the convex (suction) surface, three blowing rates, M = 0.5, 1.0, and 1.5, are used for each density ratio. On the concave (pressure) surface where the endwall does not greatly affect the film cooling performance, only two test conditions—one with blowing rate of 1.38 and density ratio of 0.96; the other with blowing rate of 1.5 and density ratio of 2.0—are used.

The velocity of the approaching flow is measured 14 cm upstream of the leading edge of the blades. The free stream has a velocity of 10.2 m/s and a turbulence intensity of 1.2 percent. The boundary layer on the endwall is turbulent with a thickness δ_{99} of 10 mm corresponding to 4.2 D; the momentum thickness is 1.2 mm and the displacement thickness is 1.8 mm. Calculating a virtual origin of the boundary layer and assuming growth similar to that on a flat plate, the boundary

Nomenclature

a_1-a_2 = attachment line, Fig. 2
C_{iw} = concentration of foreign gas at impermeable wall
C_2 = concentration of foreign gas
C_∞ = concentration of foreign gas in the mainstream
D = diameter of injection hole
h = heat transfer coefficient
H = distance along blade surface from the endwall
M = blowing rate = $\rho_2 U_2/\rho_\infty U_\infty$
q_w = wall heat flow per unit time and area density ratio = ρ_2/ρ_∞
Re_∞ = Reynolds number = $U_\infty D/\nu$
S_{s1} = saddle point, Fig. 2
s_1-s_2 = separation line, Fig. 2
T_{aw} = film cooling adiabatic wall temperature
T_r = mainstream recovery temperature
T_w = wall temperature
T_2 = temperature of secondary air
U_2 = mean velocity in injection hole
U_∞ = mainstream velocity at the first injection hole location
X = distance downstream for the downstream edge of second injection row
Z = transverse distance from center of injection hole of the second row to sampling hole
δ_{99} = thickness of boundary layer where mean velocity is 99 percent of the potential flow mean velocity
η_{aw} = local adiabatic wall effectiveness
$\bar{\eta}_{iw}$ = average impermeable wall effectiveness
η_{iw} = local impermeable wall effectiveness
ν = kinematic viscosity of the mainstream
ρ_2 = density of foreign gas
ρ_∞ = density of the mainstream

Downloaded 01 Jun 2010 to 171.66.16.57. Redistribution subject to ASME license or copyright; see http://www.asme.org/terms/Terms_Use.cfm

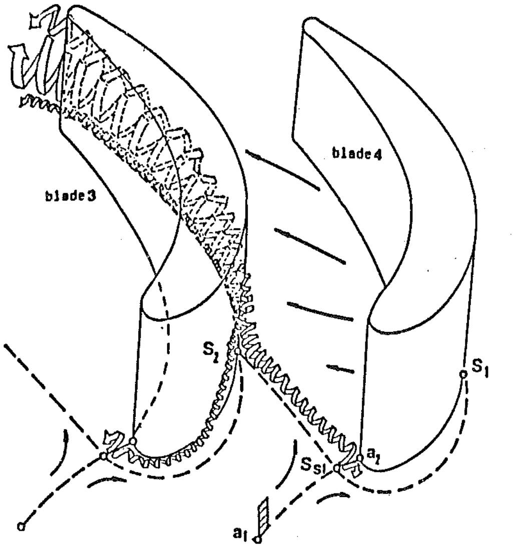

Fig. 2 Sketch of the secondary flow near endwall between blade passage

layer thicknesses at the location of the stagnation line of the blade would be about 6 percent larger than the values measured. The mainstream velocity near the injection holes of the first row is 17.8 m/s on the convex surface and 4.2 m/s on the concave surface.

The sampled gases are analyzed using a gas chromatograph. The uncertainty of the measured impermeable wall effectiveness is about 6 percent for values of effectiveness greater than 10 percent. The uncertainties in the blowing rate and density ratio are 7 and 6 percent, respectively.

Flow Field

Because of a strong relation between film cooling and the flow field, a detailed description of the flow field is essential to explain the results of the film cooling measurements. A sketch of the flow field, based on results of flow visualization [4], is shown in Fig. 2. The main structure is clear but, without more investigations, some details, especially close to the blade, are still ambiguous. In Fig. 2, the attachment (stagnation) line, indicated by a_1–a_2, extends from the stagnation point on the blade into the mainstream. The separation line, indicated by s_1–s_2, lies in front of the leading edge of the blade. A saddle point, S_{s1}, is a singular separation point and is located at the intersection of the attachment line and the separation line. Several flow regions are bounded by these two separation lines and two attachment lines. When the mainstream approaches the leading edge of the blade, the inlet boundary layer separates and a horseshoe vortex is generated behind the separation line. After the mainstream travels into the blade passage, a pressure variation is produced, high pressure near the concave surface and low pressure near the convex surface. Behind the separation line, the leg of the horseshoe vortex on the concave side traveling downstream is driven by the pressure difference in the blade passage and becomes part of the passage vortex. The other leg of the horseshoe vortex, on the convex side, is confined near the blade wall and moves up the blade when it encounters the passage vortex from the adjacent blade. On the endwall, a boundary layer is driven by the pressure difference from the concave side to the convex side.

Essentially, the passage vortex is formed from the concave side leg of the horsehoe vortex and fed from the cross flow on the endwall and the mainstream in the blade passage. It grows bigger as it travels downstream. When the passage vortex encounters the convex surface of the adjacent blade, it apparently lifts up the convex side leg of the horseshoe vortex from that blade. Also, a counter vortex is generated underneath the passage vortex. Near the endwall, the limiting streamlines on the blade surfaces are not two-dimensional. On the concave surface, the limiting streamlines are skewed downward because fluid feeds into the crossflow on the endwall. On the convex surface, the limiting streamlines are pushed up by the passage vortex. Initial work on film cooling near the endwall [4] indicated a triangular region on the convex surface in which the coolant is essentially absent.

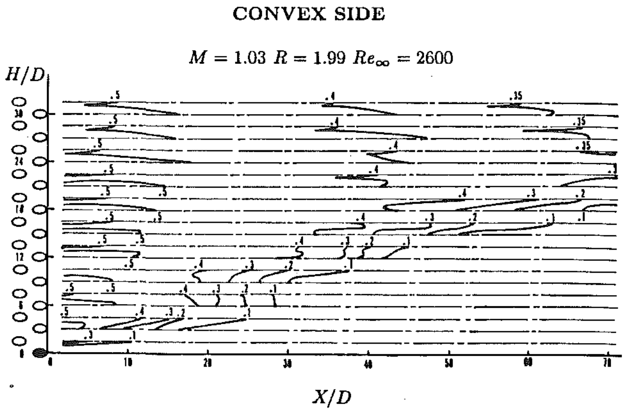

Fig. 3 Iso-effectiveness lines on convex surface at $M = 1.03$ and $R = 1.99$

Impermeable Wall Effectiveness

Convex Surface. For $M = 1.0$ and $R = 2.0$, iso-effectiveness lines of the convex surface are shown in Fig. 3. These lines are constructed in the measurement regions which start at $X/D = 1.88$ and end at $X/D = 70.93$. Note that these measurement regions only cover the half areas between two adjacent injection holes.

In the region near $H/D = 30$ the coolant flow appears symmetric around the line downstream of the injection hole centerlines. This can be seen from the periodicity of local effectiveness of two adjacent measurement regions, $28.5 > H/D > 27.0$ and $31.5 > H/D > 30$. Secondary flow in the blade passage has little effect on the film cooling performance at distances over 30 diameters from the endwall.

For $H/D < 30$, the variation of local effectiveness of two adjacent measurement regions is no longer periodic. For $H/D < 18$, the local effectiveness over much of the region studied is under 0.1; this is discussed below. For $H/D < 1.5$ low effectiveness results from: (*a*) low mainstream velocity in this region causing a high blowing rate with coolant blown from the surface, and (*b*) plugging of the hole embedded in the endwall.

Due to limited numbers of sampling taps, it is hard to determine the downstream location at which the local effectiveness essentially reaches zero. The locations of iso-effectiveness lines are calculated by interpolation and the iso-effectiveness lines with a value of 0.1 are somewhat questionable because of the difficulty in measuring very small concentrations.

Figures 4 and 5 show spanwise-average effectiveness $\bar{\eta}_{iw}$, as a function of the dimensionless distance H/D. Values of $\bar{\eta}_{iw}$ are determined by numerically interpolating the four local values measured, which represent the center of each half space (cf. Fig. 1 and Fig. 3) in which measurements are taken. Results for two density ratios are presented. Solid symbols on the right axis represent $\bar{\eta}_{iw}$ in the two-dimensional flow region, at $H/D = 69$. These values compare well with the results in [3]. The data at each downstream position (x) have a similar trend. As H/D decreases the average effectiveness at first

Downloaded 01 Jun 2010 to 171.66.16.57. Redistribution subject to ASME license or copyright; see http://www.asme.org/terms/Terms_Use.cfm

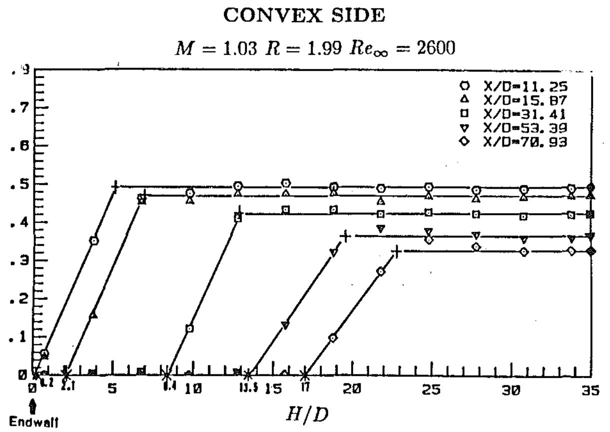
CONVEX SIDE

$M = 1.03$ $R = 1.99$ $Re_\infty = 2600$

Fig. 4 Average effectiveness on convex surface at $M = 1.03$ and $R = 1.99$

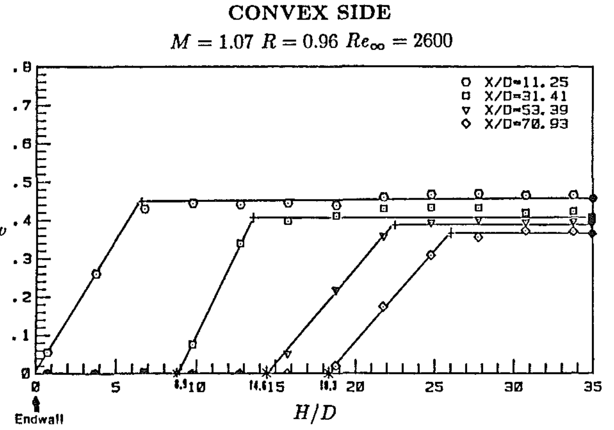
CONVEX SIDE

$M = 1.07$ $R = 0.96$ $Re_\infty = 2600$

Fig. 5 Average effectiveness on convex surface at $M = 1.07$ and $R = 0.96$

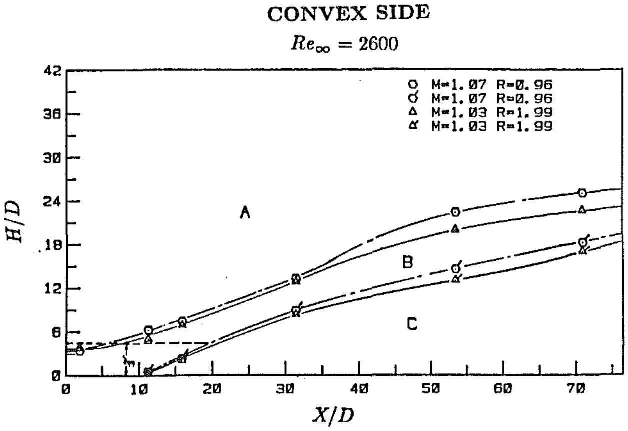
CONVEX SIDE

$Re_\infty = 2600$

Fig. 6 Distribution range of average effectiveness on the convex surface for two different density ratios, $R = 0.96$ and $R = 1.99$

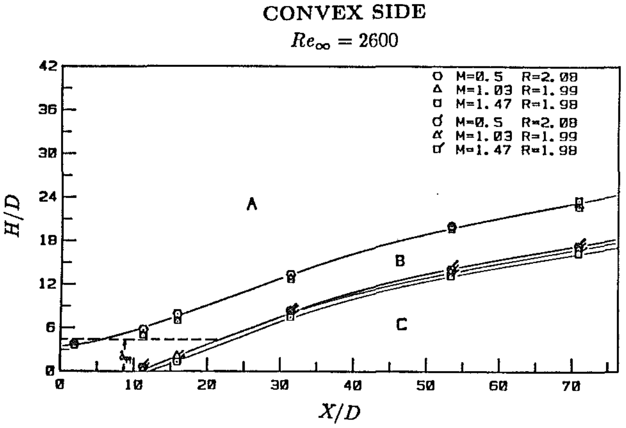
CONVEX SIDE

$Re_\infty = 2600$

Fig. 7 Distribution range of average effectiveness on the convex surface for three different blowing rates, $M = 0.5$, 1.03, and 1.47

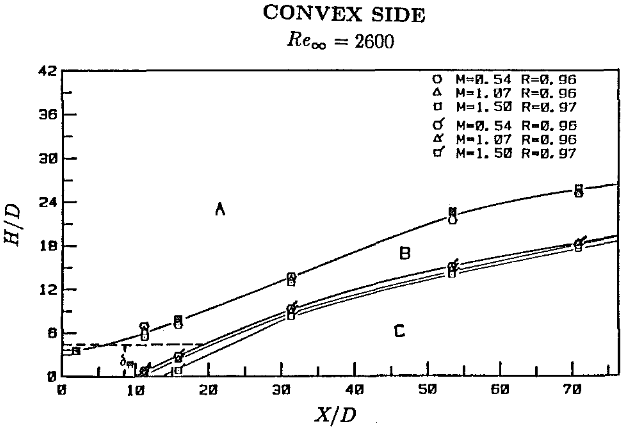
CONVEX SIDE

$Re_\infty = 2600$

Fig. 8 Distribution range of average effectiveness on the convex surface for three different blowing rates, $M = 0.54$, 1.07, and 1.50

deviates only slightly from that in the two-dimensional flow region. At a certain distance, marked by a plus symbol in Figs. 4 and 5, the values of the average effectiveness start to decrease approximately linearly to zero.

For each specified downstream location, the results can be approximated by two straight lines. One extends from the value in the two-dimensional flow region and is parallel to the horizontal axis. The slant line fits data which decrease linearly with H. Both lines intersect at the location shown by a plus symbol, which indicates where the value of the average effectiveness starts to decrease linearly. The star symbols represent the locations on the horizontal axis intersected by the slant straight lines. The region between the location of the star symbol and $H/D = 0$ has no film cooling protection. Note that these plus and star symbols are not data points.

The plus and star symbols can be mapped onto the convex surface of a blade. Figure 6 presents the ranges of the average effectiveness in the near-endwall region on the convex surface of a blade. Note that the location at a value of $X/D = 0$ is at the downstream edge of the injection holes of the second row. (For reference, the leading edge of a blade is at $X/D = -14.5$.) The star symbols (in Fig. 4 or 5) define the upper boundary of region C. The upper boundary of region B is formed by the corresponding plus symbols. The dashed line shows the extrapolated boundary thickness, δ_{99}, of the mainstream on the endwall at the leading edge of a blade.

Region C is the unprotected area where coolant flow is swept away by the passage vortex from the adjacent blade and the suction-side portion of the horseshoe vortex, which is moved up the blade by the same flow and pressure field that drives the passage vortex. The span of the unprotected area grows as the location moves toward the trailing edge because the passage vortex becomes bigger as it travels downstream. In region B, the values of the average effectiveness vanish linearly to zero as measurements are conducted toward the endwall. In this region, the coolant flow mixes with the passage vortex and the suction-side leg of the horseshoe vortex but is not totally absent. Above region B, the performance of the film cooling is slightly affected by skewed streamlines and is close to the two-dimensional flow value at $H/D \cong 30$.

The flow field near the endwall significantly affects the per-

Downloaded 01 Jun 2010 to 171.66.16.57. Redistribution subject to ASME license or copyright; see http://www.asme.org/terms/Terms_Use.cfm

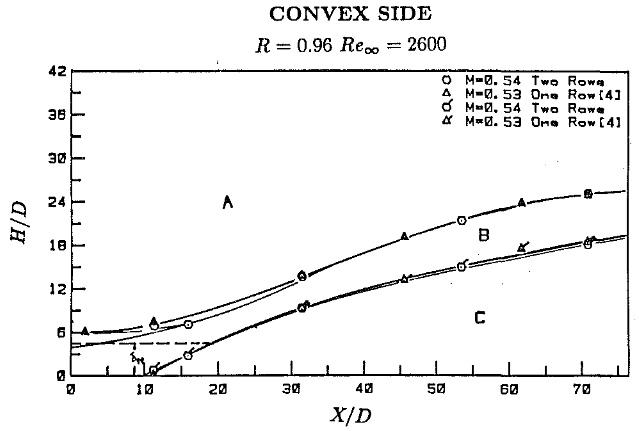

Fig. 9 Comparison of distribution range of average effectiveness between one-row injection and two-row injection

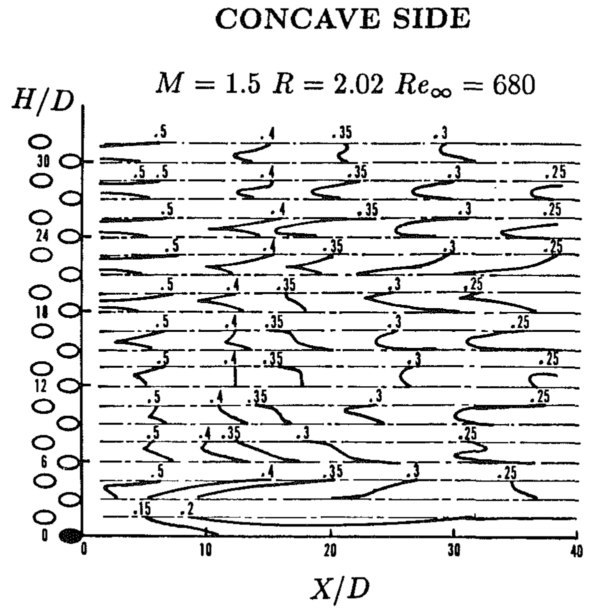

Fig. 10 Iso-effectiveness lines on concave surface at M = 1.5 and R = 2.0

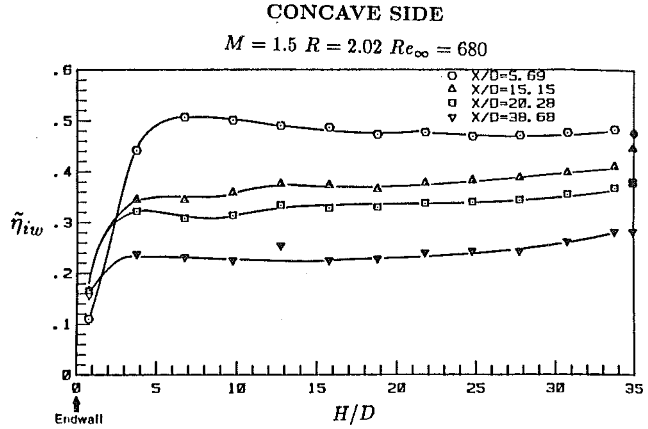

Fig. 11 Average effectiveness on concave surface at M = 1.5 and R = 2.0

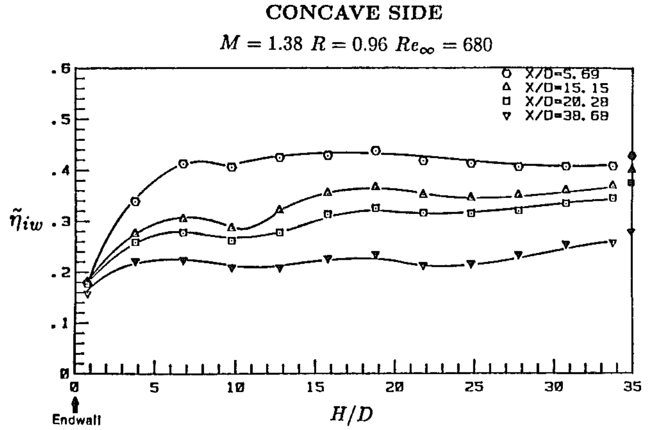

Fig. 12 Average effectiveness on concave surface at M = 1.38 and R = 0.96

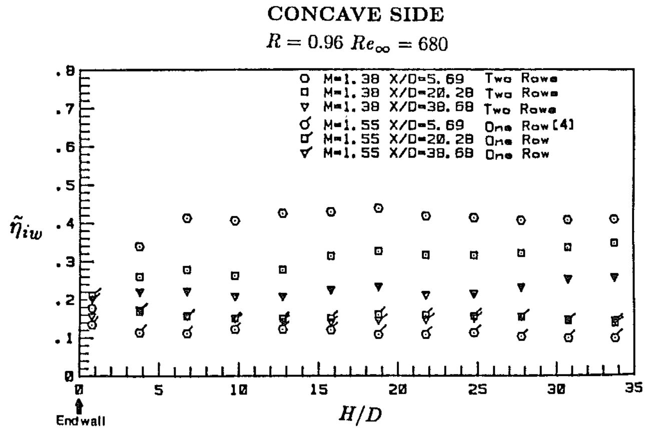

Fig. 13 Comparison of average effectiveness at R = 0.96 between one-row injection and two-row injection

formance of the film cooling on the convex surface of a blade. The passage vortex and related flow can cause a large area of a blade surface to be exposed to hot gas without coolant protection. It may be helpful to add coolant to the endwall to protect the lower convex surface of the blade. It is however uncertain that the coolant so injected would be carried up by the passage vortex to the blade surface. It might also be desirable to add coolant along the blade surface downstream of the region where the passage vortex and suction-side horseshoe vortex move up from the endwall.

The effects of some key parameters on the size of the unprotected region were studied. Figure 6 shows the effect of the density ratio on boundaries between the regions. At a blowing rate of unity, the unprotected area is smaller with the lower density ratio, but the change is slight. Figures 7 and 8 show the effect of the blowing rate on the three regions. Results for the two density ratios studied are presented. A higher blowing rate might be expected to decrease the size of the unprotected area. However, the upper boundary of region B is not affected by the change of the blowing rate and there is very little effect on the lower boundary of B (upper boundary of region C) as well. Figure 9 shows the effect of the number of rows of injection holes on the regions. Results of the one-row configuration are from [4]. There is little difference between the two sets of results in terms of the size of the regions. Outside region C, the values of the average effectiveness of the two-row configuration are of course higher than those for one-row injection, but the locations of the boundaries are not very different for the different geometries. Thus the boundaries of the regions of different (relative) film cooling performance are primarily determined by the mainstream flow, including secondary flow, and are not strongly influenced by the injected flow itself.

Concave Surface. For M = 1.5 and R = 2.0, iso-

Downloaded 01 Jun 2010 to 171.66.16.57. Redistribution subject to ASME license or copyright; see http://www.asme.org/terms/Terms_Use.cfm

effectiveness lines on the concave surface are shown in Fig. 10. Measurement regions start at $X/D = 1.10$ and end at $X/D = 38.86$. Because streamlines near the concave surface are bent toward the endwall, periodicity between two adjacent measurement regions is not present close to the endwall. The influence of the endwall on local effectiveness can be neglected for $H/D > 30$. Values of the average effectiveness are shown in Figs. 11 and 12; results for two density ratios are presented. Values of the average effectiveness are almost independent of H except very close to the endwall. The presence of the endwall does not greatly affect the performance of the film cooling on the concave surface.

Figure 13 shows a comparison of the average effectiveness between one-row and two-row configurations on the concave surface. Although the blowing rate has a 10 percent difference, a comparison is still acceptable. As expected, effectiveness wtih two-row injection is higher than that with one-row injection. In the region $H/D < 3$, one might expect that the values of the average effectiveness should be higher than those of the two-dimensional flow region for two reasons. The first is that coolant is washed toward the endwall. The other is that the values of average effectiveness on the concave surface generally increase with a higher blowing rate excluding the region close to the injection hole. On Fig. 13, this higher effectiveness is observed for the one-row configuration but not for the two-row configuration. Due to the blockage of the lowest hole of the second row, the region of $H/D < 3$ is not fully covered by two rows of injection holes.

Conclusion

The presence of the endwall has a significant effect on the performance of the film cooling on the convex surface of a blade. A triangular region where the coolant is swept from the convex surface has no film cooling protection at all. Moving away from this unprotected area, the values of the average effectiveness increase linearly from zero to a value close to that in the two-dimensional midspan region. The boundaries of these regions are only slightly changed by varying blowing rate, density ratio, and number of rows of injection hole. On the concave surface, the performance of the film cooling is not significantly altered by the presence of the endwall but the periodicity of the local effectiveness is changed due to skewing of the streamlines toward the endwall.

The film cooling effectiveness is closely related to the mainstream flow field. The incoming flow condition and the geometry of the turbine blade can play important roles in affecting the dimensions of the different regions of effectiveness variation on the convex surface.

Acknowledgments

This study was conducted with support from the U.S. Air Force Office of Scientific Research.

References

1 Peterson, D. R., Eckert, E. R. G., and Goldstein, R. J., "Film Cooling With Large Density Difference Between the Mainstream and the Secondary Fluid Measured by the Heat-Mass Transfer Analogy," ASME *Journal of Heat Transfer*, Vol. 99, 1977, pp. 620-627.

2 Ito, S., Goldstein, R. J., and Eckert, E. R. G., "Film Cooling of a Gas Turbine Blade," ASME *Journal of Engineering for Power*, Vol. 100, 1978, pp. 476-480.

3 Goldstein, R. J., Kornblum, Y., and Eckert, E. R. G., "Film Cooling Effectiveness on a Turbine Blade," *Israel Journal of Technology*, Vol. 20, 1982, pp. 193-200.

4 Goldstein, R. J., and Chen, H. P., "Film Cooling on a Gas Turbine Blade Near the Endwall," ASME *Journal of Engineering for Gas Turbines and Power*, Vol. 107, 1985, pp. 117-122.

5 Langston, L. S., Nice, L. M., and Hopper, R. M., "Three-Dimensional Flow Within a Turbine Cascade Passage," ASME *Journal of Engineering for Power*, Vol. 99, 1977, pp. 21-28.

6 Langston, L. S., "Crossflows in a Turbine Cascade Passage," ASME *Journal of Engineering for Power*, Vol. 102, 1980, pp. 864-874.

7 Gaugler, R. E., and Russell, L. M., "Comparison of Visualized Turbine Endwall Secondary Flows and Measured Heat Transfer Patterns," ASME *Journal of Engineering for Gas Turbines and Power*, Vol. 106, 1984, pp. 168-172.

8 Sieverding, C. H., and Van Den Bosche, P., "The Use of Coloured Smoke to Visualize Secondary Flows in a Turbine-Blade Cascade," *Journal of Fluid Mechanics*, Vol. 134, 1983, pp. 85-89.

9 Sieverding, C. H., "Recent Progress in the Understanding of Basic Aspects of Secondary Flows in Turbine Blade Passages," ASME *Journal of Engineering for Gas Turbines and Power*, Vol. 107, 1985, pp. 248-257.

Downloaded 01 Jun 2010 to 171.66.16.57. Redistribution subject to ASME license or copyright; see http://www.asme.org/terms/Terms_Use.cfm

T. A. Trabold
Research Assistant.

N. T. Obot
Associate Professor.

Fluid Mechanics,
Heat and Mass Transfer Laboratory,
Department of Chemical Engineering,
Clarkson University,
Potsdam, NY 13676

Impingement Heat Transfer Within Arrays of Circular Jets: Part II—Effects of Crossflow in the Presence of Roughness Elements

An experimental investigation was carried out to determine the effects of jet-induced crossflow on impingement heat transfer from rough surfaces. The jets impinged on surfaces having repeated square ribs, with transverse flow of the spent air. Two crossflow schemes were tested: discharge of the spent air through two opposite sides (intermediate crossflow) and through one side (complete or maximum crossflow) of the rectangular impingement surface. The rib height was fixed at 0.813 mm, while the pitch-to-height ratio (p/e) *was varied between 6 and 10. The study covered standoff spacing and jet Reynolds number in the range 2 to 16 jet hole diameters and 1300 to 21,000, respectively. Three nozzle plates, having 48, 90, and 180 square-edged holes, were tested. For the maximum crossflow scheme, the presence of roughness results in small upstream reductions in heat transfer coefficient, with marked improvement in the downstream section; indicating that roughness elements can be used to compensate for the degradation that is usually associated with impingement on smooth surfaces.*

Introduction

This paper is the second part of an extensive research program dealing with impingement heat and mass transfer from complex surface geometries. The investigation, presented in the fist paper on the effects of three different spent air exhaust schemes on impingement heat transfer from smooth surfaces, is extended here to include the influence of surface roughness. The problem is of interest in numerous industrial applications (cooling of turbine and electronic components, and some aspects of drying and evaporation) because many surfaces that must be cooled or heated are by no means smooth.

It is well known that the presence of roughness elements can have profound effects on momentum, heat, and mass transfer characteristics in boundary layer flows. Extensive experimental and semi-empirical studies of transfer rates in roughened boundary layers and in ducts of circular and rectangular cross sections have been carried out over the past four decades, especially in connection with nuclear reactor applications. Although impingement transport phenomena have been studied for nearly as long, a search of the literature failed to reveal a study of effect of surface roughness.

In a study supported by one figure for heat transfer, Sakipov et al. (1975) reported that heat transfer coefficients due to a single jet, discharged parallel to a transversely grooved surface, was significantly higher than for a smooth surface under identical flow conditions. The relative pitch (p/e) and width (w/e) of their grooves were fixed at 4 and 2, respectively, with the height or depth of the grooves at 4 mm. The similarity between their wind tunnel flow configuration and that for duct flows or conventional boundary layers makes it clear that the results are not indicative of those that would prevail for normal or oblique impingement.

It would be expected that the impingement of high velocity jets on a roughened surface would have a marked effect on heat transfer. The direction of such an effect, whether favorable or unfavorable, cannot be predicted easily, due to the complex nature of a multiple jet flow field. Even for impingement on smooth surfaces, it is well known that periodic trends exist for impingement surface static pressure distribution, indicating large variations in surface pressure gradient; this is probably the most reliable quantitative flow field information available to date. Similar variations have been reported for local heat transfer coefficients (Metzger et al., 1979; Saad et al., 1980, to mention but a few), and are primarily the result of the crossflow pattern existing at the impingement surface. With roughness elements the desired effect, at least insofar as the improvement in heat or mass transfer is concerned, is to bring about a significant increase in surface pressure gradient and turbulence for any particular flow situation. To effect such a marked change in surface pressure gradient for multiple jets would require judicious design and arrangement of the roughness elements, as well as the jet holes in a given array.

Contributed by the Gas Turbine Division of THE AMERICAN SOCIETY OF MECHANICAL ENGINEERS and presented at the 32nd International Gas Turbine Conference and Exhibit, Anaheim, California, May 31–June 4, 1987. Manuscript received at ASME Headquarters February 19, 1987. Paper No. 87-GT-200.

Copyright © 1987 by ASME

Downloaded 01 Jun 2010 to 171.66.16.57. Redistribution subject to ASME license or copyright; see http://www.asme.org/terms/Terms_Use.cfm

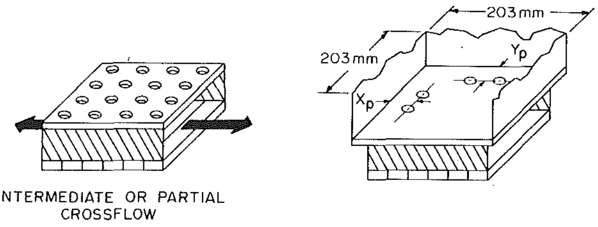

INTERMEDIATE OR PARTIAL CROSSFLOW

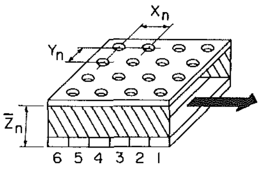

COMPLETE OR MAXIMUM CROSSFLOW

X_n	Y_n	X_p	Y_p	N_x	N_y
10	8	7	4	6	8
10	4	7	4	6	15
5.6	4	1.2	4	12	15

Fig. 1 Definition of flow schemes and geometric variables

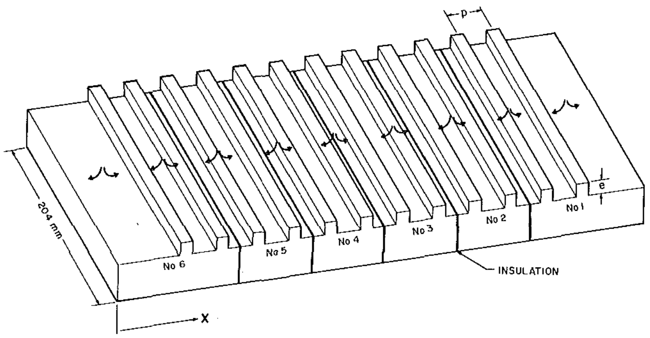

Fig. 2 Layout of rib-roughened surface

Table 1 Dimensions of test plate segments

Configuration	Streamwise Width (w) of Individual Segments of Length 204mm (all dimensions in mm)						
	#1	#2	#3	#4	#5	#6	# ribs per plate
smooth	35.0	35.0	35.0	35.0	35.0	35.0	none
p/e = 6	35.5	32.5	32.5	32.5	32.5	35.5	7
p/e = 8	34.0	31.0	31.0	31.0	31.0	34.0	5
p/e = 10	35.5	31.5	31.5	31.5	31.5	35.5	4

In the present study, the rib-roughened surfaces were the same as those used in a preliminary study (Obot, 1984). The simplified geometry consisting of transverse repeated square ribs was selected partly because of ease of fabrication and low cost, and partly because of the desire to test a well-defined configuration, especially since publications on the subject are unavailable. Instead of the single line of jets, as used in the aforementioned study, three different arrays of in-line jets were tested, the geometric configurations of which are given in Fig. 1. Two flow schemes (referred to as intermediate and complete or maximum crossflow and corresponding to discharge of spent air through two opposite sides and one side of a rectangular impingement surface, respectively) were tested.

Experimental Facility and Test Procedures

Since the test rig and experimental procedures were the same as described in detail elsewhere (Obot and Trabold, 1986), these will be briefly outlined here. Air for the experiments was supplied by a blower, and metered with a calibrated orifice prior to passing it through a 203-mm-square plenum chamber. Air temperature in the plenum chamber was measured using a chromel-constantan thermocouple. A flanged section at the downstream end of the plenum facilitated installation of the nozzle plates. The inlet and exit sections of the inline holes, each 3.17-mm in diameter, were square-edged. The geometric configurations of the three jet plates are given in Fig. 1.

The impingement surface was a 609-mm-square plexiglass plate (32.5 mm thick), the central portion of which contained an assembled heat transfer surface. The latter, a typical layout of which is illustrated in Fig. 2 for the roughened surface, is formed by cementing six aluminum plates of thickness 5.5 mm, with a 2–3 mm width of asbestos insulation between adjacent segments. The dimensions of the individual segments are given in Table 1. It may be noted that, although the six aluminum blocks that formed the smooth plate are identical, this is not the case for the roughened plates, as the two outer segments are always slightly wider than the four inner plates. This was necessitated by the desire to maintain, to the maximum extent possible, uniform rib-to-rib spacing across the entire assembled test plate. This was a very important tradeoff because, although the heat transfer trend with increasing or decreasing area is quite predictable, the effect of maintaining nonuniform pitch-to-height ratio cannot be readily assessed for this complex flow field. The height of the square ribs was fixed at 0.813 mm. The precision machining resulted in a uniform tolerance of ±0.05 mm. Provision was made to facilitate boxing in of two or three sides of the rectangular test plate. Details of this feature are provided in the aforementioned paper.

The average surface temperature of each segment was determined from the readings of six chromel-alumel thermocouples, installed in holes drilled from the back surface of the plates to within 1 mm of the surface. Since the beads at the

Nomenclature

A = heat transfer area, m^2
A_f = open area = $\pi d^2 (4x_n y_n)^{-1}$
A_n = total jet flow area, m^2
d = jet hole diameter, m
e = rib height, m
h = individual plate heat transfer coefficient, W/m^2°C
k_f = thermal conductivity based on film temperature, W/m°C
L = width of heat transfer surface in x direction, m
l = spanwise length of a test segment, m
$\dot{m}$ = air mass flow rate, kg/s
Nu = individual plate Nusselt number = hd/k_f
Nu_r = roughened plate mean Nusselt number
Nu_s = smooth plate mean Nusselt number
N_x = number of rows in the x direction
N_y = number of rows in the y direction
p = rib pitch, m
Q_c = convective heat transfer, W
Re = Reynolds number = $\dot{m}d/A_n\mu$
T_R = reference temperature, °C
T_s = average temperature of heated surface, °C
w = streamwise width of a test plate segment, m
X = location in the x direction along heat transfer surface measured from upstream end of plate #6, m
x_n = jet hole spacing in the x direction, m
X_n = nondimensional jet hole spacing = x_n/d
y_n = spanwise jet hole spacing (y direction), m
Y_n = nondimensional jet hole spacing = y_n/d
z_n = jet-to-surface spacing, m
Z_n = nondimensional jet-to-surface spacing = z_n/d
μ = fluid viscosity, Pa•s

Downloaded 01 Jun 2010 to 171.66.16.57. Redistribution subject to ASME license or copyright; see http://www.asme.org/terms/Terms_Use.cfm

thermocouple measuring junction with the 30-gage wires were comparable to the size of the square ribs, none of the couples was located directly beneath the ribs.

Each plate segment was individually heated with nichrome heaters, and separately powered with a d-c power unit. The electrical power input to each unit was computed from the current and the voltage, the latter being measured directly across each segment. Expressed as the Nusselt number, segmental results were computed using the relation

$$\mathrm{Nu} = (Q_c d)/(k_f A)(T_s - T_R) \tag{1}$$

where the convective contribution Q_c is the difference between the total power input to a segment and the losses. A layer of Kaowool insulation, 25.4 mm thick, was taped to the back surface of the segments with the objective of minimizing conduction losses.

The heat losses, determined experimentally in the absence of flow, correspond to the electrical power required to maintain the segments at the same average surface temperature as in tests with flow. As discussed in an earlier paper (Obot and Trabold, 1986), the validity of this method was verified experimentally for the maximum crossflow scheme, by comparing the Q_c values so determined with those computed using the air mass flowrate, the nearly constant specific heat, and the temperature difference of the exiting air. Since complete details are provided in the aforementioned paper, these will not be repeated here. Suffice it to state that the differences between the two sets of data did not exceed 10 percent. The reference temperature T_R in equation (1) was the average adiabatic wall temperature, taken at least one and a half hours after the establishment of the air flowrate for a run. The appropriate flat area A (i.e., exclusive of the rib surface area) was used for computation of the results shown subsequently. This is of course consistent with current practice (see, for example, Han, 1984; Han et al., 1978). It should be mentioned that all data were also reduced using the total heat transfer area (including the rib surface area) and this resulted in Nu values that were generally lower than the corresponding smooth surface data.

For the smooth or rough surface, the adiabatic wall temperatures were generally highest for the plate segment located farthest from the exhaust, decreasing slightly to its lowest value at the last downstream segment. The variations about the mean surface temperatures for the entire plate were within 1°C. Also, the differences between the mean plenum and adiabatic wall temperature were within 1°C, the latter being consistently the lower set. This resulted in mean heat transfer coefficients (averaged over the entire plate) that are essentially the same with the adiabatic wall or plenum temperature as the reference. This has been documented graphically (Obot and Trabold, 1986) for the smooth plate. The only exception to the consistent trend noted above for the nominal temperature difference between the plenum and the impingement surface occurred for $\mathrm{Re} \geq 15{,}000$, $2 \leq \bar{Z}_n \leq 16$, and $A_f = 0.0098$. For these conditions, the mean plenum temperatures were 2-4°C higher than the steady-state smooth or rough surface temperatures, the magnitudes of the segmental variations and the trend being essentially the same as noted above. In the present study, the mean temperature difference $(T_s - T_R)$ was held close to 15°C for most of the trials.

There are several general comments, and these deal with the selection and fabrication of the roughened surfaces. First, although the present design has a simplified geometry, the lack of systematic studies of impingement heat transfer from roughened surfaces did not justify the design and expensive fabrication of devices such as dimples, pedestals, or other three-dimensional geometries. Second, for large height of roughness, the inherent phenomenon of flow channeling from the central portion of the impingement surface toward the sidewalls of the enclosure precludes use of such a design. On the basis of this observation, which was the outcome of our exploratory studies, it would seem then that, for large height of roughness, the elements would be broken to provide flow paths around them. Although the present design is not as exotic as one would wish, due to the points noted above, it nonetheless should provide very useful insight on the gross effects of roughness on heat transfer, many of which could well be expected for other roughness geometries.

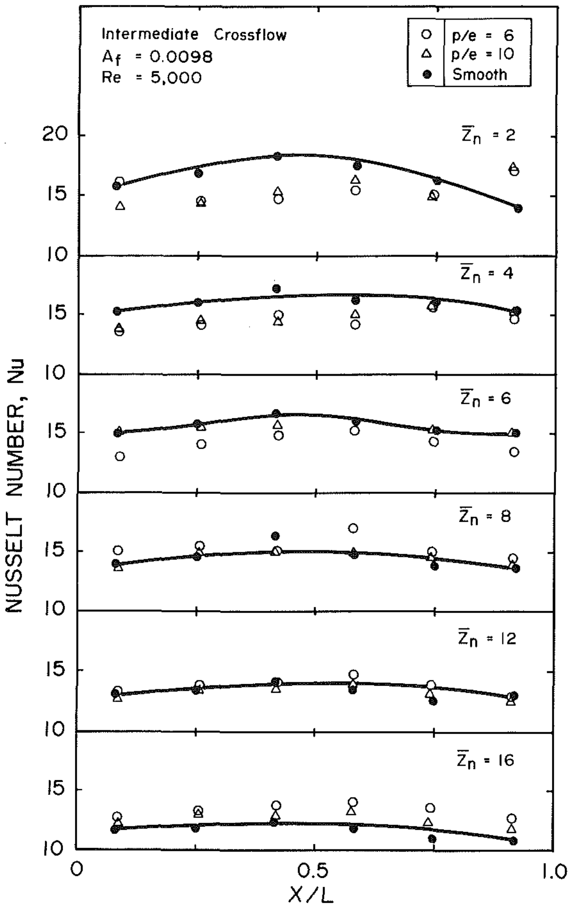

Fig. 3 Mean Nusselt number profiles with intermediate crossflow for A_f = 0.0098

For the design of the roughened test plates, there are two possibilities. One would involve maintaining the same number of ribs on each segment for all *p/e*. Aside from the fact that this would result in significant differences in the governing dimensions of the segments, the results obtained with such an arrangement might be of limited usefulness. The alternative approach, one that was adopted here, was to maintain about the same dimensions for all segments, within the constraints already discussed in this section. This is the situation in many practical applications where the real advantage to using roughness elements is to increase the heat transfer area of a body of fixed dimensions.

Results and Discussion

This presentation and discussion of results, devoted exclusively to examination of the effects of the various variables on segmental heat transfer trends instead of results averaged over the entire surface, is divided into two main sections. Typical results obtained with intermediate crossflow are presented first (Figs. 3-5) and briefly discussed, followed by a more detailed discussion of the results with complete or maximum crossflow (Figs. 6-12). In each figure, the abscissa is the

Downloaded 01 Jun 2010 to 171.66.16.57. Redistribution subject to ASME license or copyright; see http://www.asme.org/terms/Terms_Use.cfm

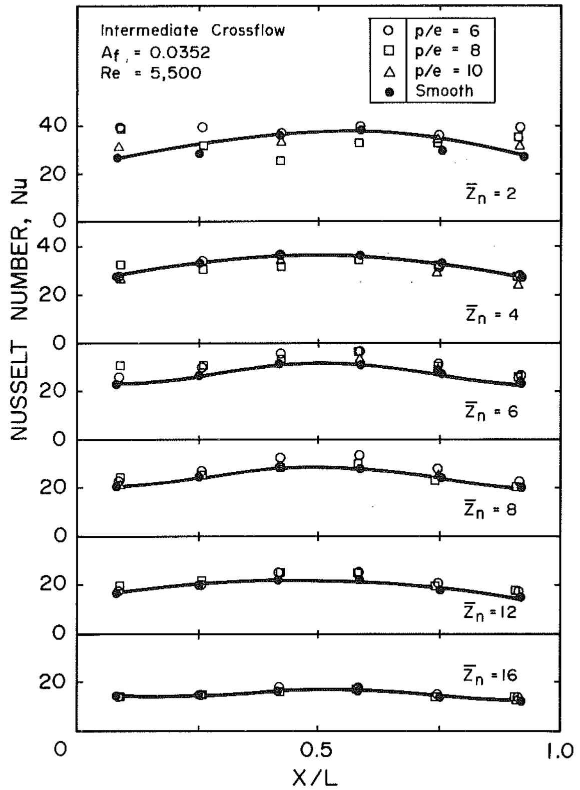

Fig. 4 Mean Nusselt number profiles with intermediate crossflow for A_f = 0.0352

nondimensional distance, X/L, where X is the distance measured from the upstream surface of the sixth segment (Figs. 1 and 2) while L is the width of the assembled plate, exclusive of the small allowances taken up by the asbestos insulation. Since an assembled plate consists of six segments, each distribution curve is characterized by six data points, the locations of which correspond closely to the center plane of the plates.

A comment prior to discussion of the results concerns the small differences in the flat area (exclusive of the rib area) between the smooth and roughened plates. We have already remarked that this was inevitable. These differences do not have any significant effect on the interpretation of the trends to be discussed. Where deviations between the smooth and roughened surface data are observed to occur, it will be noted that their magnitudes are much larger than those associated with variations in the flat area, and must therefore be due to the presence of the roughness elements.

Mean Nusselt Numbers With Intermediate Crossflow. The Nu profiles with increasing jet-to-surface spacing ($\bar{Z}_n$) are illustrated in Figs. 3 and 4 for A_f = 0.0098 and 0.0352, respectively, while a typical effect of maintaining a fixed flow rate and varying the open area is shown in Fig. 5 for the narrowest spacing of two jet hole diameters. It is pertinent to note that the larger the open area, the greater the number of jets over a given target area. All three figures indicate a common trend, that is, the presence of roughness elements can cause reductions in local mean heat transfer coefficient, notably for relatively small spacings at which the spent air is merely skimming over the repeated ribs. It will also be observed that, at these narrow spacings, each roughened plate profile, with its lowest value in the central portion, rises with increasing distance toward the exhaust openings to approach or surpass that for the smooth surface. This can be seen more clearly in Fig. 5.

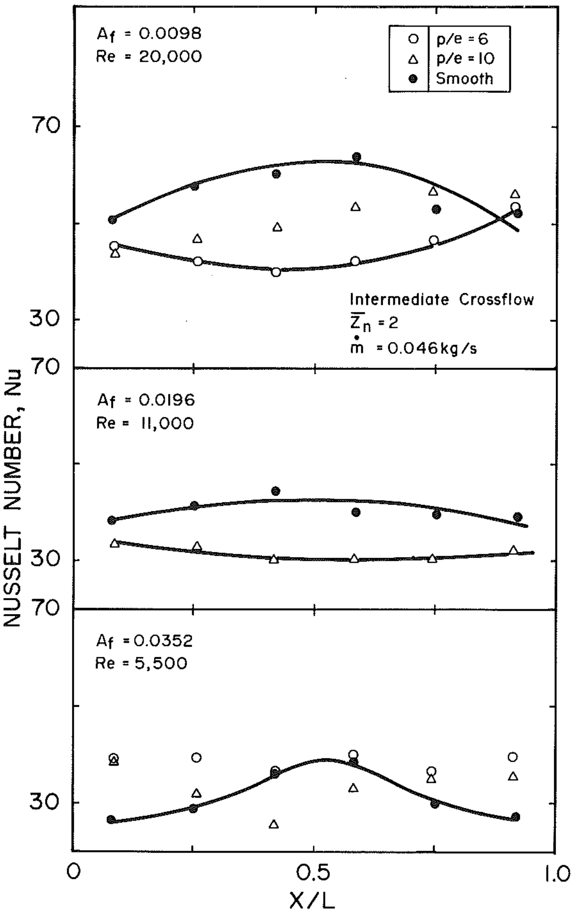

Fig. 5 Effect of open area on intermediate crossflow mean Nusselt number at $\bar{Z}_n$ = 2

For a given flowrate, since jet-induced crossflow interference becomes more pronounced with increasing open area, as well as with increasing distance from the central portion toward each exhaust opening, the A_f = 0.0352 results of Fig. 5 provide the first indication that a combination of surface roughness and crossflow might result in substantial improvement in heat transfer. In this regard it is especially noticeable that, although there are no significant differences between the three sets of data over the central portion, which is characterized by minimum crossflow, the results obtained with the roughness are consistently higher than those with the smooth surface at the downstream segments. This role of crossflow in the presence of roughness will become quite evident from the following presentation of the results for the maximum scheme.

Mean Nusselt Numbers With Maximum Crossflow. The most interesting Nu trends were obtained with complete or maximum crossflow, and some of these are shown graphically in Figs. 6–12. The common basis between Figs. 6 and 7 is that of same mass flowrate, this being also the case for Figs. 8 and 9. Comparison between each pair of figures provides information on the effect of having greater number of jets over a given target area. To provide the reader with estimates of the magnitudes of the degradation and/or enhancement in heat transfer, an alternative representation of some of the results on Figs. 6–9 is given in Fig. 10, where the roughened surface mean Nusselt numbers have been scaled with the corresponding smooth plate data. Typical trends obtained with increasing Re are presented in Fig. 11, the format of presentation being the same as in Fig. 10, while a similar effect of Re is

Downloaded 01 Jun 2010 to 171.66.16.57. Redistribution subject to ASME license or copyright; see http://www.asme.org/terms/Terms_Use.cfm

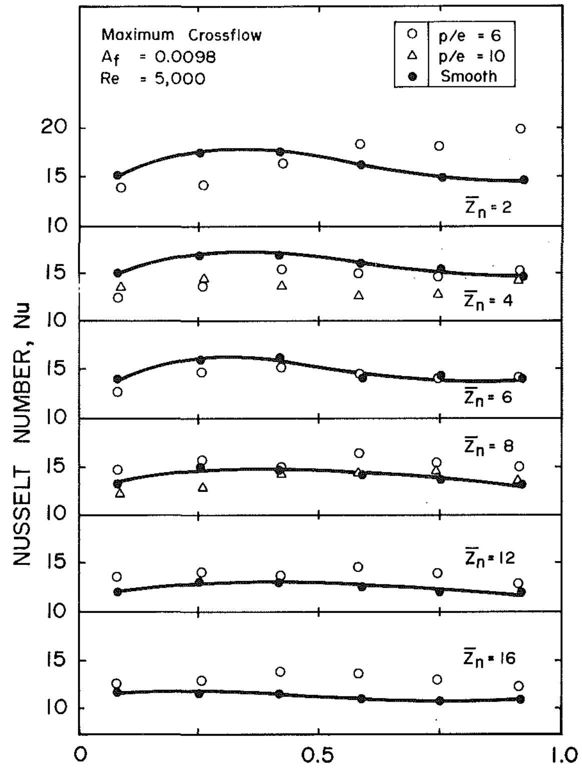

Fig. 6 Mean Nusselt number profiles with maximum crossflow for A_f = 0.0098 and Re = 5000

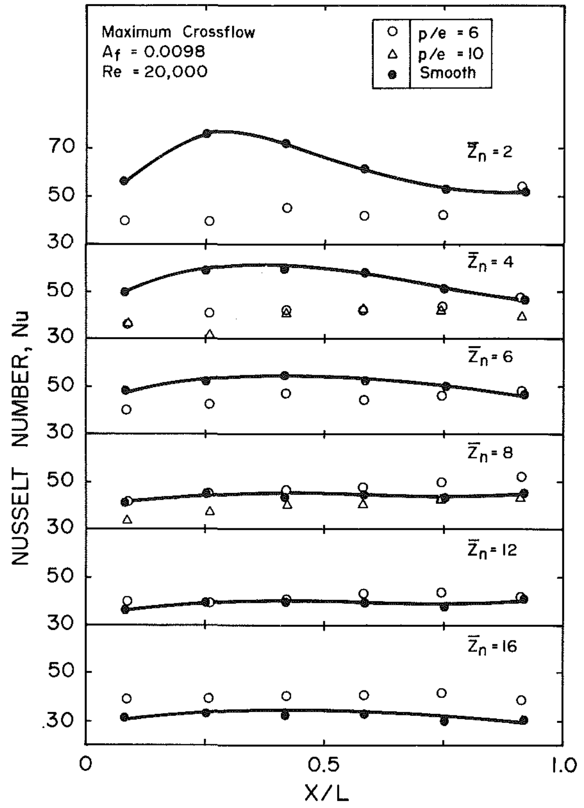

Fig. 8 Mean Nusselt number profiles with maximum crossflow for A_f = 0.0098 and Re = 20,000

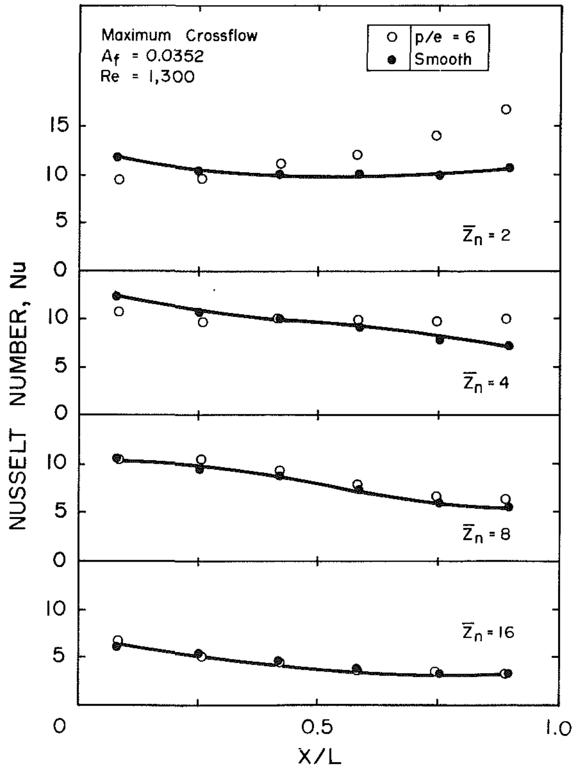

Fig. 7 Mean Nusselt number profiles with maximum crossflow for A_f = 0.0352 and Re = 1300

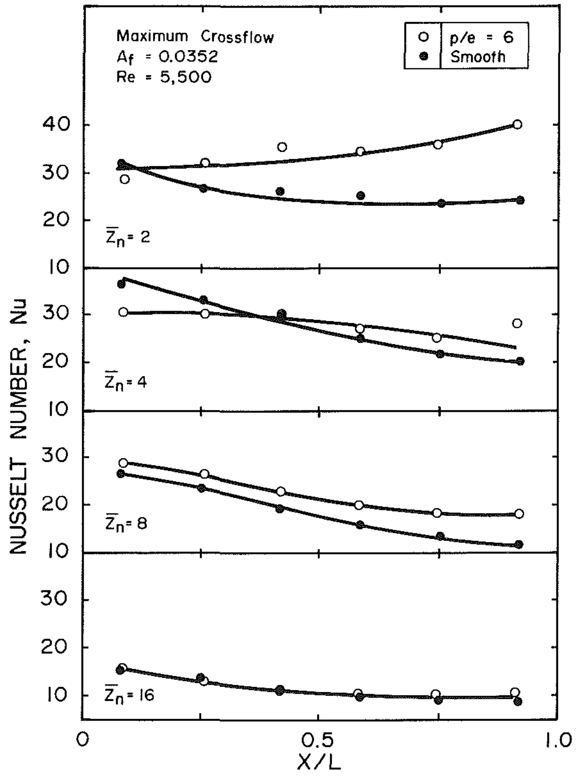

Fig. 9 Mean Nusselt number profiles with maximum crossflow for A_f = 0.0352 and Re = 5500

shown in Fig. 12. For the purpose of comparison, the smooth surface data for the highest Re are also included in Fig. 12.

We begin the discussion by considering the effect of standoff spacing $\bar{Z}_n$, the results for which are given in Figs. 6-11. At moderate spacings in the range of $\bar{Z}_n$ between 2 and 8 and for Re < 15,000, the general trend is one of small upstream degradation, followed by a marked downstream improvement, the absolute effect being somewhat dependent on

Downloaded 01 Jun 2010 to 171.66.16.57. Redistribution subject to ASME license or copyright; see http://www.asme.org/terms/Terms_Use.cfm

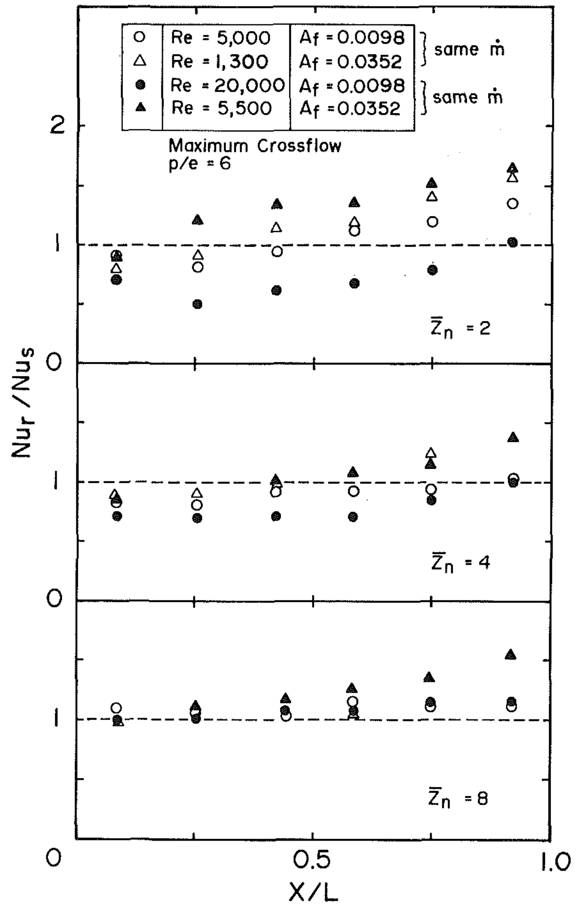

Fig. 10 Ratio of rough to smooth surface Nusselt number

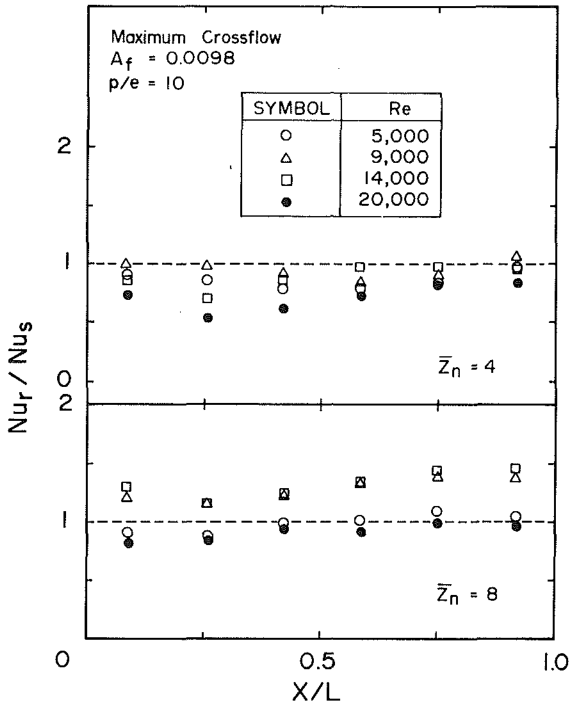

Fig. 11 Effect of Reynolds number on Nusselt number ratios for p/e = 10 and A_f = 0.0098

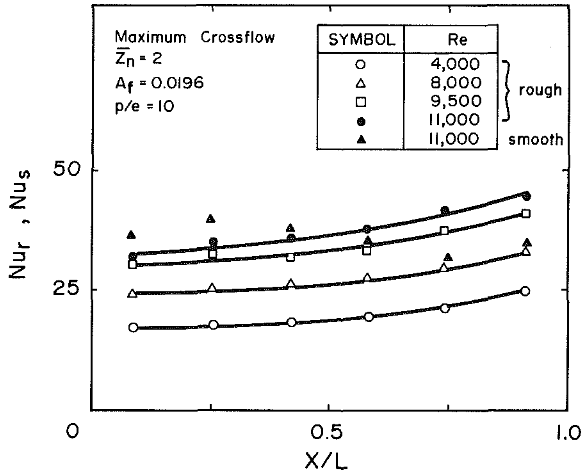

Fig. 12 Variations of Nusselt number with Reynolds number for p/e = 10 and $\bar{Z}_n$ = 2

open area and standoff spacing. It must not be inferred, however, that this is a unique feature of the present design, for obviously the influence of roughness on impingement heat transfer must depend on the cumulative effect of crossflow. Thus, since the upstream section experiences minimal crossflow interference, in sharp contrast with the prevailing situations downstream, it would be expected that, for any particular configuration of roughness and open area, the improvement in heat transfer would become more pronounced as one moves downstream toward the exhaust opening. This is verified by the present results. With increasing spacing from $\bar{Z}_n$ = 2, the roughened data can be significantly lower than those obtained with the smooth surface, depending of course on the open area and Re. However, for $\bar{Z}_n \geq 8$, all results indicate varying degrees of improvement over the smooth impingement surface.

Typical effects of open area, evident from a study of Figs. 6-9, have been consolidated into Fig. 10. It is important to note that the flowrates for Re = 5000 and 20,000 with A_f = 0.0098 correspond, respectively, to those for Re = 1300 and 5500 with A_f = 0.0352. Consistent with the lack of strong crossflow interference for the segment located farthest from the exhaust opening, it will be observed that the calculated ratios are roughly about the same, almost independent of Re or A_f. On the basis of these results and considering that for impingement on smooth surface the finding was that, the larger the open area, the more pronounced the downstream degradation in heat transfer (Obot and Trabold, 1986), it would seem that impingement on rough surfaces would be most effective with closely spaced jets in an array, especially when working with relatively short jet-to-surface spacings.

Figures 11 and 12 show the effects of Reynolds number on heat transfer coefficient. The results in both figures complement those already given in Fig. 10 for two Reynolds numbers and two values of A_f. The steady upward shift in the distribution curves with a progressive increase in Re is clearly illustrated in Fig. 12. The same general trend can also be established from comparisons of the results which are presented in Figs. 6 and 8 or Figs. 7 and 9. Although the roughened plate data can be substantially lower than those obtained with the smooth surfaces (Figs. 10 and 11), the trends displayed here on Fig. 12 were obtained at all spacings with any particular nozzle plate.

A closer examination of the maximum crossflow results reveals two distinct trends with increasing Reynolds number, the magnitudes of which do vary with $\bar{Z}_n$. At moderate Re and for open area both small and large, significant downstream enhancement in heat transfer is the dominant feature at $\bar{Z}_n$ = 2, with some degradation as $\bar{Z}_n$ is steadily increased up to $\bar{Z}_n$

Downloaded 01 Jun 2010 to 171.66.16.57. Redistribution subject to ASME license or copyright; see http://www.asme.org/terms/Terms_Use.cfm

= 6, followed by a general improvement for $\bar{Z}_n \geq 8$. At high Re and for spacings between $\bar{Z}_n = 2$ and 8, it appears that there is no intimate contact between the developing high velocity flow and the heat transfer surface. This skimming of the flow over the ribbed surface clearly results in poor heat transfer performance. For large flowrates, these undesirable heat transfer trends can be improved by using greater number of jets over the target, and the magnitudes of such improvements are strikingly illustrated in Fig. 10.

There is an additional comment on the effect of Reynolds number, and this deals with the trends which are shown on Fig. 11, in particular that for $\bar{Z}_n = 8$. In this regard it should be noted that the ratios which are plotted here for the lowest and highest Re were computed from the results already presented in Figs. 6 and 8, those for the two intermediate Re values being included to provide a more complete trend with increasing Re. It may be noted that, whereas the trends for the highest and lowest Re are the same, the data for the two intermediate Re are similar to each other. This is clearly not the result of experimental error, but a reflection of the fact that, for any particular open area and depending of course on the standoff spacing, the absolute magnitudes of the effect of roughness increase initially with Re but drop off at high Re, in line with the trends that have been reported for duct flows (Berger and Hau, 1979). For $A_f = 0.0352$, although results are presented in this paper for two Re due to the limitation of the air supply system, the above trend can be established from comparison between Fig. 7 and Fig. 9.

The general trends that have been documented in this paper can be explained in terms of the pressure gradient for several reasons. First, the static pressure, and hence the pressure gradient, is impressed on the impingement surface by both the axial velocity of the oncoming jet and the radial velocity of the developing wall flow. Second, the absolute effect of roughness depends, to a marked extent, on the nature of the pressure gradient, being most pronounced in the region of a flow field with a favorable gradient (Schlichting, 1968). For impingement on smooth surfaces, mean surface pressure distributions were reported by Florschuetz et al. (1982) and Kercher and Tabakoff (1970), the results in the latter paper being of particular importance in that they establish the trend with increasing Re.

For the region farthest from the exhaust (i.e., $X/L < 0.25$), the prevailing pressure gradient (whether positive or negative depending on the test conditions) is vanishingly small, and the addition of roughness produces marginal effect on heat transfer. For $X/L \geq 0.25$, a favorable gradient exists such that its magnitude increases with distance toward the exhaust. As might be expected, the presence of roughness results in heat transfer trends that are comparable to those for pressure gradient. The claim in the preceding paragraph that the improvement in heat transfer increases initially with Re, as well as the degradation at relatively large Re, can be inferred also from the effect of Re on mean pressure distribution (Kercher and Tabakoff, 1970).

In the present study, three values of p/e, i.e., 6, 8, and 10, were tested. No significant effect of this variable, similar to those reported for duct flows, was observed from our data. The conjecture is that this rather surprising finding might be due to the use of small ribs which result in local inter-rib flow pattern that is essentially independent of the number of ribs on a given target surface. Obviously, when the governing dimensions of the roughness elements are comparable to the jet hole diameter, the local flow conditions along the impingement surface will exhibit some dependence on p/e which, in turn, will result in variations of heat transfer coefficient with p/e. Also, for such large roughness elements, the manner of impingement, that is, whether the jets impinge directly on the elements or between them, cannot be totally ignored in assessment of the role of roughness on heat transfer. However, as has been noted, a major drawback to using large ribs of similar design is that of nonuniform distribution of spent air due to flow channeling, and this can be minimized by using broken elements.

As we have noted in the introductory section, there has been no investigation of impingement heat transfer from roughened surfaces; hence there are no data or similar observations to which ours can be compared. However, for a given height of roughness, the trend established here with increasing Re is qualitatively in agreement with the numerous results for duct flows.

Finally, a brief discussion of the relevance of the results to impingement cooling of gas turbine airfoils is appropriate. For cooling of the midchord region with a trailing edge discharge of spent air, which results in a flow scheme similar to the maximum case considered here, typical standoff spacings of interest are between one and five jet hole diameters. We have already noted earlier that, for impingement on smooth surfaces, this jet-induced crossflow results in substantial reduction in heat transfer rates in the downstream section, and that the magnitudes of the degradation become more pronounced with increasing open area and jet-to-surface spacing. However, with roughness elements and for a given mass flow rate and $1 < \bar{Z}_n < 5$, the fact that the higher the open area, the greater the improvement in heat transfer, combined with the marked enhancement near the exit of the channel, should make a combination of roughness and crossflow an attractive feature of future design. The speculation here is that there are, at least, two options that are worth considering: a smooth midchord section followed by a roughened trailing edge section, as well as a combination of impingement, roughness over both the midchord and trailing edge sections, together with a superimposed cross-flowing stream. For this particular application, as well as others involving impingement on rough surfaces, it can be readily appreciated that, because of the complex nature of the multiple jet flow field, the general recourse will be to establish the best design configuration through extensive experiments.

Concluding Remarks

An experimental investigation was carried out with the objective of determining the effects of jet-induced crossflow on impingement heat transfer from rough surfaces. The two crossflow schemes referred to as intermediate and complete (or maximum) correspond, respectively, to discharge of the spent air through two opposite sides and through one side of a rectangular impingement surface. A parametric study was made which included the effects of open area, jet-to-plate spacing, Reynolds number, and pitch-to-height ratio.

At narrow spacings and for small open area, the roughened plate heat transfer coefficients with intermediate crossflow are generally lower than the corresponding smooth surface results. With an open area of 3.5 percent and moderate Re, some improvement in heat transfer was observed to occur, but only for the immediate vicinity of the two exhaust openings.

With complete or maximum crossflow the most significant observations are as follows: small degradation in heat transfer for the upstream section which is characterized by minimum jet-induced crossflow, with substantial improvement in the downstream section. There are indications that, in the presence of roughness, the most effective design would be one that incorporates a crossflowing stream. For a given flowrate, the absolute effect of roughness on heat transfer depends on the open area and jet-to-surface spacing, both of which do determine the intensity of the prevailing crossflow at the impingement surface.

Downloaded 01 Jun 2010 to 171.66.16.57. Redistribution subject to ASME license or copyright; see http://www.asme.org/terms/Terms_Use.cfm

Acknowledgments

This work was supported by the Chemical Research and Development Center of the U.S. Army under Contract No. DAAK11-85-C-0001. Technical liaison for this project was provided by Paul Grasso, Operational Sciences Section, Physics Branch, CRDC, Aberdeen, MD.

References

Berger, F. P., and Hau, K.-F., 1979, "Local Mass/Heat Transfer Distribution on Surfaces Roughened with Small Square Ribs," *International Journal of Heat and Mass Transfer*, Vol. 22, pp. 1645-1656.

Florschuetz, L. W., Metzger, D. E., Su, C. C., Isoda, Y., and Tseng, H. H., 1982, "Jet Array Impingement Flow Distributions and Heat Transfer Characteristics: Effects of Initial Crossflow and Nonuniform Array Geometry," NASA Contractor Report 3630.

Han, J. C., Glicksman, L. R., and Rohsenow, W. M., 1978, "An Investigation of Heat Transfer and Friction for Rib-Roughened Surfaces," *International Journal of Heat and Mass Transfer*, Vol. 21, pp. 1143-1156.

Han, J. C., 1984, "Heat Transfer and Friction in Channels With Two Opposite Rib-Roughened Walls," ASME *Journal of Heat Transfer*, Vol. 106, pp. 774-781.

Kercher, D. M., and Tabakoff, W., 1970, "Heat Transfer by a Square Array of Round Air Jets Impinging Perpendicular to a Flat Surface Including the Effect of Spent Air," ASME *Journal of Engineering for Power*, Vol. 92, pp. 73-82.

Metzger, D. E., Florschuetz, L. W., Takeuchi, D. I., Behee, R. D., and Berry, R. A., 1979, "Heat Transfer Characteristics for Inline and Staggered Arrays of Circular Jets with Crossflow of Spent Air," ASME *Journal of Heat Transfer*, Vol. 101, pp. 526-531.

Obot, N. T., 1984, "Experimental Evaluation of Factors Affecting Impingement Evaporation," U.S. Army Chemical Research and Development Center, Contractor Report CRDC-CR-84111, Aberdeen, MD.

Obot, N. T., and Trabold, T. A., 1986, "Impingement Heat Transfer Within Arrays of Circular Jets. Part I: Effects of Minimum, Intermediate and Complete Crossflow for Small and Large Spacings," ASME *Journal of Heat Transfer*, in press.

Saad, N. R., Mujumdar, A. S., Abdel Messeh, W., and Douglas, W. J. M., 1980, "Local Heat Transfer Characteristics for Staggered Arrays of Circular Jets with Crossflow of Spent Air," ASME Paper No. 80-HT-23.

Sakipov, Z. B., Kozhakhmetov, D. B., and Zubareva, L. I., 1975, "Analysis of Turbulent Jets Flowing Over Smooth and Rough Flat Surfaces," *Heat Transfer–Soviet Research*, Vol. 7, pp. 125-133.

Schlichting, H., 1968, *Boundary Layer Theory*, 6th ed., McGraw-Hill, New York, pp. 467-516.

Downloaded 01 Jun 2010 to 171.66.16.57. Redistribution subject to ASME license or copyright; see http://www.asme.org/terms/Terms_Use.cfm